

BIOMIMETICS, LEARNING FROM NATURE

BIOMIMETICS, LEARNING FROM NATURE

Edited by
AMITAVA MUKHERJEE

In-Tech
intechweb.org

Published by In-Teh

In-Teh

Olajnica 19/2, 32000 Vukovar, Croatia

Abstracting and non-profit use of the material is permitted with credit to the source. Statements and opinions expressed in the chapters are those of the individual contributors and not necessarily those of the editors or publisher. No responsibility is accepted for the accuracy of information contained in the published articles. Publisher assumes no responsibility liability for any damage or injury to persons or property arising out of the use of any materials, instructions, methods or ideas contained inside. After this work has been published by the In-Teh, authors have the right to republish it, in whole or part, in any publication of which they are an author or editor, and the make other personal use of the work.

© 2010 In-teh

www.intechweb.org

Additional copies can be obtained from:

publication@intechweb.org

First published March 2010

Printed in India

Technical Editor: Goran Bajac

Cover designed by Dino Smrekar

Biomimetics, Learning from Nature,

Edited by Amitava Mukherjee

p. cm.

ISBN 978-953-307-025-4

Preface

Humans have always been fascinated by nature and have constantly made efforts to mimic it. Rapid advancements in science and technology have now made him to act beyond rather than just mimicking nature. He has now begun to understand and implement nature's principles like never before. By adapting mechanisms and capabilities from nature, scientific approaches have helped him to understand the related phenomena in order to engineer novel devices and design techniques to improve their capability. This field is now called as biomimetics or bio-inspired technology. The term biomimetics is derived from bios meaning life and mimesis meaning to imitate. While some of nature's designs can be copied, there are many ideas that are best adapted if they are to serve as an inspiration using man made capabilities. There are many characteristics that can uniquely identify a biomimetic mechanism and a major characteristic is to function autonomously in a complex environment, being adaptable to unpredictable changes and to perform multifunctional tasks.

Some of the major benefits of biomimetics include the development of dust free materials taking inspiration from the lotus effect, photovoltaic cells that have been developed by studying the photosynthesis mechanism of bacteria, airplanes constructed mimicking the dragonfly and hummingbird to name a few.

This book is a compilation of knowledge of several authors who have contributed in various aspects of bio inspired technology. It tends to bring together the most recent advances and applications in the field of biomimetics. The book is divided into twenty five chapters.

The first part of the book is entirely devoted to science and technology of biomimetic nanoparticle synthesis and identifying the various mechanisms adapted by nature. Chapters are devoted for the various strategies and applications of nanoparticles synthesized using living organisms, mimicking the various features of physiological membranes, studying the various features of photosynthetic energy conversion, neurobiology inspired design for control and learning, biomimetic oxidation catalyzed by metalloporphyrins and determining the role of carbonic anhydrase in the biomimetic zinc catalyzed activation of cumulenes.

The second part of the book deals with the various aspects of fabrication of materials drawing inspiration from nature. It discusses the assembly of organic/ inorganic nanocomposites based on nacre, hydroxyapatite microcapsules, apatite nuclei and apatite related biomaterials.

The final part of the book lists the various applications of bio-inspired technology. It discusses in detail the development of biomimetic preparation of anti tumour therapeutics, super hydrophobic surfaces based on lotus effect, micro robots with fabricated functional surfaces, electrochemical sensors based on biomimetics, use of biomimetics in dental applications,

tissue engineering, materials with improved optical properties, in drug and vaccine delivery and the development of space and earth drills drawing inspiration from the wood wasp.

The editor would like to thank the authors for their valuable contributions and to all those who were directly or indirectly involved in bringing out this work. Last but not the least; we are indebted to Vedran Kordic who was responsible for coordinating this project. We hope that readers would greatly benefit from this book by keeping abreast the research and latest advances in this field.

Amitava Mukherjee

Contents

Preface	V
1. Biomimetic Synthesis of Nanoparticles: Science, Technology & Applicability Prathna T.C., Lazar Mathew, N. Chandrasekaran, Ashok M. Raichur and Amitava Mukherjee	001
2. Immobilized redox proteins: mimicking basic features of physiological membranes and interfaces Daniel H. Murgida, Peter Hildebrandt and Smilja Todorovic	021
3. Photosynthetic energy conversion: hydrogen photoproduction by natural and biomimetic systems Suleyman I. Allakhverdiev, Vladimir D. Kreslavski, Velmurugan Thavasi, Sergei K. Zharmukhamedov, Vyacheslav V. Klimov, Seeram Ramakrishna, Hiroshi Nishihara, Mamoru Mimuro, Robert Carpentiere and Toshi Nagata	049
4. Neurobiologically inspired distributed and hierarchical system for control and learning Sungho Jo and Kazutaka Takahashi	077
5. Function-Based Biology Inspired Concept Generation J.K. Stroble Nagel, R.B. Stone and D.A. McAdams	093
6. Biomimetic chemistry: radical reactions in vesicle suspensions Chryssostomos Chatgililoglu and Carla Ferreri	117
7. Biomimetic homogeneous oxidation catalyzed by metalloporphyrins with green oxidants Hong-Bing Ji and Xian-Tai Zhou	137
8. The Carbonic Anhydrase as a Paragon: Theoretical and Experimental Investigation of Biomimetic Zinc-catalyzed Activation of Cumulenes Burkhard O. Jahn, Wilhelm A. Eger and Ernst Anders	167
9. Biomimetic Lessons Learnt from Nacre Kalpana S. Katti, Dinesh R. Katti and Bedabibhas Mohanty	193
10. Rapid Assembly Processes of Ordered Inorganic/organic Nanocomposites Chang-An Wang, Huirong Le and Yong Huang	217

11. A Biomimetic Nano-Scale Aggregation Route for the Formation of Submicron-Size Colloidal Calcite Particles Ivan Sondi, and Srečo D. Škapin	241
12. A Biomimetic Study of Discontinuous-Constraint Metamorphic Mechanism for Gecko-Like Robot ZhenDong Dai and HongKai Li	257
13. Biomimetic Fabrication of Hydroxyapatite Microcapsules by using Apatite Nuclei Takeshi Yao and Takeshi Yabutsuka	273
14. Biomimetic fabrication of apatite related biomaterials Mohammad Hafiz Uddin, Takuya Matsumoto, Masayuki Okazaki, Atsushi Nakahira and Taiji Sohmura	289
15. Podophyllotoxin and antitumor synthetic aryltetralines. Toward a biomimetic preparation Maurizio Bruschi, Marco Orlandi, Michol Rindone, Bruno Rindone, Francesco Saliu, Ricardo Suarez-Bertoa, Eva Liisa Tollpa and Luca Zoia	305
16. Superhydrophobicity, Learn from the Lotus Leaf Mengnan Qu, Jinmei He and Junyan Zhang	325
17. Micro Swimming Robots Based on Small Aquatic Creatures Seichi Sudo	343
18. Bio-Inspired Water Strider Robots with Microfabricated Functional Surfaces Kenji Suzuki	363
19. Electrochemical sensor based on biomimetic recognition utilizing molecularly imprinted polymer receptor Yusuke Fuchiwaki and Izumi Kubo	385
20. Dental tissue engineering: a new approach to dental tissue reconstruction Elisa Battistella, Silvia Mele and Lia Rimondini	399
21. Biomimetic Porous Titanium Scaffolds for Orthopedic and Dental Applications Alireza Nouri, Peter D. Hodgson and Cui'e Wen	415
22. Improved Properties of Optical Surfaces by Following the Example of the "Moth Eye" Theobald Lohmueller, Robert Brunner and Joachim P. Spatz	451
23. Wood wasp inspired planetary and Earth drill Thibault Gouache, Yang Gao, Yves Gourinat and Pierre Coste	467
24. Biomimetic Architectures for Tissue Engineering Jianming Li, Sean Connell and Riyi Shi	487
25. Lipid-based Biomimetics in Drug and Vaccine Delivery Ana Maria Carmona-Ribeiro	507

Biomimetic Synthesis of Nanoparticles: Science, Technology & Applicability

Prathna T.C. *, Lazar Mathew*, N. Chandrasekaran*,
Ashok M. Raichur# and Amitava Mukherjee*

**School of Bio Sciences & Technology, VIT University*

*#Department of Materials Engg., Indian Institute of Science
India*

1. Introduction

Nanotechnology emerges from the physical, chemical, biological and engineering sciences where novel techniques are being developed to probe and manipulate single atoms and molecules. In nanotechnology, a nanoparticle (10^{-9}m) is defined as a small object that behaves as a whole unit in terms of its transport and properties. The science and engineering of nanosystems is one of the most challenging and fastest growing sectors of nanotechnology.

This review attempts to explain the diversity of the field, starting with the history of nanotechnology, the physics of the nanoparticle, various strategies of synthesis, the various advantages and disadvantages of different methods, the possible mechanistic aspects of nanoparticle formation and finally ends with the possible applications and future perspectives. Though there are a few good reviews dealing with the synthesis and applications of nanoparticles, there appears to be scanty information regarding the possible mechanistic aspects of nanoparticle formation. This review attempts to fill the void.

The review is organized into five sections. In section 2, we discuss about the early history of nanotechnology and the significant contributions made by eminent scientists in this field. In the next section we describe about the unique properties of nanoparticles, their classification and significance of inorganic nanoparticles. The next section discusses about the various methods of synthesis of nanoparticles and the possible mechanistic aspects. The last section highlights the recent advances and possible applications of nanoparticles.

2. Early history

The concept of nanotechnology though considered to be a modern science has its history dating to as back as the 9th century. Nanoparticles of gold and silver were used by the artisans of Mesopotamia to generate a glittering effect to pots. The first scientific description of the properties of nanoparticles was provided in 1857 by Michael Faraday in his famous paper "Experimental relations of gold (and other metals) to light" (Faraday, 1857).

In 1959, Richard Feynman gave a talk describing molecular machines built with atomic precision. This was considered the first talk on nanotechnology. This was entitled "There's plenty of space at the bottom".

The 1950's and the 1960's saw the world turning its focus towards the use of nanoparticles in the field of drug delivery. One of the pioneers in this field was Professor Peter Paul Speiser. His research group at first investigated polyacrylic beads for oral administration, then focused on microcapsules and in the late 1960s developed the first nanoparticles for drug delivery purposes and for vaccines. This was followed by much advancement in developing systems for drug delivery like (for e.g.) the development of systems using nanoparticles for the transport of drugs across the blood brain barrier. In Japan, Sugibayashi *et al.*, (1977) bound 5-fluorouracil to the albumin nanoparticles, and found denaturation temperature dependent differences in drug release as well as in the body distribution in mice after intravenous tail vein injection. An increase in life span was observed after intraperitoneal injection of the nanoparticles into Ehrlich Ascites Carcinoma-bearing mice (Kreuter, 2007).

The nano- revolution conceptually started in the early 1980's with the first paper on nanotechnology being published in 1981 by K. Eric Drexler of Space Systems Laboratory, Massachusetts Institute of Technology. This was entitled "An approach to the development of general capabilities for molecular manipulation".

With gradual advancements such as the invention of techniques like TEM, AFM, DLS etc., nanotechnology today has reached a stage where it is considered as the future to all technologies.

3. Unique properties of nanoparticles

A number of physical phenomena become more pronounced as the size of the system decreases. Certain phenomena may not come into play as the system moves from macro to micro level but may be significant at the nano scale. One example is the increase in surface area to volume ratio which alters the mechanical, thermal and catalytic properties of the material. The increase in surface area to volume ratio leads to increasing dominance of the behaviour of atoms on the surface of the particle over that of those in the interior of the particle, thus altering the properties. The electronic and optical properties and the chemical reactivity of small clusters are completely different from the better known property of each component in the bulk or at extended surfaces. Some of the size dependant properties of nanoparticles are quantum confinement in semiconductors, Surface Plasmon Resonance in some metallic nanoparticles and paramagnetism in magnetic nanoparticles.

Surface plasmon resonance refers to the collective oscillations of the conduction electrons in resonance with the light field. The surface plasmon mode arises from the electron confinement in the nanoparticle. The surface plasmon resonance frequency depends not only on the metal, but also on the shape and size of the nanoparticle and the dielectric properties of the surrounding medium (Jain *et al.*, 2007). For example, noble metals, especially gold and silver nanoparticles exhibit unique and tunable optical properties on account of their Surface Plasmon Resonance.

Superparamagnetism is a form of magnetism that is a special characteristic of small ferromagnetic or ferromagnetic nanoparticles. In such superparamagnetic nanoparticles, magnetization can randomly change direction under the influence of temperature.

Superparamagnetism occurs when a material is composed of very small particles with a size range of 1- 10nm. In the presence of an external magnetic field, the material behaves in a manner similar to paramagnetism with an exception that the magnetic moment of the entire material tends to align with the external magnetic field.

Quantum confinement occurs when one or more dimensions of the nanoparticle is made very small so that it approaches the size of an exciton in the bulk material called the Bohr exciton radius. The idea behind confinement is to trap electrons and holes within a small area (which may be smaller than 30nm). Quantum confinement is important as it leads to new electronic properties. Scientists at the Washington University have studied the electronic and optical changes in the material when it is 10nm or less and have related it to the property of quantum confinement.

Some of the examples of special properties that nanoparticles exhibit when compared to the bulk are the lack of malleability and ductility of copper nanoparticles lesser than 50nm. Zinc oxide nanoparticles are known to have superior UV blocking properties compared to the bulk.

3.1. Classification of nanoparticles

Nanoparticles can be broadly grouped into two: namely organic and inorganic nanoparticles. Organic nanoparticles may include carbon nanoparticles (fullerenes) while some of the inorganic nanoparticles may include magnetic nanoparticles, noble metal nanoparticles (like gold and silver) and semiconductor nanoparticles (like titanium dioxide and zinc oxide).

There is a growing interest in inorganic nanoparticles as they provide superior material properties with functional versatility. Due to their size features and advantages over available chemical imaging drugs agents and drugs, inorganic nanoparticles have been examined as potential tools for medical imaging as well as for treating diseases. Inorganic nanomaterials have been widely used for cellular delivery due to their versatile features like wide availability, rich functionality, good biocompatibility, capability of targeted drug delivery and controlled release of drugs (Xu *et al.*, 2006). For example mesoporous silica when combined with molecular machines prove to be excellent imaging and drug releasing systems. Gold nanoparticles have been used extensively in imaging, as drug carriers and in thermo therapy of biological targets (Cheon & Horace, 2009). Inorganic nanoparticles (such as metallic and semiconductor nanoparticles) exhibit intrinsic optical properties which may enhance the transparency of polymer- particle composites. For such reasons, inorganic nanoparticles have found special interest in studies devoted to optical properties in composites. For instance, size dependant colour of gold nanoparticles has been used to colour glass for centuries (Caseri, 2009).

4. Strategies used to synthesize nanoparticles

Traditionally nanoparticles were produced only by physical and chemical methods. Some of the commonly used physical and chemical methods are ion sputtering, solvothermal synthesis, reduction and sol gel technique. Basically there are two approaches for nanoparticle synthesis namely the Bottom up approach and the Top down approach.

In the Top down approach, scientists try to formulate nanoparticles using larger ones to direct their assembly. The Bottom up approach is a process that builds towards larger and

more complex systems by starting at the molecular level and maintaining precise control of molecular structure.

4.1. Physical and chemical methods of nanoparticle synthesis

Some of the commonly used physical and chemical methods include:

- a) Sol-gel technique, which is a wet chemical technique used for the fabrication of metal oxides from a chemical solution which acts as a precursor for integrated network (gel) of discrete particles or polymers. The precursor sol can be either deposited on the substrate to form a film, cast into a suitable container with desired shape or used to synthesize powders.
- b) Solvothermal synthesis, which is a versatile low temperature route in which polar solvents under pressure and at temperatures above their boiling points are used. Under solvothermal conditions, the solubility of reactants increases significantly, enabling reaction to take place at lower temperature.
- c) Chemical reduction, which is the reduction of an ionic salt in an appropriate medium in the presence of surfactant using reducing agents. Some of the commonly used reducing agents are sodium borohydride, hydrazine hydrate and sodium citrate.
- d) Laser ablation, which is the process of removing material from a solid surface by irradiating with a laser beam. At low laser flux, the material is heated by absorbed laser energy and evaporates or sublimates. At higher flux, the material is converted to plasma. The depth over which laser energy is absorbed and the amount of material removed by single laser pulse depends on the material's optical properties and the laser wavelength. Carbon nanotubes can be produced by this method.
- e) Inert gas condensation, where different metals are evaporated in separate crucibles inside an ultra high vacuum chamber filled with helium or argon gas at typical pressure of few 100 pascals. As a result of inter atomic collisions with gas atoms in chamber, the evaporated metal atoms lose their kinetic energy and condense in the form of small crystals which accumulate on liquid nitrogen filled cold finger. E.g. gold nanoparticles have been synthesized from gold wires.

4.2. Biosynthesis of nanoparticles

The need for biosynthesis of nanoparticles rose as the physical and chemical processes were costly. So in the search of for cheaper pathways for nanoparticle synthesis, scientists used microorganisms and then plant extracts for synthesis. Nature has devised various processes for the synthesis of nano- and micro- length scaled inorganic materials which have contributed to the development of relatively new and largely unexplored area of research based on the biosynthesis of nanomaterials (Mohanpuria *et al.*, 2007).

Biosynthesis of nanoparticles is a kind of bottom up approach where the main reaction occurring is reduction/oxidation. The microbial enzymes or the plant phytochemicals with anti oxidant or reducing properties are usually responsible for reduction of metal compounds into their respective nanoparticles.

The three main steps in the preparation of nanoparticles that should be evaluated from a green chemistry perspective are the choice of the solvent medium used for the synthesis, the

choice of an environmentally benign reducing agent and the choice of a non toxic material for the stabilization of the nanoparticles. Most of the synthetic methods reported to date rely heavily on organic solvents. This is mainly due to the hydrophobicity of the capping agents used (Raveendran *et al.*, 2002). Synthesis using bio-organisms is compatible with the green chemistry principles: the bio-organism is (i) eco-friendly as are (ii) the reducing agent employed and (iii) the capping agent in the reaction (Li *et al.*, 2007). Often chemical synthesis methods lead to the presence of some toxic chemical species adsorbed on the surface that may have adverse effects in medical applications (Parashar *et al.*, 2009). This is not an issue when it comes to biosynthesized nanoparticles as they are eco friendly and biocompatible for pharmaceutical applications.

4.2.1. Use of organisms to synthesize nanoparticles

Biomimetics refers to applying biological principles for materials formation. One of the primary processes in biomimetics involves bioreduction. Initially bacteria were used to synthesize nanoparticles and this was later succeeded with the use of fungi, actinomycetes and more recently plants.

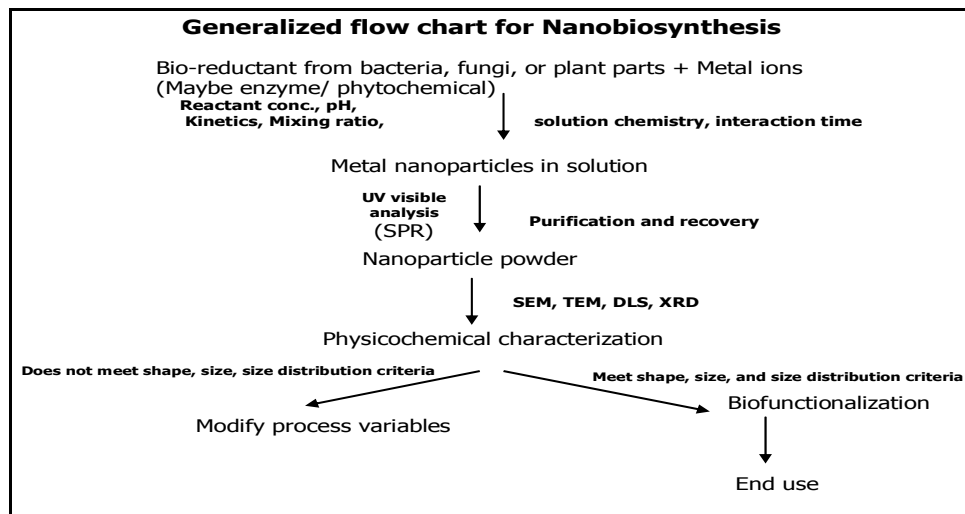


Fig. 1. Flowchart denoting the biosynthesis of nanoparticles

4.2.2. Use of bacteria to synthesize nanoparticles

The use of microbial cells for the synthesis of nanosized materials has emerged as a novel approach for the synthesis of metal nanoparticles. Although the efforts directed towards the biosynthesis of nanomaterials are recent, the interactions between microorganisms and metals have been well documented and the ability of microorganisms to extract and/or accumulate metals is employed in commercial biotechnological processes such as bioleaching and bioremediation (Gericke & Pinches, 2006). Bacteria are known to produce inorganic materials either intra cellularly or extra cellularly. Microorganisms are considered as a potential biofactory for the synthesis of nanoparticles like gold, silver and cadmium

sulphide. Some well known examples of bacteria synthesizing inorganic materials include magnetotactic bacteria (synthesizing magnetic nanoparticles) and S layer bacteria which produce gypsum and calcium carbonate layers (Shankar *et al.*, 2004).

Some microorganisms can survive and grow even at high metal ion concentration due to their resistance to the metal. The mechanisms involve: efflux systems, alteration of solubility and toxicity via reduction or oxidation, biosorption, bioaccumulation, extra cellular complexation or precipitation of metals and lack of specific metal transport systems (Husseiny *et al.*, 2007). For e.g. *Pseudomonas stutzeri* AG 259 isolated from silver mines has been shown to produce silver nanoparticles (Mohanpuria *et al.*, 2007).

Many microorganisms are known to produce nanostructured mineral crystals and metallic nanoparticles with properties similar to chemically synthesized materials, while exercising strict control over size, shape and composition of the particles. Examples include the formation of magnetic nanoparticles by magnetotactic bacteria, the production of silver nanoparticles within the periplasmic space of *Pseudomonas stutzeri* and the formation of palladium nanoparticles using sulphate reducing bacteria in the presence of an exogenous electron donor (Gericke & Pinches, 2006).

Though it is widely believed that the enzymes of the organisms play a major role in the bioreduction process, some studies have indicated it otherwise. Studies indicate that some microorganisms could reduce silver ions where the processes of bioreduction were probably non enzymatic. For e.g. dried cells of *Bacillus megaterium* D01, *Lactobacillus sp.* A09 were shown to reduce silver ions by the interaction of the silver ions with the groups on the microbial cell wall (Fu *et al.*, 1999, 2000). Silver nanoparticles in the size range of 10- 15 nm were produced by treating dried cells of *Corynebacterium sp.* SH09 with diammine silver complex. The ionized carboxyl group of amino acid residues and the amide of peptide chains were the main groups trapping $(Ag(NH_3)_2^+)$ onto the cell wall and some reducing groups such as aldehyde and ketone were involved in subsequent bioreduction. But it was found that the reaction progressed slowly and could be accelerated in the presence of OH⁻ (Fu *et al.*, 2006).

In the case of bacteria, most metal ions are toxic and therefore the reduction of ions or the formation of water insoluble complexes is a defense mechanism developed by the bacteria to overcome such toxicity (Sastry *et al.*, 2003).

4.2.3. Use of actinomycetes to synthesize nanoparticles

Actinomycetes are microorganisms that share important characteristics of fungi and prokaryotes such as bacteria. Even though they are classified as prokaryotes, they were originally designated as ray fungi. Focus on actinomycetes has primarily centred on their exceptional ability to produce secondary metabolites such as antibiotics.

It has been observed that a novel alkalothermophilic actinomycete, *Thermomonospora sp.* synthesized gold nanoparticles extracellularly when exposed to gold ions under alkaline conditions (Sastry *et al.*, 2003). In an effort to elucidate the mechanism or the processes favouring the formation of nanoparticles with desired features, Ahmad *et al.* (2003), studied the formation of monodisperse gold nanoparticles by *Thermomonospora sp.* and concluded that extreme biological conditions such as alkaline and slightly elevated temperature

conditions were favourable for the formation of monodisperse particles. Based on this hypothesis, alkalotolerant actinomycete *Rhodococcus sp.* has been used for the intracellular synthesis of monodisperse gold nanoparticles by Ahmad *et al.* (2003). In this study it was observed that the concentration of nanoparticles were more on the cytoplasmic membrane. This could have been due to the reduction of metal ions by the enzymes present in the cell wall and on the cytoplasmic membrane but not in the cytosol. The metal ions were also found to be non toxic to the cells which continued to multiply even after the formation of the nanoparticles.

4.2.4. Use of fungi to synthesize nanoparticles

Fungi have been widely used for the biosynthesis of nanoparticles and the mechanistic aspects governing the nanoparticle formation have also been documented for a few of them. In addition to monodispersity, nanoparticles with well defined dimensions can be obtained using fungi. Compared to bacteria, fungi could be used as a source for the production of large amount of nanoparticles. This is due to the fact that fungi secrete more amounts of proteins which directly translate to higher productivity of nanoparticle formation (Mohanpuria *et al.*, 2007).

Yeast, belonging to the class ascomycetes of fungi has shown to have good potential for the synthesis of nanoparticles. Gold nanoparticles have been synthesized intracellularly using the fungi *V.luteoalbum*. Here, the rate of particle formation and therefore the size of the nanoparticles could to an extent be manipulated by controlling parameters such as pH, temperature, gold concentration and exposure time. A biological process with the ability to strictly control the shape of the particles would be a considerable advantage (Gericke & Pinches, 2006).

Extracellular secretion of the microorganisms offers the advantage of obtaining large quantities in a relatively pure state, free from other cellular proteins associated with the organism with relatively simpler downstream processing. Mycelia free spent medium of the fungus, *Cladosporium cladosporioides* was used to synthesise silver nanoparticles extracellularly. It was hypothesized that proteins, polysaccharides and organic acids released by the fungus were able to differentiate different crystal shapes and were able to direct their growth into extended spherical crystals (Balaji *et al.*, 2009).

Fusarium oxysporum has been reported to synthesize silver nanoparticles extracellularly. Studies indicate that a nitrate reductase was responsible for the reduction of silver ions and the corresponding formation of silver nanoparticles. However *Fusarium moniliformae* did not produce nanoparticles either intracellularly or extracellularly even though they had intracellular and extracellular reductases in the same fashion as *Fusarium oxysporum*. This indicates that probably the reductases in *F.moniliformae* were necessary for the reduction of Fe (III) to Fe (II) and not for Ag (I) to Ag (0) (Duran *et al.*, 2005).

Instead of fungi culture, isolated proteins from them have also been used successfully in nanoparticles production. Nanocrystalline zirconia was produced at room temperature by cationic proteins while were similar to silicatein secreted by *F. oxysporum* (Mohanpuria *et al.*, 2007).

The use of specific enzymes secreted by fungi in the synthesis of nanoparticles appears promising. Understanding the nature of the biogenic nanoparticle would be equally

important. This would lead to the possibility of genetically engineering microorganisms to over express specific reducing molecules and capping agents and thereby control the size and shape of the biogenic nanoparticles (Balaji *et al.*, 2009).

Microbiological methods generate nanoparticles at a much slower rate than that observed when plant extracts are used. This is one of the major drawbacks of biological synthesis of nanoparticles using microorganisms and must be corrected if it must compete with other methods.

4.2.5. Use of plants to synthesize nanoparticles

The advantage of using plants for the synthesis of nanoparticles is that they are easily available, safe to handle and possess a broad variability of metabolites that may aid in reduction.

A number of plants are being currently investigated for their role in the synthesis of nanoparticles. Gold nanoparticles with a size range of 2- 20 nm have been synthesized using the live alfalfa plants (Torresday *et al.*, 2002). Nanoparticles of silver, nickel, cobalt, zinc and copper have also been synthesized inside the live plants of *Brassica juncea* (Indian mustard), *Medicago sativa* (Alfalfa) and *Helianthus annuus* (Sunflower). Certain plants are known to accumulate higher concentrations of metals compared to others and such plants are termed as hyperaccumulators. Of the plants investigated, *Brassica juncea* had better metal accumulating ability and later assimilating it as nanoparticles (Bali *et al.*, 2006).

Recently much work has been done with regard to plant assisted reduction of metal nanoparticles and the respective role of phytochemicals. The main phytochemicals responsible have been identified as terpenoids, flavones, ketones, aldehydes, amides and carboxylic acids in the light of IR spectroscopic studies. The main water soluble phytochemicals are flavones, organic acids and quinones which are responsible for immediate reduction. The phytochemicals present in *Bryophyllum sp.* (Xerophytes), *Cyprus sp.* (Mesophytes) and *Hydrilla sp.* (Hydrophytes) were studied for their role in the synthesis of silver nanoparticles. The Xerophytes were found to contain emodin, an anthraquinone which could undergo redial tautomerization leading to the formation of silver nanoparticles. The Mesophyte studied contained three types of benzoquinones, namely, cyperoquinone, diethequinone and remirin. It was suggested that gentle warming followed by subsequent incubation resulted in the activation of quinones leading to particle size reduction. Catechol and protocatechaldehyde were reported in the hydrophyte studied along with other phytochemicals. It was reported that catechol under alkaline conditions gets transformed into protocatechaldehyde and finally into protocatecheuic acid. Both these processes liberated hydrogen and it was suggested that it played a role in the synthesis of the nanoparticles. The size of the nanoparticles synthesized using xerophytes, mesophytes and hydrophytes were in the range of 2- 5nm (Jha *et al.*, 2009).

Recently gold nanoparticles have been synthesized using the extracts of *Magnolia kobus* and *Diopyros kaki* leaf extracts. The effect of temperature on nanoparticle formation was investigated and it was reported that polydisperse particles with a size range of 5- 300nm was obtained at lower temperature while a higher temperature supported the formation of smaller and spherical particles (Song *et al.*, 2009).

While fungi and bacteria require a comparatively longer incubation time for the reduction of metal ions, water soluble phytochemicals do it in a much lesser time. Therefore compared to

bacteria and fungi, plants are better candidates for the synthesis of nanoparticles. Taking use of plant tissue culture techniques and downstream processing procedures, it is possible to synthesize metallic as well as oxide nanoparticles on an industrial scale once issues like the metabolic status of the plant etc. are properly addressed.

4.2.6. Work on the biomimetic synthesis of nanoparticles in India

There has been considerable significant research in India in the field of biomimetic synthesis of nanoparticles. More research has been found to be concentrated in the area of biomimetic synthesis using plants.

It has been observed that a novel alkalothermophilic actinomycete, *Thermomonospora sp.* synthesized gold nanoparticles extracellularly when exposed to gold ions under alkaline conditions (Sastry *et al.*, 2003). The use of algae for the biosynthesis of nanoparticles is a largely unexplored area. There is very little literature supporting its use in nanoparticle formation. Recently stable gold nanoparticles have been synthesized using the marine alga, *Sargassum wightii*. Nanoparticles with a size range between 8nm to 12nm were obtained using the seaweed. An important potential benefit of the method of synthesis was that the nanoparticles were quite stable in solution (Singaravelu *et al.*, 2007).

Yeast, belonging to the class ascomycetes of fungi has shown to have good potential for the synthesis of nanoparticles. *Schizosaccharomyces pombe* cells were found to synthesize semiconductor CdS nanocrystals and the productivity was maximum during the mid log phase of growth. Addition of Cd in the initial exponential phase of yeast growth affected the metabolism of the organism (Kowshik *et al.*, 2002). Baker's yeast (*Saccharomyces cerevisiae*) has been reported to be a potential candidate for the transformation of Sb_2O_3 nanoparticles and the tolerance of the organism towards Sb_2O_3 has also been assessed. Particles with a size range of 2- 10 nm were obtained.

Aspergillus flavus has been found to accumulate silver nanoparticles on the surface of its cell wall when challenged with silver nitrate solution. Monodisperse silver nanoparticles with a size range of 8.92 \pm 1.61nm were obtained and it was also found that a protein from the fungi acted as a capping agent on the nanoparticles (Vigneshwaran *et al.*, 2007).

Aspergillus fumigatus has been studied as a potential candidate for the extracellular biosynthesis of silver nanoparticles. The advantage of using this organism was that the synthesis process was quite rapid with the nanoparticles being formed within minutes of the silver ion coming in contact with the cell filtrate. Particles with a size range of 5- 25nm could be obtained using this organism (Bhainsa & D Souza, 2006).

In addition to the synthesis of silver nanoparticles, *Fusarium oxysporum* has also been used to synthesize zirconia nanoparticles. It has been reported that cationic proteins with a molecular weight of 24- 28 kDa (similar in nature to silicatein) were responsible for the synthesis of the nanoparticles (Bansal *et al.*, 2004).

Recently, scientists in India have reported the green synthesis of silver nanoparticles using the leaves of the obnoxious weed, *Parthenium hysterophorus*. Particles in the size range of 30- 80nm were obtained after 10 min of reaction. The use of this noxious weed has an added

advantage in that it can be used by nanotechnology processing industries (Parashar *et al.*, 2009). *Mentha piperita* leaf extract has also been used recently for the synthesis of silver nanoparticles. Nanoparticles in the size range of 10-25 nm were obtained within 15 min of the reaction (Parashar *et al.*, 2009). Table 1 denotes the use of various organisms for the synthesis of nanoparticles.

Biological entity	Nanoparticles synthesized	Size	Intra/ Extracellular	Reference
Bacterium				
<i>Pseudomonas aeruginosa</i>	Au	15-30nm	Extracellular	Husseiny <i>et al.</i> , (2007)
<i>Bacillus subtilis</i>	Ag	5-60nm	Extracellular	Saiffudin <i>et al.</i> , (2009)
<i>Pseudomonas stutzeri</i>	Ag	Upto 200nm	Periplasmic	Joerger <i>et al.</i> , (2000) Klaus <i>et al.</i> , (1999)
Fungi				
<i>Coriolus versicolor</i>	Ag	10-75nm	Extracellular	Sanghi & Verma (2008)
<i>Fusarium semitectum</i>	Ag	10-60nm	Extracellular	Basavaraja <i>et al.</i> , (2007)
<i>Fusarium oxysporum</i>	Ag	5-15nm	Extracellular	Ahmad <i>et al.</i> , (2003)
<i>Phaenerochaete chrysosporium</i>	Ag	-	Extracellular	Vigneshwaran <i>et al.</i> , (2006)
<i>Aspergillus flavus</i>	Ag	8.92+/- 1.62nm	Intracellular	Vigneshwaran <i>et al.</i> , (2007)
Plants				
<i>Azadirachta indica</i>	Ag, Au, Ag/Au bimetallic	50-100nm	Extracellular	Shankar <i>et al.</i> , (2003), Tripathy <i>et al.</i> , (2009)
<i>Pelargonium graveolens</i>	Ag	16-40nm	Extracellular	Shankar <i>et al.</i> , (2003)
<i>Capsicum annum</i>	Ag	10-40nm	Extracellular	Li <i>et al.</i> , (2007)

Table 1. Use of biological entities for the synthesis of various nanoparticles

Azadirachta indica leaf extract has also been used for the synthesis of silver, gold and bimetallic (silver and gold) nanoparticles. Studies indicated that the reducing phytochemicals in the neem leaf consisted mainly of terpenoids. It was found that these reducing components also served as capping and stabilizing agents in addition to reduction as revealed from FT IR studies. The major advantage of using the neem leaves is that it is a commonly available medicinal plant and the antibacterial activity of the biosynthesized silver nanoparticle might have been enhanced as it was capped with the neem leaf extract.

The major chemical constituents in the extract were identified as nimbin and quercetin (Shankar *et al.*, 2004, Tripathy *et al.*, 2009). Figure 2 and 3 show the TEM micrograph of the biosynthesized silver nanoparticles (unpublished data, Prathna T.C. *et al.*, 2009).

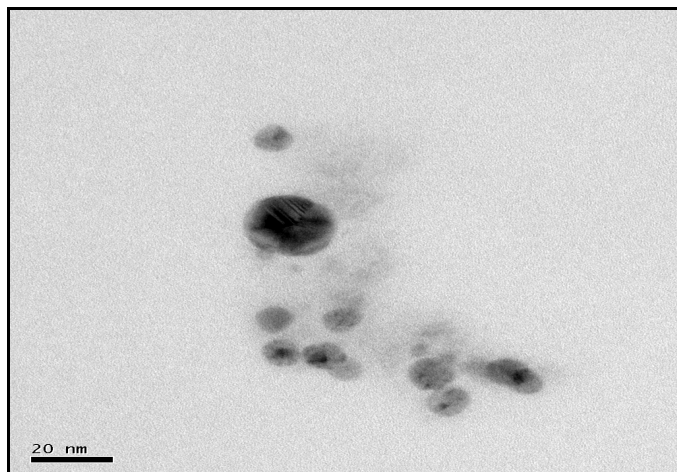


Fig. 2. Transmission electron micrograph showing silver nanoparticles synthesized using neem leaf extract (unpublished data, Prathna T.C. *et al.*, 2009)

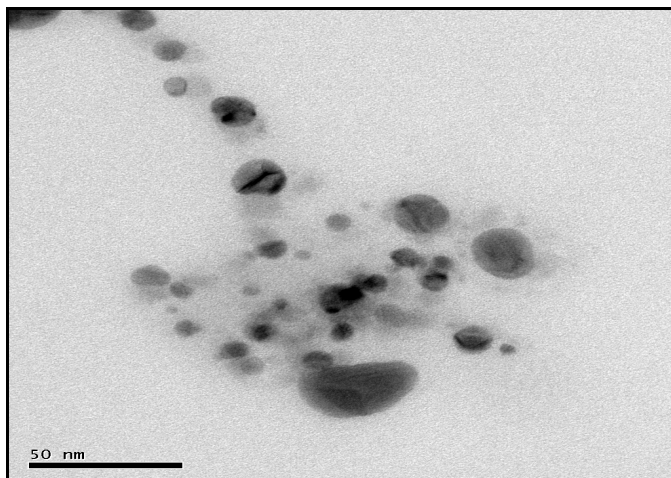


Fig. 3. Transmission electron micrograph showing silver nanoparticles synthesized using neem leaf extract (unpublished data, Prathna T.C. *et al.*, 2009).

4.2.7. Some of the mechanistic aspects of nanoparticle formation

Though there are many studies reporting the biosynthesis of various nanoparticles by bacteria, there is very little information available regarding the mechanistic aspects of nanoparticle production.

The mechanisms of gold bioaccumulation by cyanobacteria (*Plectonema boryanum* UTEX 485) from gold (III) chloride solutions have been studied and it is found that interaction of cyanobacteria with aqueous gold (III) chloride initially promoted the precipitation of nanoparticles of amorphous gold (I) sulfide at the cell walls and finally deposited metallic gold in the form of octahedral (III) platelets near cell surfaces and in solutions (Lengke *et al.*, 2006).

Scientists in Iran have investigated the extracellular biosynthesis of silver nanoparticles by the cells of *Klebsiella pneumoniae*. They hypothesize that the reduction of the metallic ions in the solution by the cell free supernatant is most likely due to the presence of nitroreductase which is produced by some members of Enterobacteriaceae. It has been widely studied that nitrate reductase is necessary for some metallic reduction.

Recently cadmium sulfide nanoparticles have been biosynthesized using the photosynthetic bacteria, *Rhodospseudomonas palustris*. The work indicated that the cysteine desulfhydrase (C-S lyase) could control crystal growth, because cysteine rich proteins can produce S²⁻ through the action of C-S lyase. The content of C-S lyase in *R.palustris* was suggested to be responsible for nanocrystal formation. C-S lyase is found to be an intracellular enzyme located in the cytoplasm and it was indicated that *R.palustris* synthesized CdS nanoparticles intracellularly, later discharging it (Bai *et al.*, 2009).

Schizosaccharomyces pombe cells were found to synthesize semiconductor CdS nanocrystals and the productivity was maximum during the mid log phase of growth. Addition of Cd in the initial exponential phase of yeast growth affected the metabolism of the organism (Kowshik *et al.*, 2002). A possible mechanism for this could be that when Cd is initially added, it causes stress to the organism triggering a series of biochemical reactions. Firstly, an enzyme phytochelatin synthase was activated to synthesize phytochelatins (PC) that chelated the cytoplasmic Cd to form a low molecular weight PC- Cd complex and ultimately transport them across the vacuolar membrane by an ATP binding cassette type vacuolar membrane protein (HMT- 1). In addition to Cd, sulfide could also be added to this complex in the membrane and this could result in the formation of high molecular weight PC- CdS complex that allows it to be ultimately sequestered into the vacuole (Mohanpuria *et al.*, 2007).

Baker's yeast (*Saccharomyces cerevisiae*) has been reported to be a potential candidate for the transformation of Sb₂O₃ nanoparticles and the tolerance of the organism towards Sb₂O₃ has also been assessed. Particles with a size range of 2- 10 nm were obtained. It has been hypothesized that membrane bound oxido reductases and quinones may have played a role in the biosynthesis. The oxidoreductases are pH sensitive and work in alternative manner. At a lower pH, oxidase gets activated while a higher pH value activates reductase. This along with a number of simple hydroxy/ methoxy derivatives of benzoquinones and toluquinones mainly found in lower fungi (and hypothesized to be present in yeast) may facilitate the redox reaction due to its tautomerization. The transformation appears to be negotiated at two levels, one at the cell membrane level immediately after the addition of SbCl₃ solution which triggers tautomerization of quinones and low pH sensitive oxidases which thereby makes molecular oxygen available for transformation. Also when Sb³⁺ enters

the cytoplasm, it might trigger the family of oxygenases harboured in the ER, meant for cellular level detoxification by a process of oxidation/ oxygenation (Jha *et al.*, 2009).

The synthesis of gold and silver nanoparticles has also been reported using black tea leaf extracts. Black tea leaf extracts are known to contain more amounts of flavonones and polyphenols. It was found that the reduction of metal ions was accompanied by oxidation of polyols (Begum *et al.*, 2009). Table 2 gives a summary of some aspects of nanoparticle formation.

Biological entity	Nanoparticle	Enzyme/ phytochemical	Reference
<i>Rhodospseudomonas palustris</i>	CdS	C-S lyase	Bai <i>et al.</i> (2009)
<i>Schizosaccharomyces pombe</i>	CdS	Phytochelatin synthase/ phytochelatins	Mohanpuria <i>et al.</i> (2007)
<i>Schizosaccharomyces cerevisiae</i>	Sb ₂ O ₃	Oxidoreductases/ quinones	Jha <i>et al.</i> ,(2009)
<i>Fusarium oxysporum</i>	Ag	NADH dependant reductase	Duran <i>et al.</i> , (2005)
Black tea leaf	Ag/ Au	Polyphenols/ flavonoids	Begum <i>et al.</i> , (2009)
<i>Azadirachta indica</i>	Ag/ Au	Terpenoids	Shankar <i>et al.</i> , (2004), Tripathy <i>et al.</i> ,(2009)
<i>Jatropha curcas</i>	Ag	Curcain, curacycline A, curacycline B	Bar <i>et al.</i> , (2009)

Table 2. Mechanistic aspects of nanoparticle formation

The latex of *Jatropha curcas*, a plant whose seeds are used to extract biodiesel has also been used for the synthesis of silver nanoparticles. Some of the major components in the latex of *Jatropha curcas* were identified as curcain, curacycline A and curacycline B. The silver nanoparticles obtained using this source had two broad distributions- one having particles in the range of 20- 40 nm and the other having larger and uneven particles. Molecular modeling studies of the peptides in the latex revealed that the silver ions were first entrapped in the core structure of the cyclic structure of the protein and were then reduced and stabilized insitu by the amide group of the peptide. This resulted in particles with radius similar to the peptides. It was also found that the larger particles with uneven shapes were stabilized by the enzyme curcain (Bar *et al.*, 2009).

Li *et al* (2007) synthesized silver nanoparticles using the *Capsicum annum* L. extract. *Capsicum annum* L. extract is known to contain a number of biomolecules such as proteins, enzymes, polysaccharides, amino acids and vitamins. These biomolecules could be used as bioreductants to react with metal ions and they could also be used as scaffolds to direct the formation of nanoparticles in solution. The mechanism responsible for the reduction was postulated as follows: the silver ions were trapped on the surface of proteins in the extract via electrostatic interactions. This stage was the recognition process. The silver ions were

then reduced by the proteins leading to changes in their secondary structure and the formation of silver nuclei. The silver nuclei subsequently grew by the further reduction of silver ions and their accumulation of the nuclei.

5. Applications of Nanoparticles

Nanotechnology has a wide range of applications in the fields of biology, medicine, optical, electrical, mechanical, optoelectronics etc.

Silver nanoparticles have also been used for a number of applications such as non linear optics, spectrally selective coating for solar energy absorption, biolabelling and antibacterial activities.

Silver nanoparticles have shown promise against gram positive *S. aureus*. Nanoparticles have also been incorporated in cloth which has shown promise to be sterile and thus helping in minimizing infections. Metal nanoparticle embedded paints have been synthesized using vegetable oils and have been found to have good antibacterial activity (Kumar *et al.*, 2008).

Current research is going on regarding the use of magnetic nanoparticles in the detoxification of military personnel in case of biochemical warfare. It is hypothesized that by utilizing the magnetic field gradient, toxins can be removed from the body. Enhanced catalytic properties of surfaces of nano ceramics or those of noble metals like platinum and gold are used in the destruction of toxins and other hazardous chemicals (Salata, 2005).

Photocatalytic activity of nanoparticles has been utilized to develop self- cleaning tiles, windows and anti- fogging car mirrors. The high reactivity of Titania nanoparticles either on their own or when illuminated by UV light have been used for bactericidal purposes in filters.

An important opportunity for nanoparticles in the area of computers and electronics is their use in a special polishing process, chemical-mechanical polishing or chemical-mechanical planarization (CMP), which is critical to semiconductor chip fabrication. CMP is used to obtain smooth, flat, and defect-free metal and dielectric layers on silicon wafers. This process utilizes slurry of oxide nanoparticles and relies on mechanical abrasion as well as a chemical reaction between the slurry and the film being polished. CMP is also used in some other applications, such as the polishing of magnetic hard disks.

Nanoscale titanium dioxide and zinc oxide have been used as sunscreens in cosmetics. The primary advantage of using these nanoparticles is that they are well dispersed and transmit visible light, acting as transparent sunblocks. On the other hand, inorganic sunscreens appear white on the skin- a potential drawback.

The interaction of silver nanoparticles with HIV I has been demonstrated in vitro. It was shown that the exposed sulfur binding residues of the glycoprotein knobs were attractive sites for nanoparticle interaction and that the silver nanoparticles had preferential binding to the gp 120 glycoprotein knobs. Due to this interaction, it was found that the silver nanoparticles inhibited the binding of the virus to the host cells in vitro (Elechiguerra *et al.*, 2005).

Magnetic nanoparticles are also used in targeted therapy where a cytotoxic drug is attached to a biocompatible magnetic nanoparticle. When these particles circulate in the bloodstream, external magnetic fields are used to concentrate the complex at a specific target site within the body. Once the complex is concentrated in the target, the drug can be released by enzymatic activity or by changes in pH or temperature and are taken up by the tumour cells (Pankhurst *et al.*, 2003).

Porous nanoparticles have also been used in cancer therapy where the hydrophobic version of a dye molecule is trapped inside the Ormosil nanoparticle. The dye is used to generate atomic oxygen which is taken up more by the cancer cells when compared to the healthy tissue. When the dye is not entrapped, it travels to the eyes and skin making the patient sensitive to light. Entrapment of the dye inside the nanoparticle ensures that the dye does not migrate to other parts and also the oxygen generating ability is not affected.

Alivisatos (2001) reported the presence of inorganic crystals in magnetotactic bacteria. The bacterium was found to have about 20 magnetic crystals with a size range of 35- 120nm diameter. The crystals serve as a miniature compass and align the bacteria with the external magnetic field. This enables the bacterium to navigate with respect to the earth's magnetic field towards their ideal environment. These bacteria immobilize heavy metals from a surrounding solution and can be separated by applying a low intensity magnetic field. This principle can be extended to develop a process for the removal of heavy metals from waste water.

Bioremediation of radioactive wastes from nuclear power plants and nuclear weapon production, such as uranium has been achieved using nanoparticles. Cells and S layer proteins of *Bacillus sphaericus* JG A12 have been found to have special capabilities for the clean up of uranium contaminated waste waters (Duran *et al.*, 2007).

Biomaterials have been formulated by using several bacteria such as *Pseudomonas aeruginosa*, *E. coli* and *Citrobacter sp.* Metal sulfide microcrystallites were formulated using *S. pombe* which could function as quantum semiconductor microcrystallite. These crystals have properties like optical absorption, photosynthetic and electron transfer.

Magnetosome particles isolated from magnetotactic bacteria have been used as a carrier for the immobilization of bioactive substances such as enzymes, DNA, RNA and antibodies (Mohanpuria *et al.*, 2007).

Gold nanoparticles are widely used in various fields such as photonics, catalysis, electronics and biomedicine due to their unique properties. *E. coli* has been used to synthesize gold nanoparticles and it has been found that these nanoparticles are bound to the surface of the bacteria. This composite may be used for realizing the direct electrochemistry of haemoglobin (Du *et al.*, 2007). p- nitrophenol is widely used in pesticides, pharmaceutical industries, explosives and in dyes and is known to be a carcinogenic agent. Gold nanoparticles have been synthesized using the barbated skullcap extract. The nanoparticles synthesized by this method have been modified to the glass electrode and this has been used to enhance the electronic transmission rate between the electrode and p- nitrophenol (Wang *et al.*, 2009).

Tripathy *et al.*, (2008) reported the antibacterial applications of the silver nanoparticles synthesized using the aqueous extract of neem leaves. The nanoparticles were coated on cotton disks and their bactericidal effect was studied against *E.coli*. Duran *et al.*, (2005) reported the significant antibacterial activities of the silver nanoparticles synthesized using *Fusarium oxysporum*.

Table 3 gives a list of a few companies which have utilized nanoparticles in their products.

Company	Product	Advantage
Air quality		
NanoStellar	Nanocomposite catalyst for use in automotive catalytic converters	Reduced cost due to less platinum use
AmericanElements	Catalyst composed of MnO ₂ nanoparticles to remove volatile organic compounds (VOC)	Capable of destroying VOC down to parts per billion level
Batteries		
Zpower	Ag-Zn battery using nanoparticles in the silver cathode	Higher power density, low combustibility
Cleaning products		
Samsung	Ag nanoparticles used in household appliances like clothes washer and refrigerator	Kills bacteria and reduces odour
Nanotec	Spray-on liquid containing nanoparticles	Repels water and dirt
Fabrics		
Aspen Aerogel	Fabric enhanced with nanopores	Insulates against heat
Nano horizons	Fabric enhanced with silver nanoparticles	Reduces odours
Sporting goods		
InMat	Nanocomposite barrier film	Prevents air loss from tennis balls
Easton	Bicycle components strengthened with C nanotubes	Strong, light weight components

Table 3. A list of few companies utilizing nanoparticles in their products (Courtesy: www.understandingnano.com)

Though the applications of nanoparticles are exhaustive, an effort has been made in this review to highlight specific applications

6. Conclusion

An important challenge in technology is to tailor optical, electric and electronic properties of nanoparticles by controlling their size and shape. Biomimetic synthesis of nanoparticles has opened its doors to a world of nanoparticles with easy preparation protocols, less toxicity and a wide range of applications according to their size and shape. Nanoparticles of desired size and shape have been obtained successfully using living organisms- simple unicellular organisms to highly complex eukaryotes. The field of nano biotechnology is still in its infancy and more research needs to be focused on the mechanistics of nanoparticle formation which may lead to fine tuning of the process ultimately leading to the synthesis of nanoparticles with a strict control over the size and shape parameters.

7. References

- Ahmad, A.; Senapati, S.; Khan, M.I.; Kumar, R. & Sastry, M. (2003). Extracellular biosynthesis of monodisperse gold nanoparticles by a novel extremophilic actinomycete, *Thermomonospora sp.* *Langmuir* 19., 3550-3553.
- Ahmad, A.; Senapati, S.; Khan, M.I.; Kumar, R.; Ramani, R.; Srinivas, V. & Sastry, M. (2003). Intracellular synthesis of gold nanoparticles by a novel alkalotolerant actinomycete, *Rhodococcus* species. *Nanotechnology* 14.; 824- 828.
- Alivisatos, A.P. (2001). Less is more in medicine. *Scientific American.*; 59- 65.
- Bai, H.J.; Zhang, Z.M.; Guo, Y. & Yang, G.E. (2009). Biosynthesis of cadmium sulfide nanoparticles by photosynthetic bacteria *Rhodospseudomonas palustris*. *Colloids and surfaces B: Biointerfaces* 70.; 142-146.
- Balaji, D.S.; Basavaraja, S.; Deshpande, R.; Mahesh, D.B.; Prabhakar, B.K. & Venkataraman, A. (2009). Extracellular biosynthesis of functionalized silver nanoparticles by strains of *Cladosporium cladosporioides* fungus. *Colloids and surfaces B: biointerfaces* 68.; 88- 92.
- Bali, R.; Razak, N.; Lumb, A. & Harris, A.T. (2006). The synthesis of metal nanoparticles inside live plants. *IEEE Xplore* DOI 10.1109/ICONN.2006.340592
- Bansal, V.; Rautaray, D.; Ahmad, A. & Sastry, M. (2004). Biosynthesis of zirconia nanoparticles using the fungus *Fusarium oxysporum*. *Journal of Materials Chemistry* 14.; 3303- 3305.
- Bar, H.; Bhui, D.K.; Sahoo, G.P.; Sarkar, P.; De, S.P. & Misra, A. (2009). Green synthesis of silver nanoparticles using latex of *Jatropha curcas*. *Colloids and surfaces A: Physicochemical and engineering aspects* 339.; 134- 139.
- Basavaraja, S.; Balaji, S.D.; Lagashetty, A.; Rajasab, A.H. & Venkataraman, A. (2007). Extracellular biosynthesis of silver nanoparticles using the fungus *Fusarium semitectum*. *Materials Research Bulletin*. Article in Press
- Begum, N.A.; Mondal, S.; Basu, S.; Laskar, R.A. & Mandal, D. (2009). Biogenic synthesis of Au and Ag nanoparticles using aqueous solutions of Black tea leaf extracts. *Colloids and surfaces B: Biointerfaces* 71.; 113- 118.
- Bhainsa, K.C. & D Souza, S.F. (2006). Extracellular biosynthesis of silver nanoparticles using the fungus *Aspergillus fumigatus*. *Colloids and surfaces B: Biointerfaces* 47.;160- 164.
- Casari, W. (2009). Inorganic nanoparticles as optically effective additives for polymers. *Chemical Engineering Communications* 196(5).; 549- 572.

- Cheon, J. & Horace, G. (2009). Inorganic nanoparticles for biological sensing, imaging and therapeutics. *J. Mater. Chem.* 19.; 6249- 6250.
- Du, L.; Jiang, H.; Liu, X. & Wang, E. (2007). Biosynthesis of gold nanoparticles assisted by *Escherichia coli* DH5 α and its application on direct electrochemistry of haemoglobin. *Electrochemistry Communications.* 9.; 1165- 1170.
- Duran, N.; Marcato, P.D.; Alves, O.L.; De Souza; G.I.H. & Esposito, E. (2005). Mechanistic aspects of biosynthesis of silver nanoparticles by several *Fusarium oxysporum* strains. *Nanobiotechnology* 3.; 8- 14.
- Duran, N.; Marcato, P.D.; De, S.; Gabriel, I.H.; Alves, O.L. & Esposito, E. (2007). Antibacterial effect of silver nanoparticles produced by fungal process on textile fabrics and their effluent treatment. *Journal of Biomedical Nanotechnology* 3.; 203- 208.
- Elechiguerra, J.L.; Burt, J.L.; Morones, J.R.; Bragado, A.C.; Gao, X.; Lara, H.L. & Yacaman, M.J. (2005). Interaction of silver nanoparticles with HIV- I. *Journal of Nanobiotechnology* 3.; 6- 16.
- Faraday, M. (1857). Experimental relations of gold (and other metals) to light. *Phil. Trans. Roy. Soc. London* 147.; 145-181.
- Fu, J.K.; Liu, Y.; Gu, P.; Tang, D.L.; Lin, Z.Y.; Yao, B.X. & Weng, S.Z. (2000). Spectroscopic characterization on the biosorption and bioreduction of Ag(I) by *Lactobacillus sp.* A09. *Acta Physico- Chimica Sinica* 16(9) .; 770-782 (in Chinese).
- Fu, J.K.; Zhang, W.D.; Liu, Y.Y.; Lin, Z.Y.; Yao, B.X. & Weng, S.Z. (1999). Characterization of adsorption and reduction of noble metal ions by bacteria. *Chem. J. Chinese Universities* 20(9).; 1452-1454 (in Chinese).
- Fu, M.; Li, Q.; Sun, D.; Lu, Y.; He, N.; Deng, X.; Wang, H. & Huang, J. (2006). Rapid preparation process of silver nanoparticles by bioreduction and their characterizations. *Chinese J. Chem. Eng.* 14(1).; 114-117.
- Gericke, M. & Pinches, A. (2006). Microbial production of gold nanoparticles. *Gold bulletin.*, 39(1).; 22-28.
- Gericke, M. & Pinches, A. (2006). Biological synthesis of metal nanoparticles. *Hydrometallurgy* 83.; 132-140.
- Husseiny, M.I.; Aziz, M.A.E.; Badr, Y. & Mahmoud, M.A. (2006). Biosynthesis of gold nanoparticles using *Pseudomonas aeruginosa*. *Spectrochimica Acta Part A* 67.; 1003-1006.
- Jain, P.K.; Huang, X.; El Sayed, L.H. & El Sayed, M.A. (2007). Review of some interesting Surface Plasmon Resonance- enhanced properties of noble metal Nanoparticles and their applications to biosystems. *Plasmonics* 2.; 107- 118.
- Jha, A.K.; Prasad, K. & Prasad, K. (2009). A green low- cost biosynthesis of Sb₂O₃ nanoparticles. *Biochemical engineering journal* 43.; 303-306.
- Jha, A.K.; Prasad, K.; Prasad, K. & Kulkarni, A.R. (2009). Plant system: Nature's nanofactory. *Colloids and Surfaces B: Biointerfaces* (in press) doi: 10.1016/j.colsurfb.2009.05.018.
- Joerger, R.; Klaus, T. & Granquist, C.G. (2000). Biologically produced silver- carbon composite materials for optically thin film coatings. *Advanced Materials.* 12.; 407-409.
- Konishi, Y.; Ohno, K.; Saitoh, N.; Nomura, T.; Nagamine, S.; Hishida, H.; Takahashi, Y. & Uruga, T.G. Bioreductive deposition of platinum nanoparticles on the bacterium *Shewanella algae*. *Journal of Biotechnology*

- Kowshik, M.; Deshmukh, N.; Vogel, W.; Urban, J.; Kulkarni, S.K. & Paknikar, K.M. (2002). Microbial synthesis of semiconductor CdS nanoparticles, their characterization and their use in the fabrication of an ideal diode. *Biotechnology and Bioengineering* 78.; 583- 588.
- Kreuter, J. (2007). Nanoparticles-a historical perspective. *International journal of pharmaceuticals* 331.; 1-10.
- Kumar, A.; Kumar, P.; Ajayan, M.P. & John, G. (2008). Silver nanoparticle embedded antimicrobial paints based on vegetable oil. *Nature Materials*. 7.; 236- 241.
- Lengke, M.; Ravel, B.; Fleet, M.E.; Wanger, G.; Gordon, R.A. & Southam, G. (2006). Mechanisms of gold bioaccumulation by filamentous cyanobacteria from gold (III) chloride complex. *Environmental Science and Technology* 40.; 6304- 6309.
- Li, S.; Shen, Y.; Xie, A.; Yu, X.; Qui, L.; Zhang, L. & Zhang, Q. (2007). Green synthesis of silver nanoparticles using *Capsicum annum* L. extract. *Green Chemistry*. 9.; 852-858.
- Mohanpuria, P.; Rana, K.N. & Yadav, S.K (2008). Biosynthesis of nanoparticles: technological concepts and future applications. *Journal of Nanoparticle Research* 10.; 507- 517.
- Mukherjee, P.; Ahmad, A.; Mandal, D.; Senapati, S.; Sainkar, S.R.; Khan, M.I.; Ramani, R.; Parischa, R.; Kumar, P.A.V.; Alam, M.; Sastry, M. & Kumar, R. (2001). Bioreduction of AuCl by the fungus, *Verticillium sp.* and surface trapping of the gold nanoparticles formed. *Angew. Chem. Int. Ed.* 40.; 3585- 3588.
- Pankhurst, Q.A.; Connolly, J.; Jones, S.K. & Dobson, J. (2003). Applications of magnetic nanoparticles in biomedicine. *Journal of physics D: Applied physics*. 36.; 167- 181.
- Parashar, U.K.; Saxena, S.P. & Srivastava, A. (2009). Bioinspired synthesis of silver nanoparticles. *Digest journal of nanomaterials and biostructures* 4(1).; 159- 166.
- Parashar, V.; Prashar, R.; Sharma, B. & Pandey., A.C. (2009). Parthenium leaf extract mediated synthesis of silver nanoparticles: a novel approach towards weed utilization. *Digest journal of nanomaterials and biostructures.*, 4(1).; 45-50.
- Raveendran, P.; Fu, J. & Wallen., S.L. (2003). Completely "Green" Synthesis and Stabilization of metal nanoparticles. *Journal of American Chemical Society*, 125(46).; 13940-13941.
- Saifuddin, N.; Wong, C.W. & Yasimura, A.A.N. (2009). Rapid biosynthesis of silver nanoparticles using culture supernatant of bacteria with microwave irradiation. *E-journal of chemistry*. 6(1).; 61-70.
- Salata, O.V. (2004). Applications of nanoparticles in biology and medicine. *Journal of Nanobiotechnology* 2.; 3- 8.
- Sanghi, R. & Verma, P. (2008). Biomimetic synthesis and characterization of protein capped silver nanoparticles. *Bioresource technology*
- Sastry, M.; Ahmad, A.; Khan, M.I. & Kumar, R. (2003). Biosynthesis of metal nanoparticles using fungi and actinomycete. *Current science* 85(2).; 162- 170.
- Shankar, S.S.; Ahmad, A. & Sastry, M. (2003). Geranium leaf assisted biosynthesis of silver nanoparticles. *Biotechnol. Prog.* 19.; 1627- 1631.
- Shankar, S.S.; Rai, A.; Ahmad, A. & Sastry, M. (2004). Rapid synthesis of Au, Ag and bimetallic Au core- Ag shell nanoparticles using neem (*Azadirachta indica*) leaf broth. *Journal of colloid and interface science*. 275.; 496-502.
- Singaravelu, G.; Arockiamary, J.S.; Kumar, V.G. & Govindaraju, K. (2007). A novel extracellular synthesis of monodisperse gold nanoparticles using marine alga, *Sargassum wightii* Greville. *Colloids and surfaces B: Biointerfaces* 57.; 97- 101.

- Song, J.Y.; Jang, H.K. & Kim, B.S. (2009). Biological synthesis of gold nanoparticles using *Magnolia kobus* and *Diopyros kaki* leaf extracts. *Process Biochemistry* 44.; 1133- 1138.
- Sugibayashi, K.; Morimoto, Y.; Nadai, T. & Kato, Y. (1977). Drug-carrier property of albumin microspheres in chemotherapy.I. Tissue distribution of microsphere-entrapped 5-fluorouracil in mice. *Chem. Pharm. Bull.* 25.; 3433-3434.
- Torresday, J.L.G.; Parsons, J.G.; Gomez, E.; Videa, J.P.; Troiani, H.E.; Santiago, P. & Yacaman, M.J. (2002). Formation and growth of Au nanoparticles inside live alfa alfa plants. *Nanoletters* 2(4).; 397- 401.
- Tripathy, A.; Chandrasekaran, N.; Raichur, A.M. & Mukherjee, A. (2008). Antibacterial applications of silver nanoparticles synthesized by aqueous extract of *Azadirachta indica* (Neem) leaves. *Journal of Biomedical Nanotechnology* 4(3); 1- 6.
- Tripathy, A.; Raichur, A.M.; Chandrasekaran, N.; Prathna, T.C. & Mukherjee, A. (2009). Process variables in biomimetic synthesis of silver nanoparticles by aqueous extract of *Azadirachta indica* (Neem) leaves. *Journal of Nanoparticle Research*. Article in press.
- Vigneshwaran, N.; Ashtaputre, N.M.; Varadarajan, P.V.; Nachane, N.P.; Paralikar, K.M. & Balasubramanya, R.H. (2007). Biological synthesis of silver nanoparticles using the fungus *Aspergillus flavus*. *Materials letters*. 61.; 1413- 1418.
- Vigneshwaran, N.; Kathe, A.A.; Varadarajan, P.V.; Nachane, R.P. & Balasubramanya, R.H. (2007). Biomimetics of silver nanoparticles by white rot fungus, *Phaenerochaete chrysosporium*. *Colloids and Surfaces B: Biointerfaces* 53.; 55- 59.
- Wang, Y.; He, X.; Wang, K.; Zhang, X. & Tan, W. (2009). Barbated Skullcap herb extract-mediated biosynthesis of gold nanoparticles and its primary application in electrochemistry. *Colloids and Surfaces B: Biointerfaces*. Article in press.
- Xu, Z.P.; Zeng, Q.H.; Lu, G.Q. & Yu, A.B. (2006). Inorganic nanoparticles as carriers for efficient cellular delivery. *Chemical Engineering Science* 61.; 1027- 1040.

Web Resources:

www.understandingnano.com

Unpublished Data:

Prathna T.C., N. Chandrasekaran, A. Mukherjee, "Kinetic evolution of silver nanoparticles synthesized using Neem leaf extract", (Manuscript in preparation)

Immobilized redox proteins: mimicking basic features of physiological membranes and interfaces

Daniel H. Murgida, Peter Hildebrandt and Smilja Todorovic
*INQUIMAE, University of Buenos Aires - CONICET,
Argentina,
Technische Universität Berlin,
Germany,
ITQB, The New University of Lisbon,
Portugal*

1. Introduction

Redox proteins perform diverse functions in cells, including electron transport, energy conversion, detoxification, enzymatic catalysis, signalling and gene regulation. The evolutionary optimised specificity and efficiency of enzymes has stimulated attempts to exploit these biocatalysts for a variety of technological applications. For example, enzymes are nowadays used to promote or to detect bio-specific interactions in biosensors (Karube, 1989). Several generations of low cost glucose oxidase-based biosensors are commercially available for monitoring the levels of glucose in diabetic individuals (Henning and Cunningham, 1998). Peroxidases are employed for biosensing of hydrogen peroxide and phenolic compounds, being relevant in environmental, pharmaceutical, clinical and industrial applications (Arya *et al.*, 2009). Cytochromes P450 possess a high potential as biocatalysts for chemical synthesis although the transfer to biotechnological applications still represents a challenge (Leland and Clark, 1989; Todorovic *et al.*, 2006; Cass, 2007).

Understanding the enzymatic processes in cellular systems as well as in technological devices strongly depends on the knowledge of the molecular functioning of the enzymes. To this end specific approaches have been designed to explore the molecular processes of enzymes and redox proteins under conditions that reproduce most closely the physiological reaction. Membrane-bound redox proteins, such as respiratory chain electron transfer (ET) complexes, are incorporated into phospholipid bilayers, thus exerting their function in a hydrophobic environment under influence of the membrane potential. Small soluble metalloproteins that shuttle electrons between ET enzymes interact with the membrane-bound redox partners and the membrane itself. As a result of these interactions, the ET processes of electron shuttles are also subjected to strong electric fields at the membrane-solution interface. These conditions are difficult to reproduce experimentally. In this respect, immobilization of redox proteins on biocompatible metal supports that function as

electrodes represents a powerful alternative, allowing application of direct electrochemistry and surface-enhanced vibrational spectroelectrochemical techniques. These methods permit determination of kinetic and thermodynamic parameters of the heterogeneous ET in a protein that is exposed to physiologically relevant electric fields. Furthermore, ET steps can be controlled in terms of directionality, distance, and driving force. In addition, spectroelectrochemical methods can simultaneously probe the active site structure and conformational dynamics concomitant to the ET.

In this chapter we will present an overview of recent developments in the field of biocompatible immobilization of membrane-bound and soluble redox proteins on metal electrodes, and of the spectroelectrochemical techniques used for the *in situ* characterization of the structure, thermodynamics and reaction dynamics of the immobilized proteins.

After a brief description of biological ET chains and their constituting complexes (Section 2), we will introduce some of the strategies for protein immobilization (Section 3), with special emphasis on self-assembled monolayers (SAMs) of functionalized alkanethiols as versatile biocompatible coatings that can be tailored according to the specific requirements. In Section 4 we will describe the basic principles of stationary and time-resolved surface-enhanced vibrational spectroscopies (SERR and SEIRA) as valuable tools for studying specifically the redox centres or the immobilized metalloproteins. The contents of the first 3 sections are integrated in Section 5, where recent progress in the immobilization and SERR/SEIRA characterization of different components of ET respiratory chains, mainly oxygen reductases and cytochromes will be discussed. We will conclude with a brief outlook (Section 6).

2. Redox proteins under physiological conditions

In this section we will provide a brief introduction to the complex ET chains involved in the energetics of organisms, i.e. respiratory and photosynthetic chains. In spite of obvious differences, these two types of systems share a number of common features that must be taken into account when investigating them using biomimetic approaches. First, both types of chains consist of a series of membrane-integrated redox active protein complexes that communicate through hydrophilic (e.g. cytochromes) and hydrophobic (e.g. quinones) electron shuttles. Second, the energy provided by the sequence of exergonic ET events is utilized by some of the constituting membrane proteins for translocating protons across the membrane against an electrochemical gradient. This gradient is, for example, utilized for driving ATP synthesis. Common to components of both ET chains are the specific reaction conditions that deviate substantially from redox processes of proteins in solution. Characteristic features are the restricted mobility of the membrane integral and peripheral proteins and the potential distribution across the membrane that displays drastic changes in the vicinity of the lipid head groups, giving origin to strong local electric fields.

2.1 Electron transfer chains

Membranes are essential in cells for defining structural and functional features, controlling intracellular conditions and responding to the environment. They permit maintaining the non-equilibrium state that keeps cells alive. Phospholipids are the main components of cell membranes, responsible for the membrane shape and flexibility. They are self-assembled in such a manner that non-polar acyl chains driven by hydrophobic interactions orient themselves towards the center of the membrane, while the polar groups remain exposed to the

solution phase, e.g., the cytoplasm and periplasm. The constituent phospholipids, which are typically asymmetrically distributed along the membrane, differ between cellular and mitochondrial membranes. Similar to smectic liquid crystals, membranes present continuous, ordered and oriented, but inhomogeneous structures (Gennis, 1989; Hianik, 2008).

A large variety of proteins are incorporated into or associated to membranes, including enzymes, transporters, receptors and structural proteins. Enzymes are the most abundant of all membrane proteins. Together with water soluble proteins and lipophilic compounds, membrane-bound enzymes compose ET chains. In eukaryotic organisms the oxidation of nutrients such as glucose and fatty acids produces reduced metabolites, namely NADH and succinate, which upon oxidation deliver electrons through ET chains to molecular oxygen. ET occurs through a series of sequential redox reactions between multisubunit transmembrane complexes (Figure 1), situated in the inner mitochondrial membrane of non-photosynthetic eukaryotic cells, or in the cytoplasmic (cell) membrane of bacteria and archaea. The complexes involved in a canonical respiratory chain are:

- Complex I (NADH : ubiquinone oxidoreductase or NADH dehydrogenase): catalyzes two-electron transfer from NADH to quinone. It is composed of 46 subunits in eukaryotic complexes, but only of 13 to 14 subunits in bacteria, which ensure the minimal functional unit. Electrons enter the enzyme through a non-covalently bound FMN primary acceptor and are then passed to the quinone molecules via several iron-sulfur clusters.
- Complex II (succinate : ubiquinone oxidoreductase or succinate dehydrogenase): couples two electron oxidation of succinate to fumarate with reduction of quinone to ubiquinol, by transferring electrons from a covalently bound FAD, via iron-sulfur clusters to heme group(s) located in the transmembrane part of the complex, and ultimately to the quinones.
- Complex III (ubiquinol : Cyt-c oxidoreductase or bc_1 complex): catalyzes the transfer of two electrons from ubiquinol to two Cyt-c molecules. It is composed of 10 to 11 subunits in mitochondria and 3 subunits in cell membranes of bacteria and archaea, which bear all prosthetic groups: two low-spin hemes b , a Rieske type iron-sulfur cluster and a heme c_1 . The last redox center is located near the docking site of the electron acceptor Cyt-c.
- Complex IV (Cyt-c : oxygen oxidoreductase or Cyt-c oxidase): catalyzes reduction of oxygen to water by utilizing four electrons received from four molecules of Cyt-c, or alternative electron donors present in some bacteria and archaea (see below).

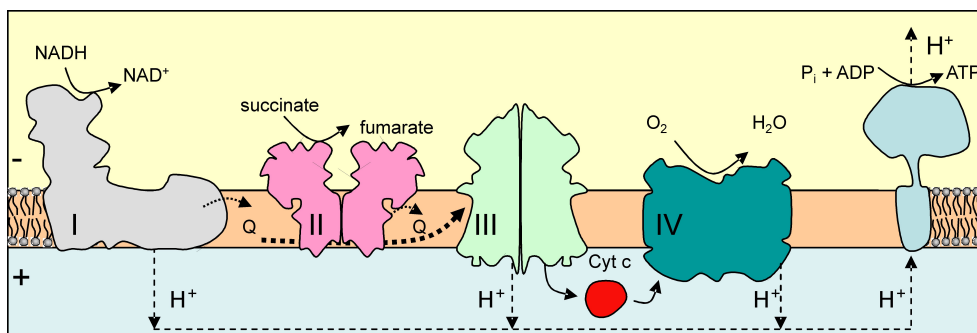


Fig. 1. Schematic representation of the mitochondrial respiratory electron transfer chain. The four complexes (I to IV), and their respective electron transfer reactions are depicted, together with proton fluxes and ATP synthase.

The ET reactions through complexes I, III and IV are coupled to proton translocation across the membrane, contributing to generation and maintenance of a transmembrane electrochemical potential. Protons move back into the mitochondrial matrix (or cytoplasm) through the ATP synthase via an energetically downhill process that provides the energy for the synthesis of ATP.

The eukaryotic photosynthetic ET chain is analogous to the respiratory chain, but structurally and functionally more complex. It is composed of: three multisubunit transmembrane complexes, namely photosystem I, photosystem II and the cytochrome *b₆f* complex, several soluble electron carriers (e.g. plastocyanin and ferredoxin), lipophilic hydrogen carrier plastoquinone, and light harvesting complexes. The trapping of the light by the two reaction centers (photosystem I and II) results in a charge separation across the stroma (thylakoid) membrane and furthermore in oxidation of water to oxygen by photosystem II. The energy produced by this process serves as the driving force for ET which is, as in respiration, coupled to proton translocation across the membrane and, thus, to the synthesis of ATP. In addition to respiratory and photosynthetic redox enzymes, membrane-bound ET chains also include i) cytochrome P450 containing microsomal and ii) mitochondrial adrenal gland cytochrome P450 systems, that carry out catabolic and anabolic reactions, with fatty acid desaturase and cytochromes P450, respectively, as terminal enzymes (Gennis, 1989).

Bacteria and archaea tend to have simpler ET complexes and more versatile respiratory chains in terms of electron donors and terminal electron acceptors that allow for alternative ET pathways and, therefore, ensure adaptation to different external conditions (Pereira and Teixeira, 2004). The gram negative bacterium *E. coli*, for example, lacks complex III. Instead, the terminal oxygen reductase in its respiratory ET chain is a quinol : oxygen oxidoreductase. Moreover, when growing under aerobic conditions, *E. coli* can express different quinol oxidases to accommodate to the external conditions. In addition to terminal oxygen reductases, it can also employ a wide range of terminal electron acceptors besides oxygen, such as nitrite, nitrate, fumarate or DMSO and express other terminal reductases, accordingly. Similarly, soil bacterium *Paracoccus denitrificans* can fine-tune the expression of the appropriate oxygen reductase (*aa₃*, *cbb₃* or *ba₃*), depending on the oxygen pressure levels in the surrounding media. Bacteria and archaea also show a high level of diversity in electron carriers, water soluble proteins (Cyt-c, HiPIP, and Cu proteins like sulfocyanin, plastocyanin and amicyanin) and structurally different lipophilic quinones.

The intricate complexity of ET chains implies that understanding their functioning on a molecular level and identification of the factors that govern electro-ionic energy transduction is virtually impossible, unless simplified biomimetic model systems are utilized. The zero-order approximation usually consists of purification of the individual proteins and their characterization by spectroscopic, electrochemical and other experimental methods (Xavier, 2004; Pitcher and Watmough, 2004). This task can be relatively simple for small soluble proteins but significantly more challenging in the case of membrane complexes, due to the typically quite large number of cofactors. The main concern towards studying the membrane components of the redox chains in solution are related to difficulties in reproducing characteristics of the natural reaction environment, governed by the structural and electrical properties of membranes. First, *mobility* of the proteins is *strongly restricted*. Integral membrane proteins are embedded into the lipid bilayer and stabilized by hydrophobic interactions. Their soluble redox partners either bind to the membrane surface or to the solvent exposed part of

the reaction partner. Second, the transition from the non-polar core to the polar surface of the lipid bilayer implies a substantial *variation of dielectric constants*, which imposes specific boundary conditions for the movement and translocation of charges. Third, different ion concentrations on the two sides of the membrane generate transmembrane potential ($\Delta\phi$), which together with the surface (ϕ_s) and the dipole (ϕ_d) potentials contributes to a complex potential profile across the membrane with particularly sharp changes and thus very *high electric field* strengths (up to 10^9 V/m) in the region of charged lipid head groups (Clarke, 2001) (Figure 2). Electric fields of such magnitude are expected to affect the dynamics of the charge transfer processes and the structures of the proteins, thereby resulting in reaction mechanisms that may differ from those observed in solution.

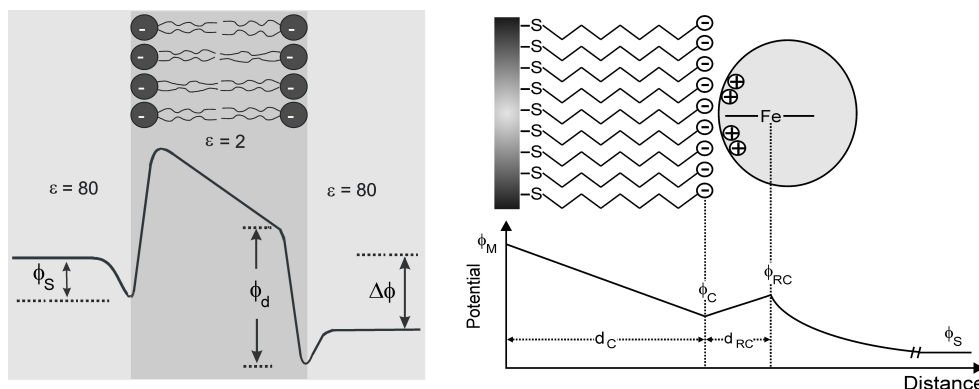


Fig. 2. Schematic representation of the interfacial potential distribution in a lipid bilayer (left) and at a SAM-coated electrode (right).

3. Biocompatible protein immobilization

Immobilization of proteins on solid supports such as electrodes may account for two distinct processes: (i) physical entrapment and (ii) attachment of proteins (Cass, 2007). The former process refers to a thin layer of protein solution trapped by a membrane or a three-dimensional polymer matrix on the solid support, resulting in non-organized and non-oriented protein deposition as, for instance, in sol-gel enzyme electrodes (Gupta and Chaudhury, 2007). The term attachment refers to covalent binding or non-covalent adsorption of the enzyme to the solid surface such as tin, indium and titanium oxide, chemically and electrochemically modified noble metal or carbon electrodes. Adsorption of proteins on bare solid supports often leads to conformational changes or even denaturation. Thus, successful immobilization relies almost exclusively on coated electrodes. Surface coating needs to be well defined in terms of chemical functionalities and physical properties. Self assembled monolayers (SAMs) of alkanethiols are among the most popular biocompatible coatings employed in studies of interfacial interactions for addressing fundamental aspects of heterogeneous ET, but also molecular recognition and cell growth processes, heterogeneous nucleation and crystallization, biomaterial interfaces, etc (Ulman, 2000).

The adsorption of proteins on the conducting, coated surface may be *non-specific* and *non-covalent*, i.e. promoted by electrostatic or van der Waals interactions between the surface functional groups of the modified electrode and amino acid residues of the protein. *Non-covalent* but *specific* interactions, based on molecular recognition, involve affinity coupling between two proteins such as antibody/antigen. This is the most commonly exploited immobilization strategy in the growing field of protein microarrays (Hodneland *et al.*, 2002). Non-covalent and specific interactions also include adsorption of a protein that possesses well defined charged (or hydrophobic) surface patches on a solid surface with opposite charge (or hydrophobic). *Covalent* binding of the protein typically accounts for cross-linking between functional groups of the protein and the surface, using carboxylate, amino or thiol side chains of amino acids on the proteins surface. Specifically, for thiol-based attachments not only natural surface cysteine side chains can be used, but Cys residues can also be introduced at a certain position on the protein surface, in order to control or to modify the attachment site.

Tailoring of novel biocompatible coatings and linkers has been a subject of intense research over the last three decades owing to the importance of protein immobilization under preservation of the native state structure for fundamental and applied purposes. Aiming to the same goal, parallel efforts have been made in the rational design of proteins. Due to the possibility of manipulating DNA sequences and the availability of bacterial expression systems for producing engineered proteins from modified genes, it is now feasible to modify their surface properties in order to promote a particular immobilization strategy (Gilardi, 2004). Such protein modifications may involve introducing of an additional sequence such as a histidine tag, or deleting hydrophobic membrane anchors to produce soluble protein variants.

3.1 Self-assembled monolayers (SAMs) of alkanethiols

Due to the high affinity of thiol groups for noble metals, ω -functionalized alkanethiols spontaneously self-assemble on metal surfaces, forming densely packed monolayers. They are commercially available in a wide variety of functional head groups and chain lengths, allowing fine tailoring of the metal coating by simple immersion of the metal support into a solution of the alkanethiols. A number of physicochemical techniques for surface analysis and spectroscopic characterization of SAMs, such as: Raman spectroscopy, reflectance absorption IR spectroscopy, X-ray photoelectron spectroscopy, high-resolution electron energy loss spectroscopy, near-edge EXAFS, X-ray diffraction, contact-angle goniometry, ellipsometry, surface plasmon resonance, surface scanning microscopy, STM and AFM, as well as electrochemical methods, are nowadays routinely used for probing monolayer assembly, structural properties and stability of SAMs (Love *et al.*, 2005). Several factors influence the stability and structure of SAMs, such as solvent, temperature, immersion time, the purity and chain length of the alkanethiols, as well as the purity and the type of the metal. The fast initial adsorption of the alkanethiol molecules, the kinetics of which is governed by surface-headgroup interactions, is followed by a slower rearrangement process driven by inter-chain interactions. Long alkanethiol molecules ($n > 10$) tend to form more robust SAMs, owing to both, kinetic and thermodynamic factors. The pKa values of acidic or basic ω -functional groups of SAMs differ significantly from those of the amphiphiles in solution. For SAMs with carboxylic head groups the pKa decreases with decreasing chain length. SAMs are electrochemically stable only within a certain range of potentials, which

depends on the chemical composition of the SAM and the type of metal support. Reductive desorption typically occurs at potentials of -1.00 ± 0.25 V (vs. Ag/AgCl). For a more detailed account on the preparation, tailoring, and characterisation of SAM coatings, the reader is referred to specialised reviews (Ulman, 1996; Love *et al.*, 2005).

3.2 Immobilization of soluble proteins

SAMs of alkanethiols provide a biocompatible interface for the immobilization of proteins on metal electrodes allowing for an electrochemical characterization of the protein under preservation of its native structure. These simple systems can be regarded as biomimetic in the sense that they reproduce some basic features of biological interfaces. The appropriate choice of the alkanthiol head group allows in some cases for specific binding of proteins, Figure 3.

Alkanethiols with pyridinyl head groups may replace the axial Met-80 ligand of the heme in mitochondrial Cyt-c to establish a direct link between the redox site and the electrode (Wei *et al.*, 2002; Murgida *et al.*, 2004b; Murgida and Hildebrandt, 2008). Similarly, apo-glucose oxidase (GOx) was successfully immobilized on a flavin (FAD)-modified metal (Xiao *et al.*, 2003). The carboxyl-terminated SAMs can be activated by carbodiimide derivatives for covalent binding of proteins via the NH_2 groups of Lys surface residues. Several enzymes, like GOx, xanthine oxidase, horse-reddish-peroxidase (HRP), were linked to modified carbon electrodes through formation of amide bond. In each case, the amperometric response of these simple bioelectronic devices could be measured upon detection of glucose, xanthine and hydrogen peroxide, respectively (Willner and Katz, 2000). Carboxylate headgroups can also provide negatively charged surfaces for the electrostatic immobilization of proteins with positively charged surface patches, as it is the case of Cyt-c that possesses a ring-shaped arrangement of positively charged lysine residues, naturally designed for interaction with the redox partners (Murgida and Hildebrandt, 2008). By changing the SAM chain length ET rates can be probed as a function of distance (Murgida and Hildebrandt, 2004a; Todorovic *et al.*, 2006). Furthermore, SAMs permit systematic control of the strength of the interfacial electric field. The potential drop across the electrode/SAM/protein interface, and thus the electric field strength experienced by the immobilized protein, can be described based on a simple electrostatic model (Figure 2) as a function of experimentally accessible parameters. Within this model, the electric field strength E_F at the protein binding site can be described in terms of the charge densities at the SAM surface (σ_c) and at the redox site (σ_{RC}) as well as of the potential drop at the redox site ($E_{RC} = E_{\text{ads}}^0 - E_{\text{sol}}^0$), which increases with the SAM thickness d_C (Equation 1) (Murgida and Hildebrandt, 2001a):

$$E_F(d_C) = \frac{\varepsilon_0 \varepsilon_S \kappa E_{RC} - \sigma_C - \sigma_{RC}}{\varepsilon_0 \varepsilon_C} \quad (1)$$

where E_{ads}^0 and E_{sol}^0 are the apparent standard reduction potentials of the protein in the adsorbed state and in solution, respectively, κ is the inverse Debye length, and ε_s and ε_c denote the dielectric constants of the solution and the SAM, respectively. For carboxylate-terminated SAMs, the electric field strength at the Cyt-c binding site is in the order of 10^9 V m^{-1} , which is comparable to the upper values estimated for biological membranes in the

vicinity of charged lipid head groups. Higher field strengths are predicted for phosphonate-terminated SAMs and sulfate monolayers for which $|\sigma_c|$ is distinctly larger. The charge density of the SAM is defined by the pK_a of the acidic head groups in the assembly, which increases with the number of methylene groups, and by the pH of the solution. Thus, the electric field strength at the protein binding site can be varied within the range ca. 10^8 - 10^9 V m^{-1} by changing the length of the alkanethiols without modifying any other parameter. The strength of the E_F can also be controlled via the electrode potential and the nature of the SAM head group, as well as via the pH and ionic strength of the solution (Murgida and Hildebrandt, 2001a; Murgida and Hildebrandt, 2001b; Murgida and Hildebrandt, 2002; Murgida and Hildebrandt, 2008).

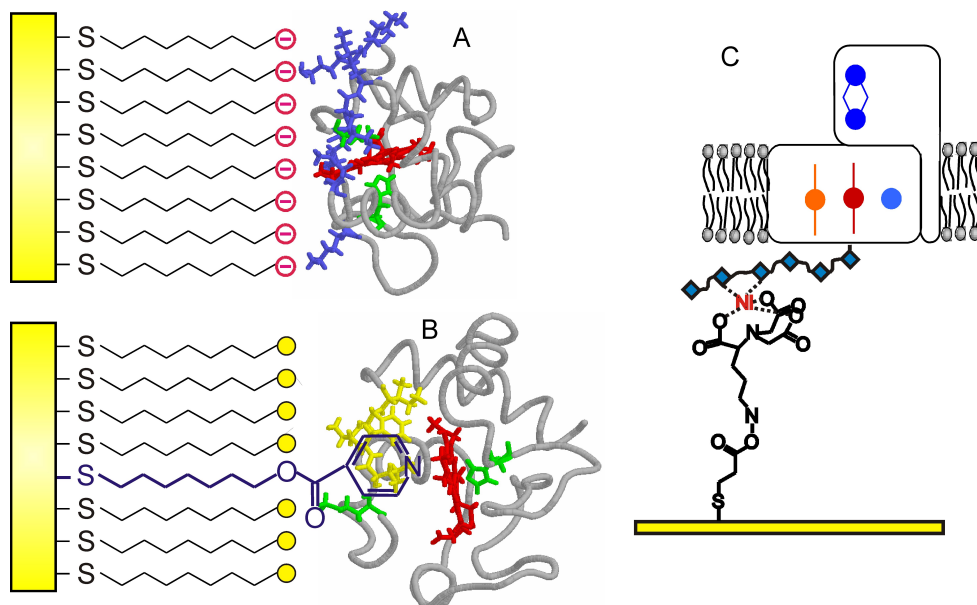


Fig. 3. Schematic representation of some strategies for biocompatible protein binding to metal electrodes: A) electrostatic binding of Cyt-c to a COOH-terminated SAM; B) coordinative binding of Cyt-c to a Py-terminated SAM; C) specific binding of a His-tagged CcO to a Ni-NTA coated electrode.

SAMs can also be formed by hydroxyl-, amino- and methyl-terminated alkanethiols. Hydroxyl-terminated alkanethiols favour polar interactions but may also allow for covalent immobilization (via chlorotriazines and Tyr or Lys amino acid residues) as shown for GOx, ferritin and urease (Willner *et al.*, 2000). Amino-terminated alkanethiols can provide positively charged surfaces for electrostatic binding of proteins rich in surface exposed carboxylic side chains of Asp and Glu, or for cross-linking upon activation of carboxylic groups of the protein (Willner *et al.*, 2000). Methyl-terminated alkanethiols are suitable for immobilization of proteins via hydrophobic interactions (Rivas *et al.*, 2002; Murgida and Hildebrandt, 2008). 'Mixed' monolayers prepared from alkanethiols with different head-groups in variable molar ratios, provide a surface engineered with gradients of charge,

capable of accommodating proteins with less well defined (or 'diluted') surface charge distribution via the interplay of different interactions. Mixed SAMs of carboxyl and methyl-terminated alkanethiols were used for HRP immobilization (Hasunuma *et al.*, 2004), while hydroxyl/methyl-terminated SAMs provided the best coating for immobilization of genetically manipulated soluble subunits of *caa₃*, *cbb₃*, and *ba₃* oxygen reductases, as well as some soluble heme proteins (Ledesma *et al.*, 2007; Kranich *et al.*, 2009). Moreover, the use of mixture of alkanethiols of different chain lengths (and headgroups) may fulfil specific steric requirements of the adsorbate. This strategy has been successfully employed for characterizing the interfacial enzymatic reaction of cutinase by electrochemical methods (Nayak *et al.*, 2007). Other possibilities include mixed SAMs composed of glycol-terminated and biological-ligand-terminated alkanethiols, which appear to be a surface of choice for immobilization of a variety of biomolecules including DNA, carbohydrates, antibodies, and whole bacterial cells that are particularly important for the design and construction of affinity immunosensors (Clarke, 2001; Love *et al.*, 2005; Collier and Mrksich, 2006).

3.3 Immobilization of membrane proteins

Membrane proteins are partially or fully integrated into the lipid bilayer, requiring, therefore, a hydrophobic environment to maintain the native structure and avoid aggregation upon isolation. Besides, they are large, typically composed of several subunits that are often prone to dissociation during the purification process. The structural and functional integrity of the proteins in the solubilized form sensitively depends on the type of detergent used to provide a hydrophobic environment *in vitro*.

Several models for physiological membranes that display different levels of complexity have been developed, including Langmuir-Blodgett (LB) lipid monolayer films (He *et al.*, 1999), bilayer lipid films and liposomes (Hianik, 2008). Protein containing lipid monolayer films formed on solid supports are frequently used for the construction of biosensors. Phospholipid bilayers can be produced in a controllable manner, with tunable thickness, surface tension, specific and electrical capacity. They are the most suitable systems for studies of membrane pores and channels. Liposomes are closed bilayer systems that can be formed spontaneously either from bacterial cell (or mitochondrial) membrane fractions containing the incorporated proteins, or from phospholipids subsequently modified by proteins. They are considered to be good model membranes in studies of transmembrane enzymes involved in coupled reactions on opposite sides of the membrane, as well as proteins involved in solute transport or substrate channeling (Gennis, 1989).

Immobilization strategies for ET membrane proteins have been developed particularly in studies of terminal oxygen reductases. In the simplest approach a detergent-solubilized protein is spontaneously adsorbed on a metal surface. Most likely, immobilization takes place via interactions of the detergent molecules with the layer of specifically adsorbed anions that the metal surface carries above the potential of zero-charge. In fact, the detergent n-dodecyl- β -D-maltoside, commonly used for solubilization of membrane proteins, has been shown to adsorb to these surfaces, providing a biocompatible interface for subsequent protein adsorption under preservation of its structural and functional integrity (Todorovic *et al.*, 2005). This finding is in contrast to the behavior observed for soluble proteins for which the direct adsorption on a bare metal, in the absence of detergent, may cause a (partial) degradation (Murgida and Hildebrandt, 2005). Mixed SAMs composed of CH₃ and OH terminated alkanethiols were shown to be a promising choice for immobilization of

detergent-solubilized membrane proteins, such as complex II from *R. marinus* (unpublished data). Direct adsorption of solubilized membrane proteins, however, cannot guarantee a uniform orientation of the immobilized enzyme. In an attempt to overcome this problem, a preformed detergent solubilized Cyt-c/CcO complex was immobilized on Au electrodes coated with hydroxyl-terminated alkanethiols at low ionic strength. It was studied by electrochemical methods, which however, do not permit unambiguous conclusions regarding the enzyme structure and orientation in the immobilized state (Haas *et al.*, 2001). A similar approach was applied to a fumarate reductase immobilized on Au electrode with hydrophobic coating (Kinnear and Monbouquette, 1993).

An alternative immobilization method has been developed for proteins that contain a genetically introduced His tag (Friedrich *et al.*, 2004; Ataka *et al.*, 2004; Giess *et al.*, 2004; Hrabakova *et al.*, 2006; Todorovic *et al.*, 2008). After functionalizing the solid support with Ni (or Zn) NTA (3,3'-dithiobis[N-(5-amino-5-carboxy-pentyl)propionamide-N, N'-diacetic acid]) dihydrochloride) monolayer, the protein can be attached via His coordination to the Ni center, Figure 3C. The high affinity of the His tag, inserted into the protein sequence either at N or C terminus, towards Ni-NTA assures large surface coverage of uniformly oriented protein molecules even at relatively high, physiologically relevant ionic strengths. The last immobilization step is the reconstitution of a lipid bilayer from 1,2-diphytanoyl-*sn*-glycero-3-phosphocholine and the removal of the detergent using biobeads. This method was recently employed for immobilization of several oxygen reductases on Au and Ag electrodes. Different steps of the assembly were demonstrated by SEIRA spectroscopy and atomic-force microscopy, providing the evidence for the formation of the lipid bilayer. Moreover, separations of the redox centers from the metal surface in the final biomimetic construct are yet not too large for applying surface enhanced vibrational spectroscopies (Friedrich *et al.*, 2004).

4. Methods for probing the structure and dynamics of immobilized proteins: vibrational spectroscopy

It is clear that the development of novel protein-based bioelectronic devices for basic and applied purposes heavily relies upon design of new biomimetic or biocompatible materials. However, it also requires appropriate experimental approaches capable of monitoring *in situ* the structure and reaction dynamics of the immobilized enzymes under working conditions. These information are crucial for understanding and eventually improving the performance of protein-based devices.

Here we will describe basic principles of SERR and SEIRA spectroelectrochemical techniques, which are among the most powerful approaches for characterization of thermodynamic, kinetic and structural aspects of immobilized redox proteins.

4.1 (Resonance) Raman and infrared spectroscopies

Raman and IR spectroscopies probe vibrational levels of a molecule, providing information on molecular structures. A vibrational mode of a molecule will be Raman active only if the incident light causes a change of its polarizability, while IR active modes require a change in dipole moment upon absorption of light. For molecules of high symmetry, these selection rules allow grouping the vibrational modes into Raman- or / and IR-active or -forbidden modes. Water gives rise to strong IR bands including the stretching and bending modes at

ca. 3400 and 1630 cm^{-1} , respectively. The bending mode represents a major difficulty in studying biological samples due to overlapping with the amide I band in the spectra of proteins (see below). In IR transmission measurements, therefore, cuvettes of very small optical paths (a few micrometers) and very high protein concentrations have to be employed. The attenuated total reflection (ATR) technique allows bypassing the problems associated with water, facilitating the studies of protein/substrate or protein/ligand interactions, and enhancing the overall sensitivity. In Raman spectroscopy water is not an obstacle at room temperature, although ice lattice modes become visible in the low frequency region in cryogenic measurements. A severe drawback of Raman spectroscopy is its low sensitivity, due to the low quantum yield of the scattering process ($< 10^{-9}$). This disadvantage can be overcome for molecules that possess chromophoric cofactors, such as metalloproteins. When the energy of the incident laser light is in resonance with an electronic transition of the chromophore, the quantum yield of the scattering process becomes several orders of magnitude higher for the vibrational modes originating from the chromophore. Thus, the sensitivity and the selectivity of Raman spectroscopy (i.e., resonance Raman – RR) are strongly increased and the resultant spectra display only the vibrational modes of the cofactor, regardless of the size of the protein matrix (Siebert and Hildebrandt, 2008).

In the last decades RR spectroscopy was proved to be indispensable in the studies of heme proteins. RR spectra obtained upon excitation into the Soret band of the porphyrin display ‘so-called’ core-size marker bands sensitive to the redox and spin state and coordination pattern of the heme iron in the 1300 – 1700 cm^{-1} region (Hu *et al.*, 1993; Spiro and Czernuszewicz, 1995; Siebert and Hildebrandt, 2008). For instance, transition from a ferric to a ferrous heme is associated with a ca. 10 cm^{-1} downshift of most of the marker bands (particularly ν_3 and ν_4). The conversion from a six-coordinated low spin (6cLS) heme to a five-coordinated high spin (5cHS) heme also causes a downshift of some bands (ν_3 and ν_2). These and further empirical relationships derived from a large experimental data basis provide valuable tools for elucidating structural details of the heme site and for monitoring ET and enzymatic processes, as shown for a variety of heme proteins including hemoglobin, myoglobin, cytochromes, peroxidases and oxygen reductases (Spiro and Czernuszewicz, 1995; Siebert and Hildebrandt, 2008).

IR spectra provide information on the secondary structure of proteins based on the analysis of the amide I (1600 – 1700 cm^{-1}) and amide II (1480 – 1580 cm^{-1}) bands. The sensitivity and selectivity of IR spectroscopy can be greatly improved upon operating in difference mode. Difference IR spectra obtained from two states of a protein only display those bands that undergo a change upon transition from one state to the other, thereby substantially simplifying the analysis (Ataka and Heberle, 2007). IR difference spectroscopy is a sensitive method for investigating structural changes of proteins that (i) accompany the redox reaction, (ii) are induced by substrate binding during the catalytic cycle, (iii) occur during protein folding and unfolding, or (iv) accompany photo-induced processes (Siebert and Hildebrandt, 2008).

4.2 Surface Enhanced resonance Raman (SERR) and surface enhanced IR (SEIRA) spectroscopy

Surface enhanced Raman (SER) spectroscopy is based on the increase of the signal intensity associated with vibrational transitions of molecules situated in close proximity to nanoscopic metal structures. Two distinct enhancement mechanisms have been identified. The chemical mechanism originates from charge transfer interactions between the metal substrate and the adsorbate, and provides a weak enhancement solely for the molecules in direct contact with the metal. The electromagnetic mechanism is based on the amplified electromagnetic fields generated upon excitation of the localized surface plasmons of nanostructured metals. It does not require specific substrate/adsorbate contacts and provides the main contribution to the overall enhancement. Among different metals tested as SER substrates, Ag affords the strongest electromagnetic enhancements, due to surface plasmon resonance in a wide spectral range from the near UV to the IR region. A drawback, however, is that Ag nanostructures are less stable and chemically less inert than their Au counterparts. In addition, the low oxidation potential of Ag narrows the range of applicable potentials in SER-based spectro-electrochemical experiments. For these reasons most efforts in recent years have been devoted to the development of Au SER substrates, including SER-active electrodes. The attractiveness of the unsurpassed sensitivity of Ag has also driven significant efforts towards use of this metal and hybrid Ag/Au structures. To this end, a large number of highly regular and reproducible Au and Ag SER substrates have been reported, making use of spheres, tubes, rods, thorns, cavities and wires as building blocks (Mahajan *et al.*, 2007; Murgida and Hildebrandt, 2008; Lal *et al.*, 2008; Banholzer *et al.*, 2008; Brown and Milton, 2008; Feng *et al.*, 2008a; Feng *et al.*, 2009).

If the excitation laser is in resonance not only with the energy of surface plasmons of the metal but also with the electronic transition of the immobilized molecule, the SER and RR effects combine. The resulting SERR spectra display exclusively the vibrational bands of the chromophore of the adsorbed species. The use of Ag as SER-active substrate is particularly suited for studying porphyrins and heme proteins since these molecules exhibit a strong electronic transition at ca. 410 nm (Soret band) and a weaker one at ca. 550 nm which both coincide with Ag (but not with Au) surface plasmon resonances. SERR spectra of heme proteins reveal the same information as RR spectra, such as the oxidation, spin, and coordination states of the heme group, and in addition their changes as a consequence of variations of the electrode potential (see below) (Siebert and Hildebrandt, 2008).

Molecules adsorbed in the vicinity of nanostructured metal surfaces, such as Ag or Au islands deposited on inert ATR crystals, experience enhanced absorption of IR radiation, which is the basis for (ATR) SEIRA spectroscopy. SEIRA spectroscopy has been successfully employed to probe the structure of immobilized biomolecules including redox proteins and enzymes (Ataka and Heberle, 2007). The enhancement of the IR bands does not exceed two orders of magnitude and therefore is smaller than the enhancement of the SERR bands which may be larger than 10^5 . The distance-dependent decay of the enhancement factor is less pronounced for SEIRA than for SERR spectroscopy, and both techniques can successfully probe molecules separated from the surface by up to 5 nm.

The nanostructured metal substrate that amplifies the signals can also serve as a working electrode in spectroelectrochemical studies. Indeed, potentiometric titrations followed by SERR and SEIRA have provided important insights into the mechanism of functioning of

several heme proteins immobilized on biocompatible metal electrodes (Murgida and Hildebrandt, 2004a; Murgida and Hildebrandt, 2005; Murgida and Hildebrandt, 2008). Both SERR and SEIRA can be employed in the time resolved (TR) mode that enables probing of dynamics of immobilized proteins. The method requires a synchronization of a perturbation event with the spectroscopic detection at variable delay times. For TR-SEIRA spectroscopy acquisition is usually performed in the rapid or step scan mode for probing events in time windows longer or shorter than 10 ms, respectively. For the study of potential dependent processes of immobilized redox proteins by TR-SERR, the equilibrium of the immobilized species is perturbed by a rapid potential jump, and the subsequent relaxation process is then monitored at different delay times. A prerequisite for applying of TR-SERR is that the underlying ET processes are fully reversible. The time resolution depends on the charge reorganization of the double layer of the working electrode and is typically on a microsecond scale (Murgida and Hildebrandt, 2004a; Murgida and Hildebrandt, 2005; Murgida and Hildebrandt 2008).

5. Recent developments in the characterization of immobilized redox proteins

In this section we will focus on selected examples of surface enhanced spectroelectrochemical characterization of ET proteins immobilized on nanostructured electrodes coated with biomimetic films. The first part is dedicated to membrane oxygen reductases whose structural, functional and spectroscopic complexity imposes some serious limits to other experimental approaches. In the second part we will describe recent studies on soluble electron carrier proteins, mainly cytochromes.

5.1 Membrane proteins: oxygen reductases

Terminal oxygen reductases are the final complexes in aerobic respiratory chains that couple the four-electron reduction of molecular oxygen to water with proton translocation across the membrane (vide supra). Intense research efforts have been made in the past decades to elucidate the mechanism of the molecular functioning of these enzymes. Although substantial progress has been made, for instance, in determining their three-dimensional structures, the coupling between the redox processes and proton translocation is not yet well understood (Garcia-Horsman *et al.*, 1994; Pereira and Teixeira, 2004). Most of the terminal oxidases are members of the heme - copper superfamily that can be classified into several families, based on amino acid sequences and intraprotein proton channels. The members of the family A are mitochondrial-like, possessing amino acid residues that compose D and K channels, the B-type enzymes have an alternative K channel, while members of the C family possess only a part of the alternative K channel. Oxygen reductases from bacteria and archaea reveal different subunit and heme-type compositions (Figure 4); they are simpler than the eukaryotic ones while maintaining the same functionality and efficiency. The mitochondrial Cyt-c oxidase (CcO) possesses 13 subunits, while the bacterial heme - copper oxidases, that are also efficient and functional proton pumps, contain three to four (Gennis, 1989; Garcia-Horsman *et al.*, 1994; Pereira and Teixeira, 2004). Investigating the catalytic reaction of bacterial complexes is therefore fundamental as the obtained insights can be extrapolated to the eukaryotic ones. A prerequisite for understanding the mechanism of functioning of these enzymes that contain multiple redox centers is determination of the individual midpoint redox potentials of the cofactors under conditions that reproduce some

basic features of the physiological environment. Published redox properties of oxygen reductases are typically determined from solution studies and are often contradictory regarding both the values and the interpretation (Todorovic *et al.*, 2005; Veríssimo *et al.*, 2007). In this respect, the use of SERR spectroelectrochemical titrations has been proven to be a valuable tool.

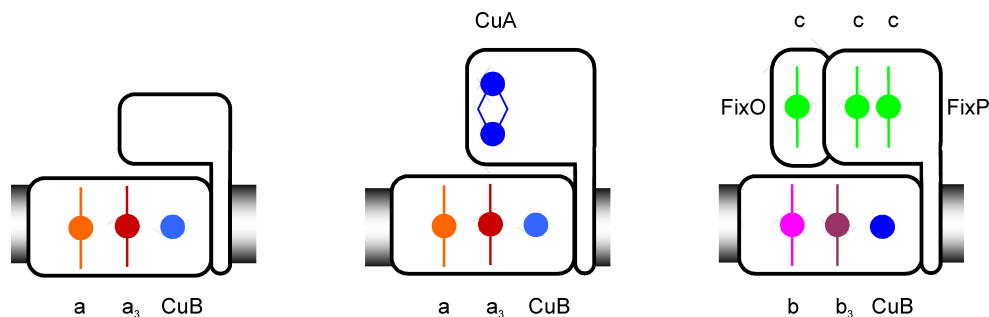


Fig. 4. Schematic representation of several oxygen reductases. A) aa_3 quinol oxidase; B) aa_3 cytochrome c oxidase; C) cbb_3 oxygen reductase. The LS hemes in the respective catalytic subunits are depicted in orange (heme a) and pink (heme b), the HS hemes are in red (a_3) and purple (b_3), the LS hemes c in FixO and FixP subunits of the cbb_3 are shown in green, and copper centers (dinuclear Cu_A and Cu_B), in blue.

aa₃ quinol oxidase (QO): The aa_3 oxygen reductase from the thermophilic archaeon *Acidianus ambivalens* receives electrons directly from the membrane quinone pool, being therefore a quinol oxidase. It is a type B oxygen reductase that in the catalytic subunit houses two heme groups, the low-spin (LS) heme a , and the high spin (HS) heme a_3 coupled to Cu_B in the catalytic (oxygen binding) center (Figure 4A). The two hemes display different RR spectral fingerprints. Detergent solubilized QO was directly adsorbed on a bare nanostructured Ag electrode and investigated by potential-dependent SERR (Todorovic *et al.*, 2005). Adsorption of the protein to the hydrophilic surface of the phosphate-coated electrode occurred without displacement of the detergent molecules, which therefore provided a biocompatible interface. This conclusion was supported by the detection of a SER signal at 2950 cm⁻¹ from the Ag electrode immersed into the protein-free buffer solution, that was attributed to the C-H stretching mode of dodecyl-maltoside. The protein retained its native structure upon immobilization as confirmed by the comparison of the RR and SERR spectra of QO in solution and in the adsorbed state (Figure 5A). Namely, all vibrational bands present in the RR spectra that were assigned to skeletal vibrations and stretching modes of the vinyl and formyl substituents of hemes a and a_3 were identified in the SERR spectra of the immobilized QO. Variations of the band intensities between the SERR and RR spectra originate from the orientation-dependence of the SERR effect, which causes different enhancements of vibrational modes of HS vs. LS hemes, but also of modes of the same heme that have different symmetry (see 5.2). The spectra of immobilized QO, measured at a series of electrode potentials, were subsequently subjected to component analysis. At intermediate potentials, over forty modes could be identified in the high frequency region of the spectra, originating from the two heme groups in two redox states. In order to simplify the analysis and to avoid uncertainties caused by the overlapping of some modes, the quantitative

spectral analysis was based on two modes, the ν_3 and $\nu_{C=O}$ that are unambiguous indicators of the redox and spin states of the two hemes. Simplified component spectra, based only on these modes of each heme group in each redox state, were constructed and used in a global fit to all experimental SERR spectra by varying the relative contributions of the individual component spectra (Figure 5B). After conversion of spectral contributions into relative concentrations, the redox potentials of the two heme sites in QO were determined. The corresponding Nernst plots display a linear behavior that reveals one-electron transfer processes, indicating, furthermore that the two hemes can be treated as independent redox couples with no significant interaction potential.

The results of the study point to a substantially different mechanistic scheme for the energy transduction in QO. The two redox centers, hemes a and a_3 are uncoupled and exhibit reversed midpoint potentials with respect to the type A enzymes. In both cases the free energy, provided by downhill ET reactions, is utilized for vectorial proton transport. However, for the type A enzymes the exergonicity of the ET cascade requires a sophisticated network of cooperativities. In contrast, downhill ET in QO is already guaranteed by the inversion of the intrinsic midpoint potentials of hemes a and a_3 such that a modulation by cooperativity effects is not required. Moreover, SERR experiments indicate that redox-linked, electric-field-modulated conformational transitions of the heme a_3 that are relevant for proton translocation, were blocked in the immobilized, but not in solubilized QO (Das *et al.*, 1999), suggesting furthermore that, when the membrane potential generated by the proton pumping activity of QO becomes sufficiently large, the resultant electric field is capable of blocking the elementary steps of proton translocation. This finding has been interpreted in terms of a self-regulation mechanism of the proton pumping activity of the QO (Todorovic *et al.*, 2005).

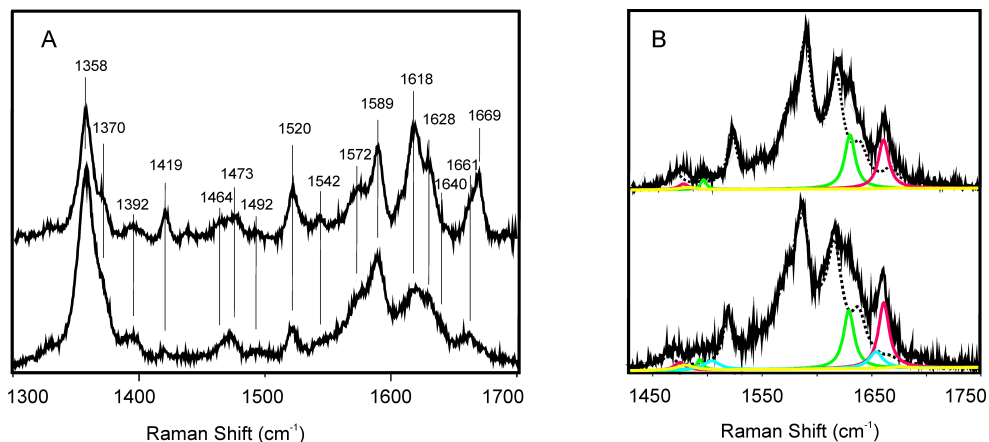


Fig. 5. RR and SERR spectra of the aa_3 QO. A) high frequency region spectra of reduced QO: RR of solubilized (upper trace) and SERR of immobilized (lower trace) protein; B) SERR spectra of the QO at -3 mV (upper trace) and at +297 mV (lower trace). Vibrational modes of the heme a are indicated in green (ferrous) and blue (ferric); modes of the heme a_3 are shown in red (ferrous) and yellow (ferric); dotted line represents the envelope that includes all non-assigned bands, black line shows experimental and overall simulated spectra.

aa₃ cytochrome c oxidase: The CcO from *Rhodobacter sphaeroides* is a member of the type A family of heme copper oxygen reductases that houses three redox centers in the catalytic subunit (subunit I) and a dinuclear copper Cu_A in the subunit II (Figure 4B). It is purified from an organism that is capable of growing heterotrophically via fermentation and aerobic and anaerobic respiration, with a genetically introduced His-tag, allowing immobilization of the CcO on a metal electrode via Ni-NTA SAMs, Figure 3C (Friedrich *et al.*, 2004; Ataka *et al.*, 2004; Giess *et al.*, 2004; Hrabakova *et al.*, 2006; Todorovic *et al.*, 2008). The protein was specifically attached, uniformly oriented and catalytically active in the biomimetic construct. The orientation of the attached protein could be controlled since the His-tag was introduced into the amino acid sequence of *R. sphaeroides* enzyme either on the C-terminus of subunit I or on the C-terminus of subunit II. Therefore, the domain that interacts with the physiological electron donor, Cyt-c, identified to be composed of residues Glu148, Glu157, Asp195, and Asp214 in subunit II, was either exposed to the solution, or was facing the metal surface (Ataka *et al.*, 2004). Catalytic currents could be measured under aerobic conditions when the Cyt-c / CcO complex was allowed to form. Proton pumping activity was also functional in the construct, as suggested by electrochemical impedance spectroscopy. SERR spectroscopic studies revealed heterogeneous ET to the heme *a*, which was selectively reduced while the heme *a₃* remained oxidized, even at the most negative electrode potentials. The ET between the two hemes is fast in solution, indicating some alterations of the intramolecular ET in immobilized CcO, possibly due to electric field dependent perturbation of internal proton translocation steps (Hrabakova *et al.*, 2006).

cbb₃ oxygen reductase: The *Bradyrhizobium japonicum cbb₃* oxidase is a type C oxygen reductase that contains three major subunits: a membrane integral subunit I (FixN), which houses a LS heme *b* and the catalytic center (HS heme *b₃* - Cu_B), and subunits II (FixO) and III (FixP), containing one (His-Met coordinated) and two (bis His and His-Met coordinated) LS hemes *c*, respectively (Figure 4C). The *cbb₃* oxygen reductases are expressed in various bacteria under microaerobic conditions and exhibit several unique characteristics (Sharma *et al.*, 2006). Phylogenetically, they are the most distant and the least understood members of the heme-copper oxygen reductase superfamily (Pereira and Teixeira, 2004; Pitcher and Watmough, 2004; Sharma *et al.*, 2006). The *cbb₃* oxygen reductases lack the Cu_A electron entry site (Garcia-Horsman *et al.*, 1994) and the highly conserved tyrosine residue covalently bound to the histidyl Cu_B ligand. Furthermore, many of the amino acid residues involved in proton conduction through the D- and K- channels of the A-type enzymes are absent in *cbb₃* oxygen reductases. These enzymes exhibit the highest NO reductase activity among the members of the superfamily (Forte *et al.*, 2001; Pitcher and Watmough, 2004; Verissimo *et al.*, 2007). The *cbb₃* oxygen reductase from *B. japonicum* possesses a genetically introduced His tag on the C-terminus of subunit I, i.e. on the cytoplasmic side. As in the previous example, it was immobilized on Ag (and Au) electrode coated with a (Ni-NTA) SAM, embedded into a reconstituted phospholipid bilayer, Figure 3C, and studied by surface-enhanced vibrational spectroscopy and cyclic voltammetry (Figure 6) (Todorovic *et al.*, 2008).

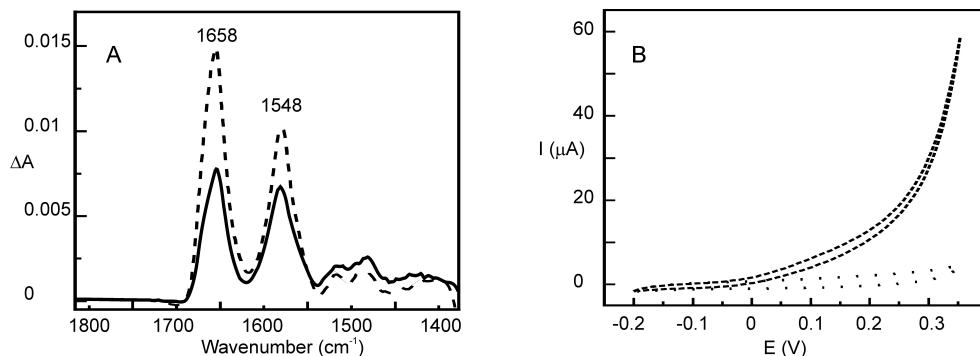


Fig. 6. Immobilized *cbb3* oxygen reductase. A) SEIRA spectra of the *cbb3* immobilized via His-tag/Ni-NTA (dashed line) and detergent coated electrode (solid line); B) cyclic voltammetry of the *cbb3* embedded into biomimetic construct in the presence (dashed line) and absence (dotted line) of electron donor.

SEIRA spectra of the immobilized *cbb3* are dominated by the amide I and II modes (Figure 6A). For membrane proteins with a high content of preferentially parallel helices such as the subunit I of *cbb3* (Zufferey *et al.*, 1998; Pitcher and Watmough, 2004), SEIRA spectra are sensitive to the orientation of the helices with respect to the electrode surface, which is reflected in the intensity ratio of amide I and amide II bands. The amide I mode, that is mainly composed by the C=O stretching coordinates of the peptide bonds, is associated with dipole moment changes parallel to the axis of the helices, such that it gains surface enhancement when the C=O groups, and thus the helices, are oriented perpendicular to the surface. Conversely, the dipole moment changes of the amide II mode that is mainly composed of N-H in-plane bending and C-N stretching coordinates, are perpendicular to the helix axis and therefore gain a weaker enhancement for helices oriented in an upright position (Marsh *et al.*, 2000). In the SEIRA spectrum of *cbb3* the amide I is observed at 1658 cm^{-1} , a characteristic position for a largely α -helical peptide. Its intensity is distinctly higher than that of the amide II (1548 cm^{-1}), which is consistent with a largely perpendicular orientation of the helices with respect to the electrode surface. A more random orientation of the enzyme is obtained upon non-specific adsorption of the solubilized *cbb3* on a detergent-coated electrode as reflected by a ca. two times weaker amide I band and a 1.5 times lower amide I / amide II intensity ratio, as compared with the His-tag bound *cbb3* (Figure 6A) (Todorovic *et al.*, 2008). The oxygen reductase catalytic activity of the immobilized *cbb3* was controlled *in situ* by cyclic voltammetry. As shown in Figure 6B, large electrocatalytic currents are observed under aerobic conditions in the presence of the electron donor, while only capacitive currents were observed in its absence.

Unlike the *aa3* QO and CcO, the *cbb3* oxygen reductase possesses five heme groups, three of which are 6cLS c-type hemes that are spectroscopically indistinguishable. Moreover, four out of five hemes are LS, displaying higher Raman cross sections, and therefore partially obscuring the spectroscopic features of catalytic HS heme *b3*. Reliable component analysis of the SERR spectra was further aggravated by the high photoreducibility of the enzyme. Therefore, in order to facilitate the assignment of individual redox transitions to each heme group of the pentahemic *cbb3*, the individual FixO and FixP subunits (Figure 4C) were

overexpressed in *E. coli* with their transmembrane domain truncated, purified in soluble form, and characterized by SERR spectroelectrochemistry. Upon combining the SERR-spectroelectrochemical data for the subunits and for the integral enzyme, it was possible to provide a consistent analysis of redox potentials of the individual cofactors in the *cbb*₃ oxidase. On the basis of these findings, a sequence of ET events in the *cbb*₃ enzyme was postulated. The Met/His heme *c* of either the FixO or FixP subunit, which exhibit the lowest redox potentials, serves as the electron entry site of the complex. According to the order of redox potentials, the subsequent electron acceptor was identified as the bis-His heme *c* in the FixP or/and the HS heme *b* in the catalytic subunit, and the final one is the heme *b*₃ (Todorovic, *et al.*, 2008). The obtained data also shed light on a controversially discussed role of the FixP subunit in *cbb*₃ oxygen reductases. The values of redox potentials obtained by SERR potentiometric titration reveal that the presence of FixP can be considered as redundant in the ET pathway. Rather, it can be associated with oxygen sensing properties, as also suggested for the *cbb*₃ enzyme from *P. stutzeri* (Pitcher and Watmough, 2004b).

5.2 Soluble proteins

As discussed in previous sections, small soluble redox proteins that transport electrons between different membrane-bound complexes along biological ET chains are exposed to relatively intense electric fields which may have a substantial impact on their structure and function. Among these electron shuttles, cytochromes and particularly Cyt-*c*, constitute the best studied examples. Electric field effects on the structure, thermodynamics and reaction dynamics of cytochromes have been extensively investigated using Ag electrodes coated with SAMs of ω -substituted alkanethiols as biomimetic interfaces that allow a systematic variation of the field strength (see 3.2).

Electric field effects on redox potential. Among other parameters, electric fields of biologically relevant magnitude may affect the most fundamental thermodynamic property of a redox protein, i.e. its reduction potential. This has been shown by potential-dependent SERR spectroscopy for the soluble tetraheme protein cytochrome *c*₃ (Cyt-*c*₃) (Rivas *et al.*, 2005). Electrostatic adsorption of Cyt-*c*₃ on Ag electrodes coated with mercaptoundecanoic acid occurs without significant structural alterations at the level of the heme groups. SERR potentiometric titrations, however, indicate that the redox potentials of the four hemes are significantly downshifted with respect to their values in solution, to such an extent that the order of reduction is actually reversed. The experimental results, that were in excellent agreement with electrostatic calculations, revealed that electric fields tend to downshift the redox potentials by stabilizing the ferric form. This effect is partially compensated by the low dielectric constant of the SAM which shifts the redox potentials in the opposite direction. Indeed, the resulting downshift was more pronounced for the hemes that are closer to the interface, i.e. under the influence of higher electric fields.

A similar interplay of different effects on the redox potential has been observed for cytochrome P450 from *P. putida* immobilized on coated Ag electrodes, although in this case the adsorbed protein was almost quantitatively converted into the P420 form as judged from the SERR spectra (Todorovic *et al.*, 2006). In contrast, electrostatic adsorption of Cyt-*c* on similar coatings does not appear to have any significant effect on the redox potential but may have distinct structural implications (Murgida and Hildebrandt, 2001a; Murgida and Hildebrandt, 2004a).

Electric field effects on protein structure and function. It has been established, using RR and SERR spectroscopy, that the electrostatic interaction of the positively charged Cyt-c with negatively charged model systems, such as phospholipid vesicles, (Droghetti *et al.*, 2006), polyelectrolytes (Weidinger *et al.*, 2006), or the binding domain of the natural reaction partner CcO, may promote the formation of the conformational state of mitochondrial Cyt-c (denoted as B2), in which the axial Met80 ligand is removed from the heme iron. At physiological pH, this coordination site may remain vacant, resulting in 5cHS Cyt-c, or may be occupied by a His residue (most likely His26 or His33). The disruption of the Fe-Met80 bond significantly alters the properties of Cyt-c. On the one hand, the B2 state has a reduction potential which is more than 300 mV lower than that of the native protein (denoted as state B1) as determined by potential-dependent SERR spectroscopy (Murgida and Hildebrandt, 2004a). On the other hand, the B2 state shows a substantial increase of peroxidase activity by allowing the access for hydrogen peroxide to the heme iron (Kagan *et al.*, 2005; Godoy *et al.*, 2009). Thus, *in vivo* the B1 to B2 transition would have profound physiological consequences since the B2 state cannot accept electrons from complex III but is capable of catalyzing the peroxidation of cardiolipin, the main charged lipid component of the inner mitochondrial membrane (Kagan *et al.*, 2009). Degradation of cardiolipin increases the permeability of the membrane, thus facilitating the transfer of Cyt-c to the cytosol where it binds to Apaf-1, in one of the initial events of the cell apoptosis. Thus, it is likely that the switch from the "normal" redox function of Cyt-c (B1 state) to the apoptotic function (B2 state) depends on the local electric field which is, in turn, modulated by the membrane potential. To check this hypothesis the structure of Cyt-c electrostatically bound to electrodes coated with anionic SAMs was investigated. Variation of the electrode potential and of the charge density on the film surface shows that the equilibrium between the B1 and B2 states of the protein is shifted towards B2 upon raising the electric field strength at the interface of the biomimetic construct (Murgida and Hildebrandt, 2001a; Murgida and Hildebrandt, 2004a). Detailed spectroscopic studies, including a variety of techniques, have demonstrated that the B1 to B2 transition occurs without substantial alteration of the protein secondary structure. Based on these observations, the influence of the electric field on the dissociation energy of the Fe-Met80 bond in model porphyrins were studied using density functional theory (DFT). In that case, i.e., for the isolated heme moiety lacking the protein environment, no significant effect on the Fe-S(Met) bond stability was predicted for biologically meaningful electric field strengths (De Biase *et al.*, 2007). On the other hand, molecular dynamics simulations performed on the entire protein, show that biologically relevant electric fields induce an increased mobility of the key protein segments that lead to the detachment of the sixth axial ligand, Met80, from the heme iron. This electric-field induced conformational transition is both energetically and entropically driven (De Biase *et al.*, 2009). It was proposed, based on these theoretical and experimental investigations using biomimetic systems, that the variable transmembrane potential may modulate the structure of Cyt-c, thus playing the role of a switch that can alternate its redox function in the respiratory chain to peroxidase function in the early events of apoptosis.

Electric field effects on protein dynamics. Protein dynamics has been recently recognized as a key factor in controlling or limiting inter- and intra-protein ET reactions. However, in most of the cases the complexity of biological systems impairs direct observations of processes such as conformational gating, configurational fluctuations or rearrangement of protein complexes under reactive conditions. In this context simplified model systems, like proteins

immobilized on SAM-coated electrodes, can greatly contribute to the understanding of the biophysical fundamentals in better detail, even though they unavoidably deviate from the true physiological conditions. A specific advantage of this approach is facilitating the determination of ET rate constants as a function of distance by simply varying the chain length of the alkanethiols without modifying other experimental parameters (Murgida and Hildebrandt, 2001a; Murgida and Hildebrandt, 2001b). For redox proteins immobilized on SAM-coated metal electrodes one can anticipate a nonadiabatic ET mechanism. Therefore, the kinetics of the heterogeneous ET reaction can be described according to the high temperature limit of Marcus semiclassical expression, including integration to account for all the electronic levels of the metal, ε , contributing to the process (Marcus, 1965):

$$k_{ET} = \frac{\pi}{\hbar} \frac{|V|^2 \rho}{\sqrt{\pi \lambda k_B T}} \int_{-\infty}^{\infty} \exp \left[- \left(\frac{\lambda + (\varepsilon_F - \varepsilon) + e\eta^0}{4\lambda k_B T} \right)^2 \right] \frac{1}{1 + \exp[(\varepsilon - \varepsilon_F)/k_B T]} d\varepsilon \quad (2)$$

where $\rho(\varepsilon)$, $f(\varepsilon)$, $|V|$, ε_F , and λ are the density of electronic states in the electrode, the Fermi-Dirac distribution, the magnitude of the electronic coupling, the energy of the Fermi level, and the reorganization energy of the redox active molecule. The quantity $\eta^0 = (E - E^0)$ refers to the standard overpotential, with E denoting the actual electrode potential and E^0 the standard potential for the redox couple; the other parameters in Equation 2 have the usual meaning. The electronic coupling decays exponentially with the distance separating the redox center from the electrode.

Notably, the characteristic exponential decay of k_{ET} with the distance predicted by the theory is verified only partially in most studies reported so far. Indeed, several research groups have studied the distance-dependence of the ET rates for a variety of proteins immobilized on Au and Ag electrodes coated with pure and mixed SAMs of ω -functionalized alkanethiols using TR-SERR and electrochemistry. These studies include Cyt-c immobilized on COOH-, COOH/OH, CH₃-, and pyridine-terminated SAMs, (Murgida and Hildebrandt, 2001a; Murgida and Hildebrandt, 2002; Yue *et al.*, 2006; Murgida *et al.*, 2004b; Feng *et al.*, 2008b) cytochrome *b*₅₆₂ on NH₂-terminated SAMs (Zuo *et al.*, 2009), azurin on CH₃-terminated SAMs (Murgida *et al.*, 2001a) and cytochrome *c*₆ (Kranich *et al.*, 2009) and Cu_A (Fujita *et al.*, 2004) centers on mixed SAMs, among others. In all the cases, the measured ET rates verify the expected exponential decay with distance, but only for relatively thick SAMs. For thinner SAMs, however, the measured rate was distance-independent even though, due to the still long donor-acceptor separation (> 6 Å), a non-adiabatic ET mechanism should apply (Figure 7A). The origin of this behavior has been elusive and controversial for the last ten years.

Recently, the use of SER selection rules for analyzing the reaction dynamics of immobilized heme proteins has shed some light onto this issue (Kranich *et al.*, 2008). In a SER experiment, i.e. under off-resonance conditions, the individual components of the scattering tensor of the heme are modified depending on the direction of the electric field vector and the orientation of the heme plane. Assuming an ideal *D*_{4h} porphyrin symmetry, one can anticipate that the *A*_{1g} modes will experience preferential enhancement when the heme plane is parallel to the surface, while for a perpendicular orientation *A*_{1g}, *A*_{2g}, *B*_{1g} and *B*_{2g} will all be enhanced. Therefore, different orientations of the adsorbed heme protein are expected to lead to different intensity ratios of modes of different symmetries, e.g. $v_{10}(B_{1g})/v_4(A_{1g})$. These SER

selection rules do not hold when the experiments are performed under electronic resonance conditions (SERR), i.e. Soret excitation, typically used in the studies of heme proteins.

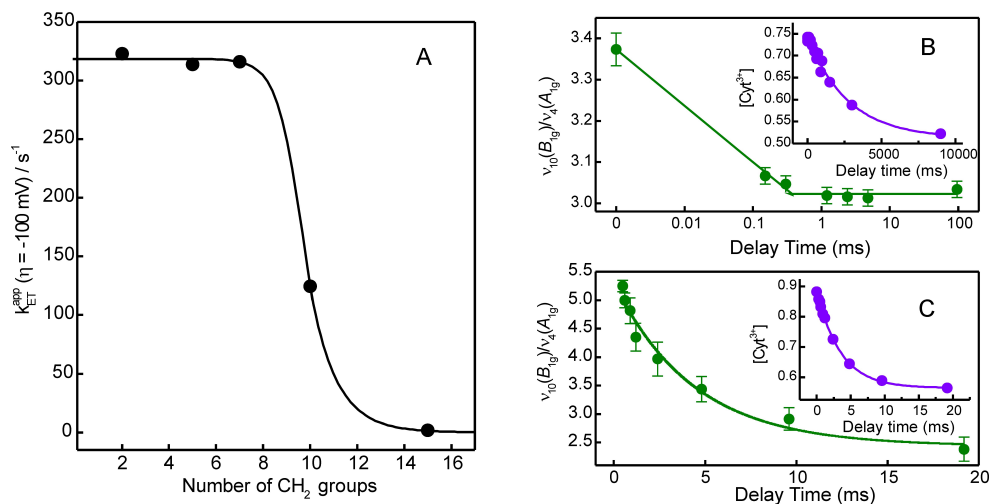


Fig. 7. TR-SERR data of Cyt-c electrostatically adsorbed to COOH-terminated SAMs. A) distance-dependence of the apparent ET rates determined at $\eta = -100$ mV; B) time-dependence of the v_{10}/v_4 intensity ratio (green, $\lambda_{exc} = 514$ nm) and of the concentration of ferric protein (violet, $\lambda_{exc} = 413$ nm) for Cyt-c adsorbed on SAM with 15 CH_2 groups; C) idem (B) for a SAM with 5 CH_2 groups.

In that case SERR spectra are largely dominated by the totally symmetric modes A_{1g} , which, in addition to partial scrambling of the radiation, result in an almost complete loss of orientation information. However, a reasonable compromise between acceptable enhancement and qualitatively predictable selection rules can still be achieved upon excitation into the less intense Q electronic transition of heme, by which non-totally symmetric modes are also enhanced.

This strategy has been applied for investigating the reaction dynamics of Cyt-c and Cyt-c₆ electrostatically adsorbed on Ag electrodes coated with SAMs of ω -carboxyl alkanethiols. TR-SERR experiments performed under Q-band excitation show that, upon applying a potential jump, the protein reorients within the electrostatic complex. The reorientation is fast in the low electric field regime, i.e. long SAMs, but becomes slower at shorter SAMs due to the barrier imposed by the increasing electric field. Indeed it has been observed that the measured ET rates in the plateau region of the k_{ET} vs. distance plots are identical to the reorientation rates, implying that reorientation is the rate limiting step (Figure 7). To understand these results at a molecular level, molecular dynamics simulations of the biomimetic systems were performed (Paggi *et al.*, 2009). The simulations show that Cyt-c can adsorb on SAMs in a variety of orientations that imply two major binding sites situated around the partially exposed heme group. In the low electric field regime, the electrostatic complexes are characterized by a large mobility of the protein that leads to significant fluctuations of the electronic coupling ($|V|$ in equation 2). For examples, a 7° change of tilt

angle of the heme with respect to the electrode plane may change the ET rate constant by more than two orders of magnitude. Moreover, the protein mobility is significantly restricted upon increasing the interfacial electric field. Thus, TR-SERR studies of heme proteins in biomimetic devices suggest that the initial electrostatic complex is not necessarily optimized for ET in terms of electronic pathway efficiency. Therefore, for the ET reaction to take place, the protein needs to reorient in search for higher electronic couplings. While at low interfacial electric fields and long tunneling distances this process is comparatively fast, it may become rate limiting at higher field strengths.

Electric field control of ET rates via modulation of protein dynamics seems to be a widespread phenomenon in bioelectrochemistry and protein-based bioelectronics. One can envisage similar effects controlling inter-protein ET *in vivo*, for example in photosynthetic and respiratory chains. In fact, the results obtained with the biomimetic systems are consistent with the biphasic kinetics observed for the inter-protein ET reactions between Cyt-c and CcO, on one hand, and between Cyt-c₆ and photosystem I, on the other (Murgida and Hildebrandt, 2008). In both cases, the cascade of ET reactions is coupled to proton translocation across the membrane generating a gradient that drives the ATP synthesis. This implies variable electric field strength during turnover, affecting the sampling rate of optimal ET pathways in transient and long-lived complexes between membrane bound proteins and soluble electron carriers. Such an effect might constitute the basis for a feedback regulating mechanism (Murgida and Hildebrandt, 2008).

6. Conclusions and Outlook

Within the past two decades, enormous progress has been achieved in developing tailored strategies for immobilizing proteins on functionalized metal surfaces. These achievements are reflected by the increasing number of biotechnological applications of enzyme-based bioelectronic devices. Yet, the behavior of the immobilized proteins is by far not understood, which aggravates employing rational design principles for the fabrication and optimization of bioelectronic devices. In this respect, surface-enhanced vibrational spectroscopies that have been introduced in this contribution are promising tools for elucidating structure and reaction dynamics of immobilized proteins. The examples presented in the previous section document the high potential of these techniques that are not only relevant for promoting the biotechnological development in this field but may also substantially improve the understanding of fundamental biophysical and biochemical processes *in vivo*. Nevertheless, both SERR and SEIRA spectroscopies are currently associated with some restrictions which narrow the range of applications. Specifically, these techniques require nanostructured Ag and Au surfaces as signal-amplifying media. These metals are usually not the type of solid supports used in biotechnological applications. Furthermore, the nanoscopic surface morphology might perturb the structure of membrane-like coatings, a drawback for using these devices as biomimetic systems for biological membranes. However, these limitations may be overcome in the near future taking into account recent promising developments in nanotechnology and material science such as the fabrication of bi-metallic hybrid systems, tailored metal nanoparticles, or surfaces with ordered nanoscopic morphologies.

7. References

- Arya, SK, Solanki PR, Datta M, and Malhotra BD (2009) Recent advances in self-assembled monolayers based biomolecular electronic devices. *Biosens. Bioelectron.*, 24, 2810-2817.
- Ataka K, Giess F, Knoll W, Naumann R, Haber-Pohlmeier S, Richter B, and Heberle J (2004) Oriented attachment and membrane reconstitution of his-tagged cytochrome c oxidase to a gold electrode: In situ monitoring by Surface-Enhanced Infrared Absorption spectroscopy. *J. Am. Chem. Soc.*, 126, 16199-16206.
- Ataka K and Heberle J (2007) Biochemical applications of Surface-Enhanced Infrared Absorption spectroscopy. *Anal. Bioanal. Chem.*, 388, 47-54.
- Banholzer MJ, Millstone JE, Qin L, and Mirkin CA (2008) Rationally designed nanostructures for surface-enhanced Raman spectroscopy. *Chem. Soc. Rev.* 37, 885-897.
- Brown RJC and Milton MJT (2008) Nanostructures and nanostructured substrates for surface - enhanced Raman scattering (SERS). *J. Ram. Spec.*, 39, 1313-1326.
- Cass T (2007) Enzymology, in Marks, RS, Cullen, DC, Karube, I, Lowe, CR, and Weetall, H H (Eds.), *Handbook of biosensors and biochips 1*. John Wiley & Sons Ltd, Chichester, 84-99.
- Clarke JR (2001) The dipole potential of phospholipid membranes and methods for its detection. *Adv. Colloid. Interface Sci.* 89-90, 263-281.
- Collier JH and Mrksich M (2006) Engineering a biospecific communication pathway between cells and electrodes. *Proc. Natl. Acad. Sci.*, 103, 2021-2025.
- Das TK, Gomes CM, Teixeira M, and Rousseau DL (1999) Redox-linked transient deprotonation at the binuclear site in the *aa₃*-type quinol oxidase from *Acidianus ambivalens*: Implications for proton translocation. *Proc. Natl. Acad. Sci.*, 96, 9591-9596.
- De Biase PM, Doctorovich F, Murgida DH, and Estrin DA (2007) Electric field effects on the reactivity of heme model systems. *Chem. Phys. Lett.*, 434, 121-126.
- De Biase PM, Paggi DA, Doctorovich F, Hildebrandt P, Estrin DA, Murgida D, and Marti MA (2009) Molecular basis for the electric field modulation of cytochrome c structure and function. *J. Am. Chem. Soc.*, in press.
- Droghetti E, Oellerich S, Hildebrandt P, and Smulevich G (2006) Heme coordination states of unfolded ferrous cytochrome c. *Biophys. J.*, 91, 3022-3031.
- Feng JJ, Gernert U, Sezer M, Kuhlmann U, Murgida DH, David C, Richter M, Knorr A, Hildebrandt P, and Weidinger IM (2009) Novel Au-Ag hybrid device for electrochemical SE(R)R spectroscopy in a wide potential and spectral range. *Nano Lett.*, 9, 298-303.
- Feng JJ, Hildebrandt P, and Murgida DH (2008a) Silver nanocoral structures on electrodes: A suitable platform for protein-based bioelectronic devices. *Langmuir*, 24, 1583-1586.
- Feng JJ, Murgida D, Kuhlmann U, Utesch T, Mroginski MA, Hildebrandt P, and Weidinger I (2008b) Gated electron transfer of yeast iso-1 cytochrome c on self-assembled-monolayer-coated electrodes. *J. Phys. Chem. B*, 112, 15202-15211.
- Forte E, Urbani M, Saraste M, Sarti P, Brunori M, and Giuffrè A (2001) The cytochrome *cbb₃* from *Pseudomonas stutzeri* displays nitric reductase activity. *Eur. J. Biochem.*, 268, 6486-6491.

- Friedrich MG, Gie F, Naumann R, Knoll W, Ataka K, Heberle J, Hrabakova J, Murgida D, and Hildebrandt P (2004) Active site structure and redox processes of cytochrome c oxidase immobilised in a novel biomimetic lipid membrane on an electrode. *Chem. Commun.*, 7, 2376-2377.
- Fujita K, Nakamura N, Ohno H, Leigh BS, Niki K, Gray H, and Richards JH (2004) Mimicking protein-protein electron transfer: voltammetry of *Pseudomonas aeruginosa* azurin and the *Thermus thermophilus* Cu_A domain at omega-derivatized self-assembled-monolayer gold electrodes. *J. Am. Chem. Soc.*, 126, 13954-13961.
- Garcia-Horsman JA, Barquera B, Rumbley J, Ma J, and Gennis RB (1994) The superfamily of the heme-copper respiratory oxidases. *J. Bacteriol.* 176, 5587-5600.
- Gennis RB (1989). *Biomembranes: molecular structure and function*. Springer-Verlag, New York.
- Giess F, Friedrich MG, Heberle J, Naumann R, and Knoll W (2004) The protein-tethered lipid bilayer: A novel mimic of the biological membrane. *Biophys. J.*, 87, 3213-3220.
- Gilardi G (2004) Protein Engineering for Biosensors, in Cooper, J and Cass, AEG (Eds.), *Biosensors*, Oxford University Press, Oxford.
- Godoy LC, Munoz-Pinedo C, Castro L, Cardaci S, Schonhoff CM, King M, Tortora V, Marin M, Miao Q, Jiang JF, Kapralov A, Jemmerson R, Silkstone GG, Patel JN, Evans JE, Wilson MT, Green DR, Kagan VE, Radi R, and Mannick JB (2009) Disruption of the M80-Fe ligation stimulates the translocation of cytochrome c to the cytoplasm and nucleus in nonapoptotic cells. *Proc. Natl. Acad. Sci.*, 106, 2653-2658.
- Gupta R and Chaudhury NK (2007) Entrapment of biomolecules in sol-gel matrix for applications in biosensors: problems and future prospects. *Biosens. Bioelectron.*, 22, 2387-2399.
- Haas AS, Pilloud KS, Reddy KS, Babcock GT, Moser CC, Blasie JK, and Dutton PL (2001) Cytochrome c and cytochrome c oxidase: Monolayer assemblies and catalysis. *J. Phys. Chem. B*, 105, 11351-11362.
- Hasunuma T, Kuwabata S, Fukusaki E, and Kobayashi A (2004) Real-time quantification of methanol in plants using a hybrid alcohol oxidase-peroxidase biosensor. *Anal. Chem.*, 76, 1500-1506.
- He JA, Samuelson L, Li J, Kumar J, and Tripathy SK (1999) Bacteriorhodopsin thin-film assemblies - immobilization, properties, and applications. *Adv. Mater.*, 11, 435-446.
- Henning TP and Cunningham DD (1998) *Commercial Biosensors*. Wiley, New York, 3-46.
- Hianik T (2008) Biological membranes and membrane mimics, in Bartlett, PN (Ed.) *Bioelectrochem.*, John Wiley and Sons, Chichester, 87-156.
- Hodneland CD, Lee YS, Min DH, and Mrksich M (2002) Selective immobilization of proteins to self-assembled monolayers presenting active site-directed capture ligands. *Proc. Natl. Acad. Sci.*, 99, 5048-5052.
- Hrabakova J, Ataka K, Heberle J, Hildebrandt P, and Murgida D (2006) Long distance electron transfer in cytochrome c oxidase immobilised on electrodes. A Surface Enhanced Resonance Raman spectroscopic study. *Phys. Chem. Chem. Phys.*, 8, 759-766.
- Hu S, Morris IK, Dingh JP, Smith KM, and Spiro TG (1993) Complete assignment of cytochrome c resonance Raman spectra via enzymatic reconstitution with isotopically labeled hemes. *J. Am. Chem. Soc.*, 115, 12446-12458.

- Kagan VE, Bayir HA, Belikova NA, Kapralov O, Tyurina YY, Tyurin VA, Jiang J, Stoyanovski DA, Wipf P, Kochanek PM, Greenberger JS, Pitt B, Shvedova AA, and Borisenko G (2009) Cytochrome c/cardiolipin relations in mitochondria: a kiss of death. *Free Radic. Biol. Med.*, 46, 1439-1453.
- Kagan VE, Tyurin VA, Jiang J, Tyurina YY, Ritov VB, Amoscato AA, Osipov AN, Belikova NA, Kapralov A, Kini V, Vlasova II, Zhao Q, Zou M, Di P, Svistunenka DA, Kurnikov IV, and Borisenko G (2005) Cytochrome c acts as a cardiolipin oxygenase required for release of proapoptotic factors. *Nat. Chem. Biol.*, 1, 223-232.
- Karube I (1989) Micro-organism based sensors, in Turner, APF, Karube, I, and Wilson, GS (Eds.), *Biosensors: Fundamentals and Applications*, Oxford Science Publications, Oxford, 13-29.
- Kinnear KT and Monbouquette HG (1993) Direct electron transfer to *Escherichia coli* fumarate reductase in self- assembled alkanethiol monolayers on gold electrodes. *Langmuir*, 9, 2255-2257.
- Kranich A, Ly HK, Hildebrandt P, and Murgida DH (2008) Direct observation of the gating step in protein electron transfer: Electric-field-controlled protein dynamics. *J. Am. Chem. Soc.*, 130, 9844-9848.
- Kranich A, Naumann H, Molina-Heredia FP, Moore HJ, Lee TR, Lecomte S, de la Rosa MA, Hildebrandt P, and Murgida DH (2009) Gated electron transfer of cytochrome c_6 at biomimetic interfaces: A time-resolved SERR study. *Phys. Chem. Chem. Phys.*, 11, 7390-7397.
- Lal S, Grady NK, Kundu J, Levin CS, Lassiter JB, and Halas NJ (2008) Tailoring plasmonic substrates for surface enhanced spectroscopies. *Chem. Soc. Rev.*, 37, 898-911.
- Ledesma GN, Murgida DH, Ly HK, Wackerbarth H, Ulstrup J, Costa AJ, and Vila AJ (2007) The met axial ligand determines the redox potential in Cu-A sites. *J. Am. Chem. Soc.*, 129, 11884-11885.
- Leland C and Clark JR (1989) The enzyme electrode, in Turner, APF, Karube, I, and Wilson, GS (Eds.), *Biosensors: Fundamentals and applications*, Oxford Science Publications, Oxford, 3-12.
- Love JC, Estroff LA, Kriebel JK, Nuzzo RG, and Whitesides GM (2005) Self- assembled monolayers of thiolates on metals as a form of nanotechnology. *Chem. Rev.*, 105, 1103-1169.
- Mahajan M, Baumberg JJ, Russell AE, and Bartlett PN (2007) Reproducible SERRS from structured gold surfaces. *Phys. Chem. Chem. Phys.*, 9, 6016-6020.
- Marcus RA (1965) On the theory of electron-transfer reactions. VI. Unified treatment for homogeneous and electrode reactions. *J. Chem. Phys.*, 43, 679-702.
- Marsh D, Muller M, and Schmitt FJ (2000) Orientation of the infrared transition moments for an α -helix. *Biophys. J.*, 78, 2499-2510.
- Murgida DH and Hildebrandt P (2001a) Heterogeneous electron transfer of cytochrome c on coated silver electrodes. Electric field effects on structure and redox potential. *J. Phys. Chem. B*, 105, 1578-1586.
- Murgida DH and Hildebrandt P (2001b) Proton-coupled electron transfer of cytochrome c. *J. Am. Chem. Soc.*, 123, 4062-4068.
- Murgida DH and Hildebrandt P (2001c) Active-site structure and dynamics of cytochrome c immobilized on self-assembled monolayers - a time-resolved Surface Enhanced Resonance Raman spectroscopy study. *Angew. Chem. Int. Ed.*, 40, 728-731.

- Murgida DH and Hildebrandt P (2002) Electrostatic-field dependent activation energies modulate electron transfer of cytochrome *c*. *J. Phys. Chem. B*, 106, 12814-12819.
- Murgida DH and Hildebrandt P (2004a) Electron-transfer processes of cytochrome *c* at interfaces. New insights by Surface Enhanced Resonance Raman Spectroscopy. *Acc. Chem. Res.*, 37, 654-661.
- Murgida DH, Hildebrandt P, Wei JJ, He YF, Liu HY, and Waldeck DH (2004b) Surface-Enhanced Resonance Raman spectroscopy and electrochemical study of cytochrome *c* bound on electrodes through coordination with pyridinyl-terminated self-assembled monolayers. *J. Phys. Chem. B*, 108, 2261-2269.
- Murgida DH and Hildebrandt P (2005) Redox and redox-coupled processes of heme proteins and enzymes at electrochemical interfaces. *Phys. Chem. Chem. Phys.*, 7, 3773-3784.
- Murgida DH and Hildebrandt P (2008) Disentangling interfacial redox processes of proteins by SERR spectroscopy. *Chem. Soc. Rev.*, 37, 937-945.
- Nayak S, Yeo W-S, and Mrksich M (2007) Determination of kinetic parameters for interfacial enzymatic reactions on self-assembled monolayers. *Langmuir*, 23, 5578-5583.
- Paggi DA, Martin DF, Kranich A, Hildebrandt P, Marti MA, and Murgida DH (2009) Computer simulation and SERR detection of cytochrome *c* dynamics at SAM-coated electrodes. *Electrochim. Acta*, 54, 4963-4970.
- Pereira MM and Teixeira M (2004) Proton pathways, ligand binding and dynamics of the catalytic site in haem-copper oxygen reductases: a comparison between the three families. *Biochim. Biophys. Acta*, 1655, 241-247.
- Pitcher RS and Watmough NJ (2004) The bacterial cytochrome *cbb₃* oxidases. *Biochim. Biophys. Acta*, 1655, 388-399.
- Rivas L, Murgida DH, and Hildebrandt P (2002) Conformational and redox equilibria and dynamics of cytochrome *c* immobilized on electrodes via hydrophobic interactions. *J. Phys. Chem. B*, 106, 4823-4830.
- Rivas L, Soares CM, Baptista AM, Simaan J, Di Paolo R, Murgida D, and Hildebrandt P (2005) Electric-field-induced redox potential shifts of tetraheme cytochromes *c₃* immobilized on self-assembled monolayers: Surface Enhanced Resonance Raman spectroscopy and simulation studies. *Biophys. J.*, 88, 4188-4199.
- Sharma V, Puustinen A, Wikstorm M, and Laakkonen L (2006) Sequence analysis of the *cbb₃* oxidases and an atomic model for the *Rhodobacter sphaeroides* enzyme. *Biochemistry*, 45, 5754-5765.
- Siebert F and Hildebrandt P (2008) *Vibrational Spectroscopy in Life Science*. Wiley-VCH, Weinheim
- Spiro TG and Czernuszewicz R (1995) Resonance Raman spectroscopy of metalloproteins. *Methods Enzymol.*, 26, 867-876.
- Todorovic S, Jung C, Hildebrandt P, and Murgida DH (2006) Conformational transitions and redox potential shifts of cytochrome P450 induced by immobilization. *J. Biol. Inorg. Chem.*, 11, 119-127.
- Todorovic S, Pereira M, Bandeiras T, Teixeira M, Hildebrandt P, and Murgida DH (2005) Midpoint potentials of hemes *a* and *a₃* in the quinol oxidase from *Acidianus ambivalens* are inverted. *J. Am. Chem. Soc.*, 127, 13561-13566.

- Todorovic S, Verissimo A, Pereira M, Teixeira M, Hildebrandt P, Zebger I, Wisitruangsakul N, and Murgida D (2008) SERR-spectroelectrochemical study of a *cbh₃* oxygen reductase in a biomimetic construct. *J. Phys. Chem. B*, 112, 16952-16959.
- Ulman A (2000) Self-assembled monolayers of rigid thiols. *Rev. Mol. Biotech.*, 74, 175-188.
- Ulman A (1996) Formation and structure of self-assembled monolayers. *Chem. Rev.*, 96, 1533-1554.
- Verissimo A, Sousa FL, Baptista AM, Teixeira M, and Pereira M (2007) Thermodynamic redox behavior of the heme centers of *cbh₃* heme-copper oxygen reductase from *Bradyrhizobium japonicum*. *Biochemistry*, 46, 13245-13253.
- Wei JJ, Liu HY, Dick AR, Yamamoto H, He YF, and Waldeck DH (2002) Direct wiring of cytochrome c's heme unit to an electrode: electrochemical study. *J. Am. Chem. Soc.*, 124, 9591-9599.
- Weidinger IM, Murgida DH, Dong WF, Mohwald H, and Hildebrandt P (2006) Redox processes of cytochrome c immobilized on solid supported polyelectrolyte multilayers. *J. Phys. Chem. B*, 110, 522-529.
- Willner I and Katz E (2000) Integration of layered redox proteins and conductive supports for bioelectronic applications. *Angew. Chem. Int. Ed.*, 39, 1180-1218.
- Xavier AV (2004) Thermodynamic and choreographic constraints for energy transduction by cytochrome c oxidase. *Biochim. Biophys. Acta*, 1658, 23-30.
- Xiao Y, Patolsky F, Katz E, Hainfeld JF, and Willner I (2003) Plugging into enzymes: nanowiring of redox enzymes by a gold nanoparticle. *Science*, 299, 1877-1881.
- Yue HJ, Khoshtariya D, Waldeck DH, Grochol J, Hildebrandt P, and Murgida DH (2006) On the electron transfer mechanism between cytochrome c and metal electrodes. Evidence for dynamic control at short distances. *J. Phys. Chem. B*, 110, 19906-19913.
- Zufferey R, Arslan E, Thony-Meyer L, and Hennecke H (1998) How replacement of the 12 conserved histidines of subunit I affects assembly, cofactor binding, and enzymatic activity of the *Bradyrhizobium japonicum cbb₃*-type oxidase. *J. Biol. Chem.*, 273, 6452-6459.
- Zuo P, Albrecht T, Barker PD, Murgida DH, and Hildebrandt P (2009) Interfacial redox processes of cytochrome *b₅₆₂*. *Phys. Chem. Chem. Phys.*, 11, 7430-7436.

Photosynthetic energy conversion: hydrogen photoproduction by natural and biomimetic systems

Suleyman I. Allakhverdiev^{a,*}, Vladimir D. Kreslavski^a,
Velmurugan Thavasi^b, Sergei K. Zharmukhamedov^a,
Vyacheslav V. Klimov^a, Seeram Ramakrishna^b, Hiroshi Nishihara^c,
Mamoru Mimuro^d, Robert Carpentier^e and Toshi Nagata^f

^a*Institute of Basic Biological Problems, Russian Academy of Sciences, Pushchino, Moscow Region, 142290 Russia.*

^b*Nanoscience and Nanotechnology Initiative, National University of Singapore, 2, Engineering Drive 3, Singapore 117576, Singapore.*

^c*Department of Chemistry, School of Science, The University of Tokyo, 7-3-1 Hongo, Bunkyo-ku, Tokyo 113-0033, Japan*

^d*Graduate School of Human and Environmental Studies, Kyoto University, Kyoto 606-8501, Japan*

^e*Groupe de recherche en biologie végétale, Université du Québec à Trois-Rivières, CP 500, Trois-Rivières, Québec, G9A 5H7, Canada.*

^f*Research Center for Molecular Scale Nanoscience, Institute for Molecular Science, 5-1 Higashiyama, Myodaiji, Okazaki 444-8787, Japan*

"I believe that water will one day be used as a fuel, because the hydrogen and oxygen which constitute it, used separately or together, will furnish an inexhaustible source of heat and light. I therefore believe that, when coal deposits are oxidized, we will heat ourselves by means of water. Water is the coal of the future"

Jules Verne, 1875

Abstract

The main function of the photosynthetic process is to capture solar energy and to store it in the form of chemical fuels. Many fuel forms such as coal, oil and gas have been intensively used and are becoming limited. Hydrogen could become an important clean fuel for the future. Among different technologies for hydrogen production, oxygenic natural and artificial photosynthesis using direct photochemistry in synthetic complexes have a great

potential to produce hydrogen as both use clean and cheap sources - water and solar energy. Photosynthetic organisms capture sunlight very efficiently and convert it into organic molecules. Artificial photosynthesis is one way to produce hydrogen from water using sunlight by employing biomimetic complexes. However, splitting of water into protons and oxygen is energetically demanding and chemically difficult. In oxygenic photosynthetic microorganisms water is splitted into electrons and protons during primary photosynthetic processes. The electrons and protons are redirected through the photosynthetic electron transport chain to the hydrogen-producing enzymes-hydrogenase or nitrogenase. By these enzymes, e^- and H^+ recombine and form gaseous hydrogen. Biohydrogen activity of hydrogenase can be very high but it is extremely sensitive to photosynthetic O_2 . At the moment, the efficiency of biohydrogen production is low. However, theoretical expectations suggest that the rates of photon conversion efficiency for H_2 bioproduction can be high enough ($> 10\%$). Our review examines the main pathways of H_2 photoproduction using photosynthetic organisms and biomimetic photosynthetic systems and focuses on developing new technologies based on the effective principles of photosynthesis.

1. Introduction

More than 3 billion years ago living organisms developed the capacity to efficiently capture solar energy and use it to power the synthesis of organic molecules. This photosynthetic process set into motion an unprecedented explosion in biological activity, allowing life to prosper and diversify on an enormous scale as witnessed by the fossil records and by the extent and diversity of living organisms on our planet today (Barber, 2007). It is estimated that photosynthesis produces more than 100 billion tons of dry biomass annually, which would be equivalent to a hundred times the weight of the total human population on our planet at the present time and equivalent to a mean annual rate of energy storage of approximately 100 TW. The success of this energy generating and storage system stems from the fact that the raw materials and energy needed to drive the synthesis of biomass are available in almost unlimited amounts, i.e. sunlight, water and carbon dioxide (Barber, 2007). Indeed, solar energy is the most abundant and accessible renewable energy source available for future sustainable production of fuel and, finally, electricity. For effective use of solar energy it is important to develop more cost-effective systems with improved ability to convert solar energy into chemical energy conserved in fuel, such as H_2 . Hydrogen is one of the most promising clean fuels for the future (Abraham, 2002). The combustion of the evolved H_2 yields only H_2O and thereby completes a clean energy cycle. A variety of process technologies have been employed for H_2 production, including splitting of water by water-electrolysis, photoelectrolysis and photo-biological production. However, for all H_2 production processes there is a need for significant improvement in efficiencies, reduced capital costs, and enhanced reliability and operating flexibility (Riis et al., 2005). For instance, the photo-electrolysis is at an early stage of development and material cost and much practical issues have to be solved for application. Photo-biological H_2 production may be one of the alternatives to chemical and electrochemical technologies. Photosynthesis is a base for all biological solar-driving methods of H_2 production. Therefore, these approaches examine a link between photosynthetic efficiency, photosynthetic products and H_2 production.

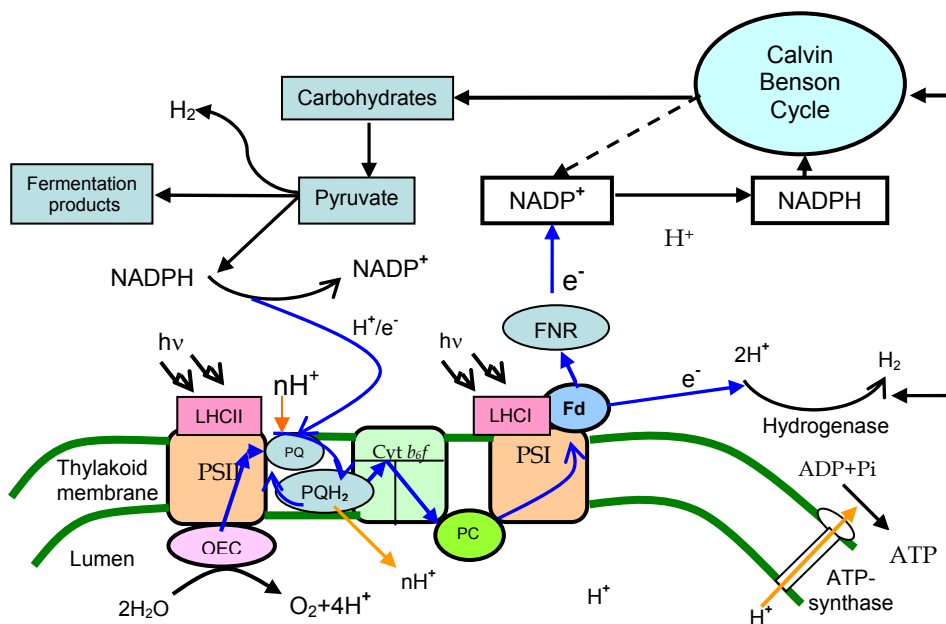


Fig. 1. The scheme of solar-powered H_2 production during oxygenic photosynthesis and subsequent formation of carbohydrates in microalgae. The oxygenic “light reactions” of photosynthesis are driven by the solar energy captured by the light-harvesting complexes of PSI and PSII. Electrons extracted from H_2O by the oxygen-evolving complex of PSII are passed along to the photosynthetic electron transport chain via plastoquinone (PQ), the cytochrome b_6/f complex (Cyt b_6/f), plastocyanin (PC), photosystem I (PSI), and ferredoxin (Fd), then by ferredoxin-NADP⁺ oxidoreductase to NADP⁺ with final production of NADPH. H^+ are released into the thylakoid lumen by PSII and the PQ/PQH₂ cycle and used for ATP production via ATP synthase. The ATP and NADPH generated during primary photosynthetic processes are consumed for CO_2 fixation in the Calvin-Benson cycle, which produces sugars and ultimately starch. Under anaerobic conditions, hydrogenase can accept electrons from reduced Fd molecules and use them to reduce protons to H_2 . Certain algae under anaerobic conditions can use starch as a source of H^+ and e^- for H_2 production (via NADPH, PQ, cyt b_6/f , and PSI) using the hydrogenase. In cyanobacteria the H^+ and e^- derived from H_2O can be converted to H_2 via a nitrogenase or fermentation. During fermentation process carbohydrate stores such as starch can be converted to sugars and subsequently pyruvate via glycolysis, before producing H_2 and organic acids (e.g., formate, acetate, and butyrate). Thylakoid membrane is denoted with green color. Electron transfer is shown with blue color and protons with brown color. Adapted from (refs. Blankenship, 2002; Kruse et al., 2005b; Rupprecht et al., 2006; Melis et al., 2007; Allakhverdiev et al., 2009).

Photosynthesis is based on conversion of solar energy into chemical energy by a series of electron transfer steps (Figure 1) (Blankenship, 2002; Chow, 2003; LaVan and Cha, 2006;

Allakhverdiev et al., 2009). Photosynthesis can be divided into oxygenic (O_2 producing) and anoxygenic photosynthesis (LaVan and Cha, 2006; Kruse et al., 2005a,b; Rupprecht et al., 2006; Allakhverdiev et al., 2009). Oxygenic organisms (higher plants, algae and cyanobacteria) use solar energy to extract electron and proton from water mainly for CO_2 assimilation cycle, and to produce oxygen (Figure 1) (Chow, 2003; LaVan and Cha, 2006; Kruse et al., 2005b; Allakhverdiev et al., 2009). Anoxygenic photosynthesis occurs in simpler organisms such as green sulfur and purple non-sulfur bacteria. This review focuses only on oxygenic organisms such as algae and cyanobacteria that are able to split water and evolve H_2 . All oxygenic organisms can extract electrons and protons from water and use them to reduce $NADP^+$ and plastoquinone (or form ATP) for use as energy sources for metabolic processes such as the Calvin cycle (CO_2 fixation) and other pathways. However, oxygenic phototrophs such as cyanobacteria and microalgae can transiently produce H_2 under anaerobic conditions via proton reduction, catalyzed by a hydrogenase (or nitrogenase) in competition with other intracellular processes. In this case the electrons and protons, ultimately produced by water oxidation, are redirected at the level of ferredoxin/NADPH into hydrogenase.

One attractive way to harvest solar energy is to adopt the concept of natural photosynthesis to build artificial systems for H_2 bioproduction. Artificial photosynthesis employs synthetic complexes as photosensitizers (Pn) to harvest solar energy and utilize the energy to produce hydrogen from water (Alstrum-Acevedo et al., 2005). This is an emerging field and the hydrogen generation efficiency of such man-made molecular systems is not however high enough at the moment, but encouraging for researchers.

There are some problems in this field. One or several sensitizers are required for artificial photosynthetic cell (Figure 2). Excited Pn donate electrons to the reductive site of the artificial photosynthetic system and extract electrons from the oxidative site. A catalyst that operates at a very high redox potential is needed for the water-oxidation reaction, performs a four-electron reaction so as to maximize the energetic efficiency, avoid production of reactive intermediates such as hydroxyl radicals, and mediates proton-coupled redox reactions (Figure 2).

To develop active and stable catalysts for water oxidation, it is important to use multinuclear structure, which can accumulate and delocalize four oxidizing equivalents. Di- and tetra-nuclear manganese complexes as well as mono-, di-, and tri-nuclear ruthenium complexes have been reported as molecular catalysts capable of evolving O_2 from water (Allakhverdiev et al., 1999; Yagi and Kaneko, 2001; Lomoth et al., 2006; McEvoy and Brudvig, 2006; Nagata et al., 2007, 2008). The presence of oxygen at the catalytic site for hydrogen production can inactivate or decrease the performance of the many known catalysts. Therefore, biomimetic systems have to be developed to spatially separate the catalytic centers for production of hydrogen and oxygen.

Catalysts such as Co (Hu et al., 2005; Nagasawa and Nagata, 2007) and molecules mimicking hydrogenase structure and possessing hydrogenase activity (Licheng et al., 2005; Ogo et al., 2007; Rauchfuss, 2007) are more favorable for hydrogen production. In any case, whether the devices mimicking photosynthesis are composed of natural biomolecules or organic or inorganic molecules, the architecture and spatial arrangements at multiple length scales play a crucial role (LaVan and Cha, 2006).

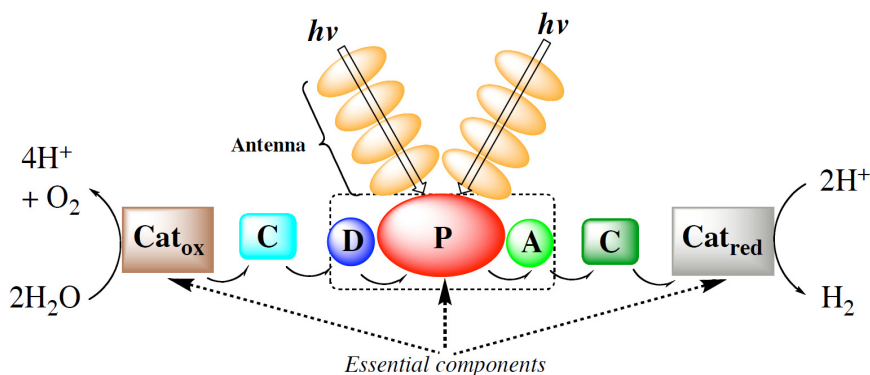


Fig. 2. The schematic view of the artificial photosynthetic system for production of hydrogen. P, photosensitizer; A, electron acceptor; D, electron donor; C, electron carrier; Cat_{ox} , catalyst for oxidation of water; Cat_{red} , catalyst for reduction of H^+ .

2. Natural systems

2.1. Oxygenic organisms (cyanobacteria and microalgae)

Photosynthesis involves a sequential chain of reactions that include light absorption, charge separation, water splitting, electron transport, reduction of $NADP^+$, and creation of a proton gradient. Several major complexes are involved in the process of oxygenic photosynthesis: Photosystem II (PSII), including water oxidation complex, Photosystem I (PSI), cytochrome b_6/f , and ATP-synthase complexes (Figure 1). The detailed composition of the photosystems and electron transport intermediates from water to $NADP^+$ are described in a number of papers (see Chow, 2003; Kruse et al., 2005b; McEvoy and Brudvig, 2006; Allakhverdiev et al., 2009).

Electrons are transferred from PSII to ferredoxin (Fd) through PSI. Normally, Fd shuttles electrons to the enzyme ferredoxin-NADP-reductase that reduces $NADP^+$ to NADPH, an important source of electrons needed to convert CO_2 into carbohydrates during the Calvin-Benson cycle. Here, protons (H^+) outside the thylakoids are carried to the inner thylakoid space thus forming a proton gradient across the thylakoid membrane. Under anaerobic conditions, hydrogenase (nitrogenase) can accept electrons from reduced Fd molecules and use them to reduce protons to molecular hydrogen (H_2). In this case, the photosynthetic reducing power can partition between at least two pathways: CO_2 reduction and H_2 production. CO_2 reduction requires ATP for using reductant from water, whereas H_2 production does not use ATP, which is the desired pathway for renewable energy production.

Under normal conditions, the competition for electron donor favors the CO_2 fixation pathway. However, in the absence or limitation of CO_2 , the favorable pathway is the H_2 production, which is down-regulated due to non-dissipation ΔpH caused by the lack of ATP utilization.

There are two major research challenges related to the conversion of protons and electrons by light energy into H_2 . 1. The level of solar light intensities that can be efficiently utilized to drive photosynthesis should be optimized for microorganisms. 2. For hydrogenases, there

are kinetic limitations on electron transport to the hydrogenase under H₂-producing conditions. Nitrogenase uses ATP during the production of H₂, therefore, the efficiency of nitrogenase system is lesser than using the hydrogenase.

2.2. Enzymes for biohydrogen production

Terrestrial plants are not capable for the H₂ photoproduction. On the contrary, most of the microalgae and cyanobacteria are able to produce hydrogen (Boichenko et al., 2004; Dutta et al., 2005; Kruse et al., 2005b; Ghirardi et al., 1997, 2000, 2005, 2007).

Cyanobacteria uses two major types of enzymes: nitrogenases that produce H₂ contaminant with N₂ fixation, and NiFe-hydrogenases (Kruse et al., 2005a; Rupprecht et al., 2006). Nitrogenase is not known to be present in any eukaryote, including the microalgae, whereas hydrogenases are widespread and synthesized in many of the microalgae and cyanobacteria (Ghirardi et al., 2005, 2007; Prince and Kheshgi, 2005). Nitrogenase can be used for H₂ production because it has the advantage of catalyzing the unidirectional production of H₂ in the presence of O₂, thus eliminating the need for a daily anaerobic production-harvesting cycle, although its theoretical maximum energy conversion efficiency is lower than that of hydrogenase (Sakurai and Masukawa, 2007). An additional process to inactivate the up-take hydrogenase is required for completion of the system. Cyanobacteria lacking hydrogenase activity were used in several researches of H₂ production, for instance *A. variabilis* ATCC29413 and its mutant PK84 with lost hydrogenase activity. The light-dependent H₂ production was maximum when the cultures synthesized vanadate-nitrogenase (Tsygankov, 2007; Tsygankov et al., 1997, 2002). A great attention is paid to enzymes participating in these processes occurring in chemotrophs and phototrophs. The basic methods of their isolation and activity determination are presented in details (Kondratieva and Gogotov, 1981).

Among microalgae, many unicellular green algae have the highest rates of H₂ photoproduction. In green algal cells, H₂ production reaction is catalyzed by the [FeFe]-hydrogenase enzyme, as shown by the following reaction equation: $2\text{H}^+ + 2\text{Fd} \rightarrow \text{H}_2 + 2\text{Fd}$. Green algal hydrogenases that belong to the class of [FeFe]-hydrogenases are involved in much higher specific activities than ones of cyanobacterial NiFe-hydrogenases (Florin et al., 2001).

Hydrogenases are oxygen-labile enzymes, which make them incompatible with the oxygen-evolving photosynthesis present in cyanobacteria. Hence, hydrogenase activity is restricted to cells with anoxic conditions. Based on our current knowledge, various strains of cyanobacteria may have no hydrogenase, only an uptake hydrogenase, only a reversible hydrogenase, or both hydrogenases. Cyanobacterial hydrogenases are Ni-Fe enzymes (Tamagnini et al., 2000, 2002). All cyanobacteria that fix nitrogen appear to have an uptake hydrogenase, whose function is to recover the electrons lost to hydrogen production by nitrogenase (Figure 3) (Tamagnini et al., 2000). The uptake hydrogenase comprises two subunits encoded by *hupS* and *hupL*. The large subunit contains the four cysteines of the active site, two of which is bridge between the Fe and Ni atoms. The small subunit has three Fe-S clusters that pass electrons from the active center to the electron acceptor in the respiratory electron transport chain, thus producing ATP and consuming oxygen, both beneficial for nitrogen fixation. In bacteria that use hydrogen as an energy source, the small subunit of hydrogenase donates electrons to another protein encoded by *hupC* or *hoxZ* that anchors the hydrogenase in the membrane and transfers the electrons to a respiratory

electron transport chain. In cyanobacteria there are no close homologs of *hupC*; thus, the anchoring protein is unknown. The uptake hydrogenase in cyanobacteria is localized on the cytoplasmic side of the cytoplasmic or thylakoid membrane (Tamagnini et al., 2002). [FeFe]-hydrogenases are quite fragile and sensitive to O₂. H₂ production is often limited mainly because of the extreme sensitive nature of hydrogenases to oxygen. A reduced O₂ sensitivity may be obtained by genetic modification of the hydrogenases. Ferredoxin, being the natural electron donor, transports the electrons to the algal [FeFe]-hydrogenase (Figure 1). As mentioned above, electrons and protons are initially extracted from water (2H₂O → 4H⁺ + 4e⁻ + O₂) by oxygenic photosynthesis. Here, the hydrogen-producing enzymes act as a H⁺/e⁻ release valve by recombining H⁺ (from the medium) and e⁻ (from the reduced ferredoxin) to produce H₂. The metal clusters of hydrogenases are unique in having CO₂ and CN ligands, but they are sensitive to O₂ and CO. [NiFe]-hydrogenases and [FeFe]-hydrogenases can be inactivated by these inhibitors especially in the latter case, the inactivation by O₂ is irreversible (Ghirardi et al., 2005, 2007). The stoichiometric release of one O₂ and two molecules of H₂ is possible only under the conditions of real anaerobiosis. This is also required for the transcription of the hydrogenase gene and supporting hydrogenase activity (Kruse et al., 2005a). However, very little is known at the moment about regulation of [FeFe]-hydrogenase gene transcription and maturation (Ghirardi et al., 2005, 2007). Such issues as well as structure and function of enzymes - [NiFe]- and [FeFe]-hydrogenases, and nitrogenase are needed to be examined.

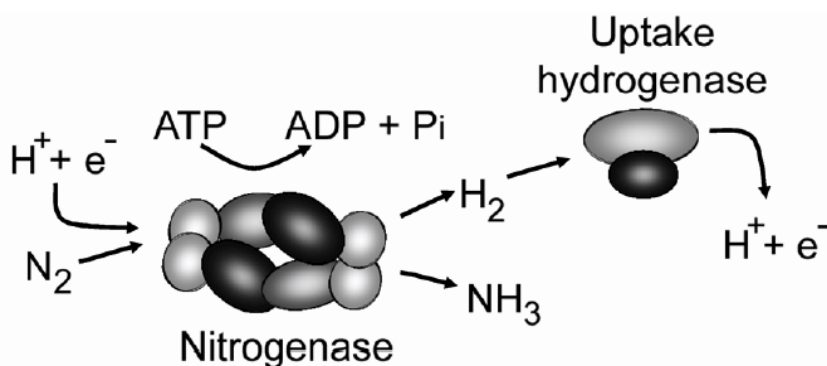


Fig. 3. Hydrogen metabolism by nitrogenase and hydrogenase. Nitrogenase comprises 3 subunits, 2 α -subunits (light gray ovals), 2 β -subunits (dark gray oval) and 4 dinitrogenase reductase subunits (light gray balls). Nitrogenase reduces N₂ to NH₃ and reduces electrons to H₂, consuming ATP. The uptake hydrogenase comprises two subunits, HupL, (the larger light gray oval) and HupS (the smaller dark gray oval), which regenerate electrons from H₂. The actual structure of HupSL has not yet been determined. Adapted from Tamagnini et al., 2002.

2.3. Pathways for H₂ production

There are several hydrogenase-dependent pathways available for H₂ production in cyanobacteria and algae (Kruse et al., 2005ab; Rupprecht et al., 2006). The first pathway is

the photo-dependent H_2 , in which the electron transport occurs via two photosystems from water to Fd (Figure 1). H^+ that is released from lumen and e^- from reduced ferredoxin are used for H_2 production by hydrogenase. This is an efficient pathway in cyanobacteria, but inefficient in green algae. However, under conditions of low activity of PSII, for instance, upon sulfur deprivation, which significantly eliminates O_2 , the rate of H_2 photoproduction can be significant (Melis et al., 2000; Kruse et al., 2005b).

The second pathway for H_2 production is photo-fermentative, which effectively occurs in two temporal stages. During the first stage, the photosynthetic processes produce carbohydrates, providing mitochondrial respiration and cell growth. During the second stage, under anaerobic conditions, hydrogenase expression is induced, and NADPH pumps electrons from stored reductants to the PQ pool.

PSI accepts e^- and H^+ delivered to the PQ pool, which is fully reduced under anaerobic conditions by enzymatic oxidation of intracellular reductants derived from fermentation. Mitochondrial oxidative phosphorylation is largely inhibited. The separation of photosynthetic O_2 -evolution and carbon accumulation from anaerobic consumption of cellular metabolites and concomitant photosynthetic H_2 -evolution is crucial for increasing the efficiency of this pathway (Melis, 2007). Thus, anaerobic conditions force some H_2 producers re-route the energy stored in carbohydrates to chloroplast hydrogenase, likely, using a NADPH-PQ electron transfer mechanism, which presumably facilitates ATP production via photophosphorylation. The two stage pathway seems to be the most effective for H_2 bioproduction (Kruse et al., 2005b).

The third pathway is similar to the second, produces H_2 from water but uses nitrogenase of cyanobacteria. Here, electrons and protons are also delivered from photosynthesis. However, this pathway requires the largest numbers of photons, which results in lower efficiency in comparison with other pathways and hence, makes it economically impractical.

2.4. Oxygen sensitivity of hydrogenases

Like nitrogenases, the majority of hydrogenases are also very sensitive to O_2 (Ghirardi et al., 2000, 2007). It is an important issue, and pathways for suppressing O_2 production and improving H_2 production yield were discussed in several recent reviews (Zhang et al., 2002; Melis, 2005; Kruse et al., 2005b; Rupprecht et al., 2006; Lubitz et al., 2008; Barber, 2007, 2009; Allakhverdiev et al., 2009). Due to the fact that hydrogenases are hypersensitive to oxygen and are located in the chloroplast, where PSII releases O_2 , H_2 production rate is usually low. Therefore it is important to decrease the O_2 concentration. Natural mechanisms that could be used for this are: the enhancement of respiration and chemical reduction of O_2 by PSI, and reversible inactivation of O_2 evolution in PSII (Kruse et al., 2005b; Rupprecht et al., 2006; Allakhverdiev et al., 2009). One of the approaches to decline in the rate of oxygenic photosynthesis is sulfur deprivation, which is described in earlier reviews (Ghirardi et al., 2000, 2007).

An effective pathway for generation of H_2 is the indirect biophotolysis that intends to bypass the oxygen sensitivity of the hydrogenases by separating H_2 -producing reactions from the oxygen evolving ones (Ghirardi et al., 2000; Laurinavichene et al., 2002; Prince and Khesghi, 2005). The properties and possible practical applications of hydrogenases of many phototrophic microorganisms are examined earlier in the review of Gogotov (1986) and in recent reviews (Vignais and Colbeau, 2004; Dutta et al, 2005).

2.5. Reduced antenna size and increased PQ pool

The efficiency of light utilization is one of the important factors that determine the H₂ photoproduction yield. Enhanced H₂ production may be achieved by engineering the antenna size to suppress fluorescence and heat dissipation that causes reduction in efficiency (Melis et al., 1999; Kruse et al., 2005b). Genes that regulate the Chl antenna size in the model green alga *Chlamydomonas reinhardtii* were identified and characterized (Melis, 2005). Analysis of the *tla1* and *tlaX* mutants with decreased Chl antenna size in comparison with the wild type demonstrated higher yields of photosynthesis in microalgae with a truncated Chl antenna size.

The increase of PQ pool capacity and strong proton buffer capacity can also be considered for improving light utilization since this leads to an accelerated electron transport to PSI, slows down the back reactions in the PSII, and oxidizes the reducing equivalents stored during CO₂ fixation. Besides, down regulation of competing pathways can redirect the fluxes of electrons via PSI and Fd into hydrogenases (Figure 1).

One additional point might be the regulation of PSI/PSII ratio (Kawamura et al., 1979). It is known that this ratio is variable depending on the light quality and quantity used for growth. The corresponding gene(s) that regulate(s) this ratio has(ve) not yet been identified but selective growth conditions may be favorable for H₂ production.

2.6. Immobilization of microbial cultures

The reported rates of H₂ production by sulfur-deprived cultures are still far below the maximum potential rate of H₂ photoproduction for an algal system (Ghirardi and Amos, 2004) mainly due to the partial inactivation of photosynthetic water oxidation (Laurinavichene et al., 2006). On the other hand, immobilized cyanobacteria produces H₂ at much higher volumetric rates than suspension cultures (Rao and Hall, 1996). The improved and longer-term H₂ photoproduction by immobilized green alga cells was successfully demonstrated (Zhang et al., 2002; Laurinavichene et al., 2002, 2006, 2008). It was shown that sulfur-deprived cultures of *C. reinhardtii* cells can be immobilized by inexpensive matrices and sulfur-deprivation stress can be successfully applied to immobilized algal cells.

Moreover, both natural cultures and future ideal artificial photobioreactors for H₂ photoproduction should be based on two reactions: photosynthetic water splitting to O₂ and H⁺ on the donor side and the H⁺ reduction on the acceptor side of PSII, using only this photosystem alone. Nevertheless in case of this approach a few problems still exist such as getting H₂ gas separately from other contaminants, first of all O₂, or the inhibition of the catalytic site of water oxidation system by molecular hydrogen. Thus, it is important to separate the processes of O₂ evolution and H₂ photoproduction. The immobilization approach may solve the problem of compartmentalization.

2.7. The use of mimics of water oxidation system

Another approach to overcome partial inactivation of photosynthetic water oxidation system leading to low efficiency and instability of H₂ photoproduction is the use of mimics of the natural Mn-cluster. It is well known that the water oxidation complex is composed of a special tetra-manganese cluster with a composition of Mn₄CaCl₂ (Loll et al., 2005; Murray et al., 2008) which is very important in photosynthetic oxygen evolution. However, the oxygen-evolving complex of PSII is not suitable for engineering application such as H₂ photoproduction due to its limited stability.

It is believed that performing a directed molecular design and broad synthesis of different artificial metal-organic complexes with different ligands spheres and matrices that mimic the natural Mn-cluster of PSII might avoid the problems associated with low H₂ photoproduction rates and scale-up of bioreactors. Such systems would have more versatility, and might split water with sun light and produce hydrogen and oxygen, with a high efficiency and long term stability.

Many synthetic Mn complexes with different ligands have been synthesized and were examined with various degree of restoration of the original function of PSII, including oxygen evolution in Mn depleted PSII complexes (Klimov et al., 1982, 1990; Allakhverdiev et al., 1994ab, 1999; Hotchandani et al., 1999, 2000; Nagata et al., 2007, 2008), and some of them even produced hydrogen peroxide (Nagata et al., 2007). If the protons emerging from the water oxidation complex could be captured and reduced to H₂, such reconstructed photosynthetic systems could provide interesting approaches for future developments. A further approach could be the combination of an artificial Mn-containing water oxidation complex with the hydrogenase system stabilized by inexpensive matrices.

2.8. Enhanced resistance to environmental stress conditions

To increase productivity, algal cells must be maintained in a healthy, active state during H₂ production for a long period of time. The tolerance of cell cultures to environmental stresses, first of all, to photoinhibition, salt stress and high temperatures, is necessary for sustainable photosynthesis and, hence, H₂ production (Kruse et al., 2005b; Rupprecht et al., 2006; Allakhverdiev et al., 2008, 2009). The efficiency of the recovery of PSII, from a damage induced by high light or environmental stress is one of the key factors in photosynthetic resistance (Kreslavski et al., 2007; Allakhverdiev and Murata, 2008; Allakhverdiev et al., 2008).

2.9. The use of mutants

An alternative approach for improving H₂ production in photosynthetic organisms is the systematic genetic screening for mutants with an increased ability for effective production of H₂. Genetic engineering has shown significant promise for increasing H₂ production both in algae and cyanobacteria (Kruse et al., 2005b; Melis, 2005, 2007; Prince and Kheshgi, 2005; Ghirardi et al., 2007; Sakurai and Masukawa, 2007).

Molecular engineering that tunes the algal hydrogenase enzyme insensitive to the presence of O₂ was suggested (Ghirardi et al., 2005, 2007). Besides, replacing the algal hydrogenase with strong oxygen tolerant, or at least reversibly inactivated, bacterial enzyme may be possible (Jones et al., 2003).

It is difficult to judge, which organisms comprise the most promising systems for H₂ production. The NiFe-hydrogenases of cyanobacteria have an advantage compared to Fe-hydrogenases of algae: they have much higher tolerance to O₂ and are resistant to various unfavorable environments (Ghirardi et al., 1997). On the other hand, algal hydrogenases can reach very high specific activities that are much higher than those of cyanobacterial hydrogenases but they are very oxygen sensitive (Ghirardi et al., 2007).

Therefore it is important to develop strategies for reducing the O₂ sensitivity. For example, it is possible to engineer an algal [FeFe]-hydrogenase resistant to O₂ inactivation or introduce a gene encoding for a [NiFe]-hydrogenase with increased resistance into photosynthetic

cyanobacterial cells. The processes of H₂ photoproduction based on using cyanobacteria and other cell cultures demonstrated relatively low conversion efficiencies (Riis et al., 2005). Besides, as mentioned, H₂ production can be improved with mutants having a reduced antenna size that decreases heat losses and fluorescence (Melis et al., 1999; Melis, 2005) and effectively redirect H⁺ and electron fluxes to their corresponding H₂-producing enzymes (Figure 1). The theory predicts that a solar light to H₂ photon conversion efficiency of 10% can be reached (Kruse et al., 2005b).

Biodiversity in cyanobacterial species is well known, therefore it is not rare to find organisms that show unique properties. In terms of H₂ production, the Chl *d*-dominated cyanobacterium, *Acaryochloris marina*, can be an interesting target. This organism contains a *hypABCDE* gene for a full complement of bidirectional hydrogenase subunits on a plasmid (pREB4) (Swingley et al. 2007). Due to the red-shifted absorption maximum of Chl *d*, this organism can utilize the light up to a near infra-red region. Due to the unique redox potentials of its electron transfer components in photosynthesis (Tomo et al., 2007, 2008) this species might be referred to as a natural mutant in this aspect.

2.10. Role of photosystems in H₂ photoproduction

Besides the activity of PSI, at least some activity of PSII is required to sustain the H₂-photoproduction. This is in line with recent observations obtained with the use of inhibitors (Kosourov et al., 2003). This last study indicated that the vast majority of the electrons driving H₂ production originates from water oxidation. The effect of progressive impairment of PSII photochemical activity in sulfur-deprived *C. reinhardtii* D1-R323 also demonstrated the progressive decrease in O₂-evolution (Makarova et al., 2007). The mutants exhibited lower H₂ yield compared to the wild type.

An interesting problem is the direct evolution of H₂ by PSII. Earlier studies have shown that H₂ can be produced from PSII under certain conditions, both in mutants lacking PSI (Boichenko et al., 1986), and in preparations of PSII (Mal'tsev et al., 1988). The wild type and mutants, lacking PSII, of green alga of *Chlamydomonas reinhardtii*, produced H₂ with high enough efficiency, but the mutant lacking PSI demonstrated low efficiency in H₂ evolution (Boichenko et al., 1986). Conversely, subchloroplast preparations enriched in PSII in the presence of the electron donor TMPD exhibited higher H₂-evolution rates (up to 30 nmol/mg Chl per h) than preparations enriched in PSI under the same conditions (Mal'tsev et al., 1988). Interestingly, H₂ photoproduction was stimulated by 10-fold after the removal of manganese (by tris-treatment) from PSII and this reaction was suppressed by DCMU (5 μM), dinoseb (10 μM), atrazine (10 μM) *o*-phenanthroline (10 μM) or CO (0.4%) (Mal'tsev et al., 1988). The data on the suppression of H₂ evolution by well-known inhibitors of PSII (DCMU, dinoseb, atrazine) prove that the H₂ photoproduction is sensitized by the reaction center of PSII. Moreover, it has been shown that the mid-point redox-potential of the intermediate electron acceptor of PSII, pheophytin (Pheo), is -0.61 V (Klimov et al., 1979). Theoretically, this potential is sufficient to allow PSII to photoreduce electron acceptors with redox-potential ca. -0.4 V (ferredoxin, NADP⁺, methylviologen, benzylviologen, NO₂⁻, NO₃⁻, SO₄²⁻, etc.) typical for PSI, and photoreduction of H₂ (-0.42V) (Allakhverdiev and Klimov, 1992).

These results demonstrate that theoretically, isolated PSII can produce H₂ under sun light. However, the detailed characterization and application of this unique approach of H₂ photoproduction by PSII should be a subject of research in the near future.

3. H₂ photoproduction in artificial systems

3.1. Principles and molecular units for artificial photosynthetic systems

Production of hydrogen from water by use of solar light energy is an important technology for hydrogen economy. Although there are many approaches towards this goal, we focus here on the “biomimetic” approach based on the mechanism of natural photosynthesis.

Figure 2 shows the conceptual overview of an artificial photosynthetic system that produces H₂ from water. The minimal system consists of three components: photosensitizer (P), oxidation catalyst (Cat_{ox}) and reduction catalyst (Cat_{red}). The photosensitizer is required to produce the photo-excited state that initiates electron transport. Cat_{ox} oxidizes water to O₂, and Cat_{red} reduces H⁺ to H₂. At present, however, no artificial systems that contain all three components have been reported. This is mainly due to the difficulty for two redox (reduction/oxidation) catalysts with opposite functions to cooperate within a single system. These catalytic sites should be spatially separated to avoid undesirable interference of each other, which presents a great challenge in the molecular architecture. In practice, the present researches focus on either of the “half” reactions, that is, formation of O₂ or H₂ by use of sacrificial electron acceptor or donors. Systems having both oxidation and reduction sites will be the subject for future study.

In addition to these “minimal” components, an artificial photosynthetic system can have other components with different functions, which are also shown in Figure 2. The light-harvesting antenna molecules will capture the incoming light and deliver the excitation energy to the photosensitizer. The donor (D) and acceptor (A) molecules will give/receive electrons to/from the excited photosensitizer. Owing to the short lifetime of the excited states, these molecules should be located in the vicinity of the photosensitizer, as is seen in the natural photosynthetic reaction centers.

Electron carriers (C) will transport electrons from the acceptors (A) to the reductive catalytic site, or from the oxidative catalytic site to the donors (D). These “carriers” act as a temporary storage of electrons, or an electron “buffer”, between the photophysical and photochemical parts of the system. This feature will allow the asynchronous operation of the photoinduced electron transfer and the electrocatalytic chemistry.

In the following part, we will discuss each of these functional components. Since we are particularly interested in H₂ production, we will first discuss Cat_{red}, which is responsible for production of H₂ from H⁺. Other functional components are described later, with special emphasis on biomimetic standpoints.

3.2. Catalysts for H₂ production

Catalysts for conversion of H⁺ into H₂ (or vice versa) will play a key role, not only in artificial photosynthesis, but also for the hydrogen economy in general (Crabtree, 2004). Many essential technologies for hydrogen economy, including fuel cells, storage, and production, depend heavily on the efficiency of H⁺/H₂ catalysts, so that the quest for better catalysts is getting more intensive these days.

The platinum metal is the most classical, and still the most efficient, catalyst for hydrogen evolution (Wohrle et al., 2003). It has almost ideal properties required for reduction of H⁺ to H₂; low overpotential, high reaction rate, good electron capacity and conductivity, and high chemical and mechanical stability. As such, Pt metal is often the best choice both for laboratory research and for practical applications. However, as the needs for catalysts grow

rapidly, the high cost and limited quantity are the major issues. In order to address this problem, many researchers are actively seeking for reasonable alternatives to Pt metal catalyst.

Particularly interesting from the biomimetic viewpoint are the efforts in the field of coordination chemistry (Koelle, 1992). The known H₂ catalysts based on coordination compounds can be classified roughly into three categories; those based on precious metals (Pt, Rh, Ir), on common metals (Co, Ni, Fe), and those related to (and/or inspired by) the natural enzyme hydrogenase. Since the enzyme hydrogenases use Fe and Ni in the active centers, there are significant overlaps in the latter two categories. Nevertheless, such classification will be beneficial for us to get a quick overview of this fast-growing research area.

3.3. H₂ catalysts with precious metals

In early studies of H₂ production, rhodium(III) polypyridine complexes such as [Rh(bpy)₃]³⁺ (bpy = 2,2'-bipyridine) were used as electron carriers together with Pt metal catalysts (Lehn and Sauvage, 1977; Brown et al., 1979a), but later it was found that these complexes were capable of generating hydrogen without Pt (Chou et al, 1982). In this system, a four-coordinate Rh(I) complex [Rh(bpy)₂]⁺ was produced during the course of the reaction (via two-electron reduction of the Rh(III) complex and subsequent departure of one bipyridine ligand), and the rhodium-hydride species such as [Rh(bpy)₂H]²⁺ is the likely intermediate for the hydrogen production. Rhodium porphyrins are also known to catalyze electrochemical generation of H₂ (Lexa et al., 1997). Iridium(III) complexes have also been used for photoproduction of H₂ (Goldsmith et al, 2005). However, in this system the iridium complexes mainly act as the photosensitizers, and the true catalysts for production of hydrogen may be the cobalt complex (used as an electron relay) rather than the iridium complexes.

From the synthetic point of view, one of the advantages of these precious metal complexes is the robustness of the metal-ligand bonds, so that sophisticated compounds with different functional groups can be prepared. One interesting approach is to combine the photosensitizer and catalyst for hydrogen evolution in one molecule; the first successful example of such "combined" photocatalyst was based on Pt for hydrogen evolution and Ru as photosensitizer (Ozawa et al., 2006). Covalent assembly of Rh center and Ru photosensitizer was also prepared, and gave good performance of rhodium-based photoproduction of H₂ (Arachchige et al., 2008; Elvington et al., 2007).

Unfortunately, these precious metal catalysts share with Pt catalyst the problem of high cost and limited availability; both Rh and Ir are even less abundant than Pt in earth crust. Although these catalysts are quite interesting from the viewpoint of coordination chemistry, it is not likely that these catalysts will become of practical importance in real world applications, unless some compounds with extremely high activity are discovered.

3.4. H₂ catalysts with common metals

Among the less precious metals in the first-row transition metal series, iron (Fe), cobalt (Co) and nickel (Ni) have shown promising results as H₂ catalysts. Complexes of cobalt, like its congener rhodium, are often used as electron carriers in photochemical H₂ producing systems (Brown et al., 1979b), but they are also useful for production of H₂ (Kellet and Spiro,

1985ab; Connolly and Espenson, 1986). Although the reaction mechanism has not yet been fully clarified, it is generally accepted that Co(III)-hydride complexes are crucial intermediates (Koelle and Paul, 1986). A BF_2 -bridged diglyoxime Co complex produces H_2 electrochemically at potentials of -0.28 V vs. SCE, which presents one of the smallest overpotentials reported for complex catalysts (Figure 4) (Hu et al., 2005). Covalent assembly of ruthenium photosensitizer and cobalt complex is also reported (Fihri et al., 2008).

Fe and Ni are particularly interesting because of their presence in the hydrogenase enzymes. Fe is also attractive because of its high abundance and low cost. Macrocyclic complexes of iron (Bhugun et al., 1996) and nickel (James et al., 1996) have been used for photochemical or electrocatalytic H_2 production. Although the active center of hydrogenase is dinuclear, a simple mononuclear Fe(I) complex can sometimes be active for H_2 production (Kayal and Rauchfuss, 2003).

In comparison with the precious metals, the difficulty of handling coordination compounds of first-row transition metals lies in their high susceptibility towards ligand exchange, particularly in aqueous solutions. This is generally due to the weaker metal-to-ligand bonds of these metals than the second- and third-row transition metals. Such characteristics, however, can also provide advantages when catalytic reactions are concerned, because weaker bonds may lead to smaller activation energies (and thus faster reactions). To utilize the inherent power of these elements, it is definitely necessary to design the coordination environment carefully, thereby improving the stability and controlling the reactivity. This is exactly what the natural enzymes do, so that it is worthwhile to see what structural features are found in the enzymes that catalyze hydrogen production (see below).

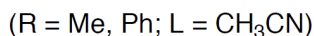
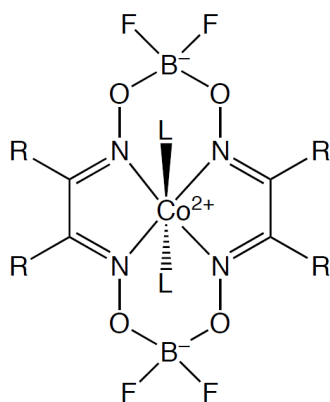


Fig. 4. The cobalt complex that produces hydrogen with small overpotential (Hu et al., 2005).

3.5. Hydrogenase and related synthetic compounds

A hydrogenase is an enzyme which presents in some anaerobic organisms, and catalyzes reversible conversion between H_2 and H^+ . In the active center of a hydrogenase enzyme, there are two metal ions (FeFe or NiFe) that cooperate during the catalytic cycle for

production (and consumption) of H₂. Recently much progress was made in researches on the structures and function of the hydrogenases by X-ray analysis, spectroscopic techniques, theoretical methods, and model studies (Artero and Fontecave, 2005; Peters et al., 1998). The schematic view of the active centers of two types of hydrogenases is shown in Figure 5.

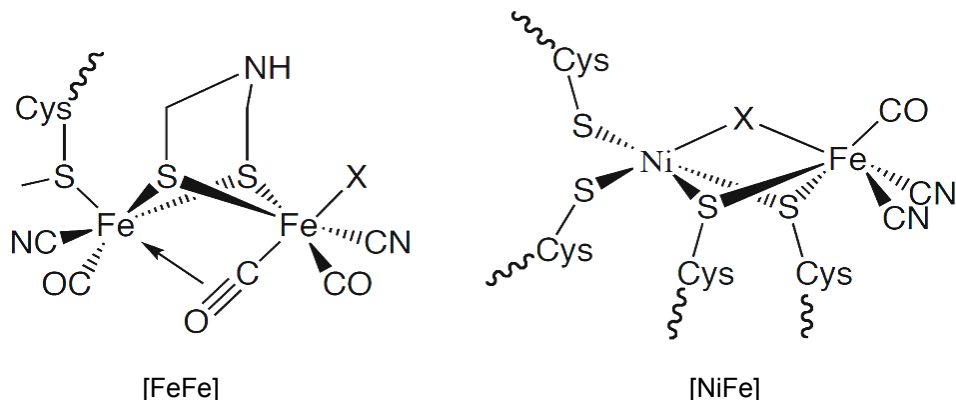


Fig. 5. The active centers of [FeFe] hydrogenase (left) and [NiFe] hydrogenase (right).

As for the synthetic model studies, much attention has been focused on the active sites of the Fe-only hydrogenases, which consist of a bimetallic iron center bridged with a dithiolate, terminal thiolate ligands and CO/CN auxiliary ligands (Rauchfuss, 2004, 2007; Tard et al., 2005). On the other hand, the syntheses of the models of [NiFe]-hydrogenases have been more challenging. By use of Ru in place of Fe (Ru is electronically similar to but more robust than Fe), a Ni-Ru complex with a bridging hydride ligand was successfully isolated (Ogo et al., 2007).

The Fe-only hydrogenases catalyze the reduction of protons to dihydrogen with almost zero overpotential (Holm et al., 1996). On the other hand, the synthetic model compounds still require large negative over-potentials (-0.4 to -1.4 V) (Tard et al., 2005; Gloaguen et al., 2001, 2002; Borg et al., 2004). There are theoretical studies to clarify the detailed mechanism of hydrogenase (Bruschi et al., 2004; Siegbahn, 2004), and zero overpotential of hydrogenase is claimed to be reproducible by computation (Norskov and Christensen, 2006). Such attempts will be helpful for designing new catalysts with better performance (Hinnermann et al., 2005; Norskov et al., 2005).

4. Other Components of Artificial Photosynthesis

4.1. Overview

While the H₂ producing catalysts are the crucial components for photoproduction of hydrogen, there are other important components as well. Obviously the most important is the photosensitizer, which converts light energy into chemical energy. The photosensitizers in photosynthesis (natural or biomimetic) are molecules that acquire light and cause photoinduced charge separation between nearby donor or acceptor molecules. This is in contrast with the semiconductor systems (e.g. solar cells), where the photoinduced charge

separation takes place between the valence and conduction bands of the semiconductor. An interesting hybrid between these systems is dye-sensitized solar cells (O'Regan and Grätzel, 1991), in which inorganic semiconductors act as the electron acceptor from the excited photosensitizers.

For photoinduced charge separation to take place efficiently, it is important that the donors and acceptors are located within short distances from the photosensitizers. This is actually the case in all resolved structures of natural photosynthetic reaction centers (Deisenhofer and Michel, 1989; Jordan et al., 2001; Zouni et al., 2001; Loll et al., 2005; Barber and Murray, 2008). In many artificial systems, donors and acceptors are simply put within the solution containing the photosensitizers, so that the efficiency of the photoinduced electron transfer depends on the random diffusion of these molecules. It is a great challenge for chemists to build the multi-component systems that are specifically designed for photoinduced electron transfer; in fact, many organic chemists were so much attracted in this subject that great progress has been achieved in the area of electron transport (Wasielewski, 2006). However, application of these sophisticated systems for redox chemical conversions is yet to be explored.

The antenna complexes, which collect light energy and transport to the photosensitizer, are also crucial components for efficient use of incident light (Kühlbrandt et al., 1994). In natural photosynthetic reaction centers, the quantum efficiency is very high because of the carefully designed molecular architecture, however the optical density of the reaction centers is very low because only one pigment in the huge reaction center complex is photoactive towards photosynthetic reactions. Antenna complexes have high optical density in the wide range of visible spectral region, and funnel the excitation energy towards the photoactive pigment in the reaction center.

The electrons for reduction of H^+ must come from somewhere. In many photochemical systems that produce hydrogen, sacrificial donors such as ethylenediaminetetraacetic acid (EDTA) or triethanolamine (TEOA) are used. Apparently, these cannot be practical sources of hydrogen because of their high cost. The ideal source of electrons is water, which is abundant and produces only dioxygen as the byproduct. Consequently, synthetic oxygen-evolving complexes are under active study (Sala et al., 2009). Another interesting approach from the biomimetic viewpoint is to follow the evolutionary pathway of natural photosynthetic organisms. Before the appearance of oxygen evolving center, old photosynthetic organisms utilized other substances such as H_2S and alcohols as electron donor. In this context, there are reports of biomimetic photosynthetic systems that utilize thiols and alcohols as electron donors (Nagata and Kikuzawa, 2007; Nagasawa et al., 2009).

4.2. Photosensitizers

The most successful photosensitizers in artificial photosynthetic systems are ruthenium polypyridyl complexes. Photoproduction of H_2 by use of $Ru(bpy)_3^{2+}$ as the photosensitizer was reported as early as 1978 (Moradpour et al., 1978). The big advantage of the ruthenium complexes as the photosensitizers is their long lifetimes of the excited MLCT states (870 μs in CH_3CN) (Jones and Fox, 1994). The strong absorption band in the visible region is also advantageous. Moreover, from the viewpoint of synthetic chemistry, the relatively slow rates of ligand exchange on the ruthenium center is beneficial for constructing elaborated multinuclear structures, as demonstrated by recent examples of "multinuclear molecular devices" for photoproduction of H_2 (Sakai and Ozawa, 2007).

Clear disadvantage of ruthenium complexes is the cost of the element. In this respect, better alternatives are the pigments that are purely organic or organic with some common metals. Inspired by the natural photosynthesis, chlorophylls and porphyrins were used for photoproduction of H₂ (Ngweniform et al., 2007; Amao and Okura, 2002). The weak points of the organic pigments are poor long-term stability and low quantum efficiency. In order to overcome these problems, we may learn from natural photosynthesis and introduce mechanisms of light-protection and/or high efficiency electron transports.

4.3. Donors, acceptors, and electron carriers

Various electron donors and acceptors were examined during the course of mimicking the primary events of photosynthesis (Wasielewski, 2006), but only a few are used in relation to photoproduction of H₂. Early studies use EDTA as the sacrificial donor and viologens as the acceptor (Moradpour et al., 1978). The viologens were also used as electron carriers that transport electrons to the reductive catalytic site. Covalent connections of viologens and photosensitizers were examined with promising results (Amao and Okura, 2002). Natural photosynthesis uses quinones for both the terminal acceptor in the photosystems and the electron carrier in the form of PQ pool. However, it is only recently that the function of the PQ pool was mimicked by use of synthetic molecules (Nagata and Kikuzawa, 2007).

Because of the inherent kinetic mismatch between the (fast) photoinduced electron transfer and (slow) electrochemical processes, it is important to select appropriate use of the electron carriers for successful photoproduction of H₂. Apparently, there are plenty of rooms for improvement in this particular area of artificial photosynthesis.

4.4. Antennas

In spite of the apparent structural complexity of the natural photosynthetic antennas, the synthetic models of photosynthetic antenna have been quite successful. This is partly because the excitation energy transfer by the Förster mechanism (Förster, 1948) has relatively mild dependence on interchromophore distances ($1/r^6$) in contrast with the case in electron transfer (exponential), so that the geometries of the chromophores need not be so rigorously controlled. Self-aggregation of amphiphilic chlorophyll analogues leads to spontaneous formation of artificial antenna (Prokhorenko et al., 2002). As for covalently bonded systems, dendritic molecules can effectively collect excitation energy, which can be used for production of H₂ (Sakamoto et al., 2001). One unique approach is to use a π -conjugated polymer embedded in dendrimer-based protecting shield (Jiang et al., 2004). The polymer acts both as the light absorber (photosensitizer) with a large absorption cross section and as the molecular wire (antenna) that transports the excitation energy to the reactive site.

4.5. Catalysts for water oxidation

The catalyst at the oxidizing side, which performs 4-electron oxidation of water to O₂, is arguably the most difficult part in artificial photosynthesis (Herrero et al., 2008). Although there have been many research works on electrochemical and photochemical production of O₂ from water (Eisenberg and Gray, 2008), it should be stated that all approaches are currently still at the developmental stage.

The natural oxygenic photosynthesis may provide hints to tackle this problem. The oxygen-evolving complex contains four manganese ions and one calcium ion (Barber and Murray, 2008). Although the detail mechanism is still under intense investigation (McEvoy and Brudvig, 2006), it is certain that these metal ions should play central roles during O₂ production.

Along this idea, multinuclear complexes that can accumulate and delocalize four oxidizing equivalents have been developed as functional models of oxygen-evolving complex. Di- and tetranuclear manganese complexes, especially a family of metal-oxo "cubane" complexes as well as mono-, di-, and trinuclear ruthenium complexes have been reported as molecular catalysts capable of evolving O₂ from water (Naruta et al., 1994; Wada et al., 2000; Carrell et al., 2002; Wu et al., 2006). Some of these complexes undergo photocatalytic oxidation of water via direct action of light into the metal core (Brimblecombe et al., 2008).

To summarize, research in artificial biomimetic photosynthesis is in its early stage and has not yet reached to the state that production of integrated and practical systems is feasible. Nevertheless, there has been significant progress in all important aspects in this area. Towards the future, there should be continuous efforts in the development of synthetic catalysts for H₂/O₂ production, photochemical conversion apparatus for controlled electron transfer, and light-harvesting units. Even more important is to integrate these components into functional assemblies, which is likely to be realized with the aid of profound understanding of the structural/functional features of biological systems.

5. Conclusion

Both the natural and biomimetic photosynthetic processes are efficient and cost-effective for water splitting, and H₂ formation. The actual photo-production of hydrogen will have to be carried out in a sealed photobioreactor, and also requires careful reactor designs (Tsygankov et al., 2002) for the substantial improvements of hydrogen production rates and yields. A prerequisite challenge is to improve current systems at the biochemical level so that they can clearly generate hydrogen at a rate and approach the 10% energy efficiency, which has been already surpassed in photoelectrical systems (Shah et al., 1999; Gratzel, 2001).

Currently and in near future, researchers could focus on increasing the O₂-tolerance of [FeFe]-hydrogenases and the use of immobilized microbial cultures to reach this target, as these methods are promising. Reduced antenna size and increased PQ pool, decreased PSI cyclic electron transport as well as enhanced resistance to environmental stress conditions should be considered for the improvement of photohydrogen production. These studies will guide further molecular engineering research aimed at improving the efficiency of hydrogen bioproduction. Thus, research is also needed to understand the diversity and capacity of natural hydrogen production systems and optimize their utilization in H₂ production processes.

Acknowledgement

This work was financially supported, in part, by grants from the Russian Foundation for Basic Research (No: 08-04-00241 and 09-04-91219-CT), from the Molecular and Cell Biology Programs of the Russian Academy of Sciences, to SIA; by Japanes Society for the Promotion

of Science (JSPS) Invitation Fellowship for Research in Japan, to SIA (ID No: S-09155); by a Grant-in-Aid for Creative Scientific Research (No. 17GS0314) from JSPS and by Scientific Research on Priority Areas "Comparative Genomics" (Nos: 17018022 and 18017016) from the Ministry of Education, Sports, Culture, Science, and Technology, Japan, to MM; by Grant-in-Aid for Scientific Research (C) (No. 19550173) from JSPS, by "Nanotechnology Support Project" of MEXT, Japan, to TN. V. Thavasi and S. Ramakrishna acknowledge the NUS, Singapore. RC was supported by Natural Sciences and Engineering Research Council of Canada.

Abbreviations

AP, artificial photosynthesis; DCMU, 3-(3',4'-dichlorophenyl)-1,1-dimethylurea; Fd, ferredoxin; PQ, plastoquinone; PSII, photosystem II; PSI, photosystem I; TMPD, N,N,N',N'-tetramethyl-p-phenylenediamine.

6. References

- Abraham, S. (2002). Toward a more secure and cleaner energy future for America: national hydrogen energy roadmap; production, delivery, storage, conversion, applications, public education and outreach, U.S. Department of Energy, Washington, DC
- Allakhverdiev, S.I.; Karacan, M.S.; Somer, G.; Karacan, N.; Khan, E.M.; Rane, S.Y.; Padhye, S.; Klimov, V.V. & Renger, G. (1994a). Reconstitution of the water-oxidizing complex in manganese depleted photosystem II complexes by using synthetic binuclear manganese complexes, *Biochemistry*, v. 33, p. 12210-12214
- Allakhverdiev S.I.; Karacan, M.S.; Somer, G.; Karacan, N.; Khan, E.M.; Rane, S.Y.; Padhye, S.; Klimov, V.V. & Renger, G. (1994b). Binuclear manganese (III) complexes as electron donors in D1/D2/cytochrome b559 preparations isolated from spinach photosystem II membrane fragments, *Z. Naturforsch.*, v.49c, p.587-592
- Allakhverdiev, S.I. & Klimov, V.V. (1992). Photoreduction of NADP⁺ in photosystem II of higher plants: requirement for manganese, *Z. Naturforsch.*, v.47c, p.57-62
- Allakhverdiev, S.I.; Kreslavski, V.D.; Thavasi, V.; Zharmukhamedov, S.K.; Klimov, V.V.; Nagata, T.; Nishihara, H. & Ramakrishna, S. (2009). Hydrogen photoproduction by use of photosynthetic organisms and biomimetic systems, *Photochem Photobiol Sci.*, v.8, p.148-156
- Allakhverdiev, S.I.; Kreslavski, V.D.; Klimov, V.V.; Los, D.A.; Carpentier, R. & Mohanty, P. (2008). Heat stress: An overview of molecular responses in photosynthesis, *Photosynth. Res.*, v.98, p.541-550
- Allakhverdiev, S.I. & Murata, N. (2008). Salt stress inhibits photosystems II and I in cyanobacteria, *Photosynth Res.*, v.98, p.529-540
- Allakhverdiev, S.I.; Ozdemir, U.; Harnois, J.; Karacan, N.; Hotchandani, S.; Klimov, V.V.; Murata, N. & Carpentier, R. (1999). Reconstruction of the water-oxidizing complex in manganese-depleted photosystem II preparations using mononuclear manganese complexes, *Photochem. Photobiol.*, v.70, p.57-63
- Alstrum-Acevedo, J.H.; Brennaman, M.K. & Meyer, T.J. (2005). Forum chemical approaches to artificial photosynthesis, *Inorg. Chem.*, v.44, p.6802-6827

- Amao, Y. & Okura, I. (2002). Photoinduced hydrogen production with the system containing water-soluble viologen-linked porphyrins and hydrogenase, *J. Mol. Catal., B*, v.17, p.9-21
- Arachchige, S.M.; Brown, J. & Brewer, K.J. (2008). Photochemical hydrogen production from water using the new photocatalyst $[(\text{bpy})_2\text{Ru}(\text{dpp})]\text{[2RhBr}_2\text{]}\text{(PF}_6\text{)}_5$, *J. Photochem. Photobiol.*, v.197, p.13-17
- Artero, V. & Fontecave, M. (2005). Some general principles for designing electrocatalysts with hydrogenase activity, *Coord. Chem. Rev.*, v.249, p.1518-1535
- Barber, J. (2007). Biological solar energy, *Phil Trans R Soc A*, v.365, p. 1007-1023
- Barber, J. (2009). Photosynthetic energy conversion: natural and artificial, *Chem Soc Rev.*, v.38, p.185-196
- Barber, J. & Murray, J. (2008). Revealing the structure of the Mn-cluster of photosystem II by X-ray crystallography, *Coord. Chem. Rev.*, v.252, p.233-243
- Bhugun, I.; Lexa, D. & Savéant, J.-M. (1996). Homogeneous catalysis of electrochemical hydrogen evolution by iron(0) porphyrins, *J. Am. Chem. Soc.*, v.118, p.3982-3983
- Blankenship, R.E. (2002). *Molecular Mechanisms of Photosynthesis*, Blackwell Science, Oxford, U.K.
- Boichenko, V.A.; Allakhverdiev, S.I.; Ladygin, V.G. & Klimov, V.V. (1986). Functional conjunction of hydrogenase with photosystem II in whole cells of *Chlamydomonas reinhardtii* mutants, *Dokl. AN SSSR*, v.290, p.995-998
- Boichenko, V.A.; Greenbaum, E. & Seibert, M. (2004). Hydrogen production by photosynthetic microorganisms, in *Photoconversion of solar energy, molecular to global photosynthesis*, (eds. M.D. Archer and J. Barber), Imperial college Press, London, v.2, pp. 397-452
- Borg, S.J.; Behrsing, T.; Best, S.P.; Razavet, M.; Liu, X.M & Pickett C.J. (2004). Electron transfer at a dithiolate-bridged diiron assembly: electrocatalytic hydrogen evolution, *J. Am. Chem. Soc.*, v.126, p.16988-16999
- Brimblecombe, R.; Swiegers, G.F.; Dismukes, G.C. & Spiccia, L. (2008). Sustained water oxidation photocatalysis by a bioinspired manganese cluster, *Angew. Chem. Int. Ed.*, v.47, p.7335-7338
- Brown, G.M.; Brunschwig, B.S.; Creutz, C.; Endicott, J.F. & Sutin, N. (1979a). Homogeneous catalysis of the photoreduction of water by visible light. Mediation by a tris (2,2'-bipyridine)ruthenium(II)-cobalt(II) macrocycle system, *J. Am. Chem. Soc.*, v.101, p.1298-1300
- Brown, G.M.; Chan, S.-F.; Creutz, C.; Schwarz, H.A. & Sutin, N. (1979b). Mechanism of the formation of dihydrogen from the photoinduced reactions of tris(bipyridine)ruthenium(II) with tris(bipyridine)rhodium(III), *J. Am. Chem. Soc.*, v.101, p.7638-7640
- Bruschi, M.; Fantucci, P. & De Gioia, L. (2004). Density functional theory investigation of the active site of Fe-hydrogenases. Systematic study of the effects of redox state and ligands hardness on structural and electronic properties of complexes related to the $[\text{2Fe}]_{\text{H}}$ subcluster, *Inorg. Chem.*, v.43, p.3733-3741
- Carrell, T.G.; Cohen, S. & Dismukes, G.C. (2002). Oxidative catalysis by $\text{Mn}_4\text{O}_4^{6+}$ cubane complexes, *J. Mol. Catal. A*, v.187, p.3-15
- Chou, M.; Creutz, C.; Mahajan, D.; Sutin, N. & Zipp, A.P. (1982). Nature of Bis(2,2'-bipyridine)rhodium(I) in Aqueous Solutions, *Inorg. Chem.*, v.21, p.3989-3997

- Chow, W.S. (2003). Photosynthesis: from natural towards artificial, *J. Biol. Phys.*, v.29, p.447-459
- Crabtree, G.W., Dresselhaus, M.S. & Buchanan, M.V. (2004). The Hydrogen Economy, *Physics Today*, v.57, p.39-44
- Connolly, P. & Espenson, J.H. (1986). Cobalt-catalyzed evolution of molecular hydrogen, *Inorg. Chem.*, v.25, p.2684-2688
- Deisenhofer, J. & Michel, H. (1989). The photosynthetic reaction centre from the purple bacterium *Rhodospseudomonas viridis*, *EMBO J.*, v.8, p.2149-2170
- Dutta, D.; De, D.; Chaudhuri, S. & Bhattacharya, S.K. (2005). Hydrogen production by cyanobacteria, *Microb. Cell Fact.*, v.4, p.36
- Eisenberg, R. & Gray, H.B. (2008). Preface on Making Oxygen, *Inorg. Chem.*, v.47, p.1697-1699
- Elvington, M.; Brown, J.; Arachchige, S.M.; Shamindri, M. & Brewer, K.J. (2007). Photocatalytic hydrogen production from water employing a Ru, Rh, Ru molecular device for photoinitiated electron collection, *J. Am. Chem. Soc.*, v.129, p.10644-10645
- Fihri, A.; Artero, V.; Razavet, M.; Baffert, C.; Leibl, W. & Fontecave, M. (2008). Cobaloxime-based photocatalytic devices for hydrogen production, *Angew. Chem. Int. Ed.*, v.47, p.564-567
- Florin, L.; Tsokoglou, A. & Happe, T. (2001). A novel type of iron hydrogenase in the green alga *Scenedesmus obliquus* is linked to the photosynthetic electron transport chain, *J. Biol. Chem.*, v.276, p.6125-6132
- Förster, T. (1948). Zwischenmolekulare Energiewanderung und Fluoreszenz, *Ann. Phys.*, v.437, p. 55-75
- Ghirardi, M.L.; King, P.; Kosourov, S.; Forestier, M.; Zhang, L. & Seibert, M. (2005). Development of algal systems for hydrogen photoproduction: addressing the hydrogenase oxygen sensitivity problem, in *Artificial Photosynthesis: From Basic Biology to Industrial Application*, (eds. A.F Collings and C. Critchley), Wiley-VCH Verlag GmbH & Co. KGaA, Weinheim, Germany, pp. 213-227
- Ghirardi, M.L. & Amos, W. (2004). Renewable hydrogen from green algae, *Biocycle*, v.45, p.59-62
- Ghirardi, M.L.; Posewitz, M.C.; Maness, P.C.; Dubini, A.; Yu, J. & Seibert, M. (2007). Hydrogenase and hydrogen photoproduction in oxygenic photosynthetic organisms, *Annu. Rev. Plant Biol.*, v.58, p.71-91
- Ghirardi, M.L.; Togasaki, R.K. & Seibert, M. (1997). Oxygen sensitivity of algal H₂-production, *Appl. Biochem. Biotechnol.*, v.63-65, p.141-151
- Ghirardi, M.L.; Zhang, L.; Lee, J.W.; Flynn, T.; Seibert, M.; Greenbaum, E. & Melis, A. (2000). Microalgae: a green source of renewable H₂, *Trends Biotechnol.*, v.18, 506-511
- Gloaguen, F.; Lawrence, J. D. & Rauchfuss, T. B. (2001). Biomimetic hydrogen evolution catalyzed by an iron carbonyl thiolate, *J. Am. Chem. Soc.*, v.123, p.9476-9477
- Gloaguen, F.; Lawrence, J.D.; Rauchfuss, T.B.; Bénard, M. & Rohmer M.-M. (2002). Bimetallic carbonyl thiolates as functional models for Fe-only hydrogenases, *Inorg. Chem.*, v.41, p.6573-6582
- Gogotov, I.N. (1986). Hydrogenases of phototrophic microorganisms, *Biochimie*, v. 68, p. 181-187.

- Goldsmith, J.I.; Hudson, W.R.; Lowry, M.S.; Anderson, T.H. & Bernhard, S. (2005). Discovery and high-throughput screening of heteroleptic iridium complexes for photoinduced hydrogen production, *J. Am. Chem. Soc.*, v.127, p.7502-7510
- Grätzel, M. (2001). Photoelectrochemical cells, *Nature*, v. 414, p. 338-344
- Herrero, C.; Lassallekaiser, B.; Leibl, W.; Rutherford, A. & Aukauloo, A. (2008). Artificial systems related to light driven electron transfer processes in PS II, *Coord. Chem. Rev.*, v.252, p.456-468
- Hinnermann, B.; Moses, P.G.; Bonde, J.; Jorgensen, K.P.; Nielsen, J.H.; Horch, S.; Chorkendorff, I. & Norskov, J.K. (2005). Biomimetic Hydrogen Evolution: MoS₂ Nanoparticles as Catalysts for Hydrogen Evolution, *J. Am. Chem. Soc.*, v.127, p.5308-5309
- Holm, H.; Kennepohl, P. & Solomon, E.I. (1996). Structural and functional aspects of metal sites in biology, *Chem. Rev.*, v.96, p.2239-2314
- Hotchandani, S.; Ozdemir, U.; Allakhverdiev, S.I.; Karacan, N.; Klimov, V.V.; Kamat, P.V. & Carpentier, R. (2000). Redox characteristics of manganese and cobalt complexes obtained from pyridine N-oxide, *Bioelectrochem.*, v.51, p.175-180
- Hotchandani, S.; Ozdemir, U.; Nasr, C.; Allakhverdiev, S.I.; Karacan, N.; Klimov, V.V.; Kamat, P.V. & Carpentier, R. (1999). Redox characterization of schiff base manganese and cobalt complexes related to water-oxidizing complex of photosynthesis, *Bioelectrochem. Bioenerg.*, v.48, p.53-59
- Hu, X.; Cossairt, B.M.; Brunschwig, B.S.; Lewis, N.S. & Peters, J.C. (2005). Electrocatalytic hydrogen evolution by cobalt difluoroboryl-diglyoximate complexes, *Chem. Commun*, v.37, p.4723-4725
- James, T.L.; Cai, L.S.; Muetterties, M.C. & Holm, R.H. (1996). Dihydrogen evolution by protonation reactions of nickel(I), *Inorg. Chem.*, v.35, p.4148-4161
- Jiang, D.-L.; Choi, C.-K.; Honda, K.; Li, W.-S.; Yuzawa, T. & Aida T. (2004). Photosensitized Hydrogen Evolution from Water Using Conjugated Polymers Wrapped in Dendrimeric Electrolytes, *J. Am. Chem. Soc.*, v.126, p.12084-12085
- Jones Jr., W. E. & Fox M.A. (1994). Determination of excited-state redox potentials by phase-modulated voltammetry, *J. Phys. Chem.*, v.98, p.5095
- Jones, A.K.; Lamle, S.E.; Pershad, H.R.; Vincent, K.A.; Albracht, S.P. & Armstrong, F.A. (2003). Enzyme electrokinetics: electrochemical studies of the anaerobic interconversions between active and inactive states of *Allochromatium vinosum* [NiFe]-hydrogenase, *J. Am. Chem. Soc.*, v.125, p.8505-8514
- Jordan, P.; Fromme, P.; Witt, H.T.; Klukas, O.; Saenger, W. & Krauss, N. (2001). Three-dimensional structure of cyanobacterial photosystem I at 2.5 Å resolution, *Nature*, v.411, p.909-917
- Kayal, A. & Rauchfuss, T.B. (2003). Protonation studies of the new iron carbonyl cyanide *trans*-[Fe(CO)₃(CN)₂]²⁻: implications with respect to hydrogenases, *Inorg. Chem.*, v.42, p.5046-5048
- Kawamura, M.; Mimuro, M. & Fujita, Y. (1979). Quantitative relationship between two reaction centers in the photosynthetic system of blue-green algae, *Plant Cell Physiol.*, v. 20, p. 697-705
- Kellett, R.M. & Spiro, T.G. (1985a). Cobalt(I) porphyrin catalysis of hydrogen production from water, *Inorg. Chem.*, v. 24, p.2378-2382

- Kellet, R.M. & Spiro, T.G. (1985b). Cobalt porphyrin electrode films as H₂ evolution catalysts, *Inorg. Chem.*, v. 24, p.2373-2377
- Klimov, V.V.; Ananyev, G.M.; Allakhverdiev, S.I.; Zharmukhamedov, S.K.; Mulay, M.; Hedge, U. & Padhye, S. (1990). Photoreaction and photoinactivation of photosystem II after a complete removal of manganese from pea subchloroplast particles, in *Current Research in Photosynthesis*, (ed. M. Baltscheffsky), Kluwer Academic Publishers, Dordrecht, pp. 247-254
- Klimov, V.V.; Allakhverdiev, S.I.; Demeter, S. & Krasnovsky, A.A. (1979). Photoreduction of pheophytin in the photosystem 2 of chloroplasts depending on the oxidation-reduction potential of the medium, *Dokl. Acad. Nauk SSSR*, v.249, p.227-230
- Klimov, V.V.; Allakhverdiev, S.I.; Shuvalov, V.A. & Krasnovsky, A.A. (1982). Effect of extraction and readdition of manganese on light reactions of photosystem II preparations, *FEBS Lett.*, v.148, p.307-312
- Koelle, U. (1992). Transition Metal-catalyzed Proton Reduction, *New J. Chem.*, v.16, p.157-169
- Koelle, U. & Paul, S. (1986). Electrochemical reduction of protonated cyclopentadienylcobalt phosphine complexes, *Inorg. Chem.*, v.25, p.2689-2694
- Kondratieva, E.N. & Gogotov I.N. (1981). Molecular hydrogen in microbia metabolism. Moscow, Nauka. pp. 344
- Kosourov, S.; Seibert, M. & Ghirardi, M.L. (2003). Effects of extracellular pH on the metabolic pathways in sulfur-deprived, H₂-producing cultures, *Plant Cell Physiol.*, v.44, p.146-155
- Kreslavski, V.D.; Carpentier, R.; Klimov, V.V.; Murata, N. & Allakhverdiev, S.I. (2007). Molecular mechanisms of stress resistance of the photosynthetic apparatus, *Membr. Cell Biol.*, v.1, p.185-205
- Kruse, O.; Rupprecht, J.; Bader, K.P.; Thomas-Hall, S.; Schenk, P.M.; Finazzi, G. & Hankamer, B. (2005a). Improved photobiological H₂ production in engineered green algal cells, *J. Biol. Chem.*, v.280, p.34170-34177
- Kruse, O.; Rupprecht, J.; Mussgnug, J.H.; Dismukes, G.C. & Hankamer, B. (2005b). Photosynthesis: a blue print for energy capture and conversion technologies, *Photochem. Photobiol.*, v.4, p.957-970
- Kühlbrandt, W.; Wang, D.N. & Fujiyoshi, Y. (1994). Atomic model of plant light-harvesting complex by electron crystallography, *Nature*, v.367, p.614-621
- Laurinavichene, T.V.; Fedorov, A.S.; Ghirardi, M.L.; Seibert, M. & Tsygankov, A.A. (2006). Demonstration of sustained hydrogen photoproduction by immobilized, sulfur-deprived *Chlamydomonas reinhardtii* cells, *Int. J. Hydrog. Ener.*, v.31, p.659 - 667
- Laurinavichene, T.V.; Kosourov, S.N.; Ghirardi, M.L.; Seibert, M. & Tsygankov, A.A. (2008). Prolongation of H₂ photoproduction by immunobilized, sulfur-limited *Chlamydomonas reinhardtii* cultures, *J. Biotech.*, v.134, p.275-277
- Laurinavichene T.V.; Tolstygina, I.V.; Galiulina, R.R.; Ghirardi, M.L.; Seibert, M. & Tsygankov, A.A. (2002). Different methods to deprive *Chlamydomonas reinhardtii* cultures of sulfur for subsequent hydrogen photoproduction, *Int. J. Hydrog. Ener.*, v.27, p.1245-1249
- LaVan, D.A. & Cha, J.N. (2006). Approaches for biological and biomimetic energy conversion, *Proc. Natl. Acad. Sci. USA*, v.103, p.5251-5255

- Lehn, J.-M. & Sauvage, J. P. (1977). Chemical storage of light energy: Catalytic generation of hydrogen by visible light or sunlight irradiation of neutral aqueous solutions, *Nouv. J. Chim.* 1, 449-451.
- Lexa, D.; Grass V. & Savéant, J.-M. (1997). Electrochemical generation of rhodium porphyrin hydride. Catalysis of hydrogen evolution, *J. Am. Chem. Soc.*, v.119, p.7526-7532
- Licheng, S.; Bjoern, A. & Sascha, O. (2005). Iron hydrogenase active site mimics in supramolecular systems aiming for light-driven hydrogen production, *Coord. Chem. Rev.*, v.249, p.1563-1663
- Loll, B.; Kern, J.; Saenger, W.; Zouni, A. & Biesiadka, J. (2005). Towards complete cofactor arrangement in the 3.0 Å resolution structure of photosystem II, *Nature*, v.438, p.1040-1044
- Lomoth, R.; Magnuson, A.; Sjödin, M.; Huang, P.; Styring, S. & Hammarström, L. (2006). Mimicking the electron donor side of Photosystem II in artificial photosynthesis, *Photosynth. Res.*, v.87, p.25-40
- Lubitz, W.; Reijerse, E.J. & Messinger, J. (2008). Solar water-splitting into H₂ and O₂: design principles of photosystem II and hydrogenases, *Energy Environ Sci.*, v.1, p.15-31
- Makarova, V.V.; Kosourov, S.; Krendeleva, T.E.; Semin, B.K.; Kukarskikh, G.P.; Rubin, A.B.; Sayre, R.T.; Ghirardi, M.L. & Seibert, M. (2007). Photoproduction of hydrogen by sulfur-deprived *C. reinhardtii* mutants with impaired photosystem II photochemical activity, *Photosynth. Res.*, v.94, p.79-89
- Mal'tsev, S.V.; Allakhverdiev, S.I.; Klimov, V.V. & Krasnovsky, A.A. (1988). Hydrogen evolution by subchloroplast preparations of photosystem II from pea and spinach, *FEBS Lett.*, v.240, p.1-5
- McEvoy, J.P. & Brudvig, G.W. (2006). Water-Splitting Chemistry of Photosystem II, *Chem. Rev.*, v.106, p.4455-4483
- Melis, A. (2007) Photosynthetic H₂ metabolism in *Chlamydomonas reinhardtii* (unicellular green algae), *Planta*, v.226, p.1075-1086
- Melis, A. (2005) Bioengineering of green algae to enhance photosynthesis and hydrogen production, in *Artificial Photosynthesis: From Basic Biology to Industrial Application*, (eds. A.F. Collings and C. Critchley), Wiley-VCH Verlag GmbH & Co. KGaA, Weinheim, Germany, pp. 229-240
- Melis, A.; Neidhardt, J. & Benemann, J.R. (1999). *Dunaliella salina* (Chlorophyta) with small chlorophyll antenna sizes exhibit higher photosynthetic productivities and photon use efficiencies than normally pigmented cells, *J. Appl. Phycol.*, v.10, p.515-525
- Melis, A.; Zhang, L.; Forestier, M.; Ghirardi, M.L. & Seibert, M. (2000). Sustained photobiological hydrogen gas production upon reversible inactivation of oxygen evolution in the green alga *Chlamydomonas reinhardtii*, *Plant Physiol.*, v.122, p.127-133
- Moradpour, A.; Amouyal, E.; Keller P. & Kagan H. (1978). Hydrogen production by visible light irradiation of aqueous solutions of tris(bipyridine)ruthenium(2+), *Nouv. J. Chim.*, v.2, p. 547-549
- Murray, J. W.; Maghlaoui, K.; Kargul, J.; Ishida, N.; Lai, T.-L.; Rutherford, A. W.; Sugiura, M.; Boussac, A. & Barber, J. (2008). X-ray crystallography identifies two chloride binding sites in the oxygen evolving centre of photosystem II, *Energy Environ Sci.*, v. 1, p. 161-166

- Nagasawa, T.; Allakhverdiev, S. I.; Kimura Y. & Nagata T. (2009). Photooxidation of alcohols by a porphyrin/quinone/TEMPO system, *Photochem. Photobiol. Sci.*, v.8, p.174-180
- Nagasawa, T. & Nagata, T. (2007). Synthesis and electrochemistry of Co(III) and Co(I) complexes having C₅Me₅ auxiliary, *Biochim. Biophys. Acta*, v.1767, p.666-670
- Nagata, T. & Kikuzawa, Y. (2007). An approach towards artificial quinone pools by use of photo- and redox-active dendritic molecules, *Biochim. Biophys. Acta*, v.1767, p.648-652
- Nagata, T.; Nagasawa, T.; Zharmukhamedov, S.K.; Klimov, V.V. & Allakhverdiev, S.I. (2007). Reconstitution of the water-oxidizing complex in manganese-depleted photosystem II preparations using synthetic binuclear Mn(II) and Mn(IV) complexes: production of hydrogen peroxide, *Photosynth. Res.*, v.93, p.133-138
- Nagata, T.; Zharmukhamedov, S.K.; Khorobrykh, A.A.; Klimov, V.V. & Allakhverdiev, S.I. (2008). Reconstitution of the water-oxidizing complex in manganese-depleted photosystem II preparations using synthetic Mn complexes: a fluorine-19 NMR study of the reconstitution process, *Photosynth. Res.*, v. 98, p.277-284
- Naruta, Y.; Sasayama M. & Sasaki T. (1994). Oxygen Evolution by Oxidation of Water with Manganese Porphyrin Dimers, *Angew. Chem. Int. Ed. Engl.*, v.33, p.1839-1841
- Ngweniform, P.; Kusumoto, Y.; Teshima, T.; Ikeda, M.; Somekawa S. & Ahmmad B. (2007). Visible-light induced hydrogen production using a polypeptide-chlorophyll complex with alpha-helix conformation, *Photochem. Photobiol. Sci.*, v.6, p.165-170
- Norskov, J. K.; Bligaard, T.; Logadottir, A.; Kitchin, J. R.; Chen, J. G.; Pandelov, S. & Stimming U. (2005). Trends in the Exchange Current for Hydrogen Evolution. *J. Electrochem. Soc.*, v.152, p.J23-J26
- Norskov, J. K. & Christensen, C. H. (2006). Toward Efficient Hydrogen Reduction at Surfaces, *Science*, v.312, p.1322-1323
- Ogo, S.; Kabe, R.; Uehara, K.; Kure, B.; Nishimura, T.; Menon, S. C.; Harada, R.; Fukuzumi, S.; Higuchi, Y.; Ohhara, T.; Tamada, T. & Kuroki, R. (2007). A dinuclear Ni(μ -H)Ru complex derived from H₂, *Science*, v.316, p.585-587
- O'Regan, B. & Grätzel M. (1991). A low-cost, high-efficiency solar cell based on dye-sensitized colloidal TiO₂ films, *Nature*, v.353, p.737-740
- Ozawa, H.; Haga, M. & Sakai, K. (2006). A Photo-hydrogen-evolving Molecular Device Driving Visible-light-induced EDTA-reduction of water into Molecular Hydrogen, *J. Am. Chem. Soc.*, v.128, p.4926-4927
- Peters, W.; Lanzilotta, W. N.; Lemon B. J. & Seefeldt L. C. (1998). X-ray crystal structure of the Fe-only hydrogenase (CpI) from *Clostridium pasteurianum* to 1.8 angstrom resolution, *Science*, v.282, p.1853-1858
- Prince, R.C. & Kheshgi, H.S. (2005). The photobiological production of hydrogen: potential efficiency and effectiveness as a renewable fuel, *Crit. Rev. Microbiol.*, v.31, p.19-31
- Prokhorenko, V. I.; Holzwarth, A. R.; Müller, M. G.; Schaffner, K.; Miyatake, T. & Tamiaki H. (2002). Energy Transfer in Supramolecular Artificial Antenna Units of Synthetic Zinc Chlorins and Co-Aggregated Energy Traps. A Time-Resolved Fluorescence Study, *J. Phys. Chem., B*, v.106, p.5761-5768
- Rao, K.K. & Hall, D.O. (1996). Hydrogen production by cyanobacteria: potential, problems and prospects, *J. Mar. Biotechnol.*, v.4, p.10-15
- Rauchfuss, T.B. (2004). Research on soluble metal sulfides: from polysulfido complexes to functional models for the hydrogenases, *Inorg. Chem.*, v.43, p.14-26

- Rauchfuss, T.B. (2007). A Promising mimic of hydrogenase activity, *Science*, 316, 553-554.
- Riis, T.; Hagen, E.F.; Vie, P.J. S. & Ulleberg, Ø. (2005). Hydrogen Production - Gaps and Priorities, HIA-HCG-Production, 2005-03-15-rev1-final. doc.
- Rupprecht, J.; Hankamer, B.; Mussgnug, J.H.; Ananyev, G.; Dismukes, G.C. & Kruse, O. (2006). Perspectives and advances of biological H₂ production in microorganisms, *Appl. Microbiol. Biotechnol.*, v.72, p.442-449
- Sakai, K. & Ozawa, H. (2007). Homogeneous catalysis of platinum(II) complexes in photochemical hydrogen production from water, *Coord. Chem. Rev.*, v.251, p.2753-2766
- Sakamoto, M.; Kamachi, T.; Okura, L.; Ueno, A. & Mihara H. (2001). Photoinduced hydrogen evolution with peptide dendrimer-multi-Zn(II)-porphyrin, viologen, and hydrogenase, *Biopolymers*, v.59, p.103-109
- Sakurai, H. & Masukawa, H. (2007). Promoting R & D in Photobiological Hydrogen Production Utilizing Mariculture-Raised Cyanobacteria, *Marine Biotechnol.*, v.9, p.128-145
- Sala, X.; Romero, I.; Rodriguez, M.; Escriche L. & Llobet A. (2009). Molecular Catalysts that Oxidize Water to Dioxygen, *Angew. Chem. Int. Ed.*, v.48, p.2842-2852
- Siegbahn, P. E. M. (2004). Proton and Electron Transfers in Ni-Fe Hydrogenase, *Adv. Inorg. Chem.*, v.56, p.101-125
- Shah, A.; Torres, P.; Tscharnner, R.; Wyrsh, N. & Keppner, H. (1999). Photovoltaic technology: The case for thin-film solar cells, *Science*, v. 285, p. 692-698
- Swingley, W. D.; Chen, M.; Cheung, P. C.; Conrad, A. L.; Dejesa, L. C.; Hao, J.; Honchak, B.M.; Karbach, L. E.; Kurdoglu, A.; Lahiri, S.; Mastrian, S. D.; Miyashita, H.; Page, L.; Ramakrishna, P.; Satoh, S.; Sattley, W. M.; Shimada, Y.; Taylor, H. L.; Tomo, T.; Tsuchiya, T.; Wang, Z. T.; Raymond, J.; Mimuro, M.; Blankenship, R. E. & Touchman J. W. (2008). Niche adaptation and genome expansion in the chlorophyll *d*-producing cyanobacterium *Acaryochloris marina*, *Proc. Natl. Acad. Sci. USA*, v.105, p. 2005-2010
- Tamagnini P, Costa JL, Almeida L, Oliveira MJ, Salema R, Lindblad P. Diversity of cyanobacterial hydrogenases, a molecular approach. *Curr Microbiol* 2000; 40:356-361
- Tamagnini P, Axelsson R, Lindberg P, Oxelfelt F, Wunschiers R, Lindblad P Hydrogenases and hydrogen metabolism of cyanobacteria. *Microbiol Mol Biol Rev* 2002;66:1-20
- Tard, C.; Liu, X. M.; Ibrahim, S. K.; Bruschi, M.; De Gioia, L.; Davies, S. C.; Yang, X.; Wang, L. S.; Sawers, G. & Pickett C. J. (2005). Synthesis of the H-cluster framework of iron-only hydrogenase, *Nature*, v.433, p.610-613
- Tomo, T.; Kato, Y.; Suzuki, T.; Akimoto, S.; Okubo, T.; Hasegawa, K.; Noguchi, T.; Tsuchiya, T.; Tanaka, K.; Fukuya, M.; Dohmae, N.; Watanabe, T. & Mimuro, M. (2008). Characterization of highly purified PS I complexes from the chlorophyll *d*-dominated cyanobacterium *Acaryochloris marina* MBIC 11017, *J. Biol. Chem.*, v.283, p.18198-18209
- Tomo, T.; Okubo, T.; Akimoto, S.; Yokono, M.; Miyashita, H.; Tsuchiya, T.; Noguchi, T. & Mimuro, M. (2007). Identification of the special pair of photosystem II in the chlorophyll *d*-dominated cyanobacterium, *Proc. Natl. Acad. Sci. USA*, v.104, p.7283-7288

- Tsygankov, A.A. (2007). Nitrogen-fixing cyanobacteria - hydrogen producers. *Applied Biochem. & Microbiol.*, v. 43, p.279-288.
- Tsygankov, A.A.; Fedorov, A.S.; Kosourov S. N. & Rao, K.K. (2002). Hydrogen production by cyanobacteria in an automated outdoor photobioreactor under aerobic conditions, *Biotechnol. Bioeng.*, v. 80, p.777-783.
- Tsygankov, A.A.; Serebryakova L.T.; Sveshnikov D.D.; Rao K.K.; Gogotov I.N. & Hall D.O. (1997). Hydrogen photoproduction by three different nitrogenases in whole cells of *Anabaena variabilis* and the dependence on pH, *Int. J. Hydr. Energy*, v. 22(9), p.859-867.
- Vignais, P.M. & Colbeau A. (2004). Molecular Biology of Microbial Hydrogenases. *Curr. Issues Mol. Biol.*, v. 6, p. 159-188.
- Wada, T.; Tsuge, K. & Tanaka K. (2000). Electrochemical oxidation of water to dioxygen catalyzed by the oxidized form of the bis(ruthenium-hydroxo) complex in H₂O, *Angew. Chem. Int. Ed.*, v.39, p.1479-1482
- Wasielewski, M. (2006). Energy, charge, and spin transport in molecules and self-assembled nanostructures inspired by photosynthesis. *J. Org. Chem.*, v.71, p.5051-5066
- Wohrle, D.; Romogailo, A.D.; Amao, Y.; Kaneko, M.; Karakhanov, E.A.; Kang, Y.S.; Maximov, A.L.; Nishide, H.; Ohsava, T.; Okura, I.; Raj, R.C. & Won J. (2003). Metal Complexes and Metal in Macromolecules, Wiley-VCH GmbH & Co. KGaA, Weinheim, Germany, pp. 573-600
- Wu, J.-Z.; Angelis, F. D.; Carrell, T. G.; Yap, G. P. A.; Sheats, J.; Car, R. & Dismukes, G. C. (2006). Tuning the photo-induced O₂-evolving reactivity of Mn₄O₄⁶⁺ and Mn₄O₄⁷⁺ manganese-oxo cubane complexes, *Inorg. Chem.*, v.45, p.189-195
- Yagi, M. & Kaneko, M. (2001). Molecular Catalysts for Water Oxidation, *Chem. Rev.*, v.101, p.21-35
- Zhang, L.; Happe, P. & Melis, A. (2002). Biochemical and morphological characterization of sulfur-deprived and H₂-producing *Chlamydomonas reinhardtii* (green alga), *Planta*, v.214, p.552-561
- Zouni, A.; Witt, H.; Kern, J.; Fromme, P. & Krauss, N. (2001). Crystal structure of photosystem II from *Synechococcus elongates* at 3.8 Å resolution, *Nature*, v.409, p.739-743

Neurobiologically inspired distributed and hierarchical system for control and learning

Sungho Jo¹ and Kazutaka Takahashi²

KAIST¹

Korea

Department of Organismal Biology and Anatomy, University of Chicago²

USA

1. Introduction

This chapter discusses potential features of neural systems that may provide insights into biomimetic system design. Recent modeling studies on the cerebrocerebellar and spinal level systems have been of huge interests because they motivate advanced biologically inspired approaches to solve various complex engineering problems in the area of control, automation, and learning. In the view of control scheme, we argue that the cerebrum loosely specifies the control space, while the cerebellum implements modular controllers that are designated to task and performance specifications. The translation of the control commands from the central nervous system to muscles is in the single-to-multiple manner. The neural circuits operate in a simple control space and distribute the commands through synergies rather than directly treat the whole redundant set of actuators. Furthermore, considering a motion task as a sequence of sub-motions controlled by multiple modules of cerebrocerebellar systems, the movement control, which can be seen as a hybrid combination of sequential command generation mechanism coupled with state dependent gainscheduled controllers, proposes interesting biomimetic design schemes. We summarize two possible such schemes: Sequential module-based or parallel module-based gain scheduling approaches. Control variables used in neural motor control may be interpreted as a hybrid of kinematic and kinetic quantities and be chosen to simplify the control dimensionality. Furthermore, mirror neuron studies show majority of those neurons are multi-modal, i.e., they appear to respond to shapes and kinematics of objects, such as limbs, of other subjects and also respond similarly to internally generated motor command for execution. Thus more biological extensions to the proposed schemes become enable to learn from imitations more efficiently. By introducing conceptual computational neural models, we suggest several functionally important *in vivo* neural circuitry and its connection which are very useful for designing biomimetic systems.

2. Cerebrocerebellar control system

Animals including humans can make a wide repertoire of limb movements effortlessly without consciously thinking about joint trajectories or muscle contractions to bring about specific motions. These movements are the outcome of a series of processes and computations carried out by the central nervous system (CNS). Even to make a simple reaching movement, for example, a number of distinct neuroanatomical areas participates to complete the task, and each area consists of numerous neurons that are densely interacting to each other. Among the supraspinal structures, the cerebrocerebellar system is central to motor control (Allen & Tsukahara 1974; Brooks 1986; Kelly & Strick 2003) and has been characterized in terms of its anatomical connections among the areas in the system. In this section, the two structures, the cerebral cortex and the cerebellar cortex are introduced, with their relevant anatomical and physiological features, as components of the cerebrocerebellar system and their functional interrelationship.

2.1 Cerebral cortex

The cerebrum is the evolutionarily newest and largest part of the brain. It participates in many different functions such as perception, decision making, memory, motor control, motion planning/execution, etc. It has been traditionally thought that each subregion of the cerebral cortex has a functionally distinct and significant role in the highly complex hierarchical cerebral structure. An interesting feature of the cerebral cortical region, particularly in sensory regions, is that the spatial extent of pyramidal cell association collaterals approximately construct a columnar assembly. The columnar assembly is a collection of cortical columns. The cortical column is a bundle of minicolumns sharing the same input connection from another cortical region or from sensory thalamic nuclei. Each cortical column may contain a specific feature presentation of sensory information such as orientation of visual stimuli. In the primary motor cortex, there has been an extensive study on modulation of spiking activities on upcoming movement direction (Georgopoulos et al. 1982). Cells with similar preferred directions tended to segregate into vertically oriented minicolumns 50-100 microm wide and at least 500 microm high. Such minicolumns are aggregated across the horizontal dimension in a secondary structure of higher order. In this structure, minicolumns with similar preferred directions were approximately 200 microm apart and were interleaved with minicolumns representing nearly orthogonal preferred directions. In addition, nonoverlapping columns, representing nearly opposite preferred directions, were approximately 350 microm apart. (Amirikian & Georgopoulos 2003). For a specific piece of movement, a group of neurons in a specific column have the most vigorous firing compared to the other columns. The specific population directional vector of the column may be regarded as a functional quantitative measure (Amirikian & Georgopoulos 2003). The activity dominated from the winning columnar assembly may be transmitted to other sensorimotor cortical columns and thence to cerebellum by larger tufted layer 5 pyramidal cells.

Experimental observations have shown task-related neural activity in both the premotor and motor cortex (Johnson & Ebner 2000). Neural activities of M1 cells in apes are directionally tuned during an epoch of reaching task movement and the preferred directions of M1 cells are very different (Cisek 2003). It is known that a population distribution in an ensemble of M1 neurons adequately points a specific direction, which is mathematically expressed by a

unit vector while the discharge of single neurons rarely identifies any direction with accuracy (Georgopoulos 1988). These observations may be related to the functional organization of the columnar assemblies in cortex.

It is shown that complex movements with multiple velocity peaks can be decomposed into a superposition of elementary, and potentially stereotypical, sub-movements that form the basis of an intermittent sub-movement-based planning mechanism (Krebs et al. 1999, Rohrer et al. 2004, Fishback et al. 2005). Such sub-movements have been identified in many types of movements: pursuit tracking (Miall et al. 1988), interception of moving targets (Lee et al. 1997), and cursor movement during isometric force task (Massey et al. 1992). Segmentations were found even in the EMG patterns during slow finger movements (Vallbo & Wessberg 1993) and during point-to-point reaching movement with a wide range of speeds (Dipietro et al. 2005), thus demonstrating that the descending command can also be inherently intermittent. Those studies suggest that the sub-movement play a fundamental role in the control or planning of primate limb movements and they may be the behavioral manifestation of neural mechanisms. Potentially a piece of sub-movement has a corresponding neural substrate so that a sequential activation of those substrates produce an overall movement. A complete motion can be repetitive such as walking such that it can be constructed by a repeated sequence of sub-movements. Each sub-movement is probably encoded within a specific spatial region. To generate a whole movement, switchings from one spatial region to another will be necessary because each sub-movement is best encoded separately in an individual region. Thus, a hypothesis is that cerebral cortex separately includes an appropriate principal spatial coordinate for each sub-movement, and the signal to the lower central nervous system from cerebral cortex informs a sequence of spatial coordinates for the whole movement. Tanji and Wise (Tanji & Wise 1981) argued that the motor cortex plays an important role in the sequencing of multiple movements. Specific spatial information at the level of intracortical processing within M1 may represent a transformation between extrinsic and intrinsic presentations. Sensed external information is in a high dimensional coordination, and internal motor system is in a low dimensional coordination (Kalaska et al. 1983). Therefore, spatial dimensional complexity of a behavior may be reduced in the world of the internal neural system. Cortical assembly may distributedly encode spatial information in a low and local dimensional space. The brain presumably can also store and combine the principal modes as needed to generate different behaviors. Thus, many situations which we encounter would be derived from combinations of previously experienced contexts (Haruno et al. 2001).

Learning a set of specific regions and corresponding neural activation patterns are probably describable by utilizing an engineering algorithm such as reinforce algorithm that provides a synaptic implementation between pre- and post-synapses (Williams 1992). The update rule consists of two components, Hebbian and anti-Hebbian. The former increases the synaptic connection strength and the latter decreases it. The update rule principally seeks to find a primary principal vector (i.e., principal mode) of correlation of a certain error trajectory. A simple generalization can find the first n principal directions with n linear neurons (Sanger 1994).

By combining those two ideas, i.e., cortical columnar organization and its functional organization in terms of spatial, and contextual, variables, it is hypothesized, to explain individual cerebellar Purkinje cell (PC) spiking activities, (Takahashi 2006) that a group of neurons in a particular cortical column in Area 3a are broadly tuned to a particular direction

of internal error signals. Each cerebral cortical column in sensorimotor cortical (SMC) area 3a (as explained in section 2.1.) is expressed by a neural population-based representation of the error-like signal (Georgopoulos 1988; Georgopoulos et al. 1983).

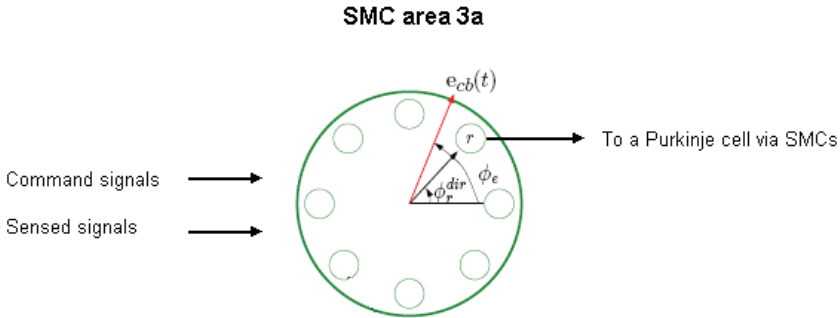


Fig. 1. A proposed cerebral cortical model from the perspective of a single Purkinje cell.

The error-like signal e_{cb} is distributed to different PCs via SMC columns in area 3a each of which has a preferred direction ϕ_{cb}^{dir} . Then, the output of each column to PCs contains the magnitude of the projection of e_{cb} vector to unit vector along ϕ_{cb}^{dir} direction. Thus the firing intensity of neurons in a given SMC column in area 3a at a given time depends on the ongoing error-like signal and its nominal tuning direction. Fig. 1 illustrates the proposed cerebral cortical model.

2.2 Cerebellar cortex

The cerebellum is the most numerous in terms of the number of the neurons and is known to coordinate and control posture and movement, and implement motor learning. Its neural circuitry is globally uniform in its cytoarchitectonics as shown in Figure 2. The cerebellar cortex can be divided into a number of sagittal zones, or microzones (Oscarsson 1979) each of which form, with its group of neurons, the operational unit of the cerebellum. This organization may be analogous to the modular columnar organization in the cerebellar cortex. In microarchitecture, three layers, e.g., molecular, Purkinje cell, and granular layers, organize the cerebellar cortex and contain five types of neurons (Kandel et al. 2000). These granule cells make excitatory connections with all the other cells, and basket, stellate, and golgi cells are inhibitory neurons. A Purkinje cell receives excitatory signals, but its output to deep cerebellar nuclei is inhibitory. Two types of inputs are conveyed to the cerebellar microzone: Mossy fibers (MFs) and Climbing fibers (CFs) (Kandel et al. 2000). MF input produces a stream of simple spikes in PCs throughout relayed circuits. The firing rate of simple spikes can extend to above a few hundred spikes per second. The frequencies encode either peripheral sensory information or central commands. CF input is composed of error-type signals originating from the inferior olivary nucleus. CFs have powerful synaptic connection with Purkinje neurons and provoke a complex spike on the dendrites of a PC, but its firing rate is very low (around 1 per second). Climbing fiber pathway is regarded as a "teaching" line for the adaptation at the parallel fiber-Purkinje cell synapse (Ito 1984).

Granule cells, the most numerous, receive neural signals through mossy fibers and transmit output signals to the Golgi cells and parallel fibers. Mossy fibers convey various forms of information (assumptions on a set of specific signals are presented in the model below). Golgi cells in the granule layer receive excitatory inputs from both mossy fibers directly and granule cells. Inhibitory inputs from stellate, basket, and Purkinje cells are also conveyed to Golgi cells which then inhibit granule cells. The signal conveyed to parallel fibers is relayed to Purkinje cells. The signal is a brief excitatory potential that evokes high frequency firing on the dendrites of the PC which has fan-like dendrites and projects into the white matter under the granular layer. A PC also receives the other input through a CF. Stellate and basket cells modulate inhibitory connections with parallel fiber to a PC.

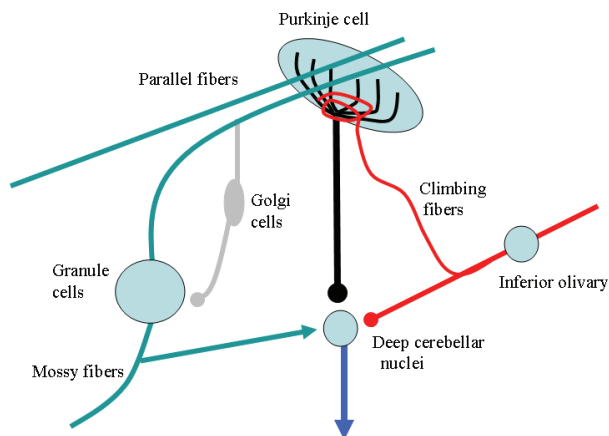


Fig. 2. The cerebellar neural circuit.

The outputs of the cerebellar cortex are sent to other areas through deep cerebellar nuclei. The neural output signals reach either motor cortex via thalamus (ventrolateral nuclei) or spinal cord via brainstem. Impairments related to the deep cerebellar nuclei indicate different behavioral functions (Thach 1998). The neural output signals from fastigials contain mainly the information on upright stance and gait. Interposed nuclei (Interpositus) in the medial region are related to reaching movements or alternating agonist-antagonist muscle. Impairment of Dentate in the lateral region causes curved motion trajectory, overshoot on reaching movement, and uncoordinated finger movements.

Many neuroanatomically feasible models to explain the cerebellar mechanism with respect to either movement control or motor learning have been proposed. The models can be roughly categorized into two types, feedback and feedforward control systems. Models (Barto et al. 1999; Kazutaka 2006) describing the cerebellar function as the feedback control system put emphasis on more robustness against the parameter variation or disturbances. The feedforward type cerebellar model implements the plant inverse dynamics (Kawato & Gomi 1992; Schweighofer et al. 1998; Miall et al. 1993) while the crude feedback controller, the cerebral system, performs. An example of each case is introduced here.

The Recurrent Integrator Proportional Integral Derivative (RIPID) cerebrocerebellar model regards the cerebellar function with the feedback controller (Jo ; Kazutaka 2006). In the RIPID model (Fig. 3), the ascending signals that percolate through the control systems are

posited to be functions of a principal tracking error formed in parietal area 5, $\theta_{target}(t) - F_3\theta(t - t_{aff})$ where t_{aff} is a sum of the spinal and peripheral delay, and more direct afferent information received via Area 3a (via F_2). The signal from area 3a is proposed to travel to intermediate cerebellum and that from area 4 to intermediate and lateral cerebellum. Those principal signals in the cerebellum and precerebellar nuclei undergo scaling, delay, recombination and reverberation to affect proportional-derivative-integral processing (G_b/s , G_k , and I_1/s , I_2/s , and I_3/s , respectively, where s denotes a Laplace variable). The cerebellar computational processing is derived from neuroanatomy (Takahashi 2006; Jo & Massaquoi 2004). These actions contribute to phase lead (by I_2/s recurrent loop) for long-loop stabilization and sculpting forward control signals (G_b/s , G_k , I_1/s) that return to motor cortex where they are collected and redistributed before descending through the spinal cord as motor command u . There is additional internal feedback to the parietal lobe and/or motor cortex via I_3/s that contributes to loop stability in the principal transcerebellar pathway. An important set of inputs is posited to consist of modulating signals (indicated by η) from spinocerebellar tracts. These signals effectively switch the values of G_b , G_k , I_1 according to limb configuration and velocity as in Fig.(3). The RIPID model also includes the direct command path from motor cortex (via MC) to spinal cord, and a hypothetical cerebral cortical integrator (I_a/s).

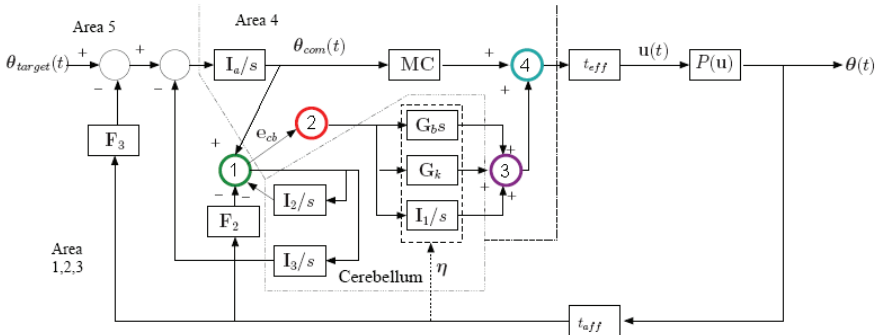


Fig. 3. The RIPID model. Numbered circles designate functional subcategories of sensorimotorcortical columns explained in section 2.1.

On the other hand, the adaptive feedback error learning (FEL) model has been rigorously investigated to describe the cerebellar function in the manner of the feedforward inverse dynamics control (Gomi & Kawato 1993; Kawato & Gomi 1992; Katayama & Kawato 1993). The cerebellum is regarded as a locus of the approximation of the plant inverse dynamics. The FEL model describes the motor learning scheme explicitly. Initially, a crude feedback controller operates influentially. However, as the system learns the estimation of the plant

inverse, the feedforward controller commands the body more dominantly. Fig. (4) illustrates the FEL scheme proposed by Gomi and Kawato (Kawato & Gomi 1992). The feedback controller can be linear, for example, as

$$\bar{\tau}_{fb} = K_1(\ddot{\bar{\theta}}_b - \ddot{\bar{\theta}}) + K_2(\dot{\bar{\theta}}_b - \dot{\bar{\theta}}) + K_3(\bar{\theta}_b - \bar{\theta}) \quad (1)$$

To acquire the inverse model, different learning schemes could be used. In general, a learning scheme $\bar{\tau}_{ff} = \phi(\bar{\theta}_d, \bar{\theta}, \dot{\bar{\theta}}_d, \dot{\bar{\theta}}, \ddot{\bar{\theta}}_d, \ddot{\bar{\theta}}, W)$ can be expressed, where W represents the adaptive parameter vector, $\bar{\theta}_d$ the desired position vector, and $\bar{\theta}$ the actual position vector. The adaptive update rule for the FEL is as follows.

$$\frac{dW}{dt} = \eta \left(\frac{\partial \phi}{\partial W} \right)^T (\bar{\tau}_{fb} + \bar{\tau}_{ext}) \quad (2)$$

where $\bar{\tau}_{ext}$ is the external torque and η the learning ratio which is small.

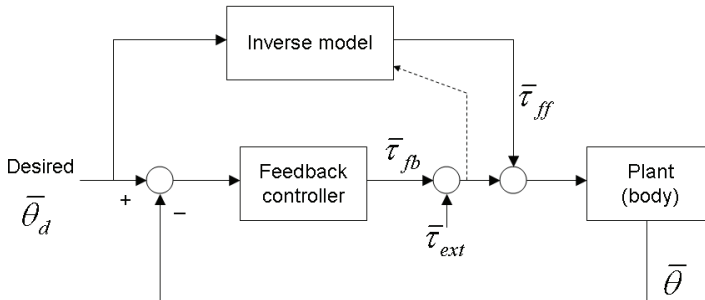


Fig. 4. The FEL model. Adapted from Kawato and Gomi (1992).

The convergence property of the FEL scheme was shown (Gomi & Kawato 1993; Nakanishi & Schaal 2004). The FEL model has been developed in detail as a specific neural circuit model for three different regions of the cerebellum and the learning of the corresponding representative movements: 1) the flocculus and adaptive modification of the vestibulo-ocular reflex and optokinetic eye movement responses, 2) the vermis and adaptive posture control, and 3) the intermediate zones of the hemisphere and adaptive control of locomotion. The existence of inverse internal model in the cerebellum is argued based on studies (Wolpert & Kawato 1998; Wolpert et al. 1998; Schweighofer et al. 1998) that the Purkinje cell activities can be approximated by kinematic signals.

There have been many other models of the cerebellum (Barto et al. 1998; Miall et al. 1993; Schweighofer et al. 1998). In those models, the cerebellum is also either feedforward or feedback control system. Yet, uniform descriptions for various models would be necessary to support one model over the other as there are multiple ways to describe one model. Interestingly, a probabilistic modelling approach has been applied to explain the inverse

internal model in the cerebellum (Kåoding & Wolpert 2004). The model takes into account uncertainty which is naturally embedded in human movements and applies the Bayes rule to interpret human decision making process. Further investigation is necessary to verify the cerebellar mechanism and to better understand the principle of movement control. It is highly expected that biological principles will teach us an outstanding scheme of robotic control to perform close to that of human. Model designs to evaluate both dynamic behaviors and internal signal processing are worthwhile for neuroprosthetic device or humanoid robotics development.

2.3 Cerebellar system as a modular controller

Neural computation of microzone in cerebellar cortex under a specific principal mode may control a sub-movement over a certain spatial region. Experimental observations have shown that the directional tunings of cells in cerebellar cortex, motor cortex, and parietal cortex are strikingly similar during arm reaching tasks (Frysinger et al. 1984; Kalaska et al. 1983; Georgopoulos et al. 1983). It is also reported that directional tunings of Purkinje cells, interpositus neurons, dentate units, and unidentified cerebellar cortical cells are nearly identical (Fortier et al. 1989) so that cerebellar computational system may be considered to be in a specific coordinate. Those experimental observations suggest that the cerebrocerebellar mechanism is implemented in a similar spatial information space. A possible neural scheme can be proposed as follows. Suppose that there are some groups of mossy fiber bundles, and each individual group conveys the neural information described in a different spatial coordinate from cerebral cortex. As spatial information becomes available, some groups of mossy fiber bundles receiving the cerebral signal becomes more active. Similarly in cerebellar cortex, inhibition between different modules by stellate and basket cells accelerates competition to select a winner module. The winner module is framed in a spatial coordinate encoded in cerebral cortex. As a result, cerebellar neural computation is implemented in the restricted spatial coordinate. Thus it appears that the cerebrum determines a spatial coordinate for a specific task, and then the cerebellum and other motor system control the motion with respect to the coordinate. Therefore, a pair of modular cortical assembly and cerebellar microzone can be probably seen as a neural substrate for movement control and learning.

From the point of view of control theory, gain scheduling is an appropriate approach to describe a control system with distributed gains: each set of control gains is assigned to a specific coordinate. Furthermore, switching or scheduling of gains may depend on a command for a sub-movement. In general, gain scheduling scheme involves multiple controllers to attempt to stabilize and potentially increase the performance of nonlinear systems. A critical issue is designing controller scheduling/switching rules. It is quite possible that an internal state, probably a combination of sensed information, may define switching condition. For instance, a gain switching scheme is demonstrated by a computational model of human balance control. Two human postural strategies for balance, ankle and hip strategies (Horak & Nashner 1986), are respectively implemented by two different control gains that are represented by the cerebellar system. (Jo & Massaquoi 2004). Depending on external disturbance intensities, an appropriate postural strategy is selected by comparing sensed position and switching condition defined by an internal state (Fig.(5)). The internal state is adapted to include information on approximated body position and external disturbance (i.e., a linear combination of sensed ankle and hip angles and angular

speed at ankle). A neural implementation of the switching mechanism is shown in Fig. (5) where a beam of active parallel fibers (PF) inhibits PCs some distance away ("off beam") via basket cells (Eccles et al. 1967; Ito 1984). This diminishes the net inhibition in those modules, allowing them to process the ascending segment input through mossy fibers (AS). Conversely, the beam activates local PCs, thereby suppressing the activity of "on beam" modules. The principal assumption of PFs in this scheme is that, unlike ascending segment fibers, they should contact PCs relatively more strongly than the corresponding cerebellar deep nuclear cells - if they contact the same DCN cells at all. This appears to be generally consistent with the studies of Eccles et al (Eccles et al. 1974; Ito 1984). A prime candidate source for PFs is the dorsal spinocerebellar tract (DSCT). The elements of the DSCT are known to convey mixtures of proprioceptive and other information from multiple muscles within a limb (Oscarsson 1965; Bloedel & Courville 1981; Osborn & Poppele 1992) while typically maintaining a steady level of background firing in the absence of afferent input (Mann 1973).

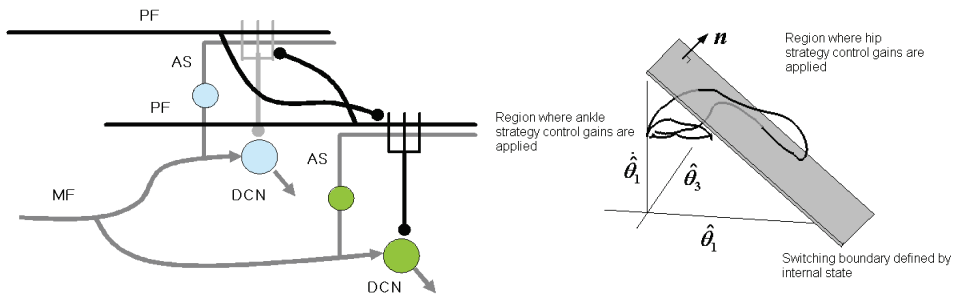


Fig. 5. Proposed switching mechanism: (left) neural circuit, and (right) postural balance switching redrawn from Jo & Massaquoi (2004). PF: parallel fibers, MF: Mossy fibers, DCN: deep cerebellar nuclei, AS: ascending segment; $\hat{\theta}_1$: sensed ankle angle, $\hat{\theta}_3$: sensed hip angle, $\hat{\dot{\theta}}_1$: sensed angular speed at ankle.

The gain scheduling mentioned so far uses an approach that spatially distributed control modules are recruited sequentially to achieve a motion task. Another possible approach is to weight multiple modules rather than pick up a module at a specific time. A slightly more biologically inspired linear parameter varying gainscheduling scheme including multiple modules each of which was responsible over a certain region in the joint angle space was developed for a horizontal arm movement (Takahashi 2007). Another example of multiple module approach is Multiple forward inverse model proposed by Wolpert and Kawato (1998). Each module consists of a paired forward inverse model and responsibility predictor. Forward models learn to divide a whole movement into sub-movements. The degree of each module activity is distributively selected by the responsibility predictor. The inverse model in each module is acquired through motor learning similar to FEL. While the degree of each contribution is adaptively decided, several modules can still contribute in synchrony unlike the previous sequential approach. The modules perform in parallel with different contributions to a movement. Learning or adaptation algorithms could be used to describe the parallel modular approach (Doya 1999; Kawato a& Gomi 1992). However, more explicit neural models based on observations have been proposed to explain adaptive behaviors

(Yamamoto et al. 2002; Tabata et al. 2001). The computational analyses generalize the relationship between complex and simple spikes in the cerebellar cortex. Error information conveyed by complex spikes synaptic weights on PCs and such changes functionally correspond to updating module gains. Further investigation is still required to understand the generality of such results and their computational counterparts as previous studies have looked mostly on simple behaviors such as eye movements or point-to-point horizontal arm movements.

2.4 Control variables and spatial coordination

Primates have many different sensors. The sensors collect a wide range of information during a specific motor task. The high-level center receives the sensed information. Neurophysiological studies propose that motor cortex and cerebellum contain much information in joint coordinates (Ajemian et al. 2001; Scott & Kalaska 1997), Cartesian coordinates (Georgopoulos et al. 1982, Ajemian et al. 2001; Scott & Kalaska 1997; Poppele et al. 2002, Roitman 2007). However other studies are consistent with the possibility that parietal and some motor cortical signals are in Cartesian (Kalaska et al. 1997) or body-centered (Graziano 2001), shoulder-centered (Soechting & Flanders 1989) workspace coordinates, or a combination (Reina et al. 2001). However, it would be highly likely that a coordinate at an area is selected to conveniently process control variables from high level command to low Level execution.

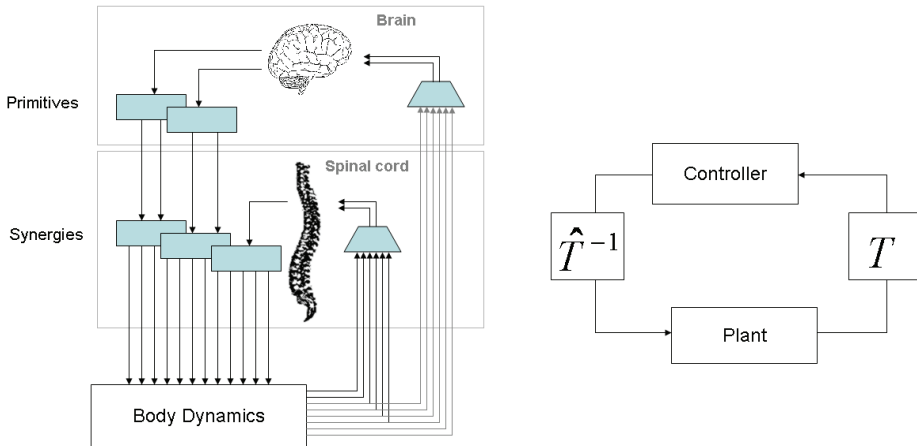


Fig. 7. Neural computational network between controller and plant.

For example, Freitas et al (2006) proposed that voluntary standing movements are maintained by stabilization of two control variables, trunk orientation and center of mass location. The control variables could be directly sensed or estimated via neural processing. It is really difficult to see what control variables are selected internally in the brain. However, redefining appropriate control variables in the high-level center can lower control dimensionality to enable efficient neural computation. Moreover, computational studies have demonstrated that workspace to sensory coordinate conversion can occur readily within a servo control loop (Ayaso et al. 2002; Barreca & Guenther 2001). As in Fig. 7, the

dimensional reduction and synergies (and/or primitives) can be viewed functionally as the inverse network of each other. The control variables in the high-level nervous center may need to be purely neither kinematic nor kinetic. A composite variable of both kinematic and kinetic information can be used, where both force and position control variables are simultaneously processed. Moreover, the position variable could be in joint or Cartesian-coordinate. Spinocerebellar pathways apparently carry a mixture of such signals from the periphery (Osborn & Poppele 1992), but the details of force signal processing in the high-level nervous center are not well understood.

Based on various investigations, it is considerable that the neural system controls behaviors using hybrid control variables. The advantage of using such types is verified in engineering applications. For teleoperation control applications, such a linear variable combination of velocity and force is called wave-variable (Sarma et al 2000). It is demonstrated that the wave-variable effectively maintains stability in a time-delayed feedback system. Application of the force controller with the position controller to a biped walker has been tested (Fujimoto et al 1998; Song et al 1999). The force feedback control mode during the support phase is effective in directly controlling interaction with the environment. The force/torque feedback controller in a computational model of human balancing facilitated attaining smooth recovery motions (Jo and Massaquoi 2004). The force feedback provided the effect of shifting an equilibrium point trajectory to avoid rapid motion.

3. Mirror neuron and learning from imitation

One form of learning a new behaviour is to imitate what others do. In order to imitate, an integration of sensory and motor signals is necessary such that perception of an action can be translated into a corresponding action. Even an infant can imitate a smile of an adult, actual processes of that consist of multiple stages. It seems that many areas in the primate brain participate in imitation. In superior temporal sulcus (STS), Perrett et al. (1985) found neurons responding to both form and motion of specific body parts. Responses of those neural systems are consistent regardless of the observer's own motion. Then, Rizzolatti's group found neurons in ventral premotor cortex, area F5, that discharged both when individuals performed a given motor task and when they observed others performing the same task. Those neurons are referred to mirror neurons which are found in premotor (F5) and inferior parietal cortices. The relation between those two areas remains unclear, but it can be hypothesized, given a known connection between F5 and area 7b in parietal cortex, that perception of a performer's objects and motions in STS is sent to F5 via 7b. Furthermore, there exist anatomical connections between dentate in cerebellum and multiple cerebral cortical areas that are related to perception, imitation, and execution of movements, i.e., area 7b, PMv, and M1 respectively (Dum & Strick 2003). Anterior intraparietal area (AIP) is a particular subregion in area 7b and sends projections to PMv (Clower et al. 2005). In addition, AIP has a unique connection to dentate nuclei in that it receives significant inputs from areas of dentate that are connected to PMv and M1. Thus, it can be further hypothesized that AIP/7b is a site where object information is extracted and can be compared to an internal estimate of actual movement, particularly of hand, and F5 recognize external and internal actions before an execution.

In relation to the RIPID model which does not have specific representation of premotor cortex and AIP, it seems that visuospatial function of cerebrotocerebellar loops, particularly

through area 7b, AIP, and PMv, may contribute to a feedforward visual stimuli dependent scheduling of cerebellar controllers that compute signals for internal or external uses. Thus, there are multiple almost simultaneous recruitment of cortical columnar assemblies and cerebellar modules based on the task specification and real time sensed state information to narrow down “effective” controller modules in the cerebellum. To train such complex dynamical control system, first a set of local controllers in the cerebellum needs to be trained (such as Schaal & Atkinson 1998 or based on limitation of the effective workspace (Takahashi 2007)). Then, a set of sub-tasks such as reaching and grasping object needs to be characterized so that the observed actions can be mapped a set of meaningfully internalized actions through a parietofrontal network of AIP/7b to PMv. Then, to perform a whole task, a higher center needs to produce a sequence of internalized actions. A model to realize this particular part of the system including mirror neurons is developed by Fagg and Arbib (1998) and a further refined version to reproduce specific classes mirror neuron responses by Bonaiuto et al. (2007) whose learning scheme was the back-propagation learning algorithm for use with anatomically feasible recurrent networks. However, no model for imitation learning has exclusively incorporated cerebellar system. Thus, it is interesting to investigate how contributions of the cerebellum and its loop structure with AIP, 7b, and PMv to learning can be realized.

4. Conclusion

In neuroscience society, the concept of modules and primitives has popularly been proposed. It facilitates controllability of redundant actuators over a large state space along the descending pathways. Meaningful control variables are extracted from the whole sensed information over the ascending pathways. The process may be interpreted that specific spatial coordinates are selected for the high nervous control system. Therefore, this provides a way to construct the control problem in the simpler dimensional description compared with body movement interacting with the environment as long as fewer control variables can be sufficient for performance. The control variables seem to be chosen in such a way as to decouple functional roles. In this way, the adjustment of a local neural control with respect to a control variable can be fulfilled substantially without affecting the neural controls related to other control variables. Furthermore, a hybrid control variable of kinematic and kinetic states may be advantageous. Under the assumption that cerebral cortex specifies an appropriate coordinate for a motion task and cerebellar cortex controls the motion in the coordinate, neural activities around the cerebrocerebellar system may be viewed as a gain scheduling or multiple modular control system with multi-modal scheduling variables. The integrated system seems to enable to estimate appropriate efforts to achieve desired tasks. Mirror neurons inspire learning algorithms, based on imitations, that specify local controllers. To shed light on the biomimetic designs, we summarize the features from human neural systems as follows.

- Functional decoupling of each controller
- Dimensional reduction in the control space
- Piecewise control by multiple modules and gain scheduling
- Hybrid control variables
- Learning from imitations

5. References

- Amirikian, B. & Georgopoulos, A.P. (2003). Modular organization of directionally tuned cells in the motor cortex: Is there a short-range order? *PNAS*, Vol. 100, No. 21, (October 2003) pp. 12474-12479, ISSN: 1091-6490
- Ajemian, R., Bullock, D. & Grossberg, S. (2001) A model of movement coordinates in the motor cortex: posture-dependent changes in the gain and direction of single cell tuning curves, *Cerebral Cortex* Vol. 11, No. 12 (December 2001) pp. 1124-1135, ISSN 1047-3211.
- Ayaso, O., Massaquoi, S.G. & Dahleh, M. (2002) Coarse gain recurrent integrator model for sensorimotor cortical command generation, *Proc of American Control Conference*, pp.1736-1741, ISSN: 0743-1619, May 2002.
- Barreca, D.M. & Guenther, F.H. (2001) A modeling study of potential sources of curvature in human reaching movements, *J Mot Behav*, Vol. 33, No.4 (December 2001) pp. 387-400, ISSN: 0022-2895.
- Barto, A.G, Fagg, A.H., Sitkoff, N. & Houk, J.C. (1998) A cerebellar model of timing and prediction in the control of reaching, *Neural Comput*, Vol.11, No.3, pp. 565-594, ISSN: 0899-7667.
- Bizzi, E., Hogan, N., Mussa-Ivaldi, F.A. & Giszter, S. (1994) Does the nervous system use equilibrium-point control to guide single and multiple joint movements? In *Movement control*, Cordo, P. & Harnad, S. (Eds.), Cambridge Univ Press, pp. 1-11, ISBN: 9780521456074.
- Bloedel, J.R. (1973) Cerebellar afferent systems: a review, *Prog Neurobiol*, Vol. 2, No. 1, pp. 3-68, ISSN: 0301-0082.
- Bonaiuto, J., Rosta, E. & Arbib, M. (2007) Extending the mirror neuron system model, I, *Biol Cybern*, Vol. 96, No. 1 (January 2007) pp. 9-38, ISSN: 0340-1200.
- Brooks, V.B. (1986) *The neural basis of motor control*, Chapter 10, Oxford Press, ISBN-13: 978-0195036848, USA.
- Cisek, P. (2003) Neural activity in primary motor and dorsal premotor cortex in reaching tasks with the contralateral versus ipsilateral arm, *J Neurophysiol*, Vol. 89 (February 2003) pp. 922-942, ISSN: 0022-3077
- Clower, D.M., Dum, R.P. & Strick, P.L. (2005) Basal ganglia and cerebellar inputs to 'AIP', *Cerebral Cortex*, Vol. 15, No. 7, pp. 913-920, ISSN: 1047-3211.
- Doya, K. (1999) What are the computations of the cerebellum, the basal ganglia and the cerebral cortex? *Neural Networks*, Vol. 12 (October 1999) pp. 961-974, ISSN: 0893-6080.
- Dum, R.P. & Strick, P.L., An unfolded map of the cerebellar dentate nucleus and its projection to the cerebral cortex, *J Neurophys*, Vol. 89, No. 1 (January 2003) pp.634-639, ISSN: 0022-3077.
- Eccles, J.C., Ito, M. & Szentágothai, J. (1967) *The cerebellum as a neuronal machine*, Springer-Verlag, Oxford, England.
- Georgopoulos, A.P. (1988) Neural integration of movement: role of motor cortex in reaching, *FASEB J*, Vol. 2 pp. 2849-2857, ISSN: 0892-6638
- Georgopoulos, A., Kalaska, J.F., Caminiti, R. & Massey, J.T. (1982) On the relations between the direction of two-dimensional arm movements and cell discharge in primate motor cortex, *J Neurosci*, Vol. 2 pp. 1527-1537, ISSN: 1529-2401.

- Fagg, A.H. & Arbib, M.A. (1998) Modeling parietal-premotor interactions in primate control of grasping, *Neural Netw*, Vol. 11, No. 7-8 (October 1998) pp. 1277-1303, ISSN: 0893-6080.
- Fishback, A., Roy, S.A. , Bastianen, C., Miller, L.E. & Houk, J.C. (2005) Kinematic properties of on-line error corrections in the monkey, *Exp Brain Res*, Vol. 164 (August 2005) pp. 442-457, ISSN: 0014-4819.
- Fortier, P.A., Kalaska, J.F. & Smith, A.M. (1989) Cerebellar neuronal activity related to whole arm reaching movements in the monkey, *J Neurophysiol*, Vol. 62 No.1 pp. 198-211, ISSN: 0022-3077.
- Freitas, S., Duarte, M. & Latash, M.L. (2006) Two kinematic synergies in voluntary whole-body movements during standing, *J Neurophysiol*, Vol. 95 (November 2005) pp. 636-645, ISSN: 0022-3077.
- Frysinger, R.C., Bourbonnais, D., Kalaska, J.F. & Smith, A.M. (1984) Cerebellar cortical activity during antagonist cocontraction and reciprocal inhibition of forearm muscles, *J Neurophysiol*, Vol. 51, pp. 32-49, ISSN: 0022-3077.
- Fujimoto, Y., Obata, S. & Kawamura, A. (1998) Robust biped walking with active interaction control between foot and ground, *Proc. of the IEEE Int Conf on Robotics & Automation*, pp. 2030-2035, ISBN 0-7803-4301-8, May 1998, Leuven, Belgium.
- Gomi, H. & Kawato, M. (1993) Neural network control for a closed-loop system using feedback-error-learning, *Neural Netw*, Vol. 6, No. 7, pp. 933-946, ISSN: 0893-6080.
- Graziano, M.S. (2001) Is reaching eye-centered, body-centered, hand-centered, or a combination? *Rev Neuosci*, Vol.12, No.2, pp.175-185, ISSN: 0334-1763.
- Haruno, M. (2001) MOSAIC model for sensorimotor learning and control, *Neural Computation*, Vol. 13 (October 2001) pp. 2201-2220, ISSN: 0899-7667.
- Horak, F.B. & Nashner, L.M. (1986) Central programming of postural movements: adaptation to altered support-surface configurations, *J Neurophysiol*, Vol. 55 pp. 1369-1381, ISSN: 0022-3077.
- Ito, M. (1984) *The cerebellum and neural control*, Raven Press, ISBN-13: 978-0890041062 , New York, USA.
- Ito, M. (2006) Cerebellar circuitry as a neuronal machine, *Prog Neurobiol*, Vol. 78 (February-April 2006), pp. 272-303, ISSN: 0301-0082.
- Jo, S. & Massaquoi, S. (2004) A model of cerebellum stabilized and scheduled hybrid long-loop control of upright balance, *Biol Cybern*, Vol. 91 (September 2004) pp. 188-202, ISSN:0340-1200.
- Johnson, M.T.V. & Ebner, T.J. (2000) Processing of multiple kinematic signals in the cerebellum and motor cortices, *Brain Res Rev*, Vol. 33 (September 2000) pp. 155-168, ISSN: 0165-0173.
- Kalaska, J.F., Caminiti, R. & Georgopoulos, A.P. (1983) Cortical mechanisms related to the direction of two-dimensional arm movements: relations in parietal area 5 and comparison with motor cortex, *Exp Brain Res*, Vol. 51 pp. 247-260, ISSN: 0014-4819.
- Kalaska, J.F., Scott, S.H., Cisek, P. & Sergio, L.E. (1997) Cortical control of reaching movements, *Curr Opin Neurobiol*, Vol. 7 (December 1997) pp. 849-859, ISSN: 0959-4388.
- Kandel, E.R., Schwartz, J.H. & Jessell, T.M. (2000) *Principles of neural science*, 4th Ed., McGraw-Hill, ISBN-13: 978-0838577011.

- Katayama, M. & Kawato, M. (1993) Virtual trajectory and stiffness ellipse during multijoint arm movement predicted by neural inverse models, *Biol Cybern*, Vol. 69 (October 1993) pp. 353-362, ISSN: 0340-1200.
- Kawato, M. & Gomi, H. (1992) A computational model of four regions of the cerebellum based on feedback-error learning, *Biol Cybern*, Vol. 682, pp. 95-103, ISSN:0340-1200.
- KÄoding, K.P. & Wolpert, D.M. (2004) Bayesian integration in sensorimotor learning, *Nature*, Vol. 427 (January 2004) pp. 244-247, ISSN: 0028-0836.
- Lee, D., Nicholas, L.P. & Georgopoulos, A.P. (1997) Manual interception of moving targets II. On-line control of overlapping submovements, *Exp Brain Res*, Vol. 116 (October 1997) pp. 421-433, ISSN: 0014-4819.
- Mann, M.D. (1973) Clarke's column and the dorsal spinocerebellar tract: A review, *Brain Behav Evol*, Vol. 7, No. 1, pp. 34-83, ISSN: 0006-8977.
- Massey, J.T., Lurito, J.T., Pellizzer, G. & Georgopoulos, A.P. (1992) Three-dimensional drawings in isometric conditions: relation between geometry and kinematics, *Exp Brain Res*, Vol. 88 (January 1992) pp. 685-690, ISSN: 0014-4819.
- Miall, R.C., Weir, D.J. & Stein, J.F. (1988) Planning of movement parameters in a visuo-motor tracking task, *Behav Brain Res*, Vol. 17 (January 1988) pp. 1-8, ISSN: 0166-4328.
- Miall, R.C., Weir, D.J., Wolpert, D.M. & Stein, J.F. (1993) Is the cerebellum a Smith predictor? *J Mot Behav*, Vol. 25, No. 3, pp. 203-216, ISSN: 0022-2895.
- Nakanishi, J. & Schaal, S. (2004) Feedback error learning and nonlinear adaptive control, *Neural Netw*, Vol. 17, No. 10, pp. 1453-1465, ISSN: 0893-6080.
- Novak, K., Miller, L. & Houk, J. (2002) The use of overlapping submovements in the control of rapid hand movements *Exp Brain Res*, Vol.144 (June 2002) pp. 351-364 ISSN: 0014-4819.
- Osborn, C.E. & Poppele, R.E. (1992) Parallel distributed network characteristics of the DSCT, *J Neurophysiol*, Vol. 68, No. 4, pp. 1100-1112, ISSN: 0022-3077.
- Oscarsson, O. (1965) Functional organization of the spino- and cuneocerebellar tracts, *Phys Rev*, Vol. 45 pp. 495-522, ISSN: 0031-9333.
- Perrett, D.I., Smith, P.A.J., Mislin, A.J., Chitty, A.J., Head, A.S., Potter, D.D., Broennimann, R., Milner, A.D., & Jeeves, M.A., (1985) Visual analysis of body movements by neurons in the temporal cortex of the macaque monkey: a preliminary report, *Behav Brain Res*, Vol. 16, No. 2-3, pp. 153-170, ISSN: 0166-4328.
- Poppele, R.E., Bosco, G. & Rankin, A.M. (2002) Independent representations of limb axis length and orientation in spinocerebellar response components, *J Neurophysiol*, Vol. 87 (January 2002) pp. 409-422, ISSN: 0022-3077.
- Reina, G.A., Moran, D.W. & Schwartz, A.B. (2001) On the relationship between joint angular velocity and motor cortical discharge during reaching, *J Neurophysiol*, Vol. 85, No.6 (June 2001) pp. 2576-2589, ISSN: 0022-3077.
- Sanger, T.D. (1994) Optimal unsupervised motor learning for dimensionality reduction of nonlinear control systems, *IEEE Trans Neural Networks*, Vol. 5, No.6, pp. 965-973, ISSN: 1045-9227.
- Sarma, S.V., Massaquoi, S. & Dahleh, M. (2000) Reduction of a wave-variable biological arm control model, *Proc. of the American Control Conf*, pp. 2405-2409, ISBN: 0-7803-5519-9, June 2000, Chicago, Illinois, USA.

- Schaal, S. & Atkeson, C. (1998) Constructive incremental learning from only local information, *Neural Comput.*, Vol. 10, No. 8 (November 1998) pp. 2047-2084, ISSN: 0899-7667.
- Schweighofer, N., Arbib, M.A. & Kawato, M.(1998) Role of the cerebellum in reaching movements in humans. II. A neural model of the intermediate cerebellum, *Eur J Neurosci*, Vol.10, No. 1 (January 1998) pp. 95-105, ISSN: 0953-816X.
- Scott, S. & Kalaska, J.F. (1997) Reaching movements with similar hand paths but different arm orientations. I. Activity of individual cells in motor cortex, *J Neurophysiol*, Vol. 77 (Februaru 1997) pp. 826-852, ISSN: 0022-3077.
- Soechting, J.F. & Flanders, M. (1989) Sensorimotor representations for pointing to targets in three-deimensional space, *J Neurophysiol*, Vol.62, No.2, pp.582-594, ISSN: 0022-3077.
- Song, J., Low, K.H. & Guo,W. (1999) A simpplified hybrid force/position controller method for the walking robots, *Robotica*, Vol.17 (November 1999) pp. 583-589, ISSN:0263-5747.
- Tabata, H. (2002) Computational study on monkey VOR adaptation and smooth pursuit based on the parallel control-pathway theory, *J Neurophysiol*, Vol. 87 (April 2002) pp. 2176-2189, ISSN: 0022-3077.
- Takahashi, K. (2006). PhD thesis, department of Aeronautics and Astronautics, Massachusetts Institute of Technology.
- Takahashi, K. & Massaquoi, S.G. (2007). Neuroengineering model of human limb control-Gainscheduled feedback control approach, *Proc of Conference on Decision and Control*, pp.5826-5832, ISBN:978-1-4244-1497-0, December 2007, New Orleans, Louisiana, USA
- Tanji, J. & Wise, S.P. (1981) Submodality distribution in sensorimotor cortex of the unanesthetized monkey, *J Neurophysiol*, Vol.45, pp.467-481, ISSN: 0022-3077.
- Thach, W.T. (1998) What is the role of the cerebellum in motor learning and cognition? *Trends in Cog Sci*, Vol. 2 (Septermber 1998) pp. 331-337, ISSN 1364-6613 .
- Vallbo, A.B. & Wessberg, J. (1993) Organization of motor output in slow finger movements in man, *J Physiol*, Vol. 469 pp. 617-691, ISSN: 0022-3751.
- Williams, R.J. (1992) Simple statistical gradient-following algorithms for connectionist reinforcement learning, *Machine learning*, Vol. 8 (May 1992) pp. 229-256, ISSN: 0885-6125.
- Wolpert, D. & Kawato, M. (1998) Multiple paired forward and inverse models for motor control, *Neural Networks*, Vol. 11 (October 1998) pp. 1317-1329, 1998. ISSN: 0893-6080.
- Wolpert, D.M., Miall, R.C. & Kawato, M. (1998) Internal models in the cerebellum, *Trends Cog Sci*, Vol.2, No.9 (September 1998) pp. 338-347, ISSN: 1364-6613.
- Yamamoto, K. (2002) Computational studies on acquisition and adaptation of ocular following responses based on cerebellar synaptic plasticity, *J Neurophysiol*, Vol. 87 (March 2002) pp. 1554-1571, ISSN: 0022-3077.

Function-Based Biology Inspired Concept Generation

J.K. Stroble Nagel¹, R.B. Stone¹ and D.A. McAdams²

¹Oregon State University; ²Texas A&M University
USA

1. Introduction

Animals, plants, bacteria and other forms of life that have been in existence for millions of years have continuously competed to best utilize the resources within their environment. Natural designs are simple, functional, and remarkably elegant. Thus, nature provides exemplary blueprints for innovative designs. Engineering design is an activity that involves meeting needs, creating function and providing the prerequisites for the physical realization of solution ideas (Pahl & Beitz 1996; Otto & Wood 2001; Ulrich & Eppinger 2004). Engineering, as a whole, is about solving technical problems by applying scientific and engineering knowledge (Pahl & Beitz 1996; Dowlen & Atherton 2005). Traditionally, the scientific knowledge of engineering is thought of as chemistry or physics, however, biology is a great source for innovative design inspiration. By examining the structure, function, growth, origin, evolution, and distribution of living entities, biology contributes a whole different set of tools and ideas that a design engineer wouldn't otherwise have.

Biology has greatly influenced engineering. The intriguing and awesome achievements of the natural world have inspired engineering breakthroughs that many take for granted, such as airplanes, pacemakers and velcro. One cannot simply dismiss engineering breakthroughs utilizing biological organisms or phenomena as chance occurrences. Several researchers were aware of this trend in the early 20th century (Schmitt 1969; Nachtigall 1989), but it was not until later that century that the formalized field of Biomimetics or Biomimicry came about. Biomimetics is devoted to studying nature's best ideas to solve human problems through mimicry of the natural designs and processes (Benyus 1997). It is evident that mimicking biological designs or using them for inspiration leads to leaps in innovation (e.g., Flapping wing micro air vehicles, self-cooling buildings, self-cleaning glass, antibiotics that repel bacteria without creating resistance).

This research focuses on making the novel designs of the natural world accessible to engineering designers through functionally representing biological systems with systematic design techniques. Functional models are the chosen method of representation, which provide a designer a system level abstraction, core functionality and individual functionalities present within the biological system. Therefore, the functional models translate the natural designs into an engineering context, which is useful for the conceptualization of biology inspired engineering designs. The biological system

information is presented to engineering designers with varying biological knowledge, but a common understanding of engineering design methods. This chapter will demonstrate that creative and novel engineering designs result from mimicking what is found in the natural world.

Although most biology inspired designs, as mentioned previously, are mechanical, structural or material, this research focuses on how biological organisms sense external stimuli for the use of novel sensor conceptualization. Sequences of chemical reactions and cellular signals during natural sensing are investigated and ported over to the engineering domain using the Functional Basis lexicon (Hirtz et al. 2002) and functional models. In the following sections, related work of biology in design, natural sensing from the biological perspective, a general methodology for functionally modeling biological systems, two conceptualization approaches and two examples are covered. The discussion and conclusion sections explain how all of the pieces fit together in the larger design context to assist with biology inspired, engineering design. For the sake of philosophical argument, it is assumed that all the biological organisms and systems in this study have intended functionality, as demonstrated through functional models.

2. Related Work

Initial problem solving by inspiration from nature may have happened by chance or through dedicated study of a specific biological organism such as a gecko. However, more recently engineering design researchers have created methods for transferring biological phenomenon to the engineering domain. Their goal is to create generalized biomimetic methods, knowledge, and tools such that biomimicry can be broadly practiced in engineering design. A short list of prominent research in biologically inspired products, theories, and design processes is: (Bregbia et al. 2002; Bregbia & Collins 2004; Chakrabarti et al. 2005; Bar-Cohen 2006; Bregbia & Technology 2006; Vincent et al. 2006; Chiu & Shu 2007). Research utilizing biological system information with systematic design techniques has recently demonstrated analogy identification, imitation and design inspiration. The work of Nagel et al. (2008) explored how to apply functional modeling with the Functional Basis to biological systems to discover analogous engineered systems; however, only engineered designs with more obvious biological counterparts were considered. Rather than start with a design need, biological systems were modeled first as a black box and functional model, and from those biological system models, functionally analogous, engineered systems were identified. Analogies between the biological and engineered systems are demonstrated through a combined morphological matrix pairing functionalities and solutions. Shu et. al (2007) explored combining functional modeling and biomimetic design to facilitate automated concept generation. Three biological strategies were extracted from natural-language descriptions of biological phenomena and functionally modeled. The single phenomenon of abscission was shown to provide solutions for different engineering problems. Additional insight was provided to an engineering designer for use during the concept generation phase than with biomimetic design alone.

In a similar vein, Stroble et. al (2008) investigated functional modeling of natural sensing for the use of conceptual biomimetic sensor design. Functional models of how an organism within the Animalia or Plantae Biological Kingdoms takes in, translates and reacts to a stimulus were created at multiple biological levels. These models were entered into a design

repository for archival and for use with existing automated concept generation techniques (Bryant et al. 2005; Bohm et al. 2008). Wilson and Rosen (2007) explored reverse engineering of biological systems for knowledge transfer. Their approach is comprised of seven steps that result in idea generation. Like other biomimetic engineering design methods, the biological system must be functionally abstracted or decomposed into physical and functional parts. A behavioral model and truth table depicting system functionality allows the designer to describe the biological system with domain-independent terms to allow for the transfer of general design principles.

The research presented in this chapter advances functional modeling of biological systems with the Functional Basis (Hirtz et al. 2002) and offers a general method for functionally representing biological systems through systematic design techniques. Traditionally, systematic design techniques have been utilized for the design of mechanical or electro-mechanical products. This treatment of engineering design theory tests the boundaries of systematic techniques to develop electrical products.

3. Background

This section provides terms used throughout this chapter that are specific to this research, and abbreviated background information about systematic design methods and biological sensing at the Kingdom level. The following sections are provided to educate the reader and support the motivation for this research.

3.1 Nomenclature

- Biomimicry - a design discipline devoted to the study and imitation of nature's methods, mechanisms, and processes to solve human problems. Also referred to as biology inspired design.
- Biological organism - a biological life form that is observed to exist.
- Biological system - any biological situation, organism, organism sub-system or portion of an organism that is observed to exist or happen (e.g., Bacteria, sensing, insect compound vision, DNA, and human heart).
- Functional Basis - a well-defined modeling language comprised of function and flow sets at the class, secondary, tertiary levels and correspondent terms.
- Functional model - a visual description of a product or process in terms of the elementary functions and flows that are required to achieve its overall function or purpose.
- Flow - refers to the material, signal or energy that travels through the sub-functions of a system.
- Function - refers to an action being carried out on a flow to transform it from an input state to a desired output state.

3.2 Systematic Design Methods

Design requirements and specifications set by a customer, internal or external, influence the product design process by providing material, economic and aesthetic constraints on the final design. In efforts to achieve the customer's needs without compromising function or form, function based design methodologies have been researched, developed and evolved

over the years. Most notable is the systematic approach of Pahl and Beitz (1996). Since the introduction of function structures, numerous functional modeling techniques, product decomposition techniques and function taxonomies have been proposed (Pahl & Beitz 1996; Stone & Wood 2000; Otto & Wood 2001; Ulrich & Eppinger 2004). The original list of five general functions and three types of flows developed by Pahl and Beitz (1984) were further evolved by Stone and Wood (2000) into a well-defined modeling language entitled the Functional Basis. The Functional Basis is comprised of function and flow sets, with definitions, correspondent terms and examples. Hirtz, et al. (2002) later reconciled the Functional Basis and NIST developed modeling taxonomy into its most current set of terms. The reconciled Functional Basis provides designers with sets of domain independent terms for developing consistent, hierarchical functional models, which describe the core functionality of products and systems.

3.3 Natural Sensing

To claim that a biomimetic sensor is one that simply transduces a stimulus, as explained in this section, would designate all sensors on today's market biomimetic. Instead, there must be a unique feature or method of detecting the stimulus, which mimics, directly or analogically, a biological sensing solution to classify the sensor as biomimetic. Thus, for biomimetic sensor conceptualization it is imperative to understand the biology behind natural sensing to leverage nature's elegance in engineering design. This section covers fundamental knowledge of the biological processes involved during natural sensing at multiple biological levels - termed scales, in the Animalia and Plantea Kingdoms.

Natural sensing occurs by stimuli interacting with a biological system, which elicits a positive or negative response. All organisms possess sensory receptor cells that respond to different types of stimuli. The receptors that are essential to an organism understanding its environment and surroundings, and are of most interest to the engineering community for mimicry, are grouped into the class known as extroreceptors (Sperelakis 1998). The three classes of receptors are (Aidley 1998; Sperelakis 1998):

- Proprioceptors - Internal - vestibular, muscular, etc.
- Interoceptors - Internal without conscious perception - blood pressure, oxygen tension, etc
- Extroreceptors - External - chemoreceptors, electroreceptors, mechanoreceptors, magnetoreceptors, photoreceptors, and thermoreceptors.

Proprioceptors and interoceptors are excellent biological sensing areas to study for developing medical assistive technologies, however, they are not investigated in this research. The receptors of interest are within the six families under the class of extroreceptors. Once a stimulus excites the biological organism, a series of chemical reactions occur converting the stimulus into a cellular signal the organism recognizes. Converting or transforming a stimulus into a cellular signal is termed transduction. Although all biological organisms share the same sensing sequence of perceive, transduce, and respond, they do not transduce in the same manner. Biological organisms that are capable of cognition have the highest transduction complexity and all stimuli result in electrical cellular signals (Sperelakis 1998). Other organisms have varying levels of simpler transduction that result in chemical cellular signals (Spudich & Satir 1991). For more detailed information about natural sensing than provided in the following subsections and

how it could be utilized for engineering design, consult Barth et al. (2003) and Stroble et al. (2009).

3.3.1 Animalia Kingdom

Biological organisms of the Animalia Kingdom are multi-cellular, eukaryotic organisms capable of cognitive tasks (Campbell & Reece 2003). Within this set of organisms, transduction occurs in one of two ways (Aidley 1998; Sperelakis 1998):

- Direct coupling of external stimuli energy to ion channels, allowing direct gating; or
- activation of 2nd messengers - the external stimuli energy triggers a cascade of messengers which control ion channels.

Transduction in this Kingdom is a quick process that happens within 10 μ s - 200ms per stimulus (Aidley 1998). During transduction, a sequence of four events occur as shown in Table 1, which are uniform across the six receptor families (Sperelakis 1998). Recognition of a stimulus happens within the nervous system, as denoted by discrimination in the transduction sequence. Mechano, chemo, thermo and photoreceptors are the dominant receptors in organisms of the Animalia Kingdom, however fish and birds utilize electro and magnetoreceptors, respectively, for important navigational tasks.

3.3.2 Plantae Kingdom

The Plantae Kingdom simply refers to multi-cellular, eukaryotic organisms that obtain nutrition by photosynthesis (Campbell & Reece 2003). Transduction in this Kingdom converts external stimuli into internal chemical responses and occurs by either (Mauseth 1997; Sperelakis 1998):

- Direct coupling of external stimuli energy to ion channels, allowing direct gating; or
- activation of 2nd messengers - the external stimuli energy triggers a cascade of messengers which control ion channels (most common).

Transduction within plants is a slow process, often taking hours to complete. Cross talk between signaling pathways permits more finely tuned regulation of cell activity than would the action of individual independent pathways (Berg et al. 2007). However, inappropriate cross talk can cause second messengers to be misinterpreted (Berg et al. 2007), much like high frequency circuits that couple to other electronic devices causing an undesired effect. During transduction a sequence of three events occur as shown in Table 1, which are uniform across the six receptor families (Sperelakis 1998).

Photo, mechano, chemo, magneto and thermoreceptors, in that order, are the dominant receptors in organisms of the Plantae Kingdom. Particular stimuli result in particular reactions, which are known as tropisms in this Kingdom. Electroreceptors are the least understood in Plantae Kingdom organisms and experiments do not provide consistent results, however, it has been suggested that electrical signals can traumatize organisms of this Kingdom (Spudich & Satir 1991).

Transduction Sequence	Animalia Kingdom	Plantae Kingdom
Detection	Protein binding and signal propagation about receptor cell	Protein binding and signal propagation about receptor cell
Amplification	Cascade of intracellular chemical signals	Cascade of intracellular chemical signals
Discrimination	Modulation of chemical signals into an electrical code sent to the nervous system	N/A
Adaptation	Over time, a prolonged stimulus has less of an effect	Change in turgor pressure or chloroplast orientation

Table 1. Transduction sequence for two biological Kingdoms

4. Modeling Biology

Representing the world in terms of its function (i.e., what the world does) as opposed to its form (i.e., what comprises the world) is commonly used to abstract problems in engineering design. Functional representation enables a thorough understanding of the requirements while decreasing the tendency of designers to fixate on some particular physical solution for a problem. When viewed functionally, biological systems operate in much the same way that engineered systems operate (French 1994). Each part or piece in an overall biological system has an intended function. Function, therefore, may be utilized as the link to connect natural and engineering domains to identify analogies. Functional representation of biological systems has the potential to provide several advantages for engineering design:

- Systematic approach for establishing and representing functionality;
- functionality, morphology or strategy captured at multiple levels of fidelity;
- identification of characteristics that can be mimicked by engineering means;
- creativity in concept generation; and
- archival and transmittal of information.

4.1 Mapping Biology to Function

Representing biological functionally using the lexicon of the Functional Basis allows biological solutions to be stored in an engineering design repository and utilized for concept generation. These biological solutions can then be recalled and adapted to engineered systems. However, modeling biological systems is not as straightforward as modeling engineered systems. One cannot easily take apart a biological system, examine the parts and associate function as one would an engineered system. Rather, the designer must rely on biological literature or biologists for detailed information about the desired system. To facilitate biological functional modeling, an engineering-to-biology thesaurus (Stroble et al. 2009) mapping biological correspondent terms to the Functional Basis is employed.

Our approach to modeling biology with the Functional Basis aims to accurately reflect the material, signal, or energy flows carrying out biological system functions. For example, the Functional Basis flow set lists fifteen different forms of energy, of which biological energy is included. However, since labeling all forms of energy that flow through an organism *biological energy* would not be descriptive enough for engineering designers to relate, create and utilize analogies, therefore equivalent engineering energies are identified to accurately describe functionality of a biological system.

Consider again natural sensing as the biological system to illustrate the mapping of biological terminology to the Functional Basis. Chemoreception of the Animalia Kingdom will be the focus. Mapping terms is one of the early steps leading to a biological functional model; however, a designer first needs to clearly define the research goal. To scope a functional model of an engineered system a design question must be posed. The same holds true for biological systems and, more importantly, it provides a designer a starting point for researching the biological system. Consider the following question for natural sensing: How does a biological organism of the Animalia Kingdom take in, interpret and react to an external chemical stimulus? Table 2 lists the flows that aid in answering the research question and how they can be represented using the Functional Basis.

Biological Information	Functional Basis Flow
Protein	Solid liquid mixture material
Receptor cell	Solid liquid mixture material
2nd Messenger	Solid solid mixture material
Chemical stimulus	Chemical energy
<i>Signal propagation about receptor cell</i>	Chemical energy
<i>Cascade of intracellular chemical signals</i>	Chemical energy
<i>Modulation of chemical signals into an electrical code</i>	Electrical energy

Table 2. Relationship between sensing and Functional Basis terms (Hirtz et al. 2002)

4.2 Defining Mimicry Categories

Mimicking a biological system for the creation of biology inspired technology happens in multiple ways. Traditionally, biomimetic designs have tended to mimic the observable aspects of biological systems, such as how the system gathers or transports food and liquid, without considering mimicry boundaries. It was observed, however, that functional analogies occurring from a strategic or process perspective tend to be less obvious and require more detailed information about the biological system (Nagel et al. 2008). To aid with identifying potential mimicry aspects of a biological system a set of mimicry categories is established, which are: function (principle), morphology, strategy (behavior),

manufacture, or any combination of these. The definitions of the mimicry categories with regards to biological systems are:

- **Function:** the fundamental principle, quality or attribute of a biological system.
- **Morphology:** the form of a living system, and the associations amongst an system's structures.
- **Strategy:** the reaction of a biological system in response to a particular situation or stimulus; its behavior.
- **Manufacture:** the production of something by a biological system.

These mimicry categories aid the designer with defining a boundary when developing a functional model. It is very easy to overstep the scope of the functional model when modeling a biological system. In addition to answering a research question related to the biological system, the biological functional model must also comply with a chosen biological scale (described in Section 4.3).

Reconsider natural sensing and the research question posed in Section 4.1. Understanding how an organism of the Animalia Kingdom takes in and interprets an external chemical stimulus requires knowledge of the principal functionalities of cellular communication, transduction and the primary energy an organism creates during transduction. One could argue that this also includes the category of strategy because the question considers the reaction to an external stimulus. However, the functional model would also need to include states for reactions of fear, surprise, neutral and no reaction. Natural sensing involves transduction of a stimulus and cellular communication, which always results in a cellular reaction; it is not the behavior of the system that is in question. Once the energy is released from the system (e.g., propulsion or movement) a behavior can be observed. Therefore, consider that the functional model boundary set for natural sensing of a chemical stimulus is the category of *function*.

4.3 Identifying Biological Scales

Biological scale deals with how much detail is required for an adequate representation of the biological system to utilize the information with a chosen engineering design method. Comparison of biological terms to Functional Basis terms at deeper, more defined levels is time consuming as each part of a biological system has a unique way of interacting with the world around it, thus terminology becomes a problem. Any desired functional model level can be achieved with enough effort and resources; however the questions become, where can inspiration be most readily achieved, and what scales must be modeled to best capture this biological information to achieve inspiration?

To define the level of biological information required for a functional model, the biological scale utilized in multi-scale biological computational models is employed. A biological computational model ranges from atomic level to population, and has the following order: atomic, molecular, molecular complexes, sub-cellular, cellular, multi-cell systems, tissue, organ, multi-organ systems, organism, population and behavior (White et al. 2009). This scale can be utilized for functional representation of biological systems, allowing engineers to clearly define the level of a biological model. Although the biological scale can be viewed as a constraint on the model, it is also a creative analogical reasoning challenge. Analogies from the same biological system can be derived at more than one scale. This has been demonstrated by (Shu et al. 2007). Advantageous starting points are the cellular, organ and organism biological scales, which are readily defined in biological literature.

When generating a biological functional model, the biological scale is often constrained to a single level (i.e., the model contains only elements from the organ level). Generating models constrained by biological scale tends to be more analogous to how engineered systems are modeled; however, functional models can represent mixed biological scales to demonstrate specific biological phenomena of interest to the designer. It is important when modeling mixed, biological scale models, to remember that any final concepts derived from analogies between natural and engineered systems will also be of mixed scale. This concept of mixed model analogies was demonstrated by the lichen example in (Nagel et al. 2010), which inspired symbiotic electronic devices.

Biological models at a very low level (i.e., molecular, sub-cellular) are not always helpful because they can provide too much detail, which results in a number of engineering components that do not work together. The converse can be said about biological models at a very high level (i.e., organism). A high level functional model may not be descriptive enough for concept generation, or may not convey the innovative principle of the biological system. However, the functional model level of fidelity is at the discretion of the designer. It is important when developing functional representations of biological systems to not mix information at one scale with information at another, unless a mixed model desired (the same could be said for an engineering system).

The functional model of Animalia chemoreception can best be captured with a model at the cellular biological scale, due to the cellular communication aspect of natural sensing. Modeling at the organ level would convey that a stimulus is converted and a reaction is the result. This result is not descriptive enough to utilize for concept generation of novel sensor technology. However, before a functional model is created, a black box representation is developed to abstract the system in question. Realizing that sensing occurs by transduction, which involves interpretation of a stimulus, the black box model of the system is described as detect (i.e., to discover information about a flow) (Hirtz et al. 2002). The flows, identified in Section 4.1 include the chemical stimulus and the electrical response as the energies, and multiple mixture materials. This black box model is provided in Figure 1.

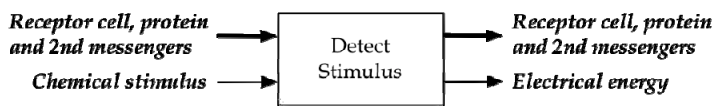


Fig. 1. Black box model of natural sensing

4.4 General Biological Modeling Methodology

During the course of this research several functional models of biological systems were created, edited and finalized. Based on these experiences, the following general methodology for functionally representing biological systems is formalized. The methodology offers a designer direction when creating a biological functional model and provides empirical guidelines to improve model accuracy. The methodology is as follows:

1. Identify a good reference (e.g., biology text book) for the biological system of interest.
2. Read the overview of the biological system to understand the core functionality of the system.

- Make note of materials, energies and signals utilized while reading about the biological system. Refer to the engineering-to-biology thesaurus for guidance on how biological flows relate to flows found in engineered systems.
3. Define the research question the functional model aims to answer.
 4. Define the category of the functional model.
 5. Define the desired scale of the model.
 - Begin by modeling the black box for the biological system defining the overall functionality with the Functional Basis modeling language.
 - Investigate what occurs at the desired biological scale to achieve the black box functionality (i.e., sub-functions).
 - Read about the biological system noting the sequential and parallel events that occur to achieve the black box functionality.
 6. Develop a functional model of the biological system using the Functional Basis modeling language within the bounds set by the research question, biological category and scale.
 - Use the engineering-to-biology thesaurus to choose the most suitable functions to accurately represent the biological system.
 - Make sure implied functions such as transfer, transmit, and guide are added to the model between major biological events.
 - Do not mix the function of the supporting structure with the core functionality of interest within the functional model (e.g., the stalk of a sunflower transports nutrients and water from the soil to the head for producing fruit, and should not be mixed with the stalk as a support for the sunflower).
 - Utilize a software program that allows quick rearrangement of blocks to make this process quicker (i.e. FunctionCAD (Nagel et al. 2009), Omni Group's OmniGraffle, and Microsoft's Visio).
 7. Double-check and/or validate (e.g., have a biologist review model hierarchies) the functional model against the research question, biological category and scale, and black box model.
 - Keep in mind that familiar terms to engineers could be used in a different context in the biological system description. (e.g., the term bleaching does not refer to the removal of color; with respect to vertebrate eyes, it means the retinal and the opsin eventually separate, which causes loss of photosensitivity (Campbell & Reece 2003).

In this section, the chemical sensing example developed through Sections 4.1-4.3 is continued. Previously, Steps 1 through 5 were developed by investigating the sensing functions, the flows required, the biological system scale and category. Now following Step 6, the functional model, shown in Figure 2, is decomposed from the black box (Figure 1). The functional principles of cellular communication and transduction, which perform the natural sensing sequence of perceive, transduce and respond are depicted within Figure 2. Perceive and respond are represented as sense and actuate, respectively. The functions of detect, change, process and condition are what comprise transduce, the organ level function of convert. As one can see, the number of material and energy interactions at the cellular level can become complex. For comparison, the organ level functional model of chemical sensing is provided in Figure 3.

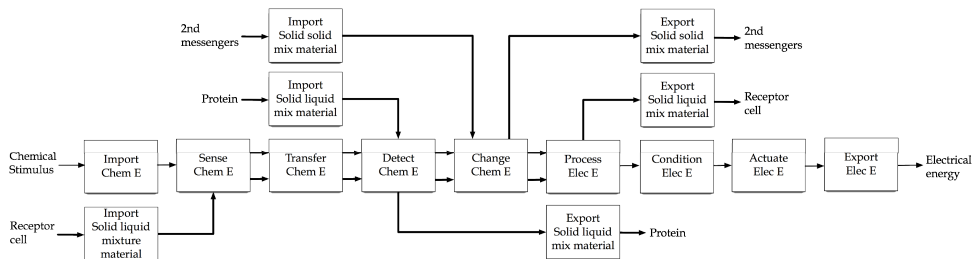


Fig. 2. Functional model of chemical sensing at the cellular scale

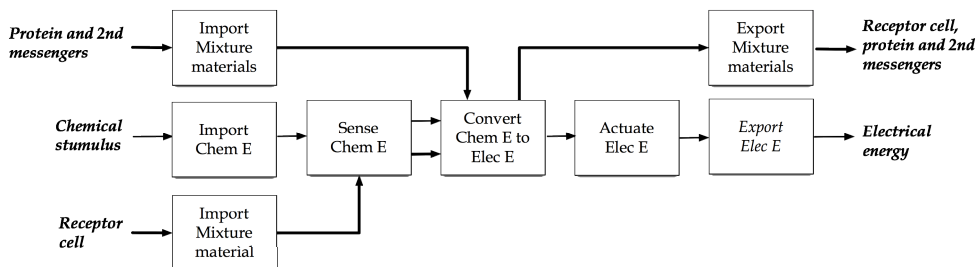


Fig. 3. Functional model of chemical sensing at the organ scale

The detailed biological events occurring during chemoreception, recognition of a taste or smell, by an organism of the Animalia Kingdom are provided in Table 3. Table 3 demonstrates in list format the Functional Basis terms that should be used for creating functional models at a sub-cellular scale for chemical sensing; also allowing one to comprehend the similarities between the two domains. The final action of the sensing sequence, respond, is described in the model as the function actuate. This term is preferred to describe response at a general level because the resultant electrical energy from sensing, once processed and conditioned, will be directed to the portion of the system that elicits the response. However, at a deeper level the exact response can be chosen. Possible function term choices are: regulate, change, guide, indicate, stop, position or inhibit.

A biologist of the Biology department at Missouri University of Science and Technology validated the biological functional models of chemoreception and the information in Table 3. However, a brief analysis of existing model abstractions and known flows, and the model's ability to answer to the designated research question is performed. The functionality in question is how chemoreception occurs within an organism of the Animalia Kingdom. By capturing perceive, transduce and respond, the functional model can be abstracted to—a chemical stimulus enters the organism boundary, which is translated by the receptor cells and changed into an electrical energy to trigger a response. At the black box level the chemical sense is modeled as having the function of detect. To discover information about a flow (stimulus) is a natural occurrence during chemical sensing. It is evident that both abstractions support the initial research question, thereby supporting the validity of the model. As a final check, both the black box and functional models have the same number of input/output flows. All requirements initially identified through flow mappings (Section 4.1) have been satisfied. It is therefore concluded that the biological functional model is valid.

Biological Term		Engineering Term	
Action	Description of events the action is comprised of....	Functional Basis Term	
Perceive	Chemical stimulus occurs	Sense	Import
	First signal propagation about receptor cell		Sense
	Second signal propagation about receptor cell		Transfer
Detect	Receptor cell transforms external stimulus into a biological stimulus of the same type	Detect	Detect
Amplify	Fluctuation of second messengers for a chemical cascade	Change	Increment, Decrement
	Ion channels open or close for Na ⁺ or K ⁺		Actuate
	Cell membrane depolarizes		Change
Discriminate	Change electrical signal into a frequency	Process	Change
	Send frequency to brain		Transmit
	Recognize chemical stimulus		Process
Adapt	Adapt to prolonged chemical stimulus	Condition	Condition
Respond	Electrical energy produced by the chemical reaction, it is based on the stimulus	Actuate	Actuate, regulate, stop, etc.
	Reaction is now external		Export

Table 3. Animalia chemoreception biological and engineering terms

5. Concept Generation

Function-based automated concept generation may be extended in three ways with the addition of biological information. The typical approach would generate functional models based on customer needs. Then automated concept generator software, such as MEMIC (Bryant et al. 2005), would be used with the Design Repository (2009) to identify potential solutions for each component. This approach, as well as the three extensions that can lead to biological inspiration, are illustrated with Figure 4. The three new approaches utilize either biological information stored in the Design Repository or biological information modeled functionally to focus queries on analogous engineered solutions. The first approach, shown as a dashed line in Figure 4, uses a functional model developed from a biological system (discussed in Section 4) to discover corresponding engineering components to mimic the functionality of the biological system. The second approach, shown as a solid line in Figure 4, uses a conceptual functional model developed from customer needs and

constraints to discover which biological components currently stored in a design repository inspire functional solutions to fill engineering requirements. The third approach represents a hybrid of the two prior approaches. In this third hybrid approach, shown as a double line in Figure 4, a biological system is modeled functionally and is used to discover other analogous biological systems priorly stored in a design repository. These analogous biological systems can then be used by the designer to inspire novel engineered solutions for each function. In this chapter the first two approaches (shown as either a dashed or solid line in Figure 4) are discussed further.

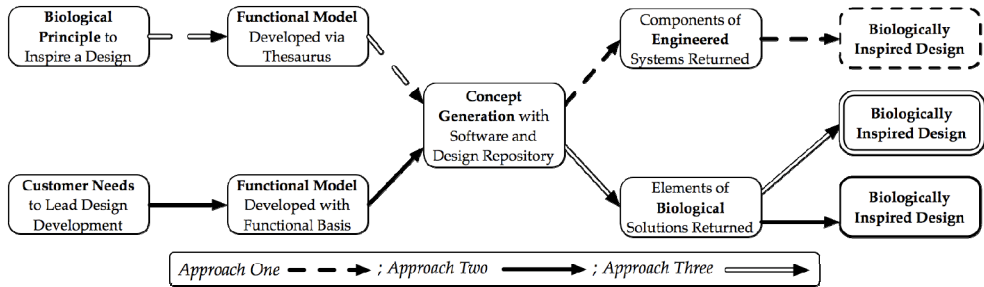


Fig. 4. Summary of concept generation approaches

The two approaches to biologically inspired design discussed in the following subsections utilize a design repository and automated concept generation software; for this research the examples access the Design Repository housed at Oregon State University (2009), the automated morphological matrix tool (Bohm et al. 2008) and the concept generator software, MEMIC (Bryant et al. 2005). The Design Repository at Oregon State currently houses descriptive product information such as functionality, component physical parameters, manufacturing processes, failure, and component connectivity for over 113 consumer products and 18 biological phenomena amounting to over 5,600 physical artifacts. Both the automated morphological matrix tool and MEMIC access the Design Repository to return potential solutions for each function in a system. Where the morphological matrix tool returns all possible solutions for each function, the MEMIC software ranks viable concepts with a matrix algebra based algorithm to provide those concepts that are feasible by considering the engineering component relationships, thus only components with a predetermined relationship are provided to the designer for concept generation. Functional models created with the software FunctionCAD (Nagel et al. 2009) can be exported directly to MEMIC to speed up the concept generation process. All design tools mentioned in this chapter can be found at the Design Engineering Lab's website: www.designengineeringlab.org.

5.1 Approach One

Concept generation approach one is a new proposal for concept generation of innovative products that utilizes functional models based on systems of interest, rather than deriving a product directly from customer needs. This particular method is useful for product redesign and improvement. By taking a product originally derived from customer needs and identifying features that need improvement, to meet the customer expectations, the designer

can take inspiration from another system—in this case biology—to discover product innovations. A designer could utilize approach one to explore the possibilities that other systems offer.

For this approach to work, the system of interest is a biological organism or strategy. A functional model of the biological system is first created. The functional model is then used to query the Design Repository for potential engineered solutions to each function using MEMIC and/or the automated morphological matrix tool. The input is processed, and a set of engineering components is returned for each function-flow pair in the functional model of the biological system. The designer must choose from the resulting component suggestions to develop a complete conceptual design. This methodology is formalized below:

1. Generate a functional model of the biological system to be mimicked following the procedure outlined in Section 4.
2. Utilize an automated concept generator to query a design repository for potential solutions for each function in the functional model of the biological system.
3. Review the engineering components returned by the automated concept generator that fulfill the same functionalities as the functions in the biological system.
4. Choose conceptual design variants from the automated concept generator.
5. Continue with the conceptual design process and/or proceed to detailed design.

This approach is limited by the data available in the design repository being queried for analogies; when data is available, analogies are easily discovered between biological and engineered systems. The solutions returned, however, often do not fit together as they would in a traditional engineered system and require a large amount of insight from the designer to be able to draw analogies leading to an engineered system. This approach therefore lends itself more toward innovate design problems where novel solutions tend to dominate.

Consider again the chemoreception example utilized through Section 4 where the Animalia chemical sense was used to demonstrate the generation of a functional model of a biological system. Chemoreception will be used to explore engineering possibilities with concept generation approach one. In the previous section, Step 1 of this approach is completed; the functional model of chemoreception is provided in Figure 2. To query the Design Repository with the MEMIC software for Step 2, the biological model of Figure 2 was created in FunctionCAD and exported as an adjacency matrix (a 2D matrix capturing the topology of the functional model) to MEMIC. MEMIC returned engineering components for half of the function/flow pairs; for the remaining half of the function flow pairs, MEMIC returned an incompatibility error meaning that engineering systems in the Design Repository were not known to solve function-flow pairs in the same order as the biological system. To find solutions for these remaining functions, the Design Repository was queried with the morphological matrix tool, and available solutions were chosen from the resultant morphological matrix. Not all of the function/flow pairs have solutions. However, the chosen engineered solutions have been substituted for each function in the functional model of the biological system and is provided in Figure 5.

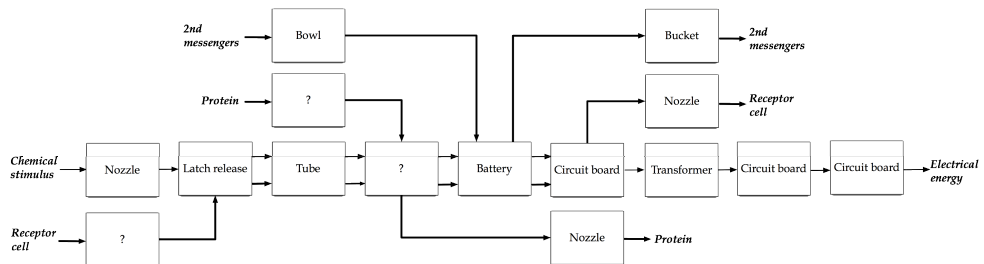


Fig. 5. Animalia chemoreception model with engineering components

It is not surprising that the biological functional model of chemical sensing did not return a complete set of engineering components that solve the biological functions. However, the blank spaces give the designer freedom to innovate or leverage knowledge from any source when developing the concept. Of the engineering components given in Figure 5, many of the import and export functions suggested a nozzle as a solution, which is a means to move material (of most types) from one location to another. The notion of nozzle inspires thoughts of tubes or channels, all of which could achieve the same function. Circuit board replaced three of the functions within the model and incorporation of a transformer on the circuit board is feasible, further simplifying the design. The function of sense suggested a latch release, a device that gives way in the presence of enough energy, or could be used as an automatic switch to activate the device. Detect chemical energy did not return a component such as a sensor; however, this allows the designer to innovate. Cutting edge research that interfaces with chemical energy to generate an electrical signal could be applied. Up to this point in the analysis, one could envision an analogous lab-on-chip device to chemoreception with the following characteristics: a chemical is introduced to the chip which automatically turns on the device, the chemical stimulus passes over the sensing interface and the results are sent by electronic signal to a computer or data storage device.

The battery that is suggested for the change chemical energy function/flow pair does not immediately make sense for a lab-on-chip device other than to power it. However, after given more thought, the battery could possibly be used in the following ways: clean the chemical stimulus before exiting the system (e.g., electrodeionization), provide a second measure for the output data or enhance the sensor reading. If investigated further, this concept could lead to a novel chemical detection system that closely mimics the principle functionality of the natural sense of chemoreception.

Reconsidering the biological scale of cellular, used to scope the functional model of Figure 2, the resultant concept is a device that is manufactured at the micro/nano scale, which is roughly the same size as the natural system. The final concept is not required to mimic the biological scale, as shown by the chemoreception example, but the suggestion of physical size is just one more piece of information the designer can leverage during biomimetic inspiration. It is important to understand that the concept generation approach does not generate a complete and final concept; that is the task of the designer. The approach, however, does facilitate discovering analogies between the biology and engineering domains, so that it may be easier for the designer to make the necessary connections leading to innovative biology inspired designs. Furthermore, the experience and expertise of the designer plays a critical role in developing the final concept. In this case, the designer

analyzing the automated concept generation results has a background in electrical engineering, which lead to the analogy of a lab-on-a-chip.

5.2 Approach Two

The second concept generation approach leading to biologically analogous products follows the typical method of automated concept generation outlined in (Bryant et al. 2005). First, the potential customer is interviewed to identify customer needs. The customer needs are translated into functionality for the product being designed. A black box model and functional model are developed and used to query a design repository for solutions to each function. In order for biological inspiration to occur using this typical method, the design repository being queried requires biological entries. Then, when the designer queries the repository, biological solutions are returned for functionality in the conceptual functional model. The designer would then have the choice to choose the biological solutions as inspiration to novel engineered solutions.

Entries into the design repository can be any of the biological categories or scales previously described, and often one biological system will offer multiple functional models where each describes a different category and/or scale. Descriptions and images are provided with each artifact to assist a designer with overcoming any potential knowledge gap between biology and engineering, thus facilitating inspiration and analogical reasoning during the design process. The Design Repository housed at Oregon State currently is populated with biological entries, which can be returned with both the automated morphological matrix tool and with the MEMIC software. The following methodology formalizes this approach:

1. Create a conceptual functional model of the desired engineering system based on mappings of customer needs and constraints to flows (Pahl & Beitz 1996; Otto & Wood 2001; Ullman 2002; Ulrich & Eppinger 2004).
2. Utilize an automated concept generator to query potential solutions for each function in the conceptual functional model.
3. Review engineering and biological components from the potential components retrieved by the automated concept generator.
4. Explore biological components for inspiration to functionalities (i.e., view the repository entry and functional model, read more about it in a biological text).
5. Identify novel engineering solutions for functions that are inspired by biology, or if none are identified, choose alternative solutions from the concept generator software.
6. Continue with the conceptual design process and/or proceed to detailed design.

To illustrate concept generation approach two and to continue the chemical sensor idea, a conceptual functional model of a chemical sensing device will be the focus of the example in this section. The needs and constraints of the chemical sensing device are derived from (Fraden 2004): selectivity (only senses the desired chemical in the presence of other species), quick response time, reusable, and utilizes an indirect sensing mechanism. These needs and constraints are mapped to flows as shown in Table 4. Figure 6 provides the conceptual functional model, which completes Step 1. The functional model is created at a system level to facilitate analogical reasoning as the majority of information in the Design Repository is at a comparable level.

Customer Need/Constraint	Functional Basis Flow
Selectivity	Status signal
Response time	Electrical energy
Reusable	Device substrate (material)
Indirect sensing mechanism	Device substrate (material)/Chemical stimulus (energy)

Table 4. Chemical sensing needs mapped to conceptual flows

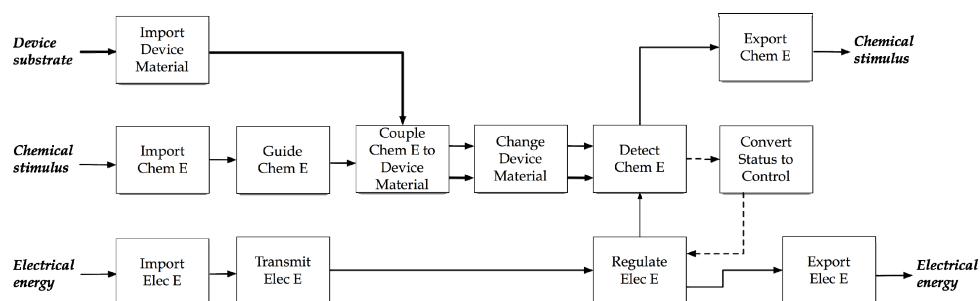


Fig. 6. Chemical sensing conceptual functional model

The chemical sensing device conceptual functional model in Figure 6 shows the generalized form of a chemical stimulus (i.e., chemical energy). This allows the designer to query all possible forms of a chemical stimulus. The device substrate is also generalized as material to include all possible forms of material in the Design Repository. Figure 6 demonstrates the indirect sensing mechanism with *couple* and *change*, sensor with *detect*, and transducer with the *convert* and *regulate* function blocks, respectively. Electrical energy is utilized to power the transducer and transfer the detection signal to the device capable of interpreting such signals, such as a computer. The boundary of the conceptual functional model includes the sensing element and the transducer.

To query the Design Repository with an automated concept generator for Step 2, the model of Figure 6 was created in FunctionCAD and exported as an adjacency matrix to MEMIC just as in Section 5.1. Again, MEMIC returned engineering components for half of the function/flow pairs; for the remaining half of the function flow pairs, the Design Repository was queried with the morphological matrix tool, and available solutions were chosen from the resultant morphological matrix. Utilizing both tools, components for each function/flow pair were returned. For 10 of the 12 functions the component list was short and easy to choose from as noted by the engineering components replacing the function/flow pairs in Figure 7. The functions of *change* and *detect* returned many possible components, of which, need to be analyzed before one can be chosen for the remaining two chemical sensing device conceptual functions. The five engineering components identified that *change* materials are: a heating coil, impeller, filter, punch, staple plate, and blade. The four biological components identified that *detect* chemical energy are: a protein of the two component

Biological inspiration leads to a sensor element surface that has specifically shaped cavities or is uniformly porous, and is a good conductor. Any material that can be patterned by photolithography can achieve the desired surface. The collection of engineering and biological components presented here, inspires the conceptual design variant of a device that supports a housing containing an electrified element (not for the production of heat) acting as a barrier that chemical energy is guided to from the container, or space. The subsequent chemical energy is attracted to the electrified element and once bonding occurs, particles (e.g., electrons) are released on the sensing element side to fill the sensor element surface cavities and generate a signal to be transduced. The filling of cavities by particles fulfills the requirement of an indirect sensing mechanism, which also supports reusability as the particles within the closed environment could return to the barrier element using a simple calibration procedure. An electronic circuit powers the sensing element, decodes the sensor signal and produces an electrical voltage or current analogous to the input. Further material property research needs to be completed before this design can be designated as feasible.

Multiple conceptual design variants for this example are possible, just as there are a number of materials applicable for the sensing element. A designer, when presented with the biological principle of natural sensing, organs of the fly, or strategies of proteins, is subsequently required to investigate the biological counterparts to each of the desired functionalities. It is through this correlation that the designer can take inspiration from the biological strategies. Again, the software does not generate a finalized concept; that is the task of the designer.

6. Discussion

Functional representation of a biological system as described in Section 4, results in a description of the biological system's functionality at a specified biological category and scale. By viewing the biological system from an engineering perspective and breaking it down into manageable parts, a designer can identify parallels between the engineering domain and biology or find inspiration for the development of novel, engineering solutions. Functional decomposition works for identifying analogies between biological and engineering systems as it creates a common approach for system decomposition. Also, with biological systems, it tends to be impractical for a designer to randomly try to match comparable engineering components to each biological component, especially for those who are biology novices. Functional modeling holds the potential to provide a translator between these domains. Concept generation techniques with function-based biological models facilitate the processes by making the task both manageable and worthwhile as demonstrated by Section 5.

When developing a functional model of a biological system, it is important that a designer consider a number of key points: (1) The category and scale of the model must be chosen carefully such that the model may be valid to the research question and accurate to the system. (2) The energies associated with the biological system must be defined appropriately using analogous engineered system equivalents (e.g., Had change biological energy been used to model change chemical energy battery would not have been returned as an analogous component.) (3) Biological scale based on the detail of information provided might be a good place to start, but when developing the final model, the scale must

represent the question being asked of the model. (4) The choice of a low-level scale, such as molecular or sub-cellular, are not only hard to define, but often may be too detailed to lead a designer to inspiration. (5) Choosing a category serves to refine the boundary, but, like scale, it should be flexible through the concept generation process, and its consideration might prompt the designer to consider the same biological system in a new and unique way leading to new ideas. (6) Utilizing the Functional Basis aids in concept generation and should be used when developing a functional model. The flows, however, should be represented as their biological correspondents when validating the functional model of a biological system.

With concept generation approach one, a functional model is first generated of a biological system. This biological system is then used to seed inspiration for innovative engineered systems. The biology-based functional model is used to query engineered solutions to facilitate biomimicry. This approach does not begin from the traditional starting point of customer needs, and could, thus, be considered a creativity tool to open a designer's mind to the possibility of finding analogy in nature. Research has shown that while approach one can quickly lead to biological mappings to engineered systems, these mappings do not consistently make sense in an engineering context, and if taken at face value by the designer, the mappings would often result in infeasible conceptual designs (e.g., the sensor to battery to circuit mapping discovered in the chemoreception example presented in Section 5). To make the concept work, a leap is required from the designer to understand that the component mapping is an analogy that relates the biological system to the engineered system. The approach assists with making the leap from biology to engineering, but to arrive at the final concept, the designer is required to make the leap within the engineering domain.

Concept generation approach number two begins more traditionally and is better suited for customer-based product design methodologies. Customer needs are first gathered. Then, the customer needs are translated to function, and function is used to direct a query for potential solutions. Instead of engineered solutions being returned, however, biology—in the form of strategies, principles, organisms, organs, etc.—is returned. At this point, approach two relies on the designer to analyze each of the biological results for potential inspiration. Where approach one helped to link biology to engineering, approach two reverses this by assisting with the link or analogy from engineering to biology. In this second approach, the engineer is not required to have any prior knowledge of biological systems; the biological information would be pre-populated in a design repository, and it is from this pre-populated data that the designer may choose to make the leap to a biology inspired design.

The approaches discussed here demonstrate the feasibility of utilizing biological information during conceptual design. However, the concept generation approaches, require work by the designer to develop at least a basic understanding of analogous biological systems. The approaches do, however, provide a starting point to guide a designer toward potential analogies reducing the biological overhead. To make this work, the conceptual system design must be heavily reliant on database content—both engineering and biological domains. Finally, it is important to understand that the approaches do not generate concepts; that is the task of the designer. They do, however, provide analogies between the domains, so that it may be easier for the designer to make the final connections leading to biology inspired designs.

7. Conclusion

Utilization of engineering design tools such as functional models and automated concept generation with biological systems allows designers to be inspired by nature such that its insight might be more readily incorporated into engineering design. To facilitate biology inspired design, a general method for functionally representing biological systems through functional-based design techniques and two approaches of concept generation utilizing biological information, engineering knowledge and automatic concept generation software are formalized, presented, and illustrated through examples. Biological organisms operate in much the same way that engineered systems operate; each part or piece in the overall system has a function, which provides a common ground between the engineering and biology domains. This research demonstrates that using functional representation and abstraction to describe biological functionality presents the natural designs in an engineering context. Thus, the biological system information is accessible to engineering designers with varying biological knowledge, but a common understanding of engineering design methodologies. Biology contributes a whole different set of tools and ideas that a design engineer would not otherwise have. For the sake of philosophical argument, it was assumed that all biological organs and systems in this study have intended functionality.

The process of Animalia chemoreception was presented from the biology and engineering viewpoints and referenced throughout this chapter, allowing one to comprehend the similarities between the two domains. Each step of the general biological modeling methodology is demonstrated and the results are reviewed through the common chemoreception example. Through concept generation approach one Animalia chemoreception inspired a possible novel lab-on-a-chip device. Although the initial findings from the Design Repository did not indicate a lab-on-a-chip device, the designer leveraged prior knowledge to make the connection. Concept generation approach two identified analogies between the principles of the fly antennae sensing mechanism and engineering components. Furthermore, the approach took inspiration from biology to develop a unique concept for a chemical sensing device. The biological repository entries served as design inspiration for conceptual sensor designs by guiding the designer to a pertinent biological topic, which provides a starting point for mimicry in engineering designs.

To facilitate the development of functional models of biological systems, key points that are important for the designer to consider are summarized in the discussion. But to follow these points, the designer must remain flexible throughout the concept generation process and be open to consider biological systems from different viewpoints, which might prompt the designer to discover novel and innovative ideas. By placing the focus on function rather than form or component, the utilization of biological systems during concept generation has shown to inspire creative or novel engineering designs. The biological domain provides many opportunities for identifying analogies between what is found in the natural world and engineered systems. It is important to understand that the concept generation approaches developed do not generate concepts; that is the task of the designer. They do, however, provide a systematic method for discovering analogies between the biology and engineering domains, so that it may be easier for the designer to make the necessary connections leading to biologically inspired designs.

8. Future Research

Biological Kingdoms that are not as well known to engineers could be explored for unique functionality. The Eubacteria Kingdom consists of bacteria, which are unicellular microorganisms. Bacteria are interesting because they have several different morphologies that fulfill the same purpose. The Fungi Kingdom contains various types of fungus that are invisible to the human eye and those that are closely related to plants and animals such as mold, yeast and mushrooms. An interesting and less known Kingdom is the Protista Kingdom. It is comprised of a diverse group of microorganisms whose cells are organized into complex structures enclosed by a membrane, without specialized tissues, which are unclassifiable under any other Kingdom. The Protista Kingdom has animal, plant and fungus like organisms, of which, exhibit characteristics familiar to organisms in other Kingdoms.

Functional modeling has shown successful for transferring biological knowledge to the engineering domain by focusing on functionality. Biological processes, natural sensing as a whole and various biological phenomena and organisms have been modeled. The investigative work in this study could be extended to other specific areas of biology, such as motors or energy harvesting. Continually developing the biological correspondent terms for the Functional Basis function and flow sets would further reduce confusion when modeling biological systems.

A third hybrid approach is postulated in Figure 4, but not further discussed. In this approach, biological systems would be modeled functionally following the outlined methodology in Section 4. A database would then be queried for functional matches and analogous biological systems would be returned. With the hybrid approach, knowledge of the initial biological system modeled is required, and it is upon the designer to perform research on the analogous biological systems returned from the database. Further research will be required to identify the feasibility of such an approach to concept generation in engineering design.

Further work will include refinement of the general biological functional modeling methodology, as well as, the two conceptual design approaches. This research successfully demonstrated the use of functional representation and abstraction to describe biological functionality; however, the models are not hierarchal. Future investigation of hierarchal biological system representation using the Function Design Framework (FDF) (Nagel et al. 2008) could allow for the creation of more accurate functional models through the inclusion of environment and process representations. We wish to continue adding biological and engineered system entries in to the Design Repository to improve the usefulness of these methodologies via increased biological information and to facilitate future biology inspired conceptual designs.

9. References

- (2009). "Design Engineering Lab." Retrieved 2009, from www.designengineeringlab.com
- Aidley, D.J. (1998). *The physiology of excitable cells*, Cambridge University Press, Cambridge, UK
- Bar-Cohen, Y. (2006). *Biomimetics Biologically Inspired Technologies*, CRC/Taylor & Francis, Boca Raton, FL
- Barth, F.G., J.A.C. Humphrey & T.W. Secomb (2003). *Sensors and sensing in biology and engineering*, Springer, 321183771X 9783211837719, Wien; New York

- Benyus, J.M. (1997). *Biomimicry Innovation Inspired by Nature*, Morrow, New York
- Berg, J.M., J.L. Tymoczko & L. Stryer (2007). *Biochemistry*, W. H. Freeman, New York
- Bohm, M., J. Vucovich & R. Stone (2008). Using a Design Repository to Drive Concept Generation. *Journal of Computer and Information Science in Engineering*, Vol.8, No.1, 14502
- Brebbia, C.A. & M.W. Collins (2004). *Design and nature II: Comparing design in nature with science and engineering*, WIT, 1853127213 9781853127212, Southampton
- Brebbia, C.A., L.J. Sucharov & P. Pascolo (2002). *Design and nature: Comparing design in nature with science and engineering*, WIT, 1853129011 9781853129018, Southampton; Boston
- Brebbia, C.A. & W.I.o. Technology (2006). *Design and nature III: Comparing design in nature with science and engineering*, WIT, 1845641663 9781845641665, Southampton
- Bryant, C., D. McAdams, R. Stone, T. Kurtoglu & M. Campbell (2005). A Computational Technique for Concept Generation. ASME 2005 Design Engineering Technical Conferences and Computers and Information in Engineering Conference Long Beach, CA, 2005
- Bryant, C., R. Stone, D. McAdams, T. Kurtoglu & M. Campbell (2005). Concept Generation from the Functional Basis of Design. Proceedings of International Conference on Engineering Design, ICED 05, pp. Melbourne, Australia
- Campbell, N.A. & J.B. Reece (2003). *Biology*, Pearson Benjamin Cummings, San Francisco
- Chakrabarti, A., P. Sarkar, B. Leelavathamma & B.S. Nataraju (2005). A functional representation for aiding biomimetic and artificial inspiration of new ideas. *Artificial Intelligence for Engineering Design, Analysis and Manufacturing*, Vol.19, 113-132
- Chiu, I. & L.H. Shu (2007). Biomimetic design through natural language analysis to facilitate cross-domain information retrieval. *Artificial Intelligence for Engineering Design, Analysis and Manufacturing*, Vol.21, No.1, 45-59
- Dowlen, C. & M. Atherton (2005). What is Design?, In: *Nature and Design*, M. W. Collins, M. A. Atherton and J. A. Bryant, WIT Press, Southampton
- Fraden, J. (2004). *Handbook of modern sensors : physics, designs, and applications*, Springer, 0387007504 9780387007502, New York
- French, M.J. (1994). *Invention and evolution design in nature and engineering*, Cambridge University Press, 0521465036 9780521465038 0521469112 9780521469111, Cambridge; New York
- Hirtz, J., R. Stone, D. McAdams, S. Szykman & K. Wood (2002). A Functional Basis for Engineering Design: Reconciling and Evolving Previous Efforts. *Research in Engineering Design*, Vol.13, No.2, 65-82
- Mauseth, J.D. (1997). *Botany: an introduction to plant biology*, Saunders College Publishing, Philadelphia
- Mitchell, B.K. (2003). Chemoreception, In: *Encyclopedia of insects*, 169-174, Academic Press. 0125869908 9780125869904, Amsterdam; Boston
- Nachtigall, W. (1989). *Konstruktionen : Biologie und Technik*, VDI, D,sseldorf
- Nagel, R., R. Hutcheson, J. Donndelinger, D. McAdams & R. Stone (2008). Function Design Framework (FDF): Integrated Process and Functional Modeling for Complex System Design. ASME IDETC/CIE 2008, New York City, NY, 2008
- Nagel, R., K. Perry, R. Stone & D. McAdams (2009). FunctionCAD: An Open Source Functional Modeling Application Based on the Function Design Framework. ASME IDETC/CIE 2009, San Diego, CA, 2009

- Nagel, R., A. Tinsley, P. Midha, D. McAdams, R. Stone & L. Shu (2008). Exploring the use of functional models in biomimetic design. *Journal of Mechanical Design*, Vol.130, No.12, 11-23
- Otto, K.N. & K.L. Wood (2001). *Product Design: Techniques in Reverse Engineering and New Product Development*, Prentice-Hall, Upper Saddle River, New Jersey
- Pahl, G. & W. Beitz (1984). *Engineering Design: A Systematic Approach*, Springer-Verlag, London, UK
- Pahl, G. & W. Beitz (1996). *Engineering Design: A Systematic Approach*, Springer-Verlag, Berlin; Heidelberg; New York
- Schmitt, O.H. (1969). Some interesting and useful biomimetic transforms. Proceedings of International Biophysics Congress, pp. 297, Boston, Massachusetts
- Shu, L.H., R.B. Stone, D.A. McAdams & J.L. Greer (2007). Integrating Function-Based and Biomimetic Design for Automatic Concept Generation. International Conference on Engineering Design, Paris, France, 2007
- Sperelakis, N. (1998). *Cell physiology source book*, Academic Press, San Diego
- Spudich, J.L. & B.H. Satir (1991). *Sensory receptors and signal transduction*, Wiley-Liss, New York
- Stock, A.M., V.L. Robinson & P.N. Goudreau (2000). Two-component signal transduction. *Annual Review of Biochemistry*, Vol.69, 183-215
- Stone, R. & K. Wood (2000). Development of a Functional Basis for Design. *Journal of Mechanical Design*, Vol.122, No.4, 359-370
- Nagel, J.K.S., R.L. Nagel, R.B. Stone & D.A. McAdams (2010). Function-Based Biologically-Inspired Concept Generation. *Accepted to the special issue of Artificial Intelligence for Engineering Design, Analysis and Manufacturing on Feb. 16, 2010*, Vol.24, No.4
- Stroble, J.K., R.B. Stone & D.A. McAdams (2009). Conceptualization of Biomimetic Sensors Through Functional Representation of Natural Sensing Solutions. Proceedings of International Conference of Engineering Design, pp. Stanford, California
- Stroble, J.K., R.B. Stone, D.A. McAdams & S.E. Watkins (2009). An Engineering-to-Biology Thesaurus to Promote Better Collaboration, Creativity and Discovery. CIRP Design Conference 2009, Cranfield, Bedfordshire, UK, 2009
- Stroble, J.K., S.E. Watkins, R.B. Stone, D.A. McAdams & L.H. Shu (2008). Modeling the Cellular Level of Natural Sensing with the Functional Basis for the Design of Biomimetic Sensor Technology. IEEE Region 5 Technical Conference, Kansas city, MO, 2008
- Ullman, D.G. (2002). *The Mechanical Design Process 3rd Edition*, McGraw-Hill, Inc., New York
- Ulrich, K.T. & S.D. Eppinger (2004). *Product design and development*, McGraw-Hill/Irwin, Boston
- Vincent, J.F.V., O.A. Bogatyreva, N.R. Bogatyrev, A. Bowyer & A.-K. Pahl (2006). Biomimetics: its practice and theory. *Journal of the Royal Society Interface*, Vol.3, 471-482
- White, R.J., G.C.Y. Peng & S.S. Demir (2009). Multiscale Modeling of Biomedical, Biological, and Behavioral Systems (Part 1). *IEEE EMBS Magazine*. 28: 12-13
- Wilson, J.O. & D. Rosen (2007). Systematic Reverse Engineering of Biological Systems. ASME 2007 International Design Engineering Technical Conferences and Computers and Information in Engineering Conference, Las Vegas, Nevada, 2007

Biomimetic chemistry: radical reactions in vesicle suspensions

Chryssostomos Chatgililoglu and Carla Ferreri
*ISOF, Consiglio Nazionale delle Ricerche, Bologna
Italy*

1. Introduction

Chemical reactivity represents the fundamental basis for studying processes in life sciences. In particular, the last years have seen the affirmation of the interdisciplinary field of chemical biology, which has motivated a strong interest in modeling chemical reactivity of biological systems, that is, improving chemical methodologies and knowledge in order to understand complex reaction pathways related to cellular processes. In this context the reactivity of free radicals revealed its enormous importance for several biological events, including aging and inflammation (Cutler & Rodriguez, 2003), therefore the modeling of free radical reactions under naturally occurring conditions has become a basic step in the research of fundamental mechanisms in biology. The assessment of modes of free radical reactivity has been found to be important at least in three areas: i) the examination of interactions at a molecular level leading to the discovery of radical-based processes involved in enzymatic activities, e.g., ribonucleotide reductase (Reichard & Ehrenberg, 1983), cyclooxygenase (Marnett, 2000), the drug effects of antitumorals (Goldberg, 1987), vitamin activities (Buettner, 1993); ii) The clarification of free radical processes that can lead to damage of biomolecules, together with the individuation of products, opening the way for the evaluation of the *in vivo* damage and its role in the overall cellular status (Kadiiskaa et al., 2005; Pryor & Godber, 1991); iii) the knowledge of free radical mechanisms allowing for new strategies to be envisaged in order to control the level of the damage and fight against the negative consequences (Halliwell & Gutteridge, 2000). These three main areas represent the core studies of free radicals using biomimetic models.

In the last decade our group has developed the subjects of lipid and protein damages under biomimetic conditions, and in particular envisaged novel damage pathways for the transformation of these important classes of biomolecules. In this chapter biomimetic models will be examined, also mentioning work previously done by others in the field and the advancements carried by us. Information will be given on liposome vesicles, which is the basic context for examining free radical reactivity in heterogenous conditions, where the partition of the reactants occurs between the lipid and the aqueous environments, and this can influence the biological effects. The regioselectivity driven by the supramolecular organization of lipids in the vesicle double layer is another feature of the biomimetic model that has been related to the formation of trans lipids, specific markers of radical stress in cell

membranes. Moreover, biomimetic chemistry has been developed on small radical species able to enter the hydrophobic compartment of the vesicle, evidencing the concomitant event of desulfurization involving sulfur-containing amino acid residues. Finally, in this chapter the biomimetic models will be highlighted also as a very useful tool where possible scenarios of biological consequences can be foreseen, such as those deriving from the study of the minimal cell to develop a biological life.

2. Modeling radical reactions in vesicles

The model treated in this chapter is a lipid vesicle, which is used as model of the cell membrane. The natural structure of cell membranes is a double layer of phospholipids, which are amphiphilic molecules of general formula shown in Figure 1, capable of self-organization. The hydrophobic part mostly consists of fatty acid residues, that are carboxylic acids with a long hydrocarbon chain (up to 26 carbon atoms), saturated or unsaturated with up to six double bonds. A specific structural feature of naturally occurring mono- and polyunsaturated fatty acid (MUFA and PUFA) residues is the *cis* double bond geometry, whereas PUFA have the characteristic methylene-interrupted motif of unsaturated chain. Examples of mono- and polyunsaturated fatty acid (MUFA and PUFA) structures and also of some *trans* isomers are shown in Figure 2, with the common names and the abbreviations describing the position and geometry of the double bonds (e.g., 9*cis* or 9*trans*), as well as the notation of the carbon chain length and total number of unsaturations (e.g., C18:1) (Vance & Vance, 2002). It is worth noting that being the *cis* geometry connected with biological activities, this feature is strictly controlled during MUFA and PUFA biosynthesis by the regiospecific and stereoselective enzymatic activity of desaturases (Fox et al, 2004).

In the free radical reactivity the double bonds and bis-allylic positions are the moieties that undergo the chemical transformations, and these processes have been ascertained to play relevant roles in pathological processes and aging. The subject of lipids and free radicals is typically interdisciplinary because it involves all disciplines of life sciences. In this respect, it was looked for appropriate models of free radical reactivity in membranes, and liposomes are the universally accepted models for cell membranes as they can closely simulate the bilayer structure. Liposomes can be represented as shown in Figure 3, *i.e.*, a double layer formed by spontaneous organization of the phospholipid components in water, delimiting an aqueous cavity. The fatty acid tails can be saturated or unsaturated, and the disposition of the double bonds in the vesicle depends on the supramolecular arrangement of the bilayer. Multilayer vesicles (MLV), having an onion-like structure, are obtained from dry lipids added with an aqueous medium and vortexed (New, 1990; Lasic, 1993). However, this type of vesicle are not the best membrane models, since the observation of the diffusion phenomenon through several layers cannot be directly extrapolated to the passage across a single bilayer, like it occurs in natural membranes. Monolamellar vesicles are the closest model to membranes, and they can be formed by different techniques, such as the extrusion (MacDonald et al., 1991) and the injection methodologies (Domazou & Luisi, 2002).

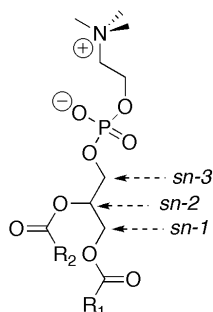


Fig. 1. The general structure of L- α -phosphatidylcholine (PC), with two hydrophobic fatty acid chains in the positions *sn-1* and *sn-2* of L-glycerol and the phosphorous-containing polar head-group in *sn-3* position.

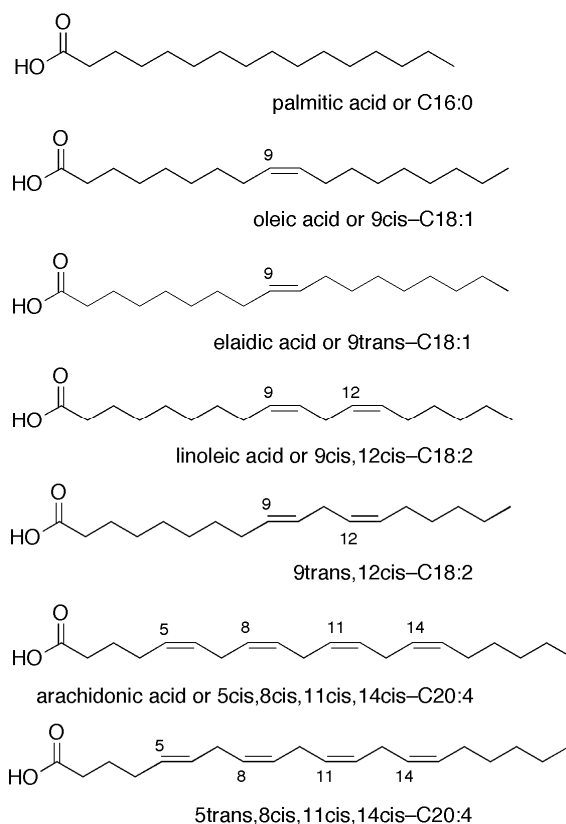


Fig. 2. Some of the most common mono- and polyunsaturated fatty acid (MUFA and PUFA) structures, with their common names and the abbreviations describing the position and geometry of the double bonds (e.g., 9cis), as well as the notation of the carbon chain length and total number of unsaturations (e.g., C18:1).

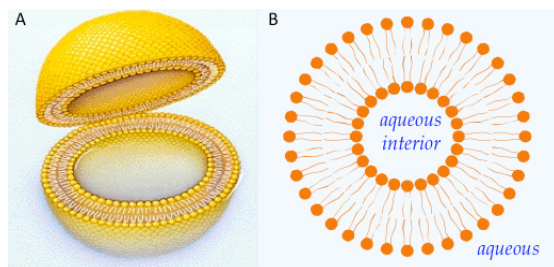


Fig. 3. Large unilamellar vesicles (LUV)

Among the lipid molecules used for liposome experiments, glycerophospholipids are relevant that account for approximately 60 mol% of total lipids in the organism, and are made of the glycerol backbone having a polar head and two hydrophobic fatty acid residues (see Figure 1). Synthetic phospholipids can have both fatty acid chains as monounsaturated residues (for example, dioleoylphosphatidylcholine DOPC with two residues of oleic acid, 9cis-C18:1), or alternatively, one unsaturated and the other saturated fatty acid chains (for example, 1-palmitoyl-2-oleoylphosphatidylcholine POPC, with one chain of saturated fatty acid residues of palmitic acid 16:0, and the other chain of the monounsaturated cis fatty acid, oleic acid 9cis-18:1), the saturated one not participating to the free radical transformation, but having the role of internal standard for the quantitative analysis of the reaction outcome. Phosphatidylcholines of natural origins can be also used, such as soybean or egg lecithins, that contain the fatty acid chains as mixtures of saturated, monounsaturated and polyunsaturated residues. For example, in egg lecithin the mean fatty acid composition is: palmitic acid (C16:0) 32%, stearic acid (C18:0) 14.1%, oleic acid (9cis-C18:1), vaccenic acid (11cis-C18:1) 1.2%, linoleic acid (9cis,12cis-C18:2) 20%, arachidonic acid (5cis,8cis,11cis,14cis-C20:4) 4.8%. Lecithins can simulate much closer the various types of fatty acids present in the natural membranes. In all these compounds another difference with the natural structures consists of the polar head, which is generally chosen as choline, whereas mixtures of choline, serine, ethanolamine and sugar derivatives are present in the real membranes. Vesicle models present in the literature are made of multilamellar vesicles, obtained by a dry film of phospholipids simply added with water and vortexed to obtain a milky suspension. Sonication can provide for a rearrangement of the starting multilamellar organization into smaller vesicles, which can be considered small liposomes, quite monolamellar in the arrangement or nearly so. As previously noted, the multilayer organization of lipids can present differences, because the diffusion of species becomes a complex process through several layers. However, information of the physical properties of all these suspensions is available and one can choose the appropriate model, which offers the heterogeneous aqueous environment where oxidative processes can be examined under a complexity still similar to the biological medium.

Free radical reactivity studied with these biomimetic models has the advantage to use a scenario closely related to a biological environment, but still simplified and controllable. During the eighties the vesicle system started to be developed in different directions: for examining membrane dynamics and transitions, (Siminovitch et al., 1987; Wolff & Entressangle, 1994) for the incorporation of proteins and the protein-lipid interactions or functioning (Gregoriadis, 1992), for studying delivery systems (Fendler & Romero, 1977) and many other applications. In free radical research, vesicles were used essentially in two directions: i) the study of free radical-based processes involving directly the lipid

components, mainly lipid peroxidation; ii) the effect of antioxidants or radical trapping agents toward radical damages to biomolecules. These aspects will be treated in the next sections. It must be underlined that experiments were also carried out with micelles and other aggregation forms involving lipid compounds, but the present chapter deals with the model closest to the membrane structure, therefore only vesicles formed by phospholipid bilayer are considered. It is also worth noting that the methodology of phospholipid vesicles has taken a while to be assessed and appropriately tuned to the experimental needs; for example, the characteristic of lipid monolamellarity is needed for simulating cell membranes, but the former models were multilamellar vesicles, and after more than two decades the results can be updated by more recent knowledge.

2.1 Oxidative transformations of lipid vesicles and the antioxidant activity

The fact that oxidative processes were found to be deeply involved in cell metabolism and also in its degradation pathways was stimulating research of the basic chemical mechanisms. Oxidation of polyunsaturated fatty acids (PUFA) by free radicals immediately acquired importance also as *in vivo* process, in particular membrane lipid damage caused either by radiation (Marathe & Mishra, 2002; Mishra, 2004) or by chemical poisons (CCl_4 , ethanol) (Kadiiska et al, 2005). Lipid polyunsaturated components are highly oxidizable materials, and membrane models have to be used to assess the phenomenon since PUFA are present also in all biological membranes and lipoproteins. In PUFA the most sensitive site to oxidative attack is the bis-allylic position, the methylene group located between two double bonds. Detailed studies of the products and mechanism of peroxidation started in the 70's by several research groups (Porter et al, 1979; Porter et al, 1980; Milne & Porter, 2001). The first products to be individuated were the hydroperoxides derived from the corresponding peroxy radicals (Figure 4). The mechanism of lipid peroxidation (a radical chain reaction) starts with the abstraction of hydrogen atom producing the bisallylic (or pentadienyl) radical L^\bullet (Figure 4). The reaction of L^\bullet with oxygen is close to a diffusion-controlled process, but is also reversible. Indeed, the peroxy radical can undergo a very rapid fragmentation. Peroxy radicals LOO^\bullet can abstract a hydrogen atom to produce lipid hydroperoxide (LOOH) together with "fresh" L^\bullet radicals to continue the chain. Termination steps occur either by radical-radical combination or by attacking other molecules, such as an antioxidant (α -tocopherol) or proteins.

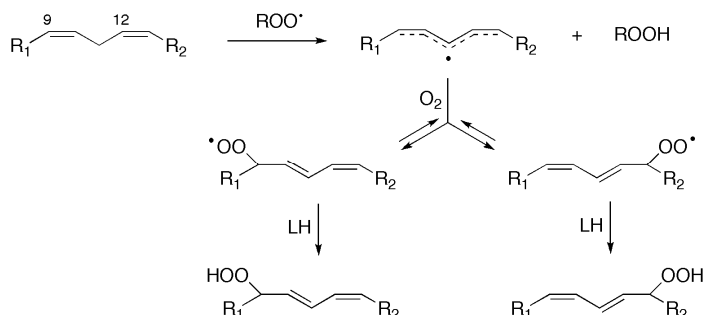
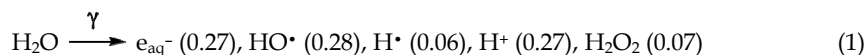


Fig. 4. Outline of the mechanism of lipid peroxidation with formation of kinetic-controlled trans-cis products

The products of lipid peroxidation are not only hydroperoxides, but also conjugated dienes (Porter et al, 1979). Further decomposition of these products by the action of transition metals in their low oxidation state (i.e., Fe⁺²) leads to aldehydes and hydrocarbon end-products, together with the subsequent combination of aldehydes to form adducts, all products that are used nowadays for testing and measuring the occurrence of oxidative stress in biological specimens (Esterbauer et al., 1989). By UV spectroscopy the quantification of conjugated dienes at 233 and 215 nm is used to follow accurately the initial stages of the process (Mihaljević et al., 1996).

The biomimetic models have been extremely useful to quantitate these events. The methodology includes the steps of preparation of vesicle suspensions and choice of the free radical initiation.

In heterogeneous systems the ability of PUFA to undergo chain oxidation (autoxidation) (Barclay et al., 1985) was examined in order to see whether differences can be found with the homogeneous solution. With these models different kinds of free radical conditions can be used, since an important point in the preparation of the experiments is the source of radical initiation. In case of the use of gamma or X-irradiations the initiation occurs in the aqueous compartment with formation of primary radical species from the interaction with water that can be quantified on the basis of the radiation dose. For example, the initiation by gamma irradiation of aqueous suspensions occurs by the Equation (1), where in parenthesis the radiation chemical yields in units of $\mu\text{mol J}^{-1}$ are shown.



The kinetics of reaction of $\cdot\text{OH}$ and e_{aq}^- with lecithin bilayers have been measured (Barber & Thomas, 1978). The rate for $\cdot\text{OH}$ with lecithin is $5.1 \times 10^8 \text{ M}^{-1}\text{s}^{-1}$, while e_{aq}^- rate is very slow. These rates are lower than those observed for similar reactions in homogeneous systems. This is explained in terms of the protective effect of the bilayer, this being especially true for e_{aq}^- which does not readily leave the aqueous phase, and in terms of the restricted diffusion imposed on the reactive species by the bilayer. Long-term alteration in the model membrane following $\cdot\text{OH}$ attack is manifested in terms of damage to the head group, increasing water penetration of the bilayer, and of cross-linking with the membrane, thereby restricting motion in the interior of the bilayer. Increased rigidity and "leakiness" of membranes is an expected consequence of radiation damage. In general, these processes modify the physical properties of the membranes, including the permeability to different solutes and the packing of lipids and proteins in the membranes, which in turn, influence membrane functions (Marathe & Mishra, 2002; Schnitzer et al., 2007). A word of caution must be spent for the compounds used for measuring the vesicle properties, which have to be added at the end of the experiments. In fact, for example the fluorescent probe pyrene solubilized in the bilayer can react with $\cdot\text{OH}$ and e_{aq}^- ($1.7 \times 10^9 \text{ M}^{-1}\text{s}^{-1}$ and $7 \times 10^7 \text{ M}^{-1}\text{s}^{-1}$, respectively). Former experiments were reported with small liposomes obtained by sonication of a vesicle suspension made of natural phospholipids, extracted from mice liver cells. X-ray at two different doses (0.8 and 8 Gy/min,) in the presence and absence of oxygen, was used for a total 100 Gy. Conjugated dienes and the main fatty acid residues were evaluated. The former were evaluated spectroscopically, as previously indicated, whereas the fatty acid composition was determined by workup of the liposome, extraction of lipids,

transesterification to fatty acid methyl esters and gas chromatographic (GC) analysis (Konings et al., 1979). Under anoxic condition there is no dose effect, whereas the irradiation in the presence of oxygen (air bubbling) lead to extensive consumption, especially of the arachidonic and docosahexaenoic acid residues. In the same paper it was also advanced the protective effect of glutathione, cysteamine and α -tocopherol, showing that the latter was the most effective. The radiation effect and lipid peroxidation were also assayed with gamma irradiation of soybean lecithin liposomes, and related to the dose-dependent formation of malondialdehyde (MDA) (Nakazawa & Nagatsuka, 1980). In the same paper the authors reported the resulting permeability of liposomes that is increasing linearly with the dose for the glucose efflux.

The kinetics of peroxidation can also be studied by free radical processes induced by an "external" generator of free radicals, like azo-compounds of general formula $R-N=N-R$, which decompose at a given temperature leading to radical $R\cdot$ and N_2 . The azo-initiators are successfully used for radical processes in homogeneous systems, but in vesicle suspensions this methodology can result in some difficulties. In fact, the nature of the initiator can be hydrophilic or hydrophobic, and therefore the effect is governed by the diffusion of the species, i.e., by the balance between the effects of membrane properties on the rate constants of propagation and termination of the free radical peroxidation in the relevant membrane domains, represented by those domains in which the oxidizable lipids reside. Both these rate constants depend similarly on the packing of lipids in the bilayer, but influence the overall rate in opposite directions. This can be the reason for quite contrasting results reported in the literature. For example, linoleic acid, taken as typical example of unsaturated fatty acid, has a similar oxidizability in different media as determined by different procedures ($0.02 - 0.04 M^{-1/2} s^{-1/2}$) (Barclay, 1993). The systematic determination of oxidizability in the extended homologous series of PUFA and comparison with the literature values have been done, indicating an increase value by increasing the number of bisallylic carbons. The relationship in the series linoleic acid/linolenic acids/arachidonic acid/docosapentaenoic acid/ docosahexaenoic acid has been shown to be $1:\sqrt{2}:2:2\sqrt{2}:4$. On the other hand, for the autoxidation of egg lecithin using AIBN [azobis(isobutyronitrile)] as lipophilic radical initiator (Barclay & Ingold, 1981) it is reported that the oxidizability of egg lecithin at 30 °C in vesicles is only 2.7% of that for the homogeneous material. It must be pointed out that the system used in those experiments was a lipid emulsion, with multilamellar vesicles, that could have influenced the viscosity of the medium and enhanced the self-termination of the initiator in the lipid bilayer, thus determining less efficiency of the peroxidation process.

The vesicle system and peroxidation process offered a good scenario also for examining the antioxidant activity. Indeed, the presence of an antioxidant network of enzymes and molecules that protects from free radical damages has been clearly demonstrated, and the consumption of these antioxidant defences has been linked to many pathological events (Halliwell & Gutteridge, 2000). Again, in the liposome models the antioxidant properties and efficiency can be studied, in order to envisage their mode of action and, more importantly, the synergies that the molecular combination of different chemical mechanisms can provide, similarly to what occurs in the biological medium. Investigations focused first on natural compounds, and peroxidation processes were found to be successfully controlled by the activity of several molecules. Among them, vitamins and thiols give a quite complete scenario of the molecular properties required for an antioxidant. Natural vitamins constitute

themselves a synergic network for the control of free radical processes; in the liposome models the combined effect of mode of action, partition coefficient and relative reactivity can be evaluated, which is different for each compounds. Vitamin E is one of the former compound to be studied and its mode of action is a chain-breaking process, due to the H-atom donation from the phenolic hydroxyl group. By this way it can scavenge the peroxy radicals stopping the chain propagation and the extensive decomposition of lipids. The partition of this compound is expected to occur in the lipophilic compartment, although a hydrophilic character can be present at the level of the hydroxyl group. Therefore, the location of this vitamin can be at the interface between the aqueous and the lipid compartments. In the liposome model this partition must be taken into account, since it is important to test both initiations, i.e., with lipid- and water-soluble azocompounds, AIBN and AAPH [(azobis(2-amidinopropane) dihydrochloride), respectively (Niki et al.,1985). Soybean multilamellar liposomes were oxidized in a similar manner with both initiation compounds, evaluated with the oxygen consumption methodology. When vitamin E or C was added in the AAPH-initiated oxidation the process was markedly suppressed. When vitamins are together added to the suspension, the first consumed is vitamin C, linearly with the time, followed by vitamin E that starts to diminish when vitamin C is consumed. In the AMVN-initiated process, vitamin E was clearly efficient in stopping the process, whereas vitamin C did not affect the reaction course. Interestingly, the use of the two vitamins together were shown to ameliorate the induction period also in the AMVN experiment, thus indicating that, although vitamin C cannot influence the formation of the lipid radicals within the bilayer, it can synergize with vitamin E activity prolonging its effect. These experiments were the first showing what is well known nowadays: vitamin E is recycled by vitamin C. As far as the synergism is concerned, liposomes allowed for the study of other compounds, such as quinone compounds (coenzyme Q) and conjugated dienes (vitamin A, carotenoids, etc), to be used in combination for antioxidant strategies.

2.2 Lipid isomerization and the vesicle effect on regioselectivity

Figure 5 shows the reaction mechanism of free radical double bond isomerization that consists of a reversible addition of radical RS^\bullet to the double bond. Indeed, the reconstitution of the double bond is obtained by β -elimination of RS^\bullet and the result is in favor of trans geometry, the most thermodynamically favorable disposition. The energy difference between the two geometrical isomers of prototype 2-butene is 1.0 kcal/mol. It is worth noting that (i) the radical RS^\bullet acts as a catalyst for cis-trans isomerization, and (ii) positional isomers cannot be formed as reaction products because the mechanism does not allow a double bond shift (Chatgililoglu & Ferreri, 2005; Ferreri & Chatgililoglu, 2005). The effectiveness of cis-trans isomerization in the presence of the most common antioxidants has also been addressed. The high efficiency of all-trans retinol and ascorbic acid as anti-isomerising agents in the lipophilic and hydrophilic compartments, respectively, parallels the well-assessed high reactivity of RS^\bullet radicals towards these two antioxidants (Chatgililoglu et al., 2002). Considering polyunsaturated substrates, the isomerization mechanism occurs as a step-by-step process depicted in Figure 6 for linoleate moiety, i.e., each isolated double bond behaves independently as discussed above (Ferreri et al., 2001).

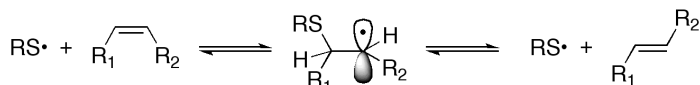


Fig. 5. The thiyl radical RS^\bullet acts as a catalyst for cis-trans isomerization by addition/elimination steps

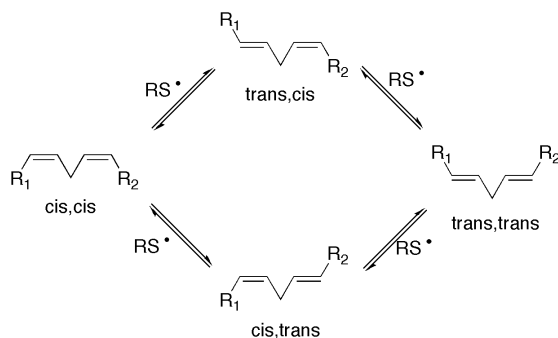


Fig. 6. Stepwise mechanism for the cis–trans isomerization of linoleate residues

Other types of free radicals (e.g., RSe^\bullet , RSO_2^\bullet , NO_2^\bullet , R_3Sn^\bullet , $(Me_3Si)_3Si^\bullet$, etc.) and atoms (e.g., Br^\bullet , I^\bullet , etc.) are known to induce cis–trans isomerization of double bonds by addition–elimination steps (Jang et al., 1999; Chatgililoglu & Ferreri, 2005). However, the efficiency of the isomerization process strongly depends on the characteristics of the attacking radicals, and although another biologically important radical is NO_2^\bullet , it should be added that thiols are known as the dominant ‘sink’ for NO_2^\bullet in cell/tissues (Equation 2). The rate constant is close to $2 \times 10^7 \text{ M}^{-1} \text{ s}^{-1}$ with generation of thiyl radicals, therefore in the biological environment thiyl radicals are likely to be the most relevant isomerizing species (Chatgililoglu et al., 2006).



It is worth noting at this point that a few years ago, the importance of trans fatty acids was known only in nutrition studies. In fact, the transformation of double bonds from the natural cis geometry to a variety of positional and geometrical trans isomers results from the processes of partial hydrogenation and deodorization used in food industry to obtain margarines and other fat shortenings. There are several books and reviews on this subject (Sébédio & Christie, 1998), therefore here it is highlighted only that the free radical-mediated isomerization is an endogenous process which has nothing to do with the chemical manipulation of fats as origin of the trans lipid geometry.

The first report highlighting the lipid isomerization mechanism as a biologically meaningful process was from our group in 1999 (Ferreri et al., 1999). Using biologically relevant compounds and phospholipids, the occurrence of such a transformation was modeled under biomimetic conditions. The subject was of interest to other research groups and all work done in this area showed that thiyl radicals are efficient and effective isomerizing agents (Chatgililoglu & Ferreri, 2005; Ferreri & Chatgililoglu, 2005). In another review the subject

of the thiyl radical production in biosystems and effects on lipid metabolism is summarized (Ferreri et al. 2005b).

Taking inspiration from the lipid peroxidation process extensively studied in liposomes, unsaturated lipid vesicles were envisaged as a good biomimetic model for the double-bond isomerization. Indeed, early reports on the use of glutathione, or other thiol compounds such as cysteine, as effective protective agents against the radiation-induced lipid peroxidation, did not mention the stability of the double-bond geometry (Konings et al., 1979; Prager et al., 1993). In our experiments large unilamellar vesicles obtained by extrusion technique (LUVET) with polycarbonate filter of 100 nm diameter were used, that form an almost transparent suspension, which is also suitable for studies under photolytic conditions. As pointed out also before, the aqueous and lipid phases are the two distinct compartments of this non-homogeneous system. There are several features to be taken into account for examining the reactivity of this system towards free radicals: i) the characteristic supramolecular arrangement of the lipid assembly, with the fatty acid chains of phospholipid molecules that form the hydrophobic core of the model membrane, and the polar heads that face the aqueous internal and external phases (see Figure 3); ii) the partition coefficient of compounds added to the system, which influences the distribution of the reactive species in the two compartments; iii) in particular, the location of the initiation step, that is, where the formation of an initial radical species, able to abstract the H-atom from the thiol group, occurs. As far as the lipid organization is concerned, there is a precise arrangement of the hydrophobic core, which can influence the position of the double bonds in the layer and the reactivity of the different fatty acids to the radical attack. This was found to be the case in the double bond isomerization, studied with an amphiphilic thiol, 2-mercaptoethanol, that is, a compound able to diffuse without restriction from the aqueous phase to the lipid bilayer, and vice versa. A regioselective process resulted where the double bonds are not involved at the same extent by the radical isomerization. In particular, using vesicles made of egg yolk lecithin, it was possible to demonstrate that the double bonds located closest to the membrane polar region are the most reactive towards the attack of diffusing thiyl radicals (Ferreri et al., 2002; Ferreri et al., 2004a). In the case of linoleic acid residues in vesicles, the double bond in position 9 resulted more reactive than that in position 12. Also arachidonic acid residues in vesicles were more reactive than oleic and linoleic acids, and two positions, i.e., the double bonds in 5 and 8 over the four present in this compound, were transformed preferentially. The scenario could be different for other long-chain PUFA, depending on their supramolecular arrangement, and in this context isomerization by diffusible thiyl radical can act as a reporter, indirectly informing on the double bond disposition in the bilayer.

From the studies carried out so far, arachidonic acid residues in membrane phospholipids emerge as very important markers to be investigated, in order to distinguish endogenous trans isomers, formed by radical processes, from the exogenous trans isomers, derived from dietary contribution. In particular, investigation can be focused on erythrocyte membrane phospholipids, which are the preferential storage for arachidonic acid after biosynthesis. As matter of fact, the case of arachidonic acid is a seminal example of how it is possible to distinguish the endogenous isomerisation from the trans isomers contained in foods. Considering the biosynthetic paths of omega-6 fatty acids represented in Figure 7, two double bonds (positions 11 and 14) originate from linoleic acid, the essential fatty acid precursor taken from the diet, whereas the two other double bonds (positions 5 and 8) are

formed by desaturase enzymes, which produce selectively the cis unsaturation. It is evident that the double bonds 5 and 8 of arachidonic acid, can only have a cis configuration, unless in the membranes these positions are involved in an isomerization process by diffusible thiyl radicals and transformed into trans isomers.

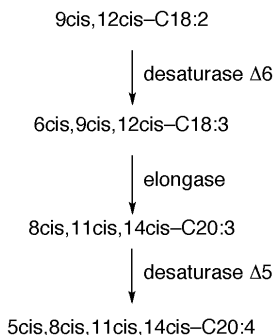


Fig. 7. Enzymatic fatty acid transformations of the omega 6 fatty acid pathway

A careful identification of membrane lipids containing arachidonic residues can be important for functional lipidomics, in order to achieve a clear understanding of the contribution from endogenous or exogenous processes. We extended the biomimetic investigation to biological systems, in order to prove the “endogenous” trans lipid formation under strictly physiological conditions. It is important to deal with “trans-free” conditions, which means that the presence of any external source of trans fatty acid isomers is carefully checked. Cell membrane lipid composition of human leukemia cell lines (THP-1) was monitored during incubation in the absence and presence of thiol compounds, ensuring that no contribution of trans compounds could come from the medium (Ferreri et al., 2004b). The experiments were based on the hypothesis that the normal cell metabolism includes several radical-based processes. Therefore, the intracellular level of sulfur-containing compounds could have produced a certain amount of thiyl radicals and consequently, caused a lipid isomerization. In parallel experiments, some thiol compounds were added in mM levels to the cell cultures during incubation, and the comparison of isomeric trends was done. Indeed, a basic content of trans lipids in THP-1 cell membranes was found during their growth before thiol addition, and by addition of the amphiphilic 2-mercaptoethanol, it was increased up to 5.6% of the main fatty acid residues. Even greater trans lipid formation was obtained by a radical stress artificially produced in the cell cultures added with thiol, and for example, by γ -irradiation a 15.5% trans content in membrane phospholipids was reached. The fatty acid residues most involved in this transformation were arachidonate moieties, and this result confirmed that these are the most important residues to be monitored in cells. The trans arachidonate content determined in THP-1 membrane phospholipids provides the first indication of the occurrence of an endogenous isomerization process, not confused with a dietary contribution, as previously explained. This opened new perspectives for the role of trans lipids in the lipidome of eukaryotic cells and was followed by several other investigations in living systems (Zamboni et al., 2006; Ferreri et al., 2005a; Puca et al., 2008). Actually, the formation of trans lipids can be evaluated in terms of relevant percentages within membranes, which means that not only can they

have a negative effect for the lipid assembly, but also act as a signaling for triggering some protective responses in cells.

3. Free radical-based tandem protein-lipid damage

3.1 Desulfurization of simple aminoacids

After the discovery of the lipid isomerization and its feasibility under physiological conditions, it was important to address what can be the real culprits of such a process occurring *in vivo*. For this reason, a variety of biologically relevant sulfur-containing compounds were examined for their potentiality to produce thiyl radicals and induce lipid isomerisation, and sulfur-containing amino acid residues came into play. Reactive oxygen species (ROS), in particular $\bullet\text{OH}$ radicals, cause oxidative damage to several amino acids, including cysteine (Cys) and methionine (Met) (Bobrowski et al., 2007; Huang & Rauk, 2004). Thiol moieties RSH can react under free radical stress (for example, caused by $\text{HO}\bullet$ radicals) by donating hydrogen atoms, therefore giving thiyl radicals $\text{RS}\bullet$. Actually, the hydrogen donation is still largely intended as a protective mechanism against radical degradation of cellular components, being the basic mechanism accepted for glutathione protective role from free radical degradation. Also some proteins, like albumin are thought to have such protective role in living systems [Roche et al., 2008]. It is worth underlining that, due to the high molecular weight, protein-bound thiyl radicals can have some restriction in the diffusion, therefore the ability to become an isomerising agent by reaching the double bond in the membrane bilayer should be considered in each case. Together with thiol, disulfide and thioether functions are also present in amino acid residues (cysteine, cystine and methionine) and are known to give a variety of reactions under free radical conditions (Alfassi, 1999). The interaction of reducing reactive species derived from the ionizing irradiation of water, namely hydrated electrons (e_{aq}^-) and $\text{H}\bullet$ atoms, with disulfides in aqueous solution is well understood (Alfassi, 1999). Figure 8 shows the disulfide radical anion ($\text{RSSR}^{\bullet-}$) derived from the direct electron attachment and its equilibrium with the protonated form, the sulfuranyl radical, which is obtained also by the $\text{H}\bullet$ atom attack directly to the sulfide moiety. Both reactive species dissociate reversibly into two entities, $\text{RS}\bullet$ and RSH (or RS^-). On the other hand, $\text{H}\bullet$ atoms were studied to selectively attack the thioether function of methionine, as shown in Figure 9 with the formation of a sulfuranyl-type radical that gives a rapid desulfurization. From this intermediate a desulfurization is produced with formation of CH_3SH , a diffusible species that under radical stress condition exists as the corresponding thiyl radical $\text{CH}_3\text{S}\bullet$. The desulfurization of methionine gives α -aminobutyric acid (Aba), which corresponds to a chemical mutation to a naturally-occurring, but not genetically-coded, amino acid.

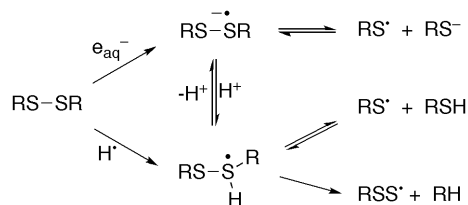


Fig. 8. The mechanism for reaction of e_{aq}^- and $\text{H}\bullet$ atom attack with disulfide moiety in aqueous solution

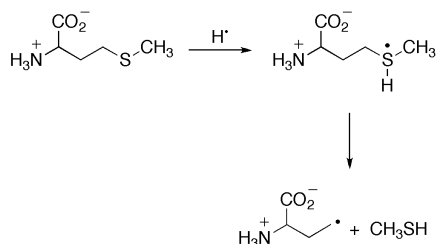


Fig. 9. The H^\bullet atom attack on the thioether moiety of methionine affords the sulfuranyl radical, which unimolecularly decomposes to give the carbon-centered radical and methanethiol.

The diffusible $\text{CH}_3\text{S}^\bullet$ radicals are able to reach the lipid bilayer of a membrane model and cause double bond isomerisation with a very high efficiency, as studied with single amino acids and peptide sequences, like Met-enkephalin. Met-enkephalin (Tyr-Gly-Gly-Phe-Met) is known as an endogenous mediator interacting with opioid receptors, therefore with several biological activities in the field of pain control. The reactivity of this substrate under reductive conditions was to generate the corresponding desulfurated sequence, with Aba instead of Met residue, which is going to be studied for its biological effects compared to the natural sequence (Mozziconacci et al., 2007). Finally, the attack of H^\bullet atoms can occur also to the sulfur moiety of cysteine residues, leading again to desulfurization reaction with the formation of H_2S and the amino acid alanine (Ala), which represents a post-translational chemical modification of natural amino acids (Ferreri et al., 2008). It is worth noting that none of these transformations are yet related to radical stress *in vivo*, therefore future developments can be envisaged concerning the presence of desulfurized amino acid residues as markers of free radical damage.

3.2 Radical-based modifications for protein libraries

Biomimetic chemistry can be successfully applied to the discovery of free radical modifications of sulfur-containing substrates based on the formation of diffusible radical species. Indeed, the reversible addition of thiyl radicals to double bonds (see Figure 5) is interesting as is a specific radical process, and indirectly amplifies the effect of a few moles of thiyl radicals, thus allowing the damage to be envisaged even at low level. This can be useful in large structures such as proteins, where radicals can attack several reactive positions, and the individuation of damages can be somehow difficult. We developed the heterogeneous system of liposome vesicles added with protein substrates as a very sensitive and reliable tool for detecting radical damage at the level of S-containing residues. This first detection is then associated to proteomic analyses, and this approach is expected to open the way to molecular libraries useful for detecting damages in biological samples. We studied bovine pancreatic RNase A individuating both methionine and cystine reactive sites, with modification of Met and Cys to α -amino butyric acid (Aba) and alanine (Ala) residues, respectively (Ferreri et al., 2006b; Ferreri et al., 2008). The sequence of amyloid β -peptide of 40 amino acids, where only the Met residue is present as a S-containing amino acid, was also studied for its connections with the alteration reported in the Alzheimer disease. In this case, reductive stress was able to produce the selective desulfurization of this sequence, and the identification of the resulting Aba-modified peptide has been possible (Kadlcik et al., 2006).

More recently, metallothioneins (MTs), small proteins extremely rich in cysteines, have been analyzed. This high-Cys content, up to a 30% of their amino acids, confers them an exceptional capacity to coordinate heavy metals through the formation of metal-thiolate bonds. The presence of labile sulfide anions as non-proteic ligands was reported in the metal-MT complexes (Capdevila et al., 2005). Therefore, the presence of both sulfur-containing amino acids and sulfide anions in the same molecular aggregate makes this system a very interesting case to determine the main targets of the reductive stress. Interestingly, a differentiation of reactivity can be assessed, since the reductive conditions seem to preferentially select the methionine and cysteine residues (Torreggiani et al., 2009). In all these experiments the protein damages were found to be coupled with the unsaturated lipid isomerisation and formation of trans fatty acids in the vesicles. As previously noted, liposomes containing double bonds are a very sensitive reporter system of the formation of diffusible thiyl radicals, since trans isomers are formed through the catalytic activity of S-centered radicals as isomerising agents. This system can be proposed as a first screening of the protein/peptide potential damage at the level of S-containing residues, in order to proceed with analytical identification of the exposed sites of radical attack along the sequence. This can be done by proteomic analysis using high resolution mass spectrometers, such as electrospray-quadrupole-time of flight (ESI-Q-TOF) instruments. Specific mass differences can be tentatively ascribed to a certain protein modification on the basis of the exact molecular mass of the atoms introduced/removed. Furthermore, a punctual characterization of the reductive modifications occurring on the protein primary structure is necessary for a better comprehension of the molecular damage produced; to this purpose, an in-deeper analysis at peptide/amino acid level has to be performed. As an example, the structural characterization of the peptide digest from irradiation-induced reductive modification of bovine pancreatic RNase A demonstrated that only 3 out of 8 Cys residues present within the whole protein primary structure were transformed into Ala, thus proving that two unique disulphide bonds were selectively reduced during reaction. These experiments also established that a unique Met residue, namely Met79, was reduced to Aba, while the remaining ones were oxidized with a variable degree, probably as consequence of the sample manipulation (Ferreri et al., 2008).

4. Biological scenarios suggested by biomimetic models

Biomimetic models can also be suggestive for scenarios that are not easily obtained directly from the biological reality, such as for example the scenario of formation of the first living cells, or protocell. This subject attracts interest from several points of view, either from the archeobiology, studying the creation of the first living entity from the primordial soup, and the biotechnology, looking for a nanosized bioreactor where biosynthesis can be created upon needs. In the former case, unilamellar liposomes are used as model for the "minimal cell", as form of minimal life that is, for assessing the minimal and sufficient conditions allowing for the start of cellular evolution. This can be viewed also as the minimal genome needed for creating the enzymatic functioning and replication of the information, but several insights can also be obtained from the point of view of the minimal physical dimension of the cell to permit the life. This section cannot comment on the various aspects related to the protocell experiments, that are treated in several reviews and books. However, it is important to focus on an aspect that emerges also from the study of the above reported

lipid cis-trans isomerization, that concerns the type of lipids used for this minimal cell experiments. Looking at the membrane composition of the first forms of life, most of the fatty acids were saturated and branched hydrocarbon chains, that defines a very small compartment of a few hundreds of nanometers. To obtain larger compartments such as those of prokaryotes ranging from 300 to 1000 nanometers and those of eukaryotes up to 2500 nanometers and more, lipids had to be differentiated (Seckbach, 2004). In this vision, the large variety offered by the families of saturated, monounsaturated and polyunsaturated fatty acids can be rationalized on the basis of their contribution to cell dimension. To deepen this subject, liposomes prepared by the injection methodology can be used because they well represent the spontaneous generation of vesicles. The resulting diameter of the cell compartment should be directly related to the type of the lipids used in the starting mixture. In this respect, a preliminary question must be addressed on the role of lipid geometry since the naturally occurring geometry in all eukaryotic cells is the cis arrangement, with exclusion of the trans isomers, which are only present in the prokaryote world where they instead mean survival (Heipieper et al., 2003). However, if the primordial conditions are considered, it is likely that, under high temperatures and irradiation, the lipid geometry presented both isomeric configurations, therefore it cannot be excluded that the cell compartment contained both forms. To verify such possibility and the corresponding compartmental dimension, different phospholipid structures were used to form unilamellar liposomes, including saturated, monounsaturated cis and trans lipids. In Table 1 the dimension obtained from dipalmitoylphosphatidylcholine (with saturated fatty acid residues of palmitic acid, 16:0) is compared with the liposomes obtained with 1-palmitoyl-2-oleoylphosphatidylcholine (with one chain of saturated fatty acid residues of palmitic acid, 16:0 and the other chain of the monounsaturated cis fatty acid, oleic acid 9cis-18:1) and those obtained with 1-palmitoyl-2-elaidoylphosphatidylcholine (with one chain of saturated fatty acid residues of palmitic acid, 16:0 and the other chain of the monounsaturated trans fatty acid, oleic acid 9trans-18:1) (Ferreri et al., 2006a).

Phospholipid	Diameter (nm)
POPC	97 ± 10
PEPC 83%	72 ± 8
DPPC	45 ± 8

Table 1. Dimension of liposomes obtained by the injection methodology from different phospholipids

It is clearly seen that saturated fatty acids are the smallest compartment followed by trans fatty acids, whereas the cis configuration is ensuring the widest compartment possible. Also the properties of the bilayer obtained by the different fatty acids showed consistent differences, as expected by the different physical parameters of the lipids (Ferreri et al., 2006c). Recent results confirmed the dimension theory since protein synthesis could be obtained in 100 nm-vesicles, formed by POPC where an ensemble made of enzymes, ribosomes, tRNA and low molecular weight molecules was enclosed (Pereira de Souza et al., 2009). This indicated the minimal cell dimension where a biosynthetic machinery can function. Extension of these results can lead to a thorough study of all possible combinations of lipid structures, which are compatible with the dimension and the functioning of the minimal cell. Indeed, the most important contribution to the dimension of the compartment

delimited by membranes is given by the cis-unsaturated geometry, therefore the variety of the polyunsaturated fatty acids present in the biological membranes can find its original reason in the creation of the best compartment compatible with life. From the studies carried out so far in liposomes, it can be logically inferred that, once formed, a minimal cell entity which certainly included cis and trans lipids, underwent a natural selection based on the resulting biophysical and biosynthetic capabilities, which above all excluded the trans geometry from eukaryotic membranes.

5. Conclusions

The chapter offered an overview of main processes studied by the membrane model of liposomes. The use of liposomes as carrier for drugs and active compound delivery cannot be forgotten, and some aspects of the liposome technology and reactivity shown in this chapter can have relevance also in this field. The system of monolamellar liposomes is expected to be extensively used for the examination of free radical reactivity, especially from a chemical biology approach exploring the biomimetic chemistry of radical species in detail, where the experimental set up of the liposomal model can satisfactorily represent the biological scenarios. In this context an improvement of interdisciplinarity is needed, among the fields of chemistry, biochemistry, biology and medicine, in order to create a common territory where the achievements of free radical reactivity can be straightforwardly transferred to a better comprehension of the biological pathways in health and diseases.

6. References

- Alfassi, Z. B., (Ed.) (1999). *S-centered radicals*, Wiley, Chichester
- Barber, D.J.W. & Thomas, J.K. (1978). Reactions of radicals with lecithin bilayers. *Radiat. Res.* 74, 51–65
- Barclay, L.R.C. & Ingold, K.U. (1981). Autoxidation of biological molecules. 2. The autoxidation of a model membrane. A comparison of the autoxidation of egg lecithin phosphatidylcholine in water and in chlorobenzene. *J. Am. Chem. Soc.* 103, 6478–6485
- Barclay, L.R.C.; Locker, S.J.; MacNeil, J.M. & Vankessel, J. (1985). Quantitative studies of the autoxidation of linoleate monomers sequestered in phosphatidylcholine bilayers. Absolute rate constants in bilayer. *Can. J. Chem.* 63, 2633–2638.
- Barclay, L.R.C. (1993). 1992 Syntex Award Lecture. Model biomembranes: quantitative studies of peroxidation, antioxidant action, partitioning, and oxidative stress. *Can. J. Chem.* 71, 1–16
- Bobrowski, K.; Hug, G.L.; Pogocki, D.; Marciniak, B. & Schoeneich, C. (2007). Stabilization of Sulfide Radical Cations through Complexation with the Peptide Bond: Mechanisms Relevant to Oxidation of Proteins Containing Multiple Methionine Residues. *J. Phys. Chem. B* 111, 9608–9620
- Buettner, G.R. (1993). The pecking order of free radicals and antioxidants: lipid peroxidation, alpha-tocopherol, and ascorbate. *Arch. Biochem. Biophys.* 300, 535–43
- Capdevila, M.; Domènech, J.; Pagani, A.; Tío, L.; Villarreal, L. & Atrian, S. (2005). Zn- and Cd-Metallothionein Recombinant Species from the Most Diverse Phyla May Contain Sulfide (S²⁻) Ligands. *Angew. Chem. Int. Ed.* 44, 4618–4622

- Chatgililoglu, C.; Zambonin, L.; Altieri, A.; Ferreri, C.; Mulazzani, Q.G. & Landi, L. (2002). Geometrical Isomerism of Monounsaturated Fatty Acids. Thiyl Radical Catalysis and Influence of Antioxidant Vitamins. *Free Radic. Biol. Med.* 33,1681-1692
- Chatgililoglu, C. & Ferreri, C. (2005). Trans Lipids: The Free Radical Path. *Acc. Chem. Res.* 36, 441-448
- Chatgililoglu, C.; Ferreri, C.; Lykakis, I.N. & Wardman, P. (2006). Trans fatty acids and radical stress: what are the real culprits? *Bioorg. Med. Chem.* 14, 6144-6148
- Cutler, R.G. & Rodriguez, H., (Eds.), (2003). *Critical Reviews of oxidative stress and aging*, World Scientific, New Jersey
- Domazou, A.S. & Luisi, P.L. (2002). Size distribution of spontaneously formed liposomes by the alcohol injection method. *J. Liposome Res.* 12, 205-220
- Esterbauer, H.; Striegl, G.; Puhl, H. & Rotheneder, M. (1989). Continuous monitoring of in vitro oxidation of human low density lipoprotein. *Free Radic. Res. Commun.* 6, 67-75
- Fendler, J.H. & Romero, A. (1977). Liposomes as drug carriers. *Life Sci.* 20, 1109-1120
- Ferreri, C.; Costantino, C.; Landi, L.; Mulazzani, Q.G. & Chatgililoglu C. (1999). The Thiyl radical Mediated Isomerization of cis-Monounsaturated Fatty Acid Residues in Phospholipids: A Novel path of membrane Damage? *Chem. Commun.* 407-408
- Ferreri, C.; Costantino, C.; Perrotta, L.; Landi, L.; Mulazzani, Q.G. & Chatgililoglu, C. (2001). Cis-trans isomerization of polyunsaturated fatty acid residues in phospholipids catalysed by thiyl radicals. *J. Am. Chem. Soc.* 123, 4459-4468
- Ferreri, C.; Faraone-Mennella, M.R.; Formisano, C.; Landi, L. & Chatgililoglu, C. (2002). Arachidonate geometrical isomers generated by thiyl radicals: the relationship with trans-lipids detected in biological samples. *Free Radic. Biol. Med.* 33, 1516-1526
- Ferreri, C.; Samadi, A.; Sassatelli, F.; Landi, L. & Chatgililoglu, C. (2004a). Regioselective cis-trans-isomerization of arachidonic double bonds by thiyl radicals: the influence of phospholipids supramolecular organization. *J. Am. Chem. Soc.* 126, 1063-1072
- Ferreri, C.; Kratzsch, S.; Brede, O.; Marciniak, B. & Chatgililoglu, C. (2004b). Trans lipid formation induced by thiols in human monocytic leukemia cells. *Free Radic. Biol. Med.* 38, 1180-1187
- Ferreri, C.; Angelini, F.; Chatgililoglu, C.; Dellonte, S.; Moschese, V.; Rossi, P. & Chini L. (2005a). Trans fatty acids and atopic eczema/dermatitis syndrome: the relationship with a free radical cis.trans isomerization of membrane lipids. *Lipids* 40, 661-667
- Ferreri, C.; Kratzsch, S.; Landi, L. & Brede, O. (2005b). Thiyl radicals in biosystems: effects on lipid structures and metabolism. *Cell. Mol. Life Sci.* 62, 834-847
- Ferreri, C. & Chatgililoglu, C. (2005c). Geometrical trans lipid isomers: a new target for lipidomics. *ChemBioChem* 6, 1722-1734
- Ferreri, C.; Pierotti, S.; Barbieri, A.; Zambonin, L.; Landi, L.; Rasi, S.; Luisi, P.L.; Barigelletti, F. & Chatgililoglu, C. (2006a). Comparison of phosphatidylcholine vesicle properties related to geometrical isomerism. *Photochem. Photobiol.* 82, 274-280
- Ferreri, C.; Manco, I.; Faraone-Mennella, M.R.; Torreggiani, A.; Tamba, M.; Manara, S. & Chatgililoglu, C. (2006b). The reaction of hydrogen atoms with methionine residues: a model of reductive radical stress causing tandem protein-lipid damage. *ChemBioChem* 7, 1738-1744
- Ferreri, C.; Pierotti, S.; Chatgililoglu, C.; Barbieri A. & Barigelletti, F. (2006c) Probing the influence of cis-trans isomers on model lipid membrane fluidity using cis-parinaric acid and stop-flow technique. *Chem. Commun.*, 529-531

- Ferreri, C.; Chatgililoglu, C.; Torreggiani, A.; Salzano, A. M.; Renzone, G. & Scaloni, A. (2008). The reductive desulfurization of Met and Cys residues in bovine RNase A is associated with trans lipids formation in a mimetic model of biological membranes. *J. Proteome Res.* 7, 2007-2015
- Fox, B.G.; Lyle, K.S. & Rogge, C.E. (2004). Reactions of the diiron enzyme stearyl-acyl carrier protein desaturase. *Acc. Chem. Res.* 37, 421-429
- Goldberg, I.H. (1987). Free radical mechanisms in neocarzinostatin-induced DNA damage. *Free Radic. Biol. Med.* 3, 41-54
- Gregoriadis, G. (1992). *Liposome Technology*, 2nd Edition, Vol 2, CRC Press, Boca Raton
- Halliwell, B. & Gutteridge, J.M.C. (Eds.) (2000). *Free Radicals in Biology and Medicine*, 3rd ed.; Clarendon Press, Oxford, U.K
- Heipieper, H.J.; Meinhardt, F. & Segura A. (2003) The *cis-trans* isomerase of unsaturated fatty acids in *Pseudomonas* and *Vibrio*: biochemistry, molecular biology and physiological function of a unique stress adaptive mechanism. *FEMS Microbiol. Lett.* 229, 1-7
- Huang, M.L. & Rauk, A. (2004). Reactions of One-Electron-Oxidized Methionine with Oxygen: An ab Initio Study. *J. Phys. Chem. A* 108, 6222-6230
- Jiang, H.; Kruger, N.; Lahiri, D.R.; Wang, D.; Vatile, J.-M. & Balazy, M. (1999). Nitrogen dioxide induces *cis-trans* isomerization of arachidonic acid within cellular phospholipids. *J. Biol. Chem.* 274, 16235-16241
- Kadiiskaa, M.B.; Gladena, B.C.; Bairda, D.D.; Germoleca, D.; Grahama, L.B. et al. (2005). Biomarkers of Oxidative Stress Study II. Are oxidation products of lipids, proteins, and DNA markers of CCl₄ poisoning? *Free Radic. Biol. Med.* 38, 698-710
- Kadlcik, V.; Sicard-Roselli, C.; Houée-Levin, C.; Ferreri, C. & Chatgililoglu, C. (2006). Reductive modification of methionine residue in amyloid β -peptide. *Angew. Chem. Int. Ed.* 45, 2595-2598
- Konings, A.W.T.; Damen, J. & Trieling, W.B. (1979). Protection of liposomal lipids against radiation induced oxidative damage. *Int. J. Radiat. Biol.* 35, 343-350
- Lasic, D.D. (1993). *Liposomes: from physics to applications*. Elsevier, Amsterdam
- MacDonald, R.C.; MacDonald, R.I.; Menco, B.P.; Takeshita, K.; Subbarao, N.K. & Hu, L.R. (1991). Small-volume extrusion apparatus for preparation of large, unilamellar vesicles. *Biochim. Biophys. Acta* 1061, 297-303
- Marathe, D. & Mishra, K.P. (2002). Radiation -induced changes in permeability in unilamellar phospholipids liposomes. *Radiation Res.* 157, 685-692
- Marnett, L.J. (2000). Cyclooxygenase mechanisms. *Curr. Opin. Chem. Biol.*, 4, 545-552
- Mihaljević, B.; Katušin-Ražem, B. & Ražem, D. (1996). The reevaluation of the ferric thiocyanate assay for lipid hydroperoxides with special considerations of the mechanistic aspects of the response. *Free Radic. Biol. Med.* 21, 53-63
- Milne, G.L. & Porter, N.A. (2001). Separation and identification of phospholipid peroxidation products. *Lipids* 36, 1265-1275
- Mishra, K.P. (2004). Cell membrane oxidative damage induced by gamma-radiation and apoptotic sensitivity. *J. Environ. Path Toxicol. Oncol.* 23, 61-66
- Mozziconacci, O.; Bobrowski, K.; Ferreri, C. & Chatgililoglu, C. (2007). Reaction of hydrogen atom with Met-enkephalin and related peptides. *Chem. Eur. J.* 13, 2029-2033

- Nakazawa, T. & Nagatsuka, S. (1980). Radiation-induced lipid peroxidation and membrane permeability in liposomes. *Int. J. Radiat. Biol.* 38, 537-544
- New, R.R.C. (1990). *Liposomes: a practical approach*. IRL Press, Oxford
- Niki, E.; Kawakami, A.; Yamamoto, Y. & Kamiya, Y. (1985). Oxidation of lipids. VIII. Synergistic inhibition of oxidation of phosphatidylcholine liposome in aqueous dispersion by vitamin E and vitamin C. *Bull. Chem. Soc. Jpn.* 58, 1971-1975
- Pereira de Souza, T.; Stano, P. & Luisi, P.L. (2009) The minimal size of liposome-based model cells brings about a remarkably enhanced entrapment and protein synthesis. *ChemBioChem* 10, 1056-1063.
- Porter, N.A.; Wolf, R.A.; Yarbrow, E.M. & Weenen, H. (1979). The autoxidation of arachidonic acid: formation of the proposed SRS-A intermediate. *Biochem. Biophys. Res. Commun.* 89, 1058-1064
- Porter, N.A.; Weber, B.A.; Weenen, H. & Khan, J.A. (1980). Autoxidation of polyunsaturated lipids. Factors controlling the stereochemistry of product peroxides. *J. Am. Chem. Soc.* 102, 5597-5601
- Prager, A., Terry, N.H.A. & Murray, D. (1993). Influence of intracellular thiol and polyamine levels on radioprotection by aminothiols. *Int. J. Radiat. Biol.* 64, 71-81
- Pryor, W.A. & Godber, S.S. (1991). Noninvasive measures of oxidative stress status in humans. *Free Radic. Biol. Med.* 10, 177-184
- Puca, A.A.; Novelli, V.; Viviani, C.; Andrew, P.; Somalvico, F.; Cirillo, N.A.; Chatgililoglu, C. & Ferreri, C. (2008). Lipid profile of erythrocyte membranes as possible biomarker of longevity. *Rejuven. Res.* 11, 63-72
- Reichard, P. & Ehrenberg, A. (1983). Ribonucleotide reductase: a radical enzyme. *Science* 221, 514-519
- Roche, M.; Rondeau, P.; Singh, N.R.; Tarnus, E. & Bourdon, E. (2008). The antioxidant properties of serum albumin. *FEBS Lett.* 582, 1783-1787
- Sébedio, J.-L. & Christie, W.W. (Eds.) (1998). *Trans Fatty Acids in Human Nutrition*. The Oily Press, Dundee
- Seckbach, J. (Ed.) (2004). *Origins. Genesis, evolution and diversity of life*. Kluwer, Dordrecht
- Schnitzer, E.; Pinchuk, I. & Lichtenberg, D. (2007). Peroxidation of liposomal lipids. *Eur. Biophys. J.* 36, 499-515
- Siminovitch, D.J.; Wong, P.T.T. & Mantsch, H.H. (1987). Effects of cis and trans unsaturation on the structure of phospholipids bilayers: a high-pressure infrared spectroscopic study. *Biochemistry* 26, 3277-3278
- Torreggiani, A.; Domènech, J.; Orihuela, R.; Ferreri, C.; Atrian, S.; Capdevila, M. & Chatgililoglu, C. (2009). Zinc and Cadmium Complexes of a Plant Metallothionein under Radical Stress: Desulfurisation Reactions Associated with the Formation of trans-Lipids in Model Membranes. *Chem. Eur. J.* 15, 6015-6024
- Vance, D.E. & Vance, J.E., (Eds), (2002). *Biochemistry of lipids, lipoproteins and membranes*, 4th ed., Elsevier, Amsterdam
- Wolff, R.L. & Entressangles, B. (1994). Steady-state fluorescence polarization study of structurally defined phospholipids from liver mitochondria of rats fed elaidic acid. *Biochim. Biophys. Acta* 1211, 198-206
- Zamboni, L.; Ferreri, C.; Cabrini, L.; Prata, C.; Chatgililoglu, C. & Landi, L. (2006). Occurrence of trans fatty acids in rats fed a trans-free diet: a free radical-mediated formation? *Free Radic. Biol. Med.* 40, 1549-1556

Biomimetic homogeneous oxidation catalyzed by metalloporphyrins with green oxidants

Hong-Bing Ji¹ and Xian-Tai Zhou²

School of Chemistry and Chemical Engineering, Sun Yat-sen University, 510275, Guangzhou, China

¹E-mail: jihb@mail.sysu.edu.cn

²E-mail: zhoux tai@mail.sysu.edu.cn

Abstract

Cytochrome P-450 mono-oxygenase enzymes play a key role in the oxidative transformation in living systems. As one kind of cytochrome P-450 models, metalloporphyrins have been widely used in selective oxygenation of hydrocarbons under mild conditions. The chapter focuses on reviewing the biomimetic homogeneous oxidation of organic compounds catalyzed by metalloporphyrins with green oxidants such as dioxygen or hydrogen peroxide, in which the oxidized substrates include alkanes, olefins, alcohols, aldehydes, sulfides etc. The mechanisms for the oxidation of different substrates were also described. We can assume that the coming decade is going to be dedicated to the development of metalloporphyrins biomimetic catalyst in petrochemical and fine chemical industries.

Keywords: Biomimetic, Cytochrome, Metalloporphyrins, Oxidation, Homogeneous

1. Introduction

Cytochrome P-450 enzymes are heme-containing monooxygenases and play a key role in the oxidative transformation of endogenous and exogenous molecules.¹⁻⁵ They are virtually ubiquitous in nature and are present in all forms of life like plants and mammals, as well as in some prokaryotic organisms such as bacteria.⁶⁻⁸ The active site of P-450s contains a highly conserved prosthetic heme IX complex coordinated by a thiolate ligand from a cysteine residue (Figure 1).

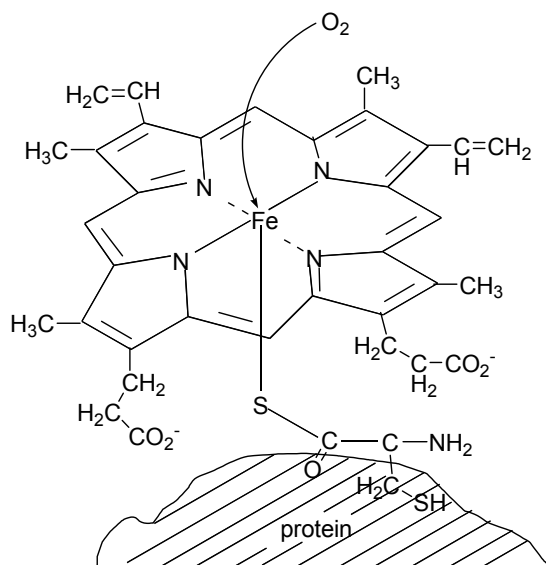
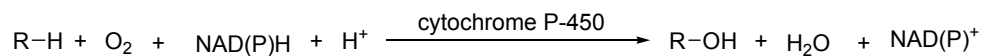


Fig. 1. Prosthetic of cysteinato-heme enzymes: an iron(III) protoporphyrin-IX covalently linked to the protein by the sulfur atom of a proximal cysteine ligand.

The primary function of cytochrome P-450 enzymes is the oxygenation of a wide variety of organic substrates by inserting one oxygen atom from O_2 to the substrate and reducing the other oxygen atom with reducing equivalents to a water molecule, utilizing two electrons provided by NAD(P)H via a reductase protein (Scheme 1).



Scheme 1. Overall oxygenation reaction catalyzed by cytochrome P-450

Being a triplet (two unpaired electrons in ground state), molecular oxygen is unreactive toward organic molecules at low temperatures. The reaction of dioxygen with the single state of organic substrates is spin-forbidden.⁹ Consequently, the oxygenation of organic molecules at physiological temperatures must involve the modification of the electronic structure of one of the partners. Living systems mainly use enzymes like cytochromes P-450 to modify the electronic structure of dioxygen to form which is adapted for the desired oxidation reaction. The mechanism of its catalytic activity and structural functions has been the subject of extensive investigation in the field of biomimetic chemistry. The high-valent iron(IV)-oxo intermediate, formed by the reductive activation of molecular oxygen via peroxo-iron(III) and hydroperoxy-iron(III) intermediates by cytochrome P-450, is responsible for the *in vivo* oxidation of drugs and xenobiotics. This high valent iron(IV)-oxo intermediate and probably other intermediates of the P450 catalytic cycle can be formed by the reaction of iron(III) porphyrins with different monooxygen donors.¹⁰⁻¹²

Therefore, cytochrome P-450 enzymes are potent oxidants that are able to catalyze the

hydroxylation of saturated carbon-hydrogen bonds, the epoxidation of double bonds, the oxidative dealkylation reactions of amines, oxidations of aromatics, and the oxidation of heteroatoms,¹³⁻¹⁵ as shown in Figure 2.

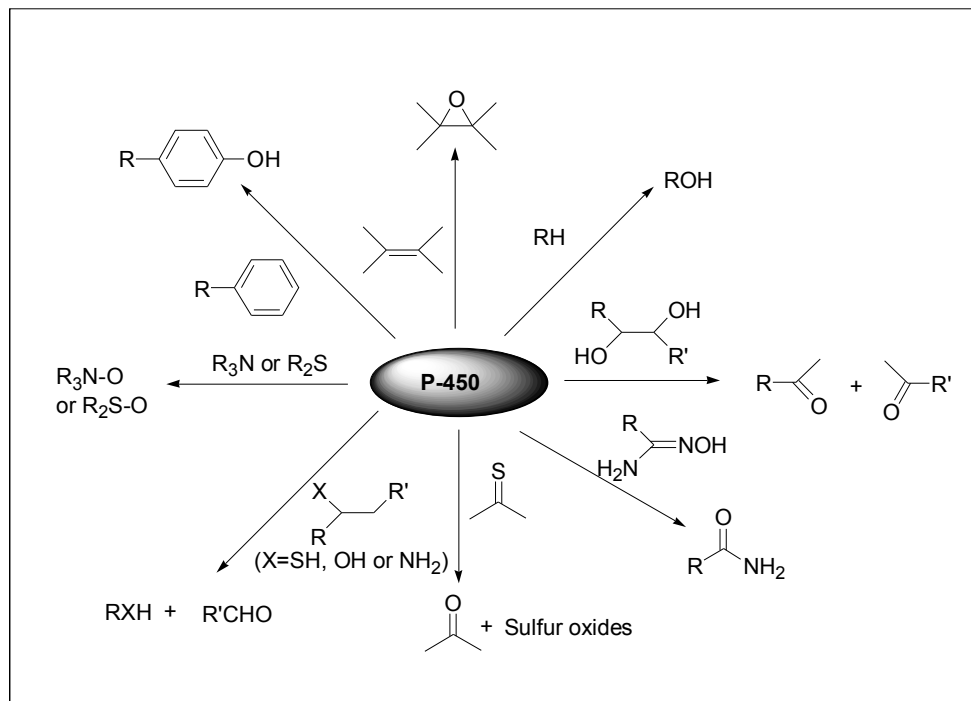


Fig. 2. Oxidations of organic compounds catalyzed by cytochrome P-450

As the isolation of P-450 enzymes from plants is extremely difficult, the first reactions employing this hemoprotein's enzymes were carried out with bacterial and mammalian P-450. Only in recent years have genes of P-450 enzymes been isolated from plants, and the first reactions confirmed that these enzymes take an active part in herbicide detoxification.¹⁶ The use of chemical model systems mimicking P-450 might therefore be a very useful tool for overcoming the difficulty in working with enzymes *in vivo* and *in vitro*.¹⁷ The synthesis of cytochrome P-450 models is a formidable challenge for chemist to establish a system that is structurally equivalent to the enzymes. The synthetic mimic is not only a structural analogue exhibiting spectroscopic features close to the enzyme's cofactor but also displays a similar reactivity and catalysis.¹⁸ In recent years, the development of efficient catalytic systems for oxidation reactions that mimic the action of cytochrome P-450 dependent monooxygenases has attracted much attention. Synthetic metalloporphyrins have been used as cytochrome P-450 models and have been found to be highly efficient homogeneous or heterogeneous catalysts for oxidation reactions, especially for the alkane hydroxylation and alkene epoxidation.¹⁹⁻²¹

In attempting to mimic the reactivity of cytochrome P-450 enzymes, many researchers have used metalloporphyrins to catalyze a variety of organic compounds oxidations, such as

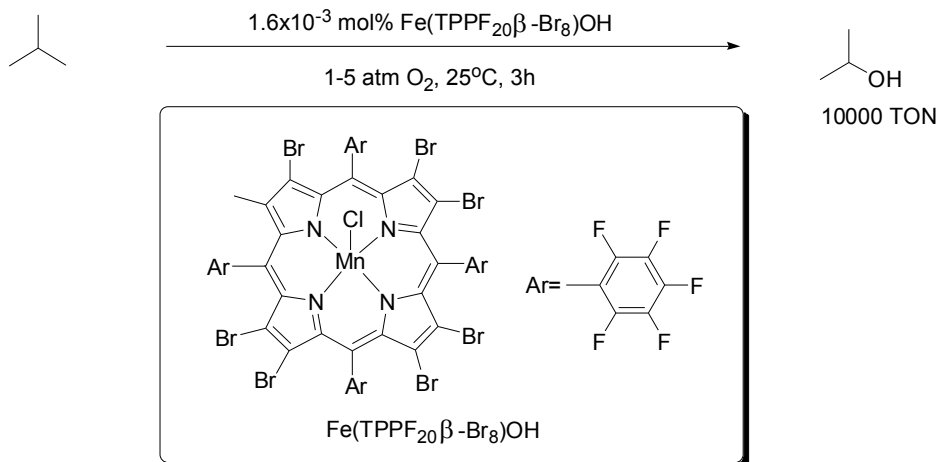
hydroxylation, epoxidation, N-oxidation and so on. An enormous range of oxidants have been used as oxygen atom transfer reagents to the metalloporphyrins in the oxidations. These include iodossylbenzenes, peroxyacids, hypochlorite, hydroperoxides, N-oxides, hydrogen peroxide, monoperoxyphthalate and potassium monopersulfate *et al.*²²⁻³⁷ However, the selective oxidation by green oxidants such as molecular oxygen or hydrogen peroxide is more attractive because of its cost-effectiveness and environmentally-friendly nature of the oxidant.³⁸⁻⁴²

The chapter will try to cover the biomimetic homogeneous oxidation of organic compounds catalyzed by metalloporphyrins with green oxidants based on our group's research works, in which the oxidized substrates include alkanes, olefins, alcohols, aldehydes, sulfides etc. Both practical and mechanistic point of view for the homogeneous oxidations of different substrates catalyzed by metalloporphyrins will be presented.

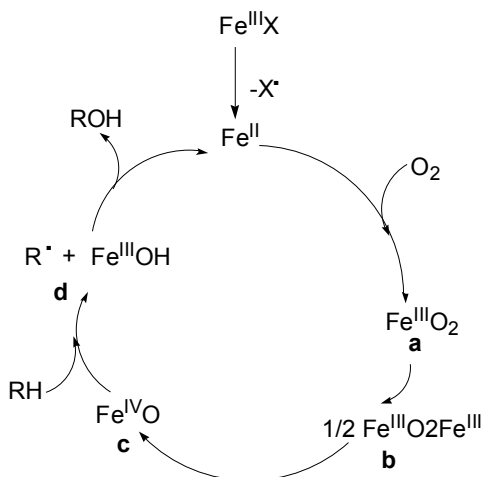
2. Hydroxylation of alkanes

The controlled and selective oxidation of saturated hydrocarbons under mild conditions is one of the most important technologies for the conversion of petroleum products to valuable commodity chemicals.⁴³ Often-used catalysts for the oxidation reactions at the industrial scale are transition metal complexes, for example, cobalt salt is used in cyclohexane oxidation. Their main drawback is the low reactivity.

In recent two decades, the catalysis of metalloporphyrins for alkane hydroxylation under mild conditions had widely received considerable attention.^{44, 45} Early reports indicated that manganese porphyrins or phthalocyanine can catalyze the oxidation of indoles or tryptophan with a product distribution different from that observed in a free-radical oxidation reaction.^{46, 47} Lyons and Ellis reported that chromium, manganese or iron complexes of *meso*-tetraphenylporphyrin with one azido as axial ligand were efficient catalysts for the oxidation of neat acyclic alkanes under molecular oxygen (1-5 atm).⁴⁸ Isobutane is oxidized to *tert*-butyl alcohol in 20000 TON in the presence of Fe(TPPF₂₀/β-Br₈)OH [Fe(TPPF₂₀/β-Br₈=tetrakis(pentafluorophenyl β-octabromo) iron porphyrin] at 100°C. Although in this reaction the catalyst decomposition is a problem at somewhat elevated temperatures (>60°C), well over 10000 catalytic turnovers can be reached at ambient temperature with no decay of the catalyst (Scheme 2).

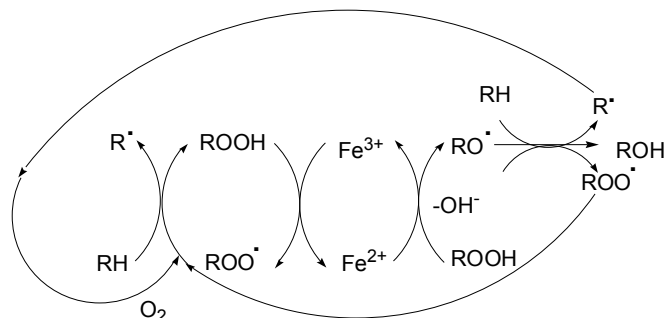
Scheme 2. Isobutane oxidation catalyzed by $\text{Fe(TPPF}_{20}\beta\text{-Br}_8\text{)OH}$

Similarly, the oxidation of propane to a 1:1:1 mixture of isopropyl alcohol and acetone is reported with 541 TON in the presence of $\text{Fe(TPPF}_{20}\beta\text{-Br}_8\text{)N}_3$ at 125°C . However, substituted alkanes such as 2-methylbutane, 3-methylpentane, 2,3-dimethylbutane, and 1,2,3-trimethylbutane are oxidized into a mixture of products due to oxidative cleavage of the carbon-carbon bond. The postulated mechanisms for these reactions are similar to those proposed for the biological oxidations by cytochrome P-450 (Scheme 3).⁴⁸



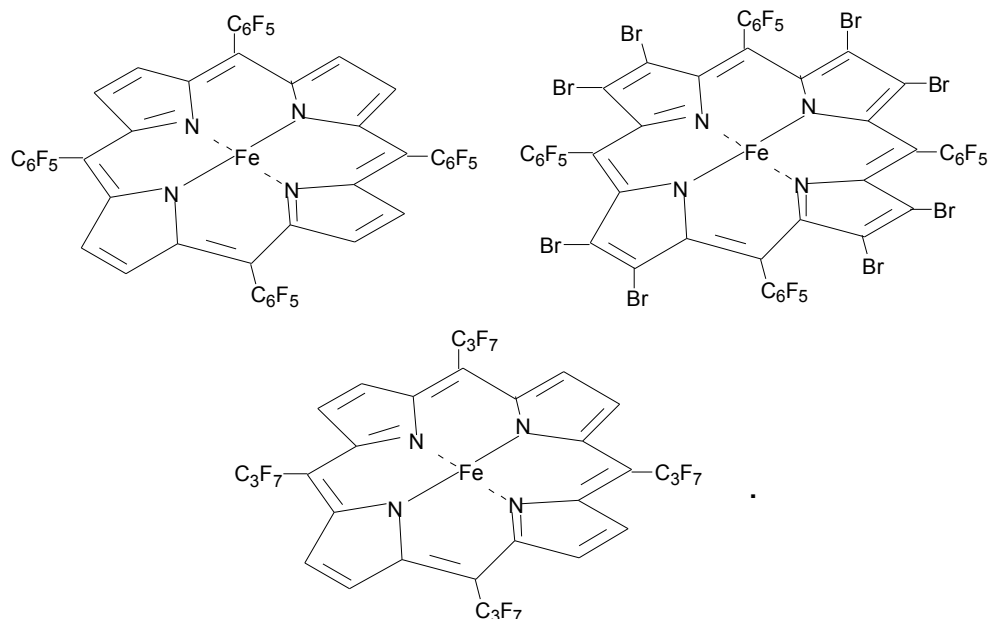
Scheme 3. Proposed mechanisms for alkane oxidation catalyzed by iron porphyrin

Gray and co-workers studied the oxidation of 3-methylpentane to 3-hydroxy-3-methylpentane (>99% selectivity) using iron-haloporphyrins and molecular oxygen in benzene at 60°C .⁴⁹ The product selectivity and radical trap experiment suggest that this reaction takes place by an autoxidation process (Scheme 4).



Scheme 4. Mechanisms for the autoxidation of alkanes catalyzed by iron-haloporphyrins

A comprehensive study of (porphinato)iron [PFe]-catalyzed isobutane oxidation in which molecular oxygen is utilized as the sole oxidant was reported by Moore and co-workers.⁵⁰ Electron-deficient PFe catalysts were examined (Scheme 5). The nature and distribution of hydrocarbon oxidation products show that an autoxidation reaction pathway dominates the reaction kinetics, consistent with a radical chain process. Evidence was present for a radical chain autoxidation mechanism, in which (porphinato)iron(III)-OH (PFe-OH) species not only are responsible for the breakdown of the *tert*-butyl hydroperoxides generated in situ during the catalytic reaction, but also play the role of radical chain initiator in the autoxidation process.



Scheme 5. Electron-deficient (porphinato) iron structures

Oxidation of cyclohexane with air to cyclohexanol and cyclohexanone is a very important industrial process from both economical and environmental aspects. Simple iron, manganese and cobalt tetraphenylporphyrins were found to be the very effective catalysts for cyclohexane oxidation with air when the reaction temperature was higher than 100°C and pressure was greater than 0.4MPa.⁵¹ The cyclohexane conversion and the yields of alcohol and ketone catalyzed by cobalt porphyrin were more than that by manganese and iron porphyrins as shown in Table 1.

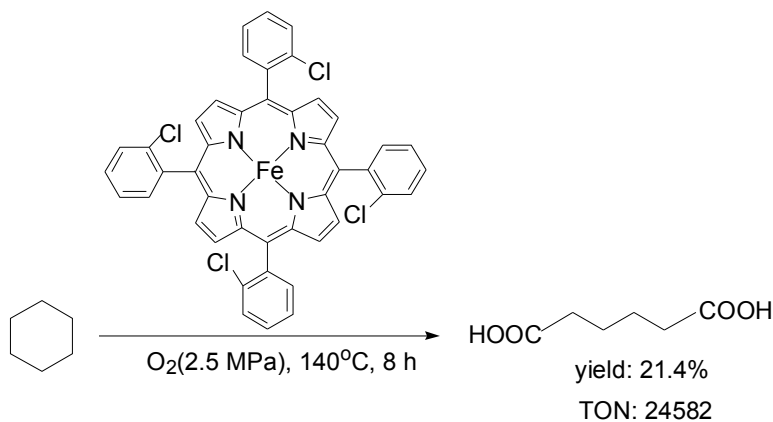
	TPP(Co)	TPP(Mn)	TPP(Fe)
Cyclohexane conversion (%)	15.0	11.9	8.54
Yields of alcohol and ketone (%)	75.6	73.4	65.1
Time until the yield maximum (H)	1.5	2.5	3.5
Ratios of alcohol to ketone	0.91	0.97	0.94
Catalyst mole turnover number	33937	26289	18866

$C_{\text{cat}}=40\text{ppm}$, $V_{\text{air}}=3\text{ l/min}$, $P=0.6\text{MPa}$, $T=140^\circ\text{C}$.

Table 1. Effect of different metalloporphyrins on the oxidation reaction

For cyclohexane oxidation catalyzed by simple cobalt tetraphenylporphyrin, the conversion of cyclohexane was up to 16.2%, general yields of cyclohexanol and cyclohexanone was 82%, and the mole turnover numbers of the catalyst reached 400,000 under the optimum conditions of 0.6MPa and 140°C and 4 ppm cobalt porphyrin.

One-pot oxidation directly from cyclohexane to adipic acid with dioxygen as oxidant is gathering increasing interest. A novel one-pot oxidation of cyclohexane to adipic acid using molecular oxygen as an oxidant catalyzed by iron-porphyrins has been developed by our research group (Scheme 6).⁵²



Scheme 6. One-pot oxidation of cyclohexane to adipic acid catalyzed by iron-porphyrin

When the reaction temperature is 140°C, oxygen pressure is 2.5 MPa, concentration of catalyst is 1.33×10^{-5} mol %, and reaction time is 8 h, the yield of adipic acid reaches 21.4%. A turnover number of about 24582 is thus far the highest one among those reported for the direct oxidation from cyclohexane to adipic acid.

3. Epoxidation of olefins

Catalytic epoxidation of olefins has attracted much attention both in industry and in organic synthesis, for epoxides are among the most useful synthetic intermediates. Access to a variety of epoxides has largely been successful due to the remarkable catalytic activity of transition metal complexes, which have a unique ability to bring the alkene substrate and the oxygen source within the coordination sphere of the metal leaving to a facial transfer of oxygen atom to the carbon-carbon double bond.⁵³⁻⁵⁶

During the past two decades, metalloporphyrins have been widely applied for epoxidation of olefins to give epoxides with high regio-, shape- and stereoselectivity since the leading works of Groves and co-workers by using iodobenzene (PhIO) as oxygen atom donor.⁵⁷

The activation of the natural oxidant, O₂, with metalloporphyrins has also been realized.

In metalloporphyrin-catalyzed homogenous epoxidation of olefins with molecular oxygen, a stoichiometric amount of reducing reagent is usually used for the activation of dioxygen. Several model systems using O₂ and reducing agents in the presence of Mn(III) porphyrins as catalyst have been described in the literature, in which including H₂/Pt,⁵⁸⁻⁶⁰ zinc powder,^{61, 62} or electrochemically on an electrode.^{63, 64}

Aldehyde is another effective reducing agent for the epoxidation of olefins with dioxygen as oxidant. Mukaiyama reported an efficient approach for epoxidation of olefins using dioxygen as oxidant under ambient conditions. The process involved use of β -diketonate complexes of Ni²⁺, Co²⁺, and Fe³⁺ as catalysts and an aldehyde as oxygen acceptor.⁶⁵⁻⁶⁷ Subsequently, many metal catalysts e.g. manganese complex, cobalt-containing molecular sieves and metalloporphyrins demonstrated highly catalytic performance for the aerobic oxidation in the presence of aldehyde.⁶⁸⁻⁷¹

Mandal and co-workers reported the epoxidation of various olefins using cobalt porphyrins in ambient molecular oxygen and 2-methylpropanal.⁷² Methyl styrene, stilbene were transformed to the corresponding epoxides in nearly quantitative yield (Table 2). It is noteworthy that trans-stilbene afforded the corresponding trans-epoxide. Limonene was readily transformed to a mixture of mono and diepoxide in 1:2.3 ratio in quantitative yield.

The simple structural metalloporphyrins has proven to be an excellent catalyst for the epoxidation of olefins in the presence of molecular oxygen and isobutylaldehyde. As a part of metalloporphyrins-catalyzed oxidations of our group works, the epoxidation of olefins catalyzed by very small amount of MnTPP (manganese *meso*-tetraphenyl porphyrin) was reported (Scheme 7), in which extremely high turnover number that could be comparable to most enzyme catalysis was obtained.⁷³

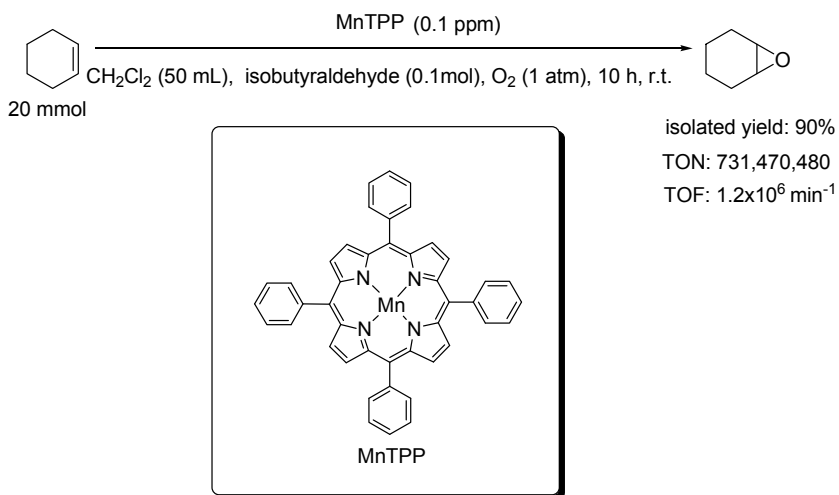
When the amount of manganese *meso*-tetraphenylporphyrin catalyst was 2.5×10^{-8} mmol, the cyclohexene oxide could be obtained with the isolated yield of 90%. It should be mentioned that the turnover number of the present catalyst could reach 731,470,480. Since commonly, TOF is used to express the catalytic efficiency of enzyme with the definition as converted substrate (mol) per enzyme (mol) per minute. The TOF of most enzymes is about 1000 min⁻¹ or more. For example, the TOF of catalase is 6×10^6 min⁻¹, and the TOF of β -galactosidase is 1.25×10^4 min⁻¹. In the present manganese *meso*-tetraphenylporphyrin catalyzed system, the TOF reaches up to 1.2×10^6 min⁻¹, which is the range for enzyme activity.

Entry	Substrate	Product ^b	Yield (%) ^a
1			94
2			100
3			80
4			100 ^c
5			83
6			51

^a Isolated yield. ^bYield determined from ¹H-NMR of the crude reaction mixture.

^cObtained as a mixture of syn-anti diastereomers

Table 2. Co(II) porphyrin catalyzed oxidation of olefins using 2-methylpropanal and dioxygen



Scheme 7. Manganese *meso*-tetraphenylporphyrin catalyzed epoxidation of olefins

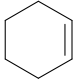
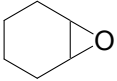
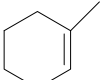
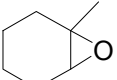
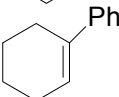
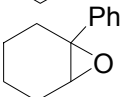
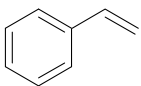
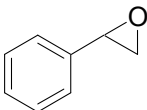
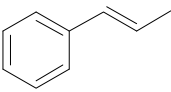
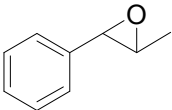
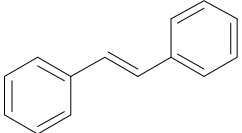
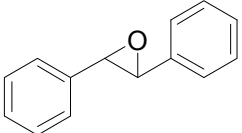
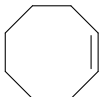
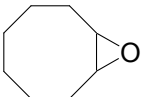
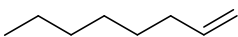
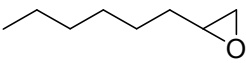
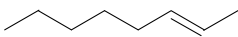
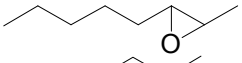
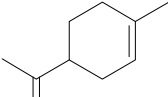
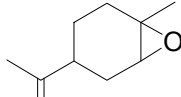
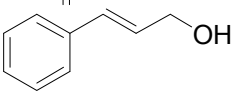
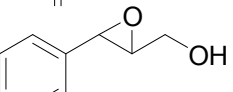
Also, various olefins could be smoothly converted to the corresponding epoxides in the catalytic system under ambient conditions. As shown in Table 3, it seems that the efficiency of epoxidation in this catalytic system is very dependent on the steric structure of substrates. The influence of steric effects could further be found when styrene and its derivatives were oxidized, the conversion rates of styrene, *trans*- β -methylstyrene and *trans*-stilbene were 95%, 89% and 86% after reacting for 4.5, 7.0 and 8.0 h, again demonstrating a steric effect (entries 4-6).

Similarly, in the epoxidation of other cycloolefin *e.g.* cyclooctene, the reaction system exhibits high catalytic performance with 93% yield of cyclooctene epoxide (entry 7). Epoxidation of linear chains *e.g.* 1-octene and *trans*-2-octene smoothly proceeded with high conversion and yield, and similar catalytic activities for the two substrates show the located position of C=C bond on linear chain alkenes could hardly influence their catalytic performance (entries 8-9).

Despite of the high efficiency of the catalyst system, another salient feature of the present epoxidation is its high regioselectivity (entry 10). In addition, the catalyst system exhibits specific selective oxidation performance towards C=C bond and hydroxyl group activation. C=C bond was preferentially activated and the corresponding epoxide as the only product with 90% yield could be obtained for the cinnamyl alcohol oxidation, and no products from hydroxyl group oxidation could be detected (entry 11).

A mechanism for the epoxidation of olefins by dioxygen in the presence of metalloporphyrins and isobutyraldehyde has been proposed from the experimental results, as shown in Figure 3.

Based on the proposed mechanism, the manganese porphyrin reacts with the aldehyde to generate an acyl radical (a) at first. The acyl radical then reacts with dioxygen to give an acylperoxy radical (b). The acylperoxy radical is assumed to play two roles. Firstly, it reacts with olefins to yield epoxides directly accompanying the generation of carboxyl radical (c), which reacts with aldehyde to generate another acyl radical and carboxylic acid (pathway A). Secondly, in pathway B, the acylperoxy radical acts as a carrier by reacting with another aldehyde molecule to give peroxyacid (d), thereby generating another acyl radical. Formation of epoxide is assumed by active high-valent Mn porphyrin intermediates (e), which are formed by the reaction of the peroxyacid with the manganese porphyrin. The evidence described above suggests that pathway B is usually superior over pathway A.

Entry	Substrate	Product	Reaction time (h)	Conv. (%)	Yield (%)
1			4.5	97	95
2			5.0	93	90
3			6.0	83	72
4			4.5	95	93
5			7.0	89	87
6			8.0	86	85
7			5.0	95	93
8			5.0	94	93
9			5.0	93	89
10			5.0	92	91
11			6.0	92	90

^asubstrate (2 mmol), isobutyraldehyde (0.01mol), CH₂Cl₂ (5 mL), O₂ bubbling, r.t.

Table 3. Epoxidation of alkenes catalyzed by manganese *meso*-tetraphenylporphyrin in the presence of molecular oxygen and isobutyraldehyde ^a

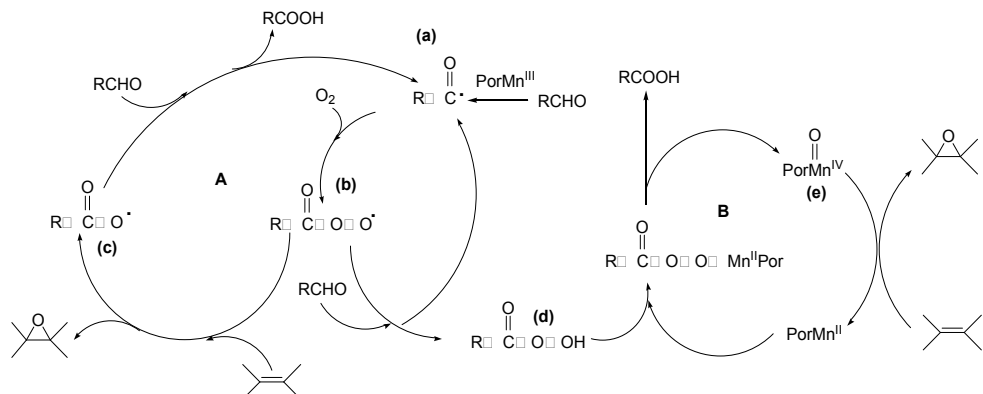
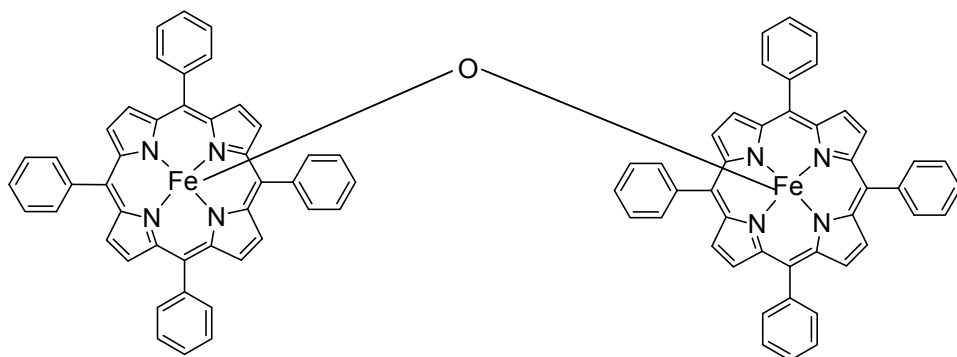


Fig. 3. Plausible mechanism of olefin epoxidation catalyzed by Mn(III) porphyrins in the presence of molecular oxygen and isobutyraldehyde

Compared with mono-metallporphyrins as catalyst, remarkable enhancement of reactivity was obtained for μ -oxo-bisiron(III) porphyrin-catalyzed olefin epoxidation system (Scheme 8), in which the turnover number (TON) of the catalyst has doubled from about 700 million to 1,400 million.⁷⁴

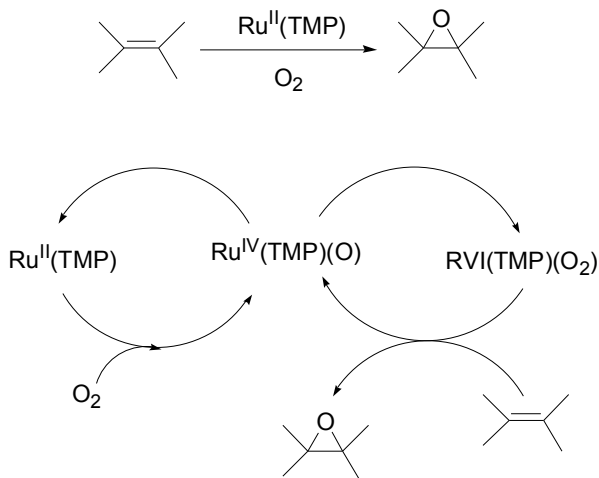


Scheme 8. Structure of μ -oxo-bisiron(III) porphyrin

It is usually considered that μ -oxo dimeric metalloporphyrins could easily form monometalloporphyrins during the catalytic process. In fact, whether the dinuclear intermediate or the mononuclear intermediate is the active species remains controversial for the oxygenation of hydrocarbons by using μ -oxo dimeric metalloporphyrins as catalyst. The results of in situ UV-vis spectra indicate that both the dinuclear and the mononuclear high-valent intermediate exist in the catalytic system. Probably two kinds of oxo-iron intermediates, that is $O=^VFe-O-Fe^V=O$ and $Fe^V=O$ were formed by series of free radical processes.

Few examples on the metalloporphyrins-catalyzed epoxidation by dioxygen in the absence of a co-reductant could be found. It is worthy mentioning that $Ru^{VI}(TMP)(O)_2$ catalyzes olefin epoxidation with O_2 without the requirement a sacrificial reductant reported by

Groves group.^{75, 76} The proposed mechanism is shown in Scheme 9. The active oxidant $\text{Ru}^{\text{VI}}(\text{TMP})(\text{O})_2$ reacts with an olefin to afford the epoxide and $\text{Ru}^{\text{IV}}(\text{TMP})(\text{O})$, and the disproportionation of the latter generates $\text{Ru}^{\text{II}}(\text{TMP})$ and the active oxidant $\text{Ru}^{\text{VI}}(\text{TMP})(\text{O})_2$. The $\text{Ru}^{\text{II}}(\text{TMP})$ re-enters the catalytic cycle after being oxidized by dioxygen to $\text{Ru}^{\text{IV}}(\text{TMP})(\text{O})$.



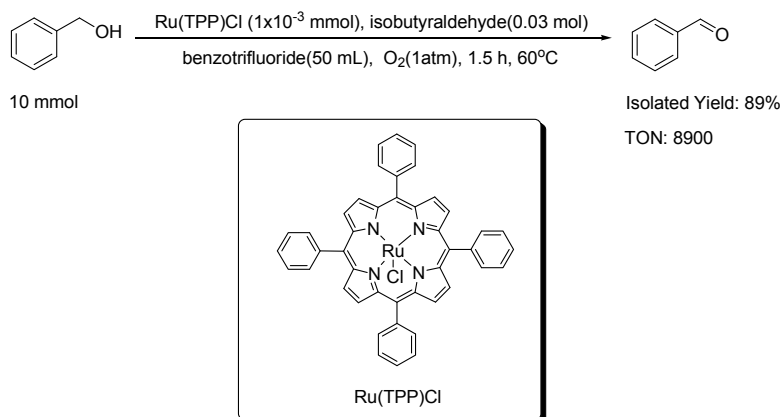
Scheme 9. Ru(TMP)-catalyzed olefins epoxidation with dioxygen

4. Oxidation of alcohols

Oxidation of alcohols to the corresponding carbonyl compounds is a very important step for organic synthesis.⁴¹ From an environmental and cost effective viewpoint, catalytic oxidation processes with molecular oxygen or air are extremely valuable and particularly attractive. Accordingly, variety of transition metal based catalysts (mainly cobalt, vanadium, ruthenium and palladium) has been intensively investigated for aerobic oxidation of alcohols so far.⁷⁷⁻⁸⁰

Although metalloporphyrins have been used to catalyze the oxidation of alcohols with PhIO , $t\text{-BuOOH}$, KHSO_5 and $m\text{-CPBA}$ (m -chloroperbenzoic acid) as oxidants,⁸¹⁻⁸⁴ few studies on metalloporphyrins-catalyzed oxidation of alcohols by molecular oxygen were reported. For examples, Woo and co-authors ever reported the aerobic homogeneous oxidation of benzyl alcohol with oxotitanium porphyrin ($\text{TTP})\text{Ti}=\text{O}$ ($\text{TTP}=\text{meso-tetra-}p\text{-tolylporphyrin}$), which gave benzaldehyde in modest yields (48%) after 94 hours in refluxing chlorobenzene.⁸⁵

Ruthenium-porphyrin has been proved to be efficient for oxidation of alcohols with high yields for carbonyl compounds under mild conditions (Scheme 10).⁸⁶ Alcohols including benzylic alcohols, secondary alcohols and primary alcohols were efficiently converted to the corresponding carbonyl compounds in the catalytic system by atmospheric dioxygen (Table 4).



Scheme 10. Oxidation of alcohols catalyzed by ruthenium (III) *meso*-tetraphenylporphyrin chloride in the presence of molecular oxygen and isobutyraldehyde

Entry	Alcohol	Product	Time (h)	Conv. (%)	Yield (%)
1			0.5	>99	>99
2			1.0	35	35
3			0.5	91	91
4			1.0	17	17
5			0.5	94	94
6			1.5	93	93
7			1.0	94	94
8			0.5	91	72
9			1.0	93	71

^aBenzyl alcohol (1mmol), Ru(TPP)Cl (1×10^{-3} mmol), isobutyraldehyde (3mmol), benzotrifluoride (5mL), O₂ bubbling (1 atm), 60°C, 0.5 h

^btoluene (5 mL) as solvent

Table 4. Oxidation of various alcohols by molecular oxygen in the presence of Ru(TPP)Cl^a

As shown in Table 4, it seems that the catalytic activity is dependent on the electronic property of substrates (entries 2-4). Secondary alcohols could be easily converted to the corresponding ketones in high yield (entries 5-8). In the case of 2-adamantanol, the catalytic system shows high activity, which gave ketone yield of 72% when the reaction continued for 30 min despite the hindrance. In the cases of saturated primary aliphatic alcohols e.g. 1-octanol and 1-hexanol, further oxidation of aldehydes to the corresponding carboxylic acids was observed under the same reaction conditions (entries 9).

A mechanism for the epoxidation of olefins by dioxygen in the presence of metalloporphyrins and isobutyraldehyde has been proposed from the experimental results, as shown in Figure 4.

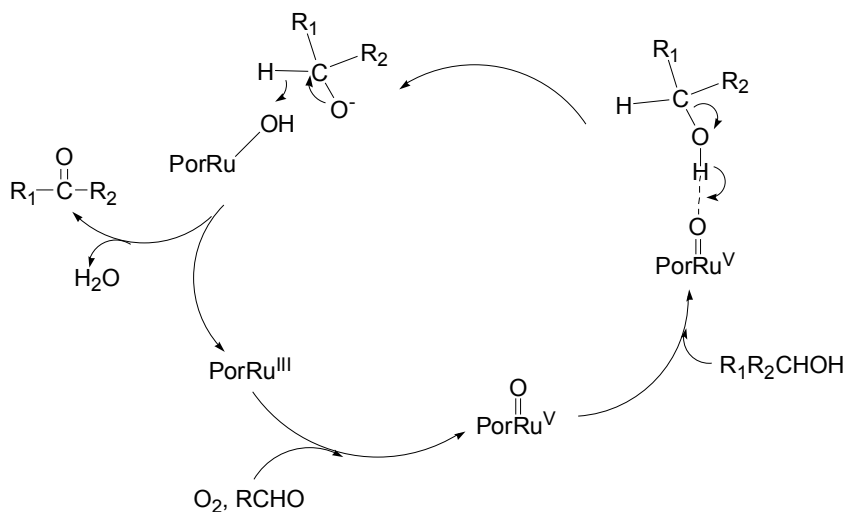
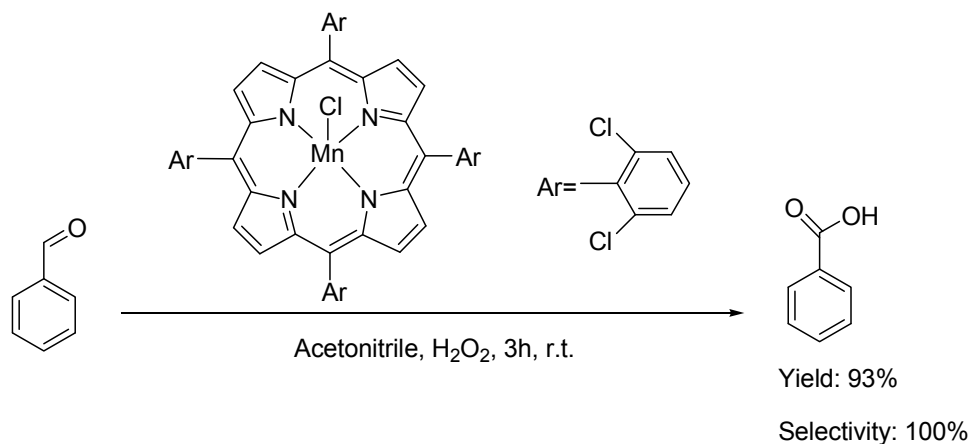


Fig. 4. Proposed mechanisms for the aerobic oxidation of alcohols catalyzed by ruthenium-porphyrin

5. Oxidation of aldehydes

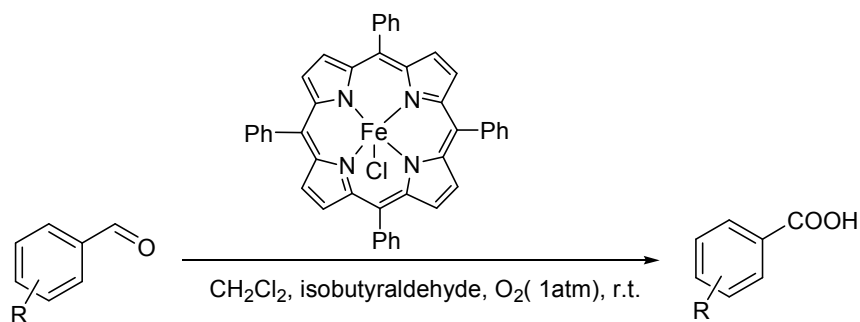
Oxidation of aldehydes to the corresponding carboxylic acids is one of the important methods in organic synthesis as carboxylic acids are versatile intermediates in a variety of synthetic transformations.⁸⁷ Few reports were found on the oxidation of aldehydes catalyzed by metalloporphyrins with hydrogen peroxide or molecular oxygen.

Rebello reported the oxidation of benzaldehyde with hydrogen peroxide in Mn(III) porphyrin/ammouium acetate system, which can give 93% yield of benzoic acid by conducting the reaction for 3 h (Scheme 11).⁸⁸



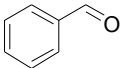
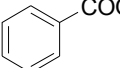
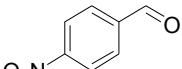
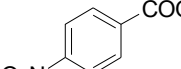
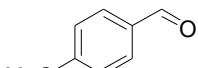
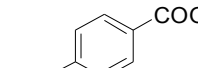
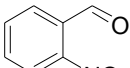
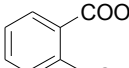
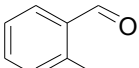
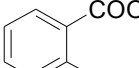
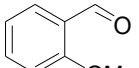
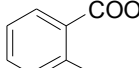
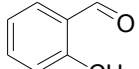
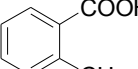
Scheme 11. Oxidation of benzaldehyde catalyzed by manganese-porphyrin with H_2O_2

First example of metalloporphyrins-catalyzed benzylic aldehyde oxidation using molecular oxygen as a sole oxidant at room temperature was developed previously by our research group (Scheme 12).⁸⁹



Scheme 12. Benzylic aldehydes aerobic oxidation catalyzed by $\text{Fe}(\text{TPP})\text{Cl}$

Various benzylic aldehydes were oxidized at room temperature in the presence of molecular oxygen and isobutyraldehyde as shown in Table 5. Most benzylic benzaldehydes could be smoothly converted to benzylic acids with high conversions by using $\text{Fe}(\text{TPP})\text{Cl}$ as a catalyst and molecular oxygen as a sole oxidant. The influence of steric effects could be clearly found for those *ortho*-position substituted substrates in comparison with those *para*-position substituted ones. For example, the oxidation of 4-methoxy-benzaldehyde for 2 h gave 93% yield of the corresponding acid; whereas only 75% yield of the corresponding acid could be obtained from the oxidation of 2-methoxy-benzaldehyde for 4 h (entries 3 and 6).

Entry	Substrate	Product	Time/h	Conv.(%)	Yield(%)
1			2.0	95	95
2			3.0	87	87
3			2.0	93	93
4			4.0	82	82
5			3.0	90	90
6			4.0	75	75
7			3.0	85	85

^aSubstrate =1.5 mmol, substrate/isobutyraldehyde (molar ratio)=1/5, catalyst(FeTPP)Cl, 1.5×10^{-3} mmol, r.t.; O₂ bubbling (1atm), 5mL CH₂Cl₂ solvent

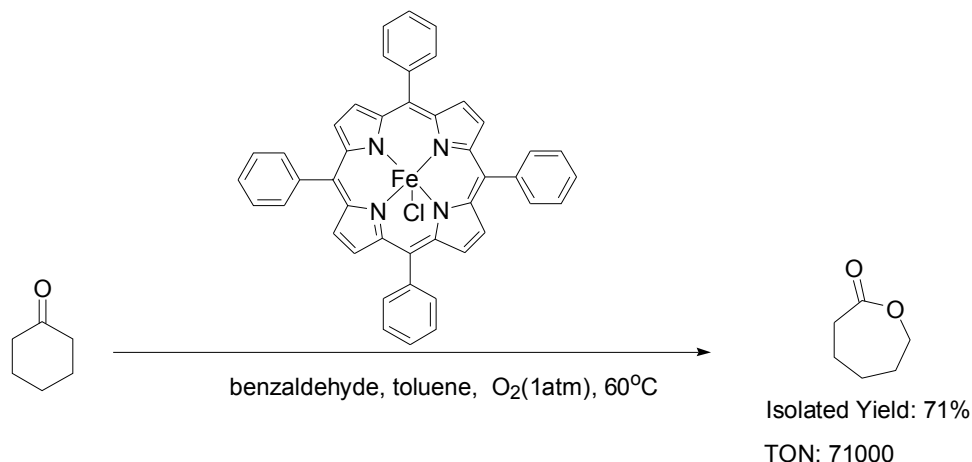
Table 5. Oxidation of various benzylic aldehydes catalyzed by Fe(TPP)Cl in the presence of molecular oxygen^a

6. Oxidation of ketones

In 1899 Adolf Baeyer and Victor Villiger reported the oxidation of menthone to the corresponding lactone using a mixture of sodium persulfate and concentrated sulfuric acid.⁹⁰ The persulfuric acid was subsequently replaced by organic peracids such as persulfuric acid, *m*-CPBA, trifluoroperacetic acid and perbenzoic acid, then the

Baeyer-Villiger (B-V) reaction became one of the most well-known and widely applied reactions in organic synthesis.⁹¹ A combination of molecular oxygen and aldehydes under heterogeneous catalyst such as silica-supported nickel complex, iron(III)-containing mesoporous silica have been extensively studied.⁹²

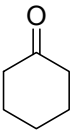
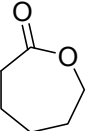
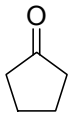
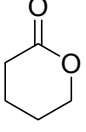
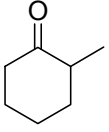
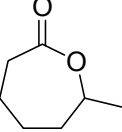
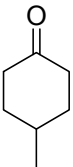
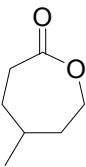
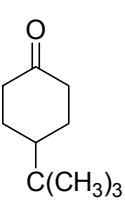
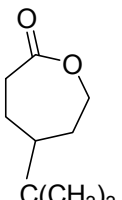
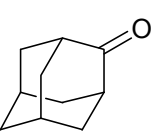
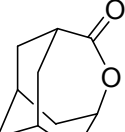
One example of B-V reaction catalyzed by metalloporphyrins with dioxygen has been developed by our group. Iron (III) *meso*-tetraphenylporphyrin chloride (Fe(TPP)Cl) was efficient for the B-V reaction of ketones to lactones in the presence of molecular oxygen and benzaldehyde (Scheme 13).



Scheme 13. Aerobic oxidation of ketones to lactone catalyzed by iron-porphyrins

The scope of substrates for the B-V reaction catalyzed by the Fe(TPP)Cl was examined and the typical results are shown in Table 6.

The oxidations of various cyclic ketones occurred smoothly to afford selectively the corresponding lactones by atmospheric dioxygen in the presence of Fe(TPP)Cl under mild conditions. It seems that cyclic ketones were more efficiently oxidized than acyclic ketones. Moreover among the cyclic ketones, six-membered cyclic ketones could be most efficiently oxidized to the corresponding lactones. For example only 32% cyclopentanone (entry 3) was converted to the corresponding lactone (entry 2) under the same reaction conditions. It might be that only those substrates with suitable steric configuration favored the conversion owing to the existence of the large ring of the metalloporphyrin catalyst in the present system. Furthermore, the substituent on the six-membered cyclic ketones was also investigated (entries 3~5), and the alkyl substitution to the ring of cyclic ketones caused no retardation of the oxidation, 96% conversion of 4-*tert*-butylcyclohexanone was obtained even increasing bulkiness of the substituent (entry 5).

Entry	Ketones	Product	Time (h)	Conv. (%)	Yield (%)
1			5	96	96
2			5	32	32
3			5	98	98
4			6	94	94
5			5	96	96
6			8	84	84

^aFe(TPP)Cl (0.2×10⁻³ M), substrate (1 mmol), toluene (5 mL), benzaldehyde (15 mmol), O₂ bubbling, 60°C

Table 6. Oxidation of various ketones by molecular oxygen in the presence of Fe(TPP)Cl^a

The possible presence of iron-oxo porphyrin was confirmed by UV-vis spectra from the oxidation of cyclohexanone, as show in Figure 5. Curves a and b show the spectra of cyclohexanone oxidation catalyzed Fe(TPP)Cl at the beginning and the point after the reaction for 30 min. A shift from 409 to 416 nm was observed, which is indicative of the existence of an active oxidation species expected as the iron high-valent intermediate.

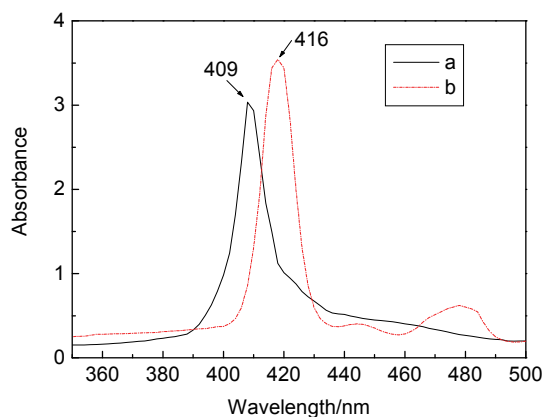


Fig. 5. UV-vis spectra of cyclohexanone oxidation by molecular oxygen in the presence of benzaldehyde and Fe(TPP)Cl. Cyclohexanone(1 mmol), Fe(TPP)Cl (0.2×10^{-3} M), benzaldehyde (15 mmol), toluene (5 mL), (a) initial point of reaction, (b) 30 min after reaction.

The reaction mechanism might be as shown in Figure 5. Based on the proposed mechanism, the iron porphyrin reacts with the benzaldehyde to generate an acyl radical at first. The acyl radical then reacts with dioxygen to give an acylperoxy radical. The acylperoxy radical acts as a carrier in a chain mechanism by reaction with another benzaldehyde molecule to give the peroxybenzoic acid, and generating another acyl radical as well. The peroxybenzoic acid is assumed to play two roles. Firstly, it reacts with another iron porphyrin molecule to generate high-valent Fe porphyrin intermediate, which combines cyclohexanone to accomplish oxygen transfer step and to generate ϵ -caprolactone (pathway A). Secondly, the peroxybenzoic acid attacks activated ketone to form a Criegee adduct, followed by protolysis to afford the lactone together with benzoic acid (pathway B).

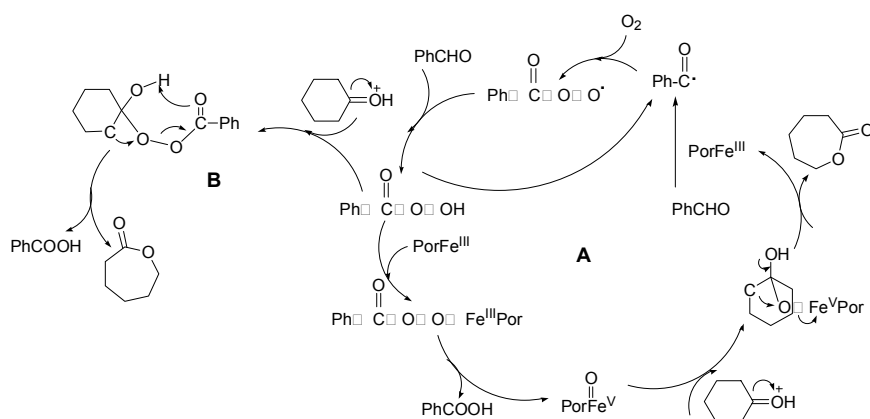


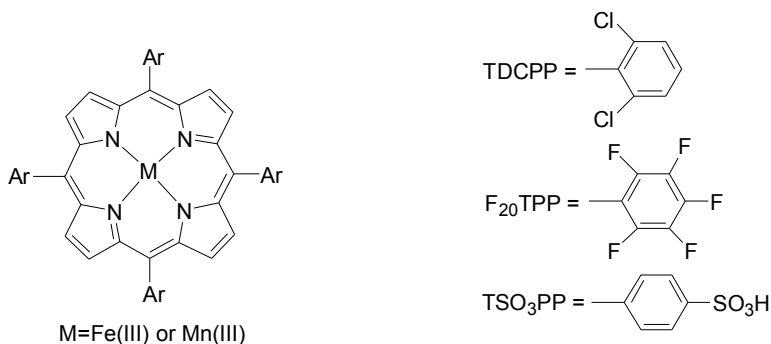
Fig. 6. Plausible mechanism of cyclohexanone oxidation in the presence of Fe(TPP)Cl and molecular oxygen

7. Oxidation of sulfides

7.1 Oxidation of sulfides to sulfones

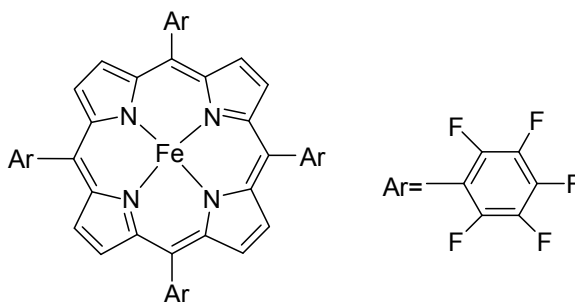
Oxidation of sulfide to sulfone has been the subject of extensive studies, since both products are useful organic intermediates for construction of various chemically and biologically significant molecules.⁹³ Hydrogen peroxide has been frequently applied to sulfoxidation system as an environmentally benign oxidant.

Sulfoxidation of sulfides catalyzed by cytochrome P-450 and peroxidase is a subject of current interest since the pioneering work of Oae and co-workers.⁹⁴ Recently, the practical application of sulfoxidation catalyzed by metalloporphyrins has been concerned increasingly. Marques reported a new approach of mustard oxidation in a protic solvent with H_2O_2 as an oxidant.⁹⁵ The results show that catalysis by Fe(III)- and Mn-(III)-tetraarylporphyrins (Scheme 14) can provide an interesting route to the transformation of mustard and related sulfides into sulfones. Differences in the behavior of Mn- and Fe-porphyrins for the efficiency in sulfide oxidation were also observed.



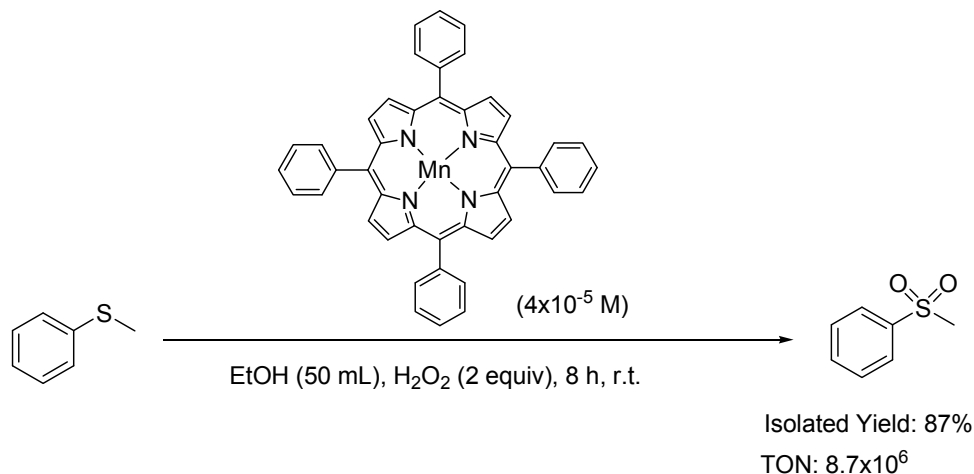
Scheme 14. Structures of metalloporphyrins used in the oxidation of mustard

Baciocchi and co-workers presented an efficient and chemically selective process for sulfide oxidation by hydrogen peroxide in the presence of complicated structural iron metalloporphyrins (tetrakis-pentafluorophenyl porphyrin, Scheme 15).⁹⁶ With a catalyst concentration between 0.09% and 0.25% of that of substrate, sulfones are obtained in almost quantitative yield and high chemoselectivity with both aromatic and aliphatic sulfides.



Scheme 15. Structures of tetrakis-pentafluorophenyl porphyrin

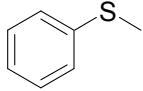
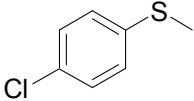
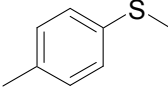
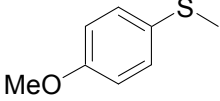
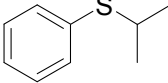
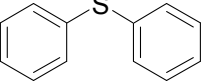
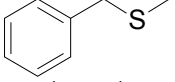
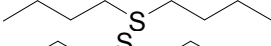
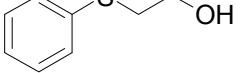
Simple structural metalloporphyrins has also been proved to be effective in the oxidation of sulfides to sulfones. As a part of our works, manganese *meso*-tetraphenyl porphyrin (MnTTP) was used for highly efficient selective oxidation of sulfide to sulfone by hydrogen peroxide at room temperature (Scheme 16).⁹⁷



Scheme 16. Oxidation of sulfide to sulfone catalyzed by manganese-porphyrin with H₂O₂

Various sulfides could be smoothly converted to the corresponding sulfones directly with high yields at room temperature as shown in Table 7. It could also be observed that the electronic property of substrate affected the conversion to some extent. Lower conversion rates could be obtained for electron-withdrawing substrates with longer reaction time (entry 2) than those substrates containing electron donating substituents that require shorter reaction time (entries 3-4).

The steric effects could be observed from the oxidation of diphenyl sulfide and isopropyl phenyl sulfide. The conversion rates of diphenyl sulfide and isopropyl phenyl sulfide were 89% and 83% after 2.0 and 3.0 h, respectively (entries 5-6). Compared with thioanisole, methyl benzyl sulfide presents similar catalytic behavior, and could be stoichiometrically converted at room temperature (entry 7). Sulfoxidation of the linear chain *di-n*-butyl sulfide smoothly proceeded with a high conversion rate and an excellent yield of sulfone in a shorter reaction time (entry 8).

Entry	Substrate	Time (h)	Conv.(%)	Select.(%)	
				sulfoxide	Sulfone
1		1.0	>99	<1	>99
2		3.0	94	7	93
3		1.5	98	9	91
4		1.5	98	7	93
5		2.0	89	<1	>99
6		3.0	83	<1	>99
7		1.5	>99	<1	>99
8		1.0	>99	3	97
9		2.0	95	12	88

^aReaction conditions: substrate (2 mmol), 30% H₂O₂(2 equiv), 5 mL of ethanol solvent, catalyst(4×10⁻⁵M), r.t.,

Table 7. Oxidation of sulfide catalyzed by Mn(TPP) using hydrogen peroxide as oxidant^a

Besides high efficiency of the present catalyst system, another salient feature of the present sulfoxidation is its high chemical selectivity. Sulfone can be conveniently synthesized from sulfide containing hydroxyl group without carbonyl compound byproduct (entry 9).

The profile of thioanisole oxidation in the presence of H₂O₂ and Mn(TPP) is shown in Figure 7, demonstrating that the reaction proceeded *via* two steps: the first step was the oxidation of sulfide to sulfoxide, and the second step was the oxidation of sulfoxide to sulfone. The sulfoxide was the reaction immediate.

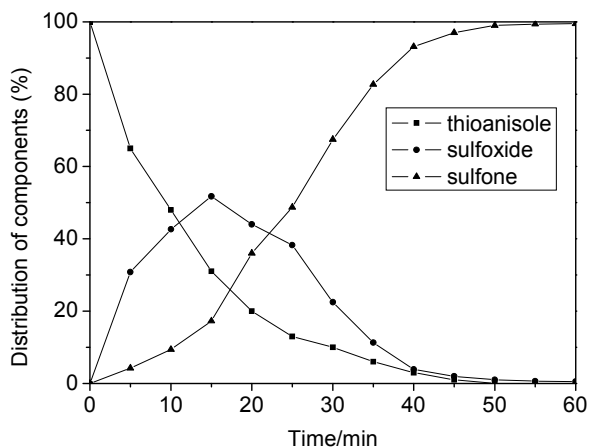


Fig. 7. Reaction profile for the oxidation of thioanisole in the presence of H_2O_2 and $\text{Mn}(\text{TPP})$ ($4 \times 10^{-5} \text{ M}$) in ethanol (5mL) at room temperature

Direct oxygen transfer from metal-oxo porphyrin radical cation to the sulfide is generally accepted to be the mechanism for sulfide oxidation in the presence of H_2O_2 and metalloporphyrins. The possible presence of metal-oxo porphyrin was confirmed by in situ UV-Vis spectrum from the thioanisole oxidation system, as shown in Figure 8.

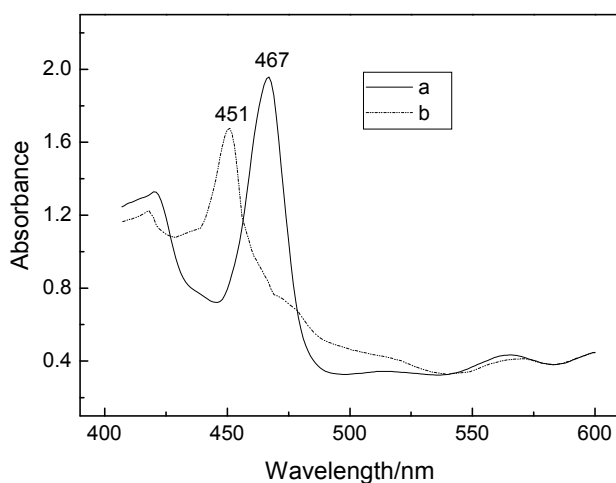


Fig. 8. In situ UV-Vis spectra of thioanisole oxidation catalyzed by $\text{Mn}(\text{TPP})$ in the presence of hydrogen peroxide, thioanisole (2mmol), 30% H_2O_2 (2 equiv), 5 mL of ethanol solvent, $\text{Mn}(\text{TPP})$ catalyst ($4 \times 10^{-5} \text{ M}$), r.t., a: initial point of reaction, b: 15 min after reaction

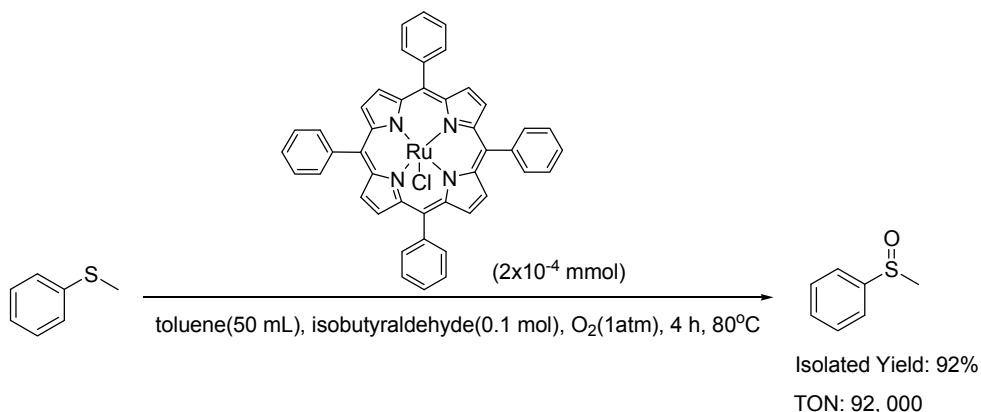
In Figure 8, a and b show the spectra of thioanisole oxidation catalyzed by Mn(TPP) at the beginning and the point after the reaction for 15 min. A shift from 467 to 451 nm with a small loss of intensity was observed. The GC control of the reaction revealed the formation of the sulfoxide and sulfone, which is indicative of the existence of an active oxidation species expected as the Mn(IV) porphyrin.

7.2 Oxidation of sulfides to sulfoxides

Selective oxidation of sulfides to the corresponding sulfoxides remains a challenge and is interesting because of the importance of sulfoxides as synthetic intermediates in organic synthesis.⁹⁸⁻¹⁰⁰ Although selective oxidation by molecular oxygen is more attractive because of its cost-effectiveness and environmentally-friendly nature of the oxidant, few reports were found for such oxidation of sulfides catalyzed by metalloporphyrins.

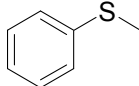
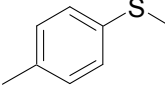
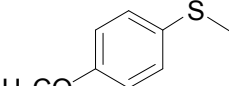
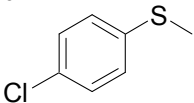
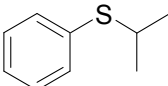
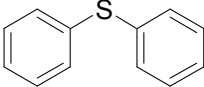
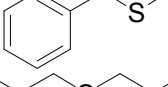
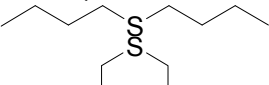
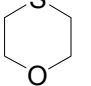
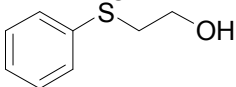
Mansuy ever reported selective aerobic oxidation of di-*n*-butylsulfide to the corresponding sulfoxide in 68% yield in the presence of Mn(TPP)Cl catalysts, zinc powder and CH₃COOH.¹⁰¹

Highly efficient selective oxidation of sulfides to sulfoxides by molecular oxygen catalyzed by ruthenium (III) *meso*-tetraphenylporphyrin chloride (Ru(TPP)Cl) with isobutyraldehyde as oxygen acceptor has been reported by our group.¹⁰² In large-scale experiment of thioanisole oxidation, the isolated yield of sulfoxide of 92% was obtained and the turnover number reached up to 92000 (Scheme 17).



Scheme 17. Ruthenium *meso*-tetraphenylporphyrin chloride catalyzed sulfoxidation

Different substrates could be smoothly converted to sulfoxides with high conversion rates, and excellent selectivities were obtained by Ru(TPP)Cl catalyst and molecular oxygen as the sole oxidant.

Entry	Substrate	Time (min)	Conv.(%)	Selectivity (%)	
				sulfoxide	sulfone
1		30	99	>99	<1
2		30	97	96	4
3		30	98	95	5
4		45	96	95	5
5		45	93	96	4
6		60	98	92	8
7		30	>99	>99	<1
8		20	>99	>99	<1
9		60	94	97	3
10		45	>99	90	<1

^aReaction conditions: substrate (2 mmol), molar ratio of substrate/isobutylaldehyde (1/5), molar ratio of catalyst/substrate (1/10000), toluene (5 mL), O₂(bubbling), 80°C

Table 8. Oxidation of various sulfides by molecular oxygen catalyzed by Ru(TPP)Cl ^a

It can be observed that the electronic property of substrate affects the reaction rate (entries 1~4). It required a slightly longer reaction time for substrate with electron-withdrawing groups (entry 4). The influence of steric effects could further be found from the oxidation of diphenyl sulfide and isopropyl phenyl sulfide. The conversion rates of diphenyl sulfide and isopropyl phenyl sulfide were 98%, 93% after much longer reactions time (entries 5-6). Compared with thianisole, methyl benzyl sulfide presents the similar reaction behavior, and it could be stoichiometrically converted at the same conditions (entry 7). Sulfoxidation of the linear chain di-n-butyl sulfide smoothly proceeded in less reaction time with high conversion and yields (entry 8). Cyclic sulfide, *i.e.* 1,4-thioxane could also be efficiently

sulfoxidated to the corresponding sulfoxide with 94% conversion and 97% selectivity (entry 9).

Despite of high efficiency, another salient feature of the present sulfoxidation system is its high chemoselectivity. For oxidation of hydroxyl group-containing sulfide e.g. 2-(phenylthio) ethanol (entry 10), sulfide can be entirely converted and the yields of sulfoxide could reach 90%, and 10% yield of the corresponding aldehyde was found in products. It demonstrates that the sulfide functional group is highly active, but hydroxyl group could hardly be activated under such reaction conditions.

It should be mentioned that the present reaction system was highly selective. Sulfoxides could be nearly stoichiometrically produced, and the generation of the corresponding sulfones was well controlled, which makes this process be a good alternative for sulfoxides production.

8. Conclusion

The foregoing sections have clearly demonstrated the impressive progress made in the area of metalloporphyrins-catalyzed aerobic oxidations. It is convincing that metalloporphyrins are very versatile oxidation catalysts which can be used in many different oxidation reactions (alkane hydroxylations, epoxidations of olefin, oxidation of compounds containing oxygen, sulfur and nitrogen, etc.). Meanwhile, many articles are dealing with mechanism studies on oxidations catalyzed by metalloporphyrins, attempting to learn the exact nature of the active species.

As described above, remarkable progress in mimicking the action of cytochrome P-450 enzymes has been made over the past decades. And this field is still seems to be achieved much attention. Biomimetic catalysis of metalloporphyrins is now a meeting for chemistry, chemical engineering, catalysis and biology. Combined efforts in such an interdisciplinary area will probably produce new applications of metalloporphyrins chemistry. Metalloporphyrins catalyzed oxidation of organic substrates with molecular oxygen is becoming an important and highly rewarding protocol for important feedstock for petrochemical and fine chemical industries. Initial successes in this area is promising and forecasts future growth in accessing oxidized organic molecules using molecular oxygen and metalloporphyrins catalysts. The efforts in this area will clearly culminate in tackling the major issues pertaining to environmentally acceptable technologies for future.

Acknowledgements

The authors thank the National Natural Science Foundation of China (20976203), the Key Fundamental Research Foundation (2008CB617511) and the Program for New Century Excellent Talents in University (NCET-06-740) for providing financial support for this project.

9. References

1. Ortiz de Montellano, P. R. *Cytochrome P450: structure, mechanism and biochemistry*; Plenum: New York, 1996.
2. Loew, G. H.; Harris, D. L. *Chem.Rev.* **2000**, *100*, 407-420.
3. Sono, M.; Roach, M. P.; Coulter, E. D.; Dawson, J. H. *Chem.Rev.* **1996**, *96*, 2841-2888.
4. Gunsalus, I. C.; Pederson, T. C.; Sligar, S. G. *Annu.Rev.Biochem.* **1975**, *44*, 377.
5. Ortiz de Montellano, P. R.; De Voss, J. J. *Nat.Prod.Rep.* **2002**, *19*, 477-493.
6. Omura, T.; Ishimura, Y.; Fujii-Kuriyama, Y. *Cytochrome P450*; Kodansha: Tokyo, 1993.
7. Hayaishi, O. *Molecular mechanism of oxygen activation*; Academic Press: New York, 1974.
8. Meunier, B.; Bernadou, J. *Top.Catal.* **2002**, *21*, 47-54.
9. Filatov, M.; Reckien, W.; Peyerimhoff, S. D.; Shaik, S. *J.Phy.Chem.A* **2000**, *104*, 12014-12020.
10. Tshuva, E. Y.; Lippard, S. J. *Chem.Rev.* **2004**, *104*, 987-1012.
11. Meunier, B.; de Visser, S. P.; Shaik, S. *Chem.Rev.* **2004**, *104*, 3947-3980.
12. Costas, M.; Mehn, M. P.; Jensen, M. P.; Que, L., Jr. *Chem.Rev.* **2004**, *104*, 939-986.
13. Meunier, B. *Biomimetic Oxidations Mediated by Metal Complexes*; Imperial College Press: London, 2000.
14. Meunier, B. *Chem.Rev.* **1992**, *92*, 1411-1456.
15. Meunier, B. *Metalloporphyrin Catalyzed Oxidation*; Kluwer Academic Publisher: 1994.
16. Reichhart, D. W.; Hehn, A.; Didierian, L. *Trends Plant Sci.* **2000**, *5*, 116-123.
17. Bernadou, J.; Meunier, B. *Adv.Synth.Catal.* **2004**, *346*, 171-184.
18. Woggon, W. D. *Acc.Chem.Res.* **2005**, *38*, 127-136.
19. Mansuy, D. *Coord.Chem.Rev.* **1993**, *125*, 129-141.
20. Ji H.B.; She Y.B. *Green Oxidation and Reduction*; China Petrochemical Press : Beijing, 2005.
21. Zhou, X. T.; Ji, H. B.; Pei, L. X.; She, Y. B.; Xu, J. C.; Wang, L. F. *Chin.J.Org.Chem.* **2007**, *27*, 1039-1049.
22. Khavasi, H. R.; Davarani, S. S. H.; Safari, N. *J.Mol.Catal.A* **2002**, *188*, 115-122.
23. Maraval, V.; Ancel, J. E.; Meunier, B. *J.Catal.* **2002**, *206*, 349-357.
24. Barkanova, S. V.; Laliya, O. L. *J.Porphyrins Phthalocyanines* **1999**, *3*, 180-187.
25. Naik, R.; Joshi, P.; Umbarkar, S.; Deshpande, R. K. *Catal.Comm.* **2005**, *6*, 125-129.
26. Balakrishnan, T.; Palani, T. *J.Appl.Polym.Sci.* **2000**, *77*, 104-111.
27. Rismayani, S.; Fukushima, M.; Sawada, A.; Ichikawa, H.; Tatsumi, K. *J.Mol.Catal.A* **2004**, *217*, 13-19.
28. Monti, D.; Pastorini, A.; Mancini, G.; Borocci, S.; Tagliatesta, P. *J.Mol.Catal.A* **2002**, *179*, 125-131.
29. Nam, W.; Kim, I.; Kim, Y.; Kim, C. *Chem.Comm.* **2001**, 1262-1263.
30. De Paula, R.; Simoes, M. M. Q.; Neves, M. G. P. M.; Cavaleiro, J. A. S. *Catal.Comm.* **2008**, *10*, 57-60.
31. Srinivas, K. A.; Kumar, A.; Chauhan, S. M. S. *Chem.Comm.* **2002**, 2456-2457.
32. Vinhado, F. S.; Gandini, M. E. F.; Yamamoto, Y.; Silva, A. M. G.; Simoes, M. M. Q.; Neves, M. G. P. M.; Tome, A. C.; Rebelo, S. L. H.; Pereira, A. M. V. M.; Cavaleiro, J. A. S. *J.Mol.Catal.A* **2005**, *239*, 138-143.
33. Nam, W.; Oh, S.-Y.; Sun, Y. J.; Kim, J.; Kim, W.-K.; Woo, S. K.; Shin, W. *J.Org.Chem.* **2003**, *68*, 7903-7906.
34. Han, J. H.; Yoo, S. K.; Seo, J. S.; Hong, S. J.; Kim, S. K.; Kim, C. *Dalton Trans.* **2005**, 402-406.
35. Groves, J. T.; Nemo, T. E.; Myers, S. E. *J.Am.Chem.Soc.* **1979**, *101*, 1032-1033.

36. Merlau, M. L.; Grande, W. J.; Nguyen, S. T.; Hupp, J. T. *J.Mol.Catal.A* **2000**, *156*, 79-84.
37. Guo, C. C.; Liu, X. Q.; Li, Z. P.; Guo, D. C. *Appl.Catal.A* **2002**, *230*, 53-60.
38. Hill, C. L. *Nature* **1999**, *401*, 436-437.
39. Neumann, R.; Dahan, M. *Nature* **1997**, *388*, 353-355.
40. Qi, J. Y.; Qiu, L. Q.; Lam, K. H.; Yip, C. W.; Zhou, Z. Y.; Chan, A. S. C. *Chem.Commun.* **2003**, 1058-1059.
41. Sheldon, R. A. *Metal-Catalyzed Oxidations of Organic Compounds*; Academic Press: New York, 1981.
42. Simandi, L. I. *Dioxygen Activation and Homogeneous Catalytic Oxidation*; Elsevier: Amsterdam, 1991.
43. Shilov, A. E.; Shul'pin, G. B. *Chem.Rev.* **1997**, 2879-2932.
44. Groves, J. T.; Han, Y. Z.; Ortiz de Montellano, P. R. *Cytochrome P-450. Structure, Mechanism and Biochemistry*; Plenum: New York, 1995.
45. Meunier, B.; Robert, A.; Prati, G.; Bernadou, J. In *Porphyrin Handbook; Metalloporphyrins in catalytic oxidations and oxidative DNA cleavage*. Academic Press: San Diego, Calif, 2000.
46. Uchida, K.; Soma, M.; Naito, S.; Onishi, T.; Tamaru, K. *Chem.Lett.* **1978**, 471-474.
47. Ji, L. N.; Liu, M.; Hsieh, A. K.; Andy Hor, T. S. *J.Mol.Catal.* **1991**, *70*, 247-257.
48. Lyons, J. E.; Ellis, P. E. *J.Catal.* **1995**, *155*, 59-73.
49. Grinstaff, M. W.; Hill, M. G.; Labinger, J. A.; Gray, H. B. *Science* **1994**, 1313.
50. Moore, K. T.; Horvath, I. T.; Therien, M. J. *Inorg.Chem.* **2000**, *39*, 3125-3139.
51. Guo, C. C.; Chu, M. F.; Liu, Q.; Liu, Y.; Guo, D. C.; Liu, X. Q. *Appl.Catal.A* **2003**, *246*, 303-309.
52. Yuan, Y.; Ji, H. B.; Chen, Y. X.; Han, Y.; Song, X. F.; She, Y. B.; Zhong, R. G. *Org.Process Res.Dev.* **2004**, *8*, 418-420.
53. Punniyamurthy, T.; Velusamy, S.; Iqbal, J. *Chem.Rev.* **2005**, *105*, 2329-2363.
54. Luts, T.; Frank, R.; Suprun, W.; Fritzsche, S.; Hey-Hawkins, E.; Papp, H. *J.Mol.Catal.A* **2007**, *273*, 250-258.
55. Serafimidou, A.; Stamatis, A.; Louloudi, M. *Catal.Commun.* **2008**, *9*, 35-39.
56. Castaman, S. T.; Nakagaki, S.; Ribeiro, R. R.; Ciuffi, K. J.; Drechsel, S. M. *Journal of Molecular Catalysis A-Chemical* **2009**, *300*, 89-97.
57. Groves, J. T.; Nemo, T. E. *J.Am.Chem.Soc.* **1983**, *105*, 5786-5791.
58. Tabushi, I.; Morimitsu, K. *Tetrahedron Lett.* **1986**, *27*, 51-54.
59. Tabushi, I.; Yazaki, A. *J.Am.Chem.Soc.* **1981**, *103*, 7371-7373.
60. Tabushi, I.; Kodera, M.; Yokoyama, M. *J.Am.Chem.Soc.* **1985**, *107*, 4466-4473.
61. Tsuda, Y.; Takahashi, K.; Yamaguchi, T.; Matsui, S.; Komura, T. *J.Mol.Catal.A* **1998**, *130*, 285-295.
62. Tsuda, Y.; Takahashi, K.; Yamaguchi, T.; Matsui, S.; Komura, T.; Nishiguchi, I. *J.Mol.Catal.A* **1999**, *138*, 145-153.
63. Bedioui, F.; Devynck, J.; Bied-Charreton, C. *J.Mol.Catal.A* **1996**, *113*, 3-11.
64. Leduc, P.; Battioni, P.; Bartoli, J. F.; Mansuy, D. *Tetrahedron Lett.* **1988**, *29*, 205-208.
65. Mukaiyama, T.; Yamada, T.; Nagata, T.; Imagawa, K. *Chem.Lett.* **1993**, 327-330.
66. Yamada, T.; Takai, T.; Rhode, O.; Mukaiyama, T. *Bull.Chem.Soc.Jpn.* **1991**, *64*, 2109-2117.
67. Nagata, T.; Imagawa, K.; Yamada, T.; Mukaiyama, T. *Chem.Lett.* **1994**, 1259-1262.
68. Qi, J. Y.; Li, Y. M.; Zhou, Z. Y.; Che, C. M.; Yeung, C. H.; Chan, A. S. C. *Adv.Synth.Catal.* **2005**, *347*, 45-49.

69. Ravikumar, K. S.; Barbier, F.; Begue, J. P.; Delpon, D. B. *Tetrahedron* **1998**, *54*, 7457-7464.
70. Raja, R.; Sankar, G.; Thomas, J. M. *Chem. Commun.* **2009**, *9*, 829-830.
71. Ellis, S.; Kozhevnikov, I. V. *J.Mol.Catal.A* **2002**, *187*, 227-235.
72. Mandal, A. K.; Iqbal, J. *Tetrahedron* **1997**, *53*, 7641-7648.
73. Zhou, X. T.; Ji, H. B.; Xu, H. C.; Pei, L. X.; Wang, L. F.; Yao, X. D. *Tetrahedron Lett.* **2007**, *48*, 2691-2695.
74. Zhou, X. T.; Tang, Q. H.; Ji H.B. *Tetrahedron Lett.* **2009**, DOI: 10.1016/j.tetlet.2009.09.061.
75. Groves, J. T.; Quinn, R. *Inorg.Chem.* **1984**, *23*, 3844-3846.
76. Groves, J. T.; Quinn, R. *J.Am.Chem.Soc.* **1985**, *107*, 5790-5792.
77. Jensen, D. R.; Schultz, M. J.; Mueller, J. A.; Sigman, M. S. *Angew.Chem., Int.Ed.* **2003**, *42*, 3810-3813.
78. Egami, H.; Shimizu, H.; Katsuki, T. *Tetrahedron Lett.* **2005**, *46*, 6049-6052.
79. Sharma, V. B.; Jain, S. L.; Sain, B. *J.Mol.Catal.A* **2004**, *212*, 55-59.
80. Gamez, P.; Arends, I. W. C. E.; Sheldon, R. A.; Reedijk, J. *Adv.Synth.Catal.* **2004**, *346*, 805-811.
81. Baciocchi, E.; Belvedere, S. *Tetrahedron Lett.* **1998**, *39*, 4711-4714.
82. Neys, P. E. F.; Vankelecom, I. F. J.; Parton, R. F.; Dehaen, W.; Labbe, G.; Jacobs, P. A. *J.Mol.Catal.A* **1997**, *126*, L9-L12.
83. Wietzerbin, K.; Meunier, B.; Bernadou, J. *Chem.Commun.* **1997**, 2321-2322.
84. Han, J. H.; Yoo, S. K.; Seo, J. S.; Hong, S. J.; Kim, S. K.; Kim, C. *Dalton Trans.* **2005**, 402-406.
85. Du, G. D.; Woo, L. K. *J.Porphyr.Phthalocya.* **2005**, *9*, 206-213.
86. Ji, H. B.; Yuan, Q. L.; Zhou, X. T.; Pei, L. X.; Wang, L. F. *Bioorg.Med.Chem.Lett.* **2007**, *17*, 6364-6368.
87. Sheldon, R. A.; Van Bekkum, H. *Fine Chemicals through Heterogeneous Catalysis*; Wiley-VCH Verlag GmbH & Co: Weinheim, 2001.
88. Rebelo, S. L. H.; Simoes, M. M. Q.; Neves, M. G. P. M.; Cavaleiro, J. A. S. *J.Mol.Catal.A* **2003**, *201*, 9-22.
89. Zhou, X. T.; Ji, H. B.; Yuan, Q. L.; Xu, J. C.; Pei, L. Y.; Wang, L. F. *Chin.Chem.Lett.* **2007**, *18*, 926-928.
90. Baeyer, A.; Villiger, V. *Ber.Deut.Chem.Ges.* **1899**, *32*, 3625-3633.
91. Krow, G. R. *Comprehensive Organic Synthesis*; Pergamon Press: New York, 1991.
92. Chisem, I. C.; Chisem, J.; Clark, J. H. *New.J.Chem.* **1998**, *22*, 81-82.
93. Patai, S.; Rappoport, Z. *Synthesis of sulfones, sulfoxides, and cyclic sulfides*; John Wiley: Chichester, 1994.
94. Oae, S.; Watanabe, Y.; Fujimori, K. *Tetrahedron Lett.* **1982**, *23*, 1192.
95. Marques, A.; Marin, M.; Ruasse, M. F. *J.Org.Chem.* **2001**, *66*, 7588-7595.
96. Baciocchi, E.; Gerini, M. F.; Lapi, A. *J.Org.Chem.* **2004**, *69*, 3586-3589.
97. Zhou, X. T.; Ji, H. B.; Yuan, Q. L.; Xu, J. C.; Pei, L. X.; Wang, L. F. *Chin.J.Chem.* **2008**, *26*, 1114-1118.
98. Fernandez, I.; Khair, N. *Chem.Rev.* **2003**, *103*, 3651-3705.
99. Carreno, M. C. *Chem.Rev.* **1995**, *95*, 1717-1760.
100. Holland, H. L. *Chem.Rev.* **1988**, *88*, 473-485.
101. Lu, W. Y.; Bartoli, J. F.; Battioni, P.; Mansuy, D. *New.J.Chem.* **1992**, *16*, 621-628.
102. Zhou, X. T.; Ji, H. B.; Cheng, Z.; Xu, J. C.; Pei, L. X.; Wang, L. F. *Bioorg.Med.Chem.Lett.* **2007**, *17*, 4650-4653.

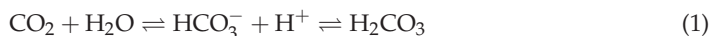
The Carbonic Anhydrase as a Paragon: Theoretical and Experimental Investigation of Biomimetic Zinc-catalyzed Activation of Cumulenes

Burkhard O. Jahn, Wilhelm A. Eger and Ernst Anders
Friedrich-Schiller-University Jena
Germany

1. Introduction

Biomimetics as an interdisciplinary concept involves learning from and imitating of nature using appropriate models. The mimicry of biological models does not only consist of the construction of engineering systems and modern technology, furthermore, it is able to be a guide for designing and architecturing in the complete range of natural sciences. In particular, the actual development of novel and uncommon chemical reactions is aimed to apply high optimized, biochemical processes to laboratory and industrially usable syntheses. Especially enzymes stand in the visual focus as highly efficient and almost extreme specialized catalysts, as nature has had a long time to develop and optimize a wide diversity of life. Nearly every organism owns different tissues, motion types, sensing functions and surviving instincts and the basis for all of these properties are highly efficient catalyzed chemical reactions. Organisms have not only to synthesize huge biopolymers for growth, but also to provide small molecules for signal transduction, energy transfers or regulation processes. Therefore, it is obvious that the study of those reactions not only gives insights in important biochemical processes, but also suggests new chemical pathways to use in synthesis or other related appliances. The possibilities of biomimetics in chemistry are outlined on the basis of the enzyme carbonic anhydrase. As this enzyme is one of the most efficient catalysts originated by nature, the investigation of such a catalytical active protein enriches not only the knowledge of biological and biochemical mechanisms and their mode of action, but also gives detailed information about the active center inside of the enzyme. In that way, one can fathom out important factors for the growth and development as well as for the investigation of diseases and glitches.

In this chapter we describe the enzymatic metal mediated reaction of the cumulene system carbon dioxide with water and its extension to the bio-analogue activation of further isoelectronic cumulenes (carbonyl sulfide, isothiocyanate and allene).



Most of the theoretical (DFT calculations) and experimental results were obtained by the authors of this chapter or in direct collaboration with former members of the Jena group (Dr. Stephan Schenk, Dr. Johannes Notni) and other researchers: Prof. Dr. Jürgen Kesselmeier (Mainz, Germany), Prof. Dr. Heinrich Vahrenkamp (Freiburg, Germany), Prof. Dr. Eckhard

Dinjus and Prof. Dr. Manfred Doering (Karlsruhe, Germany), Prof. Dr. Wolfram Koch (Frankfurt, Germany), Prof. Dr. James Weston (La Plata, Argentina), Prof. Dr. Detlef Schröder (Prag, Czech), Prof. Dr. Helmut Schwarz (Berlin, Germany), Prof. Dr. Andrea Bottoni (Bologna, Italy) and Dr. Sten Nilsson Lill (Göteborg, Sweden). We made significant efforts to cite the relevant contributions by others; nevertheless, the discussion of their results will be very brief in order to keep this chapter within a reasonable length.

2. The Model Enzyme Carbonic Anhydrase

Carbonic anhydrases (CA) are an ancient enzyme class most likely as old as life on earth. As every organism contains CA, they might be one of the most important enzyme classes. Naturally, these enzymes catalyze the reversible reaction of carbon dioxide with water to bicarbonate (see equation 1). They belong to the enzyme class of lyases, which generally catalyzes the cleavage of molecules.

At present all CAs are divided into six classes (α - ζ class). All classes developed independently and therefore are examples of convergent evolution (Hewett-Emmett & Tashian, 1996). The representatives of the α class are found in all mammals and can be subdivided into currently fifteen isoforms. Depending on the individual structure, each isoform fulfills other specialized tasks in biochemical processes. The isoform CA-I was identified in erythrocytes (Lowe et al., 1990) and is the mostly spread protein beside of globuline and responsible for the conversion of the badly water soluble gas carbon dioxide into bicarbonate, which is completely soluble and hence better transportable in water. For this reason CA-I is the base for efficient respiration. CA-II, which is one of the most active isoforms, owns turn over numbers near the diffusion controlled limit ($k_{cat} = 620\,000\text{ sec}^{-1}$) (Gibbons & Edsall, 1964) and an acceleration factor of 10^7 compared to the uncatalyzed reaction (Lindsog, 1997). Deficiency of CA-II leads to osteopetrosis with renal tubular acidosis and cerebral calcification (Sly et al., 1983). While CA-IV is involved in the ionic transport mechanisms in the endothel of the cornea (Sun et al., 2008), CA-V is placed in the mitochondria and used as a supplier for HCO_3^- in the urea cycle (Dodgson & Forster, 1986). CA-VII and CA-VIII are involved in neuronal signal forwarding and the provision of neurotransmitters in the central nervous system (Ruusuvuori et al., 2004; Yan et al., 2007). Another point of interest is the role of CAs in the development of cancer, as the activity of CA-IX and CA-XII could be proven in several tumor cells and tissues, for example breast, kidney or cerebral cancer (Barnett et al., 2008; Brennan et al., 2006; Chrastina et al., 2003; Jarvela et al., 2008).

2.1 Insights into the Enzymatic Mechanism

All CAs contain one zinc(II) cation as a cofactor (Keilin & Mann, 1939) with the exception of ζ -CAs, which possess a diatomic metal center. The central metal is not constricted to zinc in those CAs due to low zinc concentrations in the habitat of organisms containing them (Lane et al., 2005). In the catalytic core of α -class CAs the zinc ion is complexed by three histidine amino acid residues (His94, His96, His119) and a water or rather hydroxide ligand depending on the intracellular *pH* value (see Figure 1).

After getting into the hydrophobic pocket, CO_2 becomes immobilized by a hydrogen bridging bond to Thr199, which plays the role of a gatekeeper to the active center. The zinc bound hydroxide ion then initiates the hydrolysis by a nucleophilic attack on CO_2 . In the following step the produced bicarbonate is displaced by a water molecule, which is subsequently deprotonated by the help of a proton relays to His64 to give zinc bound hydroxide for the next

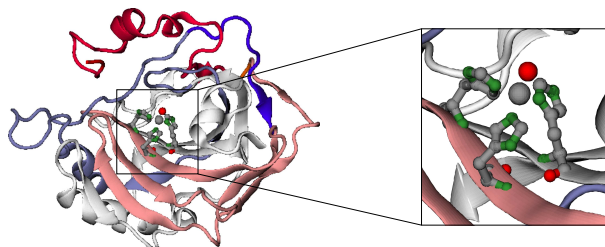


Fig. 1. An X-ray structure of CA-II depicted as a ribbon model (Eriksson *et al.*, 1988). In the representation of the active center hydrogens are not displayed.

turn of catalysis. This relay shuttle consists of several intra- and intermolecular proton shifts in a row.

The step between the nucleophilic attack and the replacement of bicarbonate was the topic of a controversial discussion in the past. While Lipscomb *et al.* (Liang & Lipscomb, 1987; Lipscomb, 1983) favored a proton shift between the two oxygens, the direct coordination by an oxygen and a rotation step was postulated by Lindskog *et al.* (Lindskog, 1984; 1997). In fact, depending on the complexity of the used model and the used quantumchemical methods respectively, each mechanism can be the favored one. Additionally, the exchange of bicarbonate for water can occur without direct coordination of an oxygen of CO_2 (see Figure 2). For further mechanistic aspects see (Mauksch *et al.*, 2001).

As the electronic configuration of the zinc(II) cation has a closed 3d shell, which is very stable, zinc compounds contain this ion nearly without any exception. Additional results of this stable state are a fairly low redox activity of the zinc(II) ion, no stabilization of the ligand field and a wide range of coordination numbers going from two to eight.

2.2 Design of Biomimetic Chemical Models

The properties of a capable model describing the biomimetics of CA depend significantly on the aim of the application. Firstly, it is important, whether the model is used in an experimental environment or for theoretical purposes, and secondly, it depends on the goal of examination.

At least a model for simulating the catalytic core of CA needs an appropriate ligand sphere and an additional nucleophilic ligand, so one of the most simplified models is the $[\text{Zn}(\text{NH}_3)_3\text{OH}]^+$ complex (see Figure 3).

2.2.1 Model for Computational Purposes

This model is only suitable for theoretical aspects, as it is not stable in solution and consists beside the zinc ion and the hydroxide ligand only of three ammonia ligands, which are a simplification of the histidine amino acid ligand sphere. Nevertheless, the so called ammonia model fulfills the needs of a theoretical model very well. One major aspect regarding calculations in chemistry is the number of atoms in the molecule. As the computation time correlates to the number of atoms like N^3 for density functional theory (DFT) and N^5 or N^6 for Post-Hartree-Fock (*ab initio*) methods, it is important to keep the molecule as small as possible for efficient calculations.

The second major aspect of choosing a model for computational chemistry is its ability to describe the geometric and electronic properties of a molecule as exact as possible in comparison

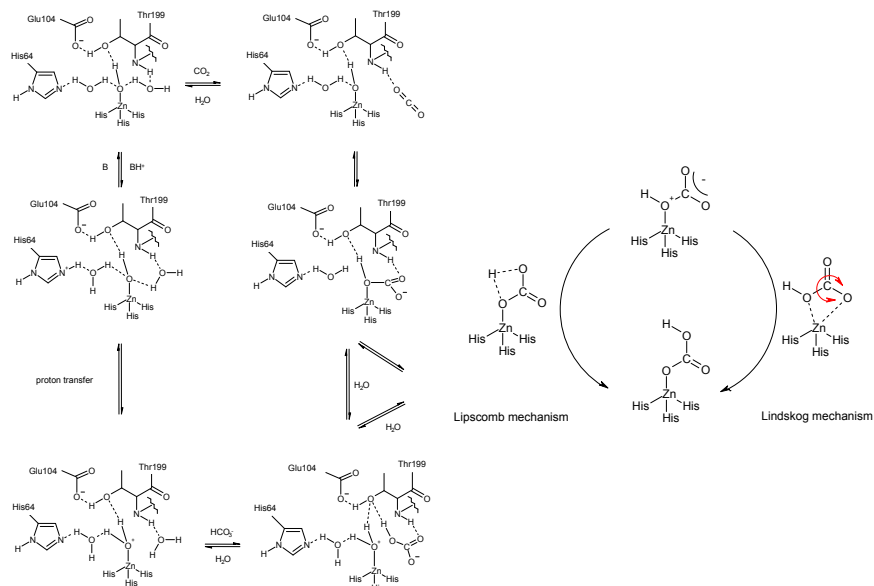


Fig. 2. Postulated enzymatic mechanism for α -CAs including the Lindskog and Lipscomb variants (Bertran et al., 1992; Krishnamurthy et al., 2008).

to reality. Describing the reaction in the real enzyme, it is better to have a bigger system, which also pays attention to parts of the peptidic backbone and its role in the mechanistic pathway. A good choice for this aim is the model of Bottoni *et al.* (Bottoni et al., 2004), which includes the mechanistically important amino acid residues Glu106 und Thr199 (see Figure 3). If it is the aim to apply the biomimetic principle to a model in synthesis, it is important to have a stable and simple molecule, what provides the basic features of the catalytic core. Depending on the reaction, the nucleophilic ligand can be varied, e. g. to a thiolate ligand.

As this chapter describes the transfer of the biomimetic principles from the enzyme CA to a model used in synthesis, the Bottoni model is not appropriate. Beneath the ammonia model one can imagine a more complex one containing imidazole rings instead of ammonia ligands. Although it resembles the ligand sphere in the catalytic core of CA better, it is not worth the calculational effort. Firstly, the imidazole rings in the enzyme have a fixed position, whereas they can turn in the model, and secondly, they do not have any significant influence on the electronic situation at the nucleophilic part of the model compared to an ammonia ligand sphere (see Table 1).

The natural charges of the ammonia model are also very similar to those calculated for the model bearing a $[12]\text{aneN}_3$ ligand (see Table 1). Contrary to the model using imidazole ligands, the ammonia and the $[12]\text{aneN}_3$ model possess amino functions directly connected to the metal center, so the ammonia ligand sphere would resemble the situation at the $[12]\text{aneN}_3$ complex better than the imidazole model. Keeping all these arguments in mind the ammonia complex is the appropriate model for our purposes. It is small and therefore can be calculated very quickly, and it is accurate enough for transferring the biomimetic principle from the catalytic core to a certain complex in synthesis. The ammonia model has already proved

model	Zn	O	bond length [Å]
human CA-II	+1.66	-0.99	1.878
ammonia	+1.62	-1.32	1.849
imidazole	+1.65	-1.31	1.879
[12]aneN ₃	+1.61	-1.31	1.851
Bottoni	+1.63	-1.32	1.910

Table 1. Natural charge distribution and Zn-O bond lengths in several CA models (calculated at the B3LYP/6-311+G(d,p) level) in comparison to the native CA.

its efficiency in extensive theoretical investigations (Bräuer et al., 2002; Eger et al., 2009; Jahn et al., 2008; Mauksch et al., 2001; Schenk et al., 2004; Schröder et al., 2003; Sinnecker et al., 2001) and serves as the structural fundament for examining reaction pathways in case of CA.

2.2.2 Model for Experimental Purposes

In the last fifty years a lot of zinc complexes were synthesized with the aim to create a good CA simulating model. Some of them are depicted in Figure 3. Beneath the nucleophilic residue, the ligand is responsible for almost all properties of the complexes like solubility, complex stability and structure. But it also has a significant effect on the catalytic effectivity of the model, as it defines the geometry in the close vicinity of the nucleophilic ligand. Most of the synthesized ligands have either a tripodal or macrocyclic geometry (see Figure 3). To the variety of ligands used for modelling CA belong tris(2-benzimidazolylmethyl)amine (BIMA) (Brandsch et al., 1997; Echizen et al., 2004; Nakata et al., 1997), different azamacrocycles, such as 1,5,9-triazacyclododecane ([12]aneN₃) (Kimura et al., 1990; Richman & Atkins, 1974), further tris(imidazolyl)carbinole (TIC) (Tang et al., 1978), tris(imidazolyl)phosphane (TIP) (Kunz et al., 2003), 1,3,5-triaminocyclohexane (tach) (Bowen et al., 1996; Cronin et al., 1996; Cronin & Walton, 2003; Urbach et al., 1968) and the representatives of hydrotris(pyrazolyl)borates (Tp) (Trofimenko, 1966; 1967; Yang et al., 1995), tris(pyrazolyl)methanes (Tp_m) (Sánchez-Méndez et al., 2004; Zvargulis et al., 1995) or tris(pyrazolyl)methanesulfonates (Tp_{ms}) (Kläui et al., 2000).

In general, complexes containing a macrocyclic ligand possess a higher complex constant and thus are more stable, this is a result of the macrocyclic effect. Common macrocyclic ligands are cyclic azaethers e.g. cyclen ([12]aneN₃) and cyclam ([12]aneN₄), whereas cyclam does not simulate the ligand sphere of CA very well, but surprisingly has better reaction rates than cyclen. With a pK_a of 7.3 [Zn([12]aneN₃)OH]⁺ is very close to the pK_a value of CA-II (about 7), whereas [Zn([12]aneN₄)OH]⁺ shows a pK_a value about 8.1 (Riccardi & Cui, 2007; Zhang & van Eldik, 1995). In aqueous solution, these complexes exist in a pH dependent equilibrium with their protonated forms, [Zn([12]aneN_x)OH₂]²⁺. Zinc hydroxide complexes of such three- and four-dentate azacycloalkanes react with CO₂ to bi- resp. mono-dentate hydrogencarbonate complexes (Schrodt et al., 1997). As [Zn([12]aneN₄)OH]⁺ coordinates this substrate only on one coordination point, van Eldik *et al.* postulated this complex to be a better CA simulating model. The azacycloalkane based models form a bridge between theory and experiment due to their easy access in synthesis and good usability for quantumchemical calculations. For a model describing the active center of CA, some criteria regarding the K_D value have to be fulfilled (Parkin, 2000; 2004). The K_D value for CA-II was measured at $K_D = 4$ pM ($pH = 7$),

what is important to prevent the metal and the ligand from dissociating, and therefore the presented models are appropriate, as they reach K_D values in the nanomolar range.

Another thoroughly investigated ligand family consists of tripodal trispyrazolyl ligands bearing either a carbon or a boron atom and trisimidazolyl ligand respectively bearing a carbon or a phosphor atom. These complexes also have very good complex constants and they allow creating different reaction pockets by varying the residues of the pyrazole and imidazole rings. The creation of such hydrophobic pockets avoids the multiple complexation of the ligand by the zinc ion. Contrary to the macrocyclic complexes those compounds can occur as neutral or cationic complexes depending on the element used at the tripodal position. The formation of cationic complexes is of importance for correctly modelling the catalytic centre of CA. The application of a charged ligand would necessarily result in a model system that does not reflect the electronic properties of the active site.

Summarizing this, both model concepts - azamacrocyclic and tripodal ligands - are appropriate to be used to apply the reaction principle of CA as chemical biomimetics to develop new syntheses. Although they have a lot in common, the differences between them define the cases they can be used in. As the azamacrocyclic complexes do not possess a hydrophobic pocket around the nucleophilic ligand, they provide a better accessibility of the catalytic center. This might be interesting when reacting bulky substrates. But the absence of this pocket gains a disadvantage as not all complexes are stable. In particular the hydrosulfide and alkyl thiolate complexes are not available. As there exist not only three- but also four-dentate azamacrocyclic ligands, the corresponding complexes can also be used to simulate the biomimetics of human CA-II. Zinc complexes of cyclic azaethers possess very high complex constants because of the macrocyclic effect, so they can be used under very harsh conditions without getting destroyed.

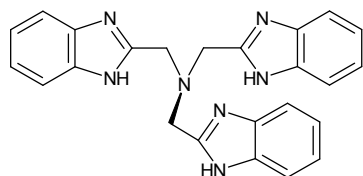
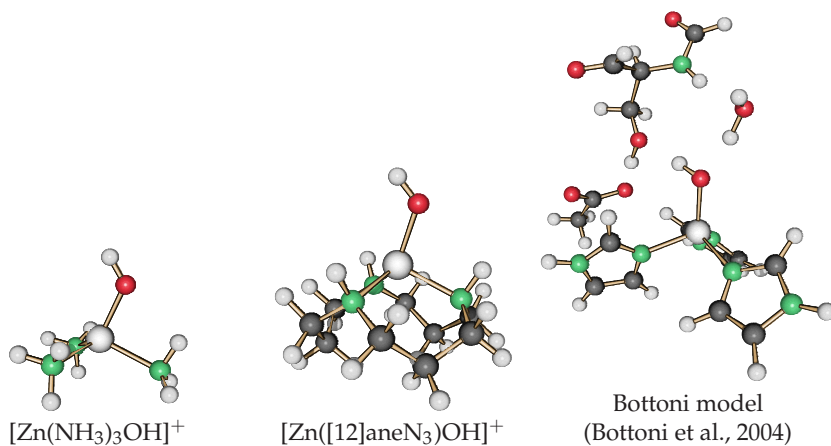
In comparison, tripodal ligands can not only simulate a hydrophobic pocket, but provide the possibility to measure the reaction rates depending on the size and composition of it. Depending on the element used at the tripodal position, they are neutral or cationic systems. Thus some tripodal ligands provide complexes, which are independent of dealing with an counterion.

3. Details about the Quantumchemical Calculations

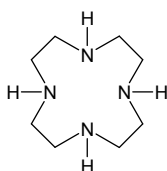
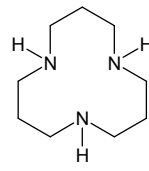
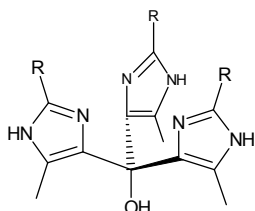
In analogy to preceding investigations on the mode of action of CA, we used density functional theory (DFT) calculations to propose a mechanism. All calculations were realized using the Gaussian 03 (Frisch et al., 2004) program package, whereas Natural Bond Orbital (NBO) analyzes were performed using NBO 5.0 (Glendening et al., 2001). Stable structure geometries were characterized by a frequency calculation, in which energetic minima must not have a imaginary mode, whereas the presence of exactly one imaginary frequency characterizes a transition state. The visualization of this mode normally illustrates the reaction path, but in several cases an intrinsic reaction coordinate (IRC) calculation is appropriate to verify the correct products and educts corresponding to a transition state.

4. Carbonyl Sulfide (COS), an Important Atmospheric Trace Gas

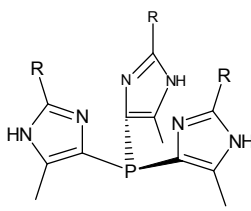
For a better understanding, in this part of our chapter we additionally will give a few explanations of the biological backgrounds. Due to the enormous catalytic effect of CA, almost all living organisms use these enzymes for important CO_2 exchange processes with the atmosphere. However, it is less well known that CA is also involved in the fixation of the atmo-



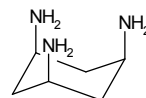
BIMA

 $[\text{12}]\text{aneN}_4$  $[\text{12}]\text{aneN}_3$ 

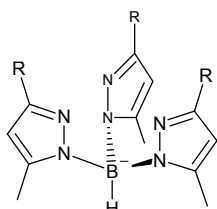
TIC



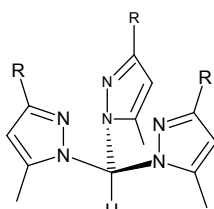
TIP



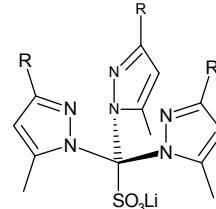
tach



Tp



Tpm



Tpms

Fig. 3. Selection of possible CA models as well as several ligands used to construct CA simulating complexes.

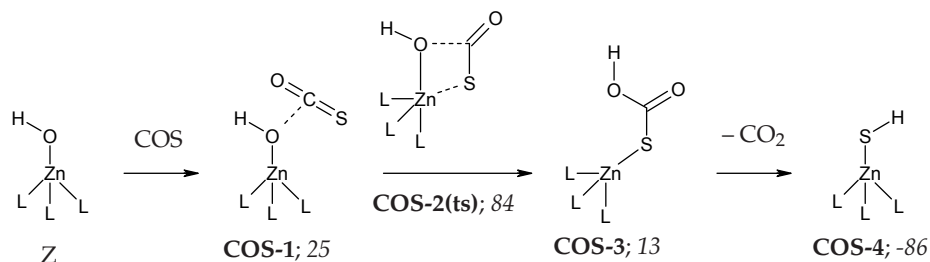


Fig. 4. Calculated mechanism of the fixation of COS, calculated at the B3LYP/6-311+G(d,p) level of theory (free energy values given in kJ/mol).

spheric trace gas carbonyl sulfide (COS) (Sandoval-Soto et al., 2005). As more recently and thoroughly investigated, COS is the most stable reduced sulfur compound in the atmosphere with a lifetime of 1-7 years. CA plays a significant role in the regulation of COS in the atmosphere and in the global distribution of sulfur (Schenk et al., 2005). Interestingly, it contributes indirectly to the global climate due to the fact that degradation of COS accounts for sulfate particles in the stratospheric aerosol layer which reflects solar radiation. Its main sources are the oceans where it is thought to be generated by photooxidation of sulfur-containing amino acids. Main sink for COS is the vegetation. The consumption of COS by many organisms, such as higher plants, algae, and lichens (Kuhn & Kesselmeier, 2000), was found to be CA-dependent. Furthermore, CA plays an important role in the interpretation of toxicity of COS. During COS consumption, H₂S is formed, which has been recognized almost thirty years ago as being the actual toxin responsible for the noxious effect of this heterocumulene (Chengelis & Neal, 1980). This has been confirmed by the finding that inhibition of CA lowers the mortality of insects upon exposition to COS, by lowering the rate of hydrolysis. In addition, CA-dependence of H₂S formation upon COS consumption has been proven for the example of algae. It can therefore be considered as being accepted that COS is a natural substrate of CA, which catalyzes its irreversible hydration according to equation 2.



The mechanism of this CA-catalyzed COS fixation according to Figure 4 has been investigated by some of us using the established computational ammonia model (Schenk et al., 2004). The reaction follows the same principle as the CO₂ reaction. The attack of the zinc-bound hydroxide occurs exclusively at the C=S bond and results in a four-centre transition structure **COS-2(ts)**, whereby a zinc-bound thiocarbonate **COS-3** is formed. Although this structure could not be observed in an experimental investigation until now, there is more than circumstantial evidence for its intermediate existence based upon our detailed calculations and related structures observed in experiments. By a water-assisted proton transfer, CO₂ is formed which is expelled and the zinc hydrosulfide complex **COS-4** is obtained. This species is stabilized by a strong ZnS bond. As a consequence, we initially assumed that the enzyme must be deactivated by this reaction. However, this contradicts the generally accepted finding that in the course of COS fixation H₂S is formed (Bleziinger et al., 2000). Furthermore, we detected an interesting side path in this reactions cascade: A water molecule helps to regenerate the original zinc hydroxide complex from the hydrosulfide complex **COS-4** and the formation of H₂S. Nevertheless, at the beginning of our investigations the mode of reactivation of the catalytic

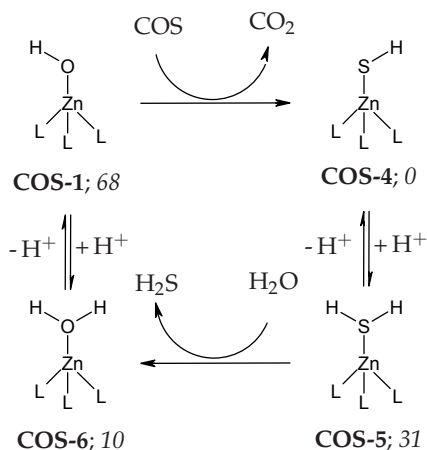


Fig. 5. Transformation of COS by the CA model complex $[\text{Zn}([\text{12}] \text{aneN}_3)\text{OH}]^+$ and mechanism of regeneration of the catalytic domain, calculated at the C-PCM(B98/G3Large)//C-PCM(B3LYP/6-311+G(d,p)) level of theory (free energy values given in kJ/mol relative to COS-4)

domain of the hydrosulfide analogue of CA was an open question, which is of special interest since some organisms apparently utilize this H_2S production process and some additional reactions steps as their only source of sulfur (Kuhn & Kesselmeier, 2000).

In case the organism is growing in sulfate-rich environment, it necessarily will not require the sulfide that stems from COS fixation. The sulfur will then be expelled in form of H_2S , since this is the main process plants utilize to free themselves from excess sulfur of any origin (Saito, 2004). However, plants which grow on sulfate deficient soils actually depend on atmospheric sources of sulfur. H_2S and particularly SO_2 are commonly considered as being the most important atmospheric sulfur compounds taken up by plants (Bertini et al., 1985). Nonetheless, in some areas where the atmospheric supply of these compounds is too low to meet the requirement of plants, H_2S formed by the COS metabolism becomes an important factor. We thus elucidated a possible mechanism for the final step of this process in order to achieve its complete understanding also at a molecular scale.

As explained above and depicted in the scheme in Figure 4, the active catalyst **Z** reacts with COS and is transformed into the zinc hydrosulfide **COS-4** (stabilized by 68 kJ/mol) (Schenk et al., 2004). Protonation resulting in the hydrogen sulfide complex **COS-5** requires only 31 kJ/mol. It can thus be assumed that **COS-4** should be protonated at least to a small extent. The replacement of H_2S by a water molecule is now enforced by two effects: First, the aquo complex **COS-6** is stabilized by 21 kJ/mol which is hardly surprising in view of the exceptionally weak coordination of H_2S ligands to zinc centres. Second, the dissociation of hydrogen sulfide is practically irreversible due to the fact that its concentration in the surrounding medium is negligible compared to water. The irreversibility of this ligand exchange ensures that all zinc-bound sulfur is eventually expelled, since the hydrosulfide protonation equilibrium (see equation 3) provides a small but constant amount of the neutral H_2S ligand which can easily dissociate.



As a consequence, the protonation of **COS-4** is the rate-determining step of the desulfuration reaction. Of course, this process is likely to proceed quite slowly. However, a minute overall reaction rate should be sufficient: due to the extraordinarily small atmospheric COS concentration, sulfur analog CA is present in only very small amounts. A fast regeneration is therefore not required. The final deprotonation of the intermediate **COS-6** results in the catalyst **COS-1**, which, according to our calculations, is endergonic by 58 kJ/mol. This deprotonation has already been extensively discussed in the context of CA-catalyzed CO₂ fixation since it is the initial step in generation of the active site, i. e. a representative of this interesting class of nucleophilic cations for which CA is the natural proton.

4.1 In vitro experimental investigations

Some years ago, a model reaction has been performed by Vahrenkamp and some of us which exemplifies the process of COS fixation (Bräuer et al., 2002). The trispyrazolylborato zinc hydroxide complex $\text{Tp}^{\text{Ph,Me}}\text{ZnOH}$ has been applied as the CA model (Notni, Schenk, Protoschill-Krebs, Kesselmeier & Anders, 2007). It has been reacted with COS, whereby CO₂ and the corresponding hydrosulfide complex $\text{Tp}^{\text{Ph,Me}}\text{ZnSH}$ comparable to **COS-4** were formed (see Figure 5). In contrast to the $[\text{Zn}([12]\text{aneN}_3)]^{2+}$ system, the $[\text{TpZn}]^+$ moiety is stable enough to bear a hydrosulfide ligand. The $\text{Tp}^{\text{Ph,Me}}\text{ZnOH}$ complex is thus excellently suited for modelling the calculated regeneration mechanism, particularly with regard to the similar deprotonation enthalpies encountered for the related trispyrazolylborato and azamacrocyclic complexes. At neutral *pH*, the reaction cascade stops at the stage of the hydrosulfide (**COS-4**). However, after repeating this reaction, we recently could demonstrate that at *pH* values below 4 the hydrosulfide ligand is apparently protonated. Upon treatment of trispyrazolylborato complex of **COS-4** with small portions of HClO₄, H₂S is formed, which can be removed from the solution by an argon stream. Since the trispyrazolylborato ligand is hydrolyzed at very low *pH*, the reaction mixture has to be kept at *pH* = 3 or above, which requires constant measurement and dropwise addition of HClO₄.

Further contributions to this subject have been made by Carrano *et al.* (Hammes et al., 2002) and Parkin *et al.* (Bergquist et al., 2003), both of whom isolated and characterized different examples of the $[\text{TpZnOH}_2]^+$ structure type with various anions. The latter authors have also shown that addition of base deprotonates the aquo ligand. From all these works with the trispyrazolylborato ligand, we derive the assumption of intermediate existence of the cation **COS-6**. We subsequently recovered the hydroxide complex **COS-1** from the alkalized solution of **COS-6** and identified it by NMR spectroscopy.

4.2 In vivo experimental investigations

The release of H₂S from cleavage of COS was investigated with the green alga *Chlamydomonas reinhardtii* as this organism contains extracellular CA localized on its outer cell membranes faced to environmental solution. Hence, the released H₂S can be expected to escape the biological metabolism quite easily. As shown in Figure 6, the release of H₂S is closely correlated to the consumption of COS but a substantial part of the expected H₂S is always missing. We assume either a metabolic consumption of H₂S and/or a loss of H₂S due to the technical needs using a headspace technique. The latter instance is most probable, as it is known that application of this technique may involve a loss of 30 to 40 % of the H₂S formed. A similar release of H₂S upon COS consumption could be reported for marine algae, although

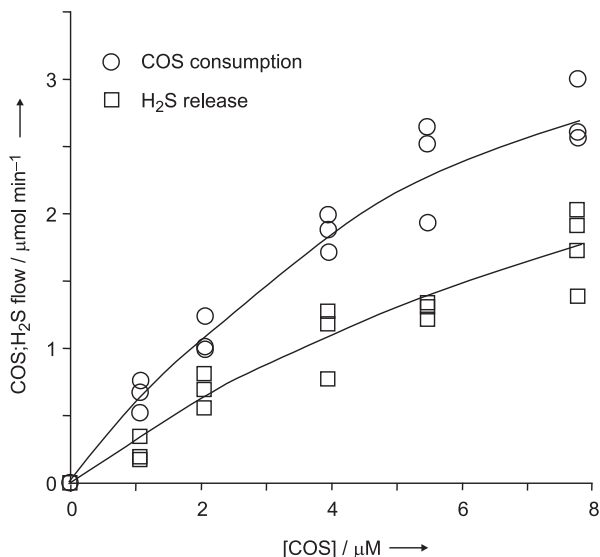
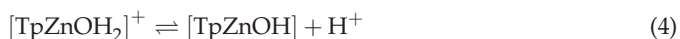


Fig. 6. COS consumption and H₂S production in correlation to increasing COS concentrations by the green alga *Chlamydomonas reinhardtii* grown under 0.03 % CO₂. Amount of algae per measurement accounts for 1.26 μg *Chl.* ml⁻¹. Measurements were performed in the light with 5 W/m in 25 mm barbital buffer at pH = 7.5. COS and H₂S in aqueous solutions were determined by a dynamic headspace technique coupled to GC-FPD analysis.

on significant lower activity levels which can be discussed as being caused by missing extracellular CA.

4.3 Discussion of the DFT calculations: Experiment meets theory

A DFT-calculation which is related to those presented in this work has been reported earlier by Parkin and coworkers (Bergquist et al., 2003). They investigated the deprotonation of a complex of the [TpZnOH₂]⁺ type according to equation 4.



For this reaction, they calculated a free energy of 1172 kJ/mol. This is substantially different to the deprotonation energy value we obtained for the zinc-bound water of the azamacrocyclic compound **COS-5** (58 kJ/mol). Although we used another model system, the energies should at least be of the same order of magnitude. Presumably, the difference results from the fact that in equation 4, the free energy of the proton has been set to zero by these authors. However, for calculations including solvent effects, the solvation free energy of the proton should be taken into account to obtain realistic deprotonation energies. For the total free energy of the proton in aquatic solution, we used a value of 1125 kJ/mol given in the literature. This value is the sum of the absolute free energy of the proton in the gas phase (26 kJ/mol) and its absolute solvation free energy (1099 kJ/mol). When this free energy value is added to the free energy of deprotonation reported by Parkin *et al.*, a corrected value of 47 kJ/mol is obtained. This is in very good agreement with our result. We therefore conclude that the selection of two

apparently completely different model systems, one with an azamacrocyclic and the other with a pyrazolyl type ligand, is not a problem. Apparently, the deprotonation energies of the zinc-bound water are very similar. Thus we assume that our experiment using the TpZnSH complex is suited to corroborate and illustrate the calculated mechanism. Although a true catalysis is not observed, the substrate COS can be transformed into CO₂ and H₂S in the presence of Tp^{Ph,Me}ZnOH just by altering the *pH* of the solution.

According to our calculations, the protonation free energies of the zinc-bound hydroxide and hydrosulfide differ by ca. 84 kJ/mol. This is in good agreement with our experimental observation that a fast desulfuration occurs only at *pH* values at which a zinc-bound water is not deprotonated. Nevertheless, a well-balanced *pH* at the active site of natural CA could allow both a predominantly deprotonated zinc-bound water ligand and small but sufficient protonation of the zinc-bound hydrosulfide. As we already pointed out above, we hold the view that a small amount of protonated hydrosulfide ligand at the zinc ion is sufficient for complete desulfuration of CA due to the fact that the dissociation of H₂S is practically irreversible. In our opinion, the calculated mechanism is thus very likely to occur the way it is depicted in Figure 5.

The role of other amino acid residues in the catalytic mechanism has been addressed in studies by Bottoni (Bottoni et al., 2004) and Liedl (Tautermann et al., 2003). They have demonstrated that some of the residues, especially Glu106 and Thr199, are directly involved in some steps of the CO₂ fixation. It has also been commented upon that a histidine residue in the enzyme cavity near the active site (so-called proton shuttle) influences the *pK_a* of the zinc-bound water. The residue which is located in a distance of approx. 7 Å from the zinc centre can be present in both protonated or deprotonated state. For both cases, different *pK_a* values for the zinc-bound water have been measured (Bertini et al., 1985). It is very probable that its protonation state will also affect a zinc-bound hydrosulfide ligand. However, the conclusions drawn in all these studies did not introduce any change in the overall qualitative picture obtained with simpler models that neglect those amino acids. We hold the view that in order to exactly calculate such effects, an expanded model system taking into account the additional residues and a study of molecular dynamics would be required. This would currently exceed by far the computational resources available to us. In addition, we do not believe that such calculation would substantially alter the proposed mechanism. Our aim was to deliver the proof of principle for the hypothesis that hydrosulfide substitution of CA does not entail inhibition of the enzyme, and nothing but a water molecule is required for reactivation and formation of H₂S. We are sure that this proposal is sufficiently supported by our model calculations and experiment.

From the *in vivo* experiments, it is obvious that there is a correlation between COS consumption and H₂S release. As stated above, the missing amount of H₂S flow is not a problem since systematic errors in experiment and partial H₂S metabolisation have been shown to be possible reasons for this finding. However, the most important observation is that there is apparently no deactivation of CA by COS: With increasing COS concentration, the plot of the H₂S release rates shows no signs of any saturation effects, i. e. non-proportionality to the COS consumption plot. This fact strongly corroborates the overall statement of this study.

5. Application of the Enzymatic Reaction Principle to further Examples of Isoelectronic Molecules

As seen in the sections above, the reaction principle of CA is not restricted to the molecule CO₂ but has been applied to COS by nature itself. So it is anticipated, that further isoelectronic molecules like allenes (R₂CCCR₂), isothiocyanates (R-NCS), carbodiimides (R-NCN-R), and

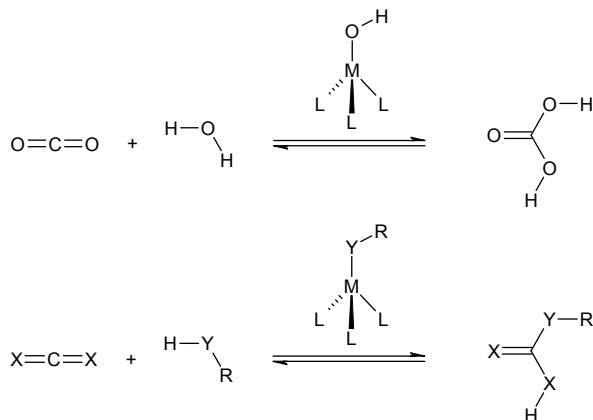


Fig. 7. Catalytic hydration of CO_2 as well as the homologous biomimetic addition reaction to heterocumulenes. $\text{X} = \text{CR}_2, \text{NR}, \text{O}, \text{S}$; $\text{Y} = \text{O}, \text{S}$; $\text{R} = \text{H}, \text{alkyl}, \text{aryl}$; $\text{M} = \text{Zn}^{2+}, \text{Co}^{2+}$; $\text{L} = \text{ligand}$

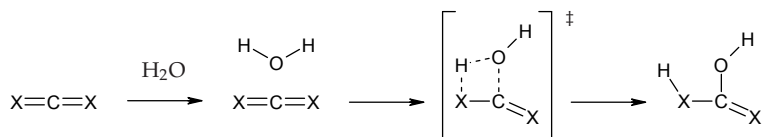


Fig. 8. Uncatalyzed reaction with water across a concerted four-membered cyclic transition state. $\text{X} = \text{CH}_2, \text{NH}, \text{O}, \text{S}$

other heterocumulenes should react resembling the mode of action of CA (see Figure 7). In principle, the structure of the adding compound is not restricted to water, as a lot of polar HX compounds, such as alcohols or H_2S and mercaptanes respectively, provide comparable properties. Hence these heterocumulenic structures are very similar, the addition of a HX compound to a heterocumulene catalyzed by a CA model can be written as depicted in Figure 7. In the next sections the reactions of two representatives will be presented.

5.1 Validation of the Catalytic Effect

A very important value for estimating the catalytic effect is the activation barrier of the rate determining step in the uncatalyzed reactions. Accordingly to the catalyzed reactions, the uncatalyzed reactions do not differ significantly between various heterocumulenes (see Figure 8). After formation of an encounter complex (EC) between water and the double bond system, a concerted transition state (TS), which normally is the rate determining step of the reaction, has to be surmounted to get to the first intermediates. In some cases, these intermediates are the final products, in other cases further transition states with minor activation barriers follow.

Depending on the used heterocumulene, the Gibbs free energies ΔG of the encounter complexes vary between 0 and 20 kJ/mol in comparison to the free non-interacting educts. However, these values might be slightly erroneous, as some DFT methods do not calculate weak intermolecular forces properly. Subsequently, the reaction coordinate leads to a four-membered

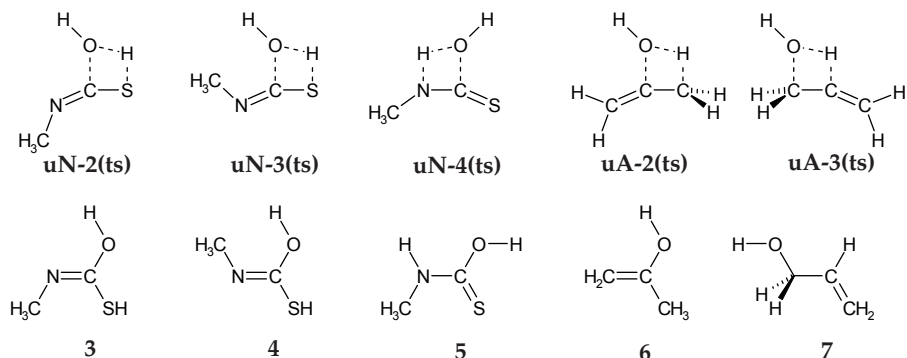


Fig. 9. Transition states and products of the uncatalyzed reaction of MeNCS and allene with water.

cyclic TS (see Figure 9), whose strained structure explains the high activation barrier of the reaction. Typical energy values for these structures can be found in Table 2. The resulting products are also shown in Figure 9. The addition reactions of allene to the products 6 and 7 are both exergonic (see Table 2) and propene-2-ol 6 tautomerizes under standard conditions to the more stable acetone. In case of isothiocyanates, the intermediates are still not exergonic, but after surmounting some minor transition states, several conformers of the exergonic carbamic thio acid can be reached (Eger et al., 2009).

To summarize this, the activation barriers of the uncatalyzed reactions of allenes and isothiocyanates are very high, as they are four-membered cyclic transition states and therefore possess Gibb's free energies between 200 and 300 kJ/mol. Keeping the estimated activation barriers of carbon dioxide and carbonyl sulfide in mind, it should be possible to see a significant catalytic effect in the reactions of allenes and isothiocyanates.

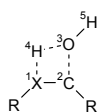
5.2 The Selectivity Problem

Contrary to the case of carbon dioxide, allenes or isothiocyanates as educts for the nucleophilic attack of hydroxide or water provide a more complex scenario. As a heterocumulene, isothiocyanate possess nitrogen and oxygen on the outer positions of the cumulenic system and additionally has an imine group, which reduces the symmetry of the molecule and introduces more reaction possibilities (see Figure 9). Looking at allene, all known problems regarding alkenes and alkynes come to mind, thus chemo- (single or double addition), regio- (Markovnikov- or anti-Markovnikov products) and stereoselectivity (cis- or trans-addition products on stereotopic sides) play a role. For substituted allenes there exists a positional selectivity (Hashmi, 2000) as the attack can take place at two different positions of the allene molecule. Therefore, additions at one of the orthogonal double bonds will lead to constitutional isomers in the case of substituted allenes and as a consequence, this inclusion of regioselectivity doubles the number of isomers.

6. Isothiocyanates (R-NCS), the Link to Synthesis

As described previously, the reaction of isothiocyanates with water and other H-X compounds, i. e. alcohols and amines, is kinetically hindered. Water and alcohols do not react

educt	MeNCS 1			allene 2	
EC ^a	uN-1 ^c 23			uA-1 ^d 22	
TS ^a	uN-2(ts) ^c 220	uN-3(ts) ^c 210	uN-4(ts) ^c 206	uA-2(ts) ^d 263	uA-3(ts) ^d 293
$\angle^1X^2CR^b$	144°	142°	145°	157°	142°
$\angle^1X^4H^3O^b$	117°	123°	114°	122°	121°
$\angle^2C^3O^4H^b$	81°	74°	73°	69°	70°
$\sphericalangle^1X^2C^3O^4H^b$	7°	2°	4°	0°	0°
$\sphericalangle^1X^4H^3O^5H^b$	114°	105°	105°	180°	179°
$^1X^2C^b$	1.716 Å	1.703 Å	1.300 Å	1.386 Å	1.392 Å
$^2C^3O^b$	1.526 Å	1.683 Å	1.629 Å	1.833 Å	1.884 Å
$^3O^4H^b$	1.179 Å	1.269 Å	1.175 Å	1.181 Å	1.190 Å
$^1X^4H^b$	1.724 Å	1.605 Å	1.364 Å	1.449 Å	1.432 Å
product ^a	3 49	4 71	5 -1	6 -92	7 -44



^a ΔG in kJ/mol

^b $^1X^2C$ denote the attacked double bond, with $X=C, N, O, S$.

Depending on the selectivity of the reaction the residue R could be H, CH₂, NMe or S (see formula left).

^c Calculated at the MP2/aug-CC-pVTZ level of theory

^d Calculated at the mPW1k/aug-CC-pVDZ level of theory

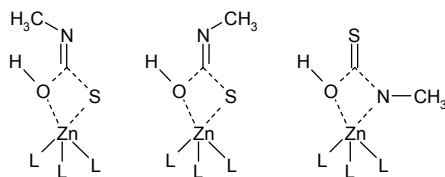
Table 2. Energies and geometries of the uncatalyzed reaction of methylisothiocyanate and allene with water.

under standard conditions, even when they are heated, it takes very long to see some product (Browne & Dyson, 1931; Hagemann, 1983; Rao & Venkataraghavan, 1962; Walter & Bode, 1967). This is only true as long as there is no acid or base present, which would open up other reaction possibilities. If the catalysis by a CA model is efficient, it would be the method of choice to hydrolyze or alcoholize isothiocyanate systems under neutral conditions. This might be interesting for the synthesis of complex and acid or base sensitive molecules.

In comparison to carbon dioxide and carbonyl sulfide, isothiocyanates bear a residue on one of the outstanding hetero atoms. As this is an imine function, it increases the degree of freedom and therefore produces more possible pathways.

		X	C	Y
carbon dioxide	X,Y=O	-0.56	1.13	-0.56
carbon oxid sulfid	X=O, Y=S	-0.48	0.50	-0.01
methylisothiocyanate	X=S, Y=N	-0.10	0.30	-0.48
allene	X,Y=C	-0.51	0.07	-0.51

Table 3. Natural Charges δ^{NC} for CO₂, COS, MeNCS, and allene.



NCS-a(ts); 82 NCS-b(ts); 89 NCS-c(ts); 97

Fig. 10. Rate determining steps in the catalyzed reaction with methyl isothiocyanate. Level of theory is B3LYP/6-311+G(d,p), given values are Gibb's free energies ΔG in kJ/mol.

6.1 Calculated Mechanistic Pathway

The calculations show only one encounter complex NCS-1, in which the isothiocyanate coordinates via the sulfur atom to two ammonia ligands using hydrogen bridging bonds. Coming from this encounter complex, three different transition states could take place. Whereas in NCS-1(ts) and NCS-2(ts) the C=S double bond adds to the Zn-O bond, the C=N double bond does this in the case of NCS-3(ts) (see Figure 10). These transition states resemble the rate determining steps in the reactions of carbon dioxide and carbonyl sulfide and also are the highest activation barriers in the pathway of isothiocyanate. Contrary to the situation in case of COS, which also possesses an unsymmetric cumulenenic system, the energies of this transition states differ not significantly, so a prediction of selectivity depends not only on the energies of the rate determining steps, but also on the further reaction paths and thermodynamic control.

Comparing the free enthalpies of the three transition states and the energies of the following reaction paths, it becomes obvious, that the attack on the C=S double bond is thermodynamically and kinetically slightly favored. Contrary to the fact, that the existence of the imine function makes the situation at the rate determining step more complex, it simplifies it at the point, where the Lindskog and Lipscomb transition states enter the scenery right after the attack of the C=S double bond. As the disturbed symmetry of isothiocyanate opens up about eight possible pathways, the kinetically and thermodynamically most favorable will be discussed shortly here (see Figure 11).

Structure NCS-2(ts) is the rate determining step, as no other transition state builds up a higher activation barrier. $\Delta G = 82$ kJ/mol relative to the separated educts (ammonia model and methyl isothiocyanate), is not as good as the corresponding values estimated for carbon dioxide and carbonyl sulfide, but it is easily surmountable in a normal experimental environment. The catalytic effect becomes very clear, when comparing the activation barriers of the rate determining steps in the catalyzed and uncatalyzed reaction, as the gap between these values is about $\Delta\Delta G = 76$ kJ/mol. This is a significant decrease in energy. The reaction path proceeds further via a Lindskog reaction mechanism (NCS-4(ts)), which is rather lower than the corresponding Lipscomb proton shift. Nevertheless, the pathway surmounting NCS-4(ts) is the thermodynamically and kinetically favored one.

The found selectivity is only true for the reaction with methyl isothiocyanate, as calculation with several residues showed different results. In general, the inductive effect of the residue of the isothiocyanate changes the selectivity. The greater the ability of the residue to pull electrons out of the cumulenenic system, the more an attack of the C=N double bond is preferred. This is mainly a result of the electronic structure in the cumulenenic system. If the residue on the nitrogen atom pulls electron density out of the double bond system, it is mainly taken from

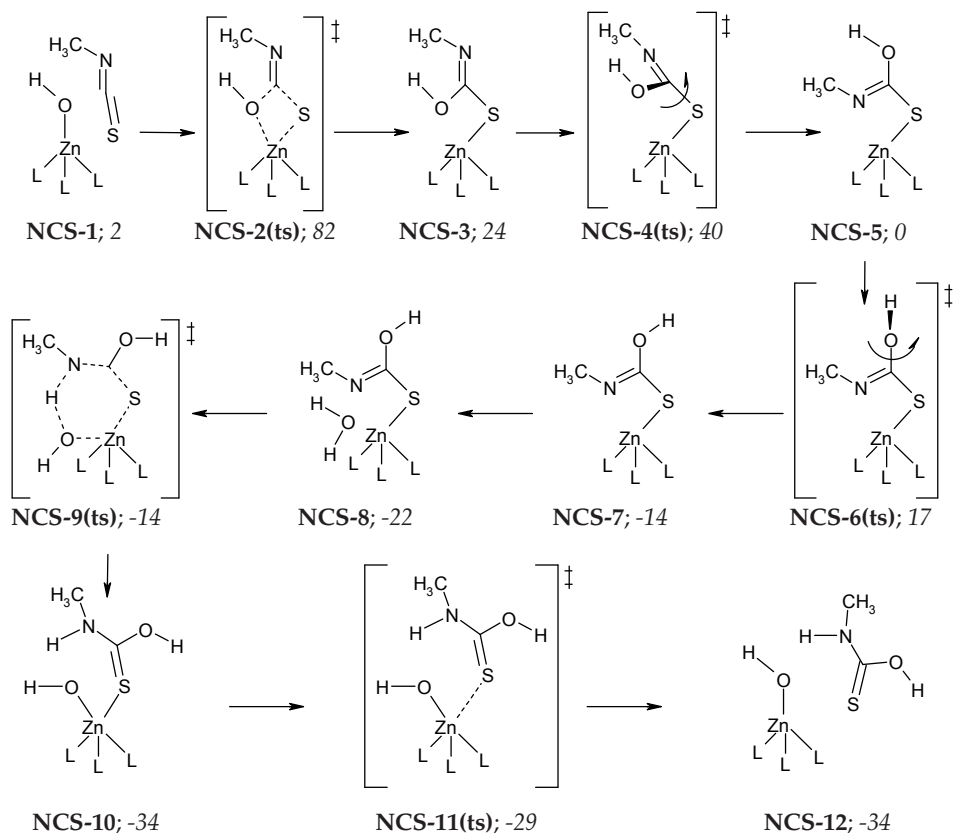


Fig. 11. Pathway of the catalyzed reaction with methyl isothiocyanate. Level of theory is B3LYP/6-311+G(d,p), given values are Gibb's free enthalpies in kJ/mol.

the C=S double bond. Thus NBO calculations show, that in such cases the C=N double bond has a strong triple, and the C=S double bond a strong single bond character (Eger et al., 2009). Further calculations with complexes not bearing a hydroxide ion but an hydrosulfide and an thiolate ion respectively, showed, that the biomimetics of CA are not only limited to hydroxide bearing complexes and thus the addition of water to cumulenic system. Furthermore a lot of different combinations of different nucleophiles and cumulenes are possible.

6.2 Experimental Results

As the reaction with a thiolate complex reduces the number of possible pathways significantly and those complexes recently proved their ability simulating CA biomimetic insertion reactions (e. g. with carbon disulfide) (Notni et al., 2006), this seems to be a good model complex to see, if isothiocyanate inserts even similar. Thiolate complexes bearing a four-dentate [12]aneN₄ ligand are known to work faster than the corresponding three-dentate complexed compounds (Notni, Günther & Anders, 2007).

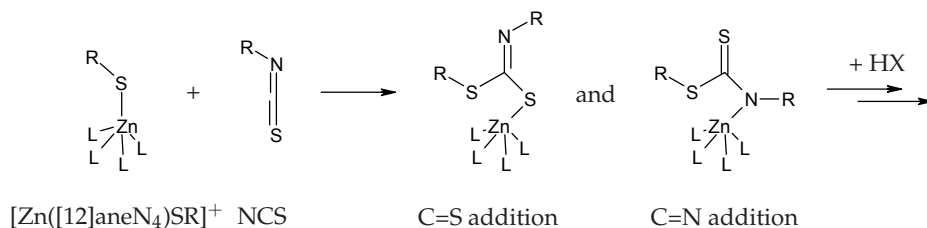


Fig. 12. Insertion possibilities of isothiocyanate to a zinc thiolate complex.

The reaction shown in Figure 12 was carried out in dimethyl sulfoxide under standard conditions at room temperature. The insertion could be proved using GC/MS and Raman spectroscopy. For different isothiocyanates different reaction rates could be determined, as mostly isothiocyanates with an electron withdrawing residue as phenyl or *p*-nitro phenyl were able to insert easily at room temperature. Depending on the purpose of the reaction those activated cumulenes can react further with an HX compound, e. g. an alcohol or mercaptan.

7. Allene

Allene is the simplest hydrocarbon with cumulated double bonds. Since van't Hoff has predicted the correct structures of allene and higher cumulenes, chemists are fascinated by the extraordinary properties like axial chirality of the elongated tetrahedron, if two different substituents at every terminal carbon exist. Allene with its isomer methyl acetylene accrues in large amounts in the C3-cut of the naphtha distillation. Currently both compounds are only hydrated to propene and propane respectively or flared off. Therefore the activation of allene has additionally to the biomimetic a strong economical aspect.

Allene could be estimated as the parent compound for heterocumulenes with two cumulated double bonds. By the formal exchange of one or both terminal carbon atoms a vast number of heterocumulenes are available.

The first investigation of a possible biomimetic activation of allene with zinc catalysts was undertaken by Breuer et al. (1999). They found catalytical activity of zinc silicates with zinc acetate in methanol to give 2-methoxypropene and 2,2-dimethoxypropene in 85 % yield.

7.1 Calculated Mechanistic Pathway

The presentation of the whole calculated reaction mechanism of the addition of water to allene goes beyond the scope of this chapter due to the immense number of reaction steps (see (Jahn et al., 2008) for further reading). Therefore the description of mechanistical pathways is confined to the variants of the initial nucleophilic attack, which lead to mechanistical important intermediates. The results show that the initial attack is the rate determining step for the whole catalytic cycle.

The zinc catalyzed addition starts with an encounter complex **A-1** between the zinc hydroxide complex and allene. This structure is the starting point for the different reaction variants, comparable to the uncatalyzed reaction described in section 5.1. Corresponding to the regio selectivity problem the attack to allene can take place at either the central or the terminal carbon atom (see Figure 13). The attack of the hydroxide on the terminal carbons leads to a concerted four-membered cyclic transition state **A-2(ts)** with an activation barrier of $\Delta G = 139$ kJ/mol.

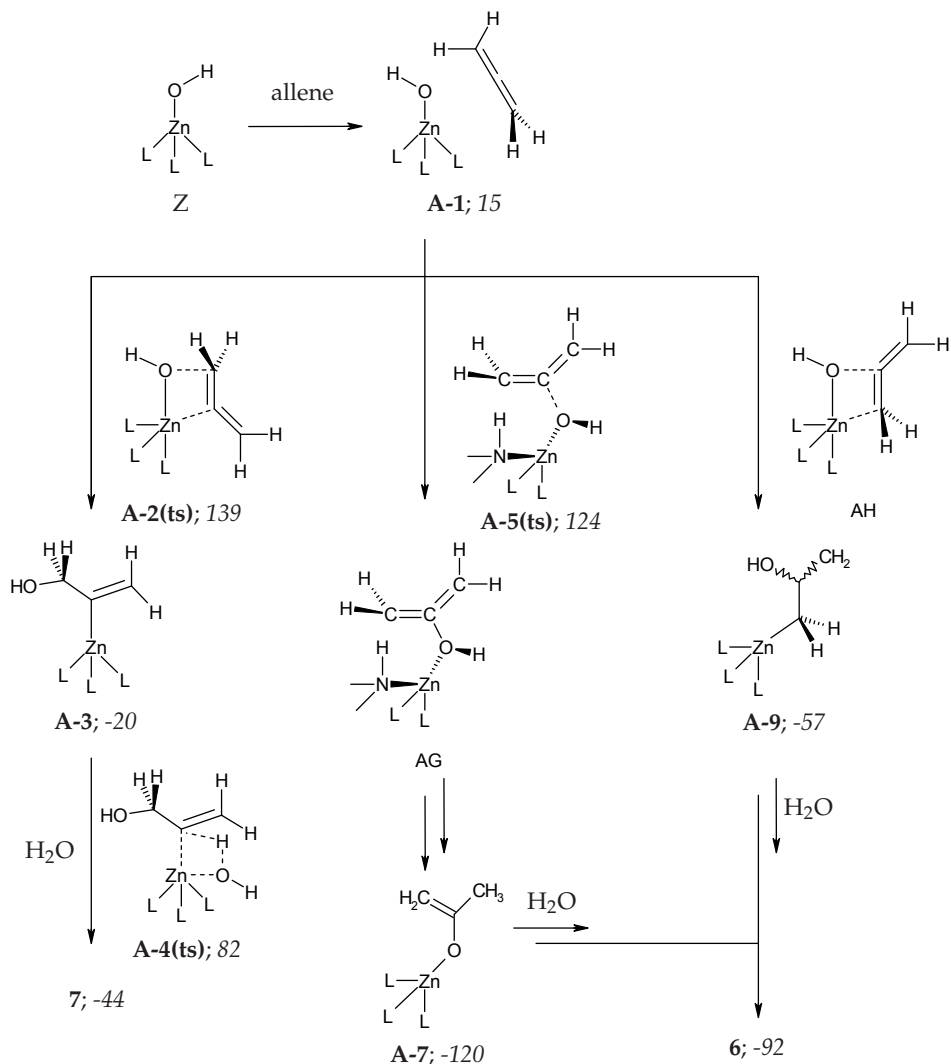


Fig. 13. Calculated mechanism of the initial, rate determining steps of the activation of allene. ΔG in kJ/mol. Level of theory is mPW1k/aug-CC-pVDZ.

This structure relaxes to the C_{2v} -symmetric, slightly exergonic intermediate **A-3**, in which the carbon backbone, the hydroxyl group, the metal ion and one nitrogen of the ligand span the symmetry plane. The hydroxyl group is placed between and in front of the ligands. There is only one possibility to close the catalytic cycle starting from intermediate **A-3**. This mechanism is an attack of a water molecule, which leads to a cleavage of the Zn-C bond. One water proton is shifted to the central carbon atom to give allyl alcohol **7** and the remaining hydroxide regenerates the catalytic model.

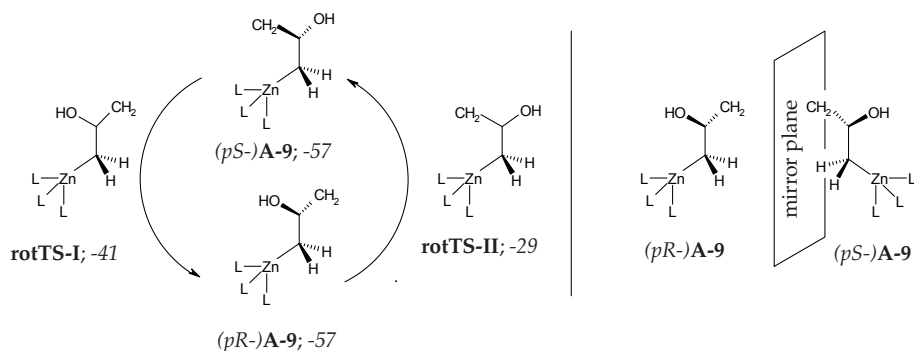


Fig. 14. Mechanism of the racemization of **A-9** via **rotTS-I** and **rotTS-II**. ΔG in kJ/mol. Level of theory is mPW1k/aug-CC-pVDZ.

Alternatively, the initial nucleophilic attack on the CA model complex can take place at the central carbon atom. Depending on the kind of the model complex, two different mechanisms of the initial reaction step can be found. This reaction path can either proceed via a stepwise or a concerted reaction mechanism, whereas the stepwise mechanism can only be found using the azamacrocyclic models. Contrary, the concerted one can be found in all cases. This shows the restrictions of the ammonia model.

Structure **A-5(ts)** is the first transition state of the stepwise variant. The activation barrier is $\Delta\Delta G = 18$ kJ/mol) higher than for the concerted TS **A-8(ts)**, which is interesting, as this TS has no sterical restrictions. As its carbon backbone stands approximatively perpendicular to the Zn-O bond, structure **A-5(ts)** differs fundamentally in its geometry compared to the cyclic concerted TSs. The reaction coordinate is only defined by the difference of the distance between oxygen and the central carbon atom of allene. The TS relaxes to the intermediate **A-6**. With $\Delta G = 113$ kJ/mol relative to the Gibb's free energy of the separated reactants allene and zinc hydroxide complex, this intermediate is only poorly stable. Intermediate **A-6** rearranges by a cascade of proton transfer steps between the substrate and the ligand to the intermediate **A-7**, which is one of the most stable structures in the calculated reaction path variants ($\Delta G = -120$ kJ/mol). Subsequently, the direct formation of acetone is facilitated by a proton shift from an attacking water molecule to the free methylenide group.

The third and most probable transition state between allene and the CA model complex is the concerted four-membered cyclic TS **A-8(ts)**. Comparably to methylisothiocyanate, **A-8(ts)** resembles the rate determining step in the reactions of carbon dioxide and carbonyl sulfide. **A-8(ts)** possesses the lowest activation barrier of all three initial TSs ($\Delta G = 124$ kJ/mol). It finally relaxes into the intermediate **A-9**.

Contrary to all other intermediates of different heterocumulenes at comparable points of the reaction coordinate, structure **A-9** has an outmost geometry. Whereas in all geometries of intermediates connected to the zinc ion by a heteroatom the former cumulated system and the metal ion are located in a plane, intermediate **A-9** has a carbon atom connected to the zinc instead, which forces the plane spanned by the carbon backbone of the allene to stand perpendicular to the Zn-C bond and parallel to the plane spanned by the ligand respectively. A reason for that is the partial double bond character of the bonding between the central and the zinc-bound carbon atoms. As a consequence, **A-9** is a chiral structure without an asymmetric center and therefore an example of planar chirality. However, the activation barrier of

the racemization TS is not high enough to ensure a separation of the enantiomers (*pR*-)**A-9** and (*pS*-)**A-9** (see Figure 14). Isomerization around the single bond between zinc and the zinc bound carbon can occur clockwise or counter-clockwise. As a result, two rotational transition states exist (**rotTS-I** and **rotTS-II**). TS **rotTS-I** is slightly preferred, as hydrogen bridging bonds between the hydroxyl group and the ligand lower the energy. Comparing their geometries, the proposed analogous transition state for catalytic cycle of the CO₂ hydration (Mauksch et al., 2001) and the transition state **A-8(ts)** are quite similar. In contrast to **A-9**, the following so-called Lindskog-type intermediate possesses a C_{2v} symmetry like **rotTS-I**. The geometry of intermediate **A-9** is comparable to the Lindskog-type rotational TS, which leads to the Lipscomb product. The latter is a geometrical equivalent to **rotTS-II**. Due to the different geometry, an alternative way like the Lipscomb mechanism (proton shift) (Liang & Lipscomb, 1987; Lipscomb, 1983) appears to be impossible for intermediate **A-9**. Intermediate **A-9** could be identified as the the key intermediate for the further possible reaction paths. Starting from here, hydrolysis recreates allene and the CA model complex, whereas another pathway directly leads to acetone. The catalytic product of all remaining possible pathways is **6**. Thus the water attack can take place on the methyldene group with and without a preceding rotation of the hydroxyl group. Further, an intramolecular proton shift from the hydroxyl to the methyldene group under generation of a carbonyl and methyl group is another possible pathway. The carbonyl group can also be attacked by a water molecule. Alternatively, a coordination change from the oxygen to the zinc bound carbon can occur. This step generates the stable structure **A-7**, which is also accessible from the initial stepwise mechanism.

7.2 Experimental Results

The reaction of allene and [Zn([12]aneN₃)OH]ClO₄ as the CA model complex was investigated under heterogeneous conditions. Due to the gaseous aggregation state of the unsubstituted allene, a pressure cell was used. The analysis was done with Raman spectroscopic methods.

8. Conclusion

In summary, we have shown that the transformation of COS by carbonic anhydrase, which finally yields H₂S and CO₂, requires no further reactant than water in order to regenerate the most important zinc-bound hydroxide [L₃ZnOH]⁺ from the hydrosulfide complex. We conclude that CA is perfectly equipped by nature to perform the task of transformation of COS into H₂S. Furthermore, we regard this special function of CA to be perfectly linked to the plant sulfur metabolism. Therefore, this regeneration mechanism can be regarded as the missing link between CA-catalyzed COS fixation and plant sulfur metabolism; an aspect of fundamental significance for the understanding of some very important biological processes. Nature has chosen an elegant and efficient system for the hydration of CO₂ and COS, the [L₃ZnOH]⁺/CO₂ or COS/H₂O group of reactants. The catalyst is able to transform both cumulenes, though the relative energies of the corresponding reactions steps differ in some details significantly. Further we have shown that it is possible to apply biomimetic principles of high optimized, biochemical processes to the laboratory as well as industrially usable syntheses. The reaction principle of carbonic anhydrase is applicable to other isoelectronic molecules than CO₂, which are normally not processed by the enzyme. These biomimetic investigations about the enzyme carbonic anhydrase could serve as a paragon for the further research on biochemical model systems.

Acknowledgement

These investigations are part of the general research field of the Collaborative Research Centre Metal Mediated Reactions Modeled after Nature (CRC 436, University of Jena, Germany, since 1997 though 2006 supported by the Deutsche Forschungsgemeinschaft).

9. References

- Barnett, D. H., Sheng, S., Howe Charn, T., Waheed, A., Sly, W. S., Lin, C.-Y., Liu, E. T. & Katzenellenbogen, B. S. (2008). Estrogen Receptor Regulation of Carbonic Anhydrase XII through a Distal Enhancer in Breast Cancer, *Cancer Research* **68**(9): 3505–3515.
- Bergquist, C., Fillebeen, T., Morlok, M. M. & Parkin, G. (2003). Protonation and Reactivity towards Carbon Dioxide of the Mononuclear Tetrahedral Zinc and Cobalt Hydroxide Complexes, $[\text{Tp}^{\text{But,Me}}]\text{ZnOH}$ and $[\text{Tp}^{\text{But,Me}}]\text{CoOH}$: Comparison of the Reactivity of the Metal Hydroxide Function in Synthetic Analogues of Carbonic Anhydrase, *Journal of the American Chemical Society* **125**(20): 6189–6199.
- Bertini, I., Dei, A., Luchinat, C. & Monnanni, R. (1985). Acid-Base Properties of Cobalt(II)-Substituted Carbonic Anhydrases, *Inorganic Chemistry* **24**(3): 301–303.
- Bertran, J., Sola, M., Lledos, A. & Duran, M. (1992). Ab Initio Study of the Hydration of CO_2 by Carbonic Anhydrase. A Comparison between the Lipscomb and the Lindskog Mechanisms, *Journal of the American Chemical Society* **114**(3): 869–877.
- Blezynger, S., Wilhelm, C. & Kesselmeier, J. (2000). Enzymatic Consumption of Carbonyl Sulfide (COS) by Marine Algae., *Biogeochemistry* **48**: 185–197.
- Bottoni, A., Lanza, C. Z., Miscione, G. P. & Spinelli, D. (2004). New Model for a Theoretical Density Functional Theory Investigation of the Mechanism of the Carbonic Anhydrase, *Journal of the American Chemical Society* **126**: 1542–1550.
- Bowen, T., Planalp, R. P. & Brechbiel, M. W. (1996). An Improved Synthesis of cis,cis-1,3,5-triaminocyclohexane. Synthesis of Novel Hexadentate Ligand Derivatives for the Preparation of Gallium Radiopharmaceuticals, *Bioorganic & Medicinal Chemistry Letters* **6**(7): 807–810.
- Brandsch, T., Schell, F.-A., Weis, K., Ruf, M., Miller, B. & Vahrenkamp, H. (1997). On the Ligating Properties of Sulfonate and Perchlorate Anions Towards Zinc, *Chemische Berichte* **130**(2): 283–289.
- Bräuer, M., Pérez-Lustres, J. L., Weston, J. & Anders, E. (2002). Quantitative Reactivity Model for the Hydration of Carbon Dioxide by Biomimetic Zinc Complexes., *Inorganic Chemistry* **41**(6): 1454–1463.
- Brennan, D. J., Jirstrom, K., Kronblad, A., Millikan, R. C., Landberg, G., Duffy, M. J., Ryden, L., Gallagher, W. M. & O'Brien, S. L. (2006). CA IX is an Independent Prognostic Marker in Premenopausal Breast Cancer Patients with One to Three Positive Lymph Nodes and a Putative Marker of Radiation Resistance, *Clinical Cancer Research* **12**(21): 6421–6431.
- Breuer, K., Teles, J. H., Demuth, D., Hibst, H., Schäfer, A., Brode, S. & Domgörgen, H. (1999). Zinksilicate: hochwirksame heterogene Katalysatoren für die Addition primärer Alkohole an Alkine und Allene, *Angewandte Chemie* **111**(10): 1497–1502.
- Browne, D. W. & Dyson, G. M. (1931). CCCCLVII. The Inhibitory Effect of Substituents in Chemical Reactions. Part II. The Reactivity of the Isothiocyano-Group in Substituted Arylthiocarbimides, *Journal of the Chemical Society* p. 3285.

- Chengelis, C. P. & Neal, R. A. (1980). Studies of Carbonyl Sulfide Toxicity: Metabolism by Carbonic Anhydrase, *Toxicology and Applied Pharmacology* **55**(1): 198–202.
- Chrastina, A., Závada, J., Parkkila, S., Kaluz, S., Kaluzová, M., RajccaronĀani, J., Pastorek, J. & Pastoreková, S. (2003). Biodistribution and Pharmacokinetics of ¹²⁵I-Labeled Monoclonal Antibody M75 Specific for Carbonic Anhydrase IX, an Intrinsic Marker of Hypoxia, in Nude Mice Xenografted with Human Colorectal Carcinoma, *International Journal of Cancer* **105**(6): 873–881.
- Cronin, L., Greener, B., Moore, M. H. & Walton, P. H. (1996). Preparations and Structures of Two cis,cis-1,3,5-triaminocyclohexane-Based Complexes Containing Hydrogen-Bonded Solvent Molecules, *Dalton Transactions* pp. 3337–3339.
- Cronin, L. & Walton, P. H. (2003). Synthesis and Structure of [Zn(OMe)(L)]*[Zn(OH)(L)]-*2(BPh₄), L = cis,cis-1,3,5-tris[(e,e)-3-(2-Furyl)acrylideneamino]cyclohexane: Structural Models of Carbonic Anhydrase and Liver Alcohol Dehydrogenase, *Chemical Communications* pp. 1572–1573.
- Dodgson, S. J. & Forster, R. E., n. (1986). Carbonic Anhydrase: Inhibition Results in Decreased Urea Production by Hepatocytes, *Journal of Applied Physiology* **60**(2): 646–652.
- Echizen, T., Ibrahim, M. M., Nakata, K., Izumi, M., Ichikawa, K. & Shiro, M. (2004). Nucleophilic Reaction by Carbonic Anhydrase Model Zinc Compound: Characterization of Intermediates for CO₂ Hydration and Phosphoester Hydrolysis, *Journal of Inorganic Biochemistry* **98**(8): 1347–1360.
- Eger, W. A., Jahn, B. O. & Anders, E. (2009). The Zinc Complex Catalyzed Hydration of Alkyl Isothiocyanates, *Journal of Molecular Modeling* **15**: 433–446.
- Eriksson, A. E., Jones, T. A. & Liljas, A. (1988). Refined Structure of Human Carbonic Anhydrase II at 2.0 Å Resolution, *Proteins: Structure, Function, and Genetics* **4**(4): 274–282.
- Frisch, M. J., Trucks, G. W., Schlegel, H. B., Scuseria, G. E., Robb, M. A., Cheeseman, J. R., J. A. Montgomery, Jr., J. A., Vreven, T., Kudin, K. N., Burant, J. C., Millam, J. M., Iyengar, S. S., Tomasi, J., Barone, V., Mennucci, B., Cossi, M., Scalmani, G., Rega, N., Petersson, G. A., Nakatsuji, H., Hada, M., Ehara, M., Toyota, K., Fukuda, R., Hasegawa, J., Ishida, M., Nakajima, T., Honda, Y., Kitao, O., Nakai, H., Klene, M., Li, X., Knox, J. E., Hratchian, H. P., Cross, J. B., Adamo, C., Jaramillo, J., Gomperts, R., Stratmann, R. E., Yazyev, O., Austin, A. J., Cammi, R., Pomelli, C., Ochterski, J. W., Ayala, P. Y., Morokuma, K., Voth, G. A., Salvador, P., Dannenberg, J. J., Zakrzewski, V. G., Dapprich, S., Daniels, A. D., Strain, M. C., Farkas, O., Malick, D. K., Rabuck, A. D., Raghavachari, K., Foresman, J. B., Ortiz, J. V., Cui, Q., Baboul, A. G., Clifford, S., Cioslowski, J., Stefanov, B. B., Liu, G., Liashenko, A., Piskorz, P., Komaromi, I., Martin, R. L., Fox, D. J., Keith, T., Al-Laham, M. A., Peng, C. Y., Nanayakkara, A., Challacombe, M., Gill, P. M. W., Johnson, B., Chen, W., Wong, M. W., Gonzalez, C. & Pople, J. A. (2004). Gaussian03.
URL: <http://www.gaussian.com>
- Gibbons, B. H. & Edsall, J. T. (1964). Kinetic Studies of Human Carbonic Anhydrases B and C, *Journal of Biological Chemistry* **239**(8): 2539–2544.
- Glendening, E. D., Badenhop, J. K., Reed, A. E., Carpenter, J. E., Bohmann, J. A., Morales, C. M. & Weinhold, F. (2001). Nbo 5.0.
URL: <http://www.chem.wisc.edu/nbo5>
- Hagemann, H. (1983). *Methoden der Organischen Chemie (Houben-Weyl): Kohlendioxid-Derivate*, Vol. E4, Georg Thieme Verlag, Stuttgart.

- Hammes, B. S., Luo, X., Carrano, M. W. & Carrano, C. J. (2002). Zinc Complexes of Hydrogen Bond Accepting Ester Substituted Trispyrazolylborates, *Inorganica Chimica Acta* **341**: 33–38.
- Hashmi, A. S. K. (2000). Neue und Selektive Übergangsmetall-Katalysierte Reaktionen von Allenen, *Angewandte Chemie* **112**(20): 3737–3740. *Angew. Chem. Int. Ed. Engl.* 2000, 39, 3590–3593.
- Hewett-Emmett, D. & Tashian, R. E. (1996). Functional Diversity, Conservation, and Convergence in the Evolution of the α -, β -, and γ -Carbonic Anhydrase Gene Families, *Molecular Phylogenetics and Evolution* **5**(1): 50–77.
- Jahn, B. O., Eger, W. A. & Anders, E. (2008). Allene as the Parent Substrate in Zinc-Mediated Biomimetic Hydration Reactions of Cumulenes, *Journal of Organic Chemistry* **73**(21): 8265–8278.
- Jarvela, S., Parkkila, S., Bragge, H., Kahkonen, M., Parkkila, A.-K., Soini, Y., Pastorekova, S., Pastorek, J. & Haapasalo, H. (2008). Carbonic Anhydrase IX in Oligodendroglial Brain Tumors, *BMC Cancer* **8**(1): 1.
- Keilin, D. & Mann, T. (1939). Carbonic Anhydrase, *Nature* **144**: 442–443.
- Kimura, E., Shiota, T., Koike, T., Shire, M. & Kodama, M. (1990). A Zinc(II) Complex of 1,5,9-Triazacyclododecane ([12]aneN₃) as a Model for Carbonic Anhydrase, *Journal of the American Chemical Society* **112**(15): 5805–5811.
- Kläui, W., Berghahn, M., Rheinwald, G. & Lang, H. (2000). Tris(pyrazolyl)methanesulfonates: A Novel Class of Water-Soluble Ligands, *Angewandte Chemie International Edition* **39**(14): 2464–2466.
- Krishnamurthy, V., Kaufman, G., Urbach, A., Gitlin, I., Gudiksen, K., Weibel, D. & Whitesides, G. (2008). Carbonic Anhydrase as a Model for Biophysical and Physical–Organic Studies of Proteins and Protein–Ligand Binding, *Chemical Reviews* **108**(3): 946–1051.
- Kuhn, U. & Kesselmeier, J. (2000). Environmental Variables Controlling the Uptake of Carbonyl Sulfide by Lichens., *Journal of Geophysical Research – Atmospheres* **105**: 26783–26792.
- Kunz, P., Reiß, G., Frank, W. & Kläui, W. (2003). A Novel Water-Soluble Tripodal Imidazolyl Ligand as a Model for the Tris(histidine) Motif of Zinc Enzymes: Nickel, Cobalt and Zinc Complexes and a Comparison with Metal Binding in Carbonic Anhydrase, *European Journal of Inorganic Chemistry* **2003**(21): 3945–3951.
- Lane, T. W., Saito, M. A., George, G. N., Pickering, I. J., Prince, R. C. & Morel, F. M. M. (2005). Biochemistry A Cadmium Enzyme from a Marine Diatom, *Nature* **435**(7038): 42–42.
- Liang, J. Y. & Lipscomb, W. N. (1987). Hydration of Carbon Dioxide by Carbonic Anhydrase: Internal Protein Transfer of Zinc(2+)-Bound Bicarbonate, *Biochemistry* **26**(17): 5293 – 5301.
- Lindskog, S. (1984). The Kinetic Mechanisms of Human Carbonic Anhydrases I and II: A Computer Approach, *Journal of Molecular Catalysis* **23**(2-3): 357–368.
- Lindskog, S. (1997). Structure and Mechanism of Carbonic Anhydrase, *Pharmacology & Therapeutics* **74**(1): 1–20.
- Lipscomb, W. N. (1983). Structure and Catalysis of Enzymes, *Annual Review of Biochemistry* **52**: 17–34.
- Lowe, N., Brady, H. J. M., Barlow, J. H., Sowdes, J. C., Edwards, M. & Butterworth, P. H. W. (1990). Structure and Methylation Patterns of the Gene Encoding Human Carbonic Anhydrase I, *Gene* **93**(2): 277–283.

- Mauksch, M., Bräuer, M., Weston, J. & Anders, E. (2001). New Insights into the Mechanistic Details of the Carbonic Anhydrase Cycle as Derived from the Model System $[(\text{NH}_3)_3\text{Zn}(\text{OH})]^+ / \text{CO}_2$, *ChemBioChem* **2**: 190–198.
- Nakata, K., Uddin, M. K., Ogawa, K. & Ichikawa, K. (1997). CO_2 Hydration by Mimic Zinc Complex for Active Site of Carbonic Anhydrase, *Chemistry Letters* **26**(10): 991–992.
- Notni, J., Günther, W. & Anders, E. (2007). Zinc Thiolate Complexes $[\text{ZnL}_n(\text{SR})]^+$ with Azamacrocyclic Ligands, Part III: The Influence of the Ligand L_n on the Reactivity of Zinc-Bound Thiolate, *European Journal of Inorganic Chemistry* **7**(7): 985–993.
- Notni, J., Schenk, S., Protoschill-Krebs, G., Kesselmeier, J. & Anders, E. (2007). The Missing Link in COS Metabolism: A Model Study on the Reactivation of Carbonic Anhydrase from its Hydrosulfide Analogue, *ChemBioChem* **8**(5): 530–536.
- Notni, J., Schenk, S., Roth, A., Plass, W., Görls, H., Uhlemann, U., Walter, A., Schmitt, M., Popp, J., Chatzipapadopoulos, S., Emmler, T., Breitzke, H., Leppert, J., Buntkowsky, G., Kempe, K. & Anders, E. (2006). Zinc Thiolate Complexes $[\text{ZnL}_n(\text{SR})]^+$ with Azamacrocyclic Ligands, Part II: Mechanism of the Reaction with CS_2 , *European Journal of Inorganic Chemistry* **14**(14): 2783–2791.
- Parkin, G. (2000). The Bioinorganic Chemistry of Zinc: Synthetic Analogues of Zinc Enzymes that Feature Tripodal Ligands, *Chemical Communications* pp. 1971–1985.
- Parkin, G. (2004). Synthetic Analogues Relevant to the Structure and Function of Zinc Enzymes, *Chemical Reviews* **104**(2): 699–768.
- Rao, C. N. R. & Venkataraghavan, R. (1962). Mechanism of the Addition of Alcohols to Substituted Phenylisothiocyanates: Electrical Effects of the Substituents on the Reaction, *Tetrahedron* **18**(5): 531–537.
- Riccardi, D. & Cui, Q. (2007). pK_a Analysis for the Zinc-Bound Water in Human Carbonic Anhydrase II: Benchmark for Multiscale QM/MM Simulations and Mechanistic Implications, *The Journal of Physical Chemistry A* **111**(26): 5703–5711.
- Richman, J. E. & Atkins, T. J. (1974). Nitrogen Analogs of Crown Ethers., *Journal of the American Chemical Society* **96**: 2268–2270.
- Ruusuvuori, E., Li, H., Huttu, K., Palva, J. M., Smirnov, S., Rivera, C., Kaila, K. & Voipio, J. (2004). Carbonic Anhydrase Isoform VII Acts as a Molecular Switch in the Development of Synchronous Gamma-Frequency Firing of Hippocampal CA1 Pyramidal Cells, *Journal of Neuroscience* **24**(11): 2699–2707.
- Saito, K. (2004). Sulfur Assimilatory Metabolism. The Long and Smelling Road, *Plant Physiology* **136**(1): 2443–2450.
- Sánchez-Méndez, A., Silvestri, G., de Jesús, E., de la Mata, F., Flores, J., Gómez, R. & Gómez-Sal, P. (2004). Tris(pyrazolyl)methane Ligands: Syntheses and Structures of Monometallic and Metallodendritic Complexes, *European Journal of Inorganic Chemistry* **2004**(16): 3287–3296.
- Sandoval-Soto, L., Stanimirov, M., von Hobe, M., Schmitt, V., Valdes, J., Wild, A. & Kesselmeier, J. (2005). Global Uptake of Carbonyl Sulfide (COS) by Terrestrial Vegetation: Estimates Corrected by Deposition Velocities Normalized to the Uptake of Carbon Dioxide (CO_2), *Biogeosciences Discussion* **2**: 183–201.
- Schenk, S., Kesselmeier, J. & Anders, E. (2004). How Does the Exchange of One Oxygen Atom with Sulfur Affect the Catalytic Cycle of Carbonic Anhydrase?, *Chemistry – A European Journal* **10**(12): 3091–3105.

- Schenk, S., Kesselmeier, J. & Anders, E. (2005). Chemical Modelling of the Uptake Process of Carbonyl Sulphide (COS) by the Enzyme Carbonic Anhydrase, *Geophysical Research Abstracts* **7**.
- Schröder, D., Schwarz, H., Schenk, S. & Anders, E. (2003). A Gas-Phase Reaction as a Functional Model for the Activation of Carbon Dioxide by Carbonic Anhydrase., *Angewandte Chemie International Edition* **42**: 5087–5090.
- Schrodt, A., Neubrand, A. & van Eldik, R. (1997). Fixation of CO₂ by Zinc(II) Chelates in Alcoholic Medium. X-ray Structures of {[Zn(cyclen)]₃(μ₃-CO₃)}(ClO₄)₄ and [Zn(cyclen)EtOH](ClO₄)₂., *Inorganic Chemistry* **36**: 4579–4584.
- Sinnecker, S., Bräuer, M., Koch, W. & Anders, E. (2001). CS₂ Fixation by Carbonic Anhydrase Model Systems - A New Substrate in the Catalytic Cycle., *Inorganic Chemistry* **40**: 1006–1013.
- Sly, W. S., Hewett-Emmett, D., Whyte, M. P., Yu, Y. S. & Tashian, R. E. (1983). Carbonic Anhydrase II Deficiency Identified as the Primary Defect in the Autosomal Recessive Syndrome of Osteopetrosis with Renal Tubular Acidosis and Cerebral Calcification, *Proceedings of the National Academy of Sciences of the United States of America* **80**(9): 2752–2756.
- Sun, X. C., Li, J., Cui, M. & Bonanno, J. A. (2008). Role of Carbonic Anhydrase IV in Corneal Endothelial HCO₃⁻ Transport, *Investigative Ophthalmology and Visual Science* **49**(3): 1048–1055.
- Tang, C. C., Davalian, D., Huang, P. & Breslow, R. (1978). Models for Metal Binding Sites in Zinc Enzymes. Syntheses of tris[4(5)-Imidazolyl]carbinol (4-TIC), tris(2-Imidazolyl)carbinol (2-TIC), and Related Ligands, and studies on metal complex binding constants and spectra, *Journal of the American Chemical Society* **100**(12): 3918–3922.
- Tautermann, C. S., Loferer, M. J., Voegele, A. F. & Liedl, K. R. (2003). About the Kinetic Feasibility of the Lipscomb Mechanism in Human Carbonic Anhydrase II, *The Journal of Physical Chemistry B* **107**(43): 12013–12020.
- Trofimenko, S. (1966). Boron-Pyrazole Chemistry, *Journal of the American Chemical Society* **88**(8): 1842–1844.
- Trofimenko, S. (1967). Boron-Pyrazole Chemistry II. Poly(1-pyrazolyl)-borates, *Journal of the American Chemical Society* **89**(13): 3170–3177.
- Urbach, F. L., Sarneski, J. E., Turner, L. J. & Busch, D. H. (1968). Nickel(II) Complexes with the Two Isomers of 1,3,5-Triaminocyclohexan, *Inorganic Chemistry* **7**(10): 2169–2171.
- Walter, W. & Bode, K.-D. (1967). Neuere Methoden der Präparativen Organischen Chemie VI. Synthesen von Thiourethanen, *Angewandte Chemie* **79**(7): 285–297.
- Yan, J., Jiao, Y., Jiao, F., Stuart, J., Donahue, L. R., Beamer, W. G., Li, X., Roe, B. A., LeDoux, M. S. & Gu, W. (2007). Effects of Carbonic Anhydrase VIII Deficiency on Cerebellar Gene Expression Profiles in the WDL Mouse, *Neuroscience Letters* **413**(3): 196–201.
- Yang, K., Yin, Y. & Jin, D. (1995). An Active Site Model for Carbonic Anhydrase. Synthesis and Crystal Structure of [[η]₃-HB(3-Phpz)₃]ZnBr, *Polyhedron* **14**(8): 1021–1023.
- Zhang, X. & van Eldik, R. (1995). A Functional Model for Carbonic Anhydrase, *Inorganic Chemistry* **34**: 5606–5614.
- Zvargulis, E. S., Buys, I. E. & Hambley, T. W. (1995). Models of the Active Sites of Zinc Containing Enzymes: The Crystal Structures of Two bis(Tripod)zinc(II) Complexes, *Polyhedron* **14**(15-16): 2267–2273.

Biomimetic Lessons Learnt from Nacre

Kalpna S. Katti, Dinesh R. Katti and Bedabibhas Mohanty
Department of Civil Engineering, North Dakota State University
USA

1. Introduction

Nacre, the inner iridescent layer of molluscan shells has been investigated for many decades due to its exceptional mechanical properties, tremendous structural redundancy and complex hierarchical structure that spans nanometer to millimeter length scale. This chapter gives an overview of past and current literature on advancements in evolution of understanding of the hierarchical microstructure of nacre, the molecular makeup of mineral and organic components, as well as recent efforts on biomimicking this structure for a variety of applications. In addition, we will also describe multiscale modeling efforts in simulating the mechanical response of this material. Modeling efforts in literature include fracture mechanics based continuum theories to molecular dynamics studies on mineral-protein interactions in nacre. The goal of this chapter would be to give the reader an in depth understanding of the existing knowledge on architecture of nacre and the structure property relationships therein. Lessons from nature to accomplish optimized mechanical response, structural redundancy and fracture toughness will be illustrated for this important material system. Also described are efforts in literature on mimicking the structure of nacre.

2. Structure and properties of nacre

2.1 Evolution

Nacre is the inner iridescent layer in many molluscan shells as shown in Figure 1. It is a type of structure which is commonly found in the molluscan classes of Gastropoda, Bivalvia and Cephalopoda (Bogild 1930, Taylor, Kennedy and Hall 1969, Mutvei 1970, Erben 1972, Taylor, Kennedy and Hall 1973, Currey 1977). The other structural type that is found in all classes of molluscan shells has the crossed lamellar structure. Nacre is considered to be the primitive structural type and it is found in those groups that have undergone less evolutionary diversification and modification. Review of the history of various structures in bivalves can be found elsewhere (Taylor 1973). It has been reported that the organic matrix components of fossil mollusk shell is preserved for 80 million years (Weiner et al. 1979). This indicates that mollusk shells have been around for at least 80 million years. Furthermore, presence of preserved amino acids in fossil shells as old as 360 million years is reported in literature (Abelson 1954). Unfortunately, a good knowledge about the history of various structural types found in molluscan shells is not available. Most of them are made of aragonite (a crystallographic form of calcium carbonate), which is less stable than calcite.

Aragonite always tends to metamorphose into calcite with disruption of its structure (Currey 1977).



Fig. 1. Picture of a seashell showing shiny nacreous layer.

2.2. Hierarchical Structure of Nacre

Nacre exhibits a work of fracture about significantly higher than that of pure ceramic (Jackson, Vincent and Turner 1988, Jackson, Vincent and Turner 1990, Currey 1977) which is its major constituent. This is the reason why it is extensively studied in the literature for over four decades. Nacre is made up of 95% of aragonitic form of calcium carbonate (CaCO_3) which is a ceramic and 5% organic material primarily composed of proteins and polysaccharides. The studies in literature suggest that the main strengthening and toughening mechanisms of nacre result from its unique micro-architecture (Jackson et al. 1988, Jackson et al. 1990, Jackson et al. 1986, Wang et al. 1995, Currey 1980). Structural hierarchy is an important characteristic of all structural materials in nature such as bone, teeth and other tissues. Nacre has a very complex hierarchical microarchitecture that spans over multiple length scales from nanoscale to macroscale. At the lowest length scale, it is considered as a nanocomposite material and the microarchitecture of nacre is often described as 'brick-and-mortar' structure as shown in Figure 2. The bricks are made of the mineral phase and the organic matrix forms the mortar. The mineral platelets are $\sim 5\text{-}8\ \mu\text{m}$ long and $\sim 200\text{-}500\ \text{nm}$ thick, depending on the species and age of the shell and they are separated by layer of the organic matrix which is $\sim 20\ \text{nm}$ thick (Currey 1977, Jackson et al. 1988, Jackson, Vincent and Turner 1989, Jackson et al. 1990, Sarikaya et al. 1990, Currey 1980). Katti et al. (Katti et al. 2005) discovered that nacre has an "interlocked" brick-and-mortar structure with interlocking influencing the mechanical response. These platelets are

mostly pseudo-hexagonal, but they may be triangular, square, or pentagonal depending on the degree of twinning on $\{110\}$ planes of orthorhombic lattice (Heuer et al. 1992, Sarikaya et al. 1990). From the X-ray diffraction results, it has been found that the aragonite platelets are organized with their $[001]$ axis perpendicular to the layers. Sarikaya (Sarikaya 1994) reported that the adjacent platelets in nacre belong to the same $[001]$ zone axis with a slight rotation among the platelets about this axis with respect to each other. Electron diffraction revealed that there is a crystallographic relationship between the adjacent platelets, i.e. each platelet is twin-related to the platelet next to it with a twin plane of $\{110\}$ type of the orthorhombic unit cell. This indicates that all the platelets on the same layer are twin-related whether they share a boundary or not. Further analysis indicated the presence of several domains with in each platelet that are crystallographically coupled. Diffraction patterns showed that two superimposed patterns can be correlated with a twin relationship with $\{110\}$ twin plane parallel to $[001]$ direction of the unit cell. Recorded patterns from all the domain boundaries showed identical twin reflections indicating that each domain is twin-related to the one next to it by a $\{110\}$ twin relation.

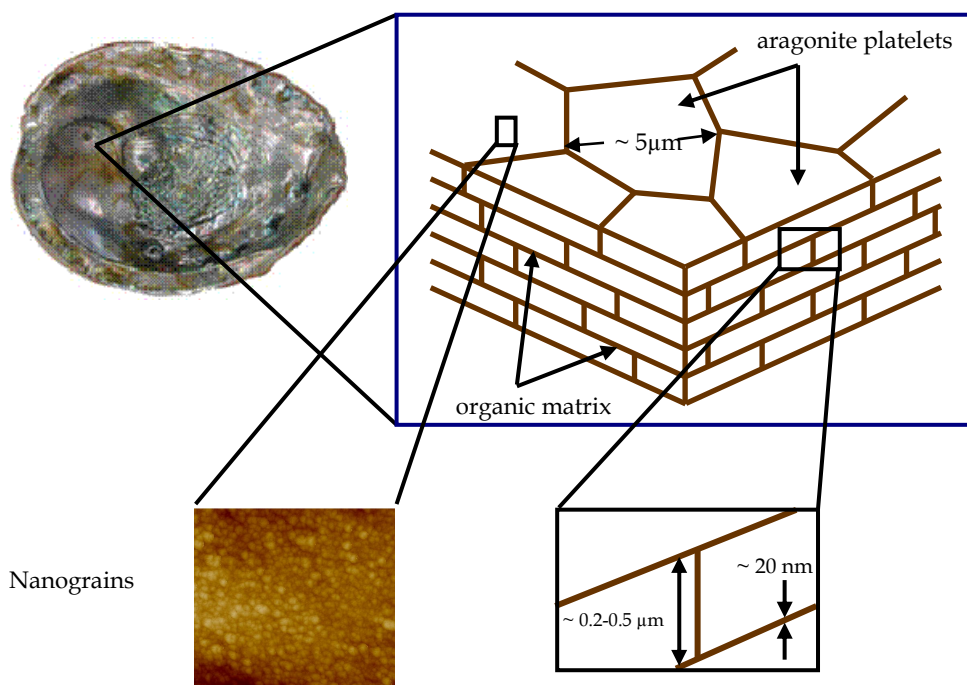


Fig. 2. Schematic representation of hierarchical structure of nacre.

Due to the large span of length scales of the hierarchical structure of nacre, various characterization methods have been utilized. Schaffer et al. (Schaffer et al. 1997) investigated the organic matrix layers of nacre by using atomic force microscope (AFM) and scanning ion conductance microscope (SICM). They observed many nanopores in the inter-lamellar organic matrix sheets. They suggested that there might be a number of mineral bridges in the organic matrix layers of nacre and proposed that the formation of nacre may be due to

continuous growth of mineral bridges through these nanopores in organic matrix layers. Later Song et al. (Song, Zhang and Bai 2002, Song and Bai 2001, Song, Soh and Bai 2003) observed nacre under transmission electron microscope (TEM) and confirmed the existence of mineral bridges in the organic matrix layers. They suggested that the microarchitecture of nacre should be considered as “brick-bridge-mortar” structure rather than the traditional “brick and mortar” arrangement. Based on their observation, they proposed a distribution law of mineral bridges in the organic matrix layers using statistical methods. These mineral bridges were circular in shape with a diameter of ~25-34 nm and the height being equal to the thickness of organic matrix. Density of the mineral bridges was estimated to be approximately $91\text{-}116\ \mu\text{m}^{-2}$. Nanoscale mineral island-like structures were observed using atomic force microscopy (AFM) and scanning electron microscopy (SEM) (Wang et al. 2001, Evans et al. 2001). These were called as nanoasperities and were about 30-100 nm in diameter, 10 nm in amplitude, and separated 60-120 nm. Later, Katti and co-workers (Katti et al. 2005) discovered the presence of interlocking between the platelets of nacre. The mineral platelets are rotated by a small angle relative to each other and form the interlocks by interpenetrating into each other. Scanning electron microscopy imaging of fractured surface of nacre first revealed the presence of extensive interlocking in nacre as shown in Figure 3. They showed that the bricks are not only stacked upon one another to form a brick wall but also interpenetrated into one another to form interlocks. Further, Li et al. (Li et al. 2004) observed that the aragonite platelets consist of polygonal nanograins which are the basic building blocks in nacre. Observation of screw dislocations in nacre has been reported as early as the 1950s in literature (Watabe 1955). Wise et al. (Wise and Devillie, J 1971) showed the significance of these screw dislocations in the crystal growth of the aragonite platelets. Yao et al. (Yao, Epstein and Akey 2006) confirmed the presence of these screw dislocations by excavating individual aragonite platelets using a nanomanipulator with in-situ SEM/FIB. They suggested that the crystal growth in nacre occurs via spiral motion which is responsible for the identical crystal orientation in the successive layers. Nacre contains 106 screw dislocations per square centimeter which is three orders of magnitude higher as compared to typical ionic or covalent crystals. Thus the architecture of nacre spans from molecular, nanograin, defect structures of crystals, mineral bridges, asperities, polygonal, interlocked bricks over the atomic to 10s of microns of length scale with strengthening and toughening mechanisms associated with each length scale.

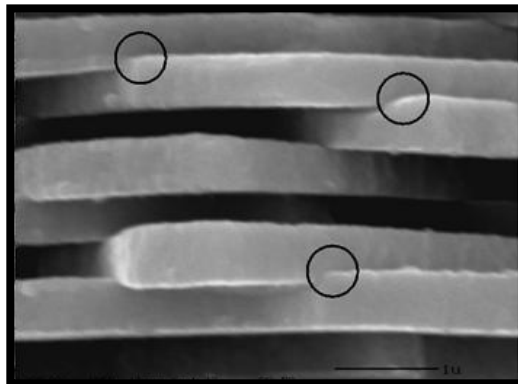


Fig. 3. SEM of nacre showing interlocks (Katti et al. 2005).

2.3. Molecular Structure

Although the molecular structures of components of nacre: the mineral platelets and organic mortar are known to have very significant role on its mechanics, far lesser studies have been conducted on evaluation of molecular structures as compared to the architectures. Weiner and co-workers (Weiner 1979, Weiner and Traub 1980, Weiner and Traub 1981, Weiner, Talmon and Traub 1983, Weiner 1983, Weiner and Traub 1984, Weiner 1984, Addadi and Weiner 1985, Addadi et al. 1987, Addadi and Weiner 1997, Nudelman et al. 2006), as well as Morse and co-workers (Fritz et al. 1994, Zaremba et al. 1995, Zaremba et al. 1996, Schaffer et al. 1997, Shen et al. 1997, Smith et al. 1999, Belcher et al. 1996, Su et al. 2002) have made significant efforts in understanding the organic matrix and biomineralization in molluscan shells. The organic matrix in nacre primarily consists of proteins, with some glycoproteins and chitin. Different proteins play different roles such as: some provide nucleation sites for the growth of aragonite crystals, some are responsible for the secretion of calcium carbonate, and many of them help in stabilizing the aragonite crystal arrangement. Presence of β -sheet structures in an antiparallel conformation was indicated by the infrared spectroscopic results and the amino acid compositions of insoluble shell matrices resembled those of silk fibroins in their content of glycine, alanine and serine, which together constitute more than 50% of the total (Weiner and Traub 1980). The silk-fibroin like protein, in some cases associated with chitin may contribute to the structural basis for the elaboration of the organic matrix framework around which the mineral is deposited. X-ray diffraction studies revealed a well defined spatial relationship between orientations of the protein, chitin and aragonite. The a-axis of the aragonite orthorhombic cell is lined up with the b-axis of chitin and the b- and c- axes of the aragonite lie along the b- and c- axes of the protein respectively. The identification of proteins present in the organic matrix has only been partially done to this date. Although researchers have succeeded in extracting protein from the shells and causing precipitation from the supersaturated solutions of Ca^{2+} and CO_3^{2-} (Addadi and Weiner 1985). Weiner and co-workers (Addadi and Weiner 1985, Weiner and Traub 1980, Addadi et al. 1987) have suggested the presence of aspartic acid-rich proteins (Asp-Y_n), and serine-rich proteins, where Y is an amino acid. The aspartic acid-rich proteins have amino acid composition: Aspartic acid, 32%; Serine, 10%; Glutamic acid, 17%; Glycine, 7% and are often associated with small amounts of polysaccharides. The serine-rich proteins have a amino acid composition: Aspartic acid, 7%; Serine, 25%; Glutamic acid, 8%; Glycine, 19%. Constituents of both these proteins bind to Ca^{2+} and undergo conformational changes. It is believed that the aspartic acid-rich proteins adopt the β -sheet conformation (Addadi and Weiner 1985). The phenomenon of stereo-selectivity has been described in considerable detail and three possible reasons have been suggested: (1) The aspartic acid rich proteins bind preferentially to the calcium atoms, (2) A favorable electric charge is created on the (001) face for the protein adsorption due to the relative position of calcium and carbonate ions, and (3) The coordination around the protein-bound calcium atoms are completed as the carboxylate groups (CO_3^-) are oriented perpendicular to the (001) face. It has been further proposed that the aspartic acid-rich domains are covalently bonded to sulfated polysaccharides, and these sulfates cooperate with β -sheet structured carboxylates for oriented calcite crystal nucleation (Addadi et al. 1987). The sulfates help concentrate calcium, creating the super-saturation required for nucleation on the structured carboxylate domains. The basis of cooperative mechanism is attributed to the distinct ways in which carboxylates and the sulfates interact with calcium ions. The sulfates are strongly associated

with calcium, and carboxylates are relatively weak binders of calcium. Carboxylates being a part of an ordered protein structure help in binding calcium ions in an ordered array.

Morse and co-workers investigated the biomineralization process in red abalone shells by inserting different materials including flat pearls as substrates between the mantle and shell (Fritz et al. 1994, Belcher et al. 1996, Zaremba et al. 1996). Exposure of mantle epithelial cells to a foreign material causes the secretion of proteins that activate growth of calcite layer with preferred {104} orientation, which is followed by the growth of nacreous aragonite. The transition from {104} oriented calcite growth to aragonite growth is abrupt. It is suggested that the formation of mineral structure and the molluscan shell architecture are controlled by the interaction at the cell-mineral interface. Belcher et al. performed *in vitro* crystallization of calcium carbonate in the presence of water-soluble polyanionic proteins extracted from abalone shell. It was found that these proteins are sufficient to control the crystal phase and govern the transition between calcite and aragonite growth. These proteins are also necessary for the control of nucleation and crystal orientation. Shen et al. characterized the cDNA coding for Lustrin A, which is a protein they identified and is present in the organic matrix in the nacreous layer of red abalone (Shen et al. 1997). Analysis of amino acid sequence of this protein revealed that it exhibits a highly modular structure with a high proportions of Serine (16%), Proline (14%), Glycine (13%) and Cystine (9%). It contains ten cystine-rich domains (C1-C10) and eight proline-rich domains (P1-P8). These proline-rich domains are present between the cystine-rich domains and act as extenders allowing them to work independently. The glycine- and serine-rich domains lie between the cystine-rich domains near the C terminus. It was shown that the mineralization of nacre is controlled by the cystine-rich domain, and the proline-rich domains act as spacers between the cystine domains. Further, Lustrin A is multifunctional protein that combines several structural elements into a single molecule. Su et al. (Su et al. 2002) characterized the growth lines in red abalone shell using X-ray diffraction, and scanning and transmission electron microscopy. The growth lines were observed to consist of two types of structures: blocklike and spherulitic, separated by a green organic matrix interlayer. Both these structures are composed of aragonite, the same CaCO_3 polymorph as in the nacreous layer. The spherulitic structure is composed of radially distributed elongated crystals and the block-like structure is made up of crystalline aggregates with irregular shape. The size of the individual aggregates is similar to that of a single crystal and the orientation is identical to that of the adjacent stack of tablets in the nacreous structure. Nudelman et al. (Nudelman et al. 2006) mapped the distribution of organic matrix components underlying a single aragonite platelet in nacre. Four different zones were observed under a single aragonite platelet: a central spot rich in carboxylates which is surrounded by a ring-shaped area rich in sulfates, third zone is the area between the central nucleation region and the imprint periphery containing carboxylates, and the fourth zone is the intertabular matrix which is rich in carboxylates and sulfates. Gilbert et al. (Gilbert et al. 2008) investigated red abalone shells using X-ray photoelectron emission spectromicroscopy and suggested that orientational ordering of aragonite tablets in nacre do not occur abruptly but gradually over a distance of 50 μm from the prismatic boundary. They suggested that different crystal orientations in nacre tablets correspond to different growth rates. All the tablets try to grow and compete for space. The oriented tablets grow faster than the misoriented ones and create ordering in nacre. It was also suggested that the ordering of the mineral phase may be independent of biological or organic-molecule control.

Kattis and co-workers have performed FT-IR (Fourier transform infrared) spectroscopic experiments (Verma, Katti and Katti 2006, Verma, Katti and Katti 2007) and molecular dynamics (MD) simulations (Ghosh, Katti and Katti 2007, Ghosh, Katti and Katti 2008) to understand the organic-inorganic interactions in nacre at molecular level. Verma et al. (Verma et al. 2006) performed PA-FTIR (photoacoustics FTIR) experiments on undisturbed nacre as well as powdered nacre and compared the results. The observed differences in PA-FTIR spectra of nacre powder and undisturbed nacre are believed to arise from two sources: breaking of bonds between organic and inorganic phases, and relaxation of residual stress that exists in the structure of nacre. They also investigated the stratification in nacre using PA-FTIR experiments in step-scan mode. Results did not indicate any significant compositional changes in the mineral and protein layers. In another study, Kattis and coworkers (Verma et al. 2007) performed 2D-FTIR spectroscopy and deconvolution analysis to investigate the nature and location of water present in nacre. They found three different forms of water present at various locations in nacre as shown in Figure 4. One of the forms is partially hydrogen bonded possibly hydrogen bonded with the organic matrix. Second form of water is fully hydrogen bonded with the surrounding water molecules and is similar to bulk water. This form of water is possibly located in the pores of the organic matrix and the organic platelets. Third form of water is the chemisorbed water present on the surface of the aragonite platelets. Polarization experiments indicated that the water present in nacre exhibits a preferred orientation. The H-O-H plane of water molecule is oriented parallel to the c-axis of aragonite platelets. Furthermore, molecular models of organic and mineral phase were built and steered molecular dynamics simulations were performed to understand the effect of mineral-protein interaction in the work of Kattis and co-workers (Ghosh et al. 2007). In this work, glycine-serine domain of a nacre protein Lustrin A was used as a model system. The protein molecule was pulled in absence and presence of mineral phase as shown in Figure 5. Obtained load-displacement curves indicated that the mechanical response of the organic phase in nacre is significantly influenced by the mineral proximity. It was observed that the energy required to pull the protein molecule in the proximity of mineral is several times higher than when the mineral is absent. Further, the pulling velocity of the protein molecule influences the factor by which additional amount of energy is required to unfold a protein domain. In another study, Kattis and co-workers (Ghosh et al. 2008) quantitatively described the specific mechanisms responsible for the differences in load-displacement (L-D) responses of protein at mineral proximity and absence of mineral. It was shown that the peaks in the L-D plot can be directly correlated to the interaction energies between the atoms involved in the latching phenomenon of amino acid side chain to aragonite surface during the early stage of pulling. Further, water plays a significant role in the mineral-protein interaction. Water close to the mineral phase is highly oriented and does not move while the protein is being pulled. The layer of water around the protein strands moves with the strand as the protein is pulled. Attractive interactions between the various constituents, the protein, protein-bound water, and the mineral are primarily responsible for the high magnitude of load required for a given displacement. These studies indicate a significant role of organic-inorganic interactions in the mechanical response of nacre and the important role of water in these interactions.

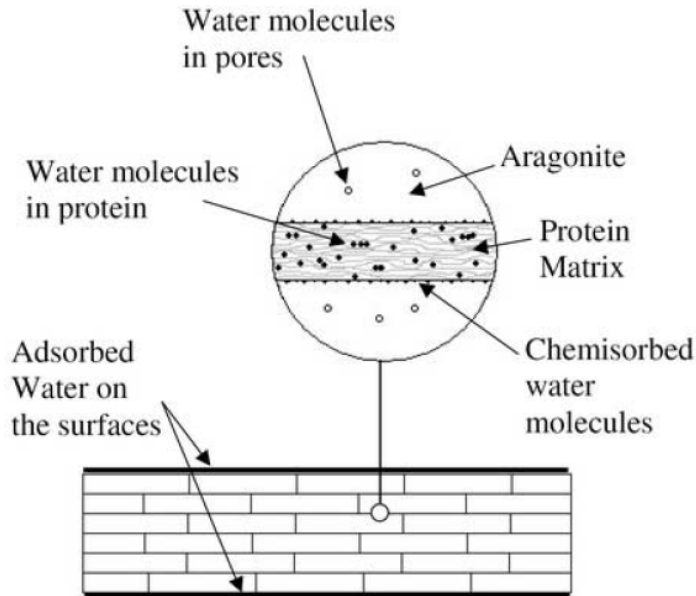


Fig. 4. Schematic showing presence of water clusters in the protein matrix and chemisorbed water molecules at the interface (Verma et al. 2007)

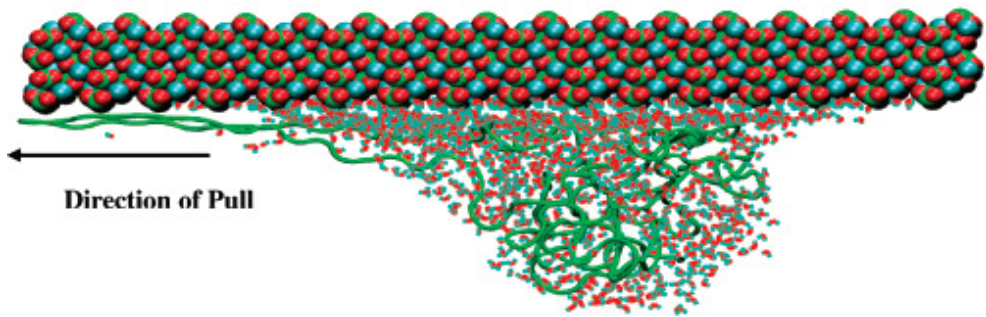


Fig. 5. Model of Glycine - Serine (GS) domain at mineral proximity as the GS domain is pulled. The ball form with the cyan, red, and green combination is atoms in aragonite, the ribbon form in green is the GS domain, and the line form with red and cyan lines represents water (Ghosh et al. 2007).

2.4. Mechanical properties

Literature shows several comparative studies on the mechanical properties of various structural types found in molluscan shells (Taylor and Layman 1972, Currey and Taylor 1974, Currey 1976). It is clear that nacre is stronger than other structures irrespective of the loading type. The extraordinary toughness possessed by nacre was first described by Currey

(Currey 1977). He suggested that the mechanical properties of nacre result from its structure and specifically, the highly organized micro-architecture with precise arrangement of mineral platelets. This arrangement of mineral platelets obstructs crack propagation. Later, Jackson et al. (Jackson et al. 1988) performed an extensive experimental study on the mechanical properties of nacre and tested nacre in dry and wet conditions. They reported Young's moduli values of 70 GPa and 60 GPa for dry and wet samples respectively. The tensile strength of nacre was found to be 170 MPa for dry and 140 MPa for wet samples. Depending on the span-to-depth (S/D) ratio and degree of hydration, the work of fracture varied between 350 to 1240 J/m². In contrast, the observed work of fracture for monolithic CaCO₃ was about 3000 times less than that of nacre. They found that the water absorbed in the organic matrix of nacre plays a significant role in the mechanical response of nacre. Presence of water reduces the Young's modulus and tensile strength, where as the work of fracture shows pronounced increment. Nacre exhibits a work of fracture which is almost three times when wet as compared to dry nacre. Water may cause reduction in shear modulus and shear strength of the organic matrix which in turn reduces the Young's modulus and tensile strength. Significant improvement in the toughness might be due to the plasticizing of organic matrix by water. This plasticizing of the organic matrix may cause debonding around the crack tip. They also pointed out that the nacre platelets have small S/D ratios making them more ductile and there by increasing the ability to absorb more energy. In another study Jackson et al. (Jackson et al. 1990) compared the properties of nacre with different synthetic composites that had high volume percent of ceramic phase and a minor organic phase as the matrix. The closely packed layered structure and soft organic matrix were the two features that distinguished nacre from other synthetic composites used in the study. Further, they found that nacre is stiffer, stronger and tougher than the synthetic composites. After these key studies by Currey and Jackson et al., literature was deluged with various kinds of studies involving experiments and modeling to understand the mechanisms responsible for the high toughness in nacre. Various experimental techniques have been used to understand the mechanical behavior of nacre at different length scales and their relationship to the microstructure. Modeling techniques such as finite element analysis (FEA) and molecular dynamics (MD) have been used to get an insight into the mechanisms enhancing the mechanical behavior of nacre.

Experimental evaluation using fractographic and ultramicrostructural analysis using scanning electron microscopy (SEM) and transmission electron microscopy respectively have also been conducted (Sarikaya et al. 1990). conducted mechanical tests on nacre samples. Similar tests were also carried out on alumina and partially stabilized zirconia samples for comparison. From the indentation experiments it was observed that cracks extend radially from the corners of the indentation in case of the pure ceramic samples, indicating brittle behavior. Similar tests on transverse direction in nacre indicated that cracks do not extend from corners of the indentation, but from regions close to corners and propagate in various directions. They suggested that these directions might be the high strain regions formed due to the complex stress distribution in the nacre structure. The path of the cracks and microcracks were very tortuous which indicated a large amount of energy absorption in the form of deformation during the crack propagation. This resulted in higher fracture toughness as compared to other monolithic ceramics. From the fractographic analysis of the fracture surfaces and indentation cracks, they suggested several possible

mechanisms for toughening of nacre. These mechanisms are crack blunting/branching, microcrack formation, platelet pull-outs, crack bridging (ligament formation), and sliding of layers. They concluded that all these mechanisms have to be operative in nacre to increase the fracture toughness and strength. High tortuosity seen in the crack propagation was mainly due to crack blunting and branching, and the tortuosity was not considered the major toughening mechanism. Wang et al. (Wang et al. 1995) used SEM, TEM and microindentation tests to study the deformation, fracture and toughening mechanisms in nacre. Their results revealed anisotropic nature in fracture and microindentation morphologies, as well as the cracking behavior of nacre. And this reflects the microstructural character of nacre. It was observed that the fracture surface parallel to the cross-sectional surface is much more tortuous as compared to the surface that is parallel to the platelet surface. Step-like crack lines were seen on the cross-sectional surface where as it is polygonal on the platelet surface. They suggested that the major plastic deformation mechanism in nacre is the sliding of the aragonite layers combined with plastic deformation in the organic matrix. They concluded that there are three major toughening mechanisms in nacre acting simultaneously: crack deflection, fiber pull-out, and organic matrix bridging. Smith et al. (Smith et al. 1999) pulled the organic molecules from a freshly cleaved nacre surface using atomic force microscope (AFM) and obtained consecutive force-extension curves without touching the surface between the pulls. They observed rupture events with a saw-tooth appearance in each of the obtained force-extension curves. Observed hysteresis after completion of a pulling cycle demonstrated that work has been done on the shell which is irreversible and is dissipated in the form of heat. The dissipated heat was found from the area between the retracting and approaching parts of the curve, and it was found to be of the order of $(0.4-1) \times 10^{-17}$ J per cycle. Each peak in saw-tooth curve indicates opening of intra-chain loops or folded domains within a single molecule. This may also indicate the successive release of sacrificial inter-chain bonds crosslinking multiple chains together in the matrix. They concluded that breaking of sacrificial inter-chain bonds and opening of folded domains absorb energy and contribute towards the high toughness of nacre. Song et al. (Song et al. 2002, Song and Bai 2001, Song et al. 2003) observed the presence of mineral bridges using TEM. To investigate the effect of mineral bridges, they performed tension and three-point bend tests on dry nacre samples and examined the fracture surface morphology. They found that the organic matrix layer is linear elastic in the direction of mineral bridges and undergoes very small deformation before crack extension. All the cracks were observed to propagate through the organic matrix layers. They suggested that the presence of mineral bridges significantly affects the organic matrix layers by enhancing the stiffness, strength and toughness. Mineral bridges in organic matrix layers are intimately associated with the two major toughening mechanisms in nacre: crack deflection and platelet pull-out, because of the unique microstructure of nacre. They concluded that nacre possesses a high toughness because of the existence of mineral bridges in the weak layers where as other synthetic materials with "brick and mortar" structure do not have a toughness comparable to nacre. It has been discussed in the previous section that nanoasperities were observed on the surface of platelets in nacre (Wang et al. 2001, Evans et al. 2001). Wang et al. (Wang et al. 2001) and Evans et al. (Evans et al. 2001) showed that deformation in nacre is inelastic both in shear and tension. And the nanoasperities on the surface of aragonite platelets govern the stress at which the inelastic deformation proceeds. The interposing arrangements of nanoasperities control the sliding resistance that facilitates the observed ductility in nacre. They suggested

that the organic matrix and nanoasperities play a key role in toughening of nacre. Based on their study, they identified four design principles that impart high toughness to nacre. (i) The mineral phase possesses tabular morphology and is optimized with plate size, aspect ratio, and topological arrangements to maximize the inelastic strain. (ii) The amplitudes and wavelengths of nanoscale asperities on the platelet surface cause strain hardening large enough to form multiple dilatation bands, but not so large which may lead to internal fracture of the platelets. (iii) Organic interlayer has sufficient adherence and transverse stretch that keeps the platelets intact in the regions between dilatation bands, where transverse tensile strains are generated. (iv) Organic matrix provides high lubrication that makes the interface slip frictionless. Meyers and co-workers studied the quasi-static as well as dynamic mechanical response of *Haliotis rufescens* (abalone) (Menig et al. 2000) and *Strombus gigas* (Menig et al. 2001) (conch) shells. From their observations, they suggested that the shell structure imparts a significant increase in the toughness of the brittle aragonite mineral. They identified two primary toughening mechanisms in nacre: (i) sliding of mineral platelets by means of viscoplastic deformation of the organic interfacial layers; (ii) arrest and deflection of cracks by the viscoplastic organic layers. These two mechanisms and the highly organized microstructure, consisting of mineral platelets, lead to delocalization of failure. Due to this delocalization of failure, one single sharp crack is replaced by a large number of smaller cracks in a broader region. Kamat et al. (Kamat et al. 2000) indicated that the cracks do not propagate catastrophically through the middle layers of mollusk shells and the crack propagation retarded by the bridging action of the first-order lamellae.

Kotha et al. (Kotha, Li and Guzelsu 2001) modeled the tensile behavior of nacre using a modified shear lag theory. They used a two-dimensional model to analyze the stress transfer between the aragonite platelets. They suggested that composites having high toughness can be made using platelets with small aspect ratios, but the matrix should be designed to have high shear strains. Organic matrix can have high shear strains through the presence of loops or domains that break at different strains.

Katti et al. (Katti et al. 2001, Katti and Katti 2001, Katti, Pradhan and Katti 2004, Katti et al. 2005) studied the mechanical response of nacre using finite element modeling and experimental techniques to understand underlying mechanisms responsible for the high toughness of nacre. Their results led to important findings that give a better insight about the mechanical behavior of nacre. 3D finite element modeling results indicated that a very high (400 MPa) yield stress of the organic phase is needed to obtain the stress-strain behavior and yield stress of nacre observed experimentally (Katti et al. 2001). This value of yield stress is higher than the observed values for real proteins and biological tissues. Necessity of the high yield stress is due to higher effective local stresses in organic phase than applied. They suggested that the organic phase might be a composite containing a high yield stress component. Also, high yield stress of the organic phase may be due to the presence of possible hard contacts between the mineral platelets through the organic layer causing higher stress in organic phase than applied. In another study using finite element simulations, Katti et al. (Katti and Katti 2001) showed that the organic phase possesses an elastic modulus of ~ 15 GPa. This value of elastic modulus is higher than the reported values for the organic phase by three orders of magnitude. Katti et al. (Katti et al. 2004) evaluated the role of nanoscale asperities present on the aragonite platelet surface. These

nanoasperities were incorporated in the finite element models as shown in Figure 6 and simulations were performed using different values for the yield stress of the organic. The results revealed that the nanoasperities have a marginal effect on the over all mechanical response of nacre. In the elastic regime, a small increase in elastic modulus was observed due to the presence of nanoasperities, part of which resulted because of increase in mineral volume and part due to the structural effect of nanoasperities. No significant effect of nanoasperities was observed in the inelastic regime. As discussed in the previous section, Katti et al. (Katti et al. 2005) discovered the presence of platelet interlocks in the structure of nacre. They also evaluated the effect of these interlocking features on the mechanical behavior of nacre by incorporating them into finite element models as shown in Figure 7. Finite element analysis results revealed that these platelet interlocks play a key role in imparting high toughness and strength to nacre. Interlocks function as physical obstacles to the relative movement of the mineral platelets. Thus, these interlocks must break before the load is completely transferred to the organic matrix. Further, these interlocking features might play a role in inhibiting crack propagation by crack branching and blunting. Platelet interlocks are spread throughout the volume of nacre and collective influence of these interlocks from different layers is translated into the bulk mechanical response of nacre. This results in a significant enhancement of fracture toughness and strength by providing a mechanism for energy dissipation.

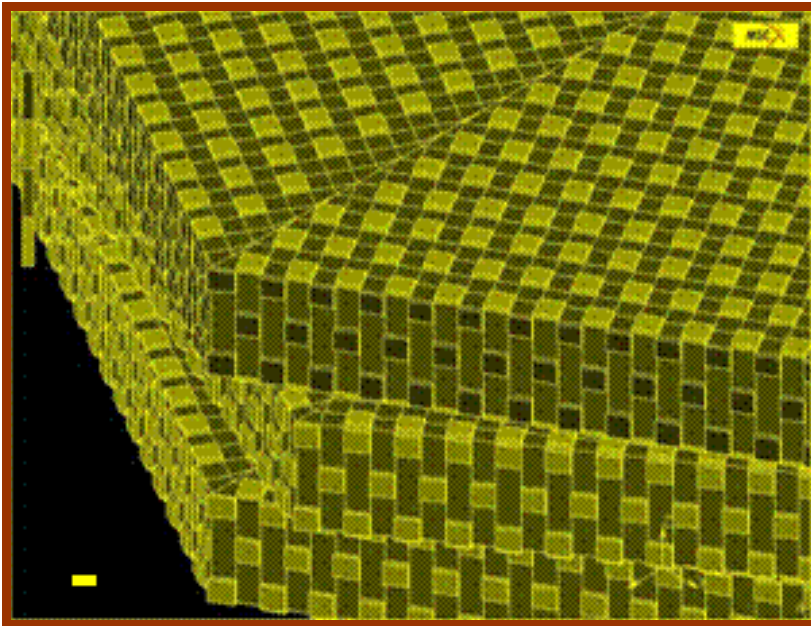


Fig. 6. 3D FE model of nacre with nanoasperities (Katti et al. 2004).

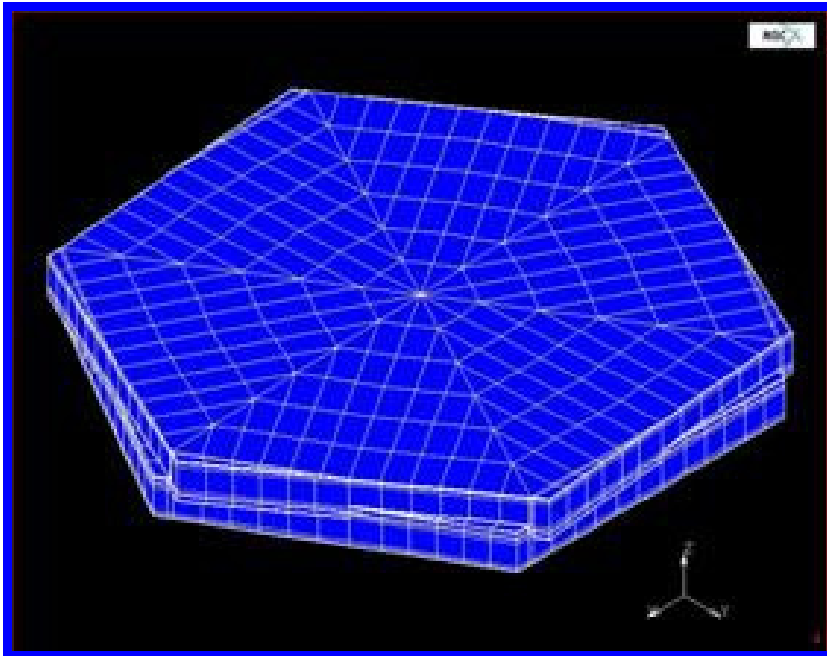


Fig. 7. 3D FE model of nacre with platelet interlocks (Katti et al. 2005).

Li et al. (Li et al. 2004) used microindentation and AFM imaging techniques to study the deformation behavior of nacre. They observed plastic deformation in the aragonite platelets around the crack tip which indicated that the aragonite platelets are not brittle in nature but somewhat ductile. The plastic deformation allows the material to redistribute stress around strain concentrated site, thereby eliminating stress concentration that results in blunting the crack tip. They believed that the ductility of aragonite platelets results from a large number of nanograins which are the basic building blocks. They suggested that the deformability of aragonite platelets along with crack deflection, platelet slip, and organic adhesive interlayer result in a unusual increase in toughness of nacre. Bruet et al. (Bruet et al. 2005) investigated deformation in nacre using atomic force microscopy (AFM) and nanoindentation. They performed nanoindentation tests on nacre and observed the deformation of the indented region using AFM. AFM images showed flattening of the nanoasperities, plastic deformation, pileup around indent and no microcracks in the pileup region. Deformation at nanoscale revealed ductile behavior of aragonite platelets that is not expected to be present in case of a ceramic which is expected to exhibit microcracking under the tensile stresses observed in the pileup region and fail in a brittle manner. The observed ductility might be due to the small length scale or may indicate that the obstructed organic molecules within the platelet lessen any defects and impart ductility to the deformation process. The pileup zones around the indents indicated the ability of nanoasperities to undergo plastic deformation to accommodate strain caused by the indenter tip. Bruet et al. suggested that plastic deformation of the nanoasperities may occur initially and can act as a safety mechanism prior to the intertablet shear. Barthelat et al. (Barthelat et al. 2006, Barthelat and Espinosa 2007) investigated the mechanical performance of nacre using experiments and

finite element modeling. They suggested that the observed ductility is because of the small length scale, and the nanoasperities and nanograins are not likely to be the key microstructural features controlling the unique mechanical response of nacre (Barthelat et al. 2006). From this experimental study, it was suggested that the viscoplastic energy dissipation in the proteins and other biopolymers present between the platelets associated with the sliding of the platelets in nacre, is a significant fracture toughening mechanism.

Kattis and co-workers (Mohanty et al. 2006) investigated the dynamic nanomechanical response of nacre using dynamic nanoindentation, AFM and Fourier transform infrared spectroscopy (FTIR). Dynamic nanoindentation tests were performed at different loads with varying frequency. Loss modulus (E'') and $\tan \delta$ values were observed to increase with increase in testing frequency. Their observation of results at lower indentation depths indicated that the mineral phase exhibits viscoelastic behavior which is not expected in case of a ceramic material. Viscoelastic nature of the aragonite platelets was attributed to the presence of nanograins and water within the platelets. Kattis and co-workers (Verma et al. 2007) further utilized 2D-FTIR spectroscopy and deconvolution analysis to describe the nature and location of water present in nacre. Later, Li et al. (Li, Xu and Wang 2006) observed nanograin rotation and deformation while pulling nacre samples in tension by in situ AFM imaging. They suggested that the nanograins are closely packed by the biopolymer adhesive to form a robust structure. When nacre is pulled in tension, the biopolymer between the nanograins is stretched that allows enough space for some nanograins to rotate. During rotation, these nanograins push neighboring nanograins and also undergo deformation. They suggested that the grain rotation and deformation results in high deformability of the aragonite platelets and are two key mechanisms for energy dissipation in nacre. Meyers et al. (Meyers et al. 2008) investigated the role of organic layer on the mechanical strength of nacre. They concluded that the primary role of the organic layer is to subdivide the CaCO_3 matrix into platelets with thickness of $0.5 \mu\text{m}$. It was also suggested that the scale of the structural components in nacre is an important parameter. Mohanty et al. (Mohanty, Katti and Katti 2008) investigated the mechanics of mineral-protein interface of nacre using force mode AFM. Protein molecules were pulled from the cleaved nacre surface using AFM and the force required to pull the protein molecules was measured. Results indicated that the protein molecules withstand a large force ($\sim 6 \text{ nN}$), before they are pulled off of the aragonite platelet. These forces are several orders of magnitude higher than those obtained for unfolding of domains in a single protein molecule. They estimated the force of adhesion between the organic phase and the aragonite platelet for the first time. They suggested that the large work of adhesion can lead to a large amount of energy dissipation by the protein molecules and contribute towards the bulk toughness of nacre. This indicates a significant role of organic-inorganic interactions on the mechanical response of nacre.

Some researchers have used micromechanical modeling to predict the mechanical behavior of nacre (Zuo and Wei 2008, Bertoldi, Bigoni and Drugan 2008). Zuo and Wei (Zuo and Wei 2008) suggested that the deformation in nacre can be well described by modified shear-lag model considering the elastic-plastic hardening property of the protein. Tushtev et al. (Tushtev, Murck and Grathwohl 2008) showed using finite element simulations that the high stiffness of nacre under tensile load in longitudinal direction is only possible, if the organic layer is incompressible. They pointed that the organic layer plays a key role on the

load transfer between the platelets which affects the stiffness of nacre. Sumitomo et al. (Sumitomo et al. 2008a, Sumitomo et al. 2008b) used transmission electron microscopy to observe the nanoscale deformation structures in nacre. They observed strong adhesion of organic phase to the mineral plates and high ductile behavior of the organic matrix (Sumitomo et al. 2008a). Viscoelastic reformation of the matrix ligaments after failure was also observed. Nanograin separation, nanograin shear, and crack bridging due to organic matrix ligament formation within the fractured platelets were observed. They suggested that toughening of nacre occurs in a hierarchical manner from nano to macroscale; i.e. from nanograins, to platelets and to bulk nacre.

As discussed in this section, various different mechanisms have been proposed in literature those contribute towards the energy dissipation in nacre. These mechanisms are summarized below:

Crack diversion and crack branching make crack propagation very tortuous.

Crack bridging by the ligaments of organic matrix.

Formation of microcracks.

Frictional resistance due to presence of nanoasperities and mineral bridges have marginal effect on the toughness of nacre.

Unfolding of protein domains and breaking of crosslinks in the organic phase.

Plasticizing effect of water present in nacre.

Platelet interlocks.

Viscoelastic behavior of the organic phase.

Viscoelastic behavior of the mineral platelets.

Rotation and deformation of nanograins.

3. Biomimicking Efforts

Highly organized microarchitecture and extraordinary mechanical response of nacre have inspired scientists to develop synthetic nanocomposite materials mimicking nacre. Till date, several attempts have been made using various reinforcing materials and different processing methods to develop layered nanocomposite materials those mimic the structure of nacre (Sellinger et al. 1998, Almqvist et al. 1999, Feng et al. 2000, Tang et al. 2003, Zhang et al. 2002, Zhang et al. 2004, Zhang et al. 2006, Gehrke et al. 2005, Bennadji-Gridi, Smith and Bonnet 2006, Wei et al. 2007, Long et al. 2007, Chen et al. 2008, Podsiadlo et al. 2007, Podsiadlo et al. 2008, Lin et al. 2008). Sellinger et al. (Sellinger et al. 1998) synthesized poly (dodecylmethacrylate)/silica nanocomposite using a self assembly process based on a simple dip-coating procedure. They started with a solution of silica, surfactant and organic monomers, formation of micelles and partitioning of the organic constituents into micellar interiors occurred due to evaporation during dip-coating. Organic and inorganic precursors get organized into the desired nanolaminated form with subsequent self-assembly silica-surfactant-monomer micellar species. Finally, the nanocomposite assembly process is completed with polymerization that fixes the structure. Almqvist et al. (Almqvist et al. 1999) fabricated laminated nanocomposite materials using talc tablets as the inorganic phase and polyvinylacetate as the organic phase and investigated seven different physical fabrication methods. In this work 10 wt% of organic was used as it was difficult to wet the talc tablets with an organic content of 5 wt%. It was suggested that align of tablets can be obtained by

using a suitable processing method. No significant improvement in the mechanical properties was observed due to improvement in tablet orientation. Feng et al. (Feng et al. 2000) synthesized alumina/aramid fiber reinforced epoxy composites containing five alumina (0.38 m thick) lamnas and four aramid fiber reinforced epoxy strips (0.18 mm thick) alternatively. The synthesized composite exhibited a work of fracture that is 80 times of that of monolithic alumina. Tang et al. (Tang et al. 2003) prepared a nanostructured composite with alternating organic and inorganic layers mimicking nacre by sequential deposition of polyelectrolytes [poly(diallyldimethylammonium) chloride polycation] and clays. The saw-tooth pattern in the stretching curves revealed gradual breakage of ionic crosslinks in polyelectrolyte chains which is similar to the unfolding of protein domains in nacre. The tensile strength of these multilayered composites was comparable to that of nacre. Zhang et al. (Zhang et al. 2004) synthesized silica/poly(methacryloxyethyl hexadecyldimethyl ammonium bromide) nanocomposite thin films by supermolecular self-assembly method on glass substrate. It was confirmed that the nanocomposite films resemble the laminated structure in nacre. Zhang et al. (Zhang et al. 2006) prepared poly(tripropylene glycol diacrylate) (i.e. poly-TPGDA)/indium-tin-oxide (ITO) nanocomposite films by dip-coating method where the self-assembly was induced by evaporation. Results indicated that the films have organic and inorganic layers with orderly arrangement. Gehrke et al. (Gehrke et al. 2005) used a unique method to synthesize artificial nacre remineralization of the insoluble matrix of natural nacre. Prior to this, nacre was demineralized and the soluble proteins were removed. Scanning electron microscope images of the fractured surface showed that the artificial nacre closely resembles the natural nacre. Bennadji-Gridi et al. (Bennadji-Gridi et al. 2006) prepared nacre-like films based on Na/Ca montmorillonite by drying the dispersions with low concentrations of delaminated platelets. A dense brick-like structure was obtained after complete drying using a sodium salt as deflocculant. The observed mechanical properties were not comparable to that of nacre. Wei et al. (Wei et al. 2007) designed a structure mimicking nacre by alternating layer-by-layer deposition of polymer films and CaCO_3 strata. The organic matrix composed of layer-by-layer polymer thin films of diazo-resins (DAR) and poly (acrylic acid) (PAA). The role of DAR is to cross-link the thin films and PAA provides a surface for facilitating the biomineralization. The inorganic layers of CaCO_3 strata were prepared via CO_2 diffusion method. The thickness of inorganic layer can be controlled by varying the diffusion time of CO_2 and the thickness of organic matrix can be controlled by the number of polymer thin film layers. Long et al. (Long et al. 2007) prepared polyacrylamide-clay nacre-like nanocomposites by electrophoretic deposition of montmorillonite modified by acrylamide monomers in an aqueous suspension. Electrophoretic deposition was carried out using the suspension of organic clay in distilled water. Then the deposit on the electrode was polymerized under ultraviolet radiation using a photo-initiator. The nanocomposite was observed to possess a uniform and organized layer-by-layer structure which was similar to the brick-and-mortar structure of natural nacre. These nacre-like composites exhibited significant improvement in elastic modulus and hardness values as compared to that of pure montmorillonite. Chen et al. (Chen et al. 2008) fabricated inorganic/organic nanocomposites using clay nano-platelets as the mineral and polyimide as the organic constituent. An ordered nanostructure with alternating organic and inorganic layers was achieved using a centrifugal deposition process. Improvement in mechanical properties was observed, but they were not comparable to that of nacre. Podsiadlo et al. (Podsiadlo et al. 2007) prepared a high-strength

nanocomposite by sequential deposition using clay and L-3,4-Dihydroxyphenylalanine (DOPA) polymer which is an amino acid present in mussel protein. DOPA was used as it is known to have high affinity for a variety of chemically distinct surfaces: organic and inorganic, via coordination, covalent and hydrogen bonds. Significant improvement in ultimate tensile strength was observed with the addition of DOPA. In another study, Podsiadlo et al. (Podsiadlo et al. 2008) prepared nacre-like structures by using poly(vinyl alcohol) (PVA) and Na-montmorillonite clay nanosheets. They undertook a layer-by-layer assembly technique. Further, PVA and montmorillonite were bound mainly through weak hydrogen bonds and PVA was crosslinked using metal cations after assembly, to introduce ionic bonds in the structure. A double network of sacrificial bonds is created with the introduction of ionic bonds. During deformation, it is expected These sacrificial cross-links can break and form again in the course of deformation. The mechanical property of these composites exhibited significant improvement. The cross-linked films exhibited an ultimate tensile strength ($\sim 320 \pm 40$ MPa) which is more than twice as high as that of nacre ($\sim 80 - 135$ MPa). Lin et al. (Lin et al. 2008) introduced a special assemble method using hydrothermal-electrophoretic techniques to prepare clay based nanocomposites that mimics nacre, both in structure and composition. In the first step, the polymer is intercalated into the interlayer space of montmorillonite by hydrothermal process and electrophoretic deposition is carried out in the second step. Results showed an increase in elastic modulus value as compared to that of pure montmorillonite. As discussed in this section, several attempts have been made to mimic the structure of nacre till date. None of the composites have exhibited an improvement in toughness as in case of nacre. One possible reason might be that all these composites do not possess the interlocking features observed in nacre. Moreover, the organic phase in case of nacre exhibits a very high elastic modulus.

4. Multiscale Modeling

Nacre is a nanocomposite that has a hierarchical microstructure and exhibits unique mechanical properties. There are several structural details at various length scales which influence the overall mechanical response of nacre. Modeling mechanical behavior of nacre through models is necessary to understand the role of structure at different length scales on overall mechanical behavior. Traditional routes of modelling composites such as those based on micromechanics and continuum theories are not applicable or practical over the large length scale (nm to mm) and time scale (fs to s) and requires unique multiscale methodologies. Kattis and co-workers have used different modeling tools along with experiments to investigate the mechanical response of nacre at different length scales based on a unique hierarchical multiscale modelling methodology (Ghosh et al. 2007, Ghosh et al. 2008, Katti et al. 2001, Katti and Katti 2001, Katti et al. 2004, Katti et al. 2005, Katti, Mohanty and Katti 2006, Katti and Katti 2006, Mohanty et al. 2006, Mohanty et al. 2008, Verma et al. 2006, Verma et al. 2007). They have quantitatively described the role of each of nanostructural details on the mechanics and deformation behavior of nacre. The identified key mechanisms influencing the overall mechanical behaviour of nacre have been quantitatively identified. Katti et al. have extensively used finite element (FE) modeling to understand the mechanical response of nacre. 3D finite element models of nacre were constructed based on interlocked brick and mortar architecture. Material properties of the constituents were included in the model. Elastic modulus of aragonite was obtained from

nanindentation tests to include in the model. Mechanical properties of organic were not available at the time of study and were predicted from finite element simulations applying tensile and compressive stresses to the model. Mineral bridges and nanoscale asperities were incorporated in the finite element models. The size, shape and distribution of these features were included according to the reported observations found in literature. Interlocks were constructed by rotating the stack of two aragonite platelets by five degrees relative to each other and then protruding the upper platelet into the lower platelet through a distance of 50 nm. This penetration distance of 50 nm was obtained from the SEM images which include the 20 nm thick organic film between two aragonite platelets. Simulations results indicated a very high elastic modulus value for the organic phase. FE simulation results revealed that the presence of mineral bridges and nanoasperities in the nacre structure have marginal effect on the mechanical response of nacre. The obtained stress-strain response of nacre from FE simulation with interlocks indicated that the observed deformations in nacre are results of deformation of the organic phase, inorganic phase and failure of the interlocks. The progressive failure of the platelet interlocks contribute to the high toughness and strength of nacre.

MD simulations have also been performed to understand role of molecular interactions on the mechanical behavior of nacre. Results showed that the mineral significantly influences the mechanical response of the organic phase. Protein molecules were pulled experimentally from the cleaved nacre surface using force mode atomic force microscopy. Experimental results were in agreement with the MD simulation results which indicated that a high force is required to pull the protein molecules. These simulation and experimental studies led to some important findings that help better understand the underlying mechanisms responsible for the unique mechanical response of nacre. Based on these studies, Katti et al. have identified the key components that contribute towards the high strength and toughness of nacre as given below:

Unique properties of the organic phase in the confined space between the platelets.

Size and shape of platelets (i.e. structure at micro scale).

Interlocking aragonite platelets.

Bonded and non-bonded molecular interactions at the organic-inorganic interface.

5. Conclusions

In summary, here we present the unique aspects of the details of the structure of nacre, the inner layer of many molluscan seashells. Also described is the state-of-art in understanding the structure-property relationships in nacre covering the length span from nanoscale features to a length scale of mm. It appears that this unique architecture of nacre and its resulting exceptional properties of fracture toughness and strength have intrigued materials scientists over decades and has been a subject of biomimetic design for over 4 decades. We also present recent attempts to mimic structure and mimic properties using engineered systems. It appears that engineering routes suffer from the inherent incapability of achieving hierarchy although details at any given length scale are easily achieved. This hierarchy itself is of paramount importance that gives properties such as toughness and structural redundancy to biological materials and structures. Unearthing the key to mechanisms of hierarchy (which are most definitely biological) needs to be the fundamental goal of the field

of biomimetics which if successful has far reaching applications in defence, structures, medicine and other areas. Unearthing details of structure in nacre has been extensively investigated but unearthing the mechanisms by which biology accomplishes hierarchy has not been sufficiently investigated. None the less, nature continues to both inspire and intrigue and we continue to be inspired to design and duplicate details copied from nature intrigued by its simple processing routes and engineering.

6. References

- Abelson, P. H. (1954) Organic constituents of fossils. *Carnegie Inst. Washington Yearb*, 53, 97-101.
- Addadi, L., J. Moradian, E. Shay, N. G. Maroudas & S. Weiner (1987) A CHEMICAL-MODEL FOR THE COOPERATION OF SULFATES AND CARBOXYLATES IN CALCITE CRYSTAL NUCLEATION - RELEVANCE TO BIOMINERALIZATION. *Proceedings of the National Academy of Sciences of the United States of America*, 84, 2732-2736.
- Addadi, L. & S. Weiner (1985) INTERACTIONS BETWEEN ACIDIC PROTEINS AND CRYSTALS - STEREOCHEMICAL REQUIREMENTS IN BIOMINERALIZATION. *Proceedings of the National Academy of Sciences of the United States of America*, 82, 4110-4114.
- Addadi, L. & S. Weiner (1997) Biomineralization - A pavement of pearl. *Nature*, 389, 912-&.
- Almqvist, N., N. H. Thomson, B. L. Smith, G. D. Stucky, D. E. Morse & P. K. Hansma (1999) Methods for fabricating and characterizing a new generation of biomimetic materials. *Materials Science & Engineering C-Biomimetic and Supramolecular Systems*, 7, 37-43.
- Barthelat, F. & H. D. Espinosa (2007) An experimental investigation of deformation and fracture of nacre-mother of pearl. *Experimental Mechanics*, 47, 311-324.
- Barthelat, F., C. M. Li, C. Comi & H. D. Espinosa (2006) Mechanical properties of nacre constituents and their impact on mechanical performance. *Journal of Materials Research*, 21, 1977-1986.
- Belcher, A. M., X. H. Wu, R. J. Christensen, P. K. Hansma, G. D. Stucky & D. E. Morse (1996) Control of crystal phase switching and orientation by soluble mollusc-shell proteins. *Nature*, 381, 56-58.
- Bennadji-Gridi, F., A. Smith & J. P. Bonnet (2006) Montmorillonite based artificial nacre prepared via a drying process. *Materials Science and Engineering B-Solid State Materials for Advanced Technology*, 130, 132-136.
- Bertoldi, K., D. Bigoni & W. J. Drugan (2008) Nacre: An orthotropic and bimodular elastic material. *Composites Science and Technology*, 68, 1363-1375.
- Boggild, O. B. (1930) The shell structure of the mollusks. *K. danske Vidensk. Selsk. Skr.*, 2, 232-325.
- Bruet, B. J. F., H. J. Qi, M. C. Boyce, R. Panas, K. Tai, L. Frick & C. Ortiz (2005) Nanoscale morphology and indentation of individual nacre tablets from the gastropod mollusc *Trochus niloticus*. *Journal of Materials Research*, 20, 2400-2419.
- Chen, R. F., C. A. Wang, Y. Huang & H. R. Le (2008) An efficient biomimetic process for fabrication of artificial nacre with ordered-nano structure. *Materials Science & Engineering C-Biomimetic and Supramolecular Systems*, 28, 218-222.

- Currey, J. D. (1976) Further studies on the mechanical properties of mollusc shell material. *J. Zool. Lond.*, 180, 445-453.
- Currey, J. D. (1977) MECHANICAL-PROPERTIES OF MOTHER OF PEARL IN TENSION. *Proceedings of the Royal Society of London Series B-Biological Sciences*, 196, 443-&.
- Currey, J. D. 1980. *The Mechanical Properties of Biological Materials*. London, UK: Cambridge University Press.
- Currey, J. D. & J. D. Taylor (1974) The mechanical behavior of some molluscan hard tissues. *J. Zool. Lond.*, 173, 395-406.
- Erben, H. K. (1972) On the structure and growth of the nacreous tablets in gastropods. *Biomineralisation*, 4.
- Evans, A. G., Z. Suo, R. Z. Wang, I. A. Aksay, M. Y. He & J. W. Hutchinson (2001) Model for the robust mechanical behavior of nacre. *Journal of Materials Research*, 16, 2475-2484.
- Feng, Q. L., F. Z. Cui, G. Pu, R. Z. Wang & H. D. Li. 2000. Crystal orientation, toughening mechanisms and a mimic of nacre. 19-25.
- Fritz, M., A. M. Belcher, M. Radmacher, D. A. Walters, P. K. Hansma, G. D. Stucky, D. E. Morse & S. Mann (1994) Flat pearls from biofabrication of organized composites on inorganic substrates. *Nature*, 371, 49-51.
- Gehrke, N., N. Nassif, N. Pinna, M. Antonietti, H. S. Gupta & H. Colfen (2005) Retrosynthesis of nacre via amorphous precursor particles. *Chemistry of Materials*, 17, 6514-6516.
- Ghosh, P., D. R. Katti & K. S. Katti (2007) Mineral proximity influences mechanical response of proteins in biological mineral-protein hybrid systems. *Biomacromolecules*, 8, 851-856.
- Ghosh, P., D. R. Katti & K. S. Katti (2008) Mineral and protein-bound water and latching action control mechanical behavior at protein-mineral interfaces in biological nanocomposites. *Journal of Nanomaterials*.
- Gilbert, P., R. A. Metzler, D. Zhou, A. Scholl, A. Doran, A. Young, M. Kunz, N. Tamura & S. N. Coppersmith (2008) Gradual Ordering in Red Abalone Nacre. *Journal of the American Chemical Society*, 130, 17519-17527.
- Heuer, A. H., D. J. Fink, V. J. Laraia, J. L. Arias, P. D. Calvert, K. Kendall, G. L. Messing, J. Blackwell, P. C. Rieke, D. H. Thompson, A. P. Wheeler, A. Veis & A. I. Caplan (1992) INNOVATIVE MATERIALS PROCESSING STRATEGIES - A BIOMIMETIC APPROACH. *Science*, 255, 1098-1105.
- Jackson, A. P., J. F. V. Vincent, D. Briggs, R. A. Crick, S. F. Davies, M. J. Hearn & R. M. Turner (1986) APPLICATION OF SURFACE ANALYTICAL TECHNIQUES TO THE STUDY OF FRACTURE SURFACES OF MOTHER-OF-PEARL. *Journal of Materials Science Letters*, 5, 975-978.
- Jackson, A. P., J. F. V. Vincent & R. M. Turner (1988) THE MECHANICAL DESIGN OF NACRE. *Proceedings of the Royal Society of London Series B-Biological Sciences*, 234, 415-&.
- Jackson, A. P., J. F. V. Vincent & R. M. Turner (1989) A PHYSICAL MODEL OF NACRE. *Composites Science and Technology*, 36, 255-266.
- Jackson, A. P., J. F. V. Vincent & R. M. Turner (1990) COMPARISON OF NACRE WITH OTHER CERAMIC COMPOSITES. *Journal of Materials Science*, 25, 3173-3178.
- Kamat, S., X. Su, R. Ballarini & A. H. Heuer (2000) Structural basis for the fracture toughness of the shell of the conch *Strombus gigas*. *Nature*, 405, 1036-1040.

- Katti, D. R. & K. S. Katti (2001) Modeling microarchitecture and mechanical behavior of nacre using 3D finite element techniques - Part I - Elastic properties. *Journal of Materials Science*, 36, 1411-1417.
- Katti, D. R., K. S. Katti, J. M. Sopp & M. Sarikaya. 2001. 3D finite element modeling of mechanical response in nacre-based hybrid nanocomposites. 397-404.
- Katti, D. R., S. M. Pradhan & K. S. Katti (2004) Modeling the organic-inorganic interfacial nanoasperities in a model bio-nanocomposite, nacre. *Reviews on Advanced Materials Science*, 6, 162-168.
- Katti, K. S. & D. R. Katti. 2006. Why is nacre so tough and strong? , 1317-1324.
- Katti, K. S., D. R. Katti, S. M. Pradhan & A. Bhosle (2005) Platelet interlocks are the key to toughness and strength in nacre. *Journal of Materials Research*, 20, 1097-1100.
- Katti, K. S., B. Mohanty & D. R. Katti (2006) Nanomechanical properties of nacre. *Journal of Materials Research*, 21, 1237-1242.
- Kothen, S. P., Y. Li & N. Guzelsu (2001) Micromechanical model of nacre tested in tension. *Journal of Materials Science*, 36, 2001-2007.
- Li, X., W. C. Chang, Y. J. Chao, R. Wang & M. Chang (2004) Nanoscale Structural and Mechanical Characterization of a Natural Nanocomposite Material: The Shell of Red Abalone. *Nanoletters*, 4, 613-617.
- Li, X. D., Z. H. Xu & R. Z. Wang (2006) In situ observation of nanograin rotation and deformation in nacre. *Nano Letters*, 6, 2301-2304.
- Lin, W., C. A. Wang, H. L. Le, B. Long & Y. Huang (2008) Special assembly of laminated nanocomposite that mimics nacre. *Materials Science & Engineering C-Biomimetic and Supramolecular Systems*, 28, 1031-1037.
- Long, B., C. A. Wang, W. Lin, Y. Huang & J. L. Sun (2007) Polyacrylamide-clay nacre-like nanocomposites prepared by electrophoretic deposition. *Composites Science and Technology*, 67, 2770-2774.
- Menig, R., M. H. Meyers, M. A. Meyers & K. S. Vecchio (2000) Quasi-static and dynamic mechanical response of *Haliotis rufescens* (abalone) shells. *Acta Materialia*, 48, 2383-2398.
- Menig, R., M. H. Meyers, M. A. Meyers & K. S. Vecchio (2001) Quasi-static and dynamic mechanical response of *Strombus gigas* (conch) shells. *Materials Science and Engineering a-Structural Materials Properties Microstructure and Processing*, 297, 203-211.
- Meyers, M. A., A. Y. M. Lin, P. Y. Chen & J. Muiyco (2008) Mechanical strength of abalone nacre: Role of the soft organic layer. *Journal of the Mechanical Behavior of Biomedical Materials*, 1, 76-85.
- Mohanty, B., K. S. Katti & D. R. Katti (2008) Experimental investigation of nanomechanics of the mineral-protein interface in nacre. *Mechanics Research Communications*, 35, 17-23.
- Mohanty, B., K. S. Katti, D. R. Katti & D. Verma (2006) Dynamic nanomechanical response of nacre. *Journal of Materials Research*, 21, 2045-2051.
- Mutvei, H. (1970) Ultrastructure of the mineral and organic components of molluscan nacreous layers. *Biomimetalisation*, 2, 49-72.
- Nudelman, F., B. A. Gotliv, L. Addadi & S. Weiner (2006) Mollusk shell formation: Mapping the distribution of organic matrix components underlying a single aragonitic tablet in nacre. *Journal of Structural Biology*, 153, 176-187.

- Podsiadlo, P., A. K. Kaushik, B. S. Shim, A. Agarwal, Z. Y. Tang, A. M. Waas, E. M. Arruda & N. A. Kotov (2008) Can Nature's Design be Improved Upon? High Strength, Transparent Nacre-Like Nanocomposites with Double Network of Sacrificial Cross Links. *Journal of Physical Chemistry B*, 112, 14359-14363.
- Podsiadlo, P., Z. Q. Liu, D. Paterson, P. B. Messersmith & N. A. Kotov (2007) Fusion of seashell nacre and marine bioadhesive analogs: High-strength nanocomposite by layer-by-layer assembly of clay and L-3,4-dihydroxyphenylalanine polymer. *Advanced Materials*, 19, 949-+.
- Sarikaya, M. (1994) AN INTRODUCTION TO BIOMIMETICS - A STRUCTURAL VIEWPOINT. *Microscopy Research and Technique*, 27, 360-375.
- Sarikaya, M., K. E. Gunnison, M. Yasrebi, D. L. Milius & I. A. Aksay. 1990. Mechanical properties-microstructure relationship in abalone shell. In *Mat. Res. Soc. Symp. Proc.*, 109-116.
- Schaffer, T. E., C. IonescuZanetti, R. Proksch, M. Fritz, D. A. Walters, N. Almqvist, C. M. Zaremba, A. M. Belcher, B. L. Smith, G. D. Stucky, D. E. Morse & P. K. Hansma (1997) Does abalone nacre form by heteroepitaxial nucleation or by growth through mineral bridges? *Chemistry of Materials*, 9, 1731-1740.
- Sellinger, A., P. M. Weiss, A. Nguyen, Y. F. Lu, R. A. Assink, W. L. Gong & C. J. Brinker (1998) Continuous self-assembly of organic-inorganic nanocomposite coatings that mimic nacre. *Nature*, 394, 256-260.
- Shen, X. Y., A. M. Belcher, P. K. Hansma, G. D. Stucky & D. E. Morse (1997) Molecular cloning and characterization of lustrin A, a matrix protein from shell and pearl nacre of *Haliotis rufescens*. *Journal of Biological Chemistry*, 272, 32472-32481.
- Smith, B. L., T. E. Schaffer, M. Viani, J. B. Thompson, N. A. Frederick, J. Kindt, A. Belcher, G. D. Stucky, D. E. Morse & P. K. Hansma (1999) Molecular mechanistic origin of the toughness of natural adhesives, fibres and composites. *Nature*, 399, 761-763.
- Song, F. & Y. L. Bai (2001) Mineral bridges of nacre and its effects. *Acta Mechanica Sinica*, 17, 251-257.
- Song, F., A. K. Soh & Y. L. Bai (2003) Structural and mechanical properties of the organic matrix layers of nacre. *Biomaterials*, 24, 3623-3631.
- Song, F., X. H. Zhang & Y. L. Bai (2002) Microstructure and characteristics in the organic matrix layers of nacre. *Journal of Materials Research*, 17, 1567-1570.
- Su, X., A. M. Belcher, C. M. Zaremba, D. E. Morse, G. D. Stucky & A. H. Heuer (2002) Structural and microstructural characterization of the growth lines and prismatic microarchitecture in red abalone shell and the microstructures of abalone "Flat pearls". *Chem. Mater.*, 14, 3106-3117.
- Sumitomo, T., H. Kakisawa, Y. Owaki & Y. Kagawa (2008a) In situ transmission electron microscopy observation of reversible deformation in nacre organic matrix. *Journal of Materials Research*, 23, 1466-1471.
- Sumitomo, T., H. Kakisawa, Y. Owaki & Y. Kagawa (2008b) Transmission electron microscopy observation of nanoscale deformation structures in nacre. *Journal of Materials Research*, 23, 3213-3221.
- Tang, Z. Y., N. A. Kotov, S. Magonov & B. Ozturk (2003) Nanostructured artificial nacre. *Nature Materials*, 2, 413-U8.
- Taylor, J. D. (1973) The structural evolution of the bivalve shell. *Palaeontology*, 16, 519-534.

- Taylor, J. D., W. J. Kennedy & A. Hall (1969) Shell structure and mineralogy of the Bivalvia: Introduction Nucleacea - Trigonacea. *Bull. Br. Mus. Hist. Zool.*, Suppl. 3, 1-125.
- Taylor, J. D., W. J. Kennedy & A. Hall (1973) The shell structure and mineralogy of the Bivalvia: Lucinacea - Clavagellacea, conclusions. *Bull. Br. Mus. nat. Hist.*, 22, 255-294.
- Taylor, J. D. & M. Layman (1972) Mechanical properties of bivalve shell structures. *Palaeontology*, 15, 73-87.
- Tushtev, K., M. Murck & G. Grathwohl (2008) On the nature of the stiffness of nacre. *Materials Science & Engineering C-Biomimetic and Supramolecular Systems*, 28, 1164-1172.
- Verma, D., K. Katti & D. Katti (2006) Photoacoustic FTIR spectroscopic study of undisturbed nacre from red abalone. *Spectrochimica Acta Part a-Molecular and Biomolecular Spectroscopy*, 64, 1051-1057.
- Verma, D., K. Katti & D. Katti (2007) Nature of water in nacre: A 2D Fourier transform infrared spectroscopic study. *Spectrochimica Acta Part a-Molecular and Biomolecular Spectroscopy*, 67, 784-788.
- Wang, R. Z., Z. Suo, A. G. Evans, N. Yao & I. A. Aksay (2001) Deformation mechanisms in nacre. *Journal of Materials Research*, 16, 2485-2493.
- Wang, R. Z., H. B. Wen, F. Z. Cui, H. B. Zhang & H. D. Li (1995) OBSERVATIONS OF DAMAGE MORPHOLOGIES IN NACRE DURING DEFORMATION AND FRACTURE. *Journal of Materials Science*, 30, 2299-2304.
- Watabe, N. (1955) The observation of the surface structure of the cultured pearls relating to color and luster. *Rep. Fac. Fish. Pref. Univ. Mie.*, 2, 18-26.
- Wei, H., N. Ma, F. Shi, Z. Q. Wang & X. Zhang (2007) Artificial nacre by alternating preparation of layer-by-layer polymer films and CaCO₃ strata. *Chemistry of Materials*, 19, 1974-1978.
- Weiner, S. (1979) ASPARTIC ACID-RICH PROTEINS - MAJOR COMPONENTS OF THE SOLUBLE ORGANIC MATRIX OF MOLLUSK SHELLS. *Calcified Tissue International*, 29, 163-167.
- Weiner, S. (1983) MOLLUSK SHELL FORMATION - ISOLATION OF 2 ORGANIC MATRIX PROTEINS ASSOCIATED WITH CALCITE DEPOSITION IN THE BIVALVE MYTILUS-CALIFORNIANUS. *Biochemistry*, 22, 4139-4145.
- Weiner, S. (1984) ORGANIZATION OF ORGANIC MATRIX COMPONENTS IN MINERALIZED TISSUES. *American Zoologist*, 24, 945-951.
- Weiner, S., H. A. Lowenstam, B. Taborek & L. Hood (1979) FOSSIL MOLLUSK SHELL ORGANIC MATRIX COMPONENTS PRESERVED FOR 80 MILLION YEARS. *Paleobiology*, 5, 144-150.
- Weiner, S., Y. Talmon & W. Traub (1983) ELECTRON-DIFFRACTION OF MOLLUSK SHELL ORGANIC MATRICES AND THEIR RELATIONSHIP TO THE MINERAL PHASE. *International Journal of Biological Macromolecules*, 5, 325-328.
- Weiner, S. & W. Traub (1980) X-RAY-DIFFRACTION STUDY OF THE INSOLUBLE ORGANIC MATRIX OF MOLLUSK SHELLS. *Febs Letters*, 111, 311-316.
- Weiner, S. & W. Traub (1981) STRUCTURE OF ORGANIC MATRICES IN MOLLUSK SHELLS - EVIDENCE FOR EPITAXIAL-GROWTH IN BIOMINERALIZATION. *Journal of Rheumatology*, 8, 1011-1012.
- Weiner, S. & W. Traub (1984) MACROMOLECULES IN MOLLUSK SHELLS AND THEIR FUNCTIONS IN BIOMINERALIZATION. *Philosophical Transactions of the Royal Society of London Series B-Biological Sciences*, 304, 425-&.

- Wise, S. W. & Devillie, J. (1971) SCANNING ELECTRON MICROSCOPY OF MOLLUSCAN SHELL ULTRASTRUCTURES - SCREW DISLOCATIONS IN PELECYPOD NACRE. *Transactions of the American Microscopical Society*, 90, 376-&.
- Yao, N., A. Epstein & A. Akey (2006) Crystal growth via spiral motion in abalone shell nacre. *Journal of Materials Research*, 21, 1939-1946.
- Zaremba, C. M., A. M. Belcher, M. Fritz, Y. L. Li, S. Mann, P. K. Hansma, D. E. Morse, J. S. Speck & G. D. Stucky (1996) Critical transitions in the biofabrication of abalone shells and flat pearls. *Chemistry of Materials*, 8, 679-690.
- Zaremba, C. M., A. M. Belcher, M. Fritz, D. E. Morse, J. S. Speck, P. K. Hansma & G. D. Stucky (1995) ORGANIC-INORGANIC INTERFACES IN THE ULTRASTRUCTURE OF RED ABALONE NACRE. *Abstracts of Papers of the American Chemical Society*, 209, 584-INOR.
- Zhang, S. M., Y. J. Gao, Z. J. Zhang, H. X. Dang, W. M. Liu & Q. J. Xue (2002) Preparation and characterization of self-assembly nanocomposite thin film mimicking nacre. *Acta Physico-Chimica Sinica*, 18, 451-454.
- Zhang, S. M., J. W. Zhang, Z. J. Zhang, H. X. Dang, W. M. Liu & Q. J. Xue (2004) Preparation and characterization of self-assembled organic-inorganic nacre-like nanocomposite thin films. *Materials Letters*, 58, 2266-2269.
- Zhang, X., C. L. Liu, W. J. Wu & J. F. Wang (2006) Evaporation-induced self-assembly of organic-inorganic ordered nanocomposite thin films that mimic nacre. *Materials Letters*, 60, 2086-2089.
- Zuo, S. C. & Y. G. Wei (2008) Microstructure observation and mechanical behavior modeling for limnetic nacre. *Acta Mechanica Sinica*, 24, 83-89.

Rapid Assembly Processes of Ordered Inorganic/organic Nanocomposites

Chang-An Wang¹, Huirong Le² and Yong Huang¹

¹ *Tsinghua University, Beijing 100084, P.R. China*

² *University of Dundee, Dundee DD1 4HN, United Kingdom*

1. Introduction

The material of seashell nacre is of great interest to material scientists due to its superior mechanical properties and unique bio-compatibility. Natural seashell nacre consists of about 95% of aragonite (a mineral form of CaCO_3) and a few percent of biological macromolecules; yet its work of fracture is about three orders of magnitude higher than its mineral constituency. The superior strength and toughness of seashell nacre are attributed to the robust nanostructure in which the protein collagen layers (10–50 nm thick) and aragonite tablets (200–900 nm thick) form an ordered brick-and-mortar structure. The macromolecules act as strong adhesives while the aragonite tablets as the rigid building blocks (Smith et al., 1999). The structure of seashell nacre has inspired material scientists to design and develop various advanced biomimetic materials in the last two decades.

A macroscopic analogue of nacre structure led to the development of laminated silicon nitride ceramic composites which exhibit superior toughness to monolithic ceramics (Clegg et al., 1990; Wang et al., 2002), however, the laminated structure in micrometer scale may not have the same performance as the one with nano-scale laminated structure. In recent years, there is an increasing interest in the development of biomimetic organic/inorganic nanocomposites. These new materials hold promise for high performance orthopaedic materials, chemical sensors and photonic functional materials.

The formation of seashell nacre is a slow process in nature. Seashell absorbs mineral elements and organic matters in seawater to form inorganic nano-platelets and macromolecules, which deposit alternately to form compact brick-and-mortar structure of nacre. There are several approaches to mimic this process. One approach is called layer-by-layer assembly, by which ultrathin films of multilayered structure were prepared by sequential adsorption of a cationic polyelectrolyte and individual platelets of the negatively charged silicate mineral (Kleinfeld & Ferguson, 1994). Kleinfeld and Ferguson reported the incorporation of these clay sheets into thin films by the electrostatic layer-by-layer assembly (LBL). The structural investigation of film thickness and interlayer spacing of clay particles was accomplished by Kotov et al (Kotov et al., 1997) through a series of surface-sensitive techniques. The determination of the mechanism of the layer-by-layer alternating self-assembly of the clay multilayers was reported (Kotov et al., 1997; Kleinfeld & Ferguson,

1996). Fan et al. (Fan et al., 2002) fabricated a sexithiophene/montmorillonite multilayered film by the electrostatic layer-by-layer deposition technique, which was considered to be the first system for the preparation of sexithiophene ultrathin films. Tang et al. (Tang et al., 2003) reported a method to reproduce an analogue of nacre by sequential deposition of polyelectrolytes and clays, of which mechanical properties approached that of nacre or lamella bones. However, since LBL assembly process requires many repeated steps to build up a practical film thickness, for example, a thin film of a thickness of 5 μm took more than 2 days to form, it is a very slow process and can only produce ultrathin films. Lu et al. (Lu et al., 1997) reported a rapid way, the evaporation-induced self-assembly, to prepare orderly laminated organic-inorganic composites. Huang et al. (Huang et al., 1998) also employed this evaporation-induced self-assembly process to prepare continuous highly ordered lamellar-phase mesostructured thin films. By this method, however, high uniformity and stability could be obtained only for thin films (Sellinger et al., 1998; Deville et al., 2006). Deville et al. (Deville et al., 2006) developed a freeze-casting process to fabricate porous, layered materials. This process offers a large number of material combinations and a wide range of dimension control. However, this method could not be extended into nanoscale. The organic content in the composites obtained by the existing methods is much higher than that contained in natural nacles. Moreover, the product is intrinsically porous and needs to be filled with a second phase to make a composite material.

As mentioned above, the deposition speed of current technologies is not efficient to fabricate orderly bulk materials. This chapter will introduce a number of efficient processes to generate ordered inorganic/organic nanocomposites currently being developed. Section 1 will describe an efficient centrifugal deposition and in-situ polymerization process to fabricate polyimide/montmorillonite (PI/MMT) nanocomposites (Chen et al., 2008). This process results in an ordered nanocomposite with alternating organic and inorganic layers and mechanical properties comparable to that of lamella bones. Section 2 will introduce an electrophoretic deposition process and in-situ polymerization to fabricate polyacrylamide-montmorillonite (PAM/MMT) composite (Long et al., 2007). The process involves preparation of water based suspension, electrophoretic deposition and ultraviolet initiated polymerization. This process can produce nano-laminated composite films, similar to nacre both in structure and organic content. The composite film displays significant enhancement in Young's modulus and hardness, compared to that of pure montmorillonite films. Section 3 will put forward a special assembly method – hydrothermal-electrophoretic assembly to prepare acrylic anodic electrophoretic resin (AAER)/montmorillonite nanocomposite that mimics nacre, both in structure and composition. The two-step assembly process includes intercalation of polymer into interlayer space of montmorillonite by hydrothermal process and the subsequent electrophoretic deposition. By constructing brick-and-mortar nanostructure, Young's modulus of the composite film is effectively enhanced even when organic content is low (Lin et al., 2008). Section 4 will present an electrophoretic deposition of aqueous suspension containing montmorillonite nano-plates and polyelectrolyte such as acrylic anodic electrophoretic resin (AAER) or cathodic electrophoretic acrylic resin (CEAR) (Lin et al., 2008; Chen et al., in press). The composite obtained has good uniformity and significant improvement in Young's modulus and strength over the polymer substrate.

2. Efficient centrifugal deposition and in-situ polymerization process to fabricate polyimide/montmorillonite (PI/MMT) Nanocomposites

In this section, an efficient centrifugal deposition and in-situ polymerization process is proposed to fabricate bulk-form polyimide/montmorillonite (PI/MMT) nanocomposites. Samples with thickness of 10–200 μm were produced in a very short time. This process resulted in an ordered nanostructure with alternating organic and inorganic layers and mechanical properties comparable to that of lamella bones.

2.1. Experimental procedure

2.1.1 Composite preparation

The raw montmorillonite, a Ca^{2+} -type montmorillonite, was provided by Deshun Montmorillonite Plant, Shunping County, Hebei Province, China. The MMT powder was first treated with sodium salt solution in hot water at 75 °C and washed to remove Ca^{2+} , to improve the organic cation exchange capacity (CEC). The MMT powder was then treated with cetyltrimethyl ammonium chloride (CTAC) under the same conditions, to convert the normally hydrophilic silicate to hydrophobic one, which is called organic-MMT. The organic-MMT platelets were thoroughly dispersed using strong ultrasonic agitator in *N,N*-dimethylacetamide solution, then added with 4,4'-diaminodiphenyl ether and pyromellitic dianhydride and finally stirred strongly at 30 °C for 4 hours. MMT platelets covered by imide monomers described above were subsequently deposited onto glass substrate by centrifugation at a speed of 3000 rpm for about 15 min. Samples were also prepared by deposition under normal gravity for comparison. All the samples were heat-treated at 300 °C for 1 hour to facilitate polymerization of imide monomers. The glass slide carrying PI/MMT was immersed into 0.5 wt.% HF solution so that the composite slices could be easily peeled off from the glass substrate.

2.1.2. Characterization

The montmorillonite platelets and microstructure of PI/MMT composites were examined using a field emission scanning electron microscopy (JEOL, JSM-6400, Japan) with an estimated resolution of about 5 nm. X-ray diffraction was taken on D8-Discover machine (Bruker Co., Germany) to examine the ordered laminated structure. FTIR absorbency (SYSTEM 2000, USA) and TGA (SETARAM TGA92, France) were used to determine the formation and content of organic compounds in the organic-inorganic composites. The tensile properties of the specimens were carried under custom-made testing device at a constant tensile speed of 0.001 mm/min, and the whole process was recorded automatically. Nanoindentations (Berkovich tip, radius of curvature 50 nm) were also taken to determine the hardness and Young's modulus. Surface topography of PI/MMT slice was measured by AFM (MI, Picoscan, USA).

2.2. Results and discussions

Montmorillonite is a naturally occurring phyllosilicate, which has a similar layered and crystalline structure as talc and mica but with a different layer charge. The MMT crystal lattice consists of a central octahedral sheet of [Al, O, OH] inserted between two [SiO₄

tetrahedral sheets (in such a way that the oxygen ions in the octahedral sheet also belong to the silica tetrahedra). The MMT's layered structure can be easily delaminated into platelets with a thickness about one to several nanometers and a length from 100 nm to several micrometers by some specific methods. Fig. 1 shows the well-dispersed and separated MMT platelets used hereby.

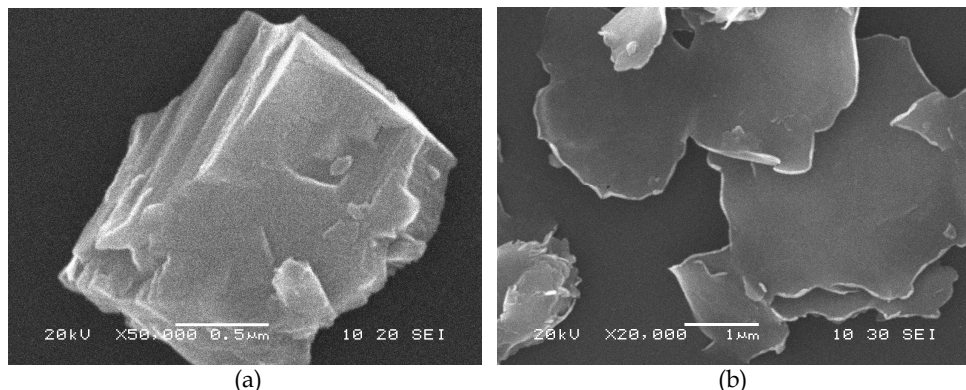


Fig. 1. (a) Stacks of platelets in original montmorillonite (b) exfoliation of the clay after organic conversion and strong sonication.

It is well known that organic ammonium salts can exchange ion with MMT to form organically modified MMT, which converts MMT from hydrophilic to hydrophobic. The organically modified MMT can be easily dispersed in water solution and absorb organic molecules in the solution. This provides a way to combine inorganic and organic components at molecular level. In the present work, the commercial MMT was treated in an organic ammonium chloride solution and dispersed in water solutions of imide monomers. The imide monomers grafted on the MMT platelet surfaces were polymerized in-situ to form polyimide (PI) macromolecules. X-ray diffraction (XRD) and infrared spectroscopy (IR) analysis (Fig. 2) showed that PI macromolecules were successfully inserted into the sodium interlayer of MMT nano-platelets to form intercalated composite. Organic ammonium chloride plays an important role in this process because it enlarges the d-spacing between adjacent montmorillonite platelets (from 1.244 nm to 1.842 nm). The adsorption of imide monomers and formation of PI macromolecules further expand the distance between MMT layers (from 1.842 nm to 2.044 nm). The results of infrared absorption spectra also indicate that the inorganic “bricks” (MMT platelets) and organic “mortar” (PI) are tightly combined together after the polymerization reaction. The nanostructure of PI/MMT composite system is similar to that of seashell nacre due to the characteristics of the inorganic and organic components.

Thermal gravimetric analysis (Fig. 3) showed the loss of organic compound when artificial nacre was heated to high temperature. There is a large weight loss around 300 °C due to the removal of free PI macromolecules surrounding the intercalated particle. Further weight loss at higher temperature might be due to the loss of organic components inside the intercalated particle. The overall composition of PI was about 20 wt.%. This is somewhat higher than the organic composition in seashell nacre.

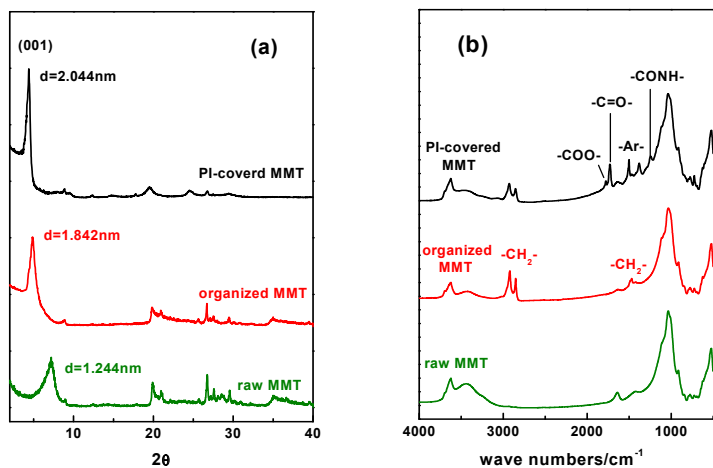


Fig. 2. XRD (a) and FTIR (b) analysis show the well combination of clay nano-platelets and polyimide

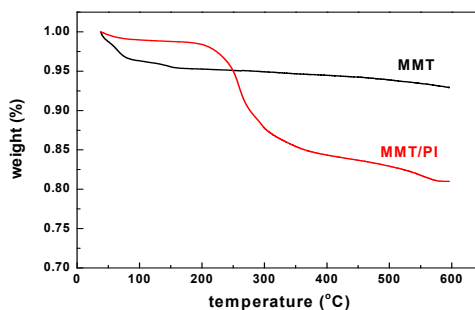


Fig. 3. Thermal gravimetric analysis shows the loss of organic content when artificial nacre heated to high temperature, and the percentage of PI is almost 20 wt. %

Montmorillonite platelets covered by PI macromolecules then form the layered nanostructure by centrifugal deposition. In this process, clay platelets become preferentially parallel to the surface of substrate as the leaves fall and spread flatly on the ground due to gravity. SEM images of the cross-sectional view of the composite exhibit a high degree of ordering of PI/MMT multilayers (Fig. 4a). AFM shows that clay platelets are glued together with adjacent platelets by polyimide macromolecules (Fig. 4b). The deposition process and formation of nanostructure can be represented by the schematics in Fig. 4c and d. The layered nanostructure is also confirmed by X-ray diffraction (Fig. 5a), the ratio of diffraction intensities of the centrifugally deposited sample is $I(001) / I(100) = 62$ which is much higher than that of normally deposited sample with $I(001) / I(100) = 12$. This confirms that the MMT platelets were preferentially aligned in parallel to the substrate in the centrifugal deposition

process. Another advantage of this technique is that the deposition process is much faster so that thick films over 100 μm can be easily obtained in a few minutes (Fig. 5b). The efficiency is much higher than other methods.

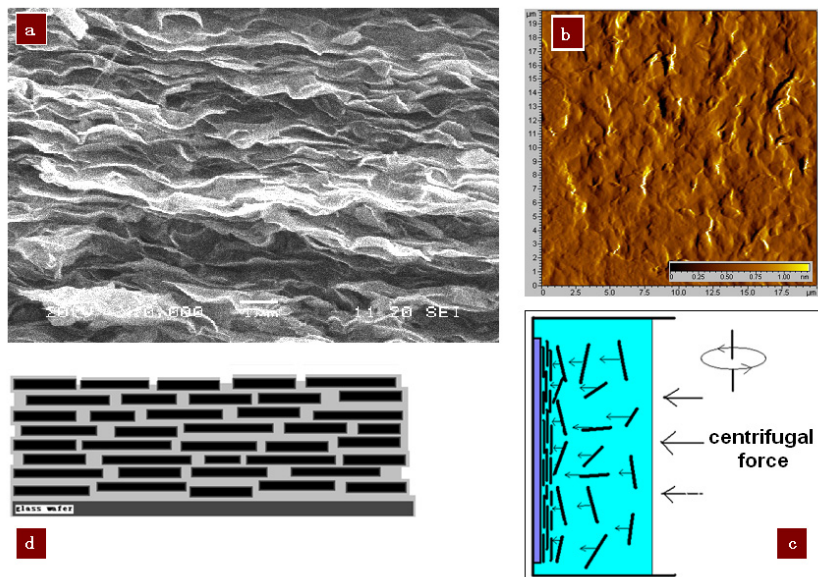


Fig. 4. The ordered nacre structure of the PI/MMT composite, a) clay platelets array in composite, b) organic platelets inset in polymer, c) the automatic alignment of clay platelets under the centrifugal force, d) representation of the general ordered nanostructure.

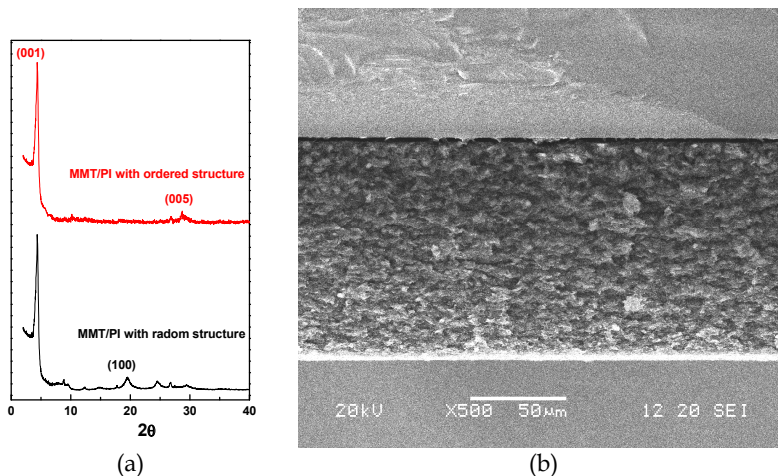


Fig. 5. Slice of PI/MMT composites acquired by the centrifugal deposition, (a) clay platelets become parallel to the substrate with the orientation of (001), (b) the sample with ordered structure in nano-scale with the thickness over 100 μm .

PI/MMT films were separated from the glass substrate using hydrofluoric acid so that the free-standing films were obtained and tested. The composites exhibited excellent and unique mechanical properties compared to PI polymer as shown in Fig. 6. Typical tensile stress-strain curves present a metal-like behaviour in which a plastic deformation stage occurs after initial elastic deformation. This is not observed in disordered composites and monolithic polyimide (PI). Under a stress below 45 MPa, both ordered and disordered artificial naces exhibit an elastic characteristic. Beyond this stress, there is a platform stage for the ordered composite which is attributed to the debonding of organic-inorganic interface as described by Evans A.G (Evans et al., 2001). The following plastic deformation and breakage stages are rather similar to polyimide polymer (PI) for both ordered and disordered artificial naces.

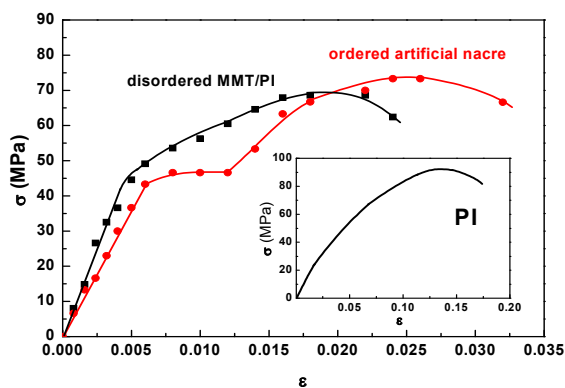


Fig. 6. In contrast to PI material and PI/MMT with disordered structure, ordered artificial nacre is yielding under a stress, which presents a unique metal-like behaviour.

The ordered nanocomposite exhibited an ultimate tensile stress (σ_u) of about 80 MPa and a Young's modulus E of 7–9 GPa as summarized in Table 1. The strength is comparable to that of clay-polyelectrolyte composites with disordered structures (Tang et al., 2003) and seashell nacre (Evans et al., 2001). The Young's modulus is lower than that of abalone seashell nacre due to higher organic content in the PI/MMT composite. Nevertheless, the obtained E values are comparable to that of plywood bones with lamellar morphology and significantly higher than that of clay-polyelectrolyte composites reported (Tang et al., 2003). Nano-indentation was used to determine the hardness of PI/MMT composites. The results are in the range of 1.4–1.6 GPa, as shown in Table 1, which is almost 10 times higher than PI. It is noted that the PI/MMT composite with ordered laminated nanostructure has lower modulus and higher hardness than that with disordered structure. This is because the inorganic platelets in disordered structure interlock with each other and exert higher resistance to the deformation of the macromolecules than the ordered brick-and-mortar structure. On the other hand, the higher hardness of the ordered structure is attributed to the higher probability for the indenter to meet the hard MMT platelets when indenter is being pressed into the surface. As a result, the ordered structure exhibits similar mechanical properties to lamella bones.

Materials	Young's modulus E (GPa)	Strength σ_u (MPa)	Extensibility (%)	Hardness (GPa)	Reference
PI/MMT-ordered	8±0.5	80±5	3.5±0.2	1.5±0.1	Present
PI/MMT-disordered	9±1	69±8	2.5±0.2	1.2±0.2	Present
PI	3±1	90±10	17±2	0.2±0.05	Present
Seashell nacles	66-81	194-248	1.1	-	Wang et al., 2001
Artificial nacre	9-13	95-109	7-10	-	Tang et al., 2003
Cortical bone	7-30	100-230	1-3	-	Bonfield et al., 1998

Table 1. Mechanical properties of PI/MMT composites

(The data was obtained at a relative humidity of 38% and T=25°C.)

2.3. Summary

In summary, the inorganic-organic (PI/MMT) composites with ordered structure in nano-scale have been successfully prepared by a simple centrifugal deposition process. The whole process is the one that simulates and accelerates the natural process of nacre growth, including the formation of organic and inorganic components, adsorption of organic compound to inorganic frameworks, and matter deposition. The structural similarity between the PI/MMT composite and natural nacre gives a similarity of properties, such as mechanical strength, which is attributed to strong interfacial interaction and high compatibility of the components. Structural and functional resemblance makes clay-polymer multilayer composite a close replica of natural biomaterials. This approach is also applicable to a wide range of artificial nacre materials with different organic and inorganic building blocks.

3. Electrophoretic deposition process and in-situ polymerization to fabricate polyacrylamide/montmorillonite (PAM/MMT) nacre-like nanocomposite

Electrophoretic deposition (EPD) is a rapid and low cost process, and capable of producing materials with complex geometry. An EPD process consists of two steps. In the first step, particles suspended in a liquid medium are driven towards an electrode by applying an electric field to the suspension (electrophoresis). In the second step, the particles are collected at one of the electrode and form a coherent deposit on it (deposition).

In this section, the fabrication of polyacrylamide/montmorillonite (PAM/MMT) nanocomposites with nacre-like structure is presented as a case study of electrophoretic deposition and in-situ polymerization process. Montmorillonite was first modified by acrylamide, and suspended in distilled water. After electrophoretic deposition, the film was polymerized by ultraviolet-radiation. The ordered "brick-and-mortar" structure was made

of montmorillonite and polyacrylamide. The composites exhibited outstanding properties that approached those of nacre.

3.1 Experimental procedure

3.1.1 Materials

Na⁺ type montmorillonite (Na-MMT) with a cation exchange capacity of 90 meq / (100 g) was provided by Zhejiang Fenghong Clay Chemicals Co. Ltd. Acrylamide was used as an intercalating agent and reacting monomer, and benzyl was used as a free-radical photon initiator. Both were used as-received without further purification. The light source was a 150 W photochemical reactor lamp (Traper, Japan). Sodium polymeta-phosphate (SPP), tetrachloromethane and methanol were chemically purified.

3.1.2 Preparation of organic clay

To make the organophilic clay (O-MMT), 10 g of Na-MMT was dispersed in 300 ml deionized water with vigorous stirring for 3 hours. Meanwhile an acrylamide solution contained 1 g of acrylamide in 60 ml of deionized water was prepared by the addition of 10 wt% HCl to adjust the pH value to about 3~4. Then the protonated acrylamide solution was added slowly to the MMT suspension. The hydrophobic clay was recovered by centrifugation and filtration of the solution, followed by repeated rinse to remove excess ammonium ions. Finally, the clay was dried at 80 °C in a vacuum oven overnight and then grinded and sieved to 200 mesh.

3.1.3 Electrophoretic deposition

The electrophoretic deposition of O-MMT onto the electrode surface was carried out in a 150 ml beaker containing 100 ml O-MMT (0.01 g/ml) aqueous solution with addition of SPP (0.001 g/ml) as a surfactant. Before the deposition, the solution was vigorously stirred for 3 hours and aged overnight to get a stable suspension. Two pre-cleaned stainless steel plates with a surface area of 4 cm² served as both the working electrode and the counter electrode. The electrophoretic deposition of O-MMT solution was performed following a potentiostatic procedure with a working voltage of 5 V. The distance between the two electrodes was 2 cm. And this procedure lasted for 5 minutes to get a uniform off-white coating. The coated electrodes were immediately withdrawn from the emulsion after electrophoretic deposition and rinsed with tetrachloromethane to remove the residue of the acrylamide monomers.

3.1.4 Photo polymerization of PAM

In a typical procedure, 7.5 g (0.075 mol) of benzyl was dissolved in 150 ml of methanol solvent under vigorous magnetically stirring for 3 hours. Then the coated electrodes were put into the solution and irradiated with a UV light for 24 hours (Fig. 7). After drying in a vacuum oven at 60 °C for 24 hours, the off-white films were peeled off from the electrodes by a sharp blade for microstructure analysis and mechanical testing.

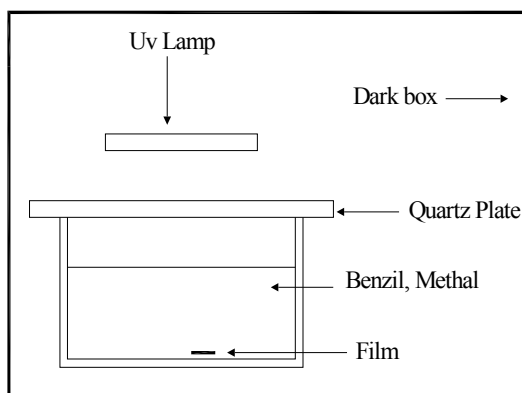


Fig. 7. Experimental setup of photo polymerization for the preparation of PAM/MMT

3.1.5. Apparatus

The montmorillonite platelets and microstructure of PAM/MMT composites were examined using field emission scanning electron microscopy (JEOL, JSM-6400, Japan) with an estimated resolution of ~ 5 nm. X-ray diffraction was taken on D8-Discover (Germany) to examine the highly ordered laminated structure, and FTIR spectrum (SYSTEM 2000, USA) was used to determine the organic compounds in this organic-inorganic composites. Nano-indentation (Berkovich tip, radius of curvature 50 nm) was taken to determine the mechanical properties. TGA (SETARAM TGA92, France) was used to determine the formation and content of organic compounds in the composites.

3.2 Results and discussion

3.2.1 Effect of monomer and polymerization on d-spacing of Na-MMT's (001) diffraction peak

The replacement of inorganic cations on the surfaces by quarternary ammonium ions expands the clay galleries. Fig. 8 shows the XRD patterns of the various MMT films obtained. The Na-MMT film was also prepared by electrophoretic deposition in the Na-MMT suspension. The d-spacing of Na-MMT's (001) diffraction peak was 1.29 nm, which was increased to 1.89 nm when modified by acrylamide monomers. It is implied that the monomer was intercalated into the interlayer of the clay. But when the monomers were polymerized, the d-spacing decreased to 1.35 nm. This is because the polymerization of AM to PAM gave a contraction of the layers. The polymer between the layers of the clay might have adopted a flattened conformation (Lan et al., 1994), whereas the monomers intercalated into the clays adopted random conformations. We can also find preferred orientation of the composites by the changes of the diffraction peaks. When the clay was intercalated by the monomers, the (001) diffraction peak became very strong. After the monomers were polymerized, it became weaker while other peaks even disappeared. This indicated that the composites exhibited a higher degree of ordering in the PAM/MMT multilayer after polymerization.

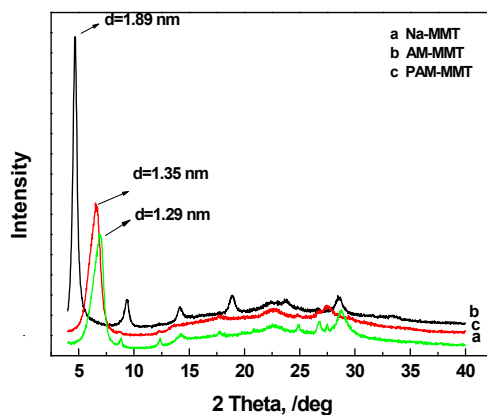


Fig. 8. XRD patterns of various MMT films: (a) Na-MMT; (b) AM-MMT and (c) PAM-MMT.

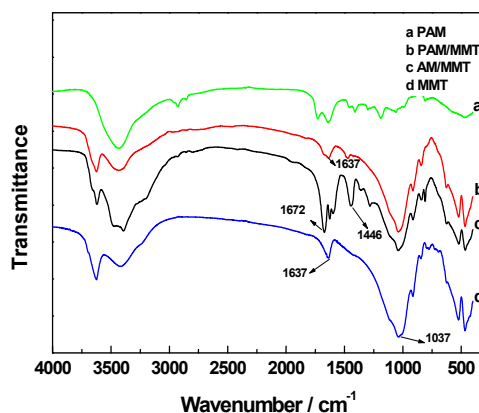


Fig. 9. FTIR spectra of the PAM (a), PAM-MMT (b), AM-MMT (c) and Na-MMT (d)

3.2.2 FTIR analysis

The characteristic FTIR spectra of the Na-MMT, AM-MMT, PAM-MMT and PAM are given in Fig. 9. The representative absorption peaks at 1037 cm^{-1} and 1637 cm^{-1} contributed to OH group on montmorillonite. The absorption peak at 1672 cm^{-1} was attributed to $-\text{CONH}_2$ on acrylamide. And the characteristic peak at 1446 cm^{-1} was attributed to $-\text{CH}_2-$. The absorption peaks of $-\text{CONH}_2$ and $-\text{CH}_2-$ became smaller when polymerized under the UV light because the OH group on the surface of montmorillonite participated in the reaction. Hence, the absorption peak at 1637 cm^{-1} contributed to OH group on PAM/MMT film became weaker compared to that of MMT.

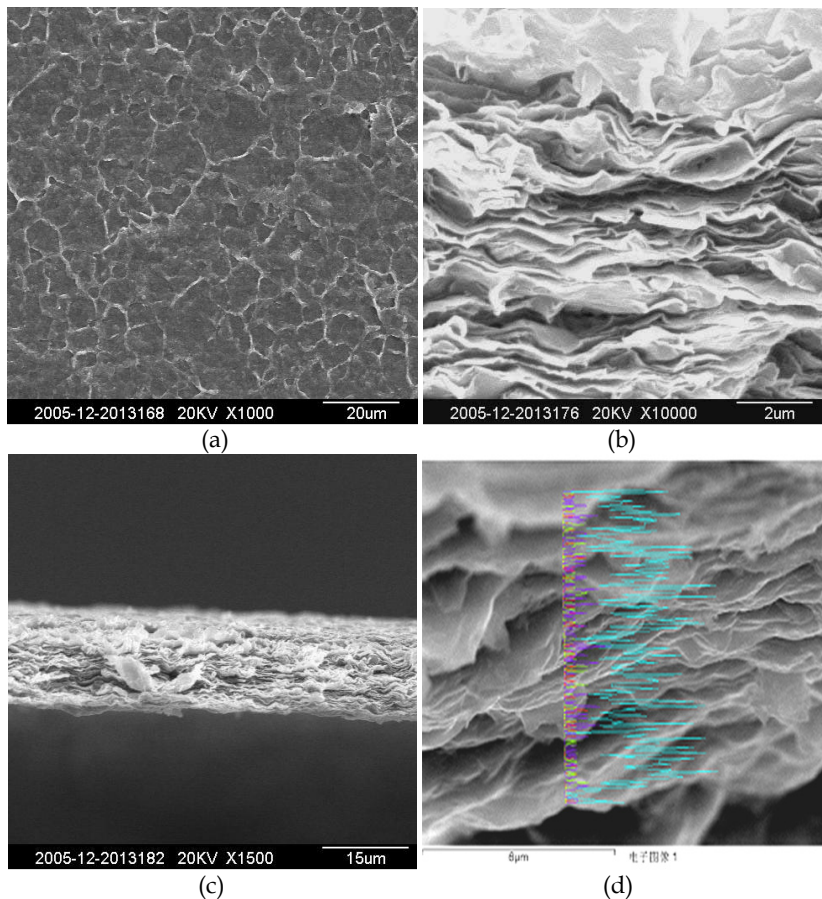


Fig. 10. SEM micrograph for electrophoretic deposited PAM/MMT film: (a) the surface of the film; (b) the cross-sectional film at a magnification of 10,000 \times ; (c) the cross-sectional film at a magnification of 1500 \times ; (d) SEM image of a cross-sectional PAM/MMT film with a EDS line scan analysis of Al (blue) , C (red) ,O (yellow) and Fe (purple) elements.

3.2.3 Microstructure of layered nanocomposites

The SEM images of the polymerized film are shown in Fig. 10. It can be seen that the polymerized film exhibits layered structure similar to the structure of nacre. The formation process of the film can be described as follows. First, the monomer is intercalated into the interlayer of MMT, which was stated before. Second, the electrophoretic deposition of MMT platelets is carried out. Montmorillonite is a clay mineral consisting of stacked silicate sheets approximately 1 nm thick and approximately 200 nm long. Its grains possess a high aspect ratio and demonstrate platelet morphology. As we know, the montmorillonite platelet presents negative charges on the large basal faces upon hydration. By contrast, the sign and density of the charges at the edges of the platelets are pH dependent, positive edges being found in acidic media (Graham et al., 1995). However, the overall particle charge is

invariably negative. In our experiment, we adjusted the pH of the emulsion to 10 to avoid the edge effect, which may affect the arrangement of the clay platelets. As we expected, the film was uniformly deposited onto the anode. From the cross section of the film (Fig. 10b and c), we obtained an orderly layered structure, which was similar to the “brick-and-mortar” structure of the nacre. The clay platelet was about decades of nanometers in thickness, and several micrometers in width. They were stacked tightly on the direction parallel to the surface of the electrodes. From Fig. 10a, we can see a uniform and smooth surface of the thin film with some overlapping clay platelets that exhibit white networking curves. The smoothness of the surface is attributed to the unique property of a high aspect ratio of the clay particle. The two-dimensional sheets can cover the defects of the underlying layers. This phenomenon was called “self-healing” by Kleinfeld and Ferguson (Kleinfeld & Ferguson, 1994). In Fig. 10d, an energy-dispersive X-ray detector attached to the SEM was used for evaluation of the Al, Fe, O and C distribution in the cross-section of the PAM/MMT film. Al, Fe and O are from MMT, and C is from PAM. The curves show an alternating distribution of the Al and C elements, which indicates the alternating organic-inorganic layered structure. From Fig. 8, we know that the interlayer of the film was filled with networking polymer which could bind clay platelets together since the d-spacing of (001) peak was enlarged by it. And in Fig. 11, the TGA curves show that the polymer content is about 4.7 wt%, i.e., the inorganic content was about 95.3 wt%. Therefore, we can draw a conclusion that the polyacrylamide-clay nacre-like nanocomposites prepared in the present work consists of ordered montmorillonite layers and the networked polyacrylamide which was located between the montmorillonite layers.

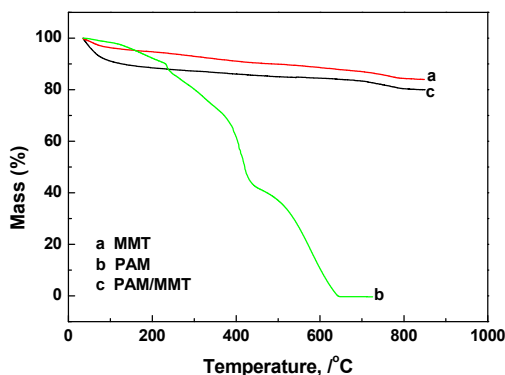


Fig. 11. TGA curves of MMT (a), PAM (b), and PAM/MMT (c).

3.2.4 Mechanical properties of the composites

Nano-indentation was used to determine mechanical properties of these samples with ordered nanostructure. With the laminated structure similar to nacre, the films demonstrated outstanding properties. Table 2 shows the typical modulus values of the ordered PAM/MMT composites acquired by nano-indentation. According to Table 2, the Young's modulus of the PAM/MMT composites is about 16.92 GPa. The high Young's modulus is attributed to a relatively high inorganic content (95.3%) and excellent

organic/inorganic bonding in the PAM/MMT composite. Nevertheless, the obtained E value was close to or even exceed the Young's modulus of plywood bones with lamellar morphology, and significantly exceed the Young's modulus of hybrid clay-polyelectrolyte composites with disordered structures reported by Tang et al, 2003. Table 2 also shows the typical hardness values of PAM/MMT composites acquired by nano-indentation. The hardness was about 0.95 GPa. For comparison, we prepared the pure montmorillonite film without polymer-intercalation under the same conditions which has a modulus of 2.92 GPa and a hardness of 0.20 GPa. It can be seen that the ordered laminated film exhibited higher strength and rigidity. This is because the brick-and-mortar structure can be stretched consistently during the elastic deformation, which is a way to absorb energy. Inorganic platelets can also interlock with each other and exert high resistance to the deformation of the macromolecules.

Materials	Young's modulus E (GPa)	Hardness (GPa)
Monolithic MMT	2.92	0.20
PAM/MMT	16.92	0.95

Table 2. Mechanical properties of pure MMT and PAM/MMT composites.

3.3 Summary

Polyacrylamide-clay nanocomposites were successfully prepared by electrophoretic deposition of montmorillonite aqueous suspension modified by acrylamide monomers and polymerized by ultraviolet-radiation. Acrylamide monomers functioned as both the intercalating agent and reacting monomers. The results show that the nanocomposites possess a uniform and ordered layer-by-layer structure with montmorillonite sheets as inorganic layers and polyacrylamide as interlayer phase, which is similar to the "brick-and-mortar" structure of the natural nacre. The nacre-like composites have outstanding mechanical properties, hardness and Young's modulus are 0.95 GPa and 16.92 GPa, respectively, which are close to or even exceed the Young's modulus of plywood bones with lamellar morphology with $E = 6\sim 16$ GPa.

4. Special assembly of laminated acrylic anodic electrophoretic resin / montmorillonite (AAER/MMT) nanocomposite that mimics nacre

In this section, a special assembly method, hydrothermal-electrophoretic assembly, is proposed to prepare acrylic anodic electrophoretic resin/montmorillonite (AAER/MMT) nanocomposite that mimics nacre, both in structure and composition. The two-step assembly process includes intercalation of polymer into interlayer space of montmorillonite by hydrothermal process and the subsequent electrophoretic deposition.

Na^+ -montmorillonite (NMMT) platelets possess high aspect ratio (the silicate sheet thickness is < 1 nm, and the lateral dimensions may vary from 30 nm to several microns or larger), with negative charges on their basal faces. It is this special character that inspired us in introducing electrophoretic deposition (EPD) into the assembly of montmorillonite platelets to form ordered nanolaminated composite films. On the other hand, acrylic anodic

electrophoretic resin (AAER) was chosen as the organic phase in the section, which has been widely used both in industry (e.g. almost all mass-produced steel car bodies) and scientific research due to its well-known electrophoretic ability, film forming ability, adhesive strength with various surfaces, corrosion resistance and insulating property.

In order to assemble bricks and mortar in nano-scale, we borrowed the method of intercalation from traditional hybrid preparation. A series of significant work done by Li and his colleagues (Li et al., 2002; Chen et al., 2002; Wang & Li, 2002) on preparing laminated structures gave us inspiration in polymer intercalation to obtain the hydrothermally-intercalated montmorillonite (HMMT) powder, under the force of the hydrothermal process.

It is hoped that the hydrothermal–electrophoretic assembly process (Scheme as shown in Fig.12) would open fascinating possibilities for assembling a variety of laminated nanocomposites.

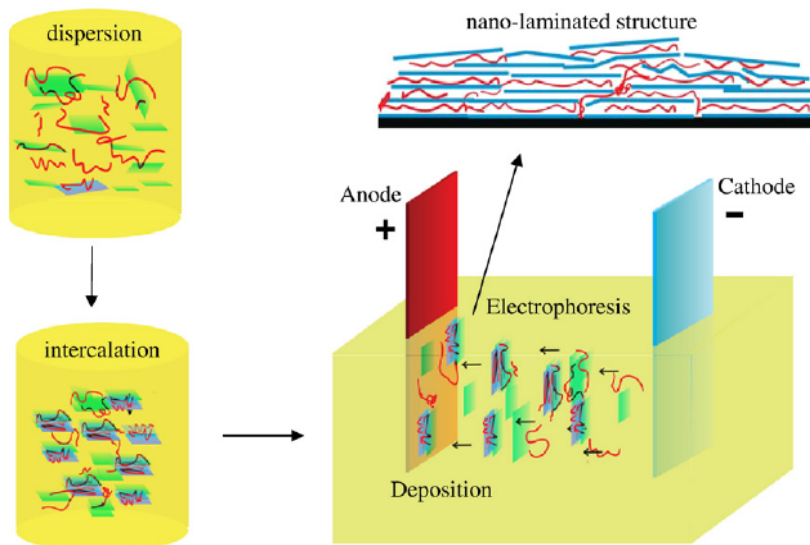


Fig. 12. The schematic showing the hydrothermal–electrophoretic assembly to construct nanolaminated film structure.

4.1. Experimental methods and materials

4.1.1. Materials

NMMT was donated by Zhejiang Fenghong Clay Chemicals Co., Ltd., with a cation exchange capacity (CEC) of 90 meq/(100 g) and average size of $\sim 1 \mu\text{m}$. AAER (Commodity No. DT323-75) synthesized from methacrylic acid, methyl methacrylate, butyl methacrylate, 2-hydroxyethyl methacrylate, styrene and glycidyl methacrylate and neutralized by triethylamine, was supplied by Tianjing Dengta Co., Ltd. The acidic value of AAER before neutralization is $\sim 105 \text{ mgKOH/g}$ (the value is provided by the supplier). The weight-

average molar mass and poly-dispersity index for the AAER used are 20,290 g/mol and 2.99, respectively, determined by gel permeation chromatography using Viscotek TriSEC Model 302. No inorganic or organic filler was present in the original AAER. Bisphenyl A type epoxy resin (E-44) was obtained from Wuxi Lanxing Co., Ltd. Cyclohexanone, dimethyl acetamide and sodium hydroxide were purchased from Beijing Chemical Reagents Company and used without further purification. Ultrasonic machine was JY92-II (Ningbo Scientz Biotechnology Co., Ltd.).

4.1.2. Preparation of aqueous suspension for subsequent EPD

NMMT suspension was prepared as follows: 1.0 g of NMMT was dispersed in 100 ml of de-ionized water, stirring for 24 hours. Then the suspension was adjusted to pH \approx 8.5 using 1 wt.% aqueous solution of sodium hydroxide, followed by ultrasonic dispersion (500 W, 20 min). Hydrothermal method was employed to prepare HMMT suspension. 0.1 g of AAER was added into 100 ml of NMMT suspension before being transferred into a Teflonlined autoclave with a stainless steel shell. The autoclave was kept at 130 °C for 24 hours and then allowed to cool to room temperature naturally. The resulting aqueous suspension was further dispersed by ultrasonic homogenizer (500 W, 20 min) for subsequent EPD directly.

4.1.3. Electrophoretic deposition (EPD)

Constant voltage was applied during the EPD process using a battery testing system (CT-3008B-5V20mAS1, NEWARE, China). The electrodes used were 18Cr8Ni type stainless steel substrates for both anode and cathode, with effective area of approximately 3 cm². Electrodes were polished before use. EPD under 2.5 V for 15 min was adopted for all the films studied in this article, with the electrode spacing of 1.0 cm. The as-deposited films (on substrate) were carefully rinsed with de-ionized water and then dried in the air.

4.1.4. Heat-treatment of films

In a typical curing process, after drying in the air, the stainless steel substrates carrying films were put into a baking oven and left at 170 °C for 1 hour to cure.

4.1.5. Preparation of powders

HMMT powder was collected by filtration from the HMMT suspension and washed with hot de-ionized water several times till ultraviolet absorption spectrum indicated the absence of C=O in water. The obtained powder was dried at 50 °C in the air for 24 hours. In an attempt to demonstrate that hydrothermal (solvent-thermal) method is universally feasible in intercalating oligomer molecules into the basal layer space of NMMT platelets, similar solvent-thermal process was also applied to intercalate E-44 epoxy resin molecules into NMMT platelets using dimethyl acetamide as the solvent; the powder obtained was designated as SMMT. For comparison, with the help of FTIR, the AAER molecules that had been intercalated into clay interlayer space and those that had been mixed physically with clay platelets without intercalation, we prepared mixture powder of AAER and NMMT by centrifugal sedimentation (from suspension containing 0.1 g of AAER and 1 g of dispersed NMMT powder).

4.1.6. Characterization

XRD experiments were carried out in D/max-rB X-ray diffractometer, using Cu K α radiation ($\lambda=1.5418 \text{ \AA}$). Care was taken to minimize the off-axis error during sample preparation. Parameters for the continuous scan mode are 0.01° , $3^\circ/\text{min}$.

Surface and cross-section observations and thickness measurement of the films were carried out by scanning electron microscope (SEM) in a JEOL JSM-6400 with an operating voltage at 10 kV. Energy Dispersive Spectroscopy (EDS) with a resolution of $\sim 1 \mu\text{m}$ was collected at 20 kV, counting for 10 min. For thickness measurement, the film was peeled off the stainless steel substrate with special care and spread on the glass plate using water-soluble glue.

FTIR experiments were performed at ambient temperature with a spectrometer (Spectrum GX, PerkinElmer, USA) at a resolution of $\sim 4 \text{ cm}^{-1}$. Care was taken when pressing KBr pellets to minimize effect of pressure on peak frequencies. 5 spectra were taken of each specimen and the average position of each peak (located automatically by peak picking software attached to the testing system) was then determined, with reproducibility of $<1 \text{ cm}^{-1}$.

Nano-indentation (XP CSM, XP-B1819n tip) was used to test elastic moduli of NMMT and HMMT films. At least 15 indentations were conducted on each sample surface. The mean and standard deviation of the reduced Young's modulus of a sample was calculated from the indentations by rejecting 2 of the highest and 2 of the lowest values to remove the outliers in a consistent manner.

The weight percentage of the organic component contained in films was determined by thermal gravimetric analysis on a TGA2050 gravimetric analyzer, and samples were heated in the air from ambient temperature to 700°C at a rate of $20^\circ\text{C}/\text{min}$.

Conductivity meter (DDS-12D, Lida, China) and Zeta Potential Analyzer (Zeta Plus, Brookhaven, USA) were employed to study the electrical conductivity and stability of powder in suspensions under ambient temperature, respectively.

4.2. Results and discussion

4.2.1. Effectiveness of hydrothermal method

Fig. 13a shows a series of XRD patterns corresponding to NMMT powder (A), HMMT powder (B), SMMT powder (C). After hydrothermal intercalation, an expansion in (001) layer space (designated as d_{001}) is observed, from 1.29 nm of NMMT powder (trace A) to 1.51 nm of HMMT powder (trace B), similar to the results reported in literatures on hybrid preparation. Trace C indicates that intercalating E-44 molecules into NMMT platelets by similar solvent-thermal method was effective too, with associated d_{001} expanded to 1.60 nm. Hereby, we may conclude that under appropriate conditions, hydrothermal (solvent-thermal) method is universally feasible in intercalating polymer/oligomer molecules into the basal layer space of NMMT.

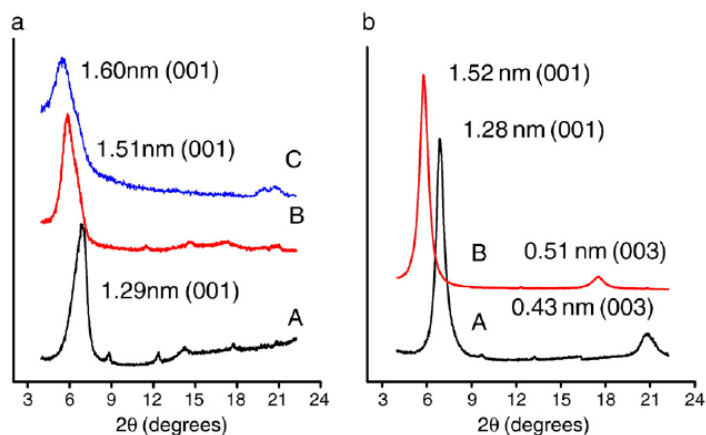


Fig. 13. a: XRD patterns of NMMT powder (A), HMMT powder (B) and SMMT powder (C). b: XRD patterns of NMMT film (A) and HMMT film (B).

Further evidence of the effectiveness of intercalation is found from FTIR, as shown in Fig. 14. In panel a, several transmittance bands and peaks typical of AAER film (trace A), which are absent in NMMT (trace D), appear in HMMT powder (trace B), including the methylene modes of 2950–2850 cm^{-1} and 1500–1400 cm^{-1} (arising from CH_2 stretching and CH_2 -scissoring vibration, respectively), and the C=O stretching at ~ 1730 cm^{-1} . Two features are observed that provide evidence of the existence of polymer molecules confined within the interlayer space in HMMT. (1) As is shown in panel b, $\nu_{\text{as}}(\text{CH}_2)$ and $\nu_{\text{s}}(\text{CH}_2)$ shift from 2934 cm^{-1} and 2877 cm^{-1} respectively in AAER to 2925 cm^{-1} and 2854 cm^{-1} respectively in HMMT powder. Panel c shows the frequency shift of $\delta(\text{CH}_2)$ from 1453 cm^{-1} in AAER to 1463 cm^{-1} in HMMT powder. According to existing FTIR research on the conformation of aliphatic chains, $\nu_{\text{as}}(\text{CH}_2)$ and $\delta(\text{CH}_2)$ are sensitive to *gauche/trans* conformer ratio, their frequency shifts reflecting preferable conformation of methylene chains in specific environment. In general, freer chains tend to assume more *gauche* conformers than less-free chains, the latter tending to assume more *trans* conformers. Increasing conformer ratio of *gauche* to *trans* usually leads to frequency shift of $\nu_{\text{as}}(\text{CH}_2)$ to lower value and of $\delta(\text{CH}_2)$ to higher value. In our study, the frequency shifts of $\nu_{\text{as}}(\text{CH}_2)$ and $\delta(\text{CH}_2)$ indicate that, in HMMT powder, AAER molecules tend to assume more *gauche* conformers, demonstrating that AAER molecules are confined (or at least partly confined) in clay layers so that interaction between AAER molecules are restricted. As for the $\nu_{\text{as}}(\text{CH}_2)$ shift, although to the author's knowledge, no definite reason is yet known, it is supposed to be closely related to the confined statement of aliphatic chains. (2) Also in panel c, peaks at 1033 cm^{-1} (Si–O in-plane vibration) that are characteristic of NMMT, shift to 1016 cm^{-1} indicating that intercalated AAER molecules most probably interact with the silicate. In contrast, all these features do not appear in the mixture powder of AAER and NMMT (trace C).

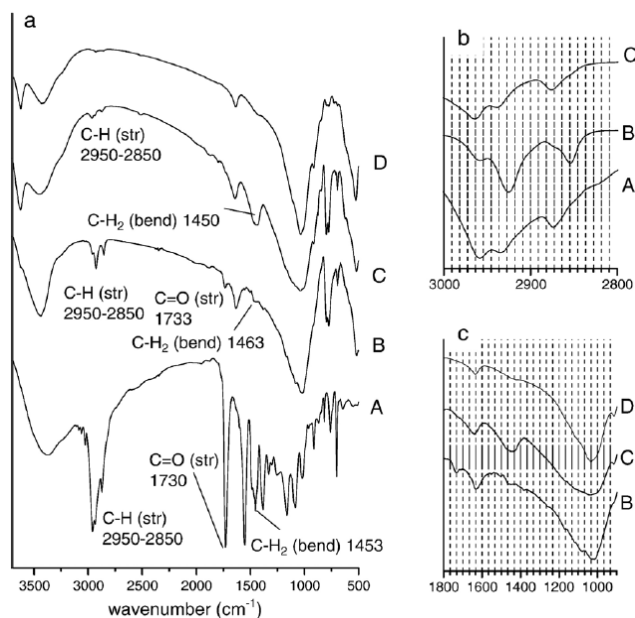


Fig. 14. a: FTIR transmittance spectra of AAER (A), HMMT powder (B), mixture powder of AAER and NMMT (C) and NMMT film (D). b and c: Enlargement of selected regions in panel a.

In thermodynamics, for the overall process, in which oligomer or polymer molecules are exchanged with the previously intercalated solvent molecules in the interlayer space, a negative variation in the Gibbs free energy is required. The driving force for the intercalation from solution is supposed to be the entropy gained by desorption of solvent molecules, which compensates for the decreased conformational entropy of the confined intercalated oligomer or polymer chains. Therefore, the variation in entropy in the overall process is positive, which means that high temperature in hydrothermal (solvent-thermal) process is beneficial in thermodynamics.

4.2.2. Morphologies and structures of films

The XRD pattern of the as-deposited HMMT film (trace B in panel b, Fig.13) displays a texture-like highly (00L) orientated structure with all other peaks generated by crystal planes besides (00L) nearly disappeared. Its d_{001} spacing was expanded to 1.52 nm for the as-deposited HMMT film, approximately consistent with that of HMMT powder (trace B in panel a, Fig.13), which means that the interlayer space is ~ 0.52 nm. In our study, no distinct variation in d_{001} was observed after heat treatment or after soaking in cyclohexanone. This is probably due to the hindrance against cross-linking for polymer molecules in the confined space. The orderly laminated structure of the HMMT film with a thickness of around 10 μm can be observed from its cross-section SEM images (Fig.15a, b, c). By adjusting the voltage (2~3 V), electrode spacing (1.0~2.0 cm) and deposition time (1~20 min), the thickness of films (from hundreds of nanometers to 20 μm) could be controlled. In the EDS result of a

line-scan (Fig.15c) on the cross-section of the HMMT film, carbon element was detected, even after the film was spoiled by ultrasonic processing in cyclohexanone, followed by washing several times with de-ionized water (Fig.15d). This once again demonstrates that polymer molecules exist in the interlayer space of the laminated composite films. But it is noted that not all platelets were intercalated with polymer, because XRD is an averaging technique and EDS gives statistical result concerning specific areas.

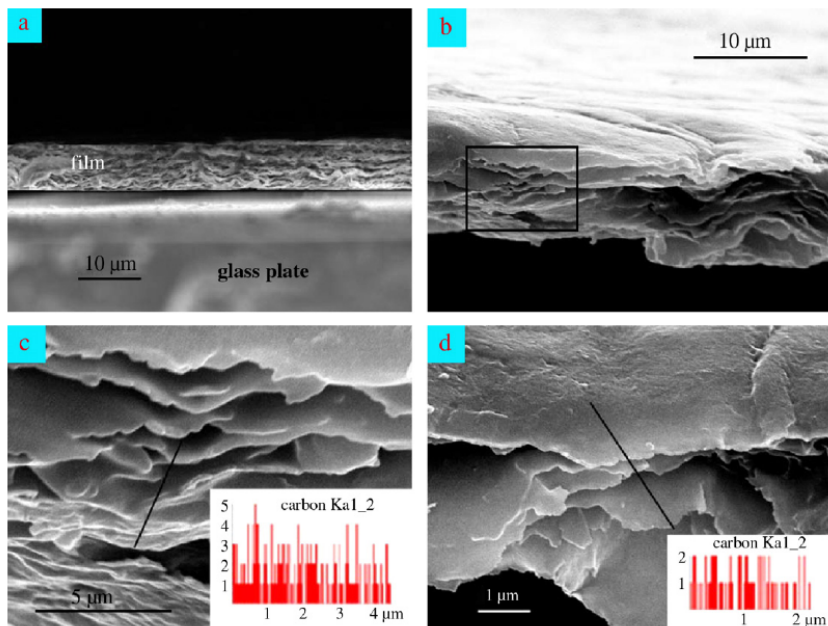


Fig. 15. SEM images of cross-section. a, b: the as-deposited HMMT film. c: enlargement of the box mark in image b (inset: EDS line-scan result showing carbon element distribution along the dark line). d: the film after being spoiled by ultrasonic processing in cyclohexanone, followed by washing several times with de-ionized water (inset: EDS line-scan result showing carbon element distribution along the dark line).

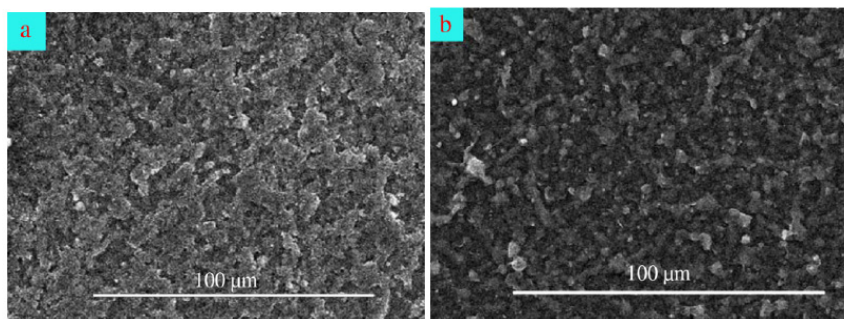


Fig. 16. SEM images of HMMT film surface (a) and NMMT film surface (b).

The surface of the HMMT film is relatively flat (Fig.16a). The clay platelets seem to overlap each other, glued together by the polymer deposited and intercalated between them, in comparison with the insular pattern characteristic of the NMMT film surface (Fig. 5b). Additionally, compliant clay platelets possess the capability of covering the defects of the underlying layers, called "self-healing" by Kleinfeld and Ferguson (Kleinfeld & Ferguson, 1994). This is why we used some deformed plates to illustrate clay platelets in Fig.12.

4.2.3. Four important roles played by AAER

What is worth our special attention are the four important roles that AAER play in the whole process, from intercalation to assembly.

Firstly, AAER serves as the intercalation agent in the hydrothermal process, ensuring the nano-laminated structure. Owing to its hydroxyl, carboxyl, epoxy groups and benzene rings introduced into the polymer molecule during polymerization, AAER possesses excellent compatibility with various materials as well as mechanical flexibility and strength. This is the first reason why we employ AAER as the organic component in this composite system.

Secondly, part of the deposited AAER from suspensions acts as the mortar in the z-direction around intercalated or non-intercalated platelets. This is evident in the TGA results of HMMT powder and HMMT film. The total organic content in HMMT films can be adjusted from ~5 wt % to ~15 wt.%, depending on the mass ratio of NMMT to AAER in aqueous suspensions. In comparison, the organic content in HMMT powder is always below 5 wt.%.

Thirdly, intercalated AAER contributes to more stable suspension for EPD. Proof is provided by the Zeta potential data: -36.69 and -63.29 mV for the aqueous suspension of NMMT and HMMT powder respectively. Furthermore, according to Scherrer's equation, from broadening of (00 L) peaks in XRD patterns, we can estimate the size of ordered domains in the direction normal to the substrate surface: 23.4 nm for the NMMT film (approximately 18 NMMT platelets piled together) and the 11.3 nm for heat-treated HMMT film (approximately 8 pieces of HMMT platelets piled together).

Finally, the electrophoretic capability of HMMT powder in water was greater than that of SMMT powder, characterized by the conductivity: 0.140 and 0.067 mS/cm for the aqueous suspension of HMMT and SMMT powder respectively. This explains why the film prepared with SMMT powder is much thinner than that prepared with HMMT powder by EPD from aqueous suspension of the same mass concentration.

4.2.4. Enhanced mechanical property of the films

Nano-indentation measurements were performed on NMMT film, AAER film and HMMT film prepared by the typical process stated in the experimental section (with ~8 wt.% polymer in the composite, determined by TGA). Results show an increase in reduced Young's modulus, from 2.9±0.4 GPa for NMMT film to 5.0±1.0 GPa for HMMT film. Given the low polymer content contained in the composite, this modulus enhancement is outstanding, which should be mainly attributed to the brick-and-mortar structure that plays a pivotal role in absorbing energy during elastic deformation of composite. As for the comparison between the mechanical property of the nanocomposite film constructed in this research and that of natural nacre, some points should be made here.

First, given the difference between testing methods, the reduced Young's modulus above cannot be directly compared with Young's modulus (~ 48.5 GPa) of nacre in the recent three-point bend test.

Second, in addition to ordered layered structure, interfacial compatibility of the organic and inorganic components is a key factor. From this aspect, only certain types of polymer are effective in dramatically enhancing mechanical properties of such composite films. Thus, whether AAER is most suitable or not is still unknown.

Third, the thicknesses of organic layers and inorganic layers in our nano-laminated films are much thinner than those in nacre. In natural naces, the biopolymer layers are usually 10–50 nm thick, providing necessary space for tight folding of polymer chains and certain degree of cross-linking of polymer. In comparison, in our laminated structure, polymer is confined within the interlayer space of smaller than 2 nm. Thus, the degree of cross-linking of AAER with its percentage in total organic content is probably low, consistent with the result that no distinction in FTIR spectra and XRD patterns were observed between the as-deposited HMMT film and the heat-treated HMMT film. Meanwhile, aragonite layers in nacre are 200–900 nm thick, hundreds of times thicker than the clay layers in our film. This may well explain why natural nacre adopts the micro/nano composite structure but not the nano/nano composites structure. Research on the preparation of micro/nano laminated organic–inorganic composites is being conducted by our group.

Fourth, properties of clay platelets are fairly different with aragonite. Clay platelets are extremely compliant, while aragonite is much more rigid. Additionally, CaCO_3 blocks have nano asperities that are about 30–100 nm in diameter, 10 nm in amplitude, providing additional friction when one block is sliding on the other.

4.3. Summary

The special assembly method—hydrothermal-electrophoretic assembly was successfully developed to prepare AAER/MMT nanocomposites that mimic nacre, both in structure and composition. The thickness of the nanocomposites film is controllable and can reach to more than 20 μm .

In this process, AAER plays four important roles as: intercalation agent in the hydrothermal process, binder around intercalated or non-intercalated platelets, stabilizing agent for MMT suspension, and improving the electric conductivity of MMT by AAER-intercalated.

Reduced Young's modulus was improved from 2.9 ± 0.4 GPa for NMMT film to 5.0 ± 1.0 GPa for HMMT film even at a low polymer content contained in the composite. The brick-and-mortar nacre-like structure is mainly attributed to the improved mechanical properties by incorporating extra energy-absorbing mechanisms during elastic deformation.

5. Conclusions

This chapter has summarized three processes that can produce laminated biomimetic nanocomposites. The high-speed centrifugal process can produce nanocomposites up to a thickness of 200 μm within minutes. The thick films produced have similar organic content and mechanical properties compared to that of lamella bones. The electrophoretic

deposition of monomers and intercalated montmorillonite clay followed by ultraviolet initiated polymerization can produce dense laminated nano-composite films up to tens of μm . The composite film exhibits four-fold improvement in Young's modulus and hardness over monolithic polyacrylamide polymers. Electrophoretic deposition combining intercalated montmorillonite nano-plates and polyelectrolyte such as acrylic anodic electrophoretic resin (AAER) can produce nanocomposites with organic content of 5 wt% to 15 wt%. The composites obtained have good uniformity and significant improvement in Young's modulus and strength over monolithic montmorillonite films. These methods hold promise to fabricate laminated biomimetic materials at increased deposition rate. With the development of synthetic hydroxyapatite nanoplates (Le et al, 2009), these methods will enable the fabrication of a new generation of biomimetic nanocomposites for bone substitutes. This is becoming an area of great interest to clinicians as well as materials scientists.

6. References

- Bonfield, W.; Wang, M. & Tanner, K. E. (1998). Interfaces in analogue biomaterials. *Acta Mater.*, 46 (7): 2509-2518
- Chen, K. Y.; Wang, C. A.; Huang, Y. & Lin, W. Preparation and characterization of polymer-clay nanocomposite films, *Science in China Series B: Chemistry*, in press
- Chen, R. F.; Wang, C. A.; Huang, Y. & Le, H. R. (2008). An efficient biomimetic process for fabrication of artificial nacre with ordered-nanostructure. *Mater. Sci. Eng. C*, 28 (2): 218-222
- Chen, X.; Sun, X. M. & Li, Y. D. (2002). Self-assembling vanadium oxide nanotubes by organic molecular templates. *Inorg. Chem.*, 41 (17): 4524-4530
- Clegg, W. J.; Kendlaa, K.; Alford, N. M.; Button, T. W. & Birchall, J. D. (1990). A simple way to make tough ceramics. *Nature*, 347 (6292) :455-457
- Deville, S.; Saiz, E; Nalla, R. K. & Tomsia, A. P. (2006). Freezing as a path to build complex composites. *Science*, 311 (5760): 515-518
- Evans, A. G.; Suo, Z.; Wang, R. Z.; Aksay, I. A.; He, M. Y. & Hutchinson, J. W. (2001). Model for the robust mechanical behavior of nacre. *J. Mater. Res.*, 16 (9): 2475-2484
- Fan, X.; Lochlin, J.; Youk, J.H.; Blanton, W.; Xia, C. & Advincula, R. (2002). Nanostructured sexithiophene/clay hybrid multilayers: a comparative structural and morphological characterization. *Chem. Mater.*, 14 (5): 2184-2191
- Fendler, J. H. (1996). Self-assembled nanostructured materials. *Chem. Mater.*, 8(8):1616-1624
- Graham, J. S.; Rosseinsky, D. R.; Slocombe, J. D.; Barrett, S. & Francis, S. R. (1995). Electrochemistry of clay electrodeposition from sols: electron-transfer, deposition and microgravimetry studies. *Colloid Surface A*, 94(2-3): 177-188
- Huang, M. H.; Dunn, B. S.; Soyez, H. & Zink, J. I. (1998). In Situ probing by fluorescence spectroscopy of the formation of continuous highlyordered lamellar-phase mesostructured thin films. *Langmuir*, 14 (26): 7331-7333
- Kleinfeld, E. R. & Ferguson, G. S. (1994). Stepwise formation of multilayered nanostructural films from macromolecular precursors. *Science*, 265 (5170): 370-372
- Kleinfeld, E. R. & Ferguson, G.S. (1996). Healing of defects in the stepwise formation of polymer/silicate multilayer films. *Chem. Mater.*, 8 (8): 1575-1778

- Kotov, N. A.; Haraszti, T.; Turi, L.; Zavala, G.; Geer, R. E.; Dekany, I. & Fendler, J. H. (1997). Mechanism of and defect formation in the self-assembly of polymeric polycation-montmorillonite ultrathin films. *J. Am. Chem. Soc.*, 119 (29): 6821-6832
- Lan, T.; Kaviratna, P. D. & Pinnavaia, T. J. (1994). On the nature of polyimide-clay hybrid composites. *Chem. Mater.*, 6 (5): 573-575
- Le, H. R.; Pranti-Haran, S.; Donnelly, K. and Keatch, R. P. (2009). Microstructure and Cell Adhesion of Hydroxyapatite/Collagen Composites. Proceedings of 11th International Congress of the IUPESM, Sept 7-12, 2009, Munich, Germany.
- Lin, W.; Wang, C. A.; Le, H. R.; Long, B. & Huang, Y. (2008). Special assembly of laminated nanocomposite that mimics nacre. *Mater. Sci. Eng. C*, 28 (7): 1031-1037
- Lin, W.; Wang, C. A.; Long, B. & Huang, Y. (2008). Preparation of polymer-clay nanocomposite films by water-based electrodeposition. *Compos. Sci Technol.*, 68 (3-4): 880-887
- Long, B.; Wang, C. A.; Lin, W.; Huang, H. & Sun, J. L. (2007). Polyacrylamide-clay nacre-like nanocomposites prepared by electrophoretic deposition. *Compos. Sci Technol.*, 67 (13) 2770-2774
- Lu, Y. F.; Ganguli, R.; Drewien, C. A.; Anderson, M. T.; Brinker, C. J.; Gong, W. L.; Guo, Y. X.; Soyez, H.; Dunn, B.; Huang, M. H. & Zink, J. I. (1997). Continuous formation of supported cubic and hexagonal mesoporous films by sol-gel dip-coating. *Nature*, 389 (6649): 364-368
- Sellinger, A.; Weiss, P. M.; Nguyen, A.; Lu, Y. F.; Assink, R. A.; Gong, W. & Brinker, C. J. (1998). Continuous self-assembly of organic-inorganic nanocomposite coatings that mimic nacre. *Nature*, 394 (6690): 256-260
- Smith, B. L.; Schaffer, T. E.; Viani, M.; Thompson, J. B.; Frederick, N. A.; Kindt, J.; Belcher, A.; Stucky, G. D.; Morse, D. E. & Hansma, P. K. (1999). Molecular mechanistic origin of the toughness of natural adhesives, fibres and composites, *Nature*, 399 (6738): 761-763
- Tang, Z. Y.; Kotov, N. A.; Magonov, S. & Ozturk, B. (2003). Nanostructured artificial nacre. *Nature Mater.*, 2 (6): 413-418
- Wang, C. A.; Huang, Y.; Zan, Q. F.; Zou, L. H. & Cai, S. Y. (2002). Control of composition and structure in laminated silicon nitride/boron nitride composites. *J. Am. Ceram. Soc.*, 85 (10): 2457-2461
- Wang, R. Z.; Suo, Z.; Evans, A. G.; Yao, N. & Aksay, I. A. (2001). Deformation mechanism in nacre. *J. Mater. Res.*, 16 (9): 2485-2493
- Wang, X. & Li, Y. D. (2002). Selected-control hydrothermal synthesis of α - and β -MnO₂ single crystal nanowires, *J. Am. Chem. Soc.*, 124 (12): 2880-2881

A Biomimetic Nano-Scale Aggregation Route for the Formation of Submicron-Size Colloidal Calcite Particles

Ivan Sondi*^a, and Srečo D. Škapin^b

^(a) *Laboratory for Geochemistry of Colloids, Center for Marine and Environmental Research, Ruđer Bošković Institute, Zagreb, Croatia (sondi@irb.hr)*

^(b) *Department for Advanced Materials, Jožef Stefan Institute, Ljubljana, Slovenia (sreco.skapin@ijs.si)*

1. Introduction

Carbonates are minerals that are frequently encountered in Nature, occurring as the main mineral constituents in rocks and sediments, and as the most common constituents of the bio-inorganic structures of the skeletons and tissues of many mineralizing organisms. The presence of bio-inorganic structures of calcium carbonate polymorphs within organisms has been intensively investigated in biology, mineralogy, chemistry, and material science (Addadi & Weiner, 1992; Ozin, 1997; Stupp & Braun, 1997; Meldrum & Cölfen, 2008) as well as in biological fields, primarily in zoology (Taylor et al., 2009) and evolutionary biology (Stanley, 2003).

The complex biomineral structures are formed through biomineralization processes, defined as the formation of inorganic crystalline or amorphous mineral-like materials by living organisms in ambient conditions (Mann, 2001; Bäuerlein, 2007). Many organisms have, during hundreds of millions of years of adaptation to the changing environment, developed their own evolutionary strategy in the formation of biominerals (Knoll, 2003). As a result, biomineralization has been a key to the historical existence of many species.

During the past decade, a number of published studies have shown that mineralizing organisms utilize the capabilities of macromolecules to initiate the crystallization process and to interact in specific ways with the surfaces of growing crystals (Mann, 1993; Falini et al., 1996; Stupp & Braun 1997; Falini, 2000; Tambutté et al., 2007). Several studies report evidence that many mineralizing organisms selectively form either intra- or extracellular inorganic precipitates with unusual morphological, mechanical, and physico-chemical properties (Falini et al., 1996; Mayers et al., 2008). These solids have surprisingly sophisticated designs, in comparison with their abiotic analogues, in particular, taking into account that they were formed at ambient pressure and temperature (Ozin, 1997; Skinner, 2005; Meldrum & Cölfen, 2008; Mayers et al., 2008). Their formation process is highly controlled, from the nanometer to macroscopic levels, resulting in complex hierarchical

architectures and shapes, providing superior multifunctional material properties (Stupp & Braun, 1997; Meldrum, 2003; Aizenberg, 2005).

The formation of biogenic calcium carbonate is controlled by organic molecules, mostly peptides, polypeptides, proteins, and polysaccharides, which are directly involved in regulating the nucleation, growth, and shaping of the precipitates (Elhadj et al., 2006a; DeOliveira & Laurusen, 1997; Sondi & Salopek-Sondi, 2004). Recently published studies have shown that mineralizing organisms utilize the capabilities of such macromolecules to interact in specific ways with the surfaces of the growing crystals, manipulating their structural and physical properties (Teng et al., 1998; Volkmer et al., 2004; Tong et al., 2004). These materials are inspiring a variety of scientists who seek to design novel materials with advanced properties, similar to those produced by mineralizing organisms in Nature.

The mechanisms of the formation of unusual bio-inorganic mineral structures have been a discussion topic for years. Lately, a new concept, the particle-mediated, non-classical crystallization process in the formation of bio-inorganic, mesoscopically structured mesocrystals, was promoted (Cölfen & Antonietti, 2005; Wang et al., 2006). These structures are composed of nanoparticle building units, and characterized by a well-faceted appearance and anisotropic properties. This microcrystal concept is much more common in biomineralization processes than has been assumed up to now, while the number of new examples of the significance of mesocrystals in biomineral formation has significantly increased in recent years.

Precipitated calcium carbonate (PCC) solids have a wide variety of important uses in numerous industrial applications. They have long been recognized as versatile additives for use in a wide range of plastic and elastomeric applications, and in many medical and dietary applications and supplements. Presently, there is a need for new approaches to the preparation of high-activity, submicron-size PCC materials with desirable physical and chemical properties, using environmentally friendly materials and methods.

So far, only modest attention has been devoted to the formation of uniform and nearly spherical calcium carbonate colloidal particles, devoid of crystal habits and anisotropic properties, but still maintaining a crystal structure (Sondi et al., 2008). The aim of this chapter is to describe recent advances in the formation of well-defined and uniform submicron-size, nanostructured colloidal calcium carbonate particles, through the non-classical *biomimetic nanoscale aggregation route* and to identify some of the problems that still need to be addressed.

2. Bioinorganic structures - learning from Nature

A large number of organisms in Nature produce, either intracellularly or extracellularly, inorganic materials, mostly modified calcium carbonate polymorphs. The number of reported studies on their function, structure and morphology has recently been increasing. A comprehensive coverage of all such studies and of biomineral structures would be impractical in this chapter. Instead, an example of functional biomineralization will be given by presenting structures of coccolithophores and their inorganic coccosphere and coccoliths, some of the remarkable and omnipresent types of marine phytoplankton assemblies in Nature (March, 2007). These are characterized by intriguing structures that can offer an answer to the question of how organisms govern the formation of complex bioinorganic structures, and how these structures are adapted to the functions of these organisms.

The aim of the present contribution is to highlight the internal structures and surface morphology of coccolith at the nano-level. Figure 1 shows a scanning electron photomicrograph (SEM) of coccosphere from the sediments of a marine lake (Malo Jezero, in the island of Mljet, Adriatic Sea). Coccolith shows its typical complex morphological feature characterized by pervasive and consistent chirality and radial symmetry (Figure 1A). However, a fairly unique observation at higher magnification is that the structural elements of coccolith are built up of much smaller, nanosize subunits (Figure 1B-D). This finding suggests that some organisms have the ability to use neoclassical mechanisms in the formation of their biomineral structures, based on the aggregation of preformed nanosize particles.

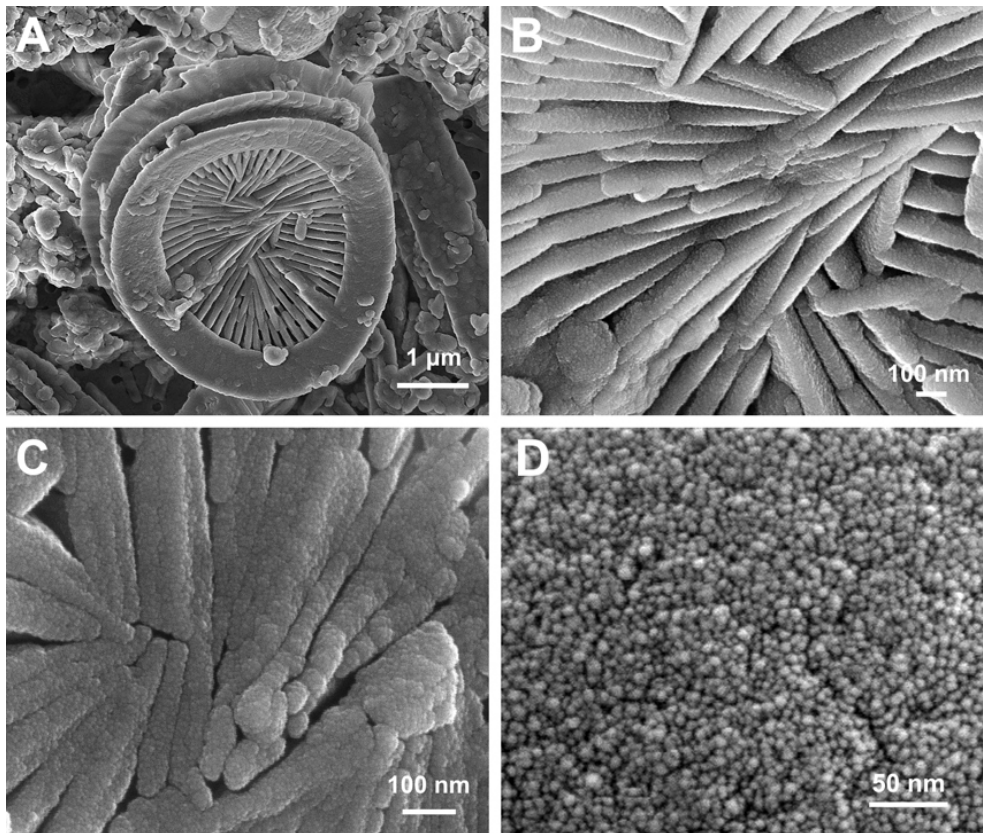


Fig. 1. SEM photomicrographs of coccosphere showing their (A) typical shape and morphology and (B-C) the composite nature of coccoliths at higher magnification. The sample originate from sediment from the marine lake of Malo Jezero on the island of Mljet, (Adriatic Sea). Unpublished illustrations.

The appearance of nanostructured biominerals in Nature is the rule rather than a chance event. Various other organisms base the functionality of their structural components on the

formation of nanostructured materials, functionally adapted to the living environment. Figure 2 shows an example of heterotrophic protozoa that build up their lorica from highly organized and nanostructured calcium carbonate solids.

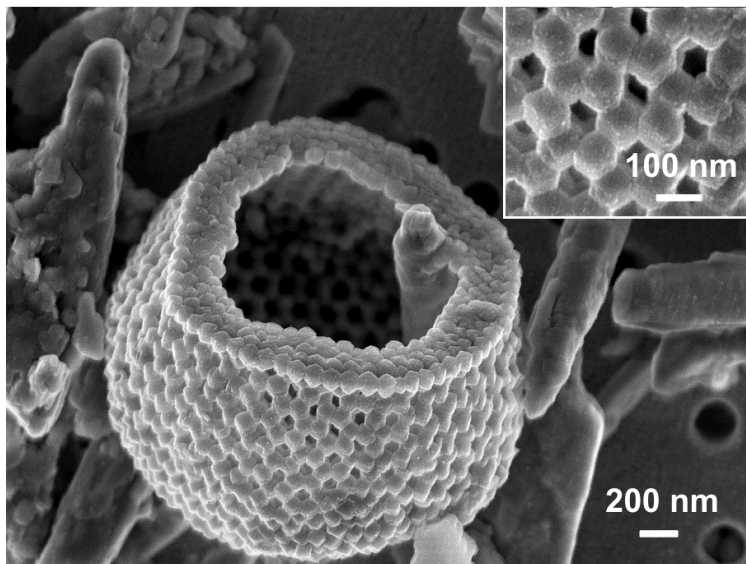


Fig. 2. SEM photomicrographs of heterotrophic protozoa showing the nanostructured shape of their lorica (the samples originate from the sediment of the marine lake of Malo Jezero on the island of Mljet, Adriatic Sea). Unpublished illustrations.

The findings obtained in natural systems have instigated laboratory experiments in producing carbonate materials by biomimetic precipitation processes. The methodology of the precipitation process, based on the aggregation of the preformed nanosize particles, is a way to produce uniform colloidal calcium carbonate solids.

3. Biomimetic formation of calcite particles

During recent decades tremendous progress in the preparation of a variety of colloids of simple and composite natures has been made. The general principles regarding the conventional formation of colloids of different structural, physical, and chemical properties have been established (Matijević, 1993). The search for innovative processing strategies to produce uniform precipitates of calcium carbonate of controlled size was advanced using the concepts and methodologies of biomimetic materials chemistry. This concept was defined by Mann (1993), who stated that *“the systematic fabrication of advanced materials will require the construction of architectures over scales ranging from the molecular to the macroscopic. The basic constructional processes of biomineralization - supermolecular pre-organisation, interfacial molecular recognition (templating) and cellular processing - can provide useful archetypes for molecular-scale building, or molecular tectonics in inorganic material chemistry”*. Some of the recent reviews have, in detail, described the biomimetic formation of carbonate solids, using

new concepts of microstructural processing techniques that either mimic, or are inspired by, biological systems (Meldrum, 2003; Cölfen, 2003; Yu & Cölfen, 2004; Xu et al., 2007).

A number of new methods and approaches, based on biomimetic processes and techniques, have been investigated and used in the preparation of calcium carbonate precipitates of different structural, morphological and surface properties. Some of them have been focused on exploring the promoting effect of matrices (templates) on the crystals' nucleation and growth (Popescu et al., 2007; Tremel et al., 2007). Several procedures have been developed, depending on the structural complexity of the templates used, such as self-assembled monolayers (Aizenberg et al., 1999; An and Cao, 2008), Langmuir monolayers (Heywood & Mann, 1994; Pichon et al., 2008), and gelatin films (Martinez-Rubi et al., 2008). Several studies have also shown that the formation of biogenic calcium carbonate structures is controlled by organic macromolecules (matrix proteins), mostly peptides and proteins, which are directly involved in regulating the nucleation, growth, and morphology of the precipitates. A variety of macromolecular additives, including proteins (Sarashina & Endo, 1998; Falini, 2000; Sondi & Salopek-Sondi, 2004), and designed peptides (DeOliveira & Laursen, 1997; Elhadj et al., 2006b; Gebauer et al., 2009), were reported. The bio-inspired production of calcium carbonates could also be accomplished by using soluble polymeric additives (Meldrum, 2003). Recently, a new class of additives was used, the double-hydrophilic block copolymers, for the effective control of the morphogenesis of inorganic precipitates in aqueous solutions, offering the possibility to obtain solids of uncommon morphologies (Sedlak & Cölfen, 2001; Cölfen, 2006).

Recently, following the protein templating concept, significant progress in the study of the bioinspired formation of calcium carbonates was accomplished through the use of catalytically active proteins, such as urease enzymes (Sondi & Matijević, 2001; Sondi & Salopek-Sondi, 2004). It was shown that during the homogeneous precipitation of carbonate solids by the urease-catalyzed reactions in aqueous solutions of calcium salts, nanosize calcite particles appeared during the early stages of the precipitation process. Following up on this work the new, bioinspired strategies for the preparation of uniform, nanostructured and submicron-size calcium carbonate solids were developed (Škapin & Sondi, 2005; Sondi et al., 2008).

Comprehensive coverage of this entire field of biomimetic material science would be impractical in this chapter. Rather, the main focus of this contribution is the role of catalytically active proteins. The complex biomimetic mechanism, acting on the crystal growth of initially formed nanocrystallites and subsequent aggregation that, finally, governs the formation of nanostructured submicron-size colloidal carbonate solids, will be discussed.

3.1. The use of urease in the formation of CaCO₃ precipitates - an overview

The first microbiological precipitation of calcium carbonate induced by urease (urea amidohydrolase, EC 3.5.1.5.), a multi-subunit, nickel-containing enzyme that converts urea to ammonia and CO₂, was described by Stocks-Fischer et al. (1999). The activity of urease in microbiologically induced calcite precipitation was also reported (Bachmeier et al., 2002). This enzyme, generated by many bacteria, certain species of yeast, and a number of plants, which allows these organisms to use exogenous and internally generated urea as a nitrogen source (Dixon et al., 1975). The chemical, structural, and surface properties and the mode of action of urease in the decomposition of urea have been described (Mobley & Hausinger,

1989; Estiu & Merz, 2004). It also appears that urease participates in systemic nitrogen-transport pathways and possibly acts as a toxic defense protein (Mobley & Hausinger, 1989). Urease, generated by certain pathogenic bacteria, during urinary tract infections, plays a significant role in the formation of intracellular urinary stones (Edinliljegren et al., 1994).

Recently, it was demonstrated that calcium carbonate polymorphs of different sizes and shapes can be obtained by homogeneous precipitation in solutions of calcium salts through the enzyme-catalyzed decomposition of urea by urease (Sondi & Matijević, 2001; Sondi & Salopek-Sondi, 2004). The role of urease in the formation of strontium and barium carbonates and their mixed compounds was also investigated (Sondi & Matijević, 2003; Škapin & Sondi, 2005). In addition to a catalytic function in the decomposition of urea, ureases also exert significant influence on the crystal-phase formation and shaping of carbonate precipitates. A recent study by the authors of this chapter has illustrated the role of the primary protein structures (amino acid sequences) of ureases on the phase formation and morphological properties of the obtained solids. As model substances, two ureases, the plant (*Canavalia ensiformis*) and the bacterial (*Bacillus pasteurii*) urease, were used in this study (Sondi & Salopek-Sondi, 2004). It was shown that despite a similar catalytic function in the decomposition of urea, these ureases exerted different influences on the crystal-phase formation and on the development of the unusual morphologies of calcium carbonate polymorphs. These differences were explained as a consequence of the dissimilarities in the amino acid sequences of the two examined ureases, causing their different roles in nucleation and physico-chemical interactions with the surface of the growing crystals. These studies have illustrated the diversity of the proteins produced by different organisms for the same function, and the drastic effects of subtle differences in their primary structures on the crystal-phase formation and the growth morphology of calcium carbonate precipitates.

3.2. Precipitation of nanostructured colloidal calcite particles by a biomimetic nanoscale aggregation route - the use of the urease enzyme as a protein-template model

Advances in the understanding of the physical and chemical principles of the formation of colloidal particles have greatly contributed to the scientific aspects of material science. It is interesting to point out, for example, that many forms of uniform colloids, built up of nanosize subunits, have been found in Nature. In considering the mechanisms of formation of colloidal materials over the range of the modal size, aggregation processes should be recognized as one of the common mechanisms (Petres et al., 1969; Lasic, 1993; Zukoski et al., 1996; Brunsteiner et al., 2005). This finding contradicts the commonly accepted classical precipitation mechanism, according to which uniform colloidal particles are formed when nuclei, arising from a short-lived burst, grow by the attachment of constituent solutes (Matijević, 1993).

Recently, a number of studies were carried out in order to employ the aggregation concept in the formation of inorganic colloids (Chow & Zukoski, 1994; Privman et al., 1999; Sondi et al., 2008). The significance of the aggregation process, in the formation of uniform colloidal particles from preformed nano-crystallites, was already observed by Težak and co-workers, in the late 1960s (Petres et al., 1969). However, this finding has long remained neglected. Recently, it has been theoretically and experimentally established that many colloids, prepared by precipitation from homogeneous solutions, are built up of nanosize subunits (Nakayama et al., 1995; Privman et al., 1999; Sondi & Matijević, 2001; 2003). Therefore, this mechanism was shown to be quite common in the formation of colloidal particles that show

crystalline characteristics. Nevertheless, there are only a few references dealing with the role of this mechanism in the precipitation of carbonates (Sondi et al., 2008; Song et al., 2009). This contribution underscores the importance of nanoscale aggregation processes in the formation of colloidal carbonate particles in the presence of model organic macromolecules (ureases), a situation commonly encountered in biomineralizing systems.

The processes of formation of bio-inorganic phases in biological systems are complex mechanisms that, almost as a rule, are characterized by several simultaneous events. An example of the complexity and of the importance of aggregation processes in the bio-inspired formation of calcium carbonate in simplified, laboratory conditions can be found in previously reported cases dealing with the role of catalytically active ureases (Sondi & Matijević, 2001; Sondi & Salopek-Sondi, 2004; Škapin & Sondi, 2005). This unique process of the biomimetic precipitation of uniform nanostructured colloidal calcite additionally explains the precipitation process based on the aggregation of preformed nanosize particles (Sondi et al., 2008).

The question is: how does the presence of urease macromolecules and of magnesium ions in the reacting solutions influence the formation of nearly spherical, submicron-size colloidal calcite particles? Obviously, the conditions under which such solids can be obtained are rather restrictive in terms of the concentration of urease, the reaction time, and the presence of magnesium and calcium salts. Details of the concentrations and methodologies used can be found elsewhere in the open literature (Sondi & Salopek-Sondi, 2004; Škapin & Sondi, 2005; Sondi et al., 2008).

In general, the process started by the rapid formation of the nanosize amorphous precursor phase is followed by simultaneous crystallization via the solid-state transformation pathway and the nanoscale aggregation processes. Three major phenomenological features, excluding the amply described decomposition of urea by urease, should be relevant in order to determine this process: (i) the role of urease macromolecules in the nucleation of the solid phase (templating), and their subsequent interaction with the inorganic phase at the solid-liquid interface, directing the growth of inorganic structures; (ii) the inhibitory effect of magnesium ions on the growth of nascent solids; and (iii) the subsequent aggregation of nanosize particles that governs the formation of submicron-size colloids.

Available reports indicate that protein macromolecules initiate the solid-phase formation, and control the crystalline nature and morphology of inorganic precipitates (Falini et al., 1996; Feng et al., 2000; Sondi & Salopek-Sondi, 2004; Xie et al., 2005; Yamamoto et al., 2008). These phenomena are the consequence of physico-chemical interactions between the active functional groups of organic macromolecules at their surface with the "building components" (ions, complexes) of the forming solids. The carboxyl-rich character of a protein, resulting from the abundance of negatively charged aspartic (*Asp*) and glutamic (*Glu*) acid residues is probably the most important factor in their biomineralization reactivity. Numerous studies have shown that these amino acids act as nucleation agents in solution and as primary active sites at the interface of organic/inorganic biomineralizing structures (Teng et al., 1998; Orme et al., 2001). The distribution of *Asp* and *Glu* on the surface of *C. ensiformis* urease is shown in the CPH model (Figure 3). Its amino acid sequence contains 12.8 % *Asp* and *Glu* residues. The initial formation of a nanosize, amorphous and metastable precursor phase may be the result of a strong interaction between the Ca^{2+} and *Asp* and *Glu* at the urease surface, forming $\text{Ca}^{2+}/\text{Asp}$ and $\text{Ca}^{2+}/\text{Glu}$ multi-carboxyl chelate complexes (Tong et al., 2004). This is in agreement with previous

studies which have shown that the *Asp* residue controls the rate of nucleation, inhibits the growth of solids and favors the formation of the amorphous phase (Aizenberg et al., 2001; Addadi et al., 2003).

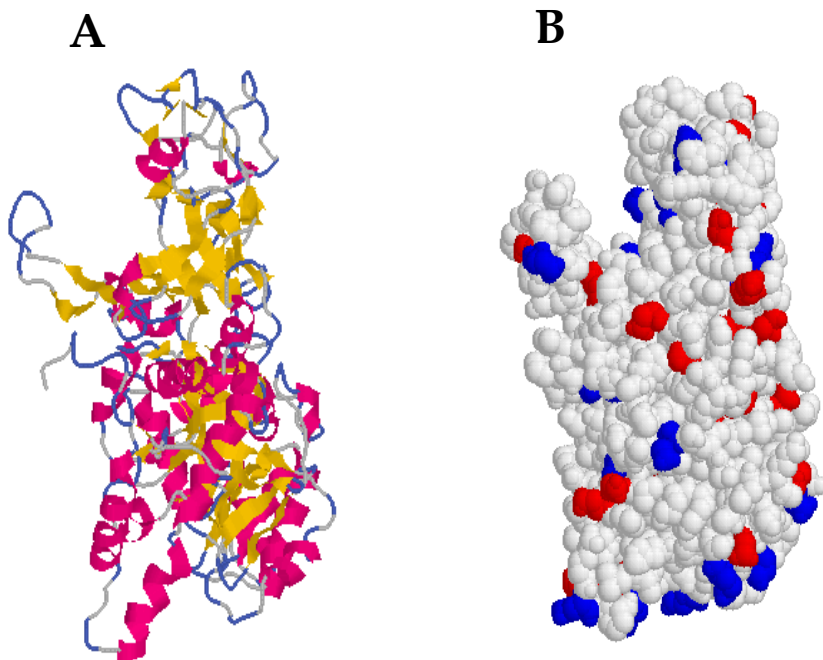


Fig. 3. CPH model of *C. ensiformis* urease (protein ID: AAA83831.1) showing (A) the tertiary structure of the protein displayed and colored according the secondary structure; (B) the distribution of *Glu* (blue) and *Asp* (red) residues on the surface of the urease molecule. The model was generated by using the ExPASy on-line program: CPH models - 2.0 for prediction of the protein tertiary structure and visualized by the RasWin 2.6 program. (Figure adapted from Sondi et al., 2008).

The presence and the activity of *Asp* and *Glu* are not sufficient to inhibit the future growth of the initially formed nanoparticles. Prolonged reaction times result in the formation of micron-size near-spheres and sequential-growth rhombohedra of calcite solids occurs (Figure 4 A-C). This observation is also corroborated by findings that, under what were otherwise the same experimental conditions, the growth of the initially formed nanoparticles was inhibited by magnesium ions (Figure 4D-F). This highlights the importance of the presence of magnesium ions during the formation of nanosize precipitates. Magnesium ions act as the main modifier of the calcite morphology in many natural environments (Davis et al., 2004). Meldrum and Hyde (2001) reported that magnesium ions, in combination with organic additives, affect the calcite morphology by adsorption to specific crystal faces, altering the nucleation and so inhibiting crystal growth.

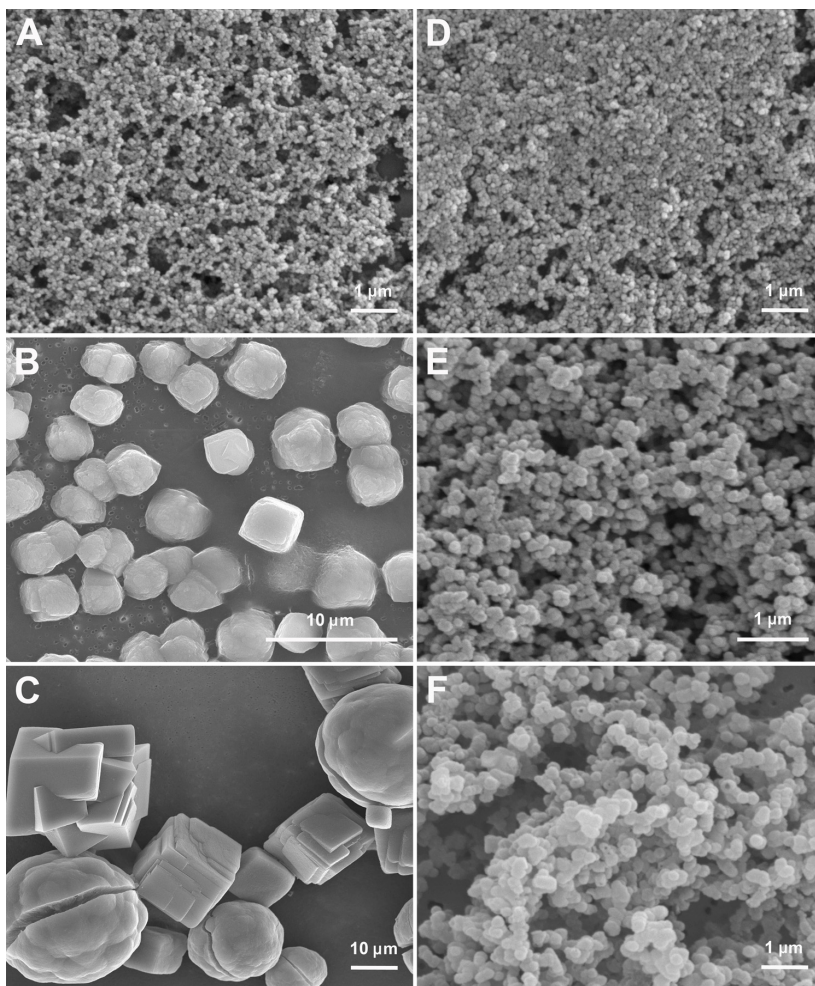


Fig. 4. Scanning electron micrographs (SEM) of calcium carbonate particles obtained by aging a solution containing 0.5 mol dm^{-3} urea, 0.25 mol dm^{-3} CaCl_2 , and 1 mg cm^{-3} *C. ensiformis* urease at $25 \text{ }^\circ\text{C}$ for (A) 10 min, (B) 30 min, and (C) 60 min, and precipitates obtained under the same experimental conditions and for the same aging time, but with the addition of 0.25 mol dm^{-3} MgCl_2 to a reacting solution (D-E). (Figure adapted from Sondi et al., 2008).

Molecular dynamic simulations (de Leeuw, 2002) are supporting evidence for the inhibitory effect of magnesium ions on calcite crystal growth. The above-described mechanisms determine the initial formation of nanosize calcium carbonate particles and inhibit their further growth. In the final stage, the aggregation of preformed nanoparticles occurs in the reacting system. More detailed morphological and structural analyses of the obtained calcium carbonate spheroids, taken at a higher TEM magnification (Figure 5), show them to be built of slightly textured nanosize subunits that, according to the XRD data, exhibit the calcium carbonate

structure. Recently, a number of experimental and theoretical studies have dealt with mechanisms of the formation of colloidal particles by the aggregation of preformed nanosize precursors. In spite of the significant contributions of these research results, most of these models have been based on a number of simplifying assumptions (Privman et al., 1999). Often, the role of the surface charge of the particles was neglected. For nanoparticles, the charge and the extent of their electrical double layer should be a major initiator of the aggregation processes (Kallay & Žalac, 2002). Our studies have shown that a negative charge, measured on the precipitates, can be assumed to originate from the charge of the same sign on the nanoparticles (Sondi et al., 2008). Since the aggregation obviously does occur, the conclusion is that the prevailing electrostatic barrier is ineffective for preventing the aggregation of the initially formed nanoparticles, the number of which in the reacting solution is continuously increasing. Indeed, it has also been shown that nanometer-scale particles cannot be stabilized by the electrostatic repulsion barrier, at the same mass, but at a higher number concentration (Kallay & Žalac, 2002). The reason for this is that these aggregate more rapidly than the larger colloidal particles. Theoretically, the main reason is the small size of the nanoparticles in comparison to the extent of their diffuse double layers. These diffuse layers overlap entirely, and the interaction between the nanoparticles can be considered as an interaction between ions. The consequence is a rapid aggregation of the preformed nanoclusters, and the formation of complex nanostructured submicron-scale spheres.

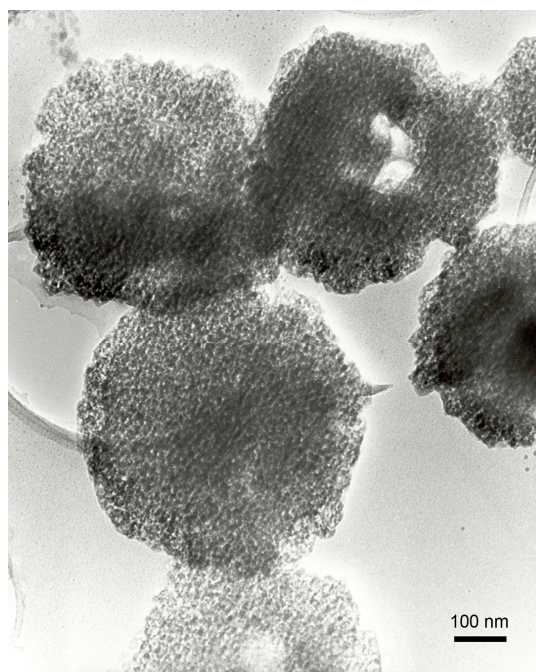


Fig. 5. Transmission electron micrograph (TEM) of spherical calcium carbonate particles obtained by aging a solution containing 0.5 mol dm^{-3} urea, 0.25 mol dm^{-3} CaCl_2 , 0.25 mol dm^{-3} MgCl_2 , and 1 mg cm^{-3} *C. ensiformis* urease at $25 \text{ }^\circ\text{C}$ for 60 min (corresponding SEM micrographs are shown in Figure 4F). (Figure adapted from Sondi et al., 2008).

4. Conclusion

This chapter aims to contribute to the understanding of the biomimetic mechanism for the synthesis of uniform and submicron-size colloidal particles of calcium carbonate. A novel, bio-inspired precipitation strategy, designated as the *biomimetic nano-scale aggregation route*, in the formation of these precipitates was discussed. This concept involves: (i) the use of functional templates, proteins, which are implicated in controlling the nucleation of solids; (ii) the inhibitory effect of magnesium ions on the crystal growth of initially formed nanocrystallites; and (iii) the subsequent aggregation of these particles that governs the formation of submicron-size and nanostructured hierarchical structures of colloidal carbonates. Understanding these mechanisms may lead to new strategies for the synthesis of novel calcium carbonate solids and to an improved insight into the sequestration of the inorganic components in the skeletons and tissues of mineralizing organisms.

5. Reference

- Addadi, L. & Weiner S. (1992). Control and design principles in biological mineralization. *Angewandte Chemie International Edition in English*, 31, 153-169, ISSN 0570-0833.
- Addadi, L., Raz, S., & Weiner, S. (2003). Taking advantage of disorder: Amorphous calcium carbonate and its roles in biomineralization. *Advanced Materials*, 15, 959-970, ISSN 0935-9648.
- Aizenberg, J. (2005). A bio-inspired approach to controlled crystallization at the nanoscale. *Bell Labs Technical Journal*, 10, 129-141, ISSN 1089-7089.
- Aizenberg, J., Black, A.J. & Whitesides, G.H. (1999). Oriented growth of calcite controlled by self-assembled monolayers of functionalized alkanethiols supported on gold and silver. *Journal of the American Chemical Society*, 121, 4500-4509, ISSN 0002-7863.
- Aizenberg, J., Lambert, G., Weiner, S. & Addadi L. (2001). Factors involved in the formation of amorphous and crystalline calcium carbonate: A study of an Ascidian skeleton. *Journal of American Chemical Society*, 124, 32-39, ISSN 0002-7863.
- An, X.Q. & Cao, C.B. (2008). Coeffect of silk fibroin and self-assembled monolayers on the biomineralization of calcium carbonate. *Journal of Physical Chemistry C*, 112, 15844-15849, ISSN 1932-7447.
- Bachmeier K.L., Williams, A.E., Warmingtton, J.R. & Bang S.S. (2002). Urease activity in microbiologically-induced calcite precipitation. *Journal of Biotechnology*, 93, 171-181, ISSN 0168-1656.
- Bäuerlein, E. (2007). Growth and form: What is the aim of biomineralization?, In: *Handbook of Biomineralization - Biological Aspects and Structure Formation*, E. Bäuerlein (Ed.), 1-20, Wiley-VCH Verlag GmbH & Co. KGaA, Weinheim, ISBN 978-3-527-31804-9.
- Brunsteiner, M., Jones, A.G., Pratola, F., Price, S.L. & Simons, S.J.R. (2005). Toward a molecular understanding of crystal agglomeration. *Crystal Growth & Design*, 5, 3-16, ISSN 1528-7483.
- Chow, M.K. & Zukoski C.F. (1994). Gold sol formation mechanisms-role of colloidal stability. *Journal of Colloid and Interface Science*, 165, 97-109, ISSN 0021-9797.
- Cölfen, H. (2003). Precipitation of carbonates: recent progress in controlled production of complex shapes. *Current Opinion in Colloid and Interface Science*, 8, 23-31, ISSN 1359-0294.

- Cölfen, H. (2007). Bio-inspired mineralization using hydrophilic polymers. *Topics in Current Chemistry*, 271, 1-77. ISBN 978-3-540-32151-4.
- Cölfen, H. & Antonietti, M. (2005). Mesocrystals: Inorganic superstructures made by highly parallel crystallization and controlled alignment. *Angewandte Chemie-International Edition*, 44, 5576-5591, ISSN 1433-7851.
- Davis, K.J., Dove, P.M., Wasylenki, L.E. & De Yoreo, J.J. (2004). Morphological consequences of differential Mg^{2+} incorporation at structurally distinct steps on calcite. *American Mineralogist*, 89, 714-720, ISSN 0003-004X.
- de Leeuw, N.H. (2002). Molecular dynamic simulations of the growth inhibiting effect of Fe^{2+} , Mg^{2+} , Cd^{2+} , and Sr^{2+} on calcite crystal growth. *Journal of Physical Chemistry B*, 106, 5241-5249, ISSN 1089-5647.
- DeOliveira, D.B. & Laursen, R.A. (1997). Control of calcite crystal morphology by a peptide designed to bind to a specific surface. *Journal of American Chemical Society*, 119, 10627-10631, ISSN 0002-7863.
- Dixon, N.E., Gazzola, C., Blakeley, R.L. & Zerner, B. (1975). Jack-bean urease (EC 3.5.1.5)-matalloenzyme - simple biological role for nickel. *Journal of American Chemical Society*, 97, 4131-4133, ISSN 0002-7863.
- Edinliljegren, A., Grenabo, L., Hedelin, H., Pettersson, S. & Wang, Y.H. (1994). Long-ter, studies of urease-induced crystallization in humane urine. *Journal of Urology*, 152, 208-212, ISSN 0022-5347.
- Elhadj, S., De Yoreo, J.J., Hoyer, J.R. & Dove, P.M. (2006a). Role of molecular charge and hydrophilicity in regulating the kinetics of crystal growth. *Proceedings of the National Academy of Science of the United States of America*, 103, 19237-19242, ISSN 0027-8424.
- Elhadj, S., Salter, E.A., Wierzbicki, A., De Yoreo, J.J. & Dove, P.M. (2006b). Peptide controls on calcite mineralization: Polyaspartate chain length affects growth kinetics and acts as a stereochemical switch on morphology. *Crystal Growth & Design*, 6, 197-201, ISSN 1528-7483.
- Estiu, G. & Merz K.M. (2004). Enzymatic catalyses of urea decomposition: Elimination or hydrolysis? *Journal of the American Chemical Society*, 126, 11832-11842, ISSN 0002-7863.
- Falini, G. (2000). Crystallization of calcium carbonates in biologically inspired collagenous matrices. *International Journal of Inorganic Chemistry*, 2, 455-461, ISSN 1466-6049.
- Falini, G., Albeck, S., Weiner, S. & Addadi, L. (1996). Control of aragonite or calcite polymorphism by mollusk shell macromolecules. *Science*, 271, 67-69, ISSN 0036-8075.
- Feng, Q.L., Pu, G., Pei, Y., Cui, F.Z., Li, H.D. & Kim, T.N. (2000). Polymorph and morphology of calcium carbonate crystals induced by proteins extracted from mollusk shell. *Journal of Crystal Growth*, 216, 459-465. ISSN 0022-0248.
- Gebauer, D., Verch, A., Borner, H.G. & Cölfen, H. (2009). Influence of selected artificial peptides on calcium carbonate precipitation - A quantitative study. *Crystal Growth & Design*, 9, 2398-2403, ISSN 1528-7483.
- Heywood, B.R. & Mann, S. (1994). Molecular construction of oriented inorganic materials-controlled nucleation of calcite and aragonite under compressed Langmuir monolayers. *Chemistry of Materials*, 6, 311-318, ISSN 0897-4756.

- Kallay, N. & Žalac S. (2002). Stability of nanodispersions: A model for kinetics of aggregation of nanoparticles. *Journal of Colloid and Interface Science*, 253, 70-76, ISSN 0021-9797.
- Knoll, A.H. (2003). Biomineralization and evolutionary history. *Reviews in Mineralogy and Geochemistry*, 54, 329-356, ISSN 1529-6466.
- Lasic, D.D. (1993). On the formation of inorganic colloid particles. *Bulletin of the Chemical Society of Japan*, 66, 709-713, ISSN 0009-2673.
- Loste, E., Wilson, R.M., Seshadri, R., & Meldrum, F.C. (2003). The role of magnesium in stabilizing amorphous calcium carbonate and controlling calcite morphology. *Journal of Crystal Growth*, 254, 206-218, ISSN 0022-0248.
- Mann, S. (1993). Molecular tectonics in biomineralization and biomimetic material chemistry. *Nature*, 365, 499-505. ISSN 0028-0836.
- Mann, S. (2001). *Biomineralization-principles and concepts in bioinorganic material chemistry*. Oxford University Press, ISBN 0-19-850882-4, New York.
- March, M. E. (2007). Regulation of Coccolith calcification in *Pleurochrysis carterae*. In: *Handbook of Biomineralization- Biological Aspects and Structure Formation*, E. Bäuerlein (Ed.), 211-226, Wiley-VCH Verlag GmbH & Co. KGaA, Weinheim, ISBN 978-3-527-31804-9.
- Martinez-Rubi, Y., Retuert, J., Azdani-Pedram, M., Barbosa, M. & Arias, J.L. (2008). Nucleation and selective growth of polymorphs of calcium carbonate on organic-inorganic hybrid films. *Journal of the Chilean Chemical Society*, 53, 1353-1357, ISSN 0717-9324.
- Matiječić, E. (1993). Preparation and properties of uniform size colloids. *Chemistry of materials*, 5, 412-426, ISSN 0897-4756.
- Mayers, M.A., Chen, P.-Y., Lin, A. Y.-M. & Seki, Y. (2008). Biological materials: structure and mechanical properties. *Progress in Materials Science*, 53, 1-206, ISSN 0079-6425.
- Meldrum, F.C. & Cölfen, H. (2008). Controlling mineral morphologies and structures in biological and synthetic systems. *Chemical Reviews*, 108, 4332-4432, ISSN 1520-6890.
- Meldrum, F.C. & Hyde, S.T. (2001). Morphological influence of magnesium and organic additives on the precipitation of calcite. *Journal of Crystal Growth*, 231, 544-558, ISSN 0022-0248.
- Meldrum, F.C. (2003). Biomimetic control of calcification. *International Materials Reviews*, 48, 187-224, ISSN 0950-6608.
- Mobley, H.L.T. & Hausinger, R.P. (1989). Microbial ureases-significance, regulation, and molecular characterization. *Microbiological Reviews*, 53, 85-108, ISSN 0146-0749.
- Nakayama, T., Nakahara, A. & Matsushita, M. (1995). Cluster-cluster aggregation of calcium carbonate colloid particles at the air-water interface. *Journal of the Physical Society of Japan*. 64, 1114-1119, ISSN 0031-9015.
- Orme, C.A. Noy, A., Wierzbicki, A., McBride, M.T., Grantham, M., Teng, H.H., Dove, P.M. & DeYoreo, J.J. (2001). Formation of chiral morphologies through selective binding of amino acids to calcite surface steps. *Nature*, 411, 775-779, ISSN 0028-0836.
- Ozin, G.A. (1997). Morphogenesis of biomineral and morphosynthesis of biomimetic forms. *Accounts of Chemical Research*, 30, 17-27, ISSN 0001-4842.
- Petres J.J., Dežalić, Gj. & Težak B. (1969). Monodisperse sols of barium sulfate. 3. Electron-microscopic study of internal structure of particles. *Croatica Chemica Acta*, 41, 183-198, ISSN 0011-1643.

- Pichon, B.P., Bomans, P.H.H., Frederik, P.M. & Sommerdijk, N.A.J.M. (2008). A quasi-time-resolved CryoTEM study of the nucleation of CaCO₃ under Langmuir monolayers. *Journal of the American Chemical Society*, 130, 4034-4040, ISSN 0002-7863.
- Popescu, D.C., Smulders, M.M.J., Pichon, B.P., Chebotareva, N., Kwak, S.Y., van Asselen, O.L.J., Sijbesma, R.P., DiMasi, E. & Sommerdijk, N.A.J.M. (2007). Template adaptability is a key in the oriented crystallization of CaCO₃. *Journal of the American Chemical Society*, 129, 14058-14067, ISSN 0002-7863.
- Privman, V., Goia, D.V., Park, J. & Matijević, E. (1999). Mechanism of formation of monodispersed colloids by aggregation of nanosize precursors. *Journal of Colloid and Interface Science*, 213, 36-45, ISSN 0021-9797.
- Sarashina, I. & Endo, K. (1998). Primary structure of soluble matrix protein of scallop shell: Implication for calcium carbonate biomineralization. *American Mineralogist*, 83, 1510-1515, ISSN 0003-004X.
- Sedlak, M. & Cölfen, H. (2001). Synthesis of double-hydrophilic block copolymers with hydrophobic moieties for the controlled crystallization of minerals. *Macromolecular Chemistry and Physics*, 202, 587-597. ISSN 1020-1352.
- Skinner, H.C.W. (2005). Biominerals. *Mineralogical Magazine* 69, 621-641, ISSN 0026-461X.
- Sondi, I. & Matijević E. (2001). Homogenous precipitation of calcium carbonate by enzyme catalyzed reactions. *Journal of Colloid and Interface Science*, 238, 208-214, ISSN 0021-9797.
- Sondi, I. & Matijević, E. (2003). Homogeneous Precipitation by enzyme-catalyzed reactions. 2. Strontium and barium carbonates. *Chemistry of Materials*, 15, 1322-1326, ISSN 0897-4756.
- Sondi, I. & Salopek-Sondi, B. (2004). The influence of the primary structures of urease enzyme on the formation of CaCO₃ polymorphs: A comparison of plant (*Canavalia ensiformis*) and bacterial (*Bacillus pasteurii*) ureases. *Langmuir* 21, 8876-8882, ISSN 0743-7463.
- Sondi, I., Škapin, S.D. & Salopek-Sondi B. (2008): Biomimetic precipitation of nanostructured colloidal calcite particles by enzyme-catalyzed reactions in the presence of magnesium ions. *Crystal Growth & Design*, 8, 435-441, ISSN 1528-7483.
- Song R.Q., Cölfen, H., Xu, A.W., Hartmann, J. & Antonietti, M. (2009). Polyelectrolyte-directed nanoparticle aggregation: Systematic morphogenesis of calcium carbonate by nonclassical crystallization. *ACS Nano*, 3, 1966-1978, ISSN 1936-0851.
- Škapin, S.D. & Sondi, I. (2005). Homogeneous precipitation of mixed anhydrous Ca-Mg and Ba-Sr carbonates by enzyme-catalyzed reactions. *Crystal Growth & Design*, 5, 1933-1938. ISSN 1528-7483.
- Stanley, D.G. (2003). The evolution of modern corals and their early history. *Earth-Science Reviews*, 60, 195-225, ISSN 0012-8252.
- Stocks-Fischer, S., Galinat, J.K. & Bang, S.S. (1999). Microbial precipitation of CaCO₃. *Soil Biology and Biochemistry*, 31, 1563-1571, ISSN 0038-0717.
- Stupp, S.I. & Braun, P.V. (1997). Molecular manipulation of microstructures: Biomaterials, ceramics, and semiconductors. *Science*, 277, 1242-1248, ISSN 0036-8075.
- Takeuchi, T., Sarashina, I., Lijima, M. & Endo, K (2008). In vitro regulation of CaCO₃ crystal polymorphism by the highly acidic molluscan shell protein Aspein. *FEBS Letters*, 582, 591-596, ISSN 0014-5793.

- Tambutté, S., Tambutté, E., Zoccola, D. Allemand, D. (2007). Organic matrix and biomineralization of scleractinian corals. In: *Handbook of Biomineralization - Biological Aspects and Structure Formation*, E. Bäuerlein (Ed.), 243-259. Wiley-VCH Verlag GmbH & Co. KGaA, Weinheim, ISBN 978-3-527-31804-9.
- Taylor, P. D., James, N.P., Bone, Y., Kuklinsky, P. & Kyser, T. K. (2009). Evolving mineralogy of Cheilostome bryozoas. *Palaios*, 24, 440-452, ISSN 0883-1351.
- Teng, H.H., Dove, P.M., Orme, C.A. & De Yoreo, J.J. (1998). Thermodynamics of calcite growth: Baseline for understanding biomineral formation. *Science*, 282, 724-727, ISSN 0036-8075.
- Tong, H., Ma, W.T., Wang, L.L., Wan, P., Hu, J.M. & Cao, L.X. (2004). Control over the crystal phase, shape, size and aggregation of calcium carbonate via L-aspartic acid including process. *Biomaterials*, 25, 3923-3929, ISSN 0142-9612.
- Tremel, W., Küther, J., Balz, M., Loges, N. & Wolf, S.E. (2007). Template surfaces for the formation of calcium carbonate. In: *Handbook of Biomineralization- Biomimetic and Bioinspired Chemistry*, P. Behrens & E. Bäuerlein (Eds.), 209-232, Wiley-VCH Verlag GmbH & Co. KGaA, Weinheim, ISBN 978-3-527-31804-9.
- Volkmer, D., Fricke, M., Hubar, T. & Sewald, N. (2004). Acidic peptides acting as growth modifiers of calcite crystals. *Chemical Communications*, 16, 1872-1873, ISSN 1359-7345.
- Wang, T.P., Antonietti, M. & Cölfen, H. (2006). Calcite mesocrystals: "Morphing" crystals by a polyelectrolyte. *Chemistry-A European Journal*, 12, 5722-5730, ISSN 0947-6539.
- Xie, A.J., Shen, Y.H., Zhang, C.Y., Yuan, Z.W., Zhu, X.M. & Zang, Y.M. (2005). Crystal growth of calcium carbonate with various morphologies in different amino acid systems. *Journal of Crystal Growth*, 285, 436-443, ISSN 0022-0248.
- Xu, A.-W., Ma, Y. & Cölfen, H. (2007). Biomimetic mineralization. *Journal of Material Chemistry*, 17, 415-449, ISSN 0959-9428.
- Yamamoto, Y., Nishimura, T., Sugawara, A., Inoue, H., Nagasawa, H. & Kato, T. (2008). Effects of peptides on CaCO₃ crystallization: Mineralization properties of an acidic peptide isolated from exoskeleton of cryfish and its derivatives. *Crystal Growth & Design*, 8, 4062-4065, ISSN 1528-7483.
- Yu, S.-H. & Cölfen, H. (2004). Bio-inspired crystal morphogenesis by hydrophilic polymers. *Journal of Material Chemistry*, 14, 2124-2147, ISSN 0959-9428.
- Zukoski C.F., Rosenbaum, D.F. & Zamora, P.C. (1996). Aggregation in precipitation reactions: Stability of primary particles. *Chemical Engineering Research & Design*, 74, 723-731, ISSN 0263-676

A Biomimetic Study of Discontinuous-Constraint Metamorphic Mechanism for Gecko-Like Robot

ZhenDong Dai and HongKai Li
*Nanjing University of Aeronautics and Astronautics
China*

1. Introduction

Mobile robots have been strong demands for defense, surveillance and counter terrorism missions as a moving platform under unconstrained environments (Eric & John, 1999; Robert et al., 2003). Two moving mechanisms, wheeled and legged, were used for mobile robots. Both of them have been studied for years. Wheeled vehicles could move much faster and have much higher efficiency than that of legged ones (Todd, 1985); they are widely used in well-structured circumstances, such as automobile and train has to be move on highway or railroad. The key point of wheeled motion is that the wheels continuously contact to the substrate. This demand makes the wheeled vehicles moving on flat surface under tens to hundreds times higher efficiency than that of legged locomotion (Todd, 1985).

On the other hand, a lot of animals that live on land have selected the legged mechanism for their locomotion. This selection comes from the advantages of legged mechanism, highly adaptability to the unstructured natural circumstance, multifunctional behaviours, such as walking, running, jumping and even climbing, and strong function compensation. The advantages that make the animals to live much more reliably were high energy efficient, and what's important is highly adaptive, robust and reliable for locomotion. Those characters are also needed for the moving system under unconstructive circumstance, unmanned intelligent situation, such as the area of defence, surveillance and counter terrorism missions, where no road existed. The legged locomotion mechanism has been demonstrated successfully in wild bumpy circumstance, so mimicking the motion mechanism and control pattern of the legged animals may greatly increase the locomotion abilities, though it's difficult to copy nature (Siegwart & Nourbakhsh, 2004).

Biomimetics on locomotion aims to reveal the secrets of legged locomotion of animals in order to understand how animals' motion and to get inspiration by the technique animals used. Now a lot of robots inspired by animals were developed in laboratory, but their performance of locomotion, such as walking, jumping, running, sliding, swimming, lagged far behind their natural counterparts in stability, agility, robustness, environmental adaptability and energy efficiency (Dickinson et al., 2000). Humanoid robots could play the

piano, dance and play Chinese GongFu, but they could not work for more than 30 minutes because of the energy supply. Research showed that the best humanoid robot, ASIMO, consumed ten times energy of human for the same motion (Collins et al., 2005). The energy efficiency of the best snake-like robot was about 25%, but a snake can move faster and longer even without food for several weeks. What makes such a big difference in energy efficiency between robots and its animal prototypes?

After millenniums years of evolution, a lot of animals that live on earth have optimized the legged mechanism for locomotion and feet for stable contact with the substrate. They selected flat hoofs with various toes to reduce the contact stress and developed several joints between bones of the foot to adapt the slope of the substrate. Research on legged machines could lead to the construction of useful legged vehicles and help us to understand legged locomotion in animals (Raibert, 1986). Developments of RHex were inspired by the biomechanics of arthropod locomotion (Altendorfer et al., 2001). The outstanding mobility of Bigdog results from the study on locomotion of dog (Raibert et al., 2008).

Gecko, have been a study highlights because of their excellent climbing ability, is a perfect object for wall-climbing robot. As a scansorial quadruped animal, gecko's locomotion abilities benefit from the adhesive pads, short strong limbs and flatten body (Cartmill, 1985; Damme et al., 1997). Morphology, kinematics (Damme et al., 1998; Damme et al., 1997; Li et al., 2009; Zaaf et al., 2001) and dynamics (Autumn et al., 2006) related to gecko's locomotion have been extensively studied. The adhesive mechanism was revealed (Autumn et al., 2000) as van der Waals force between the hierarchical structural setae on toes and substrate. Inspired by the geometric structure of seta, Carbon nanotube arrays was developed (Qu et al., 2008), the array showed strong shear binding-on and easy normal lifting-off character and may be wonderful artificial adhesive pads for gecko-like robot. Other adhesive pads were developed (Santos et al., 2007) and successfully used in a climbing robot-Sticybot (Kim et al., 2008). Though there are a lot of researches on gecko, the mechanism theory and related controlling technique are still unclearly.

In this paper, the mechanism of a gecko-like sprawling robot was proposed in section 2. In section 3 we analyzed the kinematic and dynamic characters of the robot mechanism. For well understanding how gecko moves we observed the angular regularity of gecko's each joints when moving on horizontal and vertical surface in section 4. Motion scheme including walking gait and trotting gait was introduced in section 5. And in section 6 we designed a realizable control system.

2. Mechanism of legged gecko-like robot

Limbs were the executive machine of geckos that consisted of skeleton-joint-muscle. Skeleton moved relied on the rotation of joints, and carry foot to the next support position or drive body forward. A legged mechanism for gecko-like robot (Fig. 1 A) (Dai et al.) was proposed according to the anatomic studies on gecko (Liu et al., 2005; Zaaf et al., 1999), which was generally considered as a multi-jointed serial chain (Winters & Crago, 2000). One step cycle includes an swing phase and a stance phase. During swing phase the leg lifts off and forms an open chain (Fig. 1 B). But in stance phase two or three feet, the terminal

part of legs, stably contact on the substrate and propel the body move forward, which form a closed chain by two limbs (or some time three limbs) (Fig. 1 C). When limbs of gecko shift from an swing phase to stance phase, the constrained forces acted on the foot changes discontinuously, the mechanism of the locomotion changes because of the shift from open chain to closed chain and the change of length of the equivalent bar (frame) in each leg step. We define this phenomenon as discontinuous constraint metamorphic linkage mechanism (DC-MLM). The metamorphic mechanism come from the definition given by Dai (Dai & Jones, 1999). The degree of freedom of (DoF) the cardan joint J_{BF} (J represents Joint, subscript letters BF represents Body and Femur), the revolute joint J_{FT} (FT represents Femur and Tibia), and the spherical joint J_{TD} (TD represents Tibia and Dactylust) are 2, 1, 3 respectively.

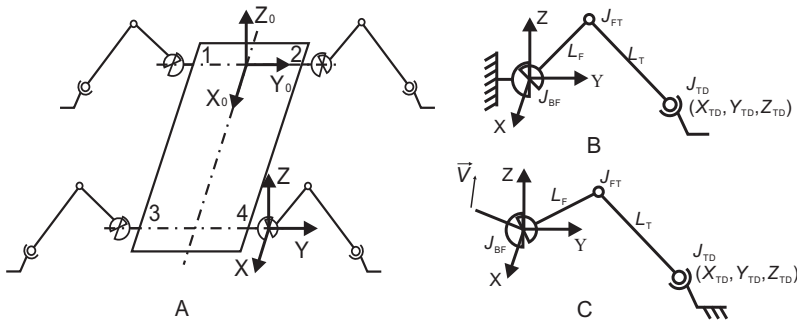


Fig. 1. A simplified mechanism of gecko-like robot (A); swing phase (B) and stance phase (C) of one leg. The gecko-like robot composed of four legs, on each leg there are two active joints J_{BF} & J_{FT} and one passive joint J_{TD} .

The adhesive force would increase with increase of real contact area, and the feet of limbs under stance phase must contact with the substrate on enough “real” area, so joint J_{TD} has evolved as a spherical joint to adapt the sole with the target surface. The mechanism needs to be driven by three active independent actuators at least (the J_{TD} as a passive joint) to allow the foot of the robot to reach the intended position and to retain enough mobility when the limb is at swing phase. The similar change was performed in folding carton, on which the metamorphic mechanism was proposed and developed (Dai & Jones, 1999; Jin et al., 2004; Jin et al., 2005).

In order to drive the robot synchronously, glenohumeral joint or Joint J_{BF} of the legs at stance phase must have the same speed vector, which need actuators of each leg drive on a concordant way. How to make them driven concordant is still a big problem. Right now spherical shaped foot was selected by a lot of legged robots that move on ground, because the design increases the adaptability of foot with substrate without passive joint. On the other hand, this foot could not meet the requirement of gecko-like robot where enough real contact area is needed to generate enough adhesive force.

There are three contact status between foot of a gecko-robot and the substrate – non-contact, sliding contact and stable contact, which is presented by the interaction force F_s – friction force parallel to the target surface and adhesive or repulsive force perpendicular to the

surface as following:

$$\left\{ \begin{array}{lll} F_s = 0 & \text{open chain} & \\ F_s = C & \text{close loop chain} & \text{Slide} \\ F_s = \infty & \text{close loop chain} & \text{Stable} \end{array} \right. \quad (1)$$

For the first case, the foot was at swing phase and lift off the substrate, so F_s would be zero, the methods of analyzing the mechanism, kinematics and dynamics of an open-chain are well developed. When the leg is at stance phase, foot contacted with substrate in two ways. When foot stably contacted on substrate, which generally falls in a self-locking situation, the contact force would increase with increase of the propel force. When foot slides on the surface, interaction force between foot and substrate would be determined by the frictional coefficient and normal force and the length of links (bar) of frame would change with sliding. This situation is much more complicated and will not discuss here.

When a legged mechanism moves, the power needed for motion should be discussed according two cases. When legs are in swing phase, the power needed is to overcome the force of inertia. When the legs are under stance phase, the power needed is to support the locomotion and depended on the carried load and the related motion. To reduce the power consummation, the legs under stance phase must move on a coordinate velocity. When a leg mechanism moves in a structured circumstance, the coordination could be transferred into a geometric question. In an unstructured circumstance, the coordination greatly depends on the unpredicted next contact position; new technique has to be introduced to meet the requirement. To obtain an idea from the animals' locomotion, it was necessary to understand the kinematics, dynamics and the control strategies of animals.

3. Kinematic and dynamic analysis

When a leg is under swing phase, it is a serial open chain with 3 active degrees of freedom with one passive sphere joint at the terminal of the leg. From the kinematics of the open chain, we will obtain the information about the working space and the trajectory of the mechanism. So the coordinates $J_{TD}(X_{TD}, Y_{TD}, Z_{TD})$ of foot point (end point of shank) in the base frame Σ -XYZ, which was coincident with $OX_0Y_0Z_0$, could be obtained by forward kinematics as following (see Fig. 1 B), Where L_F and L_T are the lengths of upper leg and shank, respectively, α (angle between YOZ plane and upper leg L_F) and β (angle between XOY plane and upper leg L_F) are the angles between the leg and body respectively, and γ represents the angle between the upper leg L_F and shank L_T :

$$\left\{ \begin{array}{l} X_{TD} = [L_F \cos \alpha - L_T \cos(\alpha + \gamma)] \cos \beta \\ Y_{TD} = [L_F \cos \alpha - L_T \cos(\alpha + \gamma)] \sin \beta \\ Z_{TD} = L_F \sin \alpha - L_T \sin(\alpha + \gamma) \end{array} \right. \quad (2)$$

The velocity components of J_{TD} could be derived from the time derivative of equations in (2). So it obvious that the linear velocity of foot tip was determined by the angular velocity of α , β and γ .

To adapt to the unstructured circumstances, point contact was selected by robots that move on land. To fit the unstructured circumstances and generate enough adhesive force to make gecko-like robot climb on walls or ceilings, a single foot with biggest contact area must be developed, and a passive spherical joint was assigned for the ankle joint (shank-foot connection) to make the foot contacted better.

4. Angular observations of joints of Geckos moving on horizontal and vertical surfaces

At present, the drive mechanism of a gecko robot depends mainly on micro-motors, and the planning and designing of motion are implemented based on angular orientation. Therefore, for the motion scheming of gecko robot, a more direct approach would be studying the orientation and angular changes of gecko's joints.

This section aims to reveal the relationship among the angles (α , β and γ) when gecko moves on floor and wall freely, and we expect the results would inspire us with a new idea for the motion plan of gecko-like robot.

4.1 Observation system and Method

A system to observe the three-dimensional locomotion behaviours of gecko was developed which consisted of a tunnel and a high speed camera (Mikrotron, MC1311 Germany) (Fig. 2). The tunnel was made up of a long flat marked track with two mirrors on left and right sides with an angle 135° to the track, a transparent polymethyl methacrylate plan which covered the top to avoid the animals falling down during experiments. The high speed camera was supported with a tripod and connected with a computer to set the frame frequency, pixels, start and stop. During the experiments the locomotion behaviour was digitally documented by the camera. The projection in two mirrors gives the lateral position of joints and, together with the real image, full spatial poses were obtained. The tunnel is wide enough to enable the geckos to move freely.

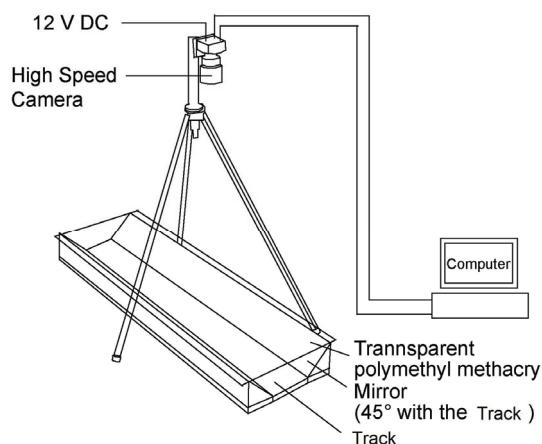


Fig. 2. Three-dimensional locomotion observation system

The tunnel was mounted horizontally or vertically to simulate floor or wall, and the geckos were induced to move along it from one end to another.

To describe the motion clearly and be in accord with our previous work, we define the reference frame following the stereotaxic method (Wang et al., 2008). We take the underside of tunnel in the three-dimensional locomotion observation system as the horizontal plane (body plane). The sagittal plane is the plane perpendicular to the body plane and passes through the bregma and nasal points. The coronal plane is the plane through the bregma point and perpendicular to the body plane and sagittal plane. The femorotibial angle (α) is the angle between femur and tibia, and is always positive. The swing angle (β) was calculated as the projection of the angle between femur and a plane through the coxa parallel with the coronal plane in the body plane. Swing angles in front of the parallel plane are considered positive, while behind this plane, negative. The lifting angle (γ) is defined as the projection of the angle between femur and a plane through the coxa parallel with the body plane in the coronal plane (Fi.3). Lifting angles are considered positive before the parallel plane, and negative behind this plane. The units of all angles are in degrees ($^{\circ}$).

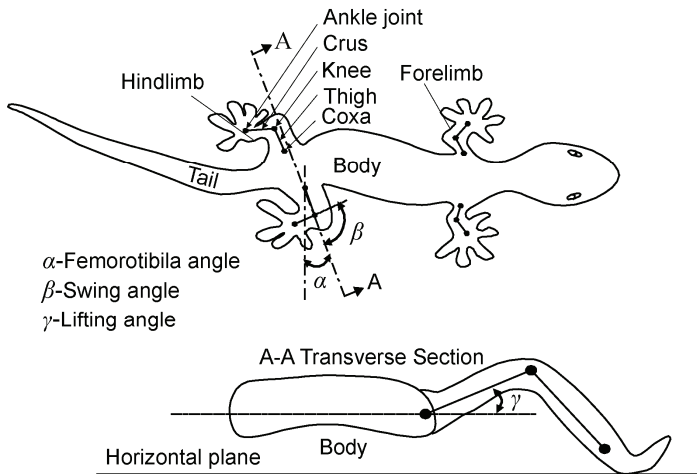


Fig. 3. The definition of femorotibial, swing and lifting angles

Experiments were grouped by gait speed and surface orientation, viz., the high speed trot gait (trot) and slow speed tripod gait (walk) on both horizontal and vertical surfaces. Four geckos were selected for the experiments. At least 20 trails were recorded in each experiment. Linear regression of step length against time was done to assess the steady speed, and four groups of complete sequences were selected for further analysis for which the R^2 values of regression were greater than 0.95. All geckos selected were marked with white non-toxic painted dots on the coxa, knee and ankle joints before experiments. The camera axis was perpendicularly oriented to the locomotion surface (track) and adjusted until there was a clear image in the computer (Fig. 4). The motion process was digitally recorded with a fixed frame frequency.

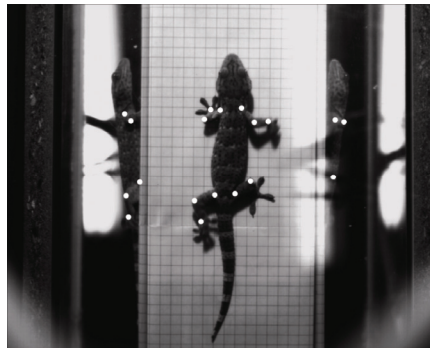


Fig. 4. One image of a free vertically climbing gecko

The middle is the real image of gecko during motion, and images on the left and right sides are the mirror images. The white plots on the images are the key points used to calculate the angles.

4.2 Ranges of each joints

From the experimental data, it was found that there are no speed limitations in gait alternation between trotting and walking. In other words, feet at diagonal direction might lift off and touch down at the same time even at slower velocities. Generally, when speeding up, geckos would transit from walking to trotting. The following four groups of data were selected for analysis and comparison: walking (66.7 mm/s) and trotting (337.1 mm/s) over a horizontal surface, and walking (30.6 mm/s) and trotting (241.5 mm/s) up a vertical surface. Extrema and ranges of fore and hindlimb angles are shown in Table 1.

Projects		Forelimb				Hindlimb			
		Horizontal		Vertical		Horizontal		Vertical	
		Trot	Walk	Trot	Walk	Trot	Walk	Trot	Walk
Swing angle(°)	Max.	59.2	59.0	36.7	33.7	77.2	85.1	82.6	79.0
	Min.	□79.2	□72.0	□87.7	□87.3	□44.3	□31.1	□64.9	□53.3
	Ra.	138.4	131.0	124.4	121.0	121.5	116.2	147.5	132.3
Lifting angle(°)	Max.	59.6	50.8	86.3	84.5	48.7	21.3	46.9	35.6
	Min.	□17.4	□11.4	15.5	5.4	□10.7	□18.0	□19.7	□16.7
	Ra.	77.0	62.2	70.8	79.1	59.4	39.3	66.6	52.3
Femorotibial angle(°)	Max.	138.3	127.2	109.1	131.8	135.2	126.7	151.3	146.9
	Min.	39.3	47.7	55.2	56.3	54.4	78.7	51.1	47.5
	Ra.	99.0	79.5	53.9	75.5	80.8	48.0	100.2	99.4

Table 1. Extrema and ranges of fore and hind-limb angles

4.3 Angular phase diagrams

Angular phase diagrams are used to show the relationship and tendencies of the two groups of angles with the same time variable (Kristiaan et al., 2002). The shape of the phase diagram shows the changing trend of angles in different phases, and the position in the coordinate

system shows the angle scope. It is very convenient to compare the same group of data in different states by their phase diagrams. The phase diagrams of swing-lifting angles and swing-femorotibial angles are shown in Fig. 5. Arrows in each figure indicate the direction of joint rotation, and swing phase is at the beginning. The time interval between two sequential plots in a diagram is the same, so the speed in each phase can be evaluated by the density of dots—the slower speed of motion the denser the points. Closed loops indicate periodicity, and the enclosed area shows the changing extent of joint angles between swing phase and stance phase.

When trotting over horizontal surfaces, swing-lifting angle plots of fore and hind limbs (Figure 5(a), (e)) and the swing-femorotibial angle plot of forelimb (Figure 5(i)) are clearly different from other plots. The density of dots is greater when swinging forward than that when swinging backward in relation to the arrow's direction.

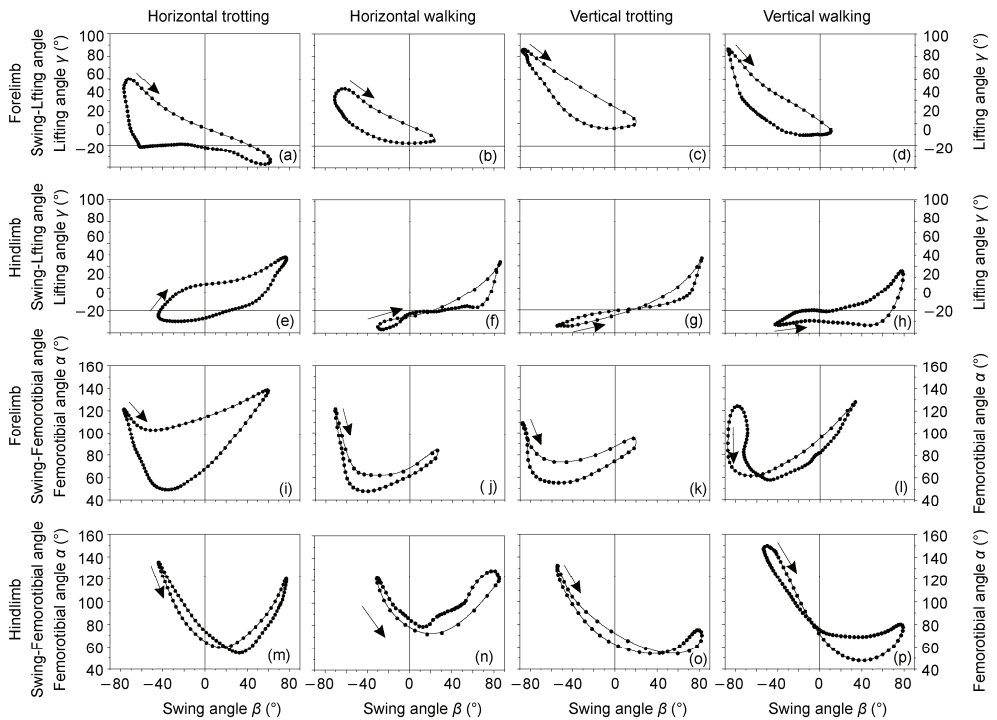


Fig. 5. Swing-lifting angle plots for forelimb trotting (a) walking; (b) on horizontal surface and trotting; (c) and walking; (c) on vertical surface; (e), (f), (g), (h) are the corresponding plots for hindlimb; (i), (j), (k), (l) are swing-femorotibial angle plots for forelimb; (m), (n), (o), (p) for Hindlimb respectively. Dots represent time slices and speed trend can be estimated by the density of dots. The arrow in each phase diagram represents the change direction of curve. Time interval of trotting and walking on horizontal surface and trotting and walking on vertical surface are 4 ms, 25 ms, 10 ms and 20 ms respectively.

There is a great difference in the shape of phase diagrams due to the different velocities when moving over horizontal surfaces, but the swing-femorotibial angle plot of the hindlimbs are similar (Figure 5(m), (n)). The enclosed areas of the swing-femorotibial angle plot in fore and hind limbs increase with the increasing speed (Figure 5(a), (b), (e), (f)). The change of femorotibial angle in forelimb is slight in the swing phase, but large bending exists in the stance phase (Figure 5(i)). The trends of the swing-lifting angle plot for forelimb (Figure 5(a) – (d)) and hindlimb (Figure 5(e) – (h)) are reversed in correspondence with the forelimb's angle curves in Figure 4. Compared with moving on horizontal surfaces, there is a lot in common between each group of phase diagrams in different gaits up vertical surfaces. And the forelimb swing- lifting angle plots (Figure 5(c), (d)) are the most obvious among these groups. Shape almost remained the same, except the position in the coordinate system when moving up vertical surfaces, which shows that the angular velocity of joints increases with speed, but the mode of joint rotation nearly keeps invariant. The swing-lifting angle plots are higher when moving up vertical surfaces than those when moving over horizontal surfaces (Figure 5(a) – (d)), and the positions as seen in Figure 5(c), (d) are all above the zero line, which means that the thigh has swung above the plane that crosses the coxa and parallels the body plane, placed the center of the body closer to the motion surface.

4.4 Influence of locomotion speed on joint rotation

The trotting gait is used when geckos move at high speed, that is, the motion cycles of fore and hind legs diagonally opposed are almost the same. The triangle gait is engaged at low speeds, namely, each swing in turn is based on the order of front right - hind left - front left - hind right - front right. Different strategies during speed adjustments are adopted when moving over horizontal and vertical surfaces at different gaits.

The experiment showed that stride frequency increased when speeding up, but step length, stride and duty factor remained unchanged when geckos moved over horizontal surfaces, and hindlimb moved more parasagittally. Both step length and stride frequency increased with increasing speed up vertical surfaces, but the relative increase of step length was small compared with that of stride frequency (Zaaf et al., 2001). Results joint angles exhibited the following rules: angular velocity should rise with increasing locomotion speed over horizontal surfaces, but the scope of swing angle remain unchanged, and the curve of the lifting angle in the stance phase should be lower to decrease the angle between thigh and sagittal plane; angular velocity should rise with increasing locomotion speed up vertical surfaces, and the scope of the swing angle should increase. Rotation speed of the joint should increase with increasing locomotion speed over the same surface, which could be derived from the dot density in the phase diagrams in Figure 5. The curve of the lifting angle corresponding to horizontal trotting was lower than that up vertical surfaces. Increased amplitude of hindlimb swing angle with increasing speed up vertical surfaces is obvious (Table 1). This experimental result was proved by our angular measurements. Moreover, in our experiments, the swing angle increase of the hindlimb was accomplished mainly during the backward swing, but did not change much during the forward swing.

When geckos trot horizontally, the task of the forelimb in the swing phase is completed by the forward extension of the crus carried by the forward rotation of the coxa, while the femorotibial angle almost remains unchanged at the end of the stance phase. The

performance looks quite smart and quick. The lifting range of the fore thigh in trotting is larger than that in walking to avoid collisions between the limb and blocks (such as stones and so on) in swing phase and body drag over the locomotion surface.

Morphology differences (Zaaf et al., 1999) between forelimb and hindlimb endow the gecko with the possession of a special adaptation. The shorter forelimb is shaped to climb. The thigh moves forward at the end of the swing phase and moves mostly hindward at the end of the stance phase. The relative height between coxa and foot in the forelimb is maximal at the end of swing phase. Regarding the coordination and compliance of movement, the limbs do not move forward at the moment of lift off, but continue to move backwards to avoid the abrupt change in acceleration.

4.5 The differences of joint rotation between moving on horizontal and vertical surfaces

Over horizontal surfaces, the body is supported by four legs on the substratum by overcoming gravity, friction and forward propulsion. Up vertical surfaces, there is the risk of tumbling backwards because of the moment of inertia when the body's center of mass leaves the wall. This moment of inertia is proportional to the gecko's mass and the perpendicular distance between the centre of mass and the wall. The influence of the moment of inertia is compensated by the pulling force of the shorter forelimb against the wall, and the torque due to the fact that the limbs in the swing phase overcome the gravity and also offer enough propulsion to move the body upward (Autumn et al., 2006).

The moment of inertia would be decreased by reducing the distance between the centre of mass and the vertical surface. Thighs in the stance phase always above the plane that crosses the coxa and paralleling the body plane to reduce the overturning moment. The lifting angles of the hindlimb are at the lowest position during most of the motion cycle, and the curves are very flat. Locomotion velocity has little influence on each limb's motion style (the shapes of the phase diagrams remain nearly the same). Over horizontal surfaces, limbs just need to overcome gravity and support propulsion, so the motions of limbs are more sprightly and agile.

The results of locomotion observation offered us a reference to scheme the robot gaits, and make the motion smoothly and have higher efficiency, though the trajectory of the joints could not be used directly to the robot because there was some difference on the size, freedoms and the actuator capability and so on between the animal and the mimetic robot.

5. Motion planning

According to the mechanism brought forward, a mode of gecko robot was built and exported to ADAMS for dynamic analysis of mechanical systems. The mode in ADAMS was showed in Fig. 6, by which the motion analysis after gait schemed was done.

It was found that during the experiments that gecko used trot gait (feet at the diagonal move nearly at the same time) most time in relative safe and certain circumstance, and used triangle gait (each foot lift off and drop down in turn, and three feet at stance phase and one

at swing phase simultaneously) at times in some difficult situations, such as walking on the ceiling and so on. Of course it's not simultaneous exactly that each foot shifts in turn, but there exists transition time, in other words, four feet maybe at stance phase in a short time during transition. So in the motion planning we insert the transition state into the locomotion cycle.

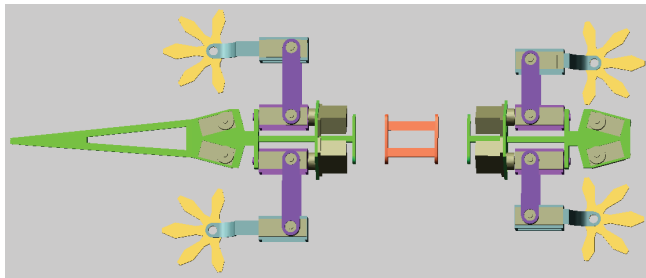


Fig. 6. ADAMS model of gecko-like robot IBSS-IV

5.1 trot gait

Just as diagram of trot gait showed in Fig. 7, the upper picture 0 was initial state. Picture 1, 3 was two motion states in which two legs in stance phase and the others two in swing phase. And picture 2, 4 was two transition states, in which two legs were in stance phase at the same time. The motion states 1, 2, 3 and 4, which correspond with the period in the below constitute the intact motion cycle.

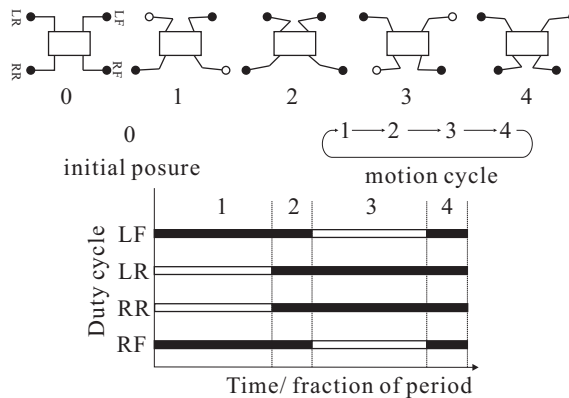


Fig. 7. Gait plan for trotting motion

Dynamic equilibrium exists in trot gait, and this is also complicated. ZMP (zero moment point) mode was a classic mode for the stability control and had been researched in depth(Kajita, 2007).

5.2 Walk gait

Triangle was often used when the circumstance is complex and at very low velocity.

According to the result of gait characters of gecko, transition state that the four feet were all at stance phase inserted between the former and latter gait state. At one moment there's just one leg at swing phase, and other three legs at stance phase to drive the robot moving forward. The legs at left front, right rear, right front and left rear direction are at swing phase in turn. The sequence of each state was showed in Fig. 8, just as the motion of trot gait.

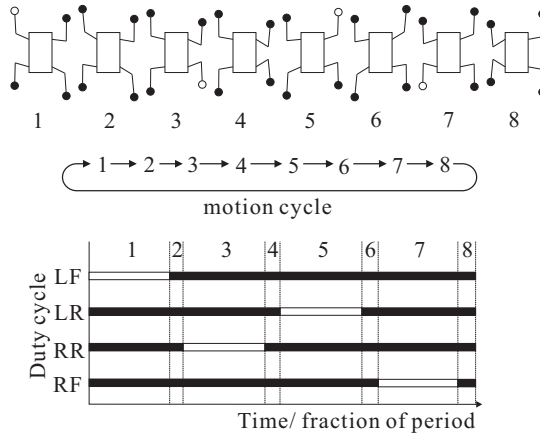


Fig. 8. Gait plan for walking motion

In Triangle gait static equilibrium, by which the center of gravity was kept in the triangle composed by the feet at stance phase, was often used in the control algorithm to keep the robot move stably. To avoid sliding between feet and contact surface, the relationship of friction angle and self-locking was widely used for the scheme of force applied to the feet. If the action line of active resultant force applied to the feet lying in the friction cone, sliding would be avoided no matter how much the active resultant force was because the self-locking had occurred. Inversely, if the action line of the resultant force was out of the friction cone, sliding must be occurred no matter how little the force was. And this principle was corresponding with the second and third situation in formula (1).

6. Design of control system

A distributed control system composed of one master - four slavers was designed to control the motion of robot. The master unit which was based on Atmega128L received orders from the host PC by wireless communication and distributed tasks to subsystems. Gait selection was also managed in the master. The subsystem was based on Atmega8L, which calculated the degrees each joints motor needed to drive the locomotion of robot leg. The I2C bus was applied to communicate between master and slaves, which need only 2 wires and the data rate up to 400 kHz. The whole control diagram was showed in Fig. 9.

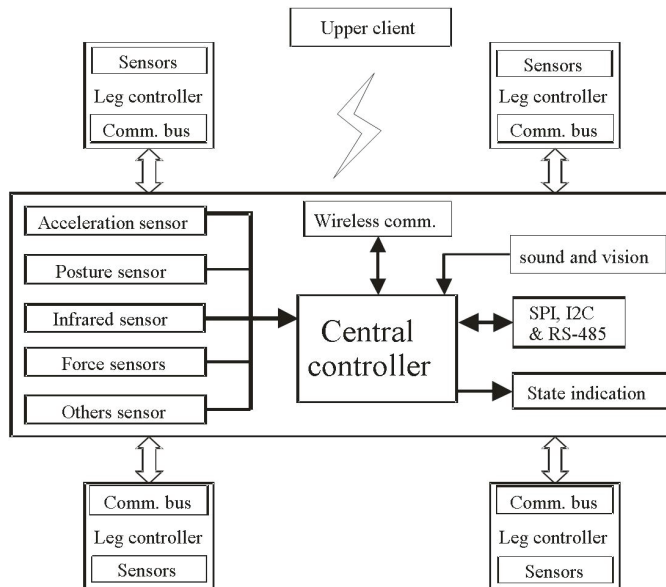


Fig. 9. Control diagram of gecko robot

Four foot pressure sensors were fixed on the sole to sense the state of feet. Foot state at each discrete step of all feet was sent to the master, according to the state master decided the next phase of each leg. The posture and acceleration sensor was used in the control system to sense the posture and motion state of robot during locomotion. Infrared sensor was for the distance detection and obstacle avoidance.

To improve the efficiency of the control system, the interrupt handing tasks were widely used on each master and slaver unit, and the main program concentrated on the task receives, send and dispatch. And subsystem calculates the geometrical relation of each leg to control the rotation of each motor on each joint.

A high power Li-polymer battery was selected which could support high current. For the electrical reliability and stability of control system, the power of control and motors were separated. The real gecko robot was shown in Fig. 10.

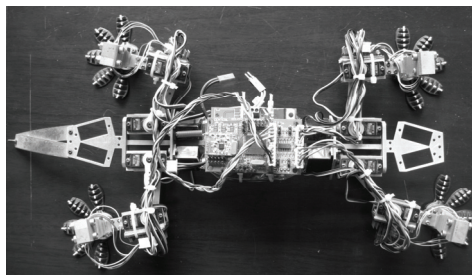


Fig. 10. A photo image of a gecko-like robot (IBSSIV)

Acknowledgement

This subject was supported by the National High Technology Research and Development Program of China (Grant No. 2007AA04Z201) and the National Natural Science Foundation of China (Grant Nos. 60535020, 30700068 and 50705043).

7. References

- Altendorfer, R. et al. (2001). RHex: a Biologically inspired hexapod runner. *Autonomous Robots*, Vol. 11, 207-213
- Autumn, K. et al. (2006). Dynamics of geckos running vertically. *Journal of Experimental Biology*, Vol. 209, 260-272
- Autumn, K. et al. (2000). Adhesive force of a single gecko foot-flair. *Nature*, Vol. 405, 681-685
- Cartmill, M. (1985). *Functional vertebrate morphology*. Harvard University Press, Cambridge, MA
- Collins, S. et al. (2005). Efficient bipedal robots based on passive-dynamic walkers. *Science*, Vol. 307, No.18, 1082-1085
- Dai, J. S. & Jones, J. R. (1999). Mobility in metamorphic mechanisms of foldable/erectable kinds. *Journal of mechanical design*, Vol. 121, No.3, 375-382
- Dai et al. (2007). Motion mechanism bionics of discontinuous-Constraint Metamorphic robot: concept and model (in Chinese). *Chinese science bulletin*, Vol. 52, No.2, 236-239
- Damme, R. V.; Aerts, P. & Vanhooydonck, B. (1998). Variation in morphology gait characteristics and speed of locomotion in two populations of lizards. *Biological Journal of the Linnean Society*, Vol. 63, 409-427
- Damme, R. V.; Aerts, P. & Vanhooydonck, B. (1997). No trade-off between sprinting and climbing in two populations of the Lizard *Podarcis hispanica*. *Biological Journal of the Linnean Society*, Vol. 60, 493-503
- Dickinson, M. H. et al. (2000). How animals move: An Integrative view. *Science*, Vol. 288, No.7, 100-106
- Eric, K. & John, B. (1999). The Defense Advanced Research Projects Agency (DARPA) Tactical Mobile Robotics Program. *Journal of Robotics Research*, Vol. 18, No.7, 769-776
- Jin, G.; Ding, X. & Zhang, Q. (2004). Research on Configuration-complete Dynamics Modeling and Numerical Simulation of Metamorphic Mechanism (in Chinese). *Acta Aeronautica ET Astronautica Sinica*, Vol. 25, 401-405
- Jin, G.; Gao, F. & Ding, X. (2005). On Classification and Configuration Analysis for Metamorphic Mechanisms (in Chinese). *Mechanical Science and Technology*, Vol. 24, 64-767
- Kajita, S. (2007). *humanoid robot*. Tsinghua University Press, 730214453, Beijing
- Kim, S. et al. (2008). Smooth Vertical Surface Climbing With Directional Adhesion. *IEEE transactions on robotics*, Vol. 24, 65-74
- Kristiaan, D. A. et al. (2002). Segment and Joint Angles of Hind Limb During Bipedal and Quadrupedal Walking of the Bonobo (*Pan paniscus*). *American Journal of Physical Anthropology*, Vol. 119, 37-51
- Li, H. et al. (2009). Angular observation of joints of Geckos moving on horizontal and vertical surfaces. *Chinese Science Bulletin*, Vol. 54, No.4, 592-598
- Liu, X. et al. (2005). A quantitative research on Gekko geckos appendicular muscle (in Chinese). *Anatomy Research*, Vol. 27, 292-301

- Qu, L. et al. (2008). Biomimetic mushroom-shaped fibrillar adhesive microstructure *Science*, Vol. 322, No.238, 238-242
- Raibert, M. et al. (2008). BigDog, the Rough-Terrain Quadruped Robot. *Proceedings of Proceedings of the 17th World Congress the International Federation of Automatic Control*, pp.10822-10825, 978-3-902661-00-5, Seoul, 2008,
- Raibert, M. H. (1986). *Legged robots that balance*. MIT Press, Cambridge MA
- Robert, G. et al. (2003). Small is beautiful: an army of small robots. *Scientific American*, Vol. 289, No.5, 63-66
- Santos, D. et al. (2007). Directional adhesion for climbing: theoretical and practical considerations. *Journal of Adhesion Science and Technology*, Vol. 21, No.12, 1317-1341
- Siegwart, R. & Nourbakhsh, I. R. (2004). *Introduction to Autonomous Mobile Robots*. The MIT press, 0-262-19502-X, Massachusetts
- Todd, D. J. (1985). *Walking Machines: an Introduction to Legged Robots*. Kogan Page Ltd, 0-85038-932-1, London
- Wang, W. et al. (2008). A stereotaxic method and apparatus for the Gekko gecko. *Chinese Science Bulletin*, Vol. 53, No.7, 1107-1112
- Winters, J. M. & Crago, P. E. (2000). *Biomechanics and neural control of posture and movement*. Springer, New York
- Zaaf, A. et al. (2001). Spatio-temporal gait characteristics of level and vertical locomotion in a ground-dwelling and a climbing gecko. *The Journal of Experimental Biology*, Vol. 204, 1233-1246
- Zaaf, A. et al. (1999). Morphology and morphometrics of the appendicular musculature in geckoes with different locomotor habits (Lepidosauria). *Zoomorphology*, Vol. 119, 9-22

Biomimetic Fabrication of Hydroxyapatite Microcapsules by using Apatite Nuclei

Takeshi Yao and Takeshi Yabutsuka
Kyoto University (Japan)

1. Introduction

1.1 Hydroxyapatite

Living bone consists of 69 wt % of inorganic substances whose main component is hydroxyapatite ($\text{Ca}_{10}(\text{PO}_4)_6(\text{OH})_2$), 22 wt% of organic substances whose main component is collagen and 9 wt% of water (Park & Lakes, 1992; Bhat, 2005). It has a skillful woven structure constructed with collagen fiber on which hydroxyapatite nano-crystals are precipitated. Hydroxyapatite is a main inorganic component of living bone and has attracted much attention as a biomaterial with high bioaffinity. It has high affinity to living bone (Jarcho et al., 1977; LeGeros & LeGeros, 1993; LeGeros & LeGeros, 2008; Oonishi et al., 2008) and cells (Deligianni et al., 2001; Rizzi et al., 2001) and an ability to absorb biopolymer such as protein (Tiselius et al., 1956). From these properties, hydroxyapatite is considered as one of the most important biomaterials.

1.2 Bioactivity

Generally, most of artificial materials implanted into living body are encapsulated with non-calcified fibrous tissue and isolated from surrounding tissue (Park & Lakes, 1992). This reaction is a normal protective reaction of living body against foreign substances.

In early 1970s, Hench et al. discovered that glass in the system $\text{Na}_2\text{O}-\text{CaO}-\text{SiO}_2-\text{P}_2\text{O}_5$, called Bioglass[®], spontaneously bonds to living bone without encapsulated with fibrous tissues (Hench et al., 1971; Hench, 1991; Hench & Andersson, 1993). Since the discovery of Bioglass[®], ceramic materials such as glass-ceramic Ceravital[®] containing crystalline hydroxyapatite (Gross et al., 1993), sintered hydroxyapatite (Jarcho et al., 1977; LeGeros & LeGeros, 1993), glass-ceramics Cerabone[®] A-W containing crystalline hydroxyapatite and wollastonite ($\text{CaO}-\text{SiO}_2$) (Kokubo et al., 1982; Kokubo, 1990a; Kokubo, 1993a; Kokubo, 2008), glass-ceramic Bioverit[®] containing crystalline hydroxyapatite and phlogopite ($(\text{Na},\text{K})\text{Mg}_3(\text{AlSiO}_{10})\text{F}_2$) (Höland & Vogel, 1993) and sintered β -tricalcium phosphate ($3\text{CaO}-\text{P}_2\text{O}_5$) (Rejda et al., 1977) have been found to bond to living bone.

Most of the ceramics mentioned above forms hydroxyapatite layer on their surface and can avoid the protective reaction in living body (Hench, 1991; Höland et al., 1985; Kitsugi et al., 1987; Kitsugi et al., 1989; Kokubo, 1990d; Ohura et al., 1991; Ohtsuki et al., 1991; Neo et al., 1992; Neo et al., 1993). This hydroxyapatite layer consists of minute crystals containing carbonate ions in chemical composition (Kokubo et al., 1990b) and is similar to

hydroxyapatite which composes living bone (Kim et al., 1999; Kim et al., 2000). On the hydroxyapatite layer, osteoblast actively proliferates and differentiates (Neo et al., 1992; Loty et al., 2000). As a result, a living bone is formed on the hydroxyapatite layer and the materials spontaneously bond to the surrounding living bone thorough the layer. This special property of the materials is termed bioactivity among researchers of ceramic-based biomaterials.

1.3 Simulated body fluid

Kokubo et al. invented a simulated body fluid (SBF) with ion concentrations nearly equal to those of human blood plasma (Kokubo et al., 1990c; Kokubo & Takadama, 2006; Takadama & Kokubo, 2008). It became possible to imitate the reaction of hydroxyapatite formation in living body by using SBF. Kokubo, Yao and Tanahashi applied the biomimetic reaction in SBF and formed hydroxyapatite thin film on the surface of various kinds of substrates (Tanahashi et al., 1992; Kokubo et al., 1993b; Tanahashi et al., 1994a; Tanahashi et al., 1994b, Tanahashi et al., 1994c; Tanahashi et al., 1995a; Tanahashi et al., 1995b).

1.4 Apatite Nuclei

When the pH or temperature of SBF is raised, fine particles of calcium phosphate are precipitated from the fluid. Yao discovered that the fine particles show high activity for forming hydroxyapatite in SBF and he named the particles Apatite Nuclei (Yao et al., 2006). The function of Apatite Nuclei is very attractive for development of various kinds of biomaterials and environmental materials in micron or nano scale.

Applying the function of Apatite Nuclei, the authors fabricated bioactive polyethylene (PE)-Apatite Nuclei composite (Yabutsuka et al., 2007) and titanium (Ti)-Apatite Nuclei composite (Yabutsuka et al., 2008a). They soaked porous PE or Ti plate formed many micropores by sulfuric acid treatment in SBF and precipitated Apatite Nuclei in the pores by raising pH or temperature of SBF. By soaking in SBF, Apatite Nuclei precipitated in the pores induce hydroxyapatite and the composites show high bioactivity. Also, formed hydroxyapatite showed high adhesive strength to the composite by a mechanical interlocking effect.

The authors also fabricated hydroxyapatite micropattern by using Apatite Nuclei (Yao, 2000; Yamaguchi et al., 2007). Resist pattern was developed on a cathode for electrophoretic deposition and a polytetrafluoroethylene (PTFE) film was set on the cathode. Then electrophoretic deposition was performed with a suspension of Apatite Nuclei in ethanol. In this process, Apatite Nuclei were deposited on a porous PTFE film so as to transcribe the resist pattern. The substrate was soaked in SBF and hydroxyapatite was selectively induced on Apatite Nuclei. As a result, apatite pattern whose resolution was as high as the resist pattern was fabricated.

1.5 Fabrication of hydroxyapatite microcapsule by biomimetic method

In living body, hydroxyapatite is not recognized as a foreign material and can avoid protective reaction of living body because hydroxyapatite induces bonelike hydroxyapatite from body fluid and forms its layer in living body. Therefore, microcapsules possessing high bioaffinity can be formed by using hydroxyapatite and the hydroxyapatite microcapsules are thought to be useful to drug delivery systems.

Yao et al. proposed that hydroxyapatite microcapsules can be fabricated by using biomimetic method (Adachi, Takeuchi, Ozawa & Yao, 2002). For the first process, Apatite Nuclei are attached to the surfaces of microspheres. For the second process, the microspheres are soaked in SBF. By this treatment, hydroxyapatite is induced from the Apatite Nuclei and grows over the whole surface area of the microspheres. As a result, hydroxyapatite is coated on the whole surface of the microspheres and hydroxyapatite microcapsules can be obtained. By this method, it is expected to encapsulate various kinds of microspheres with hydroxyapatite.

2. Fabrication of hollow hydroxyapatite microcapsule

Hollow microcapsule is expected to have many applications to the chemotherapy because it can be filled with various medical agents. In this chapter, we fabricated hollow hydroxyapatite microcapsules by using biomimetic method (Tabe et al., 2007). First, Apatite Nuclei were attached to the surfaces of polylactic acid (PLA) microspheres used as molds of hollow microcapsules. When these PLA microspheres were soaked in SBF, hydroxyapatite was induced from Apatite Nuclei on the PLA microspheres and covered the whole surface of the PLA microspheres. As a result, encapsulated PLA microspheres with hydroxyapatite were fabricated. Finally, the PLA was dissolved out in acetone and hollow hydroxyapatite microcapsules were fabricated.

2.1 Materials & Methods

2.1.1 Preparation of SBF

SBF was prepared by dissolving reagent-grade NaCl, NaHCO₃, KCl, K₂HPO₄·3H₂O, MgCl₂·6H₂O, CaCl₂ and Na₂SO₄ in ultrapure water with the composition as shown in Table 1 and buffered at pH 7.40 with tris(hydroxymethyl)aminomethane ((CH₂OH)₃CNH₂) and hydrochloric acid at 36.5 °C (Kokubo & Takadama, 2006).

	Ion concentration / mmol·dm ⁻³	
	SBF	Blood plasma
Na ⁺	142.0	142.0
K ⁺	5.0	5.0
Ca ²⁺	2.5	2.5
Mg ²⁺	1.5	1.5
Cl ⁻	147.8	103.0
HCO ₃ ⁻	4.2	27.0
HPO ₄ ²⁻	1.0	1.0
SO ₄ ²⁻	0.5	0.5

Table 1. Ion concentrations of simulated body fluid (SBF) and human blood plasma.

2.1.2 Precipitation of Apatite Nuclei

The pH of SBF was raised to pH 8.50 by dissolving (CH₂OH)₃CNH₂ at 25.0 °C, and precipitated Apatite Nuclei in the SBF, which were collected by filtration using a 50 nm polytetrafluoroethylene (PTFE) membrane filter (Millipore, USA) and washed with distilled

water, were dispersed in 200 ml of ethanol with ultrasonic vibration, and Apatite Nuclei-dispersed ethanol was obtained.

2.1.3 Fabrication of encapsulated PLA microspheres with hydroxyapatite

The ethanol contained in the Apatite Nuclei-dispersed ethanol was replaced with ultrapure water by an evaporator for the purpose of prevention of elution of PLA microsphere. By this treatment, Apatite Nuclei-dispersed water was obtained. 0.2 mg of commercially obtained PLA microspheres with 2 μm of average diameter (Corefront, Japan) were soaked in the Apatite Nuclei-dispersed water mentioned above and held for 1 d. The PLA microspheres were collected by filtration using a 100 nm PTFE membrane filter. These PLA microspheres were soaked in SBF at pH 7.40 at 36.5 °C for 7 d. After that, the PLA microspheres were collected by filtration, washed with ultrapure water, and dried at 36.5 °C. The surfaces of the PLA microspheres were analyzed by scanning electron microscopy (SEM: ESEM-2700, Nikon, Japan) and energy dispersive X-ray analysis (EDX: DX-4, EDAX International, USA). For the reference, the PLA microspheres not soaked in Apatite Nuclei suspension were also soaked in 1.0 SBF. The surfaces of these PLA microspheres were also analyzed by SEM and EDX.

2.1.3 Fabrication of hollow hydroxyapatite microcapsules

The encapsulated PLA microspheres with hydroxyapatite were soaked in acetone for 1 d. The samples thus obtained were analyzed by SEM. For the reference, not-treated PLA microspheres were also analyzed by SEM and EDX.

2.2 Results & Discussion

2.2.1 Observation of the encapsulated PLA microspheres

Fig. 1 shows (a) SEM micrograph and (b) the result of EDX analysis of not-treated PLA microsphere after the soak in SBF for 7 d. In Fig. 1(a), it was observed that the not-treated PLA microsphere have smooth surface, maybe due to the production process, and no evidence of hydroxyapatite were detected. In Fig. 1(b), no peaks of P and Ca were detected. Fig. 2 shows (a) SEM micrograph and (b) the result of EDX analysis of PLA microspheres soaked in the Apatite Nuclei-dispersed water for 1 d, and then soaked in SBF for 7 d. In Fig. 2(a), it was observed that needle like crystals characteristic to hydroxyapatite coated whole surface of the PLA microsphere. In Fig. 2(b), peaks of P and Ca, constituents of hydroxyapatite, were detected on the surface. These results indicate that hydroxyapatite was induced from the Apatite Nuclei attached to the surface of the PLA microsphere and spread over whole surface area of the PLA microsphere in SBF.

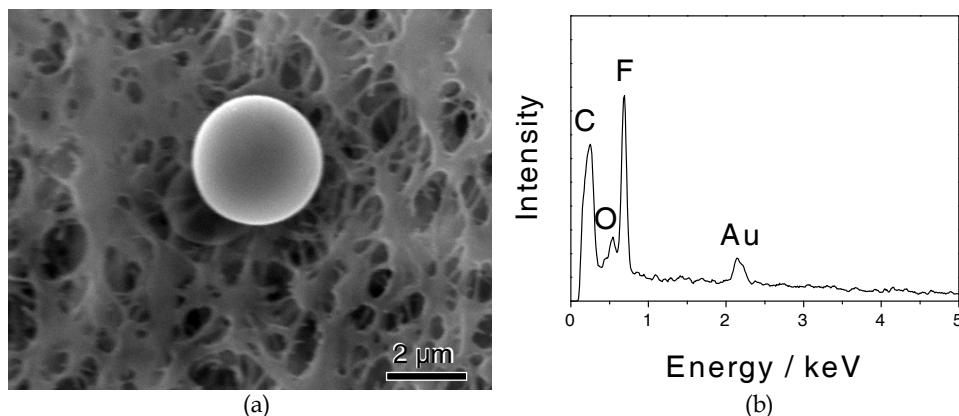


Fig. 1. (a) SEM micrograph and (b) the result of EDX analysis of the not-treated PLA microsphere after the soak in SBF for 7 d.

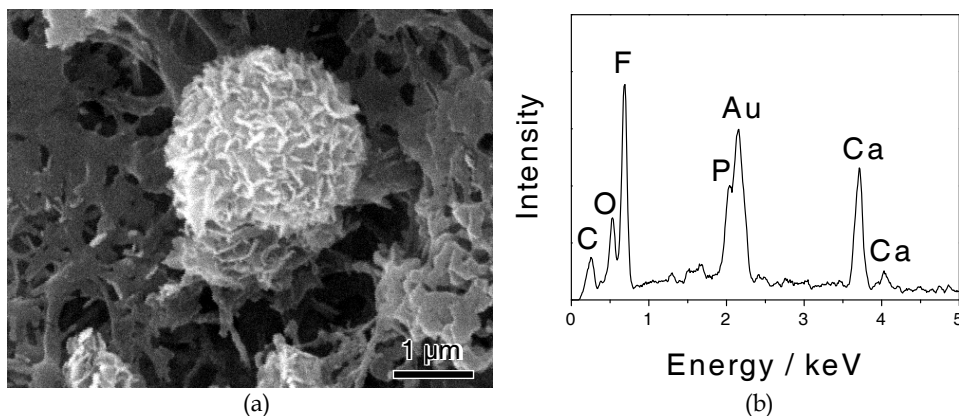


Fig. 2. (a) SEM micrograph and (b) the result of EDX analysis of PLA microsphere soaked in the Apatite Nuclei-dispersed ethanol for 1 d, and then soaked in SBF for 7 d.

2.2.2 Observation of hollow hydroxyapatite microcapsules

Fig. 3(a) and (b) show SEM micrographs of the above mentioned encapsulated PLA microspheres with hydroxyapatite after the soak in acetone for 1 d. By the soak in acetone, the PLA microsphere was dissolved out and a spherical hollow hydroxyapatite microcapsule was obtained. In Fig. 3(a), the spherical microcapsule constructed with hydroxyapatite was observed. In Fig. 3(b), a broken spherical microcapsule of hydroxyapatite was also observed. Fig. 3(b) is shown that PLA microspheres were completely dissolved by acetone and this result confirmed that the microsphere shown in Fig. 3(a) have a hollow structure. Consequently, the microcapsule constructed of hydroxyapatite was fabricated.

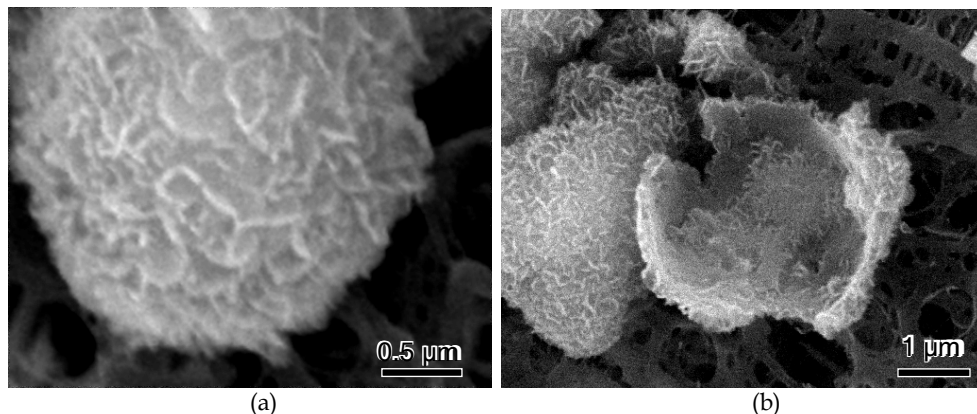


Fig. 3. SEM micrographs of encapsulated PLA microspheres with hydroxyapatite after the soak in acetone for 1 d.

3. Fabrication of encapsulated Ag microsphere with hydroxyapatite

It has been established that Ag ion has the antimicrobial activity (Russell & Hugo, 1994). If Ag ion is sustainably released at an affected part, more effective cure is expected. In this chapter, the authors fabricated encapsulated Ag microspheres with hydroxyapatite by using biomimetic method (Yabustuka et al., 2008b). First, Apatite Nuclei were attached to the surfaces of Ag microspheres. When these Ag microspheres were soaked in SBF, hydroxyapatite was induced from Apatite Nuclei on the Ag microspheres and covered the whole surface of the Ag microspheres. As a result, encapsulated Ag microspheres with hydroxyapatite were fabricated. In order to evaluate sustained-release of Ag ion, the amount of Ag ion release in saline was measured.

3.1 Materials & Methods

3.1.1 Fabrication of encapsulated Ag microspheres with hydroxyapatite

SBF was prepared by the method shown in 2.1.1. Apatite Nuclei-dispersed ethanol was prepared by the method shown in 2.1.2. 2 mg of commercially obtained Ag microspheres with 1.71 μm of average diameter (Daiken Chemical, Japan) were soaked in the Apatite Nuclei-dispersed ethanol mentioned in 2.1.2 and held for 1 d. The Ag microspheres were collected by filtration using a 100 nm PTFE membrane filter. These Ag microspheres were soaked in SBF at pH 7.40 at 36.5 °C for 7 d. After that, the Ag microspheres were collected by filtration, washed with ultrapure water, and dried at 36.5 °C. The surfaces of the Ag microspheres were analyzed by thin film X-ray diffraction (TF-XRD: Rint 2500, Rigaku, Japan), SEM and EDX. For the reference, not-treated Ag microspheres were also analyzed by TF-XRD, SEM and EDX.

3.1.2 Evaluation of sustained-release for hydroxyapatite microcapsules

2 mg of the encapsulated Ag microspheres with hydroxyapatite were soaked in 100 cm³ saline (0.01 mol·dm⁻³ phosphate buffered saline, pH at 25 °C: 7.2-7.4, Wako Pure Chemical

Industries, Japan). The saline was continued to shake by using shaking apparatus for up to 192 h in an incubator held at 36.5 °C. Changes in Ag ion concentration in saline were measured by inductively coupled plasma atomic emission spectroscopy (ICP: ICPS-7500, Shimadzu, Japan). For the reference, not-treated Ag microspheres were also dispersed in saline and conducted the same measurement.

3.2 Results & Discussion

3.2.1 TF-XRD measurement

Fig.4 shows (a) TF-XRD profile of the not-treated Ag microspheres and (b) that of the Ag microspheres soaked in the Apatite Nuclei-dispersed ethanol for 1 d, and then soaked in SBF for 7 d. After the soak in SBF for 7 d, diffraction peaks of hydroxyapatite were detected. This result indicates that hydroxyapatite was induced from the Apatite Nuclei attached to the surfaces of Ag microspheres.

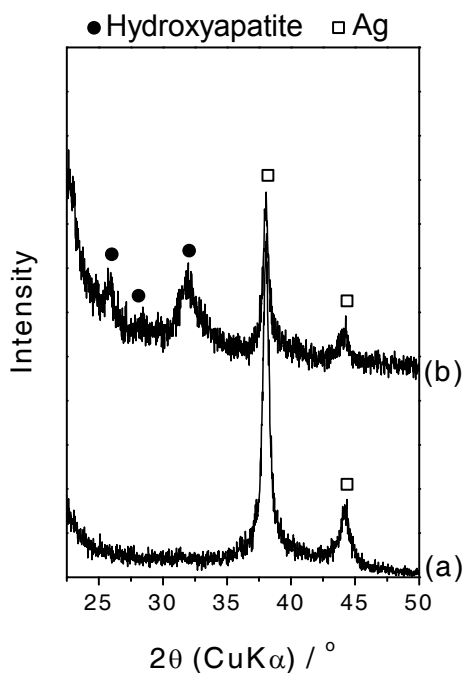


Fig. 4. TF-XRD profiles of the surface of (a) not-treated Ag microspheres and (b) Ag microspheres soaked in the Apatite Nuclei-dispersed ethanol for 1 d, and then soaked in SBF for 7 d.

3.2.2 Observation by SEM and EDX

Fig. 5 shows (a) SEM micrograph and (b) the result of EDX analysis of not-treated Ag microsphere. In Fig. 5(a), it was observed that the not-treated Ag microsphere have

characteristic wrinkle surface, maybe due to the production process. In Fig. 5(b), no peak other than Ag, except C due to a carbon tape, was detected.

Fig.6 shows SEM micrograph of the Ag microspheres soaked in the Apatite Nuclei-dispersed ethanol for 1 d, and then soaked in SBF for 7 d of low magnification. In Fig. 6, many encapsulated Ag microspheres with hydroxyapatite were observed. This result indicates that this method has high reproducibility.

Fig. 7 shows (a) picture of a microcapsule by magnification and (b) the result of EDX analysis of the Ag microspheres soaked in the Apatite Nuclei-dispersed ethanol for 1 d, and then soaked in SBF for 7 d. In Fig. 7(a), it was observed that needle like crystals characteristic to hydroxyapatite coated whole surface of the Ag microsphere. In Fig. 7(b), peaks of P and Ca, constituents of hydroxyapatite, were detected on the surface. These results indicate that hydroxyapatite was induced from the Apatite Nuclei attached to the surface of the Ag microsphere and spread over whole surface area of the Ag microsphere in SBF.

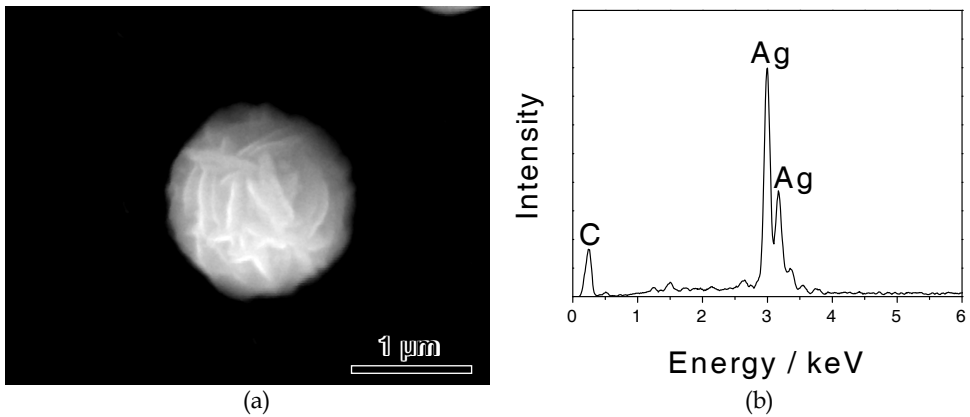


Fig. 5. (a) SEM micrograph and (b) the result of EDX analysis of the not-treated Ag microsphere.

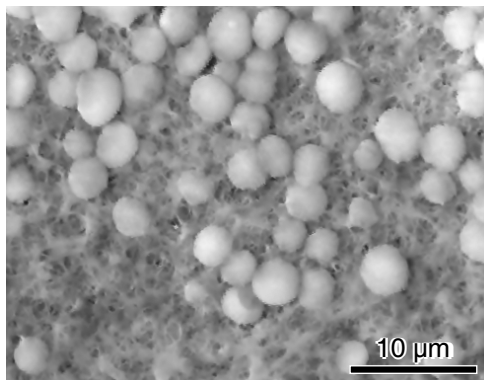


Fig. 6. SEM micrograph of Ag microspheres soaked in the Apatite Nuclei-dispersed ethanol for 1 d, and then soaked in SBF for 7 d of low magnification.

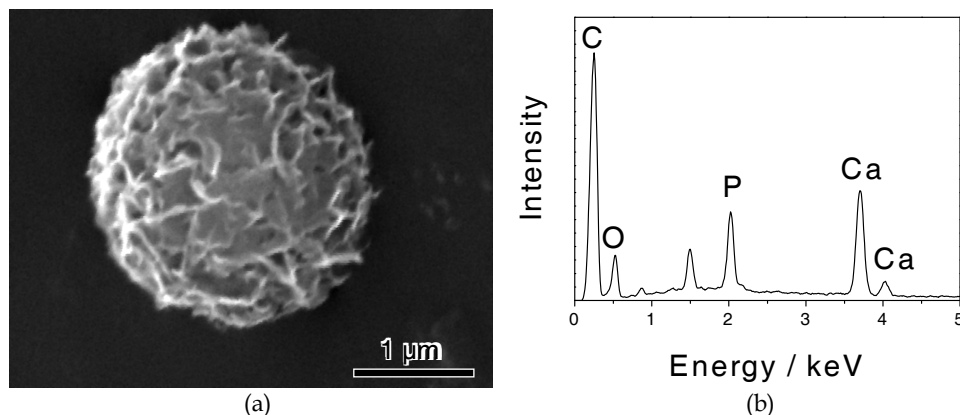


Fig. 7. (a) SEM micrograph and (b) the result of EDX analysis of Ag microsphere soaked in the Apatite Nuclei-dispersed ethanol for 1 d, and then soaked in SBF for 7 d.

4.2.3 Amount of Ag ion release

Fig.8 shows (a) the amount of Ag ion release for the not-treated Ag microspheres and (b) that for the above mentioned encapsulated Ag microspheres with hydroxyapatite in saline up to 192 h at 36.5 °C. The concentration of Ag ion for the encapsulated Ag microspheres with hydroxyapatite was approximately one over ten of that for not-treated ones. This result indicates that sustained-release of Ag ion is achieved by encapsulating Ag microsphere with hydroxyapatite.

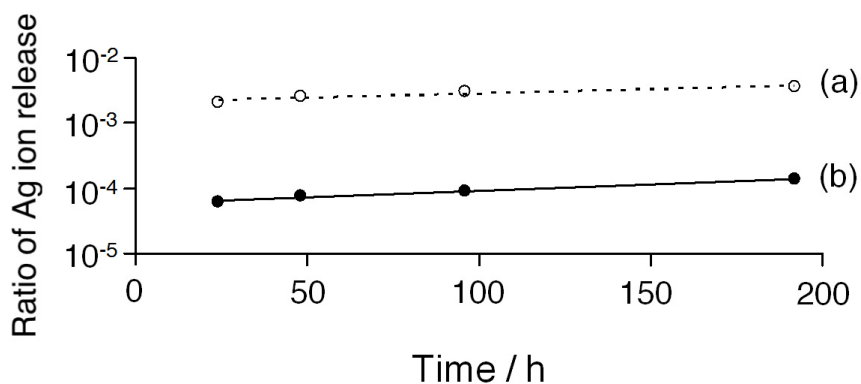


Fig. 8. Amount of Ag ion release for (a) not-treated Ag microspheres and (b) encapsulated Ag microspheres with hydroxyapatite in saline up to 192 h at 36.5 °C.

4. Fabrication of encapsulated silicagel microsphere with hydroxyapatite

Silicagel has porous structure. If medical agents are absorbed in silicagel microspheres and the silicagel microspheres are coated with hydroxyapatite, the encapsulated silicagel microspheres with hydroxyapatite are expected as carriers of drug delivery system. When

porous material is soaked in SBF and the pH is raised, Apatite Nuclei precipitated in the pores. Thus treated porous material has high bioactivity because precipitated Apatite Nuclei in the pores induce hydroxyapatite (Yao et al., 2007). In this chapter, the authors fabricated encapsulated silicagel microspheres with hydroxyapatite by using biomimetic method (Yamane et al., 2009). First, Apatite Nuclei were precipitated in the pores of silicagel microspheres. When these silicagel microspheres were soaked in SBF, hydroxyapatite was induced from Apatite Nuclei in the pores of the silicagel microspheres and covered the whole surface of the microspheres. As a result, encapsulated silicagel microspheres with hydroxyapatite were fabricated.

4.1 Materials & Methods

SBF was prepared by the method shown in 2.1.1. Silicagel microspheres (4.4 μm of average diameter, 6 nm of average pore diameter, Fuji Silysia Chemical, Japan) were soaked in SBF. The pH of SBF was raised to pH 8.60 by using $(\text{CH}_2\text{OH})_3\text{CNH}_2$ at 25.0 $^\circ\text{C}$. By this treatment, Apatite Nuclei were precipitated in the pores of the silicagel microspheres. The silicagel microspheres were collected by filtration using a 0.1 μm PTFE membrane filter (Millipore, USA), washed with ultrapure water and soaked in SBF at pH 7.40 at 36.5 $^\circ\text{C}$ for 7 d. The SBF was renewed every 4 d. After that, the silicagel microspheres were collected by filtration, washed with ultrapure water, and dried at 36.5 $^\circ\text{C}$. The surface of the silicagel microspheres were analyzed by TF-XRD, SEM and EDX.

4.2 Results and Discussion

4.2.1 TF-XRD measurement

Fig. 9 shows TF-XRD profiles of the not-treated silicagel microspheres and silicagel microspheres Apatite Nuclei precipitated then soaked in SBF for 7 d. After the soak for 7 d, diffraction peaks of hydroxyapatite were detected. This result indicates that hydroxyapatite was induced from Apatite Nuclei precipitated in the pores of silicagel microspheres.

4.2.2 Observation by SEM and EDX

Fig. 10(a) and (b) show SEM micrographs and (c) shows the result of EDX analysis of not-treated silicagel microspheres. Fig. 10(b) is higher magnification. In Fig. 10(c), peaks of Si, constituent of silicagel was detected by the EDX analysis.

Fig. 11(a) and (b) show the SEM micrographs and (c) shows the result of EDX analysis of silicagel microspheres Apatite Nuclei precipitated and soaked in SBF for 7 d. In Fig. 11(a), many encapsulated silicagel microspheres with hydroxyapatite were observed. This indicates that this method has high reproducibility. In Fig. 11(b), higher magnification, it was observed that needle like crystals characteristic to hydroxyapatite coated whole surface of the silicagel microsphere. In Fig. 11(c), peaks of P and Ca, constituents of hydroxyapatite, were detected on the surface.

From these results, it is considered that hydroxyapatite was induced from the Apatite Nuclei precipitated in the pores of the silicagel microspheres and spread over whole surface area of the silicagel microspheres in SBF.

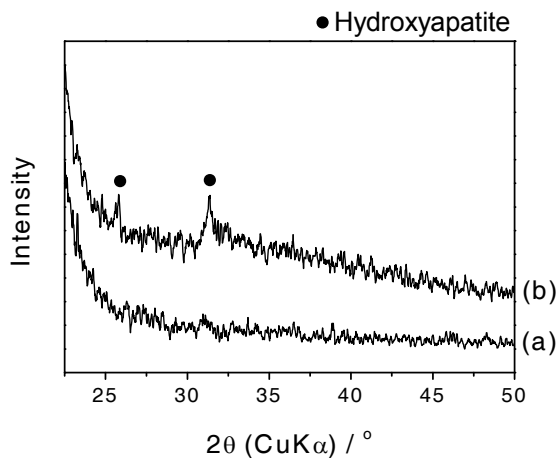


Fig. 9. TF-XRD profiles of the (a) not-treated silicagel microspheres and (b) silicagel microspheres Apatite Nuclei precipitated then soaked in SBF for 7 d.

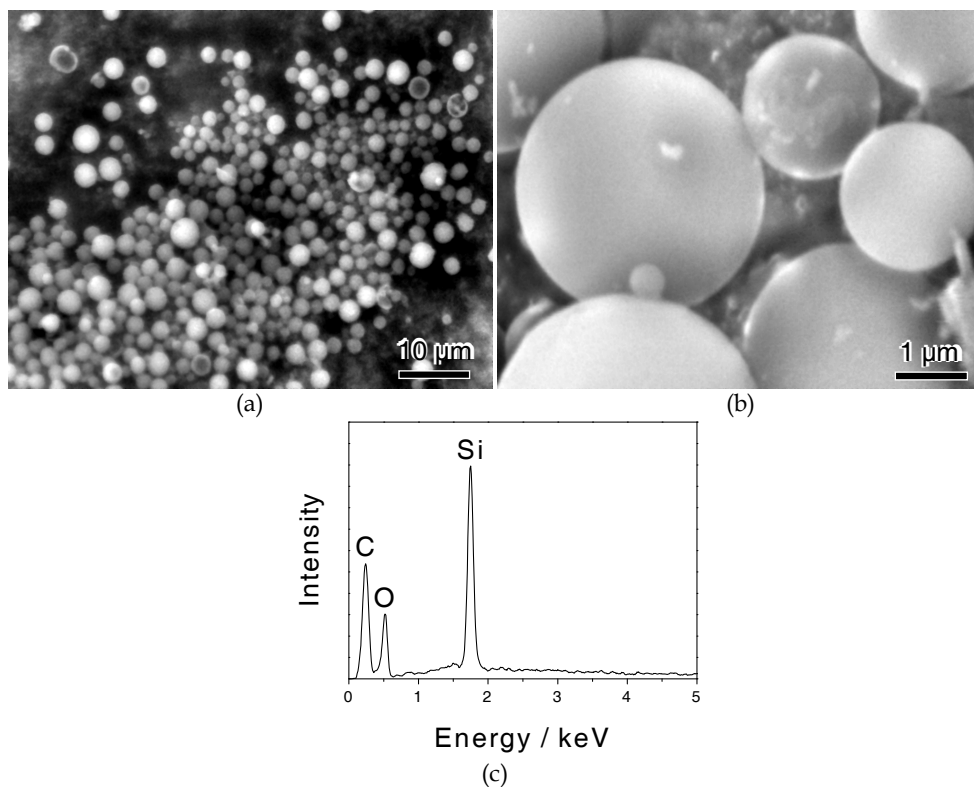


Fig. 10. SEM micrographs of (a) not-treated silicagel microspheres, (b) higher magnification of (a), and (c) result of EDX of (b).

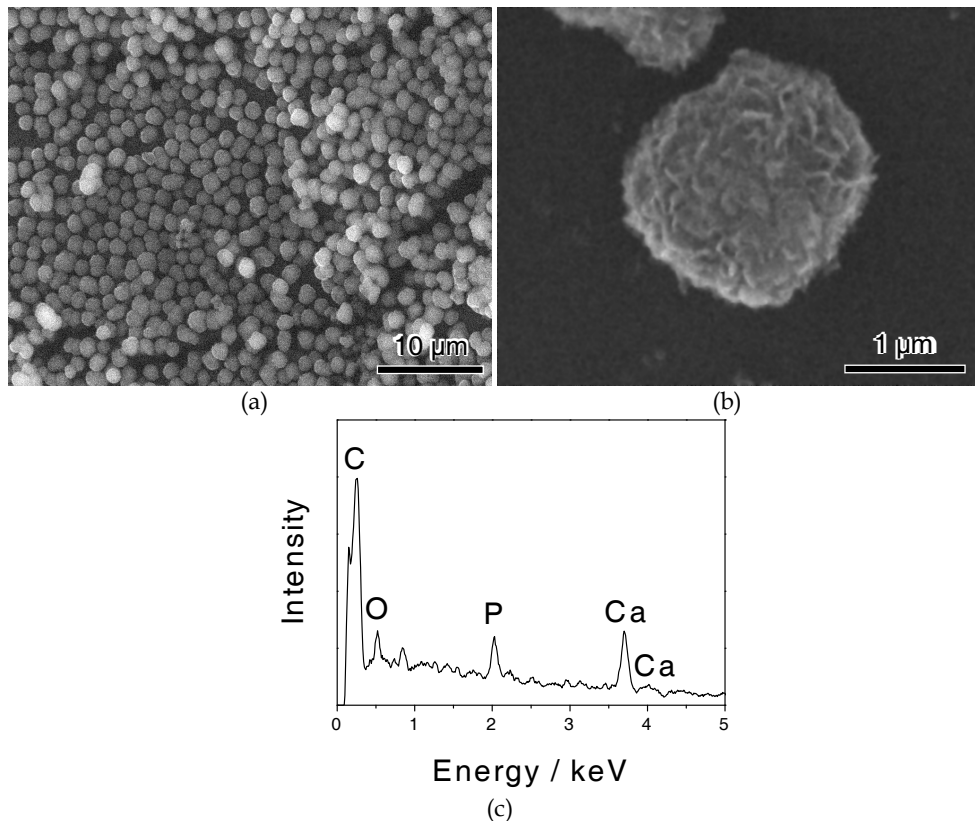


Fig. 11. SEM micrographs of (a) silicagel microspheres Apatite Nuclei precipitated and soaked in SBF for 7 d, (b) higher magnification, and (c) result of EDX of (b).

5. Conclusion

When the pH or the temperature of SBF is raised, fine particles of calcium phosphate are precipitated in the fluid. It was found that these particles are very active for forming hydroxyapatite from SBF and these particles were named Apatite Nuclei. By the discovery of Apatite Nuclei, it became possible to develop various multifunctional biomaterials possessing high bioaffinity in micron or nano scale by using biomimetic method.

The authors have successfully encapsulated Ag, PLA and silicagel microspheres with hydroxyapatite by biomimetic method. For encapsulated Ag and PLA microspheres, Apatite Nuclei were synthesized by raising pH of SBF. Hydroxyapatite was formed from Apatite Nuclei attached on the microspheres by soaking in SBF, and then the encapsulated Ag and PLA microspheres with hydroxyapatite were obtained. For encapsulated silicagel microspheres, silicagel microspheres were soaked in SBF and precipitated Apatite Nuclei in the pores of the microspheres by raising pH of SBF. Hydroxyapatite was formed from Apatite Nuclei precipitated in the pores of the microspheres by soaking in SBF, and then the encapsulated silicagel microspheres with hydroxyapatite were obtained. For the

encapsulated Ag microspheres with hydroxyapatite, sustained-release of Ag ion was achieved. Hollow hydroxyapatite microcapsules were obtained by soaking the encapsulated PLA microsphere with hydroxyapatite in acetone. These hydroxyapatite microcapsules mentioned above possessed high bioaffinity. This method is promising for fabrication of carriers for drug delivery systems.

6. References

- Adachi, M.; Takeuchi, I.; Ozawa, N. & Yao, T. (2002). Calcium phosphate capsule and method for fabrication thereof. *Japan Patent*, 2002-277662
- Bhat, S. V. (2005). *Biomaterials 2nd ed.*, Alpha Science, ISBN 1-84265-207-9, Harrow
- Deligianni, D. D.; Katsala, N. D.; Koutsoukos, P. G. & Missirlis, Y. F. (2001). Effect of surface roughness of hydroxyapatite on human bone marrow cell adhesion, proliferation, differentiation and detachment strength. *Biomaterials*, 22, 1, (Jan 2001) 87-96, ISSN 0142-9612
- Gross, U. M.; Müller-Mai, C. & Voigt, C. (1993). Ceravital® bioactive ceramics, In: *An Introduction to Bioceramics*, Hench, L. L. & Wilson, J., (Ed.), 105-124, World Scientific, ISBN 981-02-1400-6, Singapore
- Hench, L. L.; Splinter, R. J.; Allen, W. C. & Greenlee, T. K. (1971). Bonding mechanisms at the interface of ceramic prosthetic materials. *J. Biomed. Mater. Res.*, 5, 6, (Nov 1971) 117-141, ISSN 0021-9304
- Hench, L. L. (1991). Bioceramics: from concept to clinic. *J. Am. Ceram. Soc.*, 74, 7, (Jul 1991) 1487-1510, ISSN 0002-7820
- Hench, L. L. & Andersson, Ö. (1993). Bioactive glasses, In: *An Introduction to Bioceramics*, Hench, L. L. & Wilson, J., (Ed.), 42-62, World Scientific, ISBN 981-02-1400-6, Singapore
- Höland, W.; Vogel, W.; Nauman, K. & Gummel, J. (1985) Interface reactions between machinable bioactive glass-ceramics and bone. *J. Biomed. Mater. Res.*, 19, 3, (Mar 1985) 303-312, ISSN 0021-9304
- Höland, W. & Vogel, W. (1993). Machineable and phosphate glass-ceramics, In: *An Introduction to Bioceramics*, Hench, L. L. & Wilson, J., (Ed.), 125-137, World Scientific, ISBN 981-02-1400-6, Singapore
- Jarcho, M. J.; Kay, J. L.; Gumaer R. H. & Drobeck, H. P. (1977). Tissue, cellular and subcellular events at bone-ceramic hydroxyapatite interface. *J. Bioeng.*, 1, 2, (Jan 1977) 79-92, ISSN 0145-3068
- Kim, H. M.; Kishimoto, K.; Miyaji, F.; Kokubo, T.; Yao, T.; Suetsugu, Y., Tanaka, J. & Nakamura, T. (1999). Composition and structure of the apatite formed on PET substrates in SBF modified with various ionic activity products. *J. Biomed. Mater. Res.*, 46, 2, (Aug 1999) 228-235, ISSN 0021-9304
- Kim, H. M.; Kishimoto, K.; Miyaji, F.; Kokubo, T.; Yao, T.; Suetsugu, Y.; Tanaka, J. & Nakamura, T. (2000). Composition and structure of apatite formed on organic polymer in simulated body fluid with a high content of carbonate ion. *J. Mater. Sci.: Mater. Med.*, 11, 7, (Jul 2000) 421-426, ISSN 0957-4530

- Kitsugi, T.; Nakamura, T.; Yamamuro, T.; Kokubo, T.; Shibuya, T. & Takagi, M. (1987). SEM-EPMA observation of three types of apatite-containing glass-ceramics: the variance of a Ca-P-rich layer. *J. Biomed. Mater. Res.*, 21, 10, (Oct 1987) 1255-1271, ISSN 0021-9304
- Kitsugi, T.; Yamamuro, T.; Nakamura, T. & Kokubo, T. (1989) Bone-bonding behavior of MgO-CaO-SiO₂-P₂O₅-CaF₂ glass (mother glass of A/W-glass ceramics). *J. Biomed. Mater. Res.*, 23, 6, (Jun 1989) 631-648, ISSN 0021-9304
- Kokubo, T.; Shigematsu, M.; Nagashima, Y.; Tashiro, M.; Yamamuro, T. & Higashi, S. (1982). Apatite and wollastonite-containing glass-ceramics for prosthetic application. *Bull. Inst. Chem. Res., Kyoto Univ.*, 60, 3-4, (Oct 1982) 260-268, ISSN 0023-6071
- Kokubo, T. (1990a). Surface chemistry of bioactive glass-ceramics. *J. Non-Cryst. Solids*, 120, 1-3, (Apr 1990) 138-150, ISSN 0022-3093
- Kokubo, T.; Ito, S.; Huang, Z. T.; Hayashi, T.; Sakka, S.; Kitsugi, T. & Yamamuro, T. (1990b). Ca, P-rich layer formed on high-strength bioactive glass-ceramic A-W. *J. Biomed. Mater. Res.*, 24, 3, (Mar 1990) 331-343, ISSN 0021-9304
- Kokubo, T.; Kushitani, H.; Sakka, S.; Kitsugi, T. & Yamanuro, T. (1990c). Solutions able to reproduce in vivo surface-structure changes in bioactive glass-ceramic A-W. *J. Biomed. Mater. Res.*, 24, 6, (Jun 1990) 721-734, ISSN 0021-9304
- Kokubo, T. (1990d). Bonding mechanism of bioactive glass-ceramics A-W to living bone, In: *Handbook of Bioactive Ceramics, Vol. 1: Bioactive Glasses and Glass-Ceramics*, Yamamuro, T.; Hench, L. L. & Wilson, J., (Ed.), 41-49, CRC Press, ISBN 0-8493-3241-9, Boca Raton
- Kokubo, T. (1993a). A/W glass ceramics: processing and properties, In: *An Introduction to Bioceramics*, Hench, L. L. & Wilson, J., (Ed.), 75-88, World Scientific, ISBN 981-02-1400-6, Singapore
- Kokubo, T.; Yao, T.; Ogawa, M. & Shibutani, T. (1993b). Method for hydroxyapatite coating. *Japan Patent*, 1993-100380
- Kokubo, T. & Takadama, H. (2006). How useful is SBF in predicting in vivo bone bioactivity?. *Biomaterials*, 27, 15, (May 2006) 2907-2915, ISSN 0142-9612
- Kokubo, T. (2008). Bioactive glass-ceramics, In: *Bioceramics and their clinical applications*, Kokubo, T., (Ed.), 284-301, Woodhead Publishing, ISBN 1-84569-204-7, Cambridge
- LeGeros, R. Z. & LeGeros, J. P. (1993). Dense Hydroxyapatite, In: *An Introduction to Bioceramics*, Hench, L. L. & Wilson, J., (Ed.), 139-180, World Scientific, ISBN 981-02-1400-6, Singapore
- LeGeros, R. Z.; & LeGeros, J. P. (2008). Hydroxyapatite, In: *Bioceramics and their clinical applications*, Kokubo, T., (Ed.), 367-394, Woodhead Publishing, ISBN 1-84569-204-7, Cambridge
- Loty, C.; Sautier, J. M.; Boulekbache, H.; Kokubo, T.; Kim H. M. & Forest, N. (2000). In vitro bone formation on a bone-like apatite layer prepared by a biomimetic process on a bioactive glass-ceramic. *J. Biomed. Mater. Res.*, 49, 4, (Mar 2000) 423-434, ISSN 0021-9304
- Neo, M.; Kotani, S.; Nakamura, T.; Yamamuro, T.; Ohtsuki, C.; Kokubo, T. & Bando, Y. (1992). A comparative study of ultrastructure of the interface between four kinds of surface-active ceramic and bone. *J. Biomed. Mater. Res.*, 26, 11, (Nov 1992) 1419-1432, ISSN 0021-9304

- Neo, M.; Nakamura, T.; Ohtsuki, C.; Kokubo, T. & Yamamuro, T. (1993). Apatite formation on three kinds of bioactive materials at an early stage in vivo: a comparative study by transmission electron microscopy," *J. Biomed. Mater. Res.*, 27, 8, (Aug 1993) 999-1006, ISSN 0021-9304
- Ohura, K.; Yamamuro, T.; Nakamura, T.; Kokubo, T.; Ebisawa, Y.; Kotoura, Y. & Oka, M. (1991). Bone-bonding ability of P₂O₅-free CaO-SiO₂ glasses. *J. Biomed. Mater. Res.*, 25, 3, (Mar 1991) 357-365, ISSN 0021-9304
- Ohtsuki, C.; Kushitani, H.; Kokubo, T.; Kotani, S.; & Yamamuro, T. (1991). Apatite formation on the surface of Ceravital-type glass-ceramic in the body. *J. Biomed. Mater. Res.*, 25, 11, (Nov 1991) 1363-1370, ISSN 0021-9304
- Oonishi, H.; Oonishi Jr., H.; & Kim, S. C. (2008). Clinical application of hydroxyapatite, In: *Bioceramics and their clinical applications*, Kokubo, T., (Ed.), 606-687, Woodhead Publishing, ISBN 1-84569-204-7, Cambridge
- Park, J. B. & Lakes, R. S. (1992). *Biomaterials: An Introduction, 2nd ed.*, Plenum Press, ISBN 0-306-43992-1, New York
- Rejda, B. V.; Peelen J. G. J. & Groot, K. D. (1977). Tri-calcium phosphate as a bone substitute. *J. Bioeng.*, 1, 2, (Jan 1977) 93-97, ISSN 0145-3068
- Rizzi, S. C.; Heath, D. J.; Coombes, A. G. A.; Bock, N.; Textor, M.; & Downes, S. (2001). Biodegradable polymer/hydroxyapatite composites: surface analysis and initial attachment of human osteoblasts. *J. Biomed. Mater. Res.*, 55, 4, (Jun 2001) 475-486, ISSN 0021-9304
- Russell, A. D. & Hugo, W. B. (1994). Antimicrobial activity and action of silver, *Prog. Med. Chem.*, 31, (Apr 1994) 351-370, ISSN 0079-6468
- Tabe, Y.; Hibino, M. & Yao, T. (2007). Fabrication of hydroxyapatite microcapsules by biomimetic method. *Key Eng. Mater.*, 330-332, (Feb 2007) 1029-1032, ISSN 1013-9826
- Takadama, H. & Kokubo, T. (2008). In vitro evaluation of bone bioactivity, In: *Bioceramics and their clinical applications*, Kokubo, T., (Ed.), 165-182, Woodhead Publishing, ISBN 1-84569-204-7, Cambridge
- Tanahashi, M.; Hata, K.; Kokubo, T.; Minoda, M.; Miyamoto, T.; Nakamura, T. & Yamamuro, T. (1992). Effect of substrate on apatite forming by a biomimetic process, In: *Bioceramics, Vol. 5*, Yamamuro, T.; Kokubo, T. & Nakamura, T., (Ed.), 57-64, Kobunshi Kankokai, ISBN 4-7702-0060-9, Kyoto
- Tanahashi, M; Yao, T.; Kokubo, T., Minoda, M.; Miyamoto, T.; Nakamura T. & Yamamuro, T. (1994a). Apatite formation on organic polymers by biomimetic process using Na₂O-SiO₂ glasses as nucleating-agent. *J. Ceram. Soc. Jpn.*, 102, 9, (Sep 1994) 822-829, ISSN 0914-5400
- Tanahashi, M; Yao, T.; Kokubo, T., Minoda, M.; Miyamoto, T.; Nakamura T. & Yamamuro, T. (1994b). Apatite coating on organic polymer by a biomimetic process. *J. Am. Ceram. Soc.*, 77, 11, (Nov 1994), 2805-2808, ISSN 0002-7820
- Tanahashi, M; Yao, T.; Kokubo, T., Minoda, M.; Miyamoto, T.; Nakamura T. & Yamamuro, T. (1994c). Apatite coated on organic polymers by biomimetic process: improvement in its adhesion to substrate by NaOH treatment. *J. Appl. Biomater.*, 5, 4, (Win 1994) 339-347, ISSN 1045-4861

- Tanahashi, M; Yao, T.; Kokubo, T., Minoda, M.; Miyamoto, T.; Nakamura T. & Yamamuro, T. (1995a). Apatite coated on organic polymers by biomimetic process: improvement in its adhesion to substrate by glow-discharge treatment. *J. Biomed. Mater. Res.*, 29, 3, (Mar 1995) 349-357, ISSN 0021-9304
- Tanahashi, M; Yao, T.; Kokubo, T., Minoda, M.; Miyamoto, T.; Nakamura T. & Yamamuro, T. (1995b). Apatite coated on organic polymers by biomimetic process: improvement in its adhesion to substrate by HCl treatment. *J. Mater. Sci.: Mater. Med.*, 6, 6, (Jun 1995) 319-326 ISSN 0957-4530
- Tiselius, A.; Hjerten, S. & Levin; O. (1956). Protein chromatography on calcium phosphate columns. *Arch. Biochem. Biophys.*, 65, 1, (Nov 1956) 132-155, ISSN 0003-9861
- Yabutsuka, T.; Yamaguchi, S.; Hibino, M. & Yao, T. (2007). Development of bioactive polyethylene-apatite nuclei composite. *Key Eng. Mater.*, 330-332, (Feb 2007) 467-470, ISSN 1013-9826
- Yabutsuka, T.; Hibino, M. & Yao, T. (2008a). Development of bioactive titanium-apatite nuclei composite. *Key Eng. Mater.*, 361-363, (Feb 2008) 709-712, ISSN 1013-9826
- Yabutsuka, T.; Tsuboi, S., Hibino, M. & Yao, T. (2008b). Fabrication of encapsulated Ag microsphere with hydroxyapatite for sustained-release. *Key Eng. Mater.*, 361-363, (Feb 2008) 1199-1202, ISSN 1013-9826
- Yamaguchi, S.; Yabutsuka, T.; Hibino, M. & Yao, T. (2007). Formation of apatite pattern by electrophoretic deposition of apatite nuclei. *Key Eng. Mater.*, 330-332, (Feb 2007) 3-6, ISSN 1013-9826
- Yamane, S.; Yabustuka, T.; Hibino, M. & Yao, T. (2009). Fabrication of encapsulated silicagel microsphere with hydroxyapatite for sustained-release. *Key Eng. Mater.*, 396-398, (Feb 2009) 519-522, ISSN 1013-9826
- Yao, T. (2000). Apatite structures and method for forming apatite patterns. *Japan Patent*, 2000-104926
- Yao, T.; Hibino, M.; Yamaguchi, S. & Okada, H. (2006). Method for stabilizing calcium phosphate fine particles, process for production of calcium phosphate fine particles by utilizing the method, and use thereof. *PCT Patent*, PCT/JP2006/316054
- Yao, T.; Hibino, M. & Yabutsuka, T. (2007). Method of producing bioactive complex material. *PCT Patent*, PCT/JP2007/062301

Biomimetic fabrication of apatite related biomaterials

Mohammad Hafiz Uddin^{1,4}, Takuya Matsumoto^{1,4}, Masayuki Okazaki²,
Atsushi Nakahira³ and Taiji Sohmura¹

¹ *Department of Oromaxillofacial Regeneration, Osaka University, Japan*

² *Department of Biomaterials Science, Hiroshima University, Japan*

³ *Department of Material Sciences, Osaka Prefecture University, Japan*

⁴ *These authors contributed equally to this work.*

1. Introduction

Biom mineralization is the process by which mineral crystals are deposited in an organized fashion in the matrix (either cellular or extracellular) of living organisms (Boskey, 1998). In simple terms, it can be described as the widespread and fascinating process by which living organisms produce minerals (Sigel et al., 2008; Stephen and Lowenstam, 1989). In this process, a living organism provides a chemical and physical environment that controls the nucleation and growth of a unique mineral phase. Often these materials exhibit hierarchical structural order, leading to superior physical properties not found in either their inorganic counterparts or in synthetic materials. The incorporation of inorganic compounds, such as salts, into biological structures often lends the structures hardness or rigidity. Almost 70 different mineral types are known to be formed by organisms from all the kingdoms. Examples include silicates in algae, carbonates in diatoms and invertebrates, and calcium phosphates and carbonates in vertebrates. These minerals adopt complex and genetically determined shapes, are often aligned to form arrays, and fulfill many different functions. These include the mechanical functions of exo- and endo-skeletons, temporary storage of minerals, stiffening of soft tissues, and much more. In vertebrates, especially mammals, bone and tooth are major biominerals.

Bones are living, growing tissue. During our lifetime, bone is constantly being renewed; there is localized removal of old bone (resorption) and replacement with newly formed bone. This coupled process is called bone remodeling. Biom mineralization of bone—essential for its hardness and strength—involves a well orchestrated process in which crystals of calcium phosphate are deposited on the matrix produced by bone-forming cells (Weiner et al., 1999). Because bone formation consists of components including cells, matrix, and inorganics, the process is investigated by different research fields including cellular and molecular biology, organic and inorganic chemistry, crystallography, and material science (Figure 1).

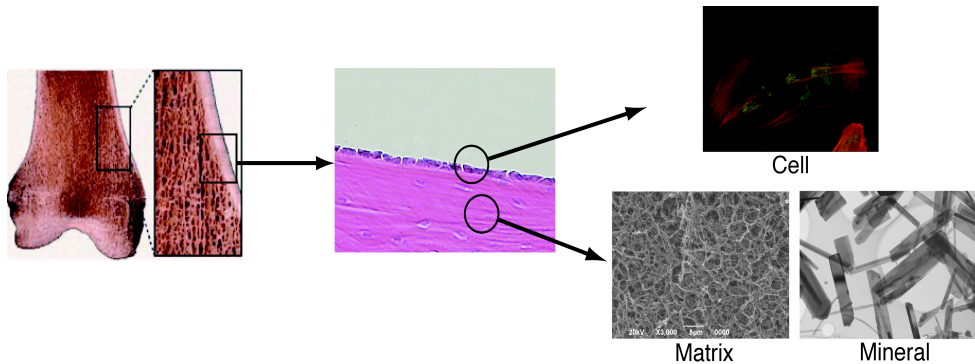


Fig. 1. Components of bone biomineralization. Bone forming cells (osteoblasts) produce extracellular matrix on which minerals are deposited.

Special attention has been paid to apatite materials because of their physicochemical properties, thermal stability, and biocompatibility that make them suitable for biomedical applications (Narasaraju et al., 1996). The usage of apatite-related biomaterials mainly focused on bone substitution or bone cements in the early years of study (Ono et al., 1990), however, the target has expanded to bone regeneration and drug delivery systems (Komleva et al., 2002). Therefore, material characteristics, including cellular and tissue compatibility, biodegradability, and drug loading capacity, should be improved. Moreover, it is desirable to create materials that can actively instruct cell fate in the area surrounding the material to enhance bone regeneration. To obtain such materials, research has focused on developing ideas based on biological mineralization systems. In this chapter, the latest research trends related to biomimetic apatite materials as well as biomimetic fabrication of apatite related biomaterials are introduced.

2. Basics of biomineralization of bones

To obtain biomimetic apatite materials or to develop biomimetic methods of fabricating them, it is crucial to understand the natural biomineralization process of bones. The biomineralization process of bone can be simply divided into three parts at the microscopic level as follows, though the process differs depending on the ossification manner (e.g. osteochondral, intramembranous), stage (e.g. development, fracture healing), region, or age.

- 1) Osteogenic differentiation of mesenchymal stem cells (MSCs).
- 2) Organization of matrix proteins secreted from osteoblasts.
- 3) Nucleation and crystal growth of apatite minerals on matrix.

2.1. Osteogenic differentiation of mesenchymal stem cells (MSCs):

As a result of the capacity for self-renewal and differentiation, bone marrow derived stromal cells were first considered as stem cells and named mesenchymal stem cells (MSCs). However, in the bone marrow, stromal cells are a rare and heterogeneous population of cells that contain a mixture of progenitors at different stages of commitment to the mesodermal lineage and only a very small number of multipotential self-renewing stem cells (Caplan,

1991). It is now accepted that most bone marrow derived progenitor stromal cells can be considered, after *in vitro* proliferation, to be MSCs (Horwitz et al., 2005). Consequently, MSCs are typically defined as adherent, fibroblastoid-like cells that differentiate to osteoblasts, adipocytes, and chondrocytes *in vitro*. Despite their functional heterogeneity, *in vitro* MSCs are defined as nonhematopoietic cells (CD45-, CD14-, CD34-) but express other molecules, the combination of which is largely used for their description: CD73+, CD44+, CD105+, CD90+ and CD146+.

Key factors	<i>In vivo</i> and <i>in vitro</i> effects
TGFbeta	Can induce osteoblast differentiation at the early stage of immature cells but can also inhibit osteogenesis in committed cells.
BMP2	Osteochondrogenic factor; might initiate bone formation and bone healing and can induce expression of other BMPs
BMP4	Osteochondrogenic factor <i>in vivo</i> and <i>in vitro</i>
BMP7	Osteogenic factor <i>in vivo</i> and <i>in vitro</i> ; active on more mature osteoblasts
Noggin	Suppresses osteoblastic differentiation
FGFb	Mutations induce chondrodysplasia and craniosynostosis; can stimulate Sox9; might be a negative regulator of postnatal bone growth and remodeling
IGF-I, II	Stimulates growth plate formation, endochondrate ossification and bone formation by osteoblasts
VEGF	Most potent angiogenic and vasculogenic factor; crucial at the onset of bone formation
PIGF	Induces proliferation and osteogenic differentiation of MSCs; crucial for vascularization
Wnts	Depending on Wnt type, crucial for osteoprogenitor proliferation; can also inhibit final osteoblast maturation
Ihh	Pivotal role for growth plate and endochondral formation; can inhibit osteoblast differentiation; might induce PTHrP expression
PTHrP	Pivotal role for growth plate and endochondral formation; can induce or inhibit osteogenesis
OPG	Strongly inhibits bone resorption and has a pivotal role in bone Remodeling.
RANKL	Strongly stimulates bone resorption and has a pivotal role in bone remodeling
MAPKs	Crucial for regulation of intracellular signaling induced by osteogenic factors (still controversial)
Runx2	Master regulator of early osteogenesis; runx2 _{-/-} mice died, with no bone formation
Osterix	Master regulator of late osteogenesis, inhibiting chondrogenesis
Dlx5	Induces osteoblast maturation but inhibits osteocyte formation
Msx2	Induces proliferation of immature cells; responses depend on Dlx5 quantity
NF-kB	Inhibits the differentiation of MSCs and committed osteoblastic cells

Table 1. Molecules involved in bone formation (Modified from Deschaseaux et al., 2009)

As shown in Table 1 a range of cytokines modulate osteoblast differentiation, including bone matrix-derived transforming growth factor beta (TGF- β), bone morphogenetic protein2 (BMP-2), BMP-4, and BMP-7, and their inhibitors noggin, chordin, gremlin, etc. Transcription factors that regulate the osteoblast include a range of homeodomain proteins: the activator protein (AP) family members Jun, Fos, and Fra, Smads, CCAAT/enhancer binding protein β (C/EBP β) and C/EBP δ , lymphoid-enhancing factor (a Wnt effector), activating transcription factor 4, Runt-related transcription factor 2 (Runx2), and osterix, the last 3 of which are considered master genes for osteoblast differentiation. Runx2 is critical for osteoblast differentiation and two homeobox protein Dlx5 and Msx2 regulate Runx2 activity via a protein-protein binding interactions (Shirakabe et al., 2001). Thus, owing to the specific signal activation including transcriptional dynamics, MSCs differentiate into osteoblasts (Figure 2).

2.2. Secretion of matrix proteins by osteoblasts

Recruited and differentiated osteoblasts play a key role in biomineralization by secreting matrix proteins including collagen and non-collagenous proteins (NCP). Most tissues have been shown to contain a mixture of different collagen types. Bone, however, appears to contain almost exclusively type I collagen, with some type V (Broek et al., 1985). Type I collagen is the most common of the collagens in vertebrates. It comprises up to 90% of the skeletons of mammals and is also widespread all over the body, giving various tissues their mechanical strength and providing the major biomechanical scaffold for cell attachment and anchorage of macromolecules. Though type I collagen has multisectorial tasks, in bones type I collagen is mineralized with apatite crystals and gives mechanical strength and bone flexibility, and, moreover, it facilitates bone mineralization (Mirja et al., 2001).

Other important matrix proteins secreted by osteoblasts are NCP, including osteopontin (OP), bone sialoprotein (BSP), osteonectin (ON), and osteocalcin (OC). OP has important roles in immune functions, acts as an important anti-apoptotic factor in many circumstances (Denhardt et al., 2001), and also functions as an adhesion protein involved in cell attachment and wound healing (Wang et al., 2008). It plays a pivotal role in anchoring osteoclasts or hematopoietic stem cells to the mineral matrix of bones and thereby regulates their fate (Nilsson et al., 2005). OP contains a string of polyaspartic acid residues as well as an RGDS sequence near the middle of the primary sequence, where it has higher affinity with hydroxyapatite (HAp). BSP is a phosphoprotein that contains large stretches of polyglutamic acids as well as the RGD integrin-binding sequence at its carboxy terminus (Ganss et al., 1999). Its expression is generally limited to the later stages of osteoblast differentiation and early stages of mineralization. BSP also has a high affinity for calcium ions. ON is an acidic, secreted extracellular matrix glycoprotein. ON binds strongly to HAp (Romberg et al., 1985) even in the presence of 4M guanidinium hydrochloride. Alkaline phosphatase (ALP) secreted by osteoblasts is responsible for increasing local inorganic phosphate concentration during apatite formation (Hoffmann et al., 2008). Notably, these NCP can adhere to collagen fibers via strong physical adsorption or covalent bindings. Therefore, NCP coupling with type I collagen is considered to be an important template for mineralization. Indeed, numerous studies indicate that HAp orientation correlates with collagen orientation (Iijima et al., 1997b). OC is abundant in the synthesized osteogenic matrix, binds to phospholipid vesicles in the presence of Ca²⁺, and also binds HAp. It has been stipulated that OC may function as a negative regulator of bone formation, although its exact role is unknown.

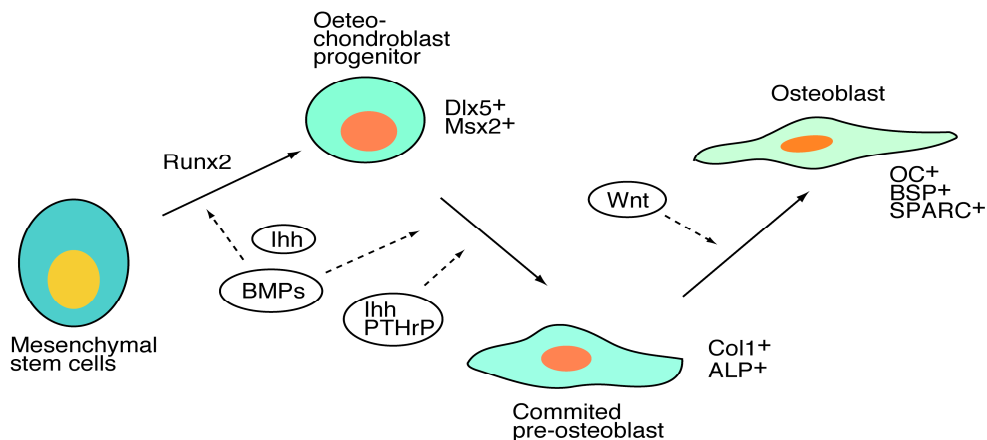


Fig. 2. Schematic illustration of differentiation of mesenchymal stem cells.

2.3. Nucleation and crystal growth of apatite minerals on matrix

It now appears clear that type I collagen alone is biologically insufficient to induce mineralization. It is thought that in bone, an interaction between anionic proteins and type I collagen fibrils may provide a stereochemical orientation of negatively charged groups that acts as a HAp nucleator. *In vitro* studies of organic matrix on biological crystal formation have proved a powerful complement to ultrastructural approaches in the ongoing attempt to determine the mechanism of calcification in bone and epiphyseal cartilage. However, much confusion has been generated by the fact that anionic matrix molecules often act as calcification inhibitors in these systems by complexing calcium ions and, in some cases, inhibiting crystal growth by adsorption onto specific crystal faces. For example, an aspartate-rich protein adsorbs to specific faces of growing apatite crystal, inhibiting the development of these faces and hence altering the crystal morphology (Addadi and Weiner, 1985). An important conceptual breakthrough has been the realization that macromolecules with a high density of negatively charged groups may act as crystal nucleators if immobilized onto solid-phase surfaces (Linde et al., 1989).

Similarly, amphipathic lipid monolayers or bilayers may promote calcification in an adjacent solution phase. Matrix vesicles secreted from osteoblasts are also considered to be a major site of biomineral nucleation (Figure 3). There are electron microscopy reports from researchers claiming that the mineralization process may involve the mobilization and translocation of insoluble mitochondrial calcium phosphate to the plasma membrane. According to this scheme, ions are 'packaged' and pinched off within trilaminar membrane-bound vesicles that are enriched and complexed with acidic phospholipid and contain NCP/proteolipid (Glinder et al., 1989). The phosphate-containing ALP within these new extracellular matrix vesicles is a species that is electrophoretically distinct from the form of the enzyme that is restricted to intracellular sites (Arsenis et al., 1976). Then, mineral formation penetrates the vesicle membrane and, in the presence of Ca^{+2} , PO_4^{-3} , and pyrophosphate, serves as the nuclei for formation of needle-shaped apatite. Finally, proliferation of the apatite spreads outwards into the matrix, rupturing the matrix vesicle (Anderson et al., 1969).

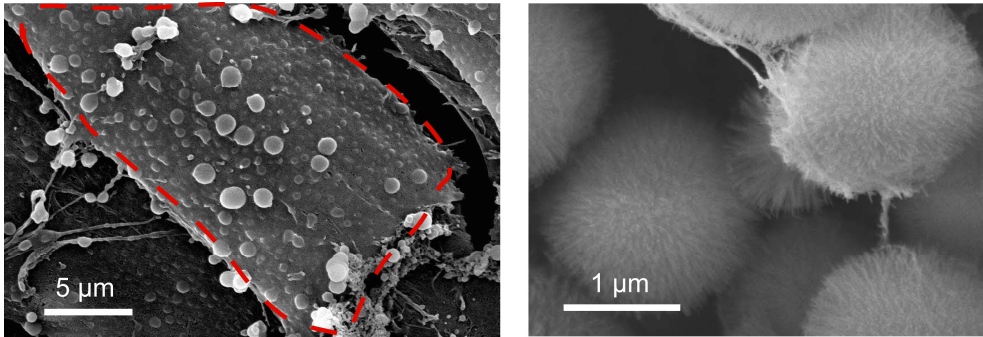


Fig. 3. Matrix vesicle secreted by osteoblasts (Left). Mineralized matrix vesicles (Right).

3. Bone minerals

The crystals of bone apatite are extremely small (crystallites). By x-ray diffraction, crystal size has been found to range in its long dimension (c-axis) from 10–25 nm (Boskey et al., 1985; Grynepas et al., 1986). By electron microscopy, bone crystal length has been found to vary from 30–70 nm (Landis et al., 1978). Therefore, bone mineral has a huge surface area of between 85 and 170 m²/g (Ortner, 2003).

There are essentially five solid phases of calcium phosphate that have been linked to biological mineralization (Table 2). Of these, HAP ($\text{Ca}_{10}(\text{PO}_4)_6(\text{OH})_2$) (Figure 4) is universally recognized as the final solid mineral phase of bone. All others have been implicated as minor or precursor phases; they are acid stable and will convert to the thermodynamically stable and insoluble HAP at a high pH. HAP alone is stable at neutral or basic pH. Tricalcium phosphate ($\text{Ca}_3(\text{PO}_4)_2$, TCP) requires the presence of Mg for its formation at room temperature. Both dicalcium phosphate dihydrate ($\text{CaHPO}_4 \cdot 2\text{H}_2\text{O}$, DCPD) and octacalcium phosphate ($\text{Ca}_8\text{H}_2(\text{PO}_4)_6 \cdot 5\text{H}_2\text{O}$, OCP) have acid phosphate groups (HPO_4) and a structural plane on which HAP can be grown epitaxially (Neuman and Neuman, 1958). Studies suggest that platelets are the dominant morphology of bone apatite (Traub et al., 1989). The formation of plate-like crystals in the mineralized collagen fibrils is still not fully understood. One possible explanation for this mineral morphology in bone is that crystal growth occurs via an OCP intermediate (Brown et al., 1962; Weiner and Traub, 1992). OCP has nearly the same crystal structure as HAP but contains an extra hydrated layer that may be responsible for the observed plate-shaped crystals in natural bone. Amorphous calcium phosphate (ACP) was also found to spontaneously precipitate to apatite at physiological values *in vitro* (Eanes et al., 1965). However, Grynepas et al. could not detect the presence of ACP in young bone (Grynepas et al., 1984). Improved methods of imaging and structure determination have since led to the identification of stable and transient forms of amorphous precursors in biomineralization of calcium carbonate in sea urchin spines and spicules (Addadi et al., 2003; Politi et al., 2004; Politi et al., 2006). As a result, the role of amorphous phases in mineralization of HAP in biological tissues such as bone continues to be a subject of great research interest.

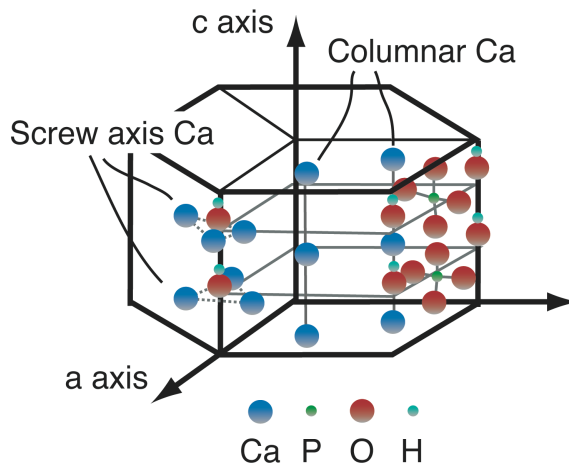


Fig. 4. Hydroxyapatite crystal

Phosphates (PO_4) in the general formula of HAp can be CO_3 , SO_4 , VO_4 , AsO_4 , or SiO_4 . A variety of metals can take the place of Ca in the formula. In case of natural apatites, the main cation is Ca and Mg is secondary. The last group $(\text{OH})_2$ can be F_2 , Cl_2 , Br_2 , or CO_3 (Zipkin, 1973). Chemical analysis has shown that in hard biological tissues, i.e., bone, enamel, and dentine, the biological apatites are not pure HAp, but contain a mixture of minor elements, including CO_3 , HPO_4 , F, Cl, Mg, and Na ions (Yoshikawa and Myoui, 2005). Based on the knowledge derived from biological mineralization systems, researchers, especially material scientists and chemists, are now seeking biomimetic apatite-related biomaterials.

Name	Formula	Abbreviation	Molar ratio
Hydroxyapatite	$\text{Ca}_{10}(\text{PO}_4)_6(\text{OH})_2$	HAp	1.67
Tricalcium phosphate	$\text{Ca}_3(\text{PO}_4)_2$	TCP	1.50
Octacalcium phosphate	$\text{Ca}_8\text{H}_2(\text{PO}_4)_5 \cdot 5\text{H}_2\text{O}$	OCP	1.33
Dicalcium phosphate dihydrate	$\text{CaHPO}_4 \cdot 2\text{H}_2\text{O}$	DCPD	1.00
Amorphous calcium phosphate		ACP	1.30-1.50

Table 2. Solid phases of biological calcium-phosphate

4. *In vitro* approaches to fabricating biomimetic inorganic materials

4.1. Biomimetic apatite: Ionically substituted apatite

Apatite powders can be synthesized via numerous production routes with a range of different reactants. Processing techniques include wet chemical methods (precipitation), hydrothermal techniques, hydrolysis of other calcium phosphates, and sol-gel methods. Since biological minerals, especially the apatite found in bone, are often ionically substituted apatite, apatite materials substituted by ions have been synthesized to control the

characteristics of apatite materials. When HAp is synthesized in the presence of Mg, Fe, CO₃, or F, these ions are readily and partly substituted at certain positions (e.g., Mg and Fe at the Ca site, CO₃ at the PO₄ site, and CO₃ and F at the OH site) in HAp crystals. The ionically substituted HAp exhibits different characteristics than normal HAp. For example, the solubility of apatite containing Mg, Fe, or CO₃ substitution increases with the increase in the concentration of the substitute ion (Gibson and Bonfield, 2002; Suchanek et al., 2004; Morrissey et al., 2005), whereas the stability of crystals increases and solubility decreases in apatite with F substitution (Okazaki et al., 1998; Okazaki et al., 1981). In addition to those, Sr- or Zn-substituted HAp crystals were synthesized by researchers. Sr-containing HAp enhanced the proliferation and differentiation of osteoblasts (e.g., MG63) (Capuccini et al., 2008). It also facilitated the nucleation of HAp, therefore, Sr-containing HAp is might be usable as a template for growing new bone (Pan et al., 2009). Zn-containing HAp increases the specific surface area (Tonegawa et al., 2007) and decreases the thermal stability of HAp (Li et al., 2008). Thus, ionic substitution, which occurs in natural apatite, is effective for controlling both material and biological characteristics of apatite.

4.2. Apatite formation via biomimetic mineralization

Researchers are also developing new synthetic, biomimetic systems to obtain apatite materials with biomimetic crystal morphology and size. Iijima et al. focused on the OCP crystal growth methods similar to the biological system. A collagen disk prepared from bovine Achilles tendon, which shows specific uniaxial alignment, was used as the template for OCP crystal formation. Consequently, the researchers were able to reproduce a ribbon-like OCP crystal formation morphologically close to the biological apatite precursors (Iijima et al., 1997b) (Figure 5a).

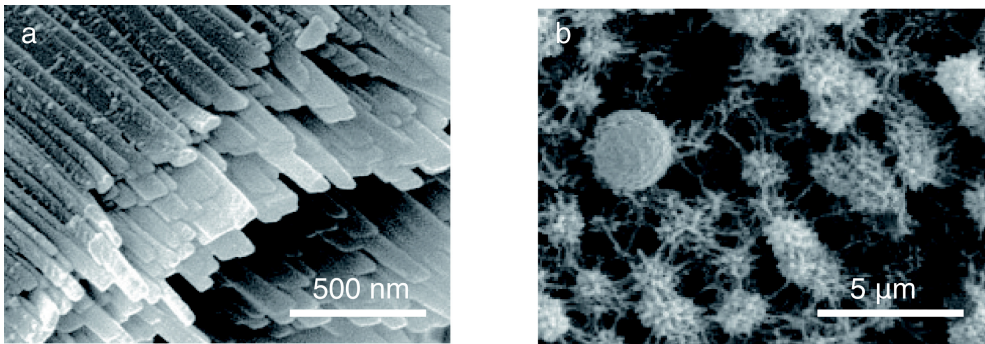


Fig. 5. a) OCP crystals (Iijima et al., 2002) Copyright 2002 IADR, b) Apatite formation on metal substrate. Copyright 2008 Elsevier.

Since simulated body fluid (SBF) containing inorganic ions similar to those in human plasma has been developed, SBF is considered to be a robust tool for reproducing biological apatite formation *in vitro*. Coating a bone-like apatite layer on substrate is expected to be a useful technique for inducing bioactivity on the substrate. The bone-like apatite layer can be formed on the surface of substrates in SBF solution when several specific functional groups are introduced to the substrates. Coating bone-like apatite layers through this biomimetic

process has received much attention in the fabrication of novel bioactive composites (Kamitakahara et al., 2007). Often, the biomimetic apatite coating is developed on the surface of titanium and its alloys. Gu et al. developed a method for biomimetic deposition of apatite coating on surface-modified NiTi alloy. They prepared a TiO₂ coating on NiTi alloy by heat treatment in air. The heat-treated NiTi alloy was then immersed in SBF for the biomimetic deposition of the apatite layer onto the surface of the TiO₂ coating. XPS and Raman results showed that this apatite layer was a carbonated and non-stoichiometric apatite with a Ca/P ratio of 1.53, which is similar to human bone (Gu et al., 2005). Ohtsuki et al. reported *in vitro* formation of small crystallinities of carbonate-containing apatite on the surface of Ceravital-type glass ceramics soaked in SBF (Ohtsuki et al., 1991).

Moreover, there are reports about biomimetic methods of apatite formation using simpler solutions than SBF. For example, Bigi et al. reported a new fast method for the development of nanocrystalline HAp coatings on Ti6Al4V substrates using a slightly supersaturated Ca/P solution with an ionic composition simpler than that of SBF (Bigi et al., 2005). Shi et al. also followed the same biomimetic approach to synthesize an apatite layer on the surface of NaOH-modified titanium coatings in supersaturated solutions containing Ca²⁺ and HPO₄²⁻ ions. They observed that, depending on the ion composition and concentration of the solution, apatite layers were formed with preferred orientation and a composition similar to that found in bone (Shi et al., 2001) (Figure 5b).

5. *In vitro* approaches to fabricate biomimetic organic/inorganic composite materials

5.1. HAp containing organics

Improvement of physico-chemical characteristics (e.g., crystallinity, solubility, adsorptive properties, etc.) of apatite is important for using apatite-based materials for biomedical applications such as bone regeneration. Since acidic molecules have a well documented affinity to HAp, researchers synthesized HAp in the presence of organics, including acidic molecules and sugars. Previous reports indicated that HAp synthesized with acidic amino acids (e.g., aspartic acid, glutamic acid) has decreased crystallinity and increased solubility (Kevin, et al., 2007; Matsumoto et al., 2002). FTIR analysis indicated that these HAp crystals contained acidic amino acids and showed selective loading capacity of positively charged molecules (Uddin et al., 2009) and enhanced osteogenic differentiation of cells (Boanini et al., 2006). Stupp et al. synthesized HAp using macromolecules such as poly(l-lysine) and poly(l-glutamic acid). Poly(l-lysine) generated large single crystals that were flat and thin, whereas poly(l-glutamic acid) generated nanoscale crystallites (Stupp et al., 1997). Stupp et al. also demonstrated biomimetic mineralization of bone apatite using self-assembling molecules known as peptide amphiphiles (Hartgerink et al., 2001). Since the peptide design is flexible, this approach would be robust for obtaining HAp crystals with desired structure and size.

5.2. Biomimetic mineralization in organic gel to fabricate organic/inorganic composite material

Basically, the methods originate from biochemical studies investigating the effect of matrix proteins on biomineralization. Silverman and Boskey developed a gel diffusion precipitation

technique for growing large HAp crystals in collagen gel. This group has shown the *inter alia* promotion of HAp formation and growth by acidic phospholipids, biglycan, and BSP (Silverman and Boskey, 2004). On the other hand, inhibition of mineralization was observed for OP, dentin sialoprotein, aggrecan, and dentin matrix protein-1 (Tartaix et al., 2004). Hunter and Goldberg used a variation of the double diffusion gel method (using double diffusion of ions from opposite directions into a gel that contains the matrix molecule of interest) to explore apatite nucleation and inhibition by a number of matrix proteins (Hunter and Goldberg, 1993). Their system uses an agarose gel separated from calcium and phosphate reservoirs by diffusion membranes. SDS-polyacrylamide electrophoretic gel was also used as gel diffusion precipitation system. Calcium and phosphate ions were diffused naturally or propelled by electric potential. Calcium phosphate was precipitated in the gel. The precipitation was affected by proteins in the gel that had been separated by electrophoresis.

From a different stand-point, gels containing precipitated minerals developed in these methods are considered to be organic/inorganic composite gel material. Yoh et al. performed *in vitro* fabrication of fibrin/apatite composite material by using gel diffusion systems at various pH conditions. The minerals generated in fibrin gel varied with the pH conditions: DCPD in the noncontrolled pH solution, a DCPD and OCP mixture at pH 7.4, and an OCP and HAp mixture at pH 9.0. The composition of minerals in the gel can be regulated by their reaction period or diffusion rate (Yoh et al., 2008) (Figure 6). Watanabe et al. demonstrated anisotropic HAp formation in an agarose gel using an electrophoretic approach and an alternate soaking process to obtain the composite materials for bone regeneration (Watanabe et al., 2007).

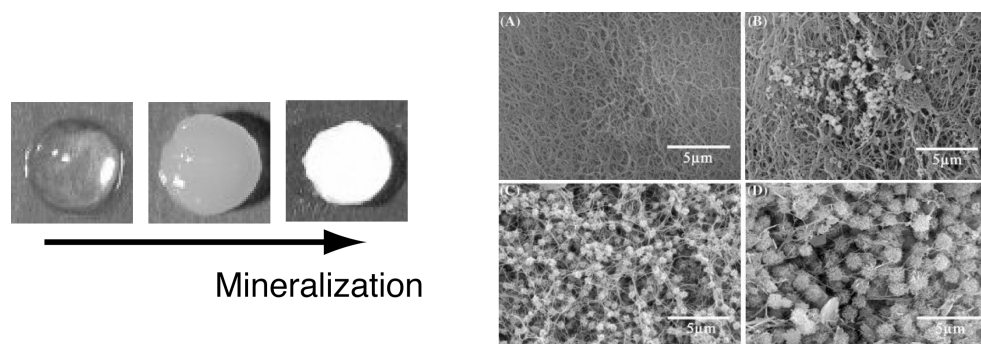


Fig. 6. Biomimetic mineralization of apatite in fibrin gel. Copyright 2008 Wiley.

5.3. Cell based fabrication of organic/inorganic composite gel

Synthesis of organic/inorganic composite materials generated by inorganic nucleation in a polymerized matrix is a unique system for obtaining biomimetic materials. Cells might also be great contributors to the synthesis of organic/inorganic composite material, because secreted proteins, especially those derived from osteogenic differentiated cells, supply regions where mineral crystals nucleate and grow. Our group demonstrated that culturing MSCs in three-dimensional (3D) gel matrix enhanced the precipitation of cell-derived matrix and minerals. The matrix and mineral content in the material can be regulated by cell culture

conditions including cell number and period. Moreover, 3D cell patterning in the gel has been found to be effective in controlling the matrix and mineral position and distribution in the gel. Thus, this type of cell-based fabrication technique would be a new approach to fabricating more biomimetic materials (Figure 7).

6. Conclusion

Biological tissue shows amazing characteristics and has functions that cannot be easily reproduced by artificial synthesis. For example, bone tissue shows fracture toughness though it is soft in nature. Therefore, learning from biological systems gives us tremendous opportunities to fabricate materials that we have not yet been able to produce. The ionically substituted HAp materials or organic-containing HAp materials introduced in this chapter are good candidates for drug delivery carriers for bone regeneration or bone-related diseases. Organic/inorganic composite gel materials fabricated by self-precipitation or by a cell-based method would be neo-bone tissue that could shorten the bone regeneration period. Thus, apatite related biomaterials inspired by nature have potential for numerical biomedical applications.

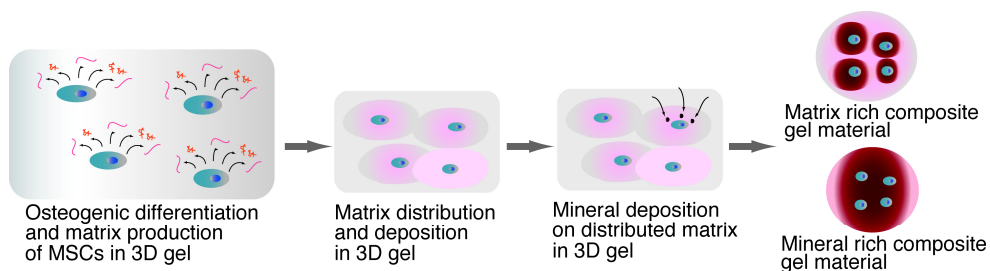


Fig. 7. Schematic illustration of biomimetic mineralization in fibrin gel culturing with MSCs.

7. References

- Addadi, L. and Weiner, S. (1985). Interactions between acidic proteins and crystals: stereochemical requirements in biomineralization. *Proceedings of the National Academy of Sciences USA*, v. 82, pp. 4110-4114.
- Addadi, L., Raz, S., Weiner, S. (2003). Taking the advantage of disorder: amorphous calcium carbonate and its roles in biomineralization. *Advanced Material*, v. 15, pp. 959-970.
- Anderson, H. C. (1969). Vesicles associated with calcification in the matrix of epiphyseal cartilage. *Journal of Cell Biology*, v. 41, pp. 59.
- Bigi, A., Boanini, E., Bracci, B., Facchini, A., Panzavolta, S., Segatti, F., Sturba, L. (2005). Nanocrystalline hydroxyapatite coatings on titanium: a new fast biomimetic method. *Biomaterials*, v. 26, pp. 4085-4089.
- Boanini, E., Torricelli, P., Gazzano M., Giardino, R., Bigi, A. (2006). Nanocomposites of hydroxyapatite with aspartic acid and glutamic acid and their interaction with osteoblast cells. *Biomaterials*, v. 27, pp. 4428-4433.
- Boskey, A. L. (1998). Biomineralization: Conflicts, challenges, and opportunities, *Journal of cellular biochemistry*, v. 72, pp. 83 - 91.

- Boskey, A. L. and Marks, S. C. (1985). Mineral and matrix alterations in the bones of incisor absent (ia) osteopetrotic rats. *Calcified Tissue International*, v. 37, pp. 287.
- Brown, W.E., Smith, J. P., Lehr, J. R., Drazier, A. W. (1962). Octacalcium Phosphate and Hydroxyapatite: Crystallographic and Chemical Relations between Octacalcium Phosphate and Hydroxyapatite. *Nature*, v. 196, pp. 1050 - 1055.
- Broek, D. L., Madri, J., Eikenberry, E. F., Brodsky, B. (1985). Characterisation of the tissue form of type v collagen from chicken bone. *Journal of Biological Chemistry*, v. 260, pp. 555-562.
- Caplan, A. I. (1991). Mesenchymal stem cells. *Journal of Orthopaedic Research*, v. 9, pp. 641-650.
- Capuccini, C., Torricell, P., Sima, E., Boanini, F., Ristoscu, C., Bracci, B., Socol, G., Fini, M., Mihailescund, I. N., Bigi, A. (2008). Strontium-substituted hydroxyapatite coatings synthesized by pulsed-laser deposition: *In vitro* osteoblast and osteoclast response. *Acta Biomaterialia*. v. 4, pp. 1985-1993.
- Choi, S. T., Kim, J. H., Kang, E. J., Lee, S. W., Park, M. C., Park, Y. B., Lee, S. K. (2008). "Osteopontin might be involved in bone remodelling rather than in inflammation in ankylosing spondylitis". *Rheumatology (Oxford)*, v. 47, pp. 1775-1779.
- Denhardt, D.T., Noda, M., O'Regan, A. W., Pavlin, D., Berman, J. S., (2001). Osteopontin as a means to cope with environmental insults: regulation of inflammation, tissue remodeling, and cell survival. *Journal of Clinical Investigation*, v. 107, pp. 1055-1061.
- Deschaseaux F, Sensébé L, Heymann D. (2009). Mechanisms of bone repair and regeneration. *Trends in Molecular Medicine*. V. 15, pp. 417-429.
- Eanes, E. D., Gillessen, I. H., Posner, A. S. (1965). Intermediate states in the precipitation of hydroxyapatite. *Nature*, v. 208, pp. 365.
- Fernandez-Moran, H. and Engstrom, A. (1957). Electron microscopy and x-ray diffraction of bone. *Biochimica et Biophysica Acta*, v. 23, pp. 260-264.
- Ganss, B., Kim, R. H., Sodek (1999). Bone sialoprotein. *Critical Reviews in Oral Biology & Medicine*. v. 10, pp. 79.
- Gibson, I. R. and Bonfield, W. (2002). Preparation and Characterisation of Magnesium/Carbonate co-substituted Hydroxyapatites". *Journal of Materials Science: Materials in Medicine*, v. 13, pp. 685-693.
- Glinder H., and Boskey, A. (1989). In: Simmons, D. J. (ed): *Nutrition and Bone Development*. Oxford University Press, N. Y.
- Grynepas, M. D., Patterson-Allen, P., Simmons, D. J. et al. (1986). The changes in quality of mandibular bone mineral in otherwise totally immobilized Rhesus monkeys. *Calcified Tissue International*, v. 39, pp. 57.
- Grynepas, M. D., Bonar, L. C. and Glimcher, M. J. (1984). Failure to detect an amorphous calcium-phosphate solid phase in bone mineral: a radial distribution function study. *Calcified Tissue International*, v. 36, pp. 291-301.
- Gu, Y. W., Tay, B. Y., Lim, C. S., Yong, M. S. (2005). Biomimetic deposition of apatite coating on surface-modified NiTi alloy. *Biomaterials*, v. 26, pp. 6916-6923.
- Hoffmann, C., Zollfrank, C., Ziegler, G. (2008). Enzyme-catalysed synthesis of calcium phosphates. *Journal of Material Science: Materials in Medicine*, v. 19, pp. 907-915.

- Horwitz, E. M., Blanc, K. Le., Dominici, M., Mueller, I., Slaper-Cortenbach, I., Marini, F. C., Deans, R. J., Krause, D. S., Keating, A. (2005). Clarification of the nomenclature for MSC: The International Society for Cellular Therapy position statement. *Cytotherapy*, v. 7, pp. 393-395.
- Hunter, G. K., and Goldberg, A. (1993). Nucleation of hydroxyapatite by bone sialoprotein. *Proceedings of the National Academy of Science, USA*. v. 90, pp. 8562-8565.
- Iijima, M., Moriwaki, Y., Yamaguchi R., Kuboki Y. (1997). Effect of solution pH on the calcium phosphates formation and ionic diffusion on and through the collagenous matrix. *Connective Tissue research*, v. 36, pp. 73-83.
- Iijima, M., Moriwaki, Y., Wen, H. B., Fincham, A. G., Moradian-Oldak, J. (2002). Elongated growth of Octacalcium phosphate crystals in recombinant amelogenin gels under controlled ionic flow. *Journal of Dental Research*, v. 81, n.1, pp. 69-73.
- Kamitakahara, M., Ohtsuki, C., Miyazaki, T. (2007). Coating of bone-like apatite for development of bioactive materials for bone reconstruction. *Biomedical Materials*, v. 2, pp. R 17-23.
- Kevin, S. J., Timothy, G. G., Matt, T. (2007). Characterization and surface properties of amino-acid modified carbonate-containing hydroxyapatite particles. *Langmuir*, v. 23, pp. 12233-12242.
- Komleva, V. S., Barinova, S. M., Koplík, E. V. (2002). A method to fabricate porous spherical hydroxyapatite granules intended for time controlled drug release. *Biomaterials*, v. 23, pp. 3449.
- Landis, W. J. and Glimcher, M. J. (1978). Electron diffraction and electron probe microanalysis of the mineral phase of bone tissue prepared by anhydrous techniques. *Journal of Ultrastructure Research*, v. 63, pp. 188.
- Li, M., Xiao, X., Liu, R., Chen, C., Huang, L. (2008). Structural characterization of zinc-substituted hydroxyapatite prepared by hydrothermal method. *Journal of Materials Science: Materials in Medicine*, v. 19, pp. 797-803.
- Linde, A., Lussi, A., and Crenshaw, M. A. (1989). Mineral induction by immobilized poly anionic protein. *Calcified Tissue International*, v. 44, pp. 286-295.
- Matsumoto, T., Okazaki, M., Inoue, M., Hamada, Y., Taira, M., Takahashi, J. (2002). Crystallinity and solubility characteristics of hydroxyapatite adsorbed amino acids. *Biomaterials*, v. 23, pp. 2241-2247.
- Mirja, L. S. (2001). Carboxyterminal degradation products of type I collagen. Department of Clinical Chemistry, University of Oulu. ISSN 1796-2234.
- Morrissey, R., Rodriguez-Lorenzo, L. M., Gross, K. A. (2005). Influence of ferrous iron incorporation on the structure of hydroxyapatite. *Journal of Material Science: Materials in Medicine*, v. 16, pp. 387.
- Nebe, J. B., Müller, L., Lüthen, F., Ewald, A., Bergemann, C., Conforto, E., Müller, F. A. (2008). Osteoblast response to biomimetically altered titanium surfaces. *Acta Biomaterialia*, v. 4, pp. 1985-1995.
- Okazaki, M., Tohda, H., Yanagisawa, T., Taira, M., Takahashi J. (1998). Differences in solubility of two types of heterogeneous fluoridated hydroxyapatites. *Biomaterials*, v. 19, pp. 611-616.
- Narasaraju, T. S. B. and Phebe, D. E. (1996). Some physico-chemical aspects of hydroxyapatite. *Journal of Material Science*, v. 31, pp. 1.

- Neuman, M. W. and Neuman, W. F. (1958). The chemical dynamics of bone mineral. University of Chicago Press, Chicago, IL. responses^l. Cytokine & Growth Factor Reviews, v. 19, pp. 333-345.
- Nilsson, S. K., Johnston, H. M., Whitty, G. A., Williams, B., Webb, R. J., Denhardt, D.T., Bertonecello, I., Bendall, L. J., Simmons, P.J., Haylock, D. N. (2005). Blood, v. 15, pp. 1232-1239.
- Ohtsuki, c., Kushitani, H., Kokubo, T., Kotani, S., Yamamuro, T. (1991). Apatite formation on the surface of Ceravital type glass-ceramics in the body. Journal of Biomedical Materials Research, v. 25, pp. 1363-1370.
- Okazaki, M., Moriwaki, Y., Aoba, T., Doi, Y., Takahashi, J. (1981). Solubility and crystallinity in relation to fluoride content of fluoridated hydroxyapatites. Journal of Dental Research, v. 60, pp.845-849.
- Okazaki, M., Tohda, H., Yanagisawa, T., Taira, M., Takahashi, J. (1998). Differences in solubility of two types of heterogeneous fluoridated hydroxyapatites. Journal of Dental Research, v. 19, pp. 611-616.
- Ono, K., Yamamuro, T., Nakamura, T., Kokubo, T. (1990) Mechanical properties of bone after implantation of apatite-wollastonite containing glass ceramic-fibrin mixture. Journal of Biomedical Materials Research, v. 24, pp. 47-63.
- Ortner, D. J., (2003). Identification of pathological conditions in human skeletal remains. Academic press. ISBN 0-12-528628-7.
- Pan, H. B., Li, Z. Y., Lam, W. M., Wong, J. C., Darvell, B. W., Luk, K. D., Lu, W. W. (2009). Solubility of strontium substituted apatite by solid titration. Acta Biomaterialia, v. 55, pp. 1678-1685.
- Politi, Y., Klein, E., Arad, T., Weiner, S., Addadi, L. (2004). Sea urchin spine calcite forms via a transient amorphous calcium carbonate phase. Science, v. 306, pp. 1161-1164.
- Politi, Y., Levi-Kalisman, Y., Raz, S., Wilt, F. H., Addadi, L., Weiner, S., and Sagi, I. (2006). Structural Characterization of the Transient Amorphous Calcium Carbonate Precursor Phase in Sea Urchin Embryos. Advanced Functional Materials, v. 16, pp. 1289-1298.
- Romberg, R. W., Werness, P. G., Lollar, P., Riggs, B. L., Maan, K. G. (1985). Isolation and characterization of native adult osteonectin. The Journal of Biological Chemistry, v. 260, pp. 2728-2736.
- Shi, J., Ding, C., Wu, Y. (2001). Biomimetic apatite layers on plasma-sprayed titanium coatings after surface modification. Surface and Coating Technology, v. 137, pp. 97-103.
- Shirakabe, K., Terasawa, K., Miyama, K., Shibuya, H. Nishida, E. (2001). Regulation of the activity of the transcription factor Runx2 by two homebox proteins, Mx2 and Dlx5. Genes to Cells, v. 6, pp. 851-856.
- Sigel, A., Sigel, H., Sigel, R. K. O., (ed) (2008). Biomineralization: From Nature to Application. Metal Ions in Life Sciences. V. 4, Wiley. ISBN 978-0-470-03525-2.
- Silverman, L., and Boskey, A. L. (2004). Diffusion systems for Evaluation of Biomineralization. Calcified Tissue International, v. 75, pp. 494-501.
- Stephen, W., and Lowenstam, H. A. (1989). On biomineralization. Oxford [Oxfordshire]: Oxford University Press. ISBN 0-19-504977-2.
- Stupp, S. I. and Braun, P. V. (1997). Molecular Manipulation of Microstructures: Biomaterials, Ceramics, and Semiconductors. Science, v. 277, pp. 1242-1248.

- Hartgerink, J.D., Beniash, E., Stupp, S. I. (2001). Self-assembly and mineralization of peptide-amphiphile nanofibers., *Science*, v. 294, pp. 1684 - 1688.
- Suchanek, W. L., Byrappa, K., Shuk, P., Riman, R. E., Janas, V. F., TenHuisen, K. S. (2004). Preparation of magnesium-substituted hydroxyapatite powders by the mechanochemical-hydrothermal method. *Biomaterials*, v. 25, pp. 4647-4757.
- Tartaux, P. H., Doulaverakis, M., George A, et al. (2004). *In vitro* effects of dentin matrix protein-1 on hydroxyapatite formation provide insights into in vivo functions. *Journal of Biological Chemistry*, v. 279, pp. 18115-18120.
- Tonegawa, T., Ikoma, T., Chen, G., Tanaka, J. (2007). Synthesis and characterization of metal ions containing hydroxyapatite microparticles with high specific surface area. *Nanoscience and Nanotechnology*, v. 7, pp. 839-843.
- Traub, W., Arad, T., Weiner, S. (1989). Three-dimensional ordered distribution of crystals in turkey tendon collagen fibers. *Proceedings of National Academy of Science USA*, v. 86, pp. 9822-9826.
- Uddin, M. H., Matsumoto, T., Ishihara, S, Nakahira, A., Okazaki, M., Sohmura, T. (2009). Aspartic acid containing hydroxyapatite particles for selective protein loading. *Journal of Dental Research* (accepted).
- Wang, K. X., Denhardt, D. T., (2008). "Osteopontin: role in immune regulation and stress responses". *Cytokine & Growth Factor Reviews*, v. 19, pp. 333-345.
- Watanabe, J., Kashii, M., Hirao, M., Oka, K., Sugamoto, K., Yoshikawa, H., Akashi, M., (2007). Quick-forming hydroxyapatite/agarose gel composites induce bone regeneration, *Journal of Biomedical Materials Research Part A*, v. 83A, pp. 845 - 852.
- Weiner, S. and Traub, W. (1992). Bone structure: from angstroms to microns. *The FASEB Journal*, v. 6, pp. 879-885.
- Weiner, S., Traub, W., Wagner, H. D.(1999). Lamellar Bone: Structure-Function Relations. *Journal of Structural Biology*, v. 126, pp. 241-255.
- Yoh, R., Matsumoto T., Sasaki, J., Sohmura T. (2008). Biomimetic fabrication of fibrin/apatite composite material. *Journal of Biomedical Materials Research Part A*, v. 87A, pp. 222-228.
- Yoshikawa, H. and Myoui, A. (2005). Bone tissue engineering with porous hydroxyapatite ceramics. *Journal of Artificial Organs*, v. 8, pp. 131-136.
- Zipkin, I. (1973). *Biological Mineralization*, Wiley-interscience: New York,. ISBN: 0471983810.

Podophyllotoxin and antitumor synthetic aryltetralines. Toward a biomimetic preparation

Maurizio Bruschi^a, Marco Orlandi^a, Michol Rindone^b, Bruno Rindone^a,
Francesco Saliu^a, Ricardo Suarez-Bertoa^a, Eva Liisa Tollpa^a and Luca Zoia^a

^a*Department of Environmental Sciences, University of Milano-Bicocca,
Piazza della Scienza, 1, 20126 Milano*

^b*SIFIT, Milano*

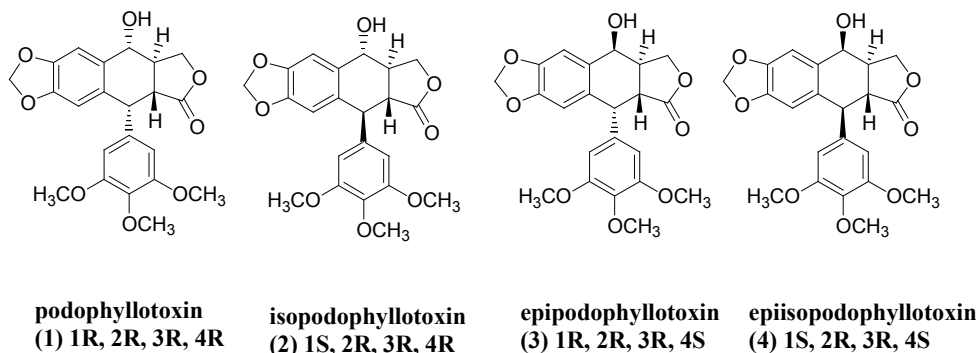
1. Introduction

Organic compounds obtained from radical coupling of phenylpropenoidic phenols have an important biological role. In fact, they constitute organic polymers such as lignin (Higuchi, 1985) lignans (Ayers & Loike, 1990), suberin (Berdards et al. 1995) and algal cell walls (Ragan, 1984). To date, several hundreds of these lignans have been isolated. Whilst their biological role in plants is unclear and remains to be fully elucidated, they have been shown to display a substantial range of biological activity and have a long and fascinating medical history that emanates from their use as folk remedies to treat an assortment of conditions (Bett, 1951). They are typically dimers and their primary physiological role in plants is in plant defense (Beutner & Ferenczy, 1997). Some lignans have found application in medicine, such as podophyllotoxin in venereal wart treatment (Meresse et al, 2004), or its semisynthetic derivatives etoposide, and teniposide in cancer therapies (Ward, 1997).

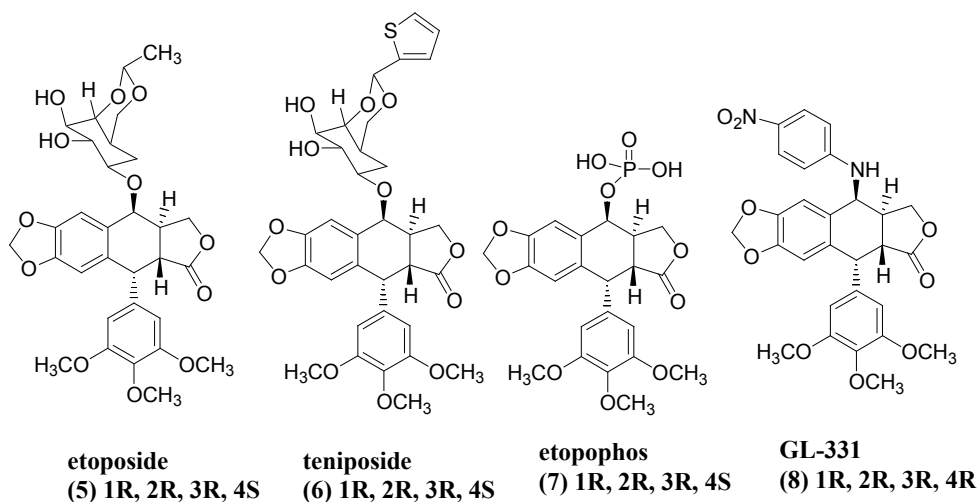
2. Aryltetraline lignans

Aryltetralin lignans are lead substances for the semi-synthetic anticancer derivatives etoposide, teniposide and etopophos (Ionkova, 2007). The most prominent member of this group of natural products is podophyllotoxin (**1**) (Scheme 1). This compound, together with analogues (**2-4**) are aryltetralin lignan lactones isolated from the American Mayapple (*Podophyllum peltatum*) and related Indian species (*Podophyllum emodi*). Podophyllotoxin (**1**) has long been known to possess anti-mitotic activity with early clinical trials showing it to be highly efficacious but also quite toxic (Jardine, 1990), (Weiss et al., 1975) (Keller-Juslen et al., 1971). Four contiguous chiral centers contained within a stereochemically unstable trans-fused tetrahydronaphthalene lactone skeleton (Ward, 1982) are present in this compound.

Scheme 1



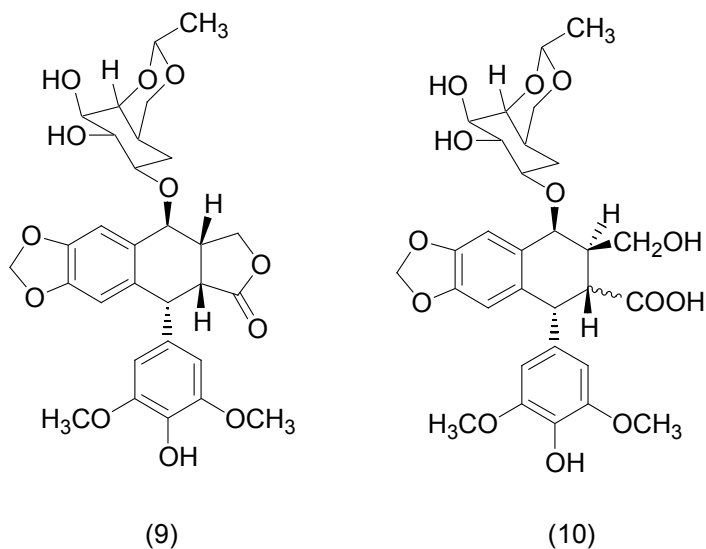
Scheme 2



A number of modifications have been done on podophyllotoxin structure (Damayanthy & Lown, 1998), and some of the congeners exhibit a potent antitumor activity. In fact, etoposide (5), teniposide (6), etopophos (7), GL-331 (8) (Kuo Hsiung-Lee, 2000) (Scheme 2) are potent chemotherapeutic agents for a variety of tumors. However, neither is optimal. For example, etoposide (5) and its analogues suffer from poor solubility and growing drug resistance. Consequently, further analogues continue to be described. GL-331 (8) is currently undergoing phase II clinical trials and has been shown to be more potent than etoposide as a topoisomerase II inhibitor and, more notably, has overcome multidrug resistance in cancer cells, including etoposide-resistant cancer cells (Xiao et al., 2004).

In vivo studies have shown that metabolic deactivation of etoposide occurs through two key pathways, giving metabolites (9-10) (Cragg & Suffness, 1988) (Dow et al., 1982) (Creaven, 1982) (Scheme 3).

Scheme 3



Epimerisation of the *trans* lactone to the *cis* isomer (**9**) leads to a 100-fold loss in activity. Hydrolysis of the lactone with concomitant epimerisation leads to the hydroxy acid (**10**), which is 500-fold less active than etoposide. It can be deduced from these two observations that the stereochemistry surrounding the C ring of podophyllotoxin (**1**) is critical for the overall activity of the molecule.

3. Antitumour Aryltetralines: Pharmacology

Lignans, and especially cyclolignans, have been the objective of numerous studies focused on preparing better and safer anticancer drugs (Gordaliza et al., 2000).

Etoposide (VP-16) and teniposide are currently in clinical use in the treatment of many cancers, particularly small cell lung carcinoma (SCLC), testicular cancer and malignant lymphoma.

Etoposide gained FDA approval in 1983 and in 1987 a soft gelatin capsule formulation was approved as well, which allowed long-term and more tolerable drug administration.

Clinical trials with etoposide began in 1971 and demonstrated its antineoplastic activity in AML (acute myeloid leukemia) (Kell, 2006), Hodgkin's disease (Advani & Horning, 2006), non-Hodgkin's lymphoma (Kluin-Nelemans et al., 2001), lung cancer, gastric cancer, breast cancer and ovarian and testicular cancer (Bookman et al. 2006).

This semisynthetic derivative, along with teniposide, is usually administered in combination chemotherapy in the treatment of lung cancer (both small cell and non-small cell), testicular cancer and in acute leukaemias. Apart from ovarian and testicular cancer, etoposide has also been tried in other solid tumours including those of the brain and thymus and also in the treatment of Kaposi's sarcoma associated with AIDS (Martindale, 2007).

In particular, cisplatin or carboplatin with etoposide remains the current standard chemotherapy regimen for small cell lung carcinoma, which accounts for about 10-20% of all lung cancers (Yee et al., 2008) and is the most aggressive form of lung cancer, with an overall 5-year survival less than 5%.

Germ cell tumours are the most common solid malignancies to affect young adult men and their incidence is increasing worldwide (Hussain et al., 2008). Advanced testicular cancer is successfully treated with etoposide, in combination chemotherapy with cisplatin and bleomycin (Feldman et al., 2008).

The dose-limiting toxicity of etoposide is myelosuppression, mainly seen as leucopenia, but also thrombocytopenia and sometimes anaemia. The nadir of the granulocyte count usually occurs 7 to 14 days after a dose, with recovery by about 21 days. Nausea and vomiting are common and gastrointestinal toxicity may be more common after oral dosage. Reversible alopecia occurs in about two-thirds of all patients. Hypersensitivity or anaphylactoid reactions can occur, characterized by flushing, chills, fever, tachycardia, bronchospasm, dyspnoea and hypotension. Peripheral or central neuropathies have been rarely observed. Tumor lysis syndrome has been reported after the use of etoposide with other chemotherapeutic drugs. Disturbances of liver function have been reported, mainly at high doses, and there have been occasional reports of cardiotoxicity.

Pharmacokinetic parameters determined from studies have shown that the area under the concentration versus time curve (AUC) and peak plasma concentrations achieved following i.v. etoposide administration are linearly related to dose (Hande et al., 1984). Etoposide's steady-state volume of distribution ranges from 5 to 171/m². Etoposide is highly bound to plasma proteins with an average free plasma fraction of 6%. Total etoposide clearance is modestly decreased in patients with renal failure, but not in patients with hepatic obstruction. The etoposide plasma binding ratio (the amount of bound drug/the amount of free drug) is directly related to the serum albumin concentration. Cancer patients, in particular those with hepatic involvement, often have reduced serum albumin concentrations. Since free etoposide is biologically active, conditions which decrease protein binding increase the pharmacological effect of a given dose.

The bioavailability of oral etoposide, ranges from 40 to 75%, changes with the drug dose and shows a considerable interindividual variability has been reported.

As etoposide is poorly soluble in water, the intravenous administration of large doses of the drug may require the administration of significant fluid volumes, and this fluid load can cause heart failure in some patients (Hande, 1998). Hypersensitivity reactions and hypotension may also occur with rapid administration of etoposide, perhaps due to the vehicles needed as solubilisers. To overcome solubility problems, etoposide phosphate (Etopophos®, Bristol-Myers Squibb Co), an etoposide prodrug for intravenous use, was produced and was approved by the FDA in 1996.

Etoposide phosphate can be administered more rapidly and seems to be associated to a reduced number of hypersensitivity reactions (Collier et al., 2008). This compound is soluble in water at concentrations up to 20 mg/ml. Several studies have shown that etoposide phosphate is rapidly and completely converted to etoposide by the action of alkaline phosphatases in blood, and it can be administered over short (5-30 min) time periods, is pharmacokinetically equivalent to etoposide and has identical toxicity. Conversion to etoposide is rapid and not saturated even at high drug doses (1.6 g/m²) used in marrow transplantation regimens.

In patients with high risk or relapsed lymphoma, high-dose etoposide phosphate proved to be bioequivalent to high-dose etoposide (Reif et al., 2001). The compound showed an acceptable toxicity and is successfully used with carboplatin in elderly patients with small-cell lung cancer (Quoix et al., 2001).

Teniposide was approved for clinical use in the US in 1993 and it is used primarily in the treatment of leukemias and lymphomas, mainly in childhood. Its toxicity is identical to those of etoposide. It can induce myelosuppression, hair loss, nausea, mild vomiting and mucositis, along with occasional hypersensitivity reactions.

4. Antitumour Aryltetralines: Mechanism of action

The mechanism by which the aryltetralin lignan podophyllotoxin (**1**) blocks cell division is related to its inhibition of microtubule assembly into the mitotic apparatus. However, etoposide and teniposide were shown not to be inhibitors of microtubule assembly. This suggested that their antitumor properties were due to another mechanism of action: their interaction with DNA. In fact, they induce a block in late phase S or early G2 by interacting with the enzyme topoisomerase II (Botta et al., 2001).

DNA topoisomerases are nuclear enzymes which make transient DNA strand breaks, allowing the cell to manipulate the topology of its DNA. These enzymes are essential for DNA replication, transcription, chromosomal segregation and DNA recombination. They act by cleaving one or both DNA strands, allowing the passage of an unbroken strand or DNA duplex through the breakage site prior to resealing the break. As a result of their double-stranded DNA passage reaction, type II topoisomerases are able to regulate over- and under-winding of the double helix and resolve nucleic acid knots and tangles.

It was not until 1979 that the name "DNA topoisomerases" was introduced. Extensive biochemical analysis of this group of enzymes was undertaken at the same time etoposide was brought to the clinic.

Etoposide was the first agent recognized as a topoisomerase II inhibiting anticancer drug: in 1984, several laboratories demonstrated that mammalian topoisomerase II was the target for etoposide action.

This compound and other topoisomerase II inhibitors do not kill cells by blocking topoisomerase catalytic function. They poison these enzymes by increasing the steady-state concentration of their covalent DNA cleavage complexes. This action converts topoisomerases into physiological toxins that introduce high levels of transient protein-associated breaks in the genome of treated cells.

The potential lethality of these drug-induced cleavage complexes rises dramatically when replication machinery or helicases attempt to traverse the covalently bound topoisomerase roadblock in the DNA. This disrupts the cleavage complex and converts transient single- or double-strand breaks into permanent double-stranded fractures which are no longer held together by proteinaceous bridges. These breaks become targets for recombinations, sister chromatid exchange, the generation of large insertions and deletions and the production of chromosomal aberrations and translocation. When these permanent DNA breaks are present at sufficient concentration, they trigger a series of events that ultimately culminate in cell death by apoptosis.

As most topoisomerase II inhibiting agents are substrates for P-glycoprotein or other multidrug resistance associated proteins, the development of newer and better

podophyllotoxin-based strategies for the treatment of malignant disease may be forthcoming (Liu et al., 2007).

Other podophyllotoxin derivatives which retain or even improve the cytotoxic activity have been studied, but these are weak inhibitors of topoisomerase II *in vitro*; the data revealed that such analogs exhibit a different, as yet unknown, mechanism of action. The main deficiency of these compounds is their cytotoxicity for normal cells and hence the side effects derived from their lack of selectivity against tumoral cells. With this regard it is necessary to investigate and prepare new more potent and less toxic analogs, with better therapeutic indices.

5. Synthetic Routes

Since its first isolation in 1953 (Hartwell et al., 1953), podophyllotoxin (**1**) and its isomers have been the subject of numerous synthetic endeavours (Pelter et al., 1998), (Ward 1990, 1992, 2004).

The particular challenge for podophyllotoxin (**1**) is in establishing the 1,2-*cis* stereochemistry together with a *trans* lactone ring fusion (Sellars & Steel, 2007). Because of the different stability of the stereoisomers, on mild base treatment, podophyllotoxin undergoes rapid epimerisation to afford a 97.5:2.5 mixture of picropodophyllin and podophyllotoxin (Gensler & Gatsonis, 1966).

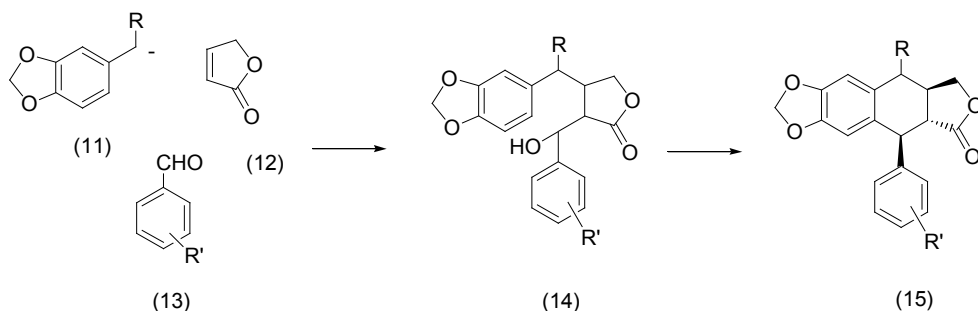
PM3 calculations show in fact that podophyllotoxin and GL-331 are 1.1 kcal/mol more stable than isopodophyllotoxin and iso-GL-331 respectively (Rindone, 2009).

a) C-Ring Formation by Aryl Substitution

The most common approach for the aryltetralin lactone skeleton is the electrophilic aromatic substitution forming the C1-C6 bond and simultaneously establishing the stereochemistry at C1. A three-component coupling strategy for aryltetralin lignan lactone synthesis is shown in Scheme 4.

This involves an acyl anion equivalent (**11**), a butenolide Michael acceptor (**12**) and an aldehyde (**13**). Intermediate (**14**) is formed and is cyclised to compound (**15**), having a 1,2-*trans*,2,3-*trans* stereochemistry (Pelter et al, 1990), (Gonzales et al., 1978) (Van Speybroek et al. 1991).

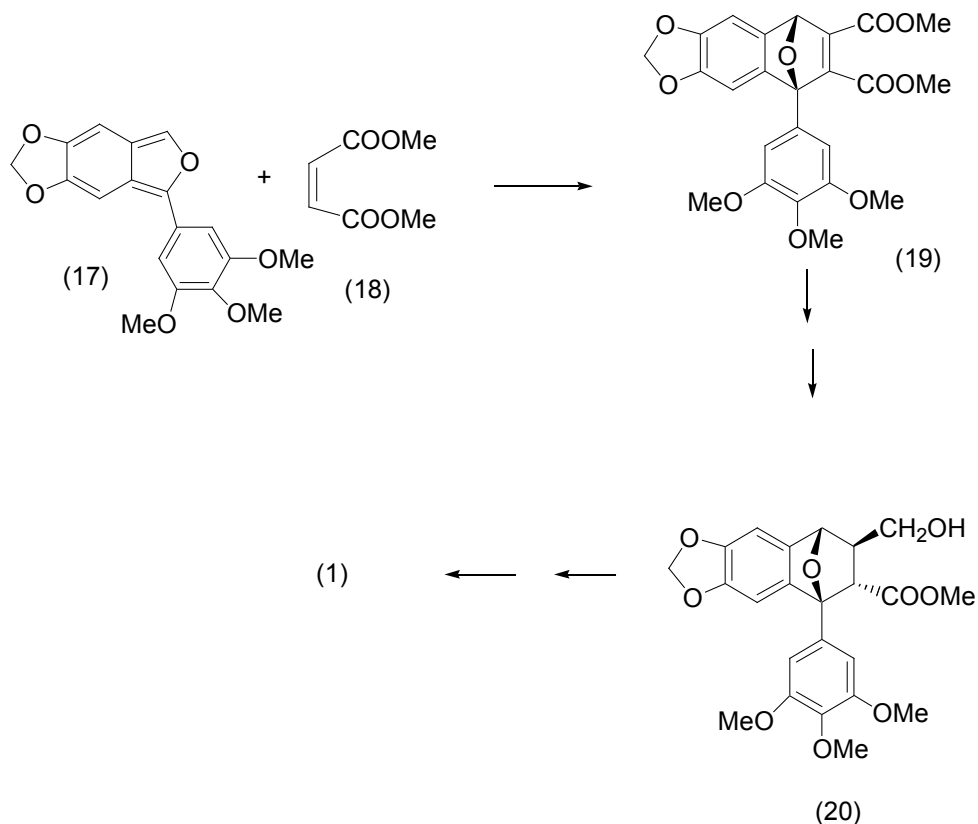
Scheme 4



b) C-Ring Formation by Cycloaddition Reactions

The other principal strategy for the construction of the cyclic system is the Diels-Alder reaction. The oxabicyclo adduct (**19**) derived from the isobenzofuran (**17**) and dimethylmaleate (**18**) gives an intermediate (**20**) which is further transformed into podophyllotoxin (**1**) (Rodrigo, 1980), (Rajapaksa & Rodrigo, 1981) (Forsey et al., 1989), (Jones et al., 1987), (Kuroda et al., 1996) (Scheme 5).

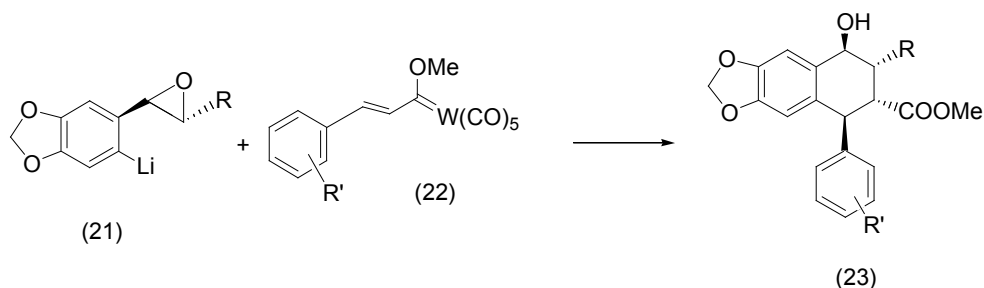
Scheme 5



c) C-Ring Construction via Michael Induced Ring Closure

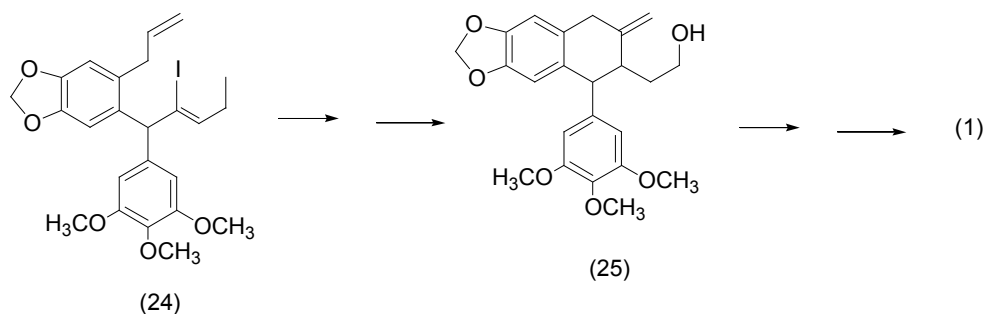
The application of a Michael-induced ring-closure using a chiral intermediate gives the formation of the *1,2-trans* stereochemistry. One example is the reaction of a tungsten-carbene (**22**) with the chiral methylenedioxyalkylstyrene epoxide (**21**) to form a reaction product (**23**) having a *1,2-trans,2,3-cis* stereochemistry (Kende et al., 1981), (Capriati et al., 2005) (Scheme 6).

Scheme 6



Alternatively, an intramolecular Heck reaction starting from the iododerivative (**24**) forms compound (**25**), subsequently transformed into podophyllotoxin (**1**) (Kennedy-Smith et al., 2004) (Scheme 7).

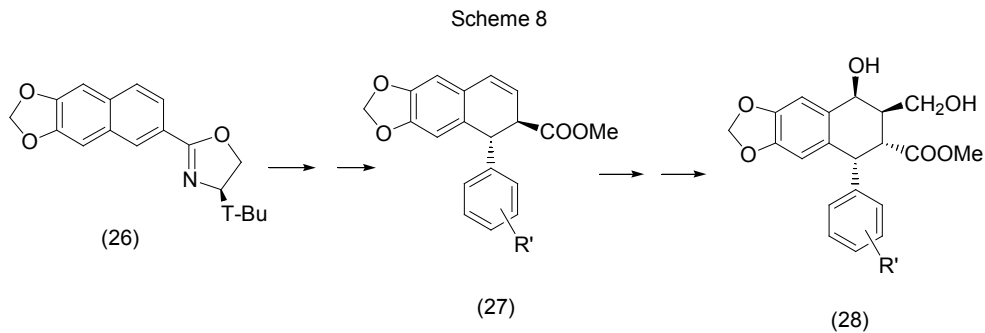
Scheme 7



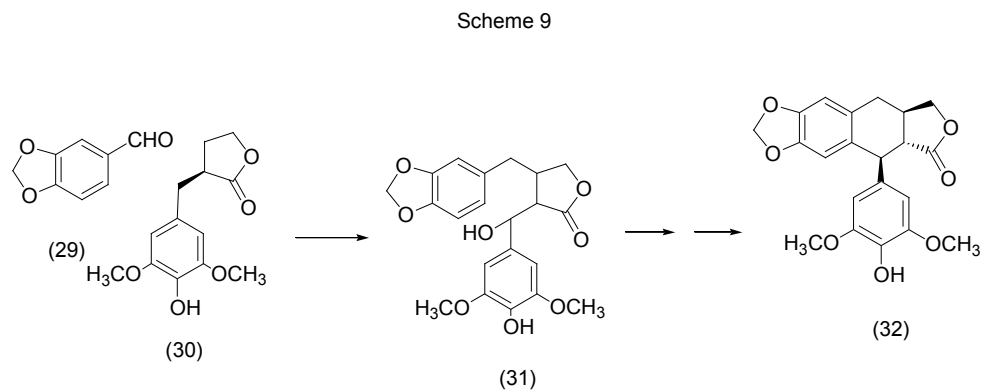
d) The use of chiral auxiliaries

Some other synthetic pathways have been performed introducing in the molecule a chiral auxiliary intended to drive the formation of the stereogenic centers in reactions performed using the methodologies exposed in the preceding paragraphs.

d1): The enantioselective dearomatisation of a naphthalene derivative (**26**) resulted in the generation of the *1,2-trans* stereochemistry in (**27**) which may be converted into (**28**), having *1,2-trans,2,3-cis* stereochemistry (Scheme 8) (Andrews et al, 1988).

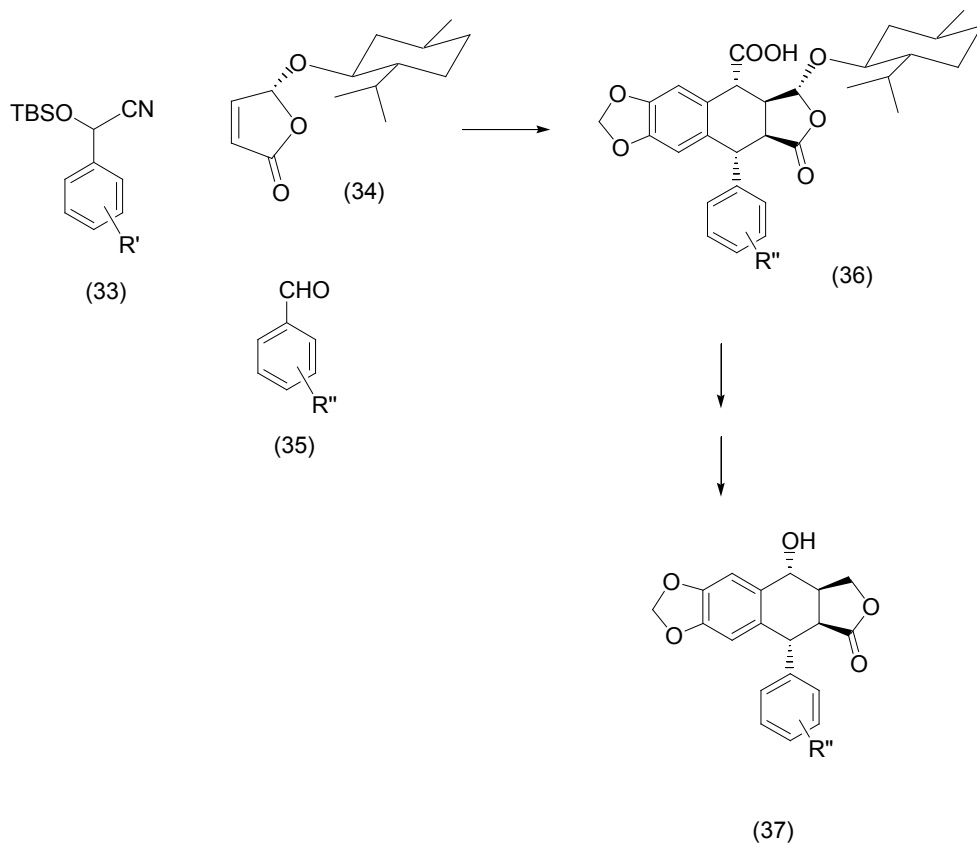


d2): The condensation of a chiral benzyl- γ -butyrolactone (**30**) with piperonal (**29**) gives compound (**31**). Subsequent alkylation and cyclization gives demethyldeoxyisopodophyllotoxin (**32**), having a *1,2-trans,2,3-trans* stereochemistry (Engelhardt et al. 2003) (Scheme 9).



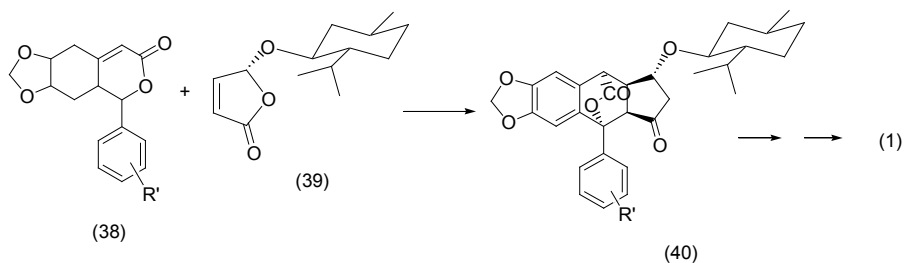
d3): The conjugate addition of the menthyl derivative (34) with the benzyl cyanide (33) and a substituted benzaldehyde (35) gave intermediate (36). Removal of the menthyl fragment resulted in the formation intermediate (36) and then of aryltetraline (37) with a 1,2-*trans*, 2,3-*cis* stereochemistry (Ward et al., 1998) (Scheme 10).

Scheme 10



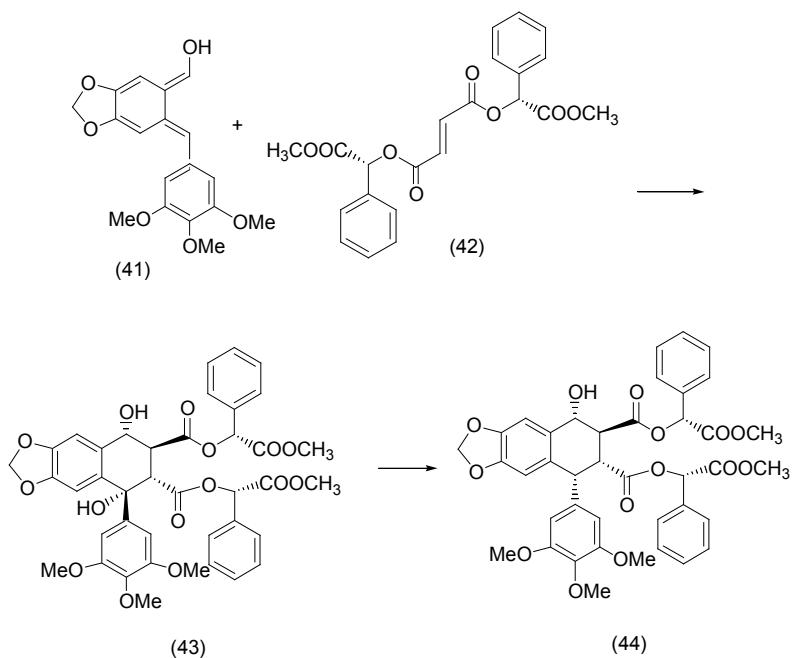
d4): Menthyloxyfuranone (**39**) and pyrones (**38**) gave the *endo* adduct (**40**) which was transformed into podophyllotoxin (**1**) with 1,2-*cis*-2,3-*trans* stereochemistry by acid-promoted elimination of the lactone bridge in intermediate (**40**) (Bush & Jones, 1996) (Scheme 11).

Scheme 11



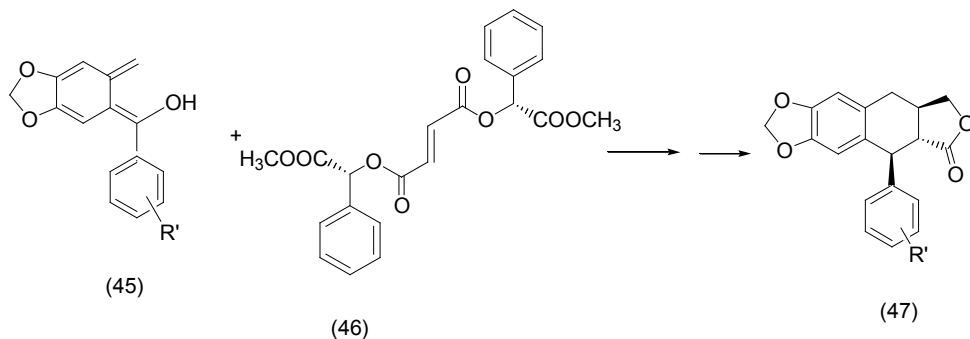
d5): A Diels-Alder cycloaddition between the fumarate of methyl (*S*)-mandelate (**42**) and α -hydroxy- α -aryl-o-quinodimethane (**41**) produces an *endo* cycloadduct (**43**) which may be converted into optically pure (-)-deoxypodophyllotoxin (**44**) having 1,2-*cis*,2,3-*trans* stereochemistry (Bogucky & Charlton, 1995) (Scheme 12).

Scheme 12



d6): A Diels-Alder cycloaddition between the fumarate of methyl (*S*)-mandelate (**46**) and α -hydroxy- α' -aryl-o-quinodimethane (**45**) gives optically pure (-)- α -dimethylretrodendrin (**47**) having a *1,2-trans-2,3-trans* stereochemistry, and three of its diastereomers (Scheme 13) (Charlton et al., 1990), (Charlton & Koh, 1992), (Maddaford & Charlton, 1993).

Scheme 13



6. The biomimetic strategy

One alternative is the biomimetic pathway, using the oxidative phenol coupling reaction which is the strategy the cell uses for the biosynthesis of lignans.

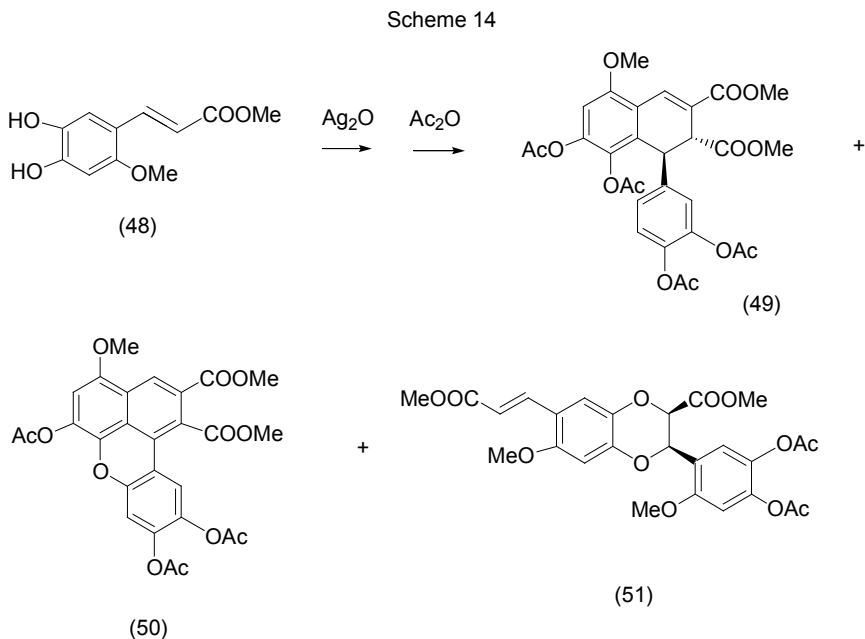
Recently Lewis has proposed a new biosynthetic pathway to enantiopure lignans. A protein isolated from *Forsythia* species is suggested to be responsible for the formation of enantiomeric pure pinoresinol from coniferyl alcohol (Lewis & Davin, 1999). In this case, the protein acts as a chiral inducer. The role of the directing protein is supposed to be at the level of 8-8 coupling of phenols.

The *in vitro* bimolecular phenoxy radical coupling reaction is not under a strictly regio- and stereospecific control. This is due to the fact that phenoxy radicals are very persistent and the dimerization reaction is slow. Hence the stereogenic carbons formed in the oxidative phenol coupling reaction *in vitro* are racemic. Sarkanen has studied the radical phenol coupling since 1973 and he has demonstrated that the 8-8 coupling of phenols such as (*E*)-isoeugenol is remarkably stereospecific and produces exclusively *threo* compounds, whereas (*Z*)-isoeugenol gives *threo*- and *erythro*-coupling products in equal amounts. He has proposed that the differences in the probabilities of coupling modes in the oxidations of (*E*) and (*Z*)-isoeugenol must be considered to be due to the characteristics of these intermediate complexes rather than to the differences in spin densities (Sarkanen & Wallis, 1993).

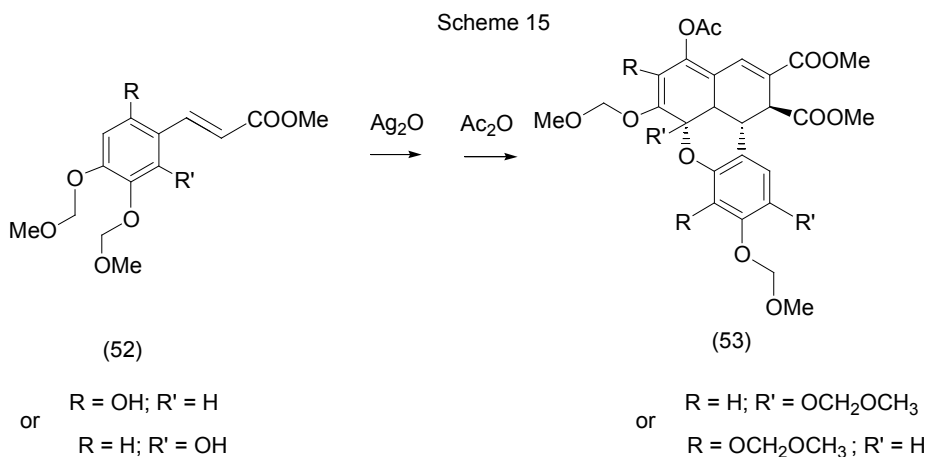
The enzymatic oxidative coupling of ferulic acid derivatives was observed by us to result in the diastereoselective synthesis of benzo[b]phenylcoumarans (Bolzacchini et al., 1998). Stereocontrol in this reaction to enantioselectively give benzo[b]phenylcoumarans has been recently shown by us to be possible (Rummalko et al., 1999) using a chiral inducer and the horseradish peroxidase (HRP)-catalyzed oxidative coupling in presence of hydrogen peroxide as the oxidant. The chiral inducers were aminoacid ethyl esters, camphorsultam and aryloxazolidinones (Bruschi et al., 2006).

6.1 Metal-mediated oxidative phenol coupling

a): The oxidative phenol coupling of compound **(48)** with silver oxide gave, after acetylation, a mixture of the aryltetraline **(49)**, with a *1,2-trans* stereochemistry and a 3,4 double bond, the benzo[*kl*]xanthene **(50)** and the benzodioxane **(51)** (Maeda et al., 1994) (Scheme 14).

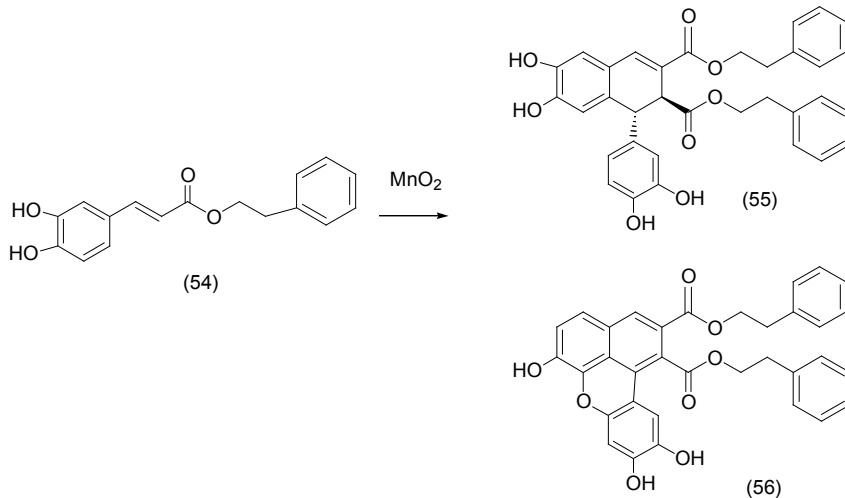


b) 2-hydroxycinnamates **(52)** underwent oxidative phenol coupling with silver oxide to give, after acetylation, compound **(53)** (Maeda et al., 1995) having *1,2-trans* stereochemistry and a 3,4-double bond (Scheme 15).



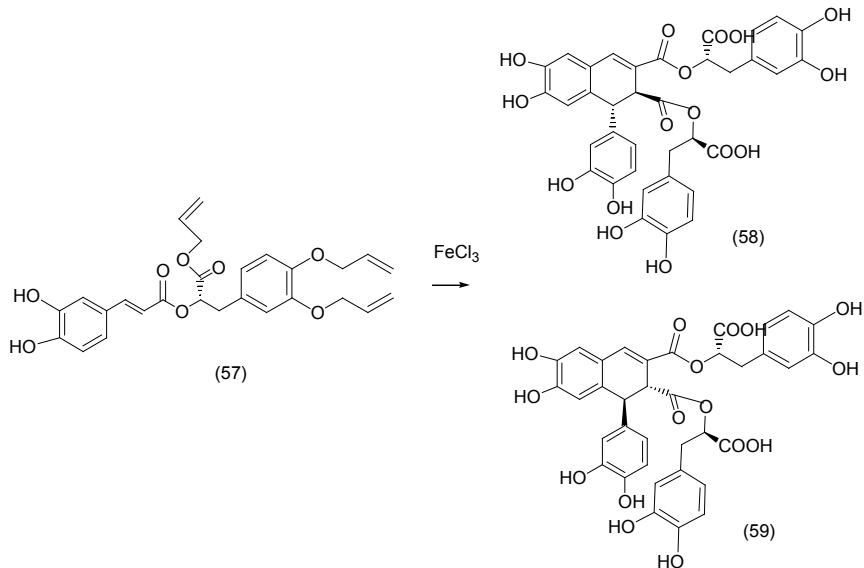
c:) With MnO_2 , the oxidative phenol coupling using compound **(54)** as the starting material gave the aryltetralin **(55)** having a *1,2-trans* stereochemistry and a *3,4*-double bond and the benzo[*k*]xanthen **(56)** (Scheme 16) (Daquino et al., 2009).

Scheme 16



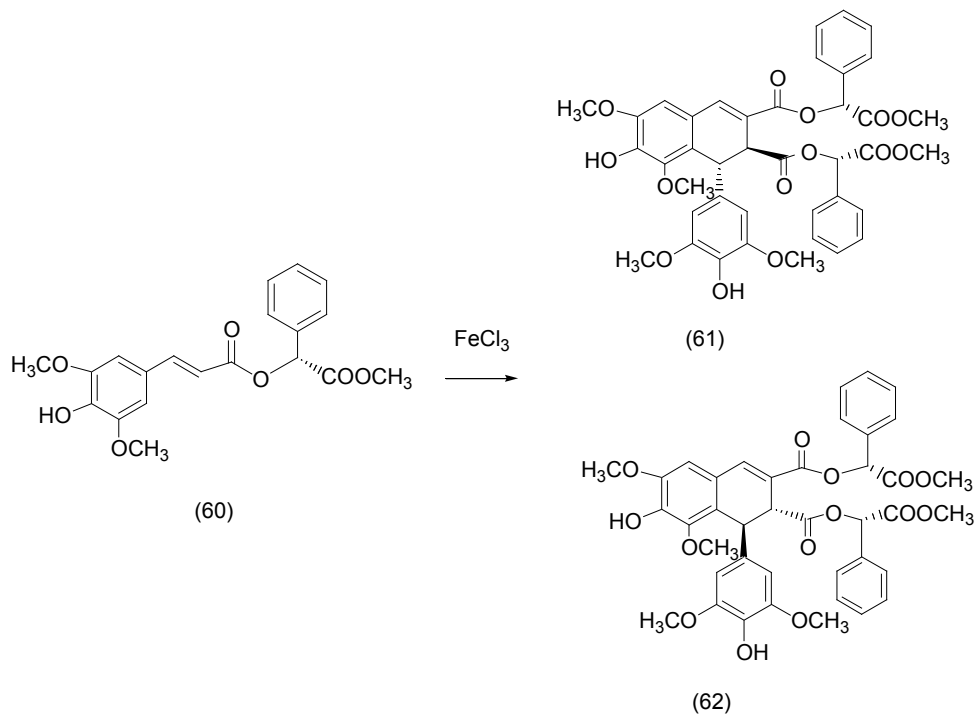
d:) The triallyl derivative of (*S*)-rosmarinic acid **(57)** was submitted to FeCl_3 -assisted oxidative phenol coupling forming the diastereoisomers **(58-59)** of rabsosin, having a *1,2-trans* stereochemistry and *3,4*-double bond (Bogucki & Charlton, 1997) (Scheme 17).

Scheme 17



e:) (*R*)-mandelyl sinapate (**60**) was diastereoselectively transformed by FeCl₃-assisted oxidative phenol coupling into trans-thomasidioate diester (**61-62**), having a *1,2-trans* stereochemistry and a 3-4 double bond (Bogucki & Charlton, 1997) (Scheme 18).

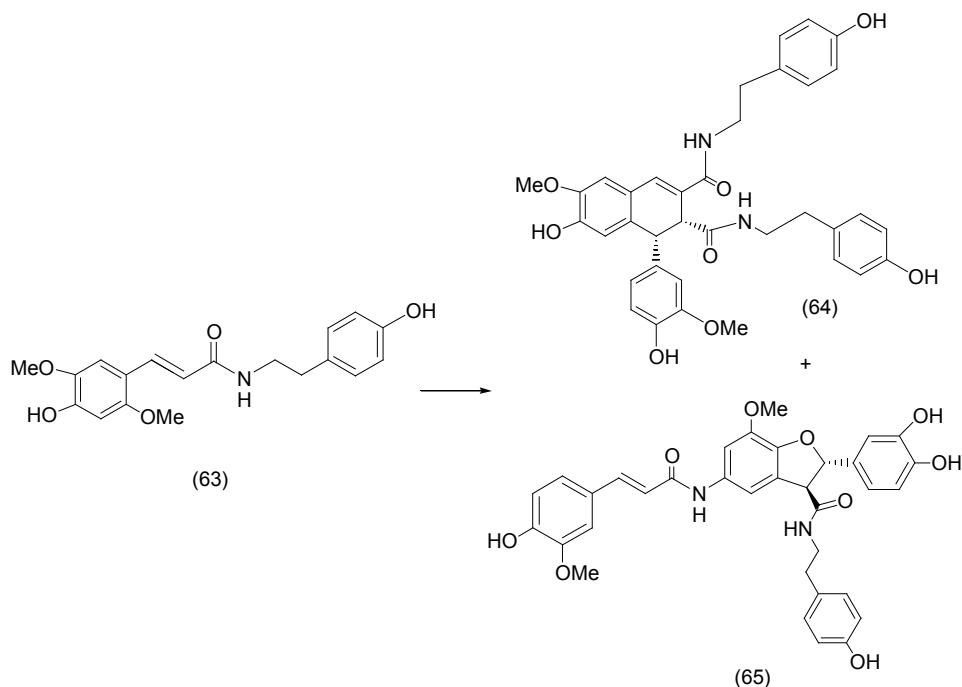
Scheme 18



6.2 Enzyme-catalyzed oxidative phenol coupling

a:) Amide (**63**), submitted to oxidative phenol coupling with hydrogen peroxide in the presence of horseradish peroxidase gave a mixture of the levorotatory isomer of the aryltetraline cannabisin (**64**), having a *1,2-cis* stereochemistry and a 3,4 double bond, and the phenylcoumaran grossamide, (**65**) (Scheme 19) (Lajide et al., 1995).

Scheme 19



b) The enantioselective oxidative phenol coupling of sinapic acid derivatives (**66**) (Scheme 18) having an amide bond with (*S*)-phenylalanine ethyl ester, (*S*)-methylbenzylamine, (*S*)-2-phenyloxazolidinone as chiral auxiliaries was performed using hydrogen peroxide as the oxidant and horseradish peroxidase as the catalyst (Zoia et al., 2008).

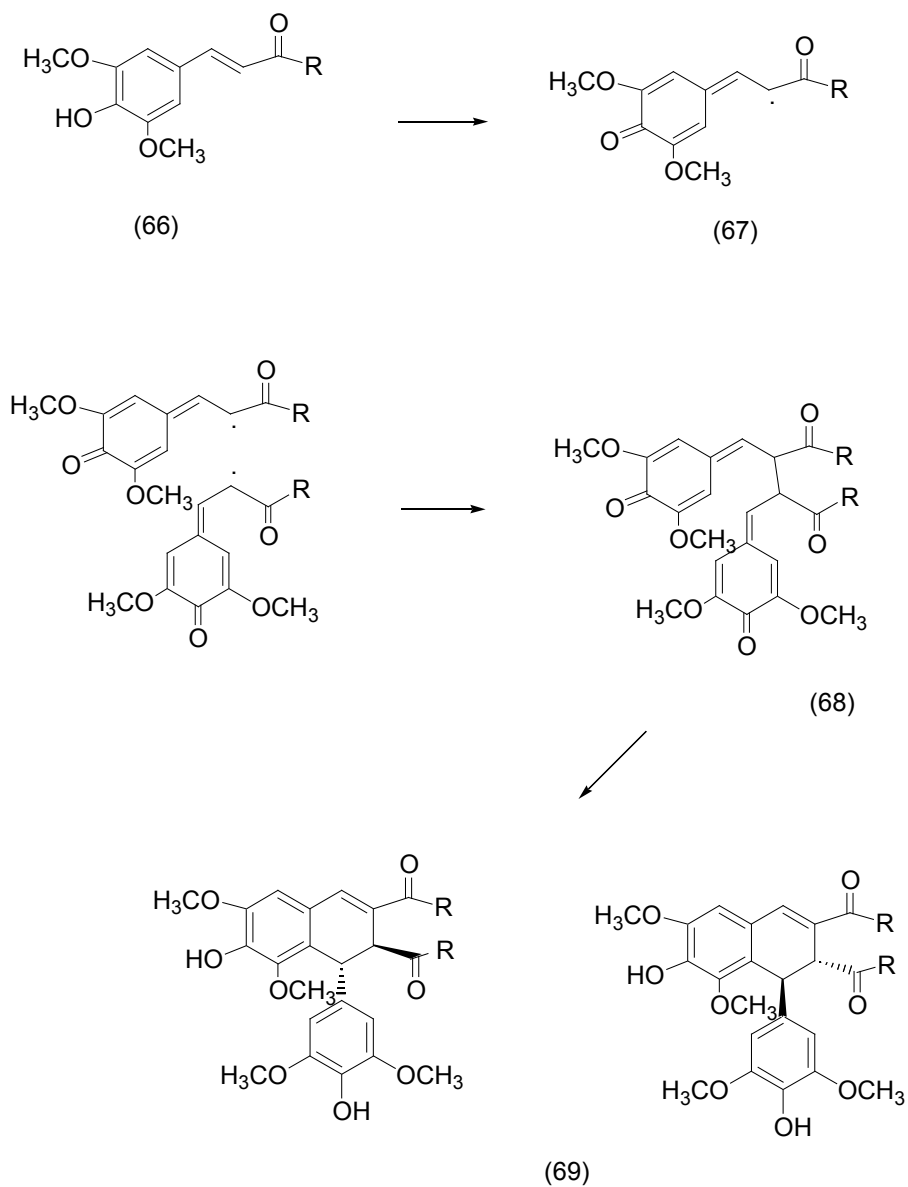
The proposed reaction pathway involves two steps; the first step is the 8-8 oxidative coupling of two phenoxy radicals (**67**) to give the bisquinomethide (**68**), and the second step is the ring closure of (**68**) to give the final product. For this mechanism the absolute configuration of thomasidioic acid amide (**69**) should be determined by the absolute configuration of the two stereogenic centers of the bisquinomethide (**68**) formed in the 8-8 oxidative coupling, and by its *trans* or *cis* ring closure (Scheme 20).

The computed profile along the reaction pathway for the 8-8 coupling at the *re-re*, *si-si*, and *re-si* faces shows that the energy barrier calculated for the *si-si* coupling is higher by more than 4 kcal mol⁻¹ than that calculated for the *re-re* and *re-si* coupling. This result suggests that the formation of the *R,R* (from *re-re* coupling), and *R,S/S,R* (from *re-si* coupling) bisquinomethide (**68**) is preferred with respect to the formation of the *S,S* (from *si-si* coupling) bisquinomethide (**68**).

The cyclization step determines the observed diastereoselection to the *trans* isomer. The diastereoselection should be controlled by the relative orientation of the two quinomethide rings which should feature a preferred conformation in order to give the "correct" ring closure, as well as to the energy of the transition state along the reaction path to give the final product.

A conformational analysis was performed in order to predict the enantioselectivity in the formation of *trans*-thomasidic acid amide (**69**) from quinomethide (**68**) having a (*S*)-2-phenyloxazolidinone chiral auxiliary group.

Scheme 20



Our computational investigation of the 8-8 oxidative coupling of quinomethide radical (67) shows that the *R,R*, *S,S* and *R,S*, *S,S* isomers of bisquinomethide (68) should be formed in larger amounts with respect to the *S,S*, *S,S* isomer. The former, after aromatization preserves only one *R* centre that gives ring closure to the *trans* 1*S*,2*R* absolute configuration, while the latter after aromatization can preserve both an *R* or *S* centre, giving ring closure to both the *trans* 1*S*,2*R*, and 1*R*,2*S* absolute configurations. Hence, the configuration of thomasidioic acid amide (69) from this enantioselective synthesis is predicted to be 1*S*,2*R*.

7. References

- Advani R., Horning S.J., *J. Natl. Compr. Canc. Netw.*, **2006**, 4 (3), 241-7.
- Andrews, R. C., Teague, S. J., Meyers, A. I., *J. Am. Chem. Soc.*, **1988**, 110, 7854-7858.
- Ayers, D., C.; Loike, J. D.; *Lignans. Chemical biological and clinical properties*; Cambridge University Press, Cambridge **1990**, pp 278-373.
- Bernards, M. A.; Lopez, M. L.; Zajicek, J.; Lewis, N. G.; *J. Biol. Chem.*, **1995**, 270, 7382-7387.
- Bett, W. R., *Practitioner* **1951**, 166, 77.
- Beutner, K. R.; Ferenczy, A. *Am. J. Med.* **1997**, 102, 28-37.
- Bolzacchini, E.; Brunow, G.; Meinardi, S.; Orlandi, M.; Rindone, B.; Rummakko, P.; Setälä, H.; *Tetrahedron Lett.*, **1998**, 39, 3291-3294.
- Bogucki; D. E., Charlton, J. L., *J. Org. Chem.*, **1995**, 60, 588-593.
- Bogucki, D. E., Charlton, J. L., *Can. J. Chem.*, **1997**, 75, 1783-1794.
- Bookman, M. A., McMeekin, D. S., Fracasso, P. M., *Gynecologic Oncology*, **2006**, 103(2), 473-478.
- Botta B., Delle Monache G., Misiti D., Vitali A., Zappia G., *Current medicinal Chemistry*, **2001**, 8 (11), 1363-81, 2001.
- Bruschi. M.; Orlandi. M.; Rindone, B.; Rummakko, P.; Zoia, L.; *J. Phys. Org. Chem.*, **2006**, 19, 592-596.
- Bush, E. J., Jones, D. W., *J. Chem. Soc. Perkin Trans. 1*, **1996**, 151-155.
- Capriati, V. Florio, S., Luisi, R., Perna, F. M., Salomone, A., Gasparrini, F., *Org. Lett.* **2005**, 7, 4895-4898.
- Charlton, J. L., Plourde, G. L., Koh, K., Secco, S., *Can. J. Chem.*, **1990**, 68, 2022-2027
- Charlton, J. L., Koh, K., *J. Org. Chem.* **1992**, 57, 1514-1516
- Collier K., Schink C., Young A.M., How K., Seckl M., Savage P., *J. Oncol. Pharm. Pract.* **2008**, 14 (1), 51-5.
- Cragg, G., Suffness, M., *Pharmacol. Ther.* **1988**, 37, 425-461
- Creaven, P. J., *Cancer Chemother. Pharmacol.* **1982**, 7, 133-140.
- Damayanthi Y., Lown J.W., *Curr Med Chem.* **1998**, Jun 5 (3), 205-52.
- Daquino, C., Spatafora, C., Tringali, C., unpublished results.
- Dow, L. W., Sinkule, J. A., Look, A. T., Horvath, A. Evans, W. E., *Cancer Res.* **1983**, 43, 5699-5706
- Engelhardt, U., Sarkar, A., Linker, T., *Angew. Chem. Int. Ed.* **2003**, 42, 2487-2489.
- Feldman D.R., Bosl G.J., Scheinfeld J., Motzer R.J., *JAMA*, **2008**, 299 (6): 672-84.
- Forsey, S. P., Rajapaksa, D., Taylor, N. J., Rodrigo, R., *J. Org. Chem.* **1989**, 54, 4280-4290
- Gensler, W. J., Gatsonis, C. D., *J. Org. Chem.* **1966**, 31, 3224-3227.
- Gonzalez, A. G., Perez, J. P., Trujillo, J. M., *Tetrahedron* **1978**, 34, 1011-1013

- Gordaliza M., Castro M.A., del Corral J.M., Feliciano A.S., *Curr Pharm Des.*, **2000**, 6 (18), 1811-39.
- Hande K.R., Wedlund P.J., Noone R.N. et al., *Cancer Res*, **1984**, 44: 379-82.
- Hande K.R., *Eur. J. Cancer*, **1998**, 34 (10), 1514-21.
- Hartwell, J. L., Johnson, J. M., Fitzgerald, D. B., Belkin, M., *J. Am. Chem. Soc.* **1953**, 75, 235-236.
- Higuchi, T.; Biosynthesis of Lignin, In *Biosynthesis and Biodegradation of Wood Component* Higuchi, T. Ed.; Academic Press Inc., New York **1985**, pp 141-148.
- Hussain S.A., Ma Y.T., Cullen M.H., *Expert Rev. Anticancer Ther*, **2008**, 8 (5): 771-84.
- Kell J., *Rev. Recent Clin. Trials* **2006**, 1 (2), 103-11.
- Keller-Juslen, C., Kuhn, M., Stahelin, H., von Wartburg, A., *J. Med. Chem.* **1971**, 14, 936-940.
- Kende, A. S., King, M. L., Curran, D. P., *J. Org. Chem.* **1981**, 46, 2826-2828
- Kennedy-Smith, J. J., Young, L. A., Toste, F. D. *Org. Lett.* **2004**, 6, 1325-1327.
- Kluin-Nelemans H.C., Zagonel V., Anastasopolou A., Bron D., Roodendaal K.J., Noordijk E.M., Musson H., Teodorovic I., Maes B., Carbone A., Carde P., Thomas J., *J. Natl. Cancer Inst.*, **2001**, 93 (1), 22-30.
- Kuo Hsiung-Lee, *Antitumor Agents* 188, 2000.
- Kuroda, T., Takahashi, M., Kondo, K., Iwasaki, T., *J. Org. Chem.* **1996**, 61, 9560-9563.
- Ionkova, I. *Pharmacognosy Reviews* **2007**, 1(1), 57-68.
- Jardine, I., *Anticancer Agents based on Natural Products*, Academic Press, New York, **1980**.
- Jones, D. W., Thompson, A. M., *J. Chem. Soc. Chem. Commun.* **1987**, 1797-1798
- Lajide, L., Escoubas, P., Mizutani, J. *Phytochemistry*, **1995**, 40, 1105-1112.
- Lewis, N, G.; Davin, L. B. *Lignans: biosynthesis and function*. In *Comprehensive Natural Products Chemistry, vol 1*; Barton, Sir D. H. R.; Nakanishi, K.; Meth-Cohn, O., (Eds.); Elsevier: Oxford, UK, **1999**; pp. 639-712.
- Liu Y.Q., Yang L.M., Tian X., *Curr. Bioactive Compounds*, **2007**, 3 (1), 37-66.
- Maddaford, S. P.; Charlton, J. L.; *J. Org. Chem.*, **1993**, 58, 4132-4138.
- Maeda, S., Masuda, H., Tokoroyama, T., *Chem. Pharm. Bull.*, **1994**, 42, 2506-2513.
- Maeda, S., Masuda, H., Tokoroyama, T., *Chem. Pharm. Bull.*, **1995**, 43, 35-40.
- Martindale, R. G., *The Complete Drug Reference*, 35th edition, **2007**.
- Meresse, P.; Dechaux, E.; Monneret, C.; Bertounesque, E. *Curr. Med. Chem.* **2004**, 11, 2443-2466.
- Pelter, A., Ward, R. S., Pritchard, M. C., Kay, I. T. *J. Chem. Soc. Perkin Trans. 1*, **1988**, 1603-1613
- Pelter, A., Ward, R. S., Jones, D. M., Maddocks, P., *Tetrahedron: Asymmetry* **1990**, 1, 855-856
- Quoix E., Breton J.L., Daniel C., Jacoulet P., Debievre D., Paillot N., Kessler R., Moreau L., Liu Y.Q., Yang L.M., Tian X., Coetmeur D., Lemarié E., Milleron B., *Ann. Oncol.*, **2001**, 12 (7), 957-62..
- Ragan, M. A.; *Phytochemistry*, **1984**, 23, 2029-2032.
- Rajapaksa, D., Rodrigo, R., *J. Am. Chem. Soc.* **1981**, 103, 6208-6209
- Reif S., Kingreen D., Kloft C., Grimm J., Siegert W., Schunack W., Jaehende U., *Cancer Chemoth. Pharmacol*, **2001**, 48 (2), 134-40.
- Rindone, B. Unpublished results
- Rodrigo, R., *J. Org. Chem.* **1980**, 45, 4538-4540
- Rummalko, P.; Brunow, G.; Orlandi, M.; Rindone, B.; *Synlett*, **1999**, 333-335.
- Sarkanen, K. V.; Wallis, A. F. A. *J. Chem. Soc. Perkin I* **1973**, 1869-1878.

- Sellars J.D., Steel P.G., *European J. of Organic Chemistry* **2007**, 23, 3815-28.
- Van Speybroeck, R., Guo, H., Van der Eycken, J., Vandewalle, M., *Tetrahedron* **1991**, 47, 4675-4682.
- Ward, R. S., *Chem. Soc. Rev.* **1982**, 11, 75-125.
- Ward, R. S., *Tetrahedron* **1990**, 46, 5029-5041.
- Ward, R. S., *Synthesis* **1992**, 719-730.
- Ward, R. S. Lignans, neolignans and related compounds. *Nat. Prod. Rep.* **1997**, 14, 43-74.
- Ward, R. S., Pelter, A., Brizzi, A., Sega, A., Paoli, P., *J. Chem. Res.* **1998**, 226-227.
- Ward, R. S., *Phytochem. Rev.* **2004**, 2, 391-400
- Weiss, S. G., Tin-Wa, M., Perdue, R. E., Farnsworth, N. R., *J. Pharm. Sci.* **1975**, 64, 95-98
- Xiao, Z., Vance, J. R., Bastow, K. F., Brossi, A., Wang, H. K., Lee K. H., *Bioorg. Med. Chem.* **2004**, 12, 3363-3369.
- Yee D., Danielson B., Roa W., *Rev. Recent Clin. Trials*, **2008**, 3 (2), 150-5.
- Zoia, L., Bruschi, M. Orlandi, M., Tollpa, E. L., Rindone, B., *Molecules*, **2008**, 13, 129-148.

Superhydrophobicity, Learn from the Lotus Leaf

Mengnan Qu^a, Jinmei He^a and Junyan Zhang^b

^a*College of Chemistry and Chemical Engineering,
Xi'an University of Science and Technology
Xi'an 710054, P.R. China*

^b*State Key Laboratory of Solid Lubrication,
Lanzhou Institute of Chemical Physics,
Chinese Academy of Sciences,
Lanzhou 730000, P.R. China*

1. Introduction

As early as the eleventh century, the Song dynasty of China, one scholar named Zhou Dunyi (1017-1073), had planted the lotus all over the poll in his home and wrote an article named *Ode to A Lotus Flower*. From then on, in the East Asian countries and regions, especially the ancient China, the lotus flower and its leaves are frequently compared to one's noble spirit and purity because of "live in the silt but not sullied". Zhou Dunyi was thus memorized by this ode and the sentence "live in the silt but not sullied" was also came down to people today from that time.

This sentence displays an interesting phenomenon to us: the lotus' flowers and leaves unfold and stayed immaculacy by the pollution even when emerging from mud and muddy waters. Furthermore, in a pond after a rainfall, spherical water droplets on the lotus leaves, carrying effortlessly the contaminations attached on the leaves when the surface is slightly tilted, showing a self-cleaning function (Fig. 1a). The lotus, furthermore, is not the only type of plant in nature that the spherical water droplets can float on the leaves. Rice, for example, the main source of food for over half of the world population, is cultivated over a geographical range from 53°N to 40°S and to elevations of more than 2500 m (Guo & Liu, 2007). According to soil and water habitat, rice is generally classified into four broad categories: irrigated or paddy-grown rice, lowland rainfed rice, upland rice, and deep-water rice. Whatever the kind of rice is, we can easily find the interesting phenomenon that the rice leaf is very similar to the lotus leaves: their surfaces have the ability to resist water, and water droplets cannot wet on the leave surfaces.

In addition to the leaves of plants, a number of insects, their wings also have the ability to resists water to spread on their surfaces. The most representative example is the water strider (*Gerris remigis*). The water striders are famous for their nonwetting legs that enable them to stand on water effortlessly (Fig. 2a). The maximal supporting force of a single leg is 152 dyn (1 dyn = 1×10^{-5} N), which is about 15 times the weight of the insect (Gao & Jiang,

2004). Furthermore, butterflies and cicadas, the evolution bestowed them the self-cleaning ability which can keep them uncontaminated by removing dust particles, dew or water droplets easily from their wings, and bestowed them water-repellent ability which can keep their wings not be wetting in the rain. Many poultry, such as the duck and the swan, have also the ability that their feathers can resist the water to spread out on the whole body surfaces when they are floating on the water.

On the surface of the lotus leaves, the almost spherical water droplets will not come to rest and simply roll off if the surface is tilted even slightly, which is now usually referred to as the “**Lotus Effect**”. This effect belongs to the subfield of the wettability of solid surface and is also named as the “**Superhydrophobicity**”. The wetting behaviour of solid surfaces by a liquid is a very important aspect of surface chemistry, which may have a variety of practical applications. When a liquid droplet contacts a solid substrate, it will either remain as a droplet or spread out on the surface to form a thin liquid film, a property which is normally characterized by means of the contact angle measurements. For a solid substrate, when the contact angle of water or oil on it is larger than 150° , it is called superhydrophobic or superoleophobic, respectively. On the other hand, when the contact angle of water or oil on a surface is almost 0° , it is called superhydrophilic or superoleophilic, respectively. Among the four kinds of surfaces, the superhydrophobic surfaces are referred to as self-cleaning surfaces and the contamination on them is easily removed by rolling droplets and as such this type of surface has obviously great potential uses, as water will not “stick” to it.

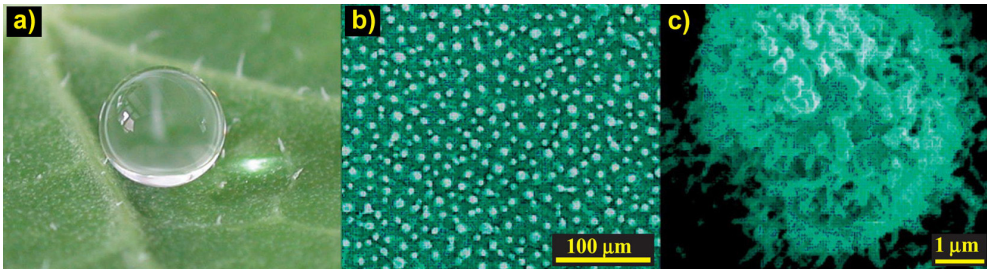


Fig. 1. (a) An almost ballshaped water droplet on a non-wettable plant leaf (Blossey, 2003). (b) Low- and (c) high-magnification scanning electron microscope images of the surface structures on the lotus leaf. Every epidermal cell forms a micrometer-scale papilla and has a dense layer of epicuticular waxes superimposed on it. Each of the papillae consists of branchlike nanostructures (Zhai et al., 2002). (Reproduced with permission from the Nature Publishing Group, Copyright 2003, and from the Chinese Physical Society, Copyright 2002.)

People have noticed these interesting nature phenomena quite a long time, while it is impossible to find out the essence under the science conditions at ancient time. The developments of analytical instruments are always promoting the level of human cognition. In the past two scores years, by means of scanning electron microscope, the studies of biological surfaces have revealed an incredible microstructural diversity of the outer surfaces of plants. Not until W. Barthlott and C. Neinhuis, Boon University, Germany, have research the lotus leaves systematically did people completely realized the mechanism of the lotus leaves to resist water. Barthlott and coworkers investigated the micro-structure of

the lotus leaves with a scanning electron microscope and hold that the surface roughness in micro-meter scale papillae and the wax layer of the surface were synergistic bestowed the superhydrophobicity to the surface of lotus leaves (Barthlott & Neinhuis, 1997). Further, detailed scanning electron microscopy images of lotus leaves indicated that their surfaces are composed of micro- and nanometer-scale hierarchical structures, that is, fine-branched nanostructures (ca. 120 nm) on top of micropapillae (5–9 μm) (Fig. 1b and 1c). The cooperation of these special double-scale surface structures and hydrophobic cuticular waxes is believed to be the reason for the superhydrophobicity (Feng et al., 2002; Zhai et al., 2002). Jiang and coworkers investigated the water strider's legs by the means of scanning electron microscope and revealed that the leg is composed of numerous needle-shaped setae with diameters on the microscale and that each microseta is composed of many elaborate nanoscale grooves (Fig. 2b and 2c). Such a hierarchical surface structure together with the hydrophobic, secreted wax is considered to be the origin of the superhydrophobicity of the water strider's legs (Gao & Jiang, 2004).

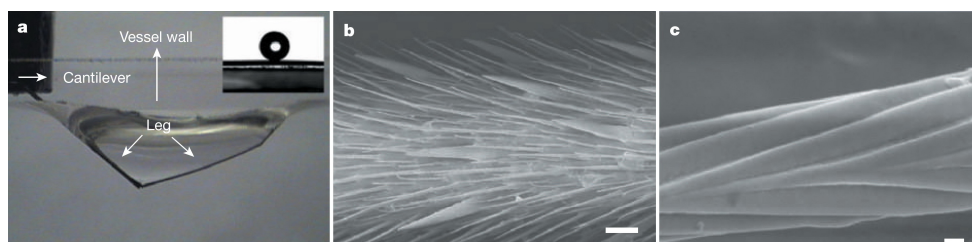


Fig. 2. The non-wetting leg of a water strider. (a) Typical sideview of a maximal-depth dimple (4.38 ± 0.02 mm) just before the leg pierces the water surface. Inset, water droplet on a leg; this makes a contact angle of $167.6 \pm 4.4^\circ$. (b), (c) Scanning electron microscope images of a leg showing numerous oriented spindly microsetae (b) and the fine nanoscale grooved structures on a seta (c). Scale bars: (b), 20 μm ; (c), 200 nm. (Gao & Jiang, 2004). (Reproduced with permission from the Nature Publishing Group, Copyright 2004.)

2. The Related Fundamental Theories

The shape of a liquid droplets on solid surface, may be flat, hemisphere or spherical, and is governed by the surface tensions. Figure 3 showed the two typical states of the liquid droplet on a solid surface. The surface tensions γ_{s-l} and γ_{v-l} attempt to make the droplet to shrink, while the tension γ_{s-v} attempts to make the droplet to spread out on the surface. When the droplets on surface reached equilibrium, the angle between the solid/liquid interface and the liquid/vapour interface was named as contact angle (θ). The value of the contact angle describes the degree of the liquid wetting the solid surface. The relationship between these parameters is commonly given by the famous Young's equation:

$$\cos\theta = (\gamma_{s-v} - \gamma_{s-l}) / \gamma_{v-l}$$

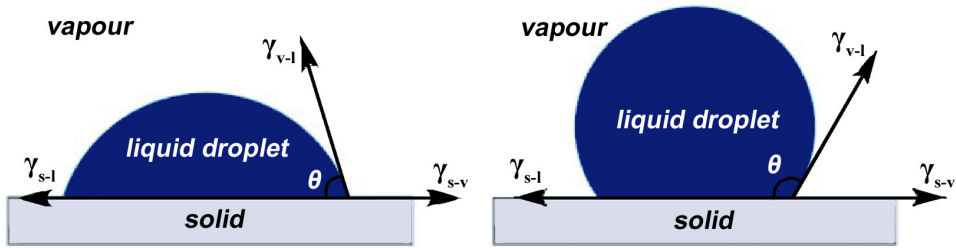


Fig. 3. The two typical states of the liquid droplets on a solid surface.

The Young's equation can be only applied for the chemical homogeneous and ideal flat surfaces. In actuality, few solid surfaces are truly flat, therefore, the surface roughness factor must be considered during the evaluation of the surface wettability. Wenzel and Cassie have developed Young's equation and worked out the Wenzel's equation and Cassie's equation, respectively. The two equations are commonly used to correlate the surface roughness with the contact angle of a liquid droplet on a solid surface. This improvement has made their application scope more wide than the Young's equation.

In 1936, Wenzel found that the surface roughness must be considered during the evaluation of the surface wettability (Wenzel, 1936). He hold that the liquid completely fills the grooves of the rough surface where they contact (Fig. 4a). The situation is described by equation:

$$\cos\theta_W = r (\gamma_{s-v} - \gamma_{s-l}) / \gamma_{v-l} = r \cos\theta$$

where θ_W is the contact angle in the Wenzel mode and r is the surface roughness factor. From this equation, it can be found that if the contact angle of a liquid on a smooth surface is less than 90° , the contact angle on a rough surface will be smaller, while the contact angle of a liquid on a smooth surface is more than 90° , the angle on a rough surface will be larger. These two situations can be described as: for $\theta < 90^\circ$, $\theta_W < \theta$; for $\theta > 90^\circ$, $\theta_W > \theta$.

In 1944, based on Wenzel's model, Cassie further developed and revised the Young's equation. He presented that the solids rough surface should be regarded as a solid-vapour composite interface and the vapour pockets were assumed to be trapped underneath the liquid (Fig. 4b). In this case, the solid-liquid-vapour three phase contact area can be represented by the f_s and f_v , which are the area fractions of the solid and vapour on the composite surface. Defining the contact angle in the Cassie mode as θ_C , θ_C can be correlated to the chemical heterogeneity of a rough surface by equation:

$$\cos\theta_C = f_s \cos\theta_s + f_v \cos\theta_v$$

Since $f_s + f_v = 1$, $\theta_s = \theta$, $\theta_v = 180^\circ$, the above equation can be written as equation:

$$\cos\theta_C = f_s (\cos\theta + 1) - 1$$

From the above equation it can be easily found that for a true contact angle more than 90° , the surface roughness will increase the apparent angle. This is unlike the Wenzel case, because even when the intrinsic contact angle of a liquid on a smooth surface is less than 90° , the contact angle can still be enhanced as a result of the as trapped superhydrophobic vapour pockets.

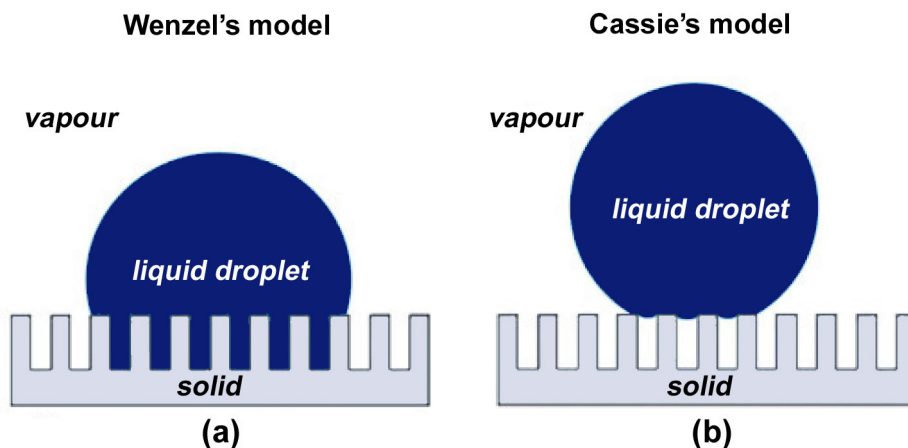


Fig. 4. (a) Wetted contact between the liquid and the rough substrate (Wenzel's model). (b) Non-wetted contact between the liquid and the rough substrate (Cassie's model).

The achievements of the Wenzel's and Cassie's models are that they have expressed the contact state between the liquid and the rough solid surface more realistically and exactly. Heretofore, Wenzel's and Cassie's models and equations are numerous applied for illustrating the mechanism of the superhydrophobic surfaces which were prepared by the material researchers in their articles.

With the emergence of the nanometer materials in 1960's, it promoted greatly the progress of the science and technology. Preparation and studies on the surface properties of the nanomaterials are the foundation of the nanoscience research. The emergence of the nanometer materials provides a good platform for the biomimetic materials research. Inspired by the microstructure of the natural water-resister, and based on the rapidly developed nanoscience and technology, material researchers have strong motivation to mimic the structure and the chemical component of the lotus leave surface for the biomimetic preparation of the superhydrophobic materials.

Heretofore, a variety of methods have been reported for constructing superhydrophobic surfaces by mimicking the surface of lotus leaves. These artificial superhydrophobic surfaces have been fabricated mostly by controlling the roughness and topography of hydrophobic surfaces and using techniques such as anodic oxidation, electrodeposition and chemical etching, plasma etching, laser treating, electrospinning, chemical vapour deposition, sol-gel processing, phase separation and so on. The materials that were used to fabricate the surface morphology ranged from carbon nanotubes, nanoparticles and nanofibers, metal oxide

nanorods, polymers to engineering alloys materials. In the following text, some most common and important preparation methods and the categories of the artificial superhydrophobic surfaces are introduced.

3. Methods for the Preparation of the Superhydrophobic Surfaces

3.1 Layer-by-Layer and colloidal assembly

The Layer-by-Layer assembly technique, which was developed by Decher's group, has been proved to be a simple and inexpensive way to build controllable chemical composition and micro- and nanometer scale (Decher & Hong, 1991). The greatest strength of the Lay-by-Layer technique is to control the thickness and the chemical properties of the thin film in molecular level by virtue of the electrostatic interaction and the hydrogen bond interaction between the molecules. Cohen, Rubner and coworkers prepared a surface structure that mimics the water harvesting wing surface of the Namib Desert beetle by means of Lay-by-Layer technique. The *Stenocara* beetle, which lived in the areas of limited water, uses their hydrophilic/superhydrophobic patterned surface of its wings to collect drinking water from fog-laden wind. In a foggy dawn, the *Stenocara* beetle tilts its body forward into the wind to capture small water droplets in the fog. After these small water droplets coalesce into bigger droplets, they roll down into the beetle's mouth, providing the beetle with a fresh morning drink. Cohen, Rubner and coworkers created the hydrophilic patterns on superhydrophobic surfaces by selectively delivering polyelectrolytes to the surface in a mixed water/2-propanol solvent to produce surfaces with extreme hydrophobic contrast (Zhai et al., 2006). Potential applications of such surfaces include water harvesting surfaces, controlled drug release coatings, open-air microchannel devices, and lab-on-chip devices. Sun and coworkers reported a facile method for preparing a superhydrophobic surface was developed by layer-by-layer deposition of poly(diallyldimethylammonium chloride)/sodium silicate multilayer films on a silica-sphere-coated substrate followed with a fluorination treatment. The superhydrophobic surface has a water contact angle of 157.1° and sliding angle of 3.1° (Zhang et al., 2007). The easy availability of the materials and simplicity of this method might make the superhydrophobic surface potentially useful in a variety of applications.

3.2 Electrochemical reaction and deposition

The electrochemical reaction and the electrochemical deposition are widely used for the preparation of the superhydrophobic materials. Zhang and coworkers reported a surface covered with dendritic gold clusters, which is formed by electrochemical deposition onto an indium tin oxide electrode modified with a polyelectrolyte multilayer, shows superhydrophobic properties after further chemisorption of a self-assembled monolayer of *n*-dodecanethiol (Zhang et al., 2004). When the deposition time exceeds 1000s, the contact angle reaches a constant value as high as 156° . Yan, Tusjii and coworkers reported a poly(alkylpyrrole) conductive films with a water contact angle larger than 150° (Fig. 5). The films were obtained by electrochemical polymerization of alkylpyrrole and are stable to temperature, organic solvents and oils. The surface of the film is a fractal and consists of an array of perpendicular needle-like structures (Yan et al., 2005).

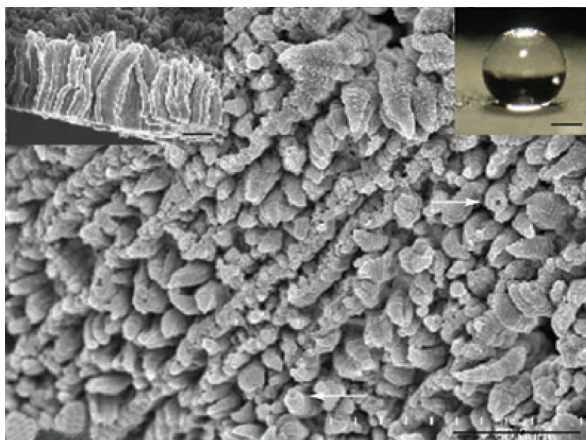


Fig. 5. Scanning electron microscopic image of the super water-repellent poly(alkylpyrrole) film (scale bar: $15\ \mu\text{m}$). Left inset: scanning electron microscopic image of the cross section of the film (bar: $15\ \mu\text{m}$). Right inset: image of a water droplet on the film (bar: $500\ \mu\text{m}$) (Yan et al., 2005). (Reproduced with permission from Wiley-VCH Verlag GmbH & Co. KGaA, Copyright 2005.)

Our group reported a Pt nanowire array superhydrophobic surface on a Ti/Si substrate by utilizing electrodeposition of Pt into the pores of anodic aluminium oxide templates and surface fluorination. The method can be extended to other metals to which the recently developed chemical etching method is not applicable (Qu et al., 2008). Zhou and coworkers reported a fabrication of superhydrophobic materials with a water contact angle of 178° using a perpendicular brucite-type cobalt hydroxide nanopin film fabricated with a bottom-up process (Fig. 6) (Hosono et al., 2005).

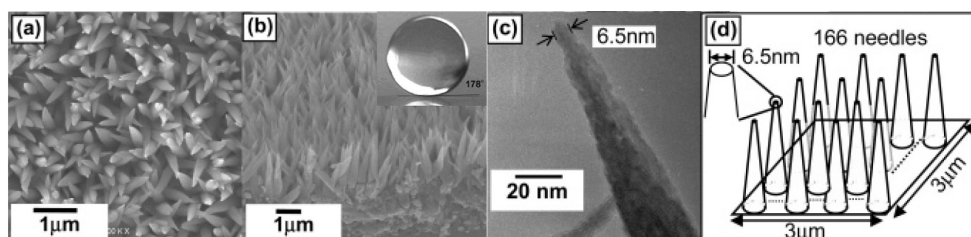


Fig. 6. (a,b) Field-emission scanning electron microscopic images of the brucite-type cobalt hydroxide films observed from the top and side, respectively. (c) Transmission electron microscope images of the films. (d) A simple model of the film with the fractal structure. Inset: image of a water droplet on the film with a contact angle of 178° (Hosono et al., 2005). (Reproduced with permission from the American Chemical Society, Copyright 2005.)

3.3 Sol-Gel Processing

For many materials, the sol-gel processing can also bestow the surface superhydrophobicity. Many research results showed that the surfaces can be made superhydrophobic while it

needs not the surface hydrophobic process after the sol-gel processing because that the low surface energy materials already exist in the sol-gel process. Shirtcliffe and coworkers reported superhydrophobic foams with contact angles greater than 150° which were prepared using a sol-gel phase-separation process. A rapid hydrophobic to hydrophilic transition was presented in the surface at around 400°C , generating a material that absorbed water rapidly (Shirtcliffe et al., 2003). Cho and coworkers reported a fabrication of superhydrophobic surface from a supramolecular organosilane with quadruple hydrogen bonding by a simple sol-gel processing at room temperature. Compared with other template syntheses, this approach to fabricating a phase-separated continuous material is a very simple way of producing a superhydrophobic coating and is made possible by the supramolecular characteristics of the novel organosilane (Han et al., 2004). Wu and coworkers prepared the ZnO surface with micro- and nanostructure via a wet chemical route. The surface showed superhydrophobic after the surface chemical modification with the moderate-length alkanolic acids (Wu et al., 2005).

3.4 Etching and Lithography

Etching is the most efficient way for the construction of rough surface. The detailed methods are plasma etching, laser etching, chemical etching et al. These methods have been greatly applied for the biomimic fabrication of the superhydrophobic surface. Teshima and coworkers formed an ultra water-repellent polymer sheet on a poly(ethylene terephthalate) substrate. Its nanotexture was formed on a poly(ethylene terephthalate) substrate surface via selective oxygen plasma etching and subsequent hydrophobic coating by means of low temperature chemical vapor deposition or plasma-enhanced chemical vapour deposition (Teshima et al., 2005). The as-prepared polymer sheets are transparent and ultra water-repellent, showing a water contact angle greater than 150° . Shen and coworkers reported fabrication of superhydrophobic surfaces by a dislocation-selective chemical etching on aluminium, copper, and zinc substrates (Qian & Shen, 2005). Our group developed a solution-immersion process to fabricate superhydrophobic surfaces on engineering materials, such as steel, copper alloy and titanium alloy by wet chemical etching and surface coating with fluoroalkylsilane (Qu et al., 2007). The synergistic effect of the two-lengthscale surface microstructures and the low surface energy of the fluorinated surface are considered to be responsible for this superhydrophobicity. Compared with the other methods, it is convenient, time-saving, and inexpensive. The as-fabricated superhydrophobic surfaces show long-term stability and are able to withstand salt solutions in a wide range of concentrations.

For the fabrication of large proportion and periodic micro- and nanopatterns, lithography, such as the electronic beam lithography, light lithography, X-ray lithography and nanospheres lithography, are fairly good methods. Riehle and coworkers fabricated ordered arrays of nanopits and nanopillars by an electronic beam writer with the desired pattern and investigated their dynamic wettability before and after chemical hydrophobization (Martines et al., 2007). These ordered patterns showed superhydrophobic after the surfaces were coated with octadecyltrichlorosilane. Tatsuma and coworkers reported superhydrophobic and superhydrophilic gold surfaces which were prepared by modifying microstructured gold surfaces with thiols (Notsu et al., 2005). The patterns required by the superhydrophobic surface were obtained by photocatalytic lithography using a TiO_2 -coated

photomask. The perfluorodecanethiol modified rough gold surface can be converted from superhydrophobic to superhydrophilic by photocatalytic remote oxidation using the TiO₂ film. On the basis of this technique, enzymes and algal cells can be patterned on the gold surfaces to fabricate biochips.

3.5 Chemical Vapor Deposition and Physical Vapor Deposition

The chemical and physical vapour depositions have been also widely used for the nanostructure fabrication and the chemical modification in the surface chemistry. Lau and coworkers deposited vertically aligned carbon nanotube forest with a plasma enhanced chemical vapor deposition technique, which is a fairly good technique that produces perfectly aligned, untangled (i.e., individually standing) carbon nanotubes whose height and diameter can be conveniently controlled (Lau et al., 2003). While after the depositing a thin hydrophobic poly(tetrafluoroethylene) coating on the surface of the nanotubes through a hot filament chemical vapor deposition process, the surface showed stable superhydrophobicity with advancing and receding contact angles are 170° and 160°, respectively. Furthermore, Lau and coworkers also reported a formation of a stable superhydrophobic surface via aligned carbon nanotubes coated with a zinc oxide thin film. The carbon nanotubes template was synthesized by chemical vapor deposition on a Fe-N catalyst layer. The ZnO film, with a low surface energy, was deposited on the carbon nanotubes template by the filtered cathodic vacuum arc technique. The ZnO-coated carbon nanotubes surface shows no sign of water seepage even after a prolonged period of time. The wettability of the surface can be reversibly changed from superhydrophobicity to hydrophilicity by alternation of ultraviolet irradiation and dark storage. Contact angle measurement reveals that the surface of the ZnO-coated carbon nanotubes is superhydrophobic with water contact angle of 159° (Huang et al., 2005). Jiang and coworkers demonstrated a honeycomb-like aligned carbon nanotube films which were grown by pyrolysis of iron phthalocyanine in the Ar/H₂ atmosphere by the physical vapour deposition (Li et al., 2002). Wettability studies revealed the film surface showed a superhydrophobic property with much higher contact angle ($163.4 \pm 1.4^\circ$) and lower sliding angle (less than 5°).

3.6 Electrospinning

Electrospinning is a very good method for the fabrication of the ultra-thin fibers. Heretofore, many groups have applied this technique to the preparation of the superhydrophobic surfaces. The merit of electrospinning is that the superhydrophobic surface can be obtained within one step. Rutledge and coworkers produced a block copolymer poly(styrene-*b*-dimethylsiloxane) fibers via electrospinning from solution in tetrahydrofuran and dimethylformamide (Ma et al., 2005). The submicrometer diameters of the fibers were in the range 150–400 nm and the contact angle measurements indicate that the nonwoven fibrous mats are superhydrophobic, with a contact angle of 163°. Jiang and coworkers reported a polyaniline/polystyrene composite film which was prepared via the simple electrospinning method (Zhu et al., 2006). The as-prepared superhydrophobic surface showed stable superhydrophobicity and conductivity, even in many corrosive solutions, such as acidic or basic solutions over a wide pH range, and also in oxidizing solutions.

4. The Category of the Artificial Superhydrophobic Materials

4.1 Carbon nanotubes

Carbon nanotubes are new type of carbon structures which was discovered in 1991. Due to their excellent electrical and mechanical properties, the carbon nanotubes are widely used in both fundamental and applied research. Jiang and coworkers prepared an aligned carbon nanotubes films with micro- and nanometer structure. The aligned carbon nanotube films showed superamphiphobic properties after the surface modification with a fluoroalkylsilane coating. The surface showed high contact angles for both water and rapeseed oil on the film and the values of the contact angles were 171° and 161° , respectively (Li et al., 2001). Lau and coworkers demonstrated a creation of a stable, superhydrophobic surface using the nanoscale roughness inherent in a vertically aligned carbon nanotube forest together with a thin, conformal hydrophobic poly(tetrafluoroethylene) coating on the surface of the nanotubes (Lau et al., 2003).

4.2 Metallic compounds nanorods and nanoparticles

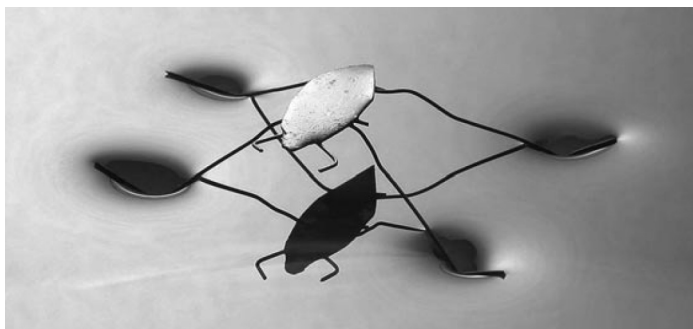


Fig. 7. A metallic model “pond skater” (body length 28 mm) standing on a water surface. Note the deformation of the water surface around the legs (Larmour et al., 2007). (Reproduced with permission from Wiley-VCH Verlag GmbH & Co. KGaA, Copyright 2007.)

With the development of the research on inorganic materials, the superhydrophobic inorganic materials were also reported numerously. For example, ZnO is a novel II - IV semiconductor material with a direct bandgap of 3.2 eV, excellent lattice, photovoltaic, pizeoelectric and dielectric properties, and it is non-toxic and low cost from cheap and abundant raw materials. Jiang and coworkers reported a controllable wettability of aligned ZnO nanorod films. This inorganic oxide films show superhydrophobicity and superhydrophilicity at different conditions, and the wettability can be reversibly switched by alternation of ultraviolet irradiation and dark storage (Feng et al., 2003). This effect is believed to be due to the cooperation of the surface photosensitivity and the aligned nanostructure of the films. Such special wettability will greatly extend the applications of ZnO films to many other important fields. Futherore, Jiang and coworkers deposited similar TiO₂ nanorod films and aligned SnO₂ nanorod films on glass substrates for the preparation of the superhydrophobic surface. The two kinds of superhydrophobic surfaces can all be switched between superhydrophobicity and superhydrophilicity by the alternation of

ultraviolet irradiation and dark storage (Feng et al., 2005; Zhu et al., 2006). Bell and coworkers reported a remarkably straightforward method for treating metals uses electroless galvanic deposition to coat a metal substrate with a textured layer of a second metal to fabricate superhydrophobic surfaces on metal surface (Larmour et al., 2007). The process is carried out under ambient conditions using readily available starting materials and laboratory equipment. The as-prepared superhydrophobic surfaces show approximately 180° contact angle. It is very striking and interesting that they have applied this preparation method to the four legs of a metallic model “pond skater” (*Gerridae*) and made this metallic model with the capacity of floating on the water (Fig. 7).

4.3 Engineering Alloy Materials

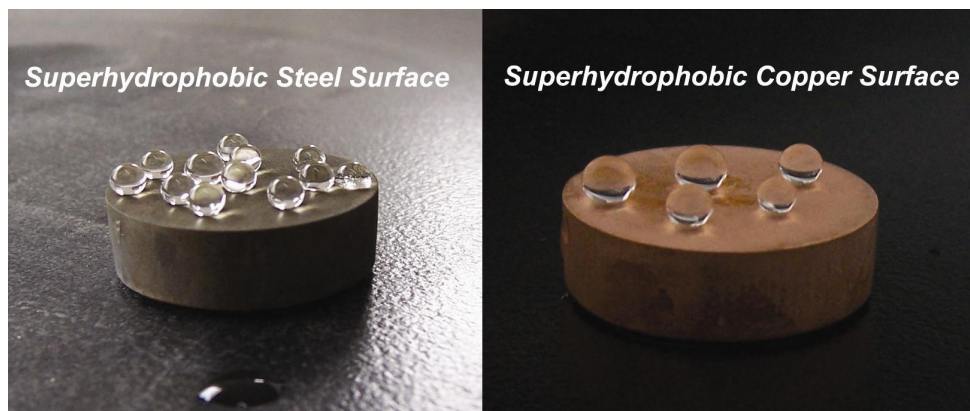


Fig. 8. Image of water droplets with different sizes on the superhydrophobic surface of steel having a contact angle of $161 \pm 1^\circ$ and on the superhydrophobic surface of copper alloy with a contact angle of $158 \pm 1^\circ$ respectively (Qu et al., 2007). (Reproduced with permission from Wiley-VCH Verlag GmbH & Co. KGaA, Copyright 2007.)

Engineering materials, such as steel, aluminium and its alloy, copper alloy and titanium alloy, have diverse technological applications in the marine, auto, aviation, and space industries. Superhydrophobicity will greatly extend their applications as engineering materials. Liu and coworkers reported a simple and inexpensive method to produce superhydrophobic surfaces on aluminium and its alloy by oxidation and chemical modification (Guo et al., 2005). The superhydrophobic surfaces show long-term stability overall wide pH range. Our group reported a novel mixed-solution system for the fabrication of superhydrophobic surfaces on steel, copper alloy and titanium alloy by a chemical etching method (Fig. 8). The superhydrophobic surfaces are able to withstand salt solutions in a wide range of concentrations, which may open a new avenue in applications especially for the marine engineering materials where salt resistance is required. We expect that this technique will accelerate the large-scale production of superhydrophobic engineering materials with new industrial applications (Qu et al., 2007).

4.4 Polymer Materials

Jiang and coworkers synthesized superhydrophobic needle-like polyacrylonitrile nanofibers via extrusion of the polyacrylonitrile precursor solution into the solidifying solution under pressure. The aligned nanofibers with different diameters and densities can be easily obtained by using anodic aluminium oxide membrane with different pore diameters, and the alignment process can be applied to different polymer precursors such as poly(vinyl alcohol), polystyrene, polyesters, and polyamides (Feng et al., 2002). The superhydrophobicity is believed that not only the nanostructure of the nanofibers but also their lower density contributes to the very large fraction of air in the surface. McCarthy and coworkers fabricated superhydrophobic polypropylene surfaces by the simultaneous etching of polypropylene and etching/sputtering of poly(tetrafluoroethylene) using inductively coupled radio frequency argon plasma. The as-prepared surfaces showed superhydrophobicity with a water contact angle of 172° (Youngblood & McCarthy, 1999). Shimomura and coworkers fabricated a honeycomb patterned fluorinated polymer films by casting of the polymer solution under humid conditions. Such honeycomb patterned films have application as transparent and superhydrophobic polymer films and it films can be formed from a large variety of materials and on a wide variety of substrates (Yabu & Shimomura, 2005). Our group prepared a polymer superhydrophobic surface on Ti/Si substrates via the fabrication of conductive polyaniline nanowire film. The polyaniline nanowire film was synthesized by electrodeposition of aniline into the pores of an anodic aluminum oxide template on Ti/Si substrate followed by the removal of the template (Qu et al., 2008). The surface showed conductivity and superhydrophobicity, even in many corrosive solutions, such as acidic or basic solutions over a wide pH range. Compared with the electrospinning method, the method in this paper is cheap and time-saving and avoided high-voltage power, and the method can be easily applied to other conducting polymers.

5. The Superhydrophobic Surfaces Related Properties and Application

With more and more in-depth study on the preparation of the superhydrophobic surfaces, the materials researchers are not only satisfy with the preparation and the contact model of the superhydrophobic surface, but the application and the related properties of the superhydrophobic surfaces. With the increase of the surface roughness, however, the surface will lost some important properties, such as the optical transparency and the mechanics property. These unfavorable factors will limit the widespread application of superhydrophobic surface greatly. Thus more and more groups have devoted to the preparation of the multi-functional superhydrophobic surfaces.

5.1 The Superhydrophobic Surfaces with the Anticorrosive Property

The pure water (pH value is 7) was commonly used for the contact angle measurements. Recently, the measurements for contact angel in whole pH range have aroused considerable interest from many researchers because of the wide application environments of this kind of superhydrophobic materials. For the engineering materials, undoubtedly, the resistance to the water or corrosive liquid will greatly enhance their anticorrosive ability, broaden its application environment and extend their service life. The superhydrophobic surfaces are able to withstand salt solutions in a wide range of concentrations, which may open a new avenue in applications especially for the marine engineering materials where salt resistance

is required. Liu's group and our group reported the superhydrophobic engineering materials such as the, steel, copper, alloy aluminium and its alloy et al (Guo et al., 2005; Qu et al., 2007). These superhydrophobic engineering materials showed superhydrophobicity in nearly the entire pH range, so they can be used in strongly corrosive environments. Furthermore, graphite carbon has intrinsic thermal and chemical resistance. Jiang and coworkers reported a nanostructured carbon films by pyrolyzing nanostructured polyacrylonitrile films (Feng et al., 2003). The films also showed superhydrophobicity in nearly the entire pH range.

5.2 The Superhydrophobic surfaces with the Optical Property



Fig. 9. Image of a glass slide coated with a transparent, superhydrophobic multilayer with antireflection properties (Bravo et al. 2007). (Reproduced with permission from the American Chemical Society, Copyright 2007.)

For many devices, such as the car windscreen and the glasses, the optical transparency is a very special and important property. Preparing the transparent superhydrophobic surface has aroused considerable interest for many materials researchers. Hydrophobicity and transparency, however, are two contradictory properties of the surface. Increasing the surface roughness is beneficial for the hydrophobicity, while the transparency decreases due to the light-scattering losses. Therefore, controlling of surface roughness to an appropriate position is to meet the requirements for both the two key factor. Watanabe and coworkers reported a sol-gel method for producing transparent boehmite films on glass substrates. The surface roughness could be precisely controlled in the range between 20 and 50 nm (Nakajima et al. 1999). This method, however, requires as high as 500 °C heating process (500 °C), which is incompatible with many optical devices. To solve this problem, a microwave plasma-enhanced chemical vapour deposition process was adapted to prepare transparent superhydrophobic films at temperatures as low as 100 °C (Hozumi & Takai, 1998; Wu et al. 2002). Jiang and coworkers prepared multifunctional ZnO nanorod films with visible-light transparency and superhydrophobic properties through controlling the diameter and length of nanorods using a low-temperature solution approach. The diameter and the spacing between the nanorods are both less than 100 nm. Such surface nanostructures are small enough not to give rise to visible light scattering. Cohen, Rubner and coworkers demonstrate a Layer-by-Layer processing scheme that can be utilized to

create transparent superhydrophobic films from SiO₂ nanoparticles of various sizes (Fig. 9). By controlling the placement and level of aggregation of differently sized nanoparticles within the resultant multilayer thin film, it is possible to optimize the level of surface roughness to achieve superhydrophobic behaviour with limited light scattering (Bravo et al. 2007).

5.3 The Superhydrophobic Surfaces with Highly Adhesive Forces

It is easy and acknowledged to imagine that a surface with a high water contact angle and small contact area should be associated with a low adhesive force. However, some research results on superhydrophobic surfaces indicate that it is not true in any situation. Feng, Jiang and coworkers reported a superhydrophobic aligned polystyrene nanotube layer via a simple template-wetting method. The surface shows superhydrophobicity, while it can hold a spherical water droplet even when it is turned upside down (Jin et al., 2005). They hold that the large contact area (the as-prepared polystyrene films are composed of about 6.76×10^6 nanotubes mm⁻²) induces a strong interacting force between the water droplet and the polystyrene nanotube films. The mechanism described here is similar to the one geckos use in nature while the difference is that the latter interactions are between two solids. Liu and coworkers also reported sticky superhydrophobic surface which were fabricated on aluminium alloy by suitable aqueous solution to control the surface roughness (Guo & Liu, 2007). These superhydrophobic surfaces with high adhesive force to liquid are expected to be used as a “mechanical hand” to transfer mini liquid droplets for microsample analyses in the future.

5.4 The Superhydrophobic Surfaces with High Electrical Conductivity

Electrical conductivity is a very important property required for many kinds of microelectrical devices, such as field-effect transistors, light-emitting diodes, and thin-film transistors. In some applications, such as biotechnology, corrosion protection, antistatics, conductive textiles and antifouling coatings, the superhydrophobic surfaces prepared with conducting material would be very useful and vital. Our group prepared conductive superhydrophobic surfaces with polyaniline by means of an anodic deposition technique on Ti/Si substrate. The method was also general to other conductive polymers, such as polythiophenes and polypyrroles. The as-prepared surface showed conductivity and superhydrophobicity, even in many corrosive solutions, such as acidic or basic solutions over a wide pH range (Qu et al., 2008). Jiang and coworkers prepared conductive hydrophobic zinc oxide thin films by means of electrochemical deposition (Li et al., 2003). They expected that the superhydrophobic conductive thin films materials have potential use, such as microfluidic devices, in the future. In fact, many reported superhydrophobic surfaces based on the metal and metallic nanomaterials are conductive naturally, while their intrinsic nature and the potential uses were ignored at the time.

6. Outlook and Summary

In this chapter, we have presented the origin model of the superhydrophobicity in nature, the lotus leaf. In the following text, the mechanism of the surface resisting water, the recent

studies on the biomimetic preparation and the properties of the superhydrophobic surface were elaborated.

The superhydrophobic surface, because of the novel aspects of surface physics and important applications ranging from selfcleaning materials, marine coatings, antiadhesive coatings, and nanobattery to microfluidic devices, has aroused considerable interest and resulted in a growing number of reports in the recent years. In addition to the superhydrophobic research, many and many researcher focused on the other wetting properties of solid surface, that is, superhydrophilicity, superoleophobicity, and superoleophilicity. For example, when superhydrophobicity/superoleophobicity or superhydrophilicity/superoleophobicity coexist, separation of water from oil (or oil from water) can be realized. Moreover, the smart surfaces whose wettability can be modulated reversibly between superhydrophobicity and superhydrophilicity or superoleophobicity and superoleophilicity are attracting more and more researchers devoted to them. Although it is very difficult that to achieve the superoleophobic surface which resists the oil, such as the chloroform or hexane, just like the superhydrophobic surfaces resists water, the preparation of the superoleophobic materials must be a research focus in the near future.

With millions of years of evolution, creatures in nature possess amazing and mysterious properties that we do not yet know. Therefore, further exploration and explanation of surfaces with special wetting behavior in nature is also necessary. Learning from nature will give us inspiration to develop simple and cheap methods to construct biomimetic multi-functional surfaces and materials.

Acknowledgment

This work was financially supported by the Natural Science Foundation of Shannxi Province, China (Grant No. 2009JQ2010), the Natural Science Research Project of Education Department of Shannxi Province, China (Grant No. 09JK580) and the Peiyu Fund of Xi'an University of Science and Technology (Grant No. 200818).

7. References

- Barthlott, W. & Neinhuis, C. (1997). Purity of the Sacred Lotus, or Escape from Contamination in Biological Surfaces. *Planta*, 202, 1-8.
- Blossey, R. (2003). Self-cleaning surfaces – virtual realities. *Nature Materials*, 2, 301-306.
- Bravo, J.; Zhai, L.; Wu, Z.; Cohen, R. E. & Rubner, M. F. (2007). Transparent Superhydrophobic Films Based on Silica Nanoparticles. *Langmuir*, 23, 7293-7298.
- Cassie, A. B. D. & Baxter, S. (1944). Wettability of Porous Surfaces. *Trans. Faraday Soc.*, 40, 546-551.
- Decher, G. & Hong, J. (1991). Buildup of Ultrathin Multilayer Films by a Self-Assembly Process. I. Consecutive Adsorption of Anionic and Cationic Bipolar Amphiphiles on Charged Surfaces. *Makromol. Chem. Macromol. Symp.*, 46, 321-327.
- ^aFeng, L.; Li, S.; Li, Y.; Li, H.; Zhang, L.; Zhai, J.; Song, Y.; Liu, B.; Jiang, L. & Zhu, D. (2002). Super-Hydrophobic Surfaces, From Natural to Artificial. *Advanced Materials*, 14, 1857-1860.

- ^bFeng, L.; Li, S.; Li, H.; Zhai, J.; Song, Y.; Jiang, L. & Zhu, D. (2002). Super-Hydrophobic Surface of Aligned Polyacrylonitrile Nanofibers. *Angewandte Chemie International Edition*, 41, 1221-1223.
- Feng, L.; Song, Y.; Zhai, J.; Liu, B.; Xu, J.; Jiang, L. & Zhu, D. (2003). Creation of a Superhydrophobic Surface from an Amphiphilic Polymer. *Angewandte Chemie International Edition*, 42, 800-802.
- Feng, X.; Feng, L.; Jin, M.; Zhai, J.; Jiang, L. & Zhu, D. (2004). Reversible Superhydrophobicity to Superhydrophilicity Transition of Aligned ZnO Nanorod Films. *Journal of the American Chemical Society*, 126, 62-63.
- Feng, X.; Zhai, J. & Jiang, L. (2005). The Fabrication and Switchable Superhydrophobicity of TiO₂ Nanorod Films. *Angewandte Chemie International Edition*, 44, 5115-5118.
- Gao, X. & Jiang, L. (2004). Water-Repellent Legs of Water Striders. *Nature*, 432, 36.
- Guo, Z.; Zhou, F.; Hao, J. & Liu, W. (2005). Stable Biomimetic Super-Hydrophobic Engineering Materials. *Journal of the American Chemical Society*, 127, 15670-15671.
- ^aGuo, Z. & Liu, W. (2007). Biomimic from the Superhydrophobic Pplant Leaves in Nature: Binary Structure and Unitary Structure. *Plant Science*, 172, 1103-1112.
- ^bGuo, Z. & Liu, W. (2007). Sticky Superhydrophobic Surface. *Applied Physics Letters*, 90, 223111.
- Han, J. T.; Lee, D. H.; Ryu, C. Y. & Cho, K. (2004). Fabrication of Superhydrophobic Surface from a Supramolecular Organosilane with Quadruple Hydrogen Bonding. *Journal of the American Chemical Society*, 2004, 126, 4796-4797.
- Hosono, E.; Fujihara, S.; Honma, I. & Zhou, H. (2005) Superhydrophobic Perpendicular Nanopin Film by the Bottom-Up Process. *Journal of the American Chemical Society*, 127, 13458-13459.
- Hozumi, A. & Takai, O. (1998). Preparation of Silicon Oxide Films having a Water-Repellent Layer by Multiple-Step Microwave Plasma-Enhanced Chemical Vapor Deposition. *Thin Solid Films*, 334, 54-59.
- Huang, L.; Lau, S. P.; Yang, H. Y.; Leong, E. S. P.; Yu, S. F. & Prawer, S. (2005). Stable Superhydrophobic Surface via Carbon Nanotubes Coated with a ZnO Thin Film. *Journal of Physical Chemistry B*, 109, 7746-7748.
- Jin, M.; Feng, X.; Feng, L.; Sun, T.; Zhai, J.; Li, T. & Jiang, L. (2005). Superhydrophobic Aligned Polystyrene Nanotube Films with High Adhesive Force. *Advanced Materials*, 17, 1977.
- Larmour, I. A.; Bell, S. E. J. & Saunders, G. C. (2007). Remarkably Simple Fabrication of Superhydrophobic Surfaces Using Electroless Galvanic Deposition. *Angewandte Chemie International Edition*, 46, 1710-1712.
- Lau, K. K. S.; Bico, J.; Teo, K. B. K.; Chhowalla, M.; Amaratunga, G. A. J.; Milne, W. I.; McKinley, G. H. & Gleason, K. K. (2003). Superhydrophobic Carbon Nanotube Forests. *Nano Letters*, 3, 1701-1705.
- Li, H.; Wang, X.; Song, Y.; Liu, Y.; Li, Q.; Jiang, L. & Zhu, D. (2001). Super-“Amphiphobic” Aligned Carbon Nanotube Films. *Angewandte Chemie International Edition*, 40, 1743-1746.
- Li, M.; Zhai, J.; Liu, H.; Song, Y.; Jiang, L. & Zhu, D. (2003). Electrochemical Deposition of Conductive Superhydrophobic Zinc Oxide Thin Films. *Journal of Physical Chemistry B*, 107, 9954-9957.

- Li, S.; Li, H.; Wang, X.; Song, Y.; Liu, Y.; Jiang, L. & Zhu, D. (2002). Super-Hydrophobicity of Large-Area Honeycomb-Like Aligned Carbon Nanotubes. *Journal of Physical Chemistry B*, 106, 9274-9276.
- Ma, M.; Hill, R. M.; Lowery, J. L.; Fridrikh, S. V. & Rutledge, G. C. (2005). Electrospun Poly(Styrene-block-dimethylsiloxane) Block Copolymer Fibers Exhibiting Superhydrophobicity. *Langmuir*, 21, 5549-5554.
- Martines, E.; Seunarine, K.; Morgan, H.; Gadegaard, N.; Wilkinson, C. D. W. & Riehle, M. O. (2005). Superhydrophobicity and Superhydrophilicity of Regular Nanopatterns. *Nano Letters*, 5, 2097-2103.
- Nakajima, A.; Fujishima, A.; Hashimoto, K. & Watanabe, T. (1999). Preparation of Transparent Superhydrophobic Boehmite and Silica Films by Sublimation of Aluminum Acetylacetonate. *Advanced Materials*, 11, 1365-1368.
- Notsu, H.; Kubo, W.; Shitanda I. & Tatsuma T. (2005) Super-Hydrophobic/Super-Hydrophilic Patterning of Gold Surfaces by Photocatalytic Lithography. *Journal of Materials Chemistry*, 15, 1523-1527.
- Qian, B. & Shen, Z. (2005). Fabrication of Superhydrophobic Surfaces by Dislocation-Selective Chemical Etching on Aluminum, Copper, and Zinc Substrates. *Langmuir*, 21, 9007-9009.
- Qu, M.; Zhang, B.; Song, S.; Chen, L.; Zhang, J. & Cao, X. (2007). Fabrication of Superhydrophobic Surfaces on Engineering Materials by a Solution-Immersion Process. *Advanced Functional Materials*, 17, 593-596.
- ^aQu, M.; Zhao, G.; Wang, Q.; Cao, X. & Zhang, J. (2008). Fabrication of Superhydrophobic Surfaces by a Pt nanowire Array on Ti/Si Substrates. *Nanotechnology*, 19, 055707.
- ^bQu, M.; Zhao, G.; Cao, X. & Zhang, J. (2008). Biomimetic Fabrication of Lotus-Leaf-like Structured Polyaniline Film with Stable Superhydrophobic and Conductive Properties. *Langmuir*, 24, 4185-4189.
- Shirtcliffe, N. J.; McHale, G.; Newton, M. I. & Perry, C. C. (2003). Intrinsically Superhydrophobic Organosilica Sol-Gel Foams. *Langmuir*, 19, 5626-5631.
- Teshimaa, K.; Sugimurab, H.; Inouec, Y.; Takaic, O. & Takano, A. (2005). Transparent Ultra Water-Repellent Poly(ethylene terephthalate) Substrates Fabricated by Oxygen Plasma Treatment and Subsequent Hydrophobic Coating. *Applied Surface Science*, 244, 619-622.
- Wenzel, R. N. (1936). Resistance of Solid Surface to Wetting by Water. *Ind. Eng. Chem.*, 28, 988-994.
- Wu, X.; Zheng, L. & Wu, D. (2005). Fabrication of Superhydrophobic Surfaces from Microstructured ZnO-Based Surfaces via a Wet-Chemical Route. *Langmuir*, 21, 2665-2667.
- Wu, Y.; Sugimura, H.; Inoue, Y. & Takai, O. (2002). Thin Films with Nanotextures for Transparent and Ultra Water-Repellent Coatings Produced from Trimethylmethoxysilane by Microwave Plasma CVD. *Chemical Vapor Deposition*, 8, 47-50.
- Yabu, H. & Shimomura, M. (2005). Single-Step Fabrication of Transparent Superhydrophobic Porous Polymer Films. *Chemistry of Materials*, 17, 5231-5234.
- Yan, H.; Kurogi, K.; Mayama, H. & Tsujii, K. (2005). Environmentally Stable Super Water-Repellent Poly(alkylpyrrole) Films. *Angewandte Chemie International Edition*, 44, 3453-3456.

- Youngblood, J. P. & McCarthy, T. J. (1999). Ultrahydrophobic Polymer Surfaces Prepared by Simultaneous Ablation of Polypropylene and Sputtering of Poly(tetrafluoro ethylene) Using Radio Frequency Plasma. *Macromolecules*, 32, 6800-6806.
- Zhai, L.; Berg, M. C.; Cebeci, F. Ç.; Kim, Y.; Milwid, J. M.; Rubner, M. F. & Cohen, R. E. (2006). Patterned Superhydrophobic Surfaces: Toward a Synthetic Mimic of the Namib Desert Beetle. *Nano Letters*, 6, 1213-1217.
- Zhai, J.; Li, H. J.; Li, Y. S.; Li, S. H. & Jiang, L. (2002). Discovery of Super-Amphiphobic Properties of Aligned Carbon Nanotube Films. *Physics*, 31, 483-486.
- Zhang, L.; Chen, H.; Sun, J. & Shen, J. (2007). Layer-by-Layer Deposition of Poly(diallyldimethyl ammonium chloride) and Sodium Silicate Multilayers on Silica-Sphere-Coated Substrate-Facile Method to Prepare a Superhydrophobic Surface. *Chemistry of Materials*, 19, 948-953.
- Zhang, X.; Shi, F.; Yu, X.; Liu, H.; Fu, Y.; Wang, Z.; Jiang, L. & Li, X. (2004). Polyelectrolyte Multilayer as Matrix for Electrochemical Deposition of Gold Clusters: Toward Super-Hydrophobic Surface. *Journal of the American Chemical Society*, 126, 3064-3065.
- Zhu, W.; Feng, X.; Feng, L. & Jiang, L. (2006). UV-Manipulated Wettability between Superhydrophobicity and Superhydrophilicity on a Transparent and Conductive SnO₂ Nanorod Film. *Chemical Communications*, 2753.
- Zhu, Y.; Zhang, J.; Zheng, Y.; Huang, Z.; Feng, L. & Jiang, L. (2006). Stable, Superhydrophobic, and Conductive Polyaniline/Polystyrene Films for Corrosive Environments. *Advanced Functional Materials*, 2006, 16, 568-574.

Micro Swimming Robots Based on Small Aquatic Creatures

Seiichi Sudo
Akita Prefectural University
Japan

1. Introduction

Earth is a sphere of life. All living things are capable of movement. Animals occur almost everywhere and make up more than half of all the living things on this planet. Most animals move about using legs, wings, or fins. The swimming of a variety of aquatic living creatures and the flying of insects have been a source of continuous fascination to scientists working in many fields. The importance of the locomotive functions of animals is well recognized with respect to a variety of robot developments. Extensive investigations on the biokinetics of swimming and flying animals have been conducted and reported by a number of researchers (Alexander, 1984; Azuma, 1992; Dickinson et al., 2000). Body size and shape of living creatures are a natural result of the adaptation of the manner of movement to environmental conditions (Azuma, 1992). In general, swimming is a far more economical way to move to a distant point than flying. Almost all swimming creatures are considerably longer in the swimming direction. The swimming motions of small aquatic creatures are fascinating to behold. With increasing interest hydrodynamicists have studied the interactions of these creatures with their surrounding fluid medium (Blake, 1972; Dresdner et al., 1980; Daniel, 1984; Jiang et al., 2002a; 2002b; 2002c). In spite of many investigations, however, there still remains a wide unexplored domain. Especially, in order to develop minute micro robots and micro mechanisms, the swimming analyses of smaller living creatures are demanded (Sudo et al., 2009). In this chapter, the swimming behaviour of small aquatic creatures was analyzed by a digital high-speed video camera system. Various swimming modes of small aquatic creatures were clarified experimentally. Furthermore, based on the swimming analyses of small aquatic creatures, some wireless micro swimming robots were made for trial purposes. Those micro swimming robots composed of a permanent magnet were driven by the external alternating magnetic field. The swimming characteristics of those micro robots were also examined, and frequency characteristics for swimming velocity of micro robots were revealed.

2. Experimental Apparatus and Procedure

Experiments on small aquatic creature swimming are conducted with a high-speed video camera system shown in authors' previous paper (Sudo et al., 2008). A schematic diagram of

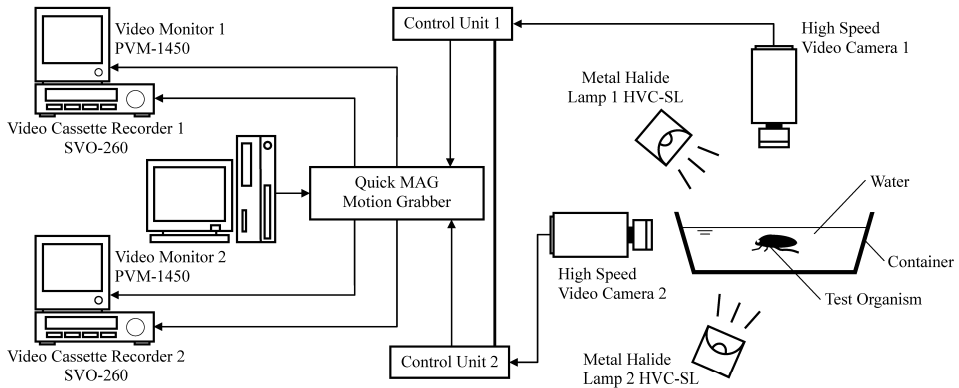


Fig. 1. Schematic diagram of experimental apparatus for free swimming analysis of small aquatic creatures

the experimental apparatus is shown in Fig.1. Some kinds of rectangular and cylindrical containers with different sizes were used in the experiments. The experimental apparatus consists of the swimming water container system, the measurement system, and the analysis system. The containers were produced with transparent acrylic plastic for optical observation. The sizes of the containers were changed by test aquatic creatures. The containers were filled up to the certain depth with water or seawater according to the test aquatic creatures. The small aquatic creatures were released in the water container. Free swimming of the test aquatic creature was observed optically with the high-speed video camera. A series of frames of free swimming behaviour of test aquatic creature were analyzed by the personal computer. In the experiment of tethered swimming analyses, the test live aquatic creature was pasted up on a human hair or a thin needle with the adhesive. The motions of the swimming legs of test aquatic creature were recorded by the high-speed video camera. A series of frames of the leg motions during swimming behaviour were also analyzed by the personal computer. In the experiment for flow visualization, the powder of chaff was scattered in the water. Movement of powder was photographed with 35mm camera. The experiments were conducted under the room temperature in summer (water temperature 18-22°C). For the purpose of the investigation on the morphological structure of swimming legs of small aquatic creatures, microscopic observations were conducted with a scanning electron microscope.

3. Swimming of Diving Beetles

3.1 Family Dytiscidae

Family Dytiscidae is one of large aquatic families with 177 species in 37 genera (Zborowski & Storey, 1995). They are found in streams, shallow lakes and ponds, brackish pools, and thermal springs. They range from 1 to 40 mm in length, and are very smooth and mostly oval for rapid underwater movement. Most species are black or dark brown but some have yellow, blown, or green marking. The hind legs are enlarged and the tarsi have a border of



Fig. 2. Dorsal view of diving beetle, *Cybister japonicus* Sharp

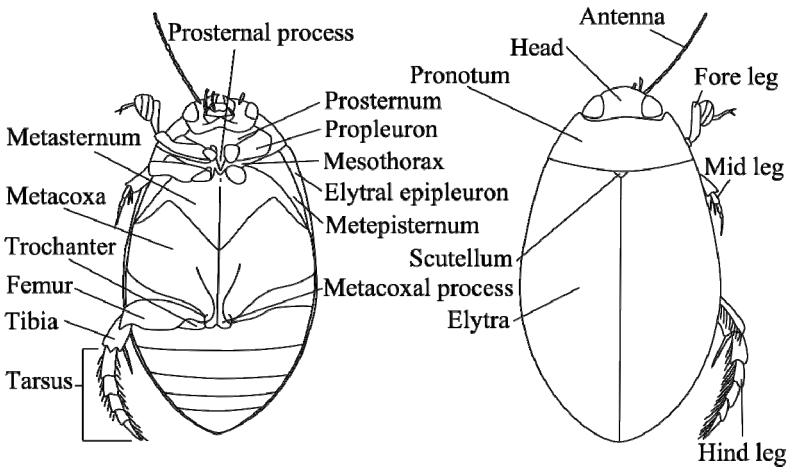


Fig. 3. A typical adult diving beetle illustrating the major parts of the body

hairs acting as oars when the legs beat in unison. The hind coxae extend to the elytra on the sides and the antennae are filiform. Highly adapted for aquatic life, they breathe by coming to the surface backwards and exposing the tip of the abdomen which draws in air to store under the elytra. They are fierce predators, attacking various preys, from insects to frogs and small fish. In this experiment, test insects were collected in stream and ponds. A diving beetle, *Cybister japonicus* Sharp, captured at Yurihonjo in Japan is shown in Fig.2. The rowing hind legs with hairs are clear in Fig.2. Figure 3 shows a schematic diagram of an

adult diving beetle and the named body parts. Adult insects have a general body plan of three main divisions; head, thorax and abdomen. In the experiment, test diving beetles were *Gaurodytes japonicas*, *Cybister lewisianus*, *Cybister japonicus*, and *Hydrogyphus japonicus*.

3.2 Swimming Behavior of diving beetle

As was stated previously, shape of diving beetles is often distinctive; elongate-oval, convex, streamlined. The hind legs are flattened and fringed with hairs. The hind tarsi have 1 or 2 claws. They are excellent swimmers, and usually when swimming move the hind legs in unison. Dytiscid beetles are the most extensively studied of these insect rowers, with excellent measurements of limb and body kinematics and drag coefficients (Nachtigall, 1980). However, the research data on the swimming behaviour of diving beetles are insufficient, and there still remains a wide unexplored domain. In this paragraph, the swimming behaviour of diving beetle in water container was examined. Figure 4 shows a sequence of photographs showing the free swimming behaviour of diving beetle. It can be seen that the

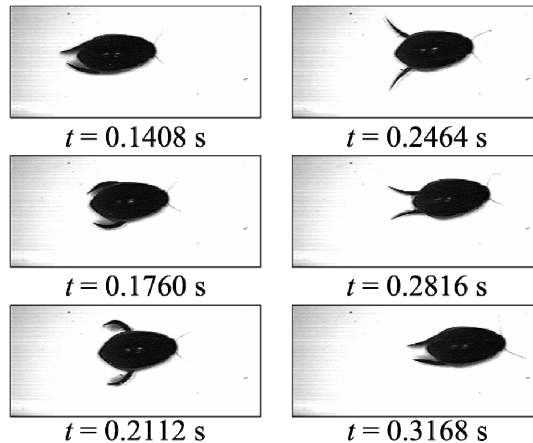


Fig. 4. A sequence of photographs showing the swimming behaviour of the diving beetle

diving beetle swims by flexing his hind legs together. During the power stroke, they are stretched and move backward. The thrust-generating mechanism is related to the motion of the hind legs. Four characteristic points on the diving beetle body were defined by the signs shown in Fig.5. These points correspond to head (H0), tail (T0), and right and left hind legtips (R3 and L3 respectively). Figure 6 shows the legtip, head, and tail orbits and the body orbit during swimming of the diving beetle. In Fig.6, L is the body length of the diving beetle, and δ_t is the time interval of plotting data. Arrows indicate the direction of the movement of the diving beetle. The orbits of right and left legtips show almost the same. The diving beetle swims by paddling its flexible hindlegs. The articulated hindlegs with hairs are fully extended in power stroke, but folded and narrowed in the recovery stroke. Let us consider the thrust-generating mechanism in a diving beetle moved with a constant velocity U . To simplify the following calculations, the leg is assumed to move backward along a straight line with a constant velocity V_p . The driving force T_p generated by the fluid

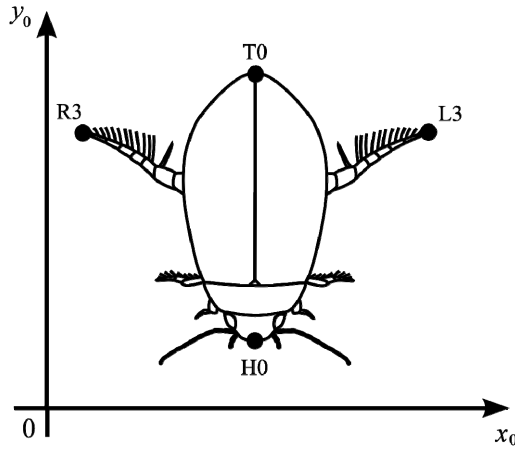


Fig. 5. Definition of signs of measurement points on the diving beetle

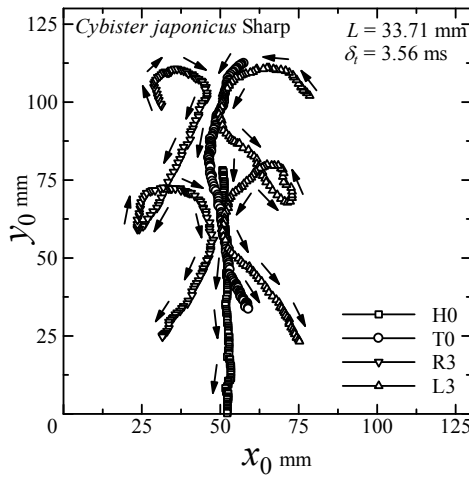


Fig. 6. Swimming trajectories of hind legtips, head, and tail of the diving beetle

dynamic drag of the leg, which is proportional to the dynamic pressure of the relative speed $V_p - U$, can be expressed as follows (Azuma, 1992);

$$T_p = \frac{1}{2} \rho (V_p - U) |V_p - U| S_p C_D \tag{1}$$

where S_p is the frontal area, and C_D is the drag coefficient. Here the inertia force has been neglected. The power P required to drive the drag is given by Eq. (2).

$$P = T_p V_p = \frac{1}{2} \rho V_p (V_p - U) V_p - U S_p C_D \quad (2)$$

In the power stroke at constant water beetle speed U , the body drag of the diving beetle D , and necessary power of the diving beetle W , are given as follows;

$$D = \frac{1}{2} \rho U^2 S_T = T_p \quad (3)$$

$$W = DU = T_p U = \frac{1}{2} \rho U^3 S_T \quad (4)$$

where S_T is the drag area of the diving beetle body. In the recovery stroke, the negative driving force T_r can be neglected, because the hindlegs are folded and swimming hairs are laid against the leg. Thus, hydrodynamic efficiency can be given as follows;

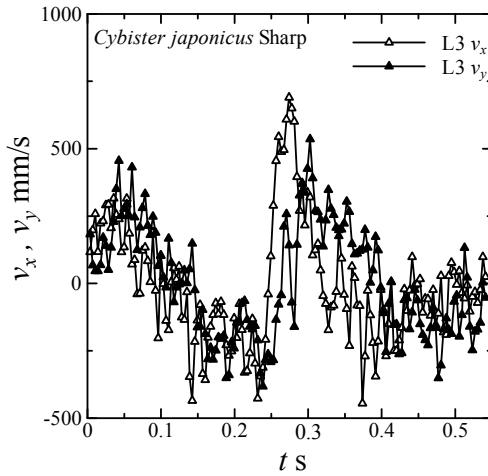
$$\eta = \frac{W}{P} = \frac{U}{V_p} = \frac{1}{1 + \sqrt{\frac{S_T}{S_p C_D}}} \quad (5)$$

It can be seen from Eq. (5) that $S_T/S_p C_D \rightarrow 0$ means higher hydrodynamic efficiency in swimming of diving beetles. In an actual diving beetle, the drag coefficient of a leg C_D is unsteady and strongly dependent on the leg structure. The diving beetle is a small insect characterized by short forelegs and long hindlegs with hairs to provide propulsion. The mean drag coefficient of a rectangular flat plate in normal flow is a function of the aspect ratio of the plate and the Reynolds number (Azuma, 1992). It changes from $C_D=1.2$ to $C_D=2.0$. The mean drag coefficient of a column is also a function of the Reynolds number Re as follows;

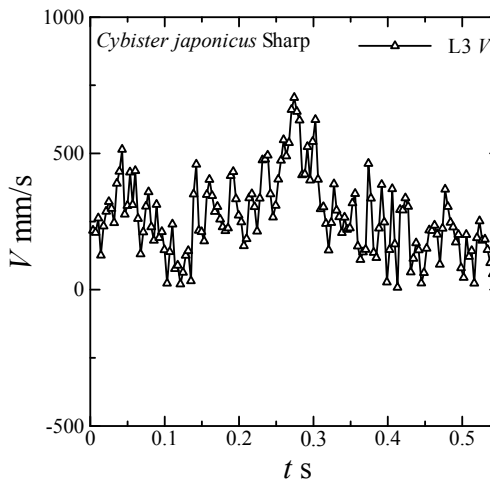
$$C_D = \frac{10.9}{Re(0.87 - \log Re)} \quad (6)$$

This equation states that the drag coefficient increases decreasing in the Reynolds number. If the flat plate leg is replaced with the set of a lot of minute columns, the drag also increases. The hind legs composed of a lot of minute hairs may generate higher drag. Since a rowing hair of diving beetle is from 20 to 2μ m in diameter from base to tip (Nachtigall, 1980a), the flow around hairs of the leg is a lower Reynolds number flow. The value of $S_T/S_p C_D$ in Eq.(5) becomes smaller with an increase in C_D . In an actual swimming of diving beetle, the driving force T is described by the difference between T_p in the power stroke and T_r in the recovery stroke, because the legs oscillate back and forth.

$$T = T_p - T_r \quad (7)$$



(a) Velocity components of legtip motion



(b) Two dimensional velocity of legtip motion

Fig. 7. Velocity variations of legtip motion during swimming of the diving beetle

Therefore, the swimming motion of diving beetle is unsteady. Fig.7 shows the velocity variations in the legtip motion of the diving beetle during swimming. The speed change in hind leg corresponds to propulsion of the entire body with diving beetle swimming. In Fig.7, v_x and v_y are x and y components of the legtip velocity respectively, and V is the two dimensional velocity described by $V=(v_x^2+v_y^2)^{1/2}$. Diving beetles swim with their strong hindlegs that they use like oars on a rowboat. If the shape of the hindlegs does not change, a quasi-steady analysis finds that the net force for a cycle of oscillation is zero. Fig.7 shows a periodic change of the velocity of the left hindlegtip. The time range of a rapid increase in

the velocity corresponds to the power stroke. On the other hand, a slowly decrease of the velocity corresponds to the recovery stroke. The diving beetle enlarges the driving force T_p , and reduces T_r .

3.3 Swimming Behavior of Small Diving Beetle

There is an interesting diving beetle that shows different swimming from usual diving beetles. In general, the third pair of legs (hindlegs) in usual diving beetles beat synchronously during the power stroke. In this paragraph, the swimming behaviour of a diving beetle, *Hydroglyphus japonicus* Sharp, is shown. The diving beetle, *Hydroglyphus japonicus* Sharp, is a small insect with the body length about 2mm as shown in the photograph in Fig.8. This test insect was collected in the rice field at Yuri Honjo in Japan . The diving beetle is confined in the water drop in Fig.8. Figure 9 shows a sequence of photographs of swimming behaviour of the diving beetle, *Hydroglyphus japonicus* Sharp. It can be seen that the diving beetle swims by alternately rowing his hind legs. In other words, the diving beetle swims by alternately paddling of right and left hind legs. Small channel with 3.3 mm in width and 3 mm in depth was used in this experiment. This channel is composed of the ditch on the tree plate and tap water. Figure 10 shows the legtip, head, and tail orbits and the body orbit during swimming of the diving beetle. The head orbit of the insect draw the sinusoidal curve, that is, the head swings right and left according to rowing the hind legs. It is uncertain why the diving beetle, *Hydroglyphus japonicus* Sharp, swims in a zigzag line. When the small diving beetle swims in mud, such swimming mode must be convenient. Fig.11 shows the velocity variations in the left hind legtip motion of the diving beetle during swimming. The variation of the velocity component of legtip motion in two dimension coordinate system is shown in Fig.11(a), and the variation of two dimensional



Fig. 8. Photograph of a small diving beetle, *Hydroglyphus japonicus* Sharp, in a water drop

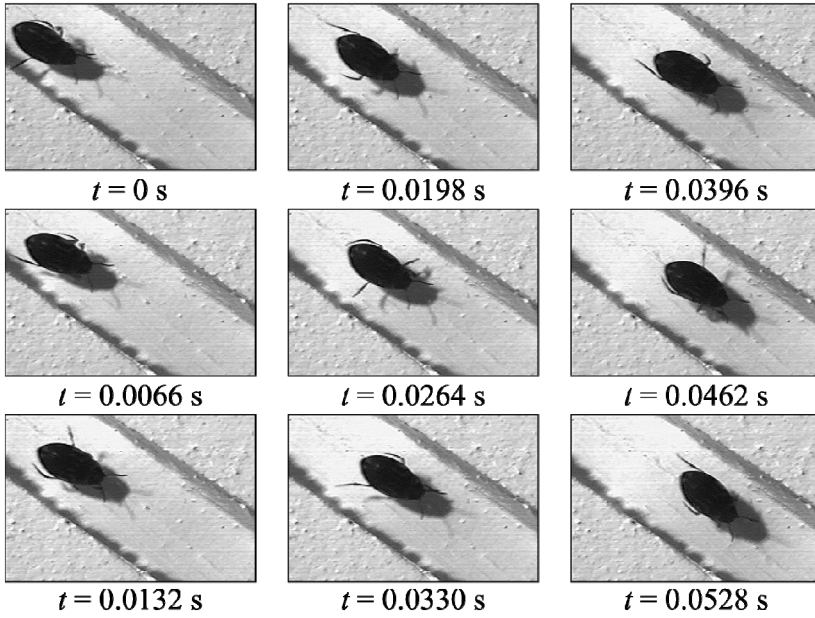


Fig. 9. A sequence of swimming behaviour of the small diving beetle in a narrow waterway

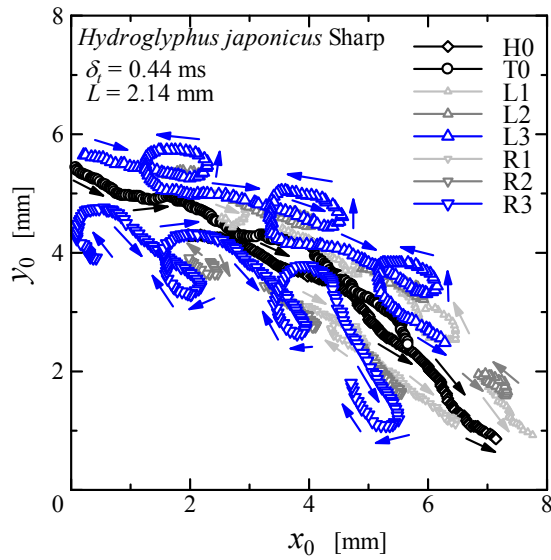
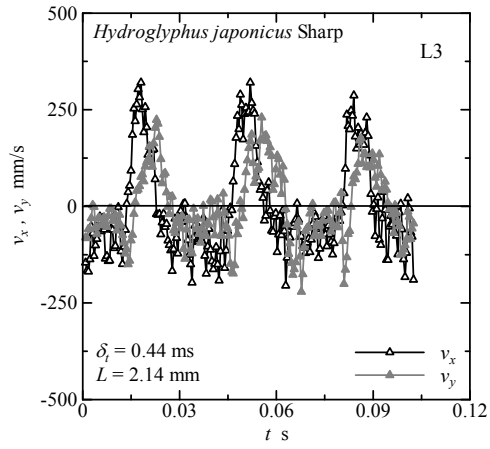
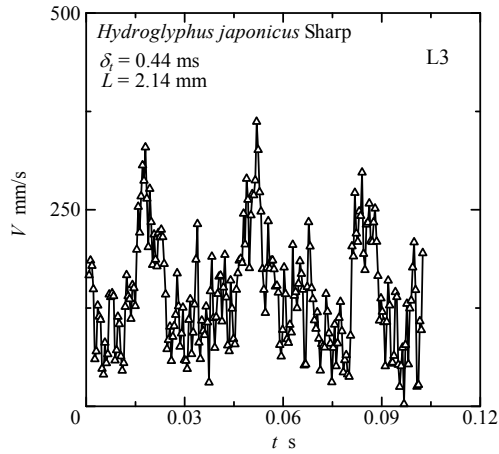


Fig. 10. Swimming trajectories of legtips, head, and tail of the diving beetle



(a) Velocity components of legtip motion



(b) Two dimensional velocity of legtip motion

Fig. 11. Velocity variations of legtip motion during swimming of the diving beetle

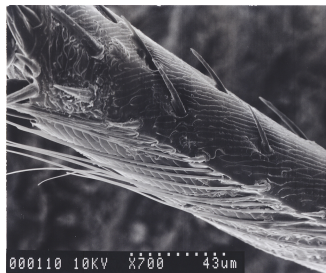


Fig. 12. Electron micrograph of a part of swimming leg of the diving beetle

resultant velocity is shown in Fig.11(b). Sharp rising up of the velocity variation corresponds to the power stroke, and gradual decreasing corresponds to the recovery stroke during swimming of the diving beetle. As stated above, swimming legs of the diving beetle, *Hydroglyphus japonicus* Sharp, are also clothed in minute hairs. The hairs increase the hydrodynamic drag of the swimming leg. Scanning electron microscopic observation of the swimming legs of the diving beetle shows existence of fine hairs on the legs. Figure 12 shows scanning electron micrograph of the rowing appendages and fine hairs of the diving beetle, *Hydroglyphus japonicus* Sharp. The thickness of the hair is about $1.5 \mu\text{m}$ in Fig.12.

4. Swimming of Dragonfly Nymph

After the dragonfly nymph emerges from the egg, it develops through a series of stages called instars. The dragonfly larvae are predatory and live in all types of freshwater. The younger nymph was selected as a test insect in the swimming experiment, because the younger nymph swam actively. The tested nymph shown in Fig. 13 was a larva of dragonfly, *Sympetrum frequens*. The swimming behavior of the nymph in water container was examined. Fig.14 shows a sequence of photographs showing the swimming behavior of dragonfly



Fig. 13. Photograph of a younger small dragonfly nymph used in the swimming experiment

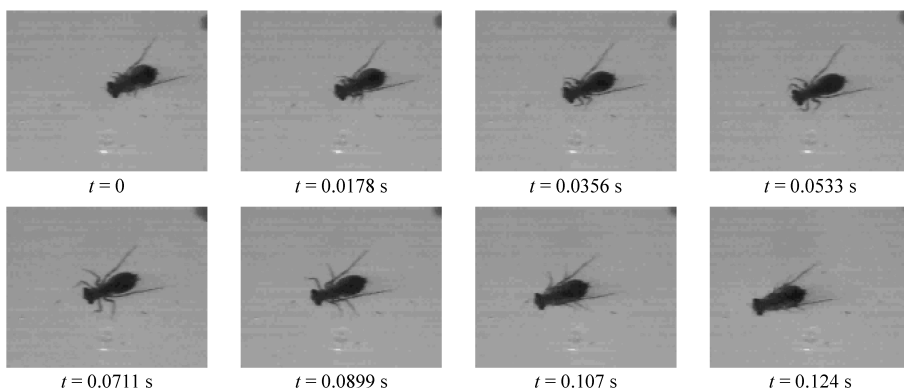


Fig. 14. A sequence of photographs showing the swimming behavior of the dragonfly nymph in water container

nymph. The process of leg movement for the nymph swimming is clear. The fore- and middle-legs beat almost synchronously. During the power stroke they are stretched and move. On the other hand, the hind-legs hardly move. The thrust-generating mechanism is related to the motion of the fore- and middle-legs. The dragonfly nymph expands and contracts its abdomen to move water during forward swimming. Figure 15 shows the change in the size of the nymph body through the swimming stroke. The changes of the body length L_s and the body width W_s are the opposite phases. The body length L_s and the body width W_s through the straight swimming are described as follows;

$$\left. \begin{aligned} L_s &= L + \alpha \sin(\omega t + \phi) \\ W_s &= W + \beta \sin(\omega t - \pi + \phi) \end{aligned} \right\} \quad (8)$$

where ω is the angular frequency of swimming stroke, t is the time, ϕ is the phase difference with the leg motion, and α and β are constants. In this experiment, constants α and β are described as follows;

$$\left. \begin{aligned} \alpha &= 0.60 \text{ mm} \\ \beta &= 0.25 \text{ mm} \end{aligned} \right\} \quad (9)$$

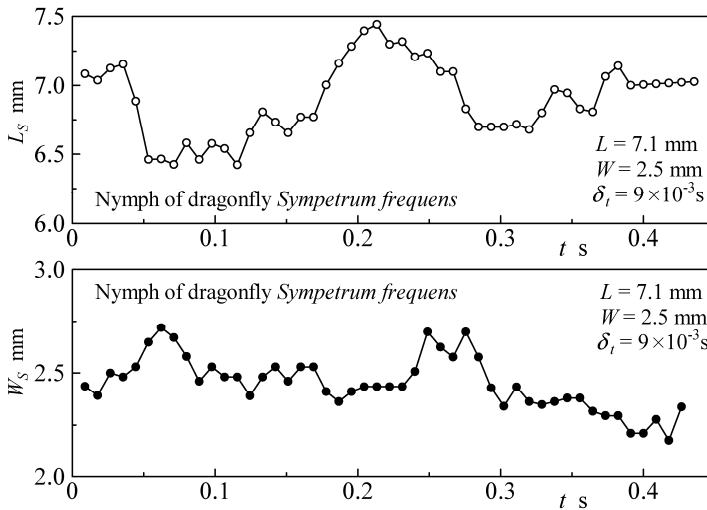


Fig. 15. Expansion and contraction of the nymph body during swimming

The change in the body size of tested nymph was about 10%. The legtips move at higher speed during the power stroke, and lower speed during the recovery stroke. Such a leg

movement generates the thrust force for nymph swimming. The swimming number S_w of this tested nymph is the following value;

$$S_w = \frac{V_{mean}}{f_s L} = \frac{77.6}{5.0 \times 7.1} \approx 2.2 \quad (10)$$

where V_{mean} is the mean swimming velocity, and f_s is the paddling frequency. The swimming number shows how many body length per beat to swim. The swimming number $S_w = 2.2$ is larger compared with fish.

5. Micro Swimming Mechanism

5.1 Driving Principle of Micro Swimming Mechanism

The biomimetic study on the swimming robot was performed. As mentioned above, small aquatic creatures swim by using their swimming legs as underwater paddles to produce hydrodynamic drag. Based on the above-mentioned swimming analysis of the aquatic creatures, the micro swimming mechanism was produced by trial and error. The micro swimming mechanism is composed of polystyrene foam body, permanent magnet, polyethyleneterephthalate film fin, copper fin stopper, and tin balancer. The dimensions of the swimming mechanism are shown in Fig.16. The swimming mechanism is propelled by the magnetic torque acting on the small permanent magnet in the alternating magnetic field. The magnet is made of NdFeB alloy, and shape is a cube of 5mm×5mm×5mm. Table 1 shows the physical properties of NdFeB permanent magnet used in the experiment. Table 2 shows the magnetic properties of the permanent magnet. The experimental apparatus is almost similar to Fig.1, but the cylindrical container coiled electric wire was used to drive the swimming robot. When the alternating magnetic field is applied to the permanent magnet, the magnet oscillates angularly due to magnetic torque and drives the propulsive robot in water. The alternating magnetic field was generated by applying AC voltage to the coil wound around container. The alternating current signal was supplied from a frequency synthesizer. A block diagram of the coiled water container and measuring devices is shown in Fig.17. The magnetic torque T_m acting on the permanent magnet with magnetic moment m in the external magnetic field H is described by Eq.(11);

$$T_m = m \times H \quad (11)$$

In this experiment, the external magnetic field was produced by the coil applied AC voltage;

$$E_c = \frac{E}{2} \sin(2\pi f_0 t) \quad (12)$$

where E is the total amplitude of AC voltage, f_0 is the frequency of AC voltage, and t is the time. Therefore, the external magnetic field generated by the coil is given by Eq.(13);

$$H = H_0 e \sin(2\pi f_0 t) \quad (13)$$

where H_0 is the amplitude of alternating magnetic field, e is a unit vector. Oscillating torque motion of the permanent magnet is excited by Eq.(13). The direction of the external magnetic

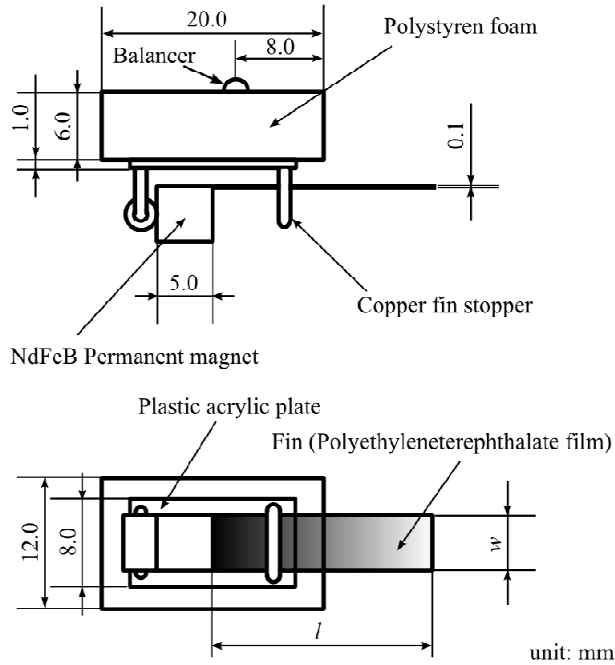


Fig. 16. Shape and dimension of the micro swimming mechanism

Permanent magnet	Nd ₂ Fe ₁₄ B
Temperature coefficient	0.12 % / °C
Density	7300 - 7500 kg/m ³
Curie temperature	310 °C
Vickers hardness	HV 500 - 600

Table 1. Physical properties of permanent magnet used in the experiment

Residual magnetic flux density B_r	1.62 - 1.33 T
Coercive force bHC	859 - 970 kA/m
Coercive force iHC	> 955 kA/m
Maximum energy product $(BH)_{max}$	302 - 334 kJ/m ³

Table 2. Magnetic properties of NdFeB magnet used in the experiment

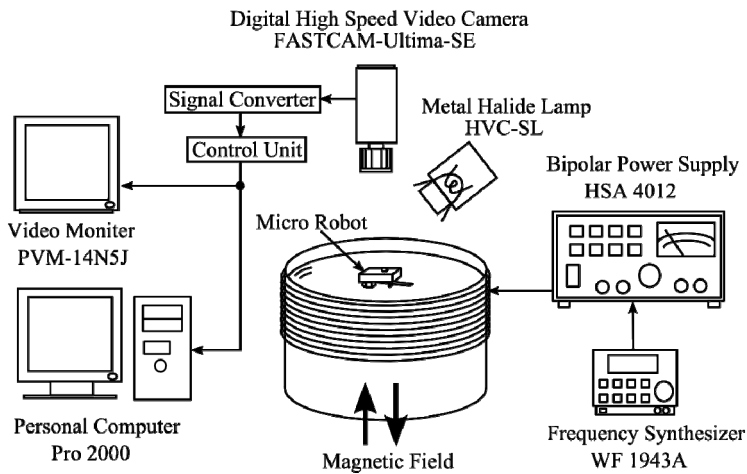


Fig. 17. Schematic diagram of experimental apparatus for locomotive characteristics of swimming robot

field is a vertical direction against the water level as shown in Fig.17. The magnet movement is connected with the fin motion directly. This mechanism swims by hydrodynamic drag produced by sweeping the fin. During one cycle of the swimming movement, the fin presses backwards against the water and this pushes the body forwards.

5.2 Frequency Characteristics of Swimming Velocity

The swimming behavior of the micro mechanism was observed with the experimental apparatus shown in Fig.17, that is, the swimming velocity of micro mechanism was examined within a certain frequency range of alternating magnetic field. In this experiment, the external magnetic field was generated with the coil around the water container shown in Fig.17. The experiment was performed on the condition of constant E in Eq.(12). Figure 18 shows the frequency characteristics of swimming velocity for the micro mechanism. In Fig.18, v is the swimming velocity, l is the fin length, w is the fin width, and the dotted lines show the unstable swimming of the micro mechanism. The effect of the applied voltage E is also shown in Fig.18. In general, an increase in the applied voltage E improves the swimming velocity of the micro mechanism. The increase in the applied voltage corresponds to the increase in the magnetic field generated by the coil. It can be seen from Fig.18 that the swimming velocity v depends on the frequency of alternating magnetic field f_0 . The spectrum of the swimming velocity in Fig.18 has the peak at the range of $f_0=4-6\text{Hz}$. The peak frequency is related to the oscillation mode of the fin in water. The swimming velocity of the micro mechanism depends on the amplitude of fin oscillation. The larger amplitude leads to higher velocity of micro mechanism swimming. The micro mechanism swims by the fin oscillation. The flow field produced by the fin oscillation was examined. The flow field around the micro mechanism was visualized by slow shutter speed photograph. Figure 19 shows one example of flow visualization on the water surface around the micro mechanism. Flow visualization was created by floating powder on the water

surface. The shutter speed of the camera is 1/2 seconds. The swimming advancement of the micro mechanism is stopped with the wire of aluminum. The forward and backward flows are generated, but the backward flow is strongly generated. The speed difference between forward and backward flows is the swimming speed of the mechanism. Figure 20 shows the flowfield produced by the live tethered opposum shrimp for the comparison. A stream is

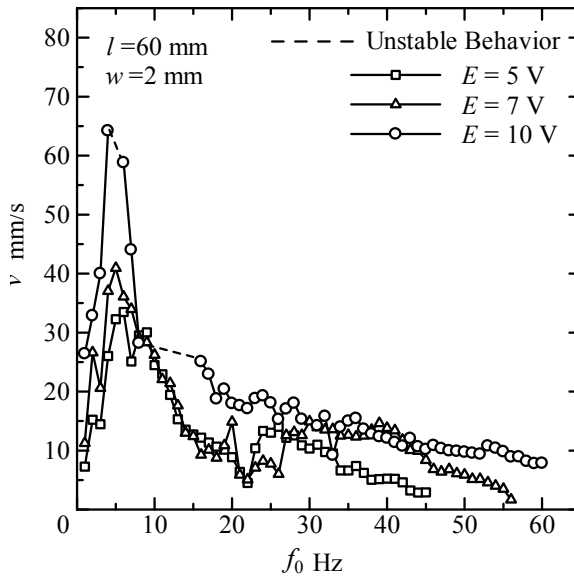


Fig. 18. Frequency characteristics of the micro swimming mechanism

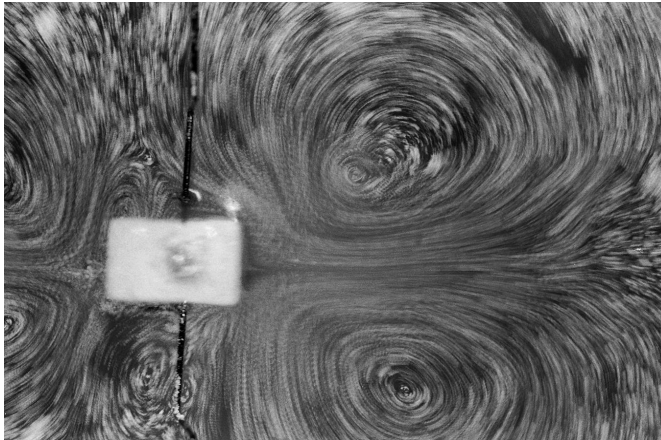


Fig. 19. Flow visualization around the micro swimming mechanism

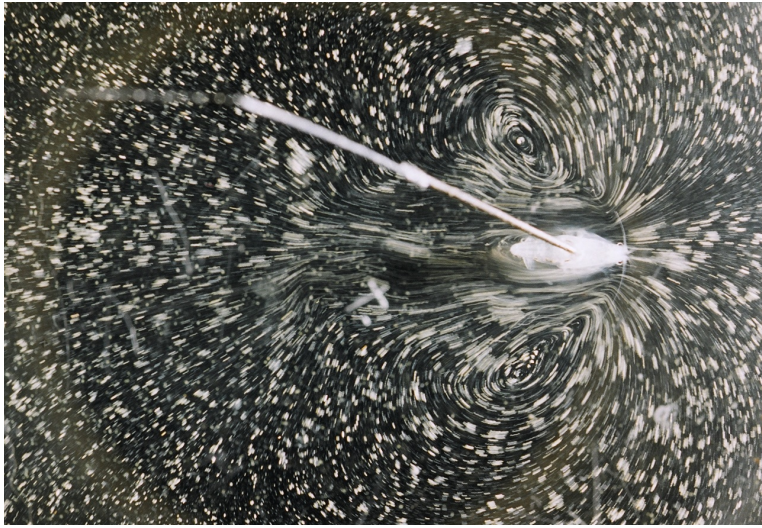


Fig. 20. Flow visualization around a tethered opossum shrimp in dorsal view

generated by beat motion of swimming legs of the opossum shrimp. The opossum shrimp swims forward, by pressing the swimming legs backwards against water. The body length of the opossum shrimp is about 10mm. This photograph was taken with a 35mm camera, shutter speed at 1/15 s.

6. Diving Beetle Robot

The micro swimming robot was developed experimentally based on the analysis of swimming behavior of diving beetle. The swimming robot was propelled by the magnetic torque acting on the small permanent magnet in the external magnetic field. The dimensions of the diving beetle robot are shown in Fig.21. The swimming robot is composed of vinyl chloride body, NdFeB permanent magnet, and polyethyleneterephthalate legs. The external magnetic field was generated by the coil wound round the cylindrical container as shown in Fig.17. Driving mechanism of the diving beetle robot is shown in Fig.22. Arrows in Fig.22 show direction of the physical quantity or direction of the motion. The magnetic torque T_m acting on the permanent magnet with magnetic moment m in the external magnetic field H is given by Eq.(11). The permanent magnet shows the rotational oscillation according to the direction of the alternating magnetic field as shown in Fig.22. In this experiment, the external magnetic field was produced by the coil applied AC voltage. The open and shut motions of the legs occur with the rotational oscillation of the permanent magnet. During such movements the legs press backwards against the water and this pushes the robot forwards. Figure 23 shows frequency characteristics of the diving beetle robot swimming. The swimming velocity of the robot shows the higher value at $f_0=4-12$ Hz. The maximum value of swimming velocity is $v_{max}=29$ mm/s. Then swimming number of the diving robot is $S_w=0.07$. The largest opening angle of the hind leg of real diving beetle is almost $\theta = \pi / 2$. However, the angle amplitude of robot leg oscillation is $\xi = 13 \pi / 180$. Therefore, the

propulsion force produced by leg motion is small. The swimming velocity of the robot was almost 29 mm/s for $f_0=4-12$ Hz, but it depended on the frequency of the alternating magnetic field.

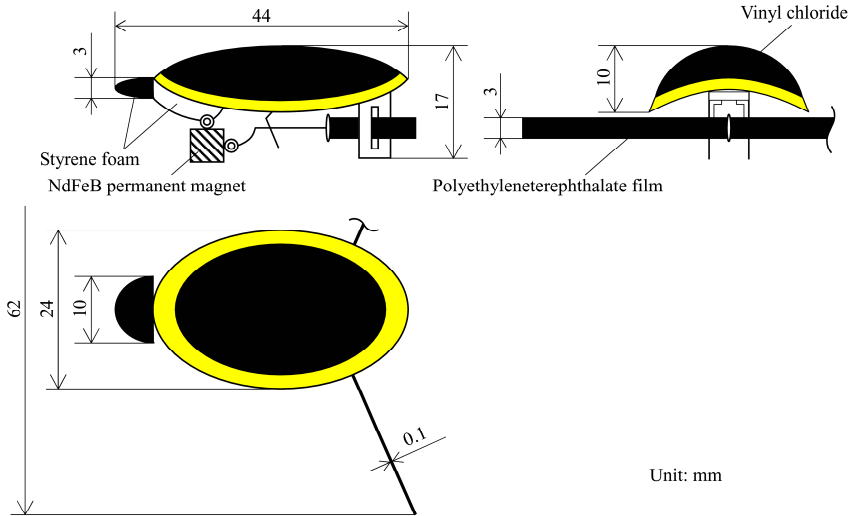


Fig. 21. Schematic diagram and dimensions of micro diving beetle robot

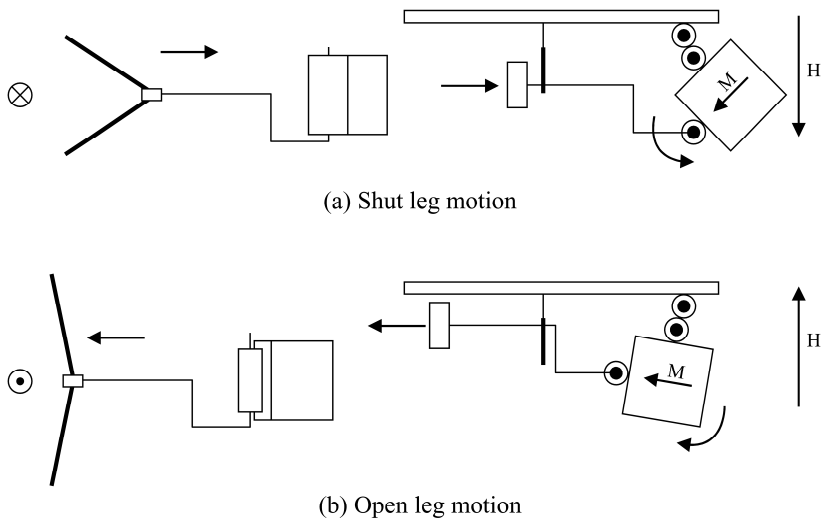


Fig. 22. Driving mechanism of micro diving beetle robot in swimming propulsion

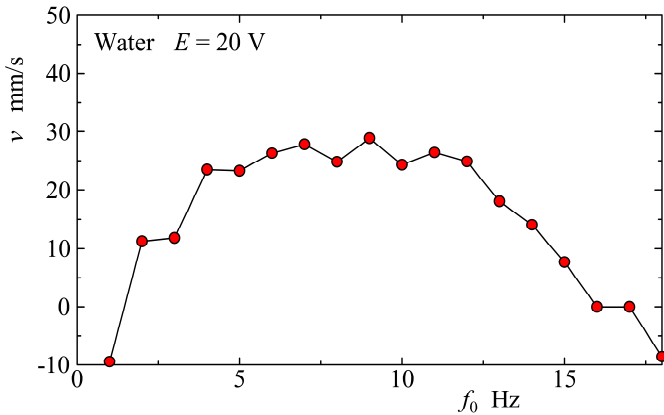


Fig. 23. Frequency characteristics of diving beetle robot in swimming velocity

7. Conclusion

The swimming behavior of small aquatic creatures was analyzed using the high speed video camera system. Based on the swimming analysis of the aquatic creatures, the micro swimming mechanism and micro diving robot propelled by alternating magnetic field were produced. The swimming characteristics of the micro mechanism and micro diving robot were developed. The swimming mechanism and diving robot swam successfully in the water. Frequency characteristics of the swimming mechanism and diving beetle robot were examined. The diving robot showed the higher swimming velocities at $f_0=4-12\text{Hz}$. These experiments show the possibility of achievement of the micro robot driving by the wireless energy supply system. The results obtained are summarized as follows;

(1) In the power stroke of the diving beetle swimming, hind legs are extended and driven backward to generate forward thrust. While in recovery stroke, hind legs are returned slowly to their initial position.

(2) In forward swimming of the dragonfly nymph, only the fore pair and the middle pair of legs are active as a thrust generator. The orbits of fore- and middle-legs show almost the same, and draw the circle partially of the orbit.

(3) The micro swimming mechanism composed of the NdFeB permanent magnet and film fin are driven by the alternating magnetic field. The swimming velocity of the micro mechanism depends on the frequency of alternating magnetic field at the constant voltage.

(4) Flow visualization around the micro mechanism was created by the motion of powder and slow shutter speed photographic technique. The forward and backward surface flows and vortex flows around the micro mechanism were generated by the robot driving.

(5) Visualization photographs of flow field around the tethered opossum shrimp show the generation of tow vortices in right and left sides of the body.

(6) The diving robot can dive into the water by sweeping the frequency of magnetic field. The diving robot can swim backward by the change of magnetic field frequency.

8. References

- Alexander, R. McN. (1984). The Gaits of Bipedal and Quadrupedal Animals. *The International Journal of Robotics Research*, Vol.3, No.2, pp.49-59
- Azuma, A. (1992). *The Biokinetics of Flying and Swimming*, pp.1-265, Springer-Verlag, ISBN 4-431-70106-0, Tokyo
- Blake, J. (1972). A model for the micro-structure in ciliated organisms. *Journal of Fluid Mechanics*, Vol.55, pp.1-23
- Dickinson, M.H.; Farley, C.T.; Full, R.J.; Koehl, M.A.R.; Kram, R. & Lehman, S. (2000). How animals move: An integrative view. *Science*, Vol.288, No.4, pp.100-106
- Dresdner, R.D.; Katz, D.F. & Berger, S.A. (1980). The propulsion by large amplitude waves of unti-flagellar micro-organisms of finite length. *Journal of Fluid Mechanics*, Vol.97, pp.591-621
- Jiang, H.; Osborn, T.R. & Meneveau, C. (2002a). The flow field around a freely swimming copepod in steady motion. Part I : Theoretical analysis. *Journal of Plankton Research*, Vol.24, No.3, pp.167-189
- Jiang, H.; Osborn, T.R. & Meneveau, C. (2002b). The flow field around a freely swimming copepod in steady motion. Part II: Numerical simulation. *Journal of Plankton Research*, Vol.24, No.3, pp.191-213
- Jiang, H.; Osborn, T.R. & Meneveau, C. (2002c). Chemoreception and the deformation of the active space in freely swimming copepods: a numerical study. *Journal of Plankton Research*, Vol.24, No.5, pp.495-510
- Nachtigall, W. (1980a). Mechanics of swimming in water-beetles, In: *Aspects of animal movement*, Elder, H.Y. & Trueman, E.R., pp.107-124, Cambridge University Press, Cambridge
- Nachtigall, W. (1980b). Swimming Mechanics and Energetics of Lovomotion of Variously Sized Water Beetles- Dytiscidae, Body Length 2 to 35 mm, In: *Aspects of animal movement*, Elder, H.Y. & Trueman, E.R., pp.269-283, Cambridge University Press, Cambridge
- Sudo, S.; Tsuyuki, K. & Honda, T. (2008). Swimming mechanics of dragonfly nymph and the application to robotics. *International Journal of Applied Electromagnetics and Mechanics*, Vol.27, pp.163-175
- Sudo, S.; Sekine, K.; Shimizu, M.; Shida, S.; Yano, T. & Tanaka, Y. (2009). Basic Study on Swimming of Small Aquatic Creatures. *Journal of Biomechanical Science and Engineering*, Vol.4, No.1, pp.23-36
- Zborowski, P. & Storey, R. (1995). *A Field Guide to Insects in Australia*, pp.111-112, Reed Books Australia, ISBN 0-7301-0414-1, Victoria

Bio-Inspired Water Strider Robots with Microfabricated Functional Surfaces

Kenji Suzuki
Kogakuin University
Japan

1. Introduction

In recent years, there has been considerable interest in insect-inspired miniature robots. Through evolutionary processes, insects have prospered by adapting themselves to diverse environments. The number of species of insects is approximately one million, which comprises approximately two-thirds of all species of animals. By taking advantage of scaling effects, insects have acquired unique locomotive abilities, such as hexapedal walking, climbing on walls, jumping, and flying by flapping, that markedly extend their fields of activity. The working principles behind these behaviours are considered to be highly efficient and optimized for miniature systems. Therefore, they provide alternative design rules for developing smart and advanced microrobotic mechanisms. For example, the flapping motion of insect wings has been investigated for micromechanical flying robots (Suzuki, et al., 1994; Wood, 2008). This chapter focuses on the locomotion of water striders. This motion is dependent on surface tension. Recent studies have demonstrated the mechanisms that enable insects to stay, as well as move, on water. Furthermore, various kinds of miniature robots that are able to move on water have been developed. Hu et al. identified the mechanism of the momentum transfer that is responsible for water strider locomotion and proposed a mechanical water strider driven by elastic thread (Hu, et al., 2003). Gao et al. showed that the legs of water striders are covered with thousands of tiny hairs that have fine nanoscale grooves (Gao & Jiang, 2004). These hierarchical micro- and nanostructures create super-hydrophobic surfaces. Suhr et al. developed a water strider robot that is driven in one of its resonant modes by using unimorph piezoelectric actuators (Suhr, et al., 2005). Song et al. numerically calculated the statics of rigid and flexible supporting legs (Song, et al., 2006; Song, et al., 2007a) and developed a non-tethered water strider robot using two miniature DC motors and a lithium-polymer battery (Song & Sitti, 2007b). The locomotion mechanisms of fisher spider (Suter & Wildman, 1997; Suter, et al., 1999) and basilisk lizard (Glasheen & McMahon, 1996a; 1996b) on the surface of water were studied. A robot that mimics the water running ability of the basilisk lizard was also developed (Floyd, et al., 2006; Floyd & Sitti, 2008).

The present authors (Suzuki, et al., 2007) have fabricated hydrophobic supporting legs with microstructured surfaces utilizing MEMS (microelectromechanical systems) techniques, and

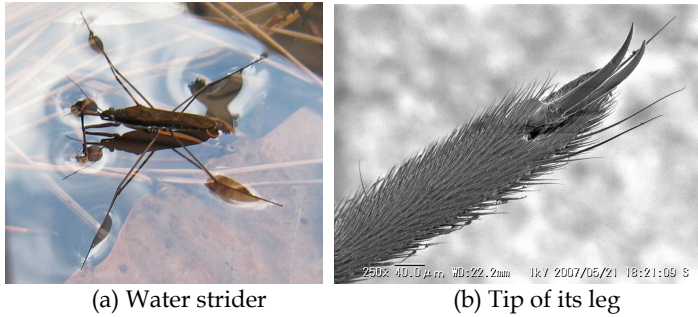


Fig. 1. The water strider, used as the robot model

developed non-tethered water strider robots with MEMS-structured legs. In this study, equations for the forces acting on a partially submerged supporting leg were derived analytically, and the effects of the diameter and contact angle of the leg on the forces were investigated. Then, various kinds of hydrophobic supporting legs with and without microfabricated surfaces were prepared, and the lift and pull-off forces on the water surface were measured to verify the theoretical analyses. In addition, two non-tethered mechanisms for water strider robots with microfabricated legs were created to demonstrate autonomous locomotion on the surface of water.

2. Theoretical model of a supporting leg

2.1 Lift force

Water striders can stay and move on the surface of water by primarily using surface tension force. Figure 1 shows a water strider on a water surface and an SEM image of the tip of its leg. The leg is covered with tiny hairs, which improve the hydrophobicity and reduce the drag force. In this section, equations of the buoyancy and surface tension forces acting on a partially submerged cylindrical leg are analytically derived

Figure 2 shows a two-dimensional model of the supporting leg. We assume that the leg is a long, rigid cylinder of uniform material with radius r and contact angle θ_c . The vertical lift force F acting on the leg of unit length consists of a buoyancy force F_B and a force due to surface tension F_S .

$$F = F_B + F_S \tag{1}$$

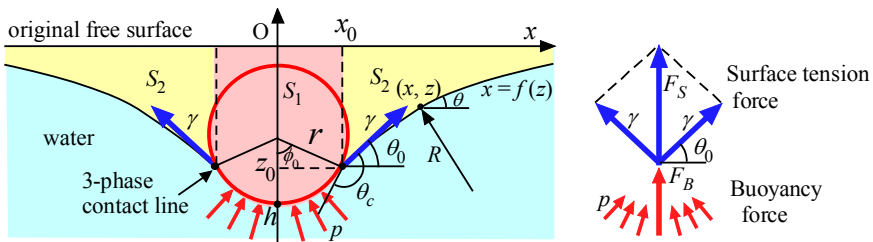


Fig. 2. Two dimensional model of the supporting leg.

The buoyancy force F_B is deduced by integrating the vertical component of hydrostatic pressure p over the body area in contact with the water. The force due to surface tension F_S is the vertical component of the surface tension per unit length γ acting on the three-phase contact line. Keller demonstrated that F_B and F_S are equal to the weights of water displaced inside and outside of the three-phase contact line, respectively (Keller, 1998). That is, F_B is proportional to the area S_1 , shown in Fig. 2, and F_S is proportional to the area S_2 .

$$F_B = \int_0^{\phi_0} p \cos \phi \cdot r d\phi = \rho g S_1 \quad (2)$$

$$= \rho g (-2 z_0 r \sin \phi_0 - r^2 \sin \phi_0 \cos \phi_0 + r^2 \phi_0)$$

$$F_S = 2 \gamma \sin \theta_0 = \rho g S_2 \quad (3)$$

where ϕ_0 is the submerged angle and θ_0 is the slope of the water surface, as shown in Fig. 2. The subscript "0" represents the value on the three-phase contact line. The relationship between ϕ_0 and θ_0 is given by:

$$\phi_0 = \pi + \theta_0 - \theta_c \quad (4)$$

From the Young-Laplace equation, hydrostatic pressure on the surface of water is:

$$p = -\rho g z = \frac{\gamma}{R} \quad (5)$$

where R is the radius of curvature of the water surface. The governing equation of the water's surface profile as a function of z , $x = f(z)$ is given by

$$\frac{\rho g z}{\gamma} = \text{Sign}(z) \frac{f''(z)}{(1 + f'(z)^2)^{\frac{3}{2}}} \quad (6)$$

The boundary conditions for $f(z)$ are

$$f(0) = \infty, \quad f(z_0) = x_0 = r \sin \phi_0 \quad (7)$$

By integrating (6) by z under the conditions (7), the following equation is obtained:

$$\frac{\rho g z^2}{2\gamma} = 1 + \text{Sign}(z) \frac{f'(z)}{\sqrt{1 + f'(z)^2}} = 1 - \cos \theta \quad (8)$$

where θ is the slope of the water surface ($f'(z) = \cot \theta$). Then, the following equations can be derived from (8).

$$z = -\text{Sign}(\theta) L_c \sqrt{2(1 - \cos \theta)} \quad (9)$$

$$L_c = \sqrt{\frac{\gamma}{\rho g}} \quad (10)$$

$$f'(z) = \frac{2L_c^2 - z^2}{-z\sqrt{4L_c^2 - z^2}} \quad (11)$$

where L_c is the capillary length. By integrating (11) by z , the equation of the surface profile of the water is given analytically:

$$x = f(z) = L_c \cosh^{-1} \left(\frac{2L_c}{|z|} \right) - \sqrt{4L_c^2 - z^2} + C \quad (12)$$

The integration constant C can be determined from the boundary conditions (7). Figure 3 shows the water surface profile given by (12). Since the maximum one-sided width of a water dimple or bump is approximately 10 mm, the maximum lift force of two supporting legs whose spacing is less than 20 mm decreases due to two water dimples overlapping with one another.

From (3), the force due to surface tension F_S reaches a maximum value 2γ at $\theta_0 = \pi/2$ if the surface of the supporting leg is hydrophobic ($\theta_c > \pi/2$). Under this condition, the depth of the three-phase contact line is $\sqrt{2} L_c$, as shown in Fig.4 (a).

$$(F_S)_{\max} = 2\gamma = 0.146 \text{ N/m} \quad (\text{at } 20^\circ\text{C}) \quad (13)$$

$$z_0 = -\sqrt{2} L_c = -3.86 \text{ mm} \quad (\text{at } 20^\circ\text{C}) \quad (14)$$

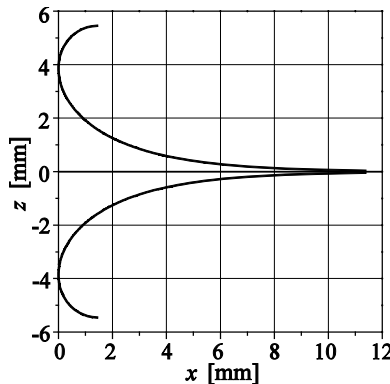


Fig. 3. Profile of the dimple and the bump of water.

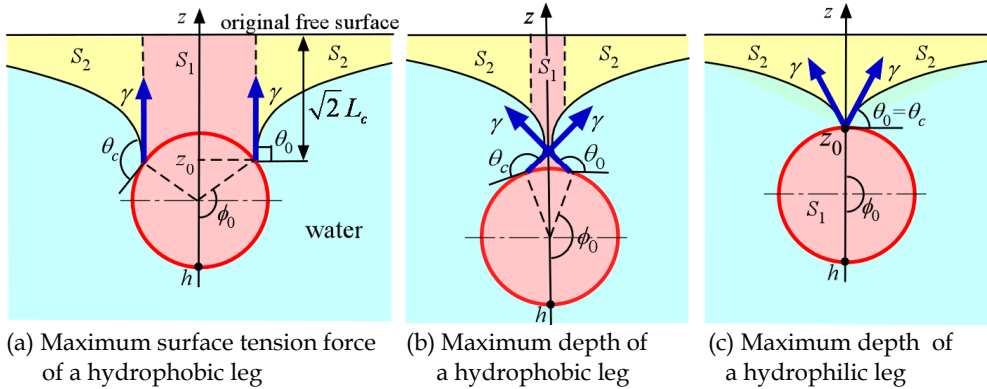


Fig. 4. Water breaking conditions

Both the maximum surface tension force and the depth of the leg do not depend on the diameter of the leg or the contact angle. In contrast, the buoyancy force F_B does depend on the diameter of the supporting leg. When the diameter is much smaller than L_c , the force due to surface tension dominates over the buoyancy force. As the depth of the three-phase contact line exceeds $\sqrt{2}L_c$, θ_0 becomes greater than $\pi/2$, and the surface tension force decreases with increasing depth. Figure 4 (b) shows the overhanging water surface just before the surface is broken.

When the surface of the supporting leg is hydrophilic ($\theta_0 < \pi/2$), the maximum surface tension force is $2\gamma \sin \theta_c$, which decreases with decreasing the contact angle θ_c (Fig. 4 (c)).

2.2 Pull-off force

When the leg is lifted out of the water, water rises with the leg, as shown in Fig. 5 (a). Both the buoyancy force and the force due to surface tension, given by (2) and (3), respectively, become negative, that is, downward forces. In this paper, the force needed to lift the leg from the water is defined as the pull-off force. Figure 5 (b) shows the water surface profile just before the leg is completely pulled off when the surface of the supporting leg is hydrophobic. In this situation, the buoyancy force becomes zero, and the maximum pull-off force is given by (15)

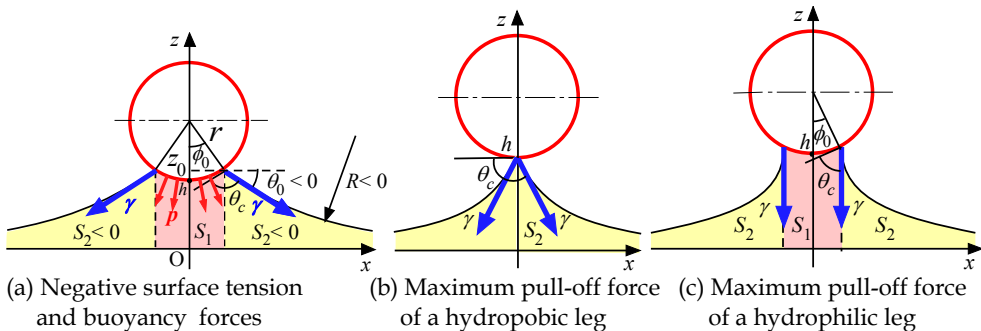


Fig. 5. Pull-off force

$$F = 2\gamma \cos \theta_c < 0 \quad (15)$$

Equation (15) indicates that a leg with a large contact angle can easily be lifted from the water surface. Therefore, super-hydrophobic legs of a water strider reduce the pull-off force instead of generating a large lift force. When the surface of the supporting leg is hydrophilic, the maximum pull-off force is approximately 2γ if the surface tension effect is dominant, which does not depend on the contact angle θ_c , as shown in Fig. 5 (c).

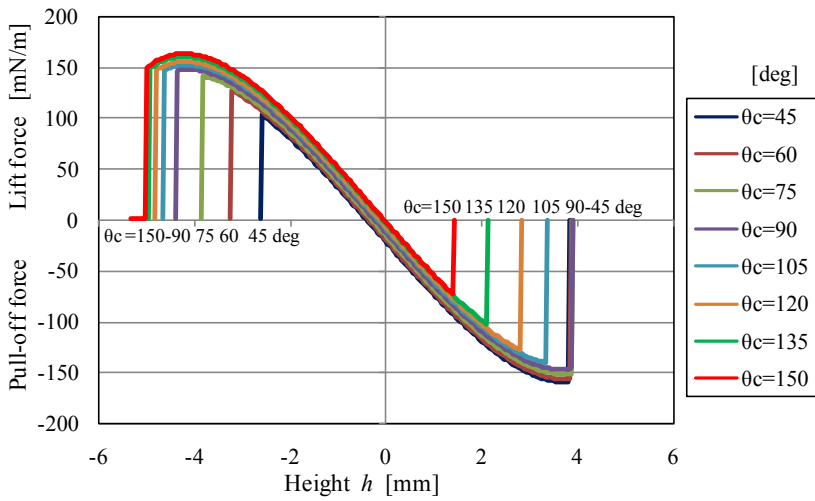
2.3 Results of the simulations

Using the theoretical model shown in the previous section, the relationship between the height of the supporting leg, h , and the force acting on the leg, F , was investigated, where h is defined as the height of the bottom of the supporting leg from the free water surface, given by:

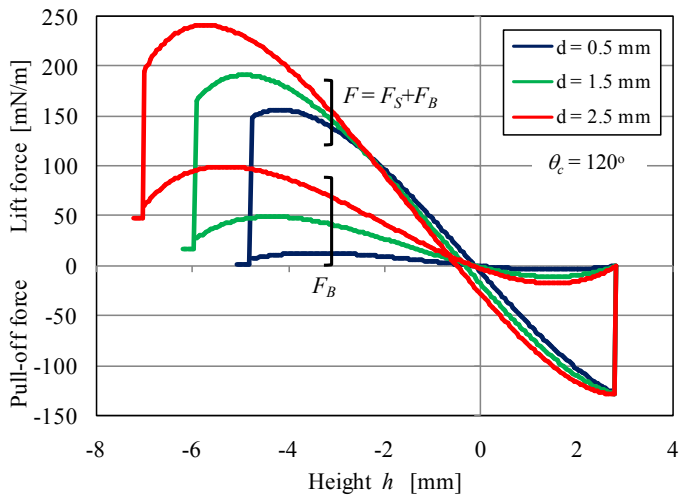
$$\begin{aligned} h &= z_0 - r(1 - \cos \phi_0) \\ &= -\text{Sign}(\theta_0) L_c \sqrt{2(1 - \cos \theta_0)} - r(1 - \cos \phi_0) \end{aligned} \quad (16)$$

The force F can be obtained by equations (1) through (4). Thus, h and F are connected by the parameter θ_0 .

The results of the calculations are shown in Fig.6. Figure 6 (a) demonstrates the effects of the contact angle of the leg surface on the lift and pull-off forces. The pull-off force is shown as the negative lift force. The results show that the lift force of the hydrophobic leg ($\theta_c > 90^\circ$) does not differ much due to the contact angle of the leg. In contrast, both the pull-off force and the height where the leg is completely pulled off increase as the contact angle decreases. In the case of the hydrophilic leg ($\theta_c < 90^\circ$), the lift force decreases as the contact angle decreases and the pull-off force is almost constant. Figure 6 (b) shows the effects of the diameter of the hydrophobic supporting leg on the lift and pull-off forces. The component of buoyancy force (F_B) is also shown in the same figure. The lift force increases as the diameter of the leg increases. The differences in lift force are derived from the differing buoyancy forces (F_B) that depend on the leg diameter. When the diameter of the leg is less than 0.5mm, the buoyancy force becomes negligibly small. The force due to surface tension, F_S , does not depend on the diameter and the contact angle of the leg, because the maximum surface tension force is 2γ per unit length if the leg surface is hydrophobic. The buoyancy force, however, is almost canceled by the weight of the leg itself if the specific gravity of the leg is greater than 1. Consequently, the increase in buoyancy force does not necessarily lead to an increase in the net loading capacity. In the case of water strider, the water-repellent hairy legs efficiently increase the loading capacity because water cannot enter the spacing between hairs, and so the apparent diameter is enlarged without increasing the mass of the leg.



(a) Effect of contact angle on the lift and pull-off forces



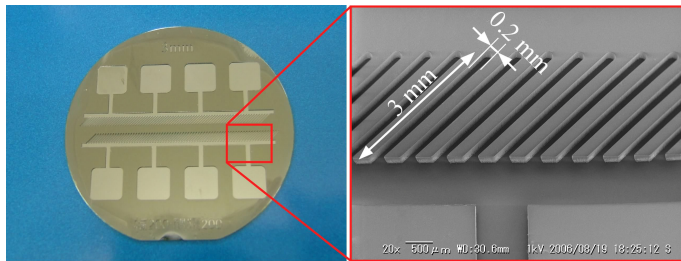
(b) Effect of diameter of supporting leg on the lift and pull-off forces

Fig. 6. Results of the simulations

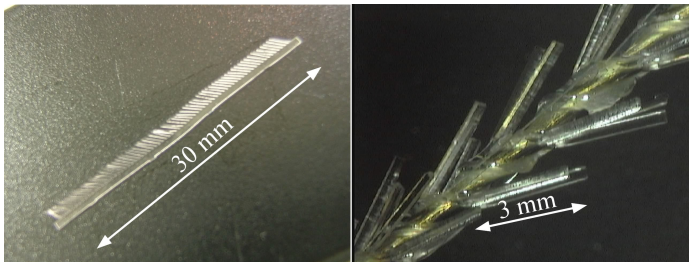
3. Fabrication Of The Microstructured Legs

According to Wenzel's law and Cassie-Baxter's law, micro structures on a surface enhance hydrophobicity. Mechanical structures as well as chemical properties help create super-hydrophobic surfaces. In the present paper, three kinds of hydrophobic supporting legs with micro structures fabricated using MEMS processes are proposed.

Figure 7 shows a PDMS (polydimethylsiloxane) hair-like structure wrapped on a 0.5-mm-diameter brass wire. The process starts with the fabrication of a mold by the patterning of SU-8, a photoresist that enables the creation of thick patterns by UV lithography (Fig.7 (a)). Then PDMS is poured into the grooves of the mold by capillary action, cured, and released from the mold to form the comb-shaped structure shown in Fig.7 (b). The PDMS structure is wrapped around the wire and adhered by a two-component epoxy adhesive. As the last step, the structure is dipped into a fluorinated hydrophobic agent (Fluoro Technology, FS-1010) to coat the surface of the structure.



(a) SU8 mold for PDMS structure



(b) PDMS comb-shaped structure (c) PDMS structure wrapped on a wire

Fig. 7. PDMS hair-like structure

The second structure, shown in Fig. 8, consists of SU-8 patterns fabricated by photolithography on a 1-mm-diameter cylindrical brass wire. The process of exposure is shown in Fig.8 (a). An 80- μm -thick SU-8 layer is coated on the wire by dipping and the surface of the SU-8 is divided into 5 faces, with each face exposed separately. Circular patterns with a diameter of 100 μm are formed by developing the SU8 layer (Fig.8 (b)). Then, the same hydrophobic agent (FS-1010) is coated on the structure by dipping. SEM micrographs of the SU-8 structure are shown in Fig.8 (c).

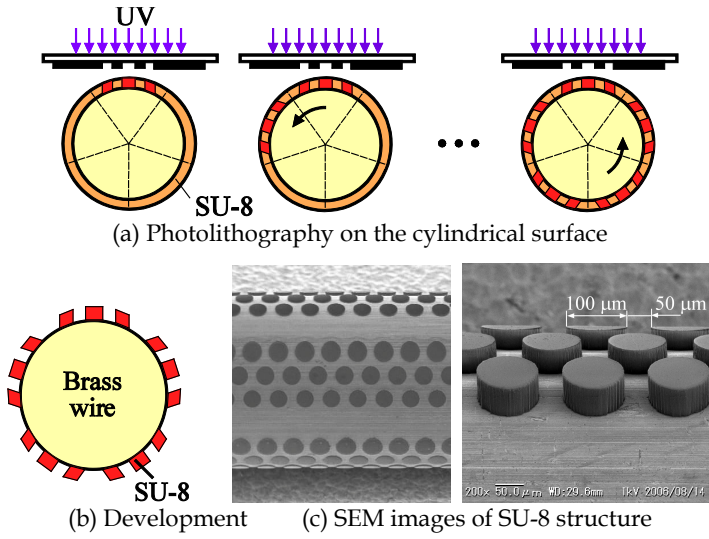


Fig. 8. SU-8 structure

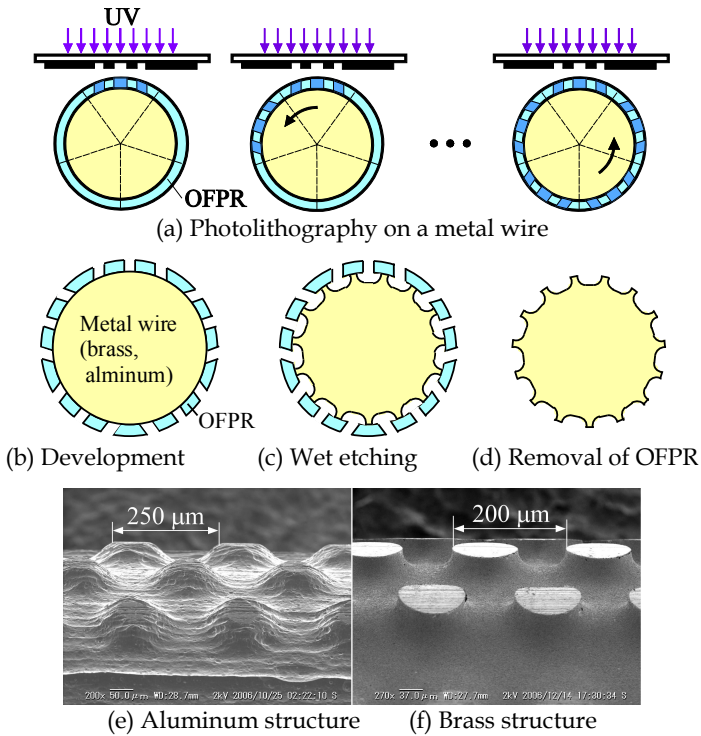


Fig. 9. Wet etching of aluminum and brass wires

The third structure is formed on the surfaces of aluminium and brass wires by wet etching. Figure 9 shows the process to fabricate the etched structures. First, photolithography on the cylindrical metal wires was carried out in the same manner as in the SU8 structure. Here, a positive type photoresist (Tokyo Ohka Kogyo, OFPR) was used instead of SU-8 (Fig. 9 (a) (b)). The wires were then patterned by isotropic wet etching (Fig. 9 (c)), followed by removal of the OFPR (Fig. 9 (d)). Finally, the same hydrophobic agent (FS-1010) was coated on the structure. SEM photographs of the aluminium and brass structures are shown in Fig. 9 (e) and (f), respectively. The brass structures have sharper edges than do the aluminium structures.

4. MEASUREMENTS OF LIFT AND PULL-OFF FORCES

4.1 Experimental setup

To investigate the performance of the supporting legs, the lift and pull-off forces of the fabricated legs were measured. The experimental setup for the measurements is illustrated in Fig. 10. The geometry of the specimen is shown in Fig.11. Both ends of the specimen are bent up in order to prevent the tip of the wire from breaking the water surface.

The surface of the water in a petri dish was moved vertically using a z stage to immerse and pull out the specimen. The lift and pull-off forces were measured by using a laser displacement sensor to detect the deformation of a parallel leaf spring fixed to the specimen. By using two laser displacement sensors, the relative height of the specimen from the water surface was also measured. Table I shows materials, surface structures, outer diameters, and contact angles of the specimens. Three kinds of the hydrophobic-agent-coated specimens, as well as four specimens with microfabricated structures on their surfaces, were prepared. The contact angles of the microfabricated wires, except for the PDMS structure, increased by 5-10 degrees compared to those of the FS-1010 coated non-structured wire. The PDMS structure was too large to show an increase in the contact angle.

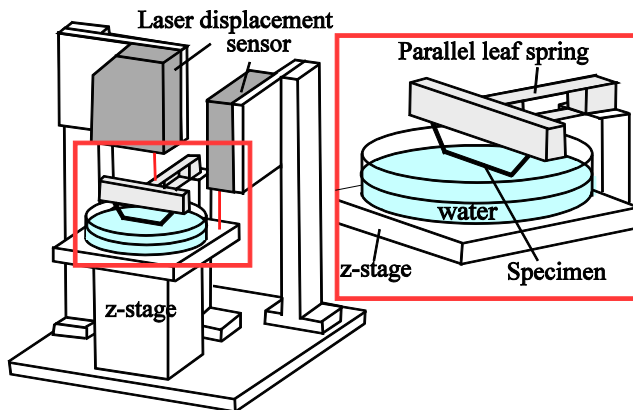


Fig. 10. Experimental setup for measuring lift and pull-off forces

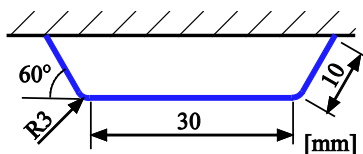


Fig. 11. Geometry of the specimen

Base wire	MEMS structure	Hydrophobic coating	Outer Diameter	Contact angle
Brass ϕ 0.5	---	FS-6130 ^{*1}	0.5 mm	105°
Brass ϕ 0.5	---	FS-1010 ^{*1}	0.5 mm	118°
Brass ϕ 0.5	---	HIREC-1450 ^{*2}	0.62 mm	135°
Brass ϕ 0.5	PDMS	FS-1010 ^{*1}	2.5 mm	117°
Brass ϕ 1.0	SU-8	FS-1010 ^{*1}	1.1 mm	128°
Aluminium ϕ 1.4	Etching	FS-1010 ^{*1}	1.4 mm	123°
Brass ϕ 1.0	Etching	FS-1010 ^{*1}	1.0 mm	123°

*1 Fluoro Technology Corp. *2 NTT Advanced Technology Corp.

Table 1. Material, Diameter, and Contact Angle of the Specimens

3.2 Experimental results

Figure 12 shows the relation of height h with lift and pull-off forces for specimens without MEMS structures. The results for the specimens with MEMS structures are shown in Fig.13. Experimental and calculated data are shown in (a) and (b), respectively, in both figures. In the experiment, the supporting leg was first immersed gradually into water. In this process, the lift force initially increased, reached a maximum, and then decreased slightly; finally, the water's surface was broken and the leg was completely submerged. After that, as the leg was pulled out of the water, the leg remained submerged until it came close to the surface of water. Then, a dimple of water formed abruptly, and it was gradually raised along with the specimen. This hysteresis is observed in the experimental results shown in Figs 12 (a) and 13 (a), although this effect was not taken into account in the calculations.

The measured lift forces are in good agreement with the calculated values. The maximum lift force depends on the diameter of the specimens rather than the surface properties of the legs. The measured pull-off force decreases with increasing contact angle. This trend agrees well with the theoretical predictions. However, the measurements for the values of the maximum pull-off force and maximum height are smaller than those calculated. This is because the meniscus bridge shrinks at one end of the leg and becomes a conical shape just before the leg is completely pulled off. Therefore, a three dimensional dynamic model of the meniscus is necessary to predict the maximum pull-off force quantitatively.

The PDMS hair-like structure wrapped on the wire of 0.5 mm in diameter enlarges to an apparent diameter of 2.5 mm and increases the maximum possible lift force efficiently, even though it does not improve the contact angle and pull-off force.

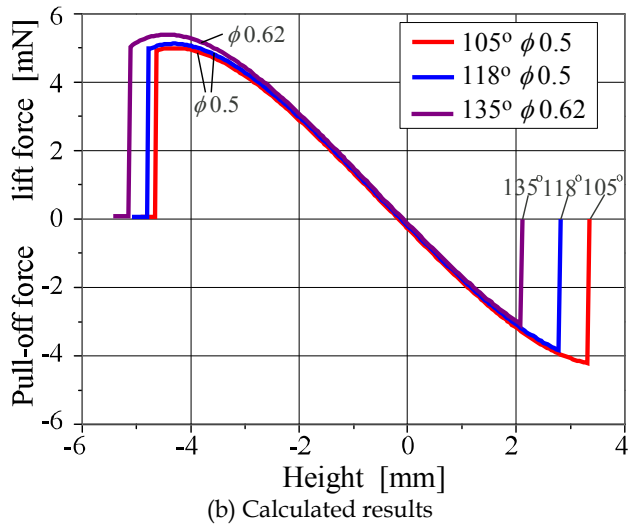
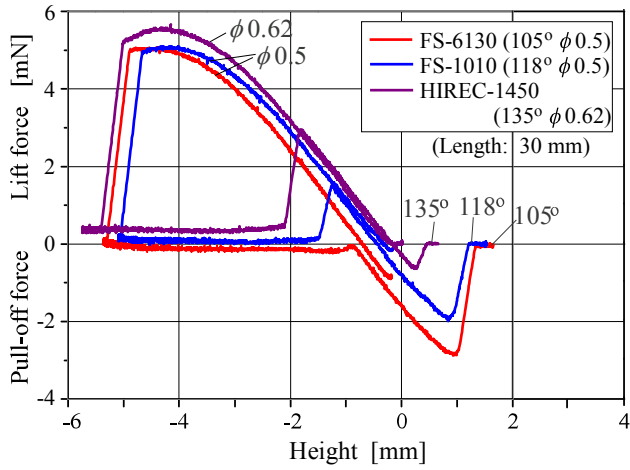
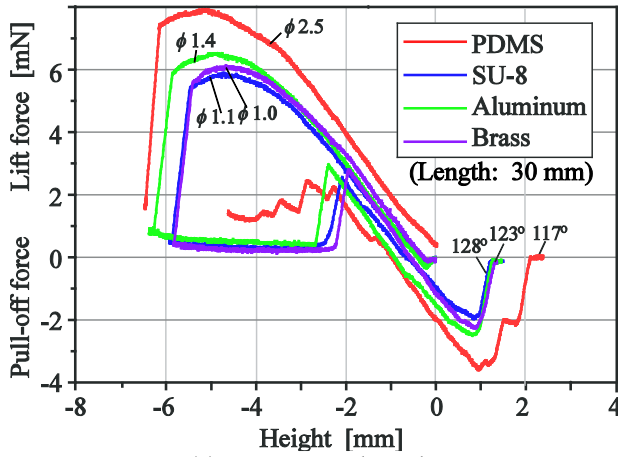
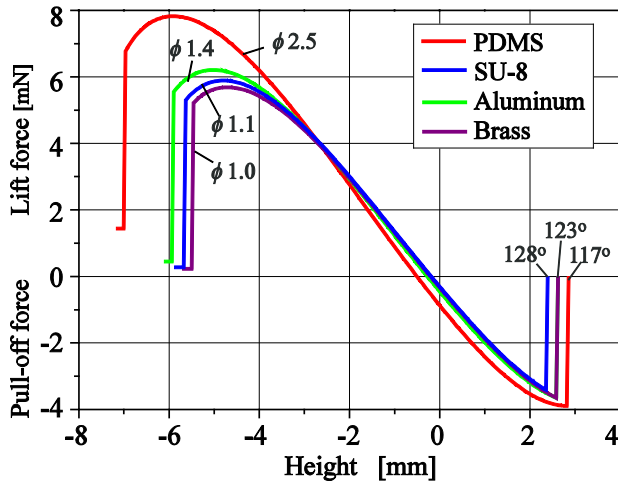


Fig. 12. Lift and pull-off forces for hydrophobic-agent-coated legs



(a) Experimental results



(b) Calculated results

Fig. 13. Lift and pull-off forces for legs with microfabricated structures

5. DEVELOPMENT OF WATER STRIDER ROBOTS

5.1 Hexapedal robot

Two different mechanisms for surface-tension-based locomotion on the water surface were developed. Figure 14 shows a hexapedal robot. The hydrophobic legs with PDMS hair-like structures were used for the forelegs and hind legs to support the weight of the body. The middle legs were attached to an actuating mechanism that creates the elliptical motion required for propulsion. The resulting hexapedal locomotion is similar to that of an insect water strider. Each supporting leg is 135 mm in length. From the results of Fig. 13 (a), the loading capacity of the four supporting legs was predicted to be 138 mN (14 gf), which is

sufficient to support a robot that weighs 5.4 gf. A DC motor and a lithium polymer battery were mounted on the body, and non-tethered actuation was achieved.

The slider-crank mechanism, shown in Fig. 15, was used for creating the elliptical motion of the middle legs. The trajectory of point P at the middle of the connecting rod is given by the following equations:

$$\begin{cases} x = r \cos \theta + \left(1 - \frac{a}{l}\right) \sqrt{l^2 - r^2 \sin^2 \theta} \\ y = \frac{ar}{l} \sin \theta \end{cases} \quad (17)$$

Definitions of r , l , a , θ and the calculated trajectory of P is shown in Fig. 16. Figure 17 illustrates the transmission mechanism for the middle leg. The 125-mm-long middle leg penetrates the connecting rod at P and is supported at Q using a flexible ring, so that the middle leg rotates conically around Q. The rowing angle of the leg is approximately 90° and the elliptical motion of P is magnified by 10 at the tip of the leg.

The hexapedal robot was put on the surface of water in a container and the middle legs were driven at 2 Hz. Forward motion was successfully achieved on the surface down to 5-mm-deep water. The velocity determined from the images of a high-speed camera is shown in Fig. 18 (a). A maximum speed of 90 mm/s and an average speed of 40 mm/s were achieved. The middle legs were swept shallowly without breaking the surface of water and pulled off during the power stroke. Consequently, deceleration starts in the middle of the power stroke. Then, acceleration starts in the middle of the recovery stroke because of the inertial force of the actuating legs. The velocity of an actual water strider obtained from high-speed video images is shown in Fig.18 (b). The water strider accelerates all the way through the power stroke and reaches a maximum speed of about 400 mm/s. Then it decelerates rapidly in the recovery stroke. After that, it glides on the surface of the water, decelerating moderately.

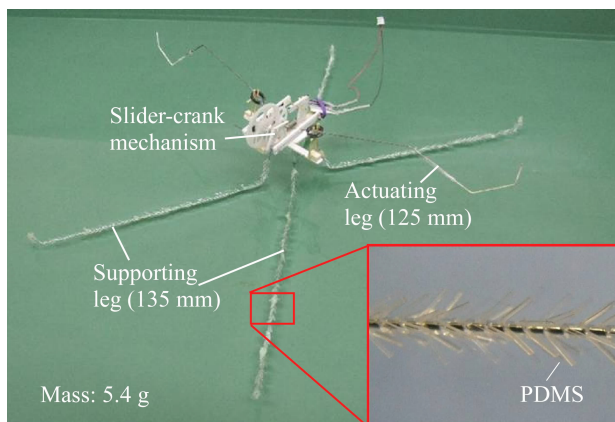


Fig. 14. Hexapedal water strider robot

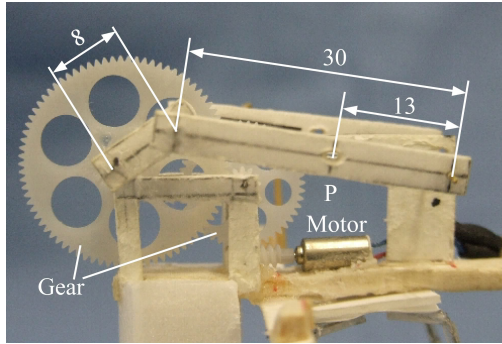


Fig. 15. Slider-crank mechanism for creating elliptical motion of middle leg.

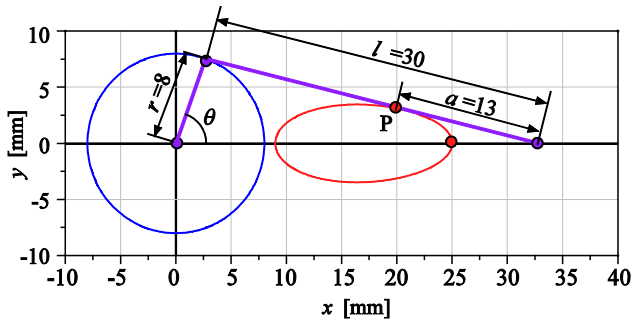


Fig. 16. Elliptical trajectory created by the slider-crank mechanism

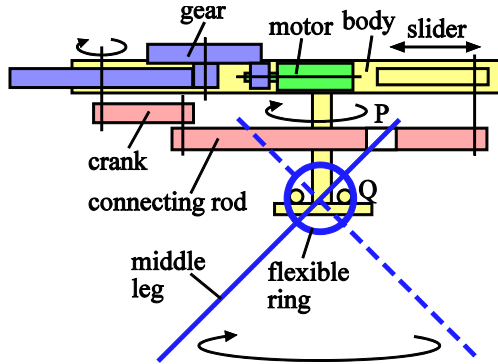


Fig. 17. Structure of the middle leg

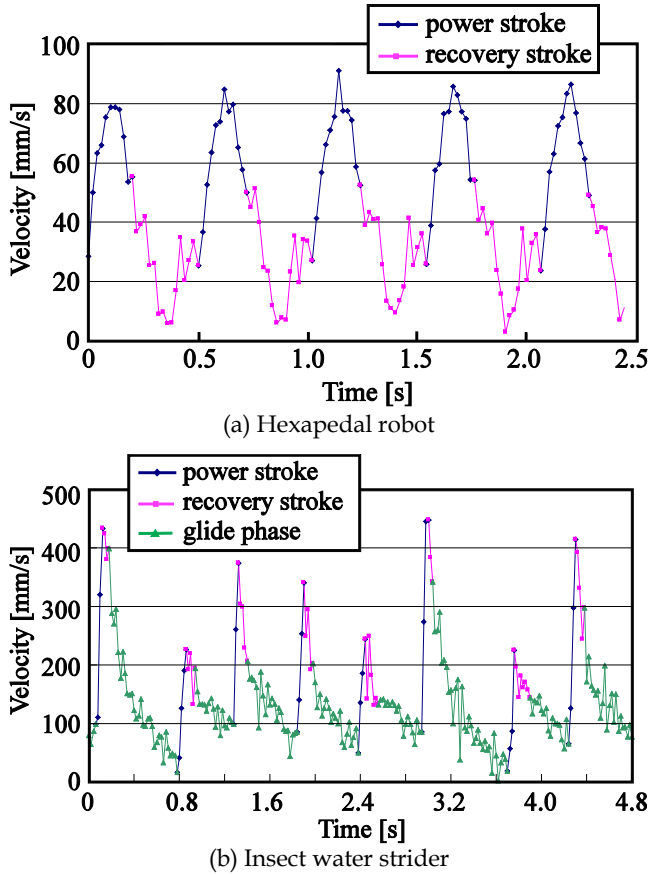


Fig. 18. Variation of the velocity during the rowing motion

5.2 Robot with a vibration motor

The other mechanism developed in the present study was a robot that moves on the water surface by the vibration of twelve supporting legs. A photograph of the robot is shown in Fig. 19. A vibration motor with an eccentric weight is mounted on the body. This type of motor is used in cell phones. Brass legs with wet-etched microstructures are used as supporting legs so that the microstructures can withstand high-frequency vibrations, as shown in the inset of Fig. 19. The geometry of both ends of the leg is the same as those of the specimen shown in Fig. 11. One end of the leg is attached to the robot's body directly. Each leg has a different length and consequently a different resonant frequency. When the rotational speed of the vibration motor is varied, different legs resonate, enabling the robot to move forward, left, and right. Thus, multiple motions can be realized using one motor without any mechanism for power transmission. The actuation method for micro mobile robots utilizing resonance with externally applied vibration was proposed by Yasuda et al.

(Yasuda et al., 1994). However, a self-contained robot with a vibrator and a power source has not been achieved.

The layout of the legs is shown in Fig.20. The roles and specifications of the legs are shown in Table 2. From the results of Fig.13 (a), total length of twelve legs is 1 m and the maximum payload is predicted to be 200mN (20.4gf). A vibration motor, lithium polymer battery, and electronics for PWM (pulse width modulation) control of rotational speed were mounted on the robot for fully autonomous actuation. The robot weighed 7.85 g and could therefore be supported by the legs with a safety factor of greater than 2.

Figure 21 shows the measured and calculated resonant frequencies of the 1st and 2nd modes in air and on the surface of the water as a function of leg length. The 2nd-mode vibration was used for locomotion, since the frequency range matches that of the PWM-controlled vibration motor. Calculated resonant frequencies were obtained from the following equation for resonant frequency of a straight cantilever:

$$f = \left(\frac{\lambda}{L}\right)^2 \sqrt{\frac{EI}{\rho A}} \tag{18}$$

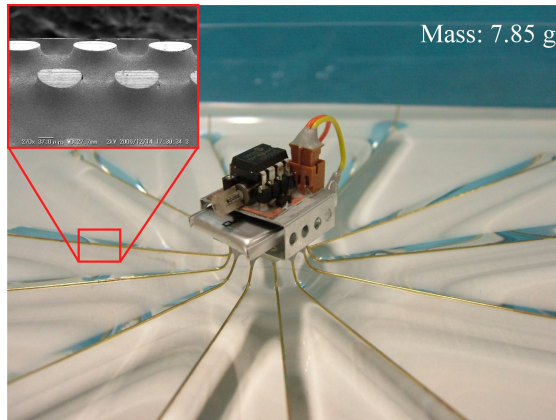


Fig. 19. Water strider robot with a vibration motor

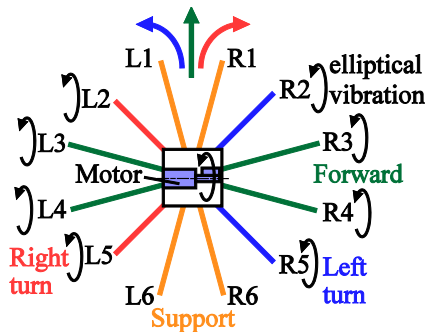


Fig. 20. Layout of the supporting legs.

where E is Young's modulus, I is the geometrical moment of inertia, ρ is the density, A is the cross sectional area, L is the length of the supporting leg including both angled ends, and λ is a constant (1st mode: 1.875, 2nd mode: 4.694). The resonant frequencies in air are in good agreement with the calculated values. The resonant frequencies on the surface of the water are lower than those in air because of the additional mass of water around the leg. Figure 22 shows the trajectory of a 90-mm-long leg (R3) resonated at 120 Hz in air. The leg rotated elliptically in sync with the eccentric mass of the vibration motor. This elliptical vibration generates the propulsive force on the surface of water

Photographs of the robot moving on the surface of an outdoor pond are shown in Fig. 23. The robot successfully moved forward and rotated left and right in accordance with the embedded program without breaking the surface of the water. The velocity of the forward motion was approximately 70 mm/s, whereas both the velocity of the left and right turns was 50 mm/s. The radius of the left and right turns was 700 mm and 800 mm, respectively. These differences are due to the differences in the number and length of the resonated legs.

Leg No.	Role	Length	Resonant Frequency	Duty factor of input pulse
L-1,6 R-1,6	Support	85 mm	---	---
L-3,4 R-3,4	Forward motion	90 mm	109 Hz	32 %
R-2,5	Left turn	80 mm	115 Hz	34 %
L-2,5	Right turn	70 mm	132 Hz	39 %

Table 2. Role, Length, and Resonant Frequency of the Leg

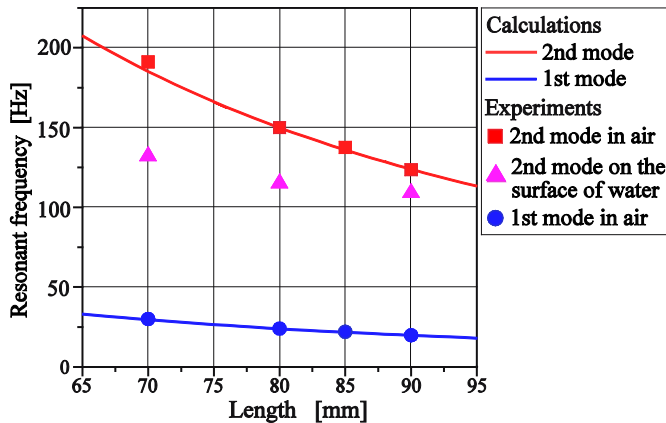


Fig. 21. Resonant frequencies in air and on the surface of water as a function of length of the supporting leg.

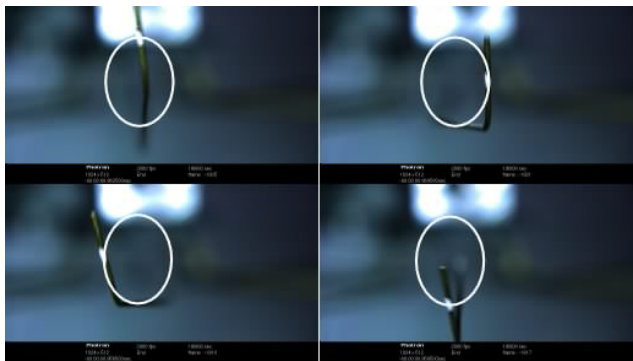
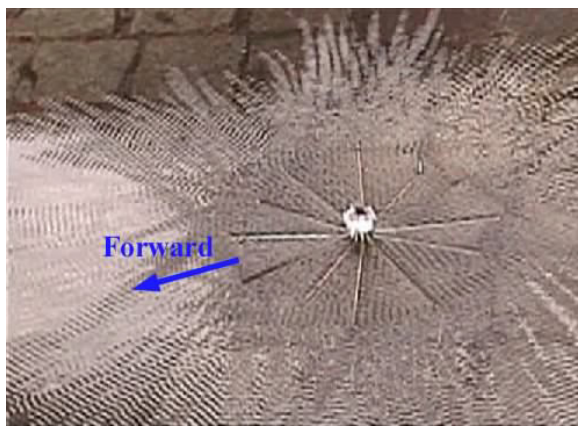
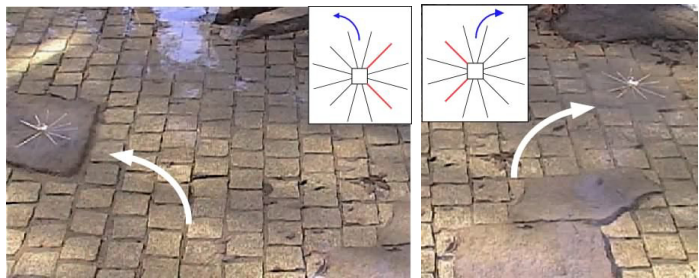


Fig. 22. Trajectory of the supporting leg resonated in air. (Leg No. R3, 120Hz)



(a) Forward motion (109Hz)



(b) Left turn (115 Hz)

(c) Right turn (132 Hz)

Fig. 23. Locomotion utilizing resonant vibration

6. Conclusion

Motivated by highly optimized working principles of small insects, we have been studying the surface-tension-based locomotion on the surface of water. Various kinds of supporting legs with microfabricated hydrophobic surfaces were developed using MEMS techniques, and the force balance between the stationary legs and the surface of water was clarified both theoretically and experimentally. Two kinds of non-tethered water strider robots with microfabricated supporting legs were developed, and autonomous locomotion on the surface of water was demonstrated. Actuation utilizing resonant vibration was effective in simplifying the mechanisms for miniature mobile robots. Dynamic analysis of the locomotion on the surface of water is left for future research.

Locomotion that depends on surface tension force provides miniature robots with efficient mobility on shallow water. In the near future, such robots with microsensors and wireless communication devices can potentially be used for entertainment and environmental monitoring, such as water quality surveys.

7. References

- Floyd, S.; Sitti, M. (2008). Design and Development of the Lifting and Propulsion Mechanism for a Biologically Inspired Water Runner Robot, *IEEE Transactions on Robotics*, Vol. 24, No. 3, pp.698-709.
- Floyd, S.; Keegan, T. & Sitti, M. (2006). A Novel Water Running Robot Inspired by Basilisk Lizards, *Proceedings of the IEEE/RSJ Intelligent Robot Systems Conference*, Beijing, pp. 5430-5436.
- Gao, X. & Jiang, L. (2004) Water-repellent legs of water strider, *Nature*, Vol. 432, p.36.
- Glasheen, J. W. & McMahon, T. A. (1996). A hydrodynamic model of locomotion in the Basilisk Lizard, *Nature*, Vol. 380, pp.340-342.
- Glasheen, J. W. & McMahon, T. A. (1996). Size-Dependence of Water- Running Ability in Basilisk Lizards, *Journal of Experimental Biology*, vol. 199, pp. 2611-2618.
- Hu, D. L.; Khan, B. & Bush, J. W. M. (2003) The hydrodynamics of water strider locomotion," *Nature*, Vol. 424, pp.663-666, 7.
- Keller, J. B. (1998). Surface Tension Force on a Partially Submerged Body, *Physics of Fluids*, Vol. 10, pp. 3009-3010.
- Song, Y. S. ; Suhr, H. & Sitti, M. (2006). Modeling of the Supporting Legs for Designing Biomimetic Water Strider Robots, *Proceedings of IEEE Int. Conf. on Robotics and Automation*, Orlando, pp.2303-2310.
- Song, Y. S. & Sitti, M. (2007)a. Surface-Tension-Driven Biologically Inspired Water Strider Robots: Theory and Experiments, *IEEE Transactions of Robotics*, Vol. 23, No. 3 pp.578-589.
- Song, Y. S. & Sitti, M. (2007)b. STRIDE: A Highly Maneuverable and Non- Tethered Water Strider Robot, *Proceedings of IEEE Int. Conf. Robotics and Automation*, Roma, 2007, pp.980-984.
- Suhr, S. H.; Song, Y., S; Lee, S. J. & Sitti, M. (2005) Biologically Inspired Water Strider Robot, *Robotics: Science and Systems*, Boston, pp. 319-325.

- Suter, R. B. & Wildman, H. (1997). Locomotion on the Water Surface: Propulsive Mechanisms of the Fisher Spider DOLOMES TRITON, *Journal of Experimental Biology*, Vol. 200, pp. 2523-2538.
- Suter, R. B.; Rosenberg, O.; Loeb, S.; Wildman, H. & Long, J. H. Jr. (1999). "Locomotion on the Water Surface: Hydrodynamic Constraints on Rowing Velocity Require a Gait Change, *Journal of Experimental Biology*, Vol. 202, pp. 2771-2785.
- Suzuki, K.; Shimoyama, I. & Miura, H. (1994). Insect-Model Based Microrobot with Elastic Hinges, *IEEE J. Microelectromechanical Systems*, Vol. 3, No. 1, pp. 4-9, March 1994.
- Suzuki, K.; Takano, H.; Noya, K.; Koike, H. & Miura, H. (2007). Water Strider Robots with Microfabricated Hydrophobic Legs, *Proceedings of. IEEE/RSJ Int. Conf. Intelligent Robots and Systems (IROS07)*, San Diego, pp.590-595.
- Wood, R. J (2008). The First Takeoff of a Biologically Inspired At-Scale Robotic Insect, *IEEE Transactions of Robotics*, Vol. 24, No. 2, pp.341-347.
- Yasuda, T.; Miura, H. & Shimoyama, I. (1994). Microrobot Actuated by a Vibration Energy Field, *Sensors and Actuators, A: physical*, Vol. 43, No. 1-3, pp.366-370.

Electrochemical sensor based on biomimetic recognition utilizing molecularly imprinted polymer receptor

Yusuke Fuchiwaki¹ and Izumi Kubo²

¹National Institute of Advanced Industrial Science and Technology (AIST)

²Soka University

1. Introduction

Biological recognition elements such as antibodies, enzymes and aptamers have been utilized as specific receptors to a target molecule in a wide variety of assays and sensors. However, many difficulties for their practical use exist as they lack stability and reusability. Moreover, it is not easy to obtain and prepare sufficient natural bioreceptors. Since practically there are many extraneous inhibitors against biological receptors, scientists have attempted to develop specific recognition elements alternative to bioreceptors.

One approach was the synthesis of hosts which possess a structure capable of binding complementary guests. The synthesis of specific recognition sites has been accomplished by coordinating functional monomers around the target molecule, and then cross-linking to position functional monomers around the target molecule (Fig. 1). Such receptors are

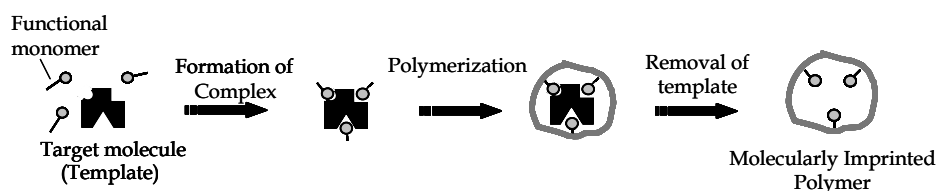


Fig. 1. Synthetic procedure of molecularly imprinted polymer

synthesized from non-biomolecules and are termed “molecularly imprinted polymers (MIPs)”.

MIPs have been synthesized to suit a large variety of templates and intensively investigated in the last decade. The application of MIPs has been demonstrated by mimicking antibody/receptor binding sites in immunoassays, chemical sensors and biosensors, while MIPs were utilized as tailor-made separation material in solid-phase extraction and screening drugs (Mosbach, 1994). Such attractive techniques using MIPs have provided a promising alternative to biological recognition elements. So far, more than 1,000 papers on

the use of MIPs in a wide range of application areas have recently been reported. Therefore, MIPs have already been used as alternatives to biological elements.

Among the application of MIPs, solid-phase extraction (SPE) has been utilized to clean-up environmental and biological samples and to exchange sorbents in liquid chromatography (Matsui et al., 1995). The application of SPE reduced the drawbacks of chromatography such as peak broadening and tailing. In addition, the application of MIPs to chromatography has been continually studied as a chiral stationary phase for enantiomer separations or to change the sorbent of capillary electrochromatography. These applications were intensively investigated and reported since molecular imprinting techniques began to attract interest among many researchers in the 1990s. In the late 1990s, due to these high affinities and selectivities, MIPs also began to be considered as alternatives to selective receptors in biosensors.

The substitution of MIPs for biological receptors is frequently reported. Although biological receptors are extremely selective as a molecular recognition element, they are labile and expensive. On the other hand, molecular imprinting-based biomimetic recognition has physical/chemical stability, tailor-made preparation and is cheaper, and also includes binding affinity comparable to a biological receptor. So, it has been expected to be a breakthrough in the limitations of biosensor technology and has thus attracted attention through studies on how to utilize MIP materials as the sensor elements more effectively.

Sensors based on electrochemical determination are potentially sensitive and inexpensive, and electrodes are easily miniaturized in the development of a sensor system. So, electrochemical sensors have been useful devices in the monitoring of a wide range of analytes. Electrochemical sensors play a crucial role in medical and clinical analysis, and in environmental and industrial monitoring. The electrochemical modes of measurements are amperometry, voltammetry, potentiometry and conductometry. Generally speaking, electrochemical analysis is sensitive and bears a reasonable cost. Since these various modes lead to several applications of sensor fabrication, electrochemical sensors are becoming important transducers in the development of sensors utilizing MIP receptors.

MIP receptors are considered as promising and inexpensive alternatives to bioreceptors. Biomimetic sensors composed of electrochemical transducers and MIPs are significantly attractive sensing devices substituting biosensors. This chapter reviews recent research on biomimetic sensors utilizing MIP receptors and electrochemical transducers. The article begins by outlining general MIP preparation and various methods of applying MIPs to recognition elements in biomimetic sensors. The article further describes recently-reported biomimetic sensors utilizing MIP materials. It focuses on electrochemical sensors that show promising practical use by utilizing MIPs, which are selective to toxic compounds such as triazine herbicides and bisphenol A, which have attracted international attention as endocrine disrupting chemicals. After the overview of biomimetic sensors, the article concludes by outlining the current state-of-the-art and issues to overcome.

2. General MIP preparation

2.1 Concept of molecular Imprinting

Great efforts to develop a specific recognition system for target molecules have been made. One approach has been the synthesis of host molecules possessing a three-dimensional structure to bind complementary guests. The synthesis of specific recognition sites has been

accomplished to coordinate functional monomers around a target molecule, and then to provide cross-linkers for positioning functional monomers around the target molecule.

It is said that the origin of molecular imprinting began from a hint by Pauling's notion regarding the working of an immune system, to assemble an antibody around the foreign intruder as a template (Pauling, 1940). Then, on the basis of this hypothesis, creation of the shape of selective sites in a silica gel was attempted using organic dyes by Dickey et al., and these silicates exhibited slight affinity (Shea, 1994).

The essential force of interaction to imprint target molecules has been either covalent or noncovalent, including electrostatic, hydrogen bonding and hydrophobic interactions. An approach based on covalent bonds has been mainly demonstrated by the Shea and Wulff groups (Shea, 1994; Wulff, 1995). On the other hand, an approach based on noncovalent bonds has been mainly demonstrated by Mosbach (Mosbach, 1994).

2.2 MIP Preparation

The recognition mechanism in a polymer network is particularly important for its great potential of molecular imprinting in the separation and purification of various biomolecules. Feasibility studies and attempts to optimize MIP-based systems have been performed. In order to investigate interactions between substrate and the polymer stationary phase, a chromatographic and ^1H NMR study involving titration of template molecule (phenylalanine anilide) with the functional monomer methacrylic acid was performed (Sellergren et al., 1998). The results were consistent with the existence of multimolecular complexes formed by electrostatic and hydrogen-bonding interactions and allowed an estimation of their formation constants and distribution. By UV-Vis adsorption spectral studies, Infrared spectroscopy (IR) and X-ray diffraction (XRD), Daniel et al. reported the characterization of palladium ion imprinted polymer. The formation of a ternary complex of ion template with functional monomer and cross-linker was confirmed by UV-Vis absorption spectra (Daniel et al., 2003). The results of XRD showed the complete removal of palladium ion from the material and the IR spectra indicated the same polymer backbone in both unleached and leached palladium ion imprinted polymer. Solid state ^{13}C -NMR and Fourier transform infrared spectroscopy (FT-IR) also have been used to investigate bonds of small molecules such as 1,3-diacetylbenzene to functionalized polymers (Shea & Sasaki, 1989). Both techniques gave a consistent picture of the manner of binding.

As the recognition mechanism of MIP was getting clearer, the application of MIP to the HPLC stationary phase began to be studied. Mosbach and co-workers extended the imprinting technique by using noncovalent bonds and optimized chiral stationary phases for degradation of amino acid derivatives in liquid chromatography (Andersson et al., 1990). The initial binding of the substrate to polymers occurred via ionic bonding between the amine group of the substrate and carboxylic residues of the polymer. The second step in the recognition process was the formation of other interactions, such as hydrogen bonds and hydrophobic forces, and it was observed that these secondary interactions gave rise to enantiometric separations. This result suggested that it was possible to use these polymers as a chiral stationary phase in column chromatography.

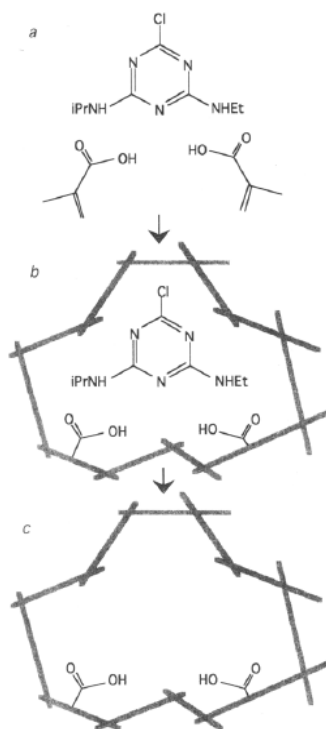


Fig. 2. Schematic illustration of the molecular imprinting procedures for atrazine (^{a,b}Matsui et al., 1995).

Molecularly imprinting can be made against a great number of organic molecules, such as drugs, metabolites, hormones and toxins. Among them, the MIP for herbicide atrazine was reported by many researchers (^{a,b}Matsui et al., 1995; Sieman et al., 1996; Muldoon & Stinker, 1995) (Fig. 2). Preparation of atrazine-imprinted polymers has been carried out mainly according to a protocol well-established by Mosbach, using methacrylic acid as functional monomer, ethylene glycol dimethacrylate as a cross linking agent, and chloroform or dichloromethane as solvent. They were studied using various analytical techniques including HPLC, a radio assay using radioactively-labeled ligand and investigations of template/functional monomer complexation were performed by an NMR spectra study. Atrazine-MIP was successful in several applications, while the MIP for simazine (Sim-MIP), similar in structure to atrazine, was hardly studied despite its stronger toxicity than atrazine. Therefore, we studied the Sim-MIP preparation according to atrazine-MIP and reported a simazine sensor based on biomimetic recognition utilizing the Sim-MIP receptor (^aFuchiwaki et al., 2007).

Although MIPs appear to be inexpensive, robust, and reusable materials, the preparation procedure has to be studied against each template, which are actually analytes. The factor for optimum MIP preparation is not yet understood, and continuous investigations are required.

3. Application of MIP to sensor

In the beginning of MIP research, the main purpose was the application to a stationary phase in liquid chromatography. So, over the last decade the use of MIPs as a biomimetic sensing materials has been investigated. Many studies on sensor fabrication using MIP materials have been reported since the 1990s, and alternatives to antibodies in immunosensors were most frequently reported (Lavignac et al., 2004). The advantage of MIP-based biomimetic sensors is the binding affinity of MIPs comparable to biological recognition elements as well as their robustness and stability against a wider range of environments. MIPs were easily synthesized in a tailor-made manner for template-analytes. MIPs have been developed against various templates such as herbicides, pharmaceuticals, proteins and vitamins.

In order to apply MIPs as biomimetic sensing materials, specific binding of analytes to the binding cavity in the MIP network to the sensor signal needs to be translated. This translating technique plays a key role in the application of MIPs to biomimetic materials. There tend to be two types of methods, labeling or labeling-free.

The binding sites in MIPs fit to unlabelled templates and labeled templates are not suitable for the binding site. Also, the preparation of selective MIP to labeled template is not easy. Therefore, in the labeling method, the sensor system is normally performed by competitive binding of an analyte with labeled analyte, and the labeled unbound analyte is inversely proportional to the amount of analyte. Radiolabeled and fluorescence-labeled analytes are frequently used for the MIP sorbent assay, whose results were compared with those in the enzyme-linked immunoassay (Vlatakis et al., 1993) (Figure 3). On the other hand, MIP-based sensing techniques that do not require labeling agents have been investigated and several interesting studies on the label-free method have been reported.

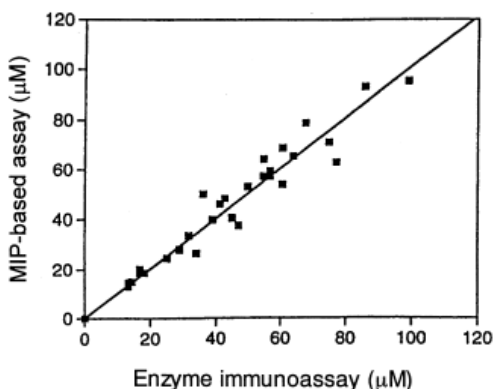


Fig. 3. Correlation between a molecularly imprinted polymer-based competitive binding assay and an enzyme immunoassay for 32 samples of serum theophylline (Vlatakis et al., 1993). The correlation coefficient was calculated to be 0.98.

There are two different types of techniques in the label-free method. They are performed by detecting the signaling activity of the analyte itself or transducing changes in the chemical/physical property of MIPs. The former includes, for example, membrane-based electrochemical and mass sensitive sensors. The specifically bound analytes close to the

binding-site in the MIP matrix directly detect the electrochemical activity on the electrode surface if the analyte has electrochemical activity. This concept could indicate the development of sensitive and precise MIP membrane-based sensors. Also, mass sensitive sensors such as the quartz crystal microbalance (QCM) and the surface acoustic wave device (SAW) have been used to study the development of an MIP membrane-based sensor (Vila et al., 2008). Determination was based on the mass change on the conducting surface electrode. So, many applications are expected because mass is a universal property of matter.

The latter involves fluorescence and conductometric detection. For sialic acid detection, *o*-phthalaldehyde was used as a reagent for fluorescence measurement of the MIP matrix containing amine residues (Piletsky et al., 1996). When sialic acid bound to the binding site, the permeability of *o*-phthalaldehyde increased due to the swelling change by binding of the template. Fluorescence intensity increased and was proportional to the amount of bound sialic acid. Turkewitsch et al. reported a fluorescent molecularly imprinted polymer for 3', 5'-cyclic monophosphate (cAMP) that contained a fluorescent dye, *trans*-4-[*p*-(*N,N*-dimethylamino)styryl]-*N*-vinylbenzylpyridinium chloride (Turkewitsch et al., 1998). The molecularly imprinted fluorescent polymer quenched fluorescence in the presence of aqueous cAMP, whereas almost no effect was observed in the presence of structurally similar molecules.

A conductometric sensor was fabricated based on the MIP membrane-modified electrode (Sergeyeva et al., 1999; Suedee et al., 2006). In the sensing principle, the conductivity decreased with an increase of bound analyte. When a different amount of analytes was bound to MIP, the MIP membrane showed differences in the degree of shrinking. This phenomenon causes a change in electro-conductivity due to changes in ion transfer.

Molecular imprinting is increasingly adopted as a biomimetic artificial receptor. Currently, many researchers have studied the improvement of MIP-based sensors by a combination of various sensing techniques for practical use.

4. Electrochemical sensor utilizing MIP

Electrochemical sensor fabrication includes various types of systems such as conductometric, voltammetric, potentiometric, capacitance, and have provided important tools to detect various analytes in environmental, clinical and biological fields due to their high sensitivity, cheapness and miniaturization.

4.1 MIP membrane-based electrochemical sensor

Membrane-based electrochemical sensor systems have become increasingly attractive for excellent affinity separation. Applications combining MIPs and membrane technology have been proposed the stable permselectivity and affinity for selective binding to analytes from a mixture containing structurally similar compounds.

4.1.1 Molecular imprinting-based conducting polymers

The application of electrosynthesis to MIP technologies is also an attractive technique. This method was first reported as a procedure for the preparation of MIPs to be utilized as a nitrate-selective potentiometric sensor by Hutchins and Bachas in 1995. By polymerizing

pyrrole in the presence of NaNO_3 , in the film produced there were pores that were complementary to the size of the nitrate ion. Both the size of the pore and the charge distribution within the polymerized film formed a host cavity for nitrate, which provides additional selectivity over conventional nitrate-selective electrodes. This molecular imprinting-based electrode demonstrated improved selectivity coefficients for perchlorate and iodide as much as 4 orders of magnitude. Therefore, molecular imprinting polymers prepared with conductive polymers (MICPs) strongly adhere to the electrode of any shape and size, and the thickness of the membrane can be easily controlled. In addition, the conductive polymer is easily obtained by chemical or electrochemical techniques. However, the physical and chemical properties of the polymers are influenced by polymerization conditions such as solvent, supporting electrolyte, electrode material and electropolymerization potential. MIPs are obtained through polymerization in the presence of a template molecule. After removing the template, specific binding cavities are created in the polymer networks. And the chemical functionality and three-dimensional shape in the binding cavity are created in the MIPs. Although electrochemical sensors combining MIPs with the conducting polymers are attractive concepts for the sensitive and real-time detection of a small molecule, it is not easy to form a specific binding site corresponding to template-analyte because the choices of functional monomers, crosslinking monomers, solvent and polymerization conditions are limited. Although such an electrochemical sensing system gave the possibility of direct communication between the polymer and the electrode surface in a simple way, there was also a problem. Conductive polymers are so electrochemically sensitive to ionic adsorption that nonspecific adsorption is not negligible. Because of these factors, there are few reports for MICP, although an electrochemical sensor, which enables the recognition of the herbicide atrazine, was recently described by Pardieu et al. (Pardieu et al., 2009) (Fig. 4). Poly-3,4-ethylenedioxythiophene-co-thiophene-acetic acid as the MICP was electrochemically synthesized onto a platinum electrode in two steps: (i) polymerization of comonomers in the presence of atrazine, already associated to the acetic acid substitute through hydrogen bonding, and (ii) removal of atrazine from the resulting polymer, which leaves the acetic acid substitutes open for association with atrazine. This electrochemical sensor showed selectivity towards the triazine moiety, with a wide range of detection (10^{-9} mol L $^{-1}$ to 1.5×10^{-2} mol L $^{-1}$ in atrazine) and low detection limit (10^{-7} mol L $^{-1}$). Therefore, this report is certainly interesting in which MICP showed selectivity to the triazine moiety; however, it was difficult to distinguish between structures similar to atrazine.

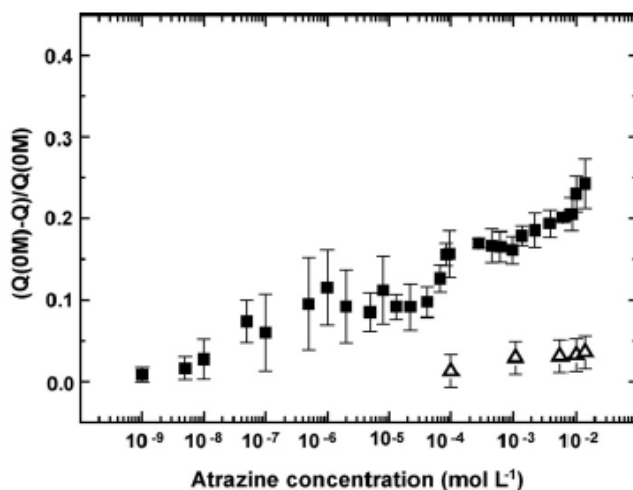


Fig. 4. Variation of the relative charge of poly(EDOT-co-AAT) MICPs (■) and poly(EDOT-co-AAT) NICPs (△) modified electrodes as a function of additional atrazine concentration (Pardieu et al., 2009). The relative charges were deduced from cyclic voltammograms.

4.1.2 Conductometric sensors

A conductometric sensor can be easily fabricated and its principle is very simple. Although a conductometric transducer is normally difficult to distinguish among different compounds, selectivity and sensitivity are considerably improved by introducing a recognition element on the electrode surface. Sergeyva et al. fabricated a conductometric sensor modified with an MIP membrane for template-atrazine, and reported the characterization of changes in the MIP membrane when the solvent, pH and functional monomer in polymerization were changed (Sergeyeva et al., 1999). The membrane containing 85% tri(ethylene glycol) dimethacrylate and 15% Oligourethane acrylate (OUA) demonstrate both a rapid and selective sensor response. The detection limit for atrazine measured in 25 mM sodium phosphate buffer, pH 7.5, containing 35 mM NaCl was found to be 5 nM. The analysis can be performed within 6-15 min. The prepared MIP membrane was shown to be a very stable and flexible membrane. Suedee et al. (2006) reported an on-line conductometric monitoring system of haloacetic acids using an MIP membrane, which was synthesized by the interaction between trichloroacetic acid (TCAA) template and a functional monomer, 4-vinylpyridine (VPD), together with a cross-linking reagent, ethylene glycol dimethacrylate (EDMA). The change in conductivity in the presence of the target molecule into the imprint cavity was investigated and responded well to TCAA in a continuous flow system with relatively good linearity. The sensitivity (range 0.5-5 $\mu\text{g l}^{-1}$) and selectivity achieved with standard TCAA and five other haloacetic acids (HAAs) (dichloro-, monochloro-, tribromo-, dibromo-, and monobromoacetic acid) in water was good enough. Minimum sample volume required was 2.5 ml and the assay time was 2 min.

4.1.3 Potentiometric sensors

A potentiometric sensor is a versatile, simple, rapid and inexpensive method for target determination. Potentiometric techniques are used for the electrochemical transduction of ion selective sensors utilizing MIP, which serves as a selective molecular recognition membrane or layer in the sensor system. There are relatively few reports dealing with potentiometric molecular sensors based on MIPs (Heng et al., 2000; Zhou et al., 2004; Kitade et al., 2004). Sadeghi et al. (2007) fabricated a potentiometric sensor based on MIPs for determination of levamisole hydrochloride. The preparation of MIPs was accomplished by using methacrylic acid as a functional monomer, *p*-divinylbenzene as the crosslinker and AIBN as initiator and the sensing membrane was prepared by mixing polyvinyl chloride powder and MIP particles with a plasticizer. Levamisole hydrochloride was measured in the activity range from 2.5 $\mu\text{mol L}^{-1}$ to 100 mmol L^{-1} and the limit of detection was 1.0 $\mu\text{mol L}^{-1}$. The response time was short (<15 s) and the membrane could be used for 4 months without any significant divergence in response. Liang et al. (2009) described a potentiometric sensor based on an MIP membrane ion-selective electrode for determination of melamine in milk, which was prepared using methacrylic acid and EDMA. The MIP membrane electrode showed a near-Nernstian response (54 mV/decade) to the protonated melamine over the concentration range of 5.0×10^{-6} to 1.0×10^{-2} mol L^{-1} . The electrode exhibited a short response time of 16 s and was stable for more than 2 months.

4.1.4 Voltammetric sensors

Studies on amperometric and voltammetric sensors have also been reported. Metallic voltammetric electrodes are particularly interesting due to their high sensitivity and versatility, with a choice of potential range, waveform and electrode material. Yoshimi et al. (2001) investigated the change in structure and diffusive permeability of the MIP layer in the presence or absence of template and reported sensitive detection of template-theophylline by measuring the peak current of ferrocyanide oxidation. A thin layer of MIP composed of methacrylic acid as functional monomer and EDMA as cross-linking monomer was grafted onto the surface of conductive indium-tin oxide (ITO). The porosity and diffusive permeability of the MIP layer, the "gate effect", is sensitive to template-analyte. The morphological change of the gate effect is still being investigated. Blanco-López et al. (2003) investigated the development of a voltammetric sensor for vanillylmandelic acid (VMA) based on acrylic MIP-modified electrodes. Their MIP-based sensors were able to give responses 5-10 times higher than those of non-imprinted electrodes in a non-excessive time lapse of 25 min. The peak current recorded with the imprinted sensor after rebinding of VMA was linear to its concentration in the range of 19-350 $\mu\text{g mL}^{-1}$, whereas the response of the control electrode was independent of its concentration.

4.2 Electrochemical sensor chips

Towards practical use, our groups have developed voltammetric sensor chips for toxic compounds such as triazine herbicides and bisphenol A, which have recently attracted international attention as endocrine disrupting chemicals (Shoji et al., 2003; Fuchiwaki et al., 2008; Kubo et al., 2008; Yokota et al., 2008). These sensor devices are composed of a gold electrode chip, which delineate an electrochemical active area with a polyimide layer, and the MIP layer as the recognition element for atrazine, simazine and bisphenol A. In

principle, the analytes penetrate into the matrix of the MIP layer and bind to the imprinted pore and the analytes close to gold surface are detected by electrochemical reaction on the gold surface. The atrazine sensor chip was fabricated by directly polymerized MIP for atrazine (Atr-MIP) composed from methacrylic acid and EDMA onto a gold surface. By introducing LiCl as electrolyte into the MIP, electrochemical reduction of atrazine was facilitated and cathodic peak current depended on the concentration of 1-10 μM atrazine (Shoji et al, 2003). The obtained results were compared to the study of Atr-MIP composed from methacrylic acid and EDMA by other groups (Table 1). The response of simazine was only 28% to atrazine although simazine was reduced electrochemically at a higher level than triazine. The optimum preparation of a thinner Atr-MIP layer for sensitive determination was then studied and the detection of an environmental concentration 50 nM (11 ppb) of atrazine was achieved with a thinner layer of Atr-MIP (Kubo et al., 2008).

	capacity factor ^b	conductometry ^c	cross reactivity of TSM ^d acoustic sensor	amperometry ^e
atrazine	100	100	100	100
simazine	78	16	55	28
prometryn	30	16	17	58 ^f
ametryn	32			2.5
triazine ^g	1	18	14	

^a Data were normalized by the data of atrazine as 100. ^b Relative capacity factor was calculated from the retention time of MIP column; see ref 12. ^c Conductometric change with use of MIP, Selectivity was calculated from the data in ref 16. ^d Thickness-shear mode (TSM) acoustic sensor. Cross reactivity at 10 μM was listed. See ref 18. ^e Present method. Current decreases at -800 mV in 0.1 M KCl (pH 3.0) of herbicides (10 μM) were compared. ^f Since peometryn was instable at acidic pH, it was compared at pH 9.0. ^g Triazine is listed for its structural interest.

Table 1. Comparison of the Selectivity of Atrazine-Imprinted Polymer (Shoji et al., 2003)

The simazine sensor chip was also fabricated by using methacrylic acid and EDMA (Fuchiwaki et al., 2008) (Fig. 5). The MIP preparation for simazine (Sim-MIP) and the electrochemical determination were investigated to establish a simazine sensor system because there were no reports for them (^{a,b}Fuchiwaki et al., 2007). Surprisingly, the simazine sensor chip was 29 times more sensitive to simazine than the bare gold electrode and the selective response to simazine compared to structural analogues such as atrazine. The bisphenol A sensor chip was fabricated by polymerizing the MIP for bisphenol A (BPA-MIP) composed from 4-vinylpyridine as a functional monomer and EDMA (Yokota et al., 2008) on a sputtered gold electrode. In order to obtain the BPA-MIP thin layer, BPA-MIP was polymerized by UV-light irradiation, and the thickness of the layer was examined by changing the time of its irradiation and observed with AFM. BPA-MIP layer prepared by 5 min irradiation could recognize BPA concentration at a 5 to 15 μM range. These sensor chips based on molecular imprinting technique allows inexpensive, stable, small devices, and *in situ* determination of analytes.

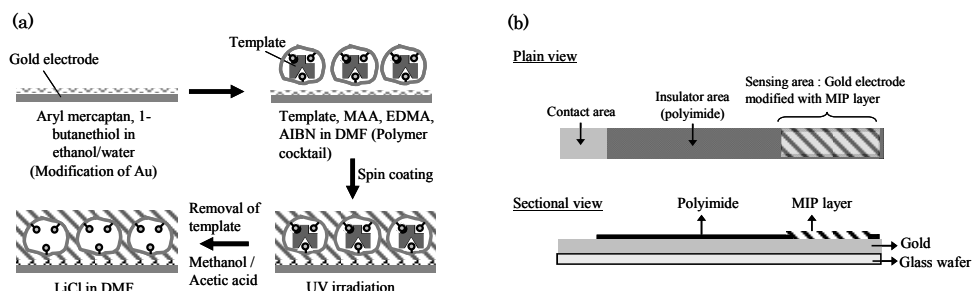


Fig. 5. MIP modified sensor chip (a) Preparation procedure of MIP layer modified electrode, (b) Schematic diagram of sensor chip (Fuchiwaki et al., 2008)

In order to improve the Membrane-based electrochemical sensor system in the future, it would be desirable to control its pore size and pore density at will because of the analyte diffusion towards the electrode surface. Analytes and substances such as electrolytes diffuse through its pore in the MIP matrix. Their size and density normally depend on the amount of polymerization solvent, which acts as a porogen in the preparation of MIP, and how the solvent interacts with template is important, too. Therefore, although the MIPs are expected to be biomimetic polymers capable of tailor-made synthesis for any analytes, detailed research to obtain selectivity, enrichment and proper permeability are still needed with respect to each template-analyte. Minimizing the thickness of the MIP membrane is very important. Controlling the thickness of MIP could be performed by a spin-coating of pre-polymer mixture. Recently, innovative approaches for the preparation of an MIP thin layer have been proposed. As a novel approach, nanotubular membranes with pores a few nm in diameter had been developed (Martin et al., 2001). Preparation was based on the controlled deposition of gold layers on the pore walls of membranes having pore sizes of about 10 nm. By combining a self-assembled functional monolayer with the obtained nano-tubules, a membrane selective to target analyte could be obtained. Therefore, such interesting approaches would allow a new way for prompting MIP-based membrane technology.

4.3 Electrochemical sensor utilizing MIP-based solid phase extraction

The application of MIPs to the field of affinity-based solid phase extraction is expected due to their strong affinity for template-analytes. So this feature is suitable for easy separation of template-analytes from a mixture containing impurities by loading several extraction solvents as commonly described in traditional chromatography. In this extraction process, the analytes are at first adsorbed to the MIP packed-column. After the undesired impurities are washed out, finally the bound analytes are recovered.

The sorbents with affinity are normally expensive and their preparation requires precious and time-consuming processes. So the application of SPE-based inexpensive MIPs (SPE-MIP) has been investigated for atrazine (herbicide), propranolol and pentamidine (medicine) (Martin et al., 1997; Matsui et al., 1997; Muldoon et al., 1997).

Our groups reported highly sensitive and selective electrochemical sensor systems by combining SPE-MIP for simazine and amperometric determination by a cyclic voltammetry method (Fuchiwaki et al., 2007; Fuchiwaki et al., 2009). As a working electrode, an amalgamated gold electrode, which was alloyed with mercury, was used for the optimum

determination of simazine. Fifteen nM of simazine, as legally regulated in Japan, was detected specifically in the mixture of other herbicides after washing nonspecifically adsorbed herbicides to the MIP column with dichloromethane. The reductive current of simazine could be detected at a negative potential around -1.0 V with a mercury electrode because there were few substances of electrochemical reaction around -1.0 V.

The electrochemical method can potentially discriminate among electroactive substances by voltammetric determination. Therefore, it could be concluded that MIP-based electrochemical sensors are very promising elements for highly selective sensors.

5. Conclusion

Molecular imprinting is an attractive technique to mimic biological recognition sites. Electrochemical measurement enables a miniature, simple and inexpensive device in the development of a sensor system. Combination of MIP technology and electrochemical measurements would allow the development of such a useful sensor device. However, there are few reports of biomimetic electrochemical sensors. The speed of development of this device would depend on the progress of MIP technology. MIPs have an advantage to overcome drawbacks of biological receptors; on the other hand, the possibility development of MIP materials as biomimetic receptors is still under investigation. Studies on MIP merge technologies from various sciences such as supermolecular chemistry and nanotechnology are on the way.

6. References

- Andersson, L.I.; O'Shannessy, D.J.; Mosbach, K. (1990) Molecular recognition in synthetic polymers: Preparation of chiral stationary phases by molecular imprinting of amino acid amides *J. Chromatogr.* 513, 167–179
- Blanco-López, M.C.; Lobo-Castañón, M.J.; Miranda-Ordieres, A.J.; Tuñón-Blanco, P. (2003) Voltammetric sensor for vanillylmandelic acid based on molecularly imprinted polymer-modified electrodes, *Biosensors and Bioelectronics*, 18, 353-362
- Daniel, S.; Gladis, J.M.; Rao, T.P. (2003) Synthesis of imprinted polymer material with palladium ion nanopores and its analytical application, *Anal. Chim. Act.*, Volume 488, 173-182
- ^aFuchiwaki, Y.; Shimizu, A.; Kubo, I. (2007) 6-Chloro-*N,N*-Diethyl-1,3,5-Triazine-2,4-Diamine (CAT) Sensor Based on Biomimetic Recognition Utilizing a Molecularly Imprinted Artificial Receptor, *Anal. Sci.*, 23 49-53
- ^bFuchiwaki, Y.; Sasaki, N.; Kubo, I. (2007) Development of an Electrochemical Sensing System for 6-Chloro-*N,N*-Diethyl-1,3,5-Triazine-2,4-Diamine (CAT) Utilizing an Amalgamated Gold Electrode and Artificial Sensor Receptor, *Electrochemistry*, 75, 709-714
- Fuchiwaki, Y.; Shoji, R.; Kubo, I.; Suzuki, H. (2008) 6-Chloro-*N,N*-Diethyl-1,3,5-Triazine-2,4-Diamine (Simazine) Electrochemical Sensing Chip Based on Biomimetic Recognition Utilizing a Molecularly Imprinted Polymer Layer on a Gold Chip. *Anal. Lett.*, 41 1398-1407

- Fuchiwaki, Y.; Sasaki, N.; Kubo, I. (2009) Electrochemical Sensing System Utilizing Simazine-Imprinted Polymer Receptor for the Detection of Simazine in Tap Water, *Journal of Sensors*, Article ID 503464, 6 pages
- Heng, L.Y. & Hall, E.A.H. (2000) Producing "self-plasticizing" ion selective membranes, *Anal. Chem.*, 72, 42-51
- Hutchins, R.S. & Bachas, L.G. (1995) Nitrate-selective electrode developed by electrochemically mediated imprinting/doping of polypyrrole. *Anal. Chem.*, 67, 1654-1660
- Kitade, T.; Kitamura, K.; Konishi, T.; Takegami, S.; Okuno, T.; Ishikawa, M.; Wakabayashi, M.; Nishikawa, K.; Muramatsu, Y. (2004) Potentiometric immunosensor using artificial antibody based on molecularly imprinted polymers, *Anal. Chem.*, 76, 6802-6807.
- Kubo, I.; Shoji, R.; Fuchiwaki, Y.; Suzuki, H. (2008) Atrazine Sensing Chip Based on Molecularly Imprinted Polymer Layer. *Electrochemistry*, 76, 541-544
- Lavignac, N.; Allender C.J.; Brain, K.R. (2004) Current status of molecularly imprinted polymers as alternatives to antibodies in sorbent assays, *Anal. Chim. Act.*, 510, 139-145
- Liang, R.; Zhang, R.; Qin, W. (2009) Potentiometric sensor based on molecularly imprinted polymer for determination of melamine in milk, *Sensors and Actuators B*, 141, 544-550
- Martin, C.R., Nishizawa, M.; Jirage, K.; Kang, M. (2001) Controlling Ion-Transport Selectivity in Gold Nanotubule Membranes, *Adv. Mater.*, 18, 1351-1362
- Martin, P.; Wilson, I.D.; Morgan, D.E.; Jones, G.R.; Jones, K. (1997) Evaluation of a Molecular-imprinted Polymer for use in the Solid Phase Extraction of Propranolol From Biological Fluids, *Anal. Commun.*, 34, 45-47
- ^aMatsui, J.; Doblhoff-Dier, O.; Takeuchi, T.; (1995) Atrazine-selective Polymer Prepared by Molecular Imprinting Technique, *Chem. Lett.*, 489
- ^bMatsui, J.; Miyoshi, Y.; Doblhoff-Dier, O.; Takeuchi, T.; (1995) A Molecularly Imprinted Synthetic Polymer Receptor Selective for Atrazine, *Anal. Chem.*, 67, 4404-4408
- ^cMatsui, J.; Okada, M.; Tsuruoka, M.; Takeuchi, T. (1997) Solid-phase Extraction of a Triazine Herbicide Using a Molecularly Imprinted Synthetic Receptor, *Anal. Commun.*, 34, 85-87
- Mosbach, K. (1994) Molecular Imprinting, *Trends Biochem. Sci.* 19, 9-14
- Muldoon, M.T. & Stanker, L.H. (1995) Molecularly Imprinted Solid Phase Extraction of Atrazine from Beef Liver Extracts, *Anal. Chem.*, 69, 803-808
- Muldoon, M.T. & Stanker, L.H. (1995) Polymer Synthesis and Characterization of a Molecularly Imprinted Sorbent Assay for Atrazine, *J. Agric. Food Chem.*, 43, 1424-1427
- Muldoon, M.T. & Stanker, L.H. (1997) Molecularly Imprinted Solid Phase Extraction of Atrazine from Beef Liver Extracts, *Anal. Chem.*, 69, 803-808
- Pardieu, E.; Cheap, H.; Vedrine, C.; Lazerges, M.; Lattach, Y.; Garnier, F.; Remita, S.; Pernelle, C. (2009) Molecularly imprinted conducting polymer based electrochemical sensor for detection of atrazine, *Anal. Chim. Act.*, 649, 236-245
- Pauling, L. (1940) A theory of the structure and process of formation of antibodies. *J. Am. Chem. Soc.*, 62, 2643-2657.

- Piletsky, S.A.; Piletskaya, E.V.; Yano, K.; Kugimiya, A.; Elgersma, A.V.; Levi, R.; Kahlow, U.; Takeuchi, T.; Karube, I.; Panasyuk, T.; El'skaya, A.V. (1996) A Biomimetic Receptor System for Sialic Acid Based on Molecular Imprinting, *Anal. Lett.*, 29, 157-170
- Sadeghi, S.; Fathi, F.; Abbasifar, J. (2007) Potentiometric sensing of levamisole hydrochloride based on molecularly imprinted polymer, *Sensors and Actuators B*, 122, 158-164
- Sellergren, B.; Lepisto, M.; Mosbach, K. (1998) Highly Enantioselective and Substrate-Selective Polymers Obtained by Molecular Imprinting Utilizing Noncovalent Interactions. NMR and Chromatographic Studies on the Nature of Recognition, *J. Am. Chemical Society*, 110, 5853-5860
- Sergeyeva, T.A.; Piletskaya, S.A.; Brovkob, A.A.; Slinchenkoa, E.A.; Sergeevab, L.M.; El'skaya, A.V. (1999) Selective recognition of atrazine by molecularly imprinted polymer membranes. Development of conductometric sensor for herbicides detection, *Anal. Chim. Act.*, 392, 105-111
- Siemann, M.; Andersson, L.I.; Mosbach, K. (1996) Selective recognition of the herbicide atrazine by non-covalent molecularly imprinted polymers. *J. Agric. Food Chem.*, 44, 141-145
- Shea, K.J. (1994) Molecular Imprinting of Synthetic Network Polymers: The De Novo Synthesis of Macromolecular Binding and Catalytic Sites, *Trends in Polymer Science*, 2, 166-173
- Shea, K.J. & Sasaki, D.Y. (1989) On the control of microenvironment shape of functionalized network polymers prepared by template polymerization, *J. Am. Chem. Soc.* 111, 3442-3444
- Shoji, R.; Takeuchi, T.; Kubo, I. (2003) Atrazine sensors based on molecularly imprinted polymer-modified gold electrode. *Anal. Chem.*, 75, 4882-4886
- Suedee, R.; Intakong, W.; Dickert, F.L. (2006) Molecularly imprinted polymer-modified electrode for on-line conductometric monitoring of haloacetic acids in chlorinated water, *Anal. Chim. Act.*, 569, 66-75
- Turkewitsch, P.; Wandelt, B.; Darling, G.D.; Powell, W.S. (1998) Fluorescent Functional Recognition Sites through Molecular Imprinting. A Polymer-Based Fluorescent Chemosensor for Aqueous cAMP, *Anal. Chem.*, 70, 2025-2030
- Vila, M. Á.; Zougagh, M.; Escarpa, A.; Ríos, Á. (2008) Molecularly imprinted polymers for selective piezoelectric sensing of small molecules, *Trends in Anal. Chem.*, 27, 54-65
- Vlatakis, G.; Andersson, L.I.; Müller, R.; Mosbach, K. (1993) Drug assay using antibody mimics made by molecular imprinting, *Nature*, 361, 645-647
- Wulff, G. (1995) Molecular Imprinting in Cross-Linked Materials with the Aid of Molecular Templates—A Way towards Artificial Antibodies, *Angew. Chem. Int. Ed. Engl.*, 34, 1812-1832
- Yokota, N.; Fuchiwaki, Y.; Kubo, I. (2008) Fabrication of bisphenol A sensor utilizing electrode modified with molecularly imprinted polymer. *ECS Transactions*, 11, 551-556
- Yoshimi, Y.; Ohdaira, R.; Iiyama, C.; Sakai, K. (2001) "Gate effect" of thin layer of molecularly-imprinted poly (methacrylic acid-co-ethyleneglycol dimethacrylate), *Sensors and Actuators B*, 73, 49-53
- Zhou, Y., Yu, B., Shiu, E., (2004) Potentiometric sensing of chemical wafer agents, surface imprinted polymer integrated with an indium tin oxide electrode, *Anal. Chem.*, 76, 2689-2693.

Dental tissue engineering: a new approach to dental tissue reconstruction

Elisa Battistella, Silvia Mele and Lia Rimondini
University of Eastern Piedmont "Amedeo Avogadro"
Novara, Italy

1. Introduction

Caries, trauma, erosion and periodontal disease are pathologies characterized by the damage and loss of dental tissues and sometimes loss of the whole tooth. These groups of diseases are very common and affect millions of people worldwide in both developing and industrialized countries.

Restorations of damaged tooth tissues and substitution of missing teeth with artificial prostheses represent the traditional therapeutic solutions. Although many sophisticated biomaterials are now available for restoration, their use is not yet completely satisfactory.

Implants, crowns, bridges and any kind of restorations are generally less functional, durable and aesthetic than intact teeth and they are aimed at repairing rather than regenerating tissues. In addition, the economical impact of such kind of therapeutic approaches is notable. The World Health Organization estimated that the dental treatment costs accounted for 5-10% of healthcare budgets in industrialized countries and adjunctive costs may be considered in terms of absences from work (Petersen, 2003).

In the last few decades the process of tooth mineralization and the role of molecular control of cellular behaviour during embryonic tooth development have received much attention. The knowledge gained in these fields has improved the general understanding about the formation of dental tissues and the whole tooth and set the basis for teeth regeneration.

The present chapter is divided as follows:

- the histology and histomorphological development of the dental hard tissues
- the re-mineralization strategies for enamel regeneration
- the potential application of stem cells to tissues regeneration

2. The histology and histomorphological development of the dental hard tissues

2.1 Enamel

Teeth are composed of several different tissues topographically assembled in order to guarantee the physiological functions. Teeth have to withstand physical and chemical processes. They are exposed to wear, compressive forces and chemical acidic attacks from

bacteria and foods. The function of external protection is made by enamel which covers the crown with a layer of 2 mm occlusally and more in correspondence with the cuspids and decreases cervically till only a few micrometers at the collar. Enamel is the most mineralized tissue in mammals. The mineral content is generally over 97% in weight and is mainly composed of various calcium phosphates (Fig.1) The mean Ca/P generally reported in normal enamel varies from 1.64 to 1.8 generally compatible with those of apatites. The stoichiometric form of hydroxyapatite $[\text{Ca}_6(\text{PO}_4)_6(\text{OH})_2]$ is rarely present in this mineralized tissue which is carbonated at various degrees ranging from 4 to 6 % . (Wilt, 2005).

The distribution of carbonate is generally homogeneous in normal teeth. On the contrary the hypomineralized enamel shows a higher content of carbonate. The hardness of enamel decreases in carbonated areas.

Fluorine is also detectable in the thickness of the enamel. There is a general agreement that the more fluoride is present, the more resistant the teeth are to acid attacks. Generally fluorine is distributed along a gradient and increases from the pulp to the outer surfaces. Some other elements are observed to be present in the enamel structures using techniques appropriate to detect elements at low concentration such as Secondary Ion Mass Spectrometry and X-ray Microanalysis (Jälevik et al., 2000; Chabala et al., 1988).

Elements such as F, Cl, Na, Mg, K and Sr are distributed in a gradient through the enamel layer from the dentine to the surface. Contents of Mg and K were reported to be slightly higher in hypomineralized areas, especially towards the surface. Also Na had a somewhat higher content toward the surface in defective enamel. Cl and Sr contents had no diversity in relation to the degree of mineralization (Jälevik et. al., 2000).

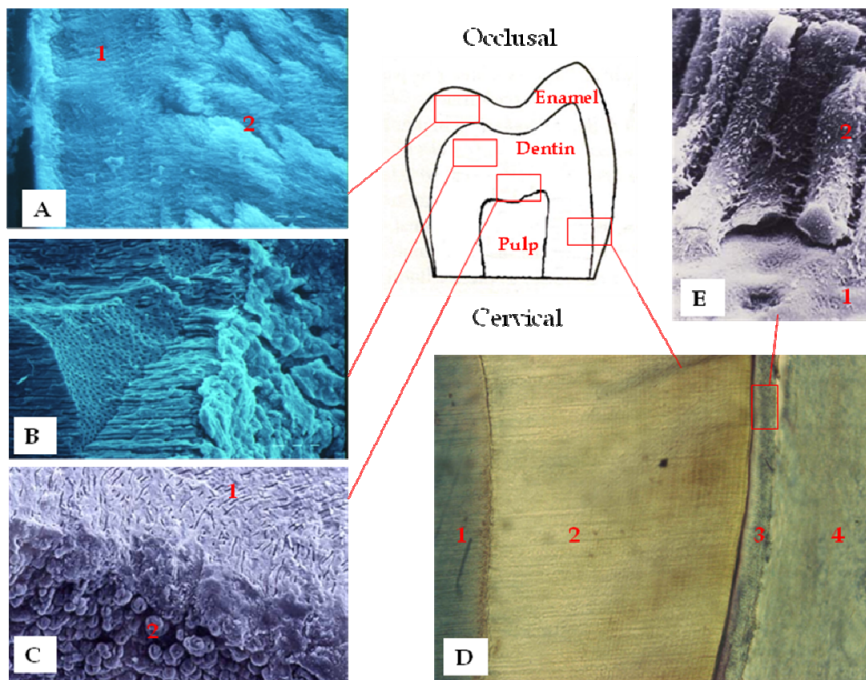


Fig. 1. Schematic representation of the crown of a tooth.

A: Enamel: 1. Prismatic enamel; 2. Prisms. Scanning Electron Microscopy of a specimen obtained by selective fracture. Original magnifications: 8000X

B: Dentin: Dentinal tubules. Scanning Electron Microscopy of a specimen obtained by selective fracture. Original magnifications: 8000X

C: Dentin: 1. Dentinal tubules and 2. Globular Dentin close to the pulp. Scanning Electron Microscopy of a specimen obtained by selective fracture. Original magnifications: 4000X

D: Histological section of the hard tissues of a tooth before eruption embedded in resin and obtained by wear. Toluidine staining. Original magnifications: 20X. 1. Dentin; 2. Enamel 3. Ameloblasts; 4. Dental papilla

E. Ameloblasts. Scanning Electron Microscopy. Original magnifications: 2000X. 1. Ameloblasts; 2. Enamel surface

Other trace elements such as Mg, Fe, Zn, Sr, Ba and Pb have been observed to be accumulated in enamel, using techniques such as laser ablation-inductively coupled plasma-mass spectrometry, in teeth of children raised in polluted areas or in consequence of particular nutrition regimes (Dolphin et al., 2005).

The teeth are made of the strongest and hardest tissue in vertebrates and they are perfectly adapted to their functions. They probably played an important role in the evolutionary success of vertebrates and later of both terrestrial (Luo, 2007) and marine mammals (Uhen, 2007).

The material and mechanical properties of the enamel can be attributed both to the gross morphology and internal architecture, as well as the nanoscale properties of the mineralized composite.

The mechanism of enamel formation and calcium phosphate deposition and crystallization into hydroxyapatite is not yet completely understood. As all mineralized tissues in living organisms it is a composite of natural polymers acting as a template for inorganic materials. The presence of natural polymers is essential to aid crystallization.

Enamel matrix is formed by the ameloblasts. The latter derive from the ectodermal epithelium when neural crest cells invade the underlying mesenchyme inducing the proliferation and formation of dental lamina and then the so called *enamel organs* or "dental papilla" (Järvinen et al., 2009). The ameloblasts are orderly disposed at the base of dental papilla which surround specialized mesenchymal cells, the odontoblasts, responsible for dentinal matrix secretion. The dentinal matrix contains a variety of molecular signals composed of structural polymers such as collagen type I, dentine sialoprotein, minerals, as well as many cytokines and signal molecules such as fibroblast growth factor and bone morphogenetic protein transforming growth factor (TGF) beta, Wnt, and Hedgehog (Thesleff et al., 2007; Tummers & Thesleff, 2009) which interfere with ameloblast cytofunctionality.

Dentin sialophosphoprotein seems to be particularly important in the early events of amelogenesis and it is strongly involved in the formation of the dentino-enamel junction and the adjacent "aprismatic" enamel. Overexpression of dentin sialoprotein, studied in trans-genic animals results in an increased rate of enamel mineralization, however, without alteration of morphology. In wild-type animals, the inclusion of dentin sialoprotein in the forming aprismatic enamel may improve the hardness and the mechanical properties of the mineralized tissue. In contrast, the over-expression of dentin phosphorprotein is associated

with hypomineralized enamels characterized by “pitted”, “chalky”, soft enamel, dis-homogeneous in thickness (Fig.2).

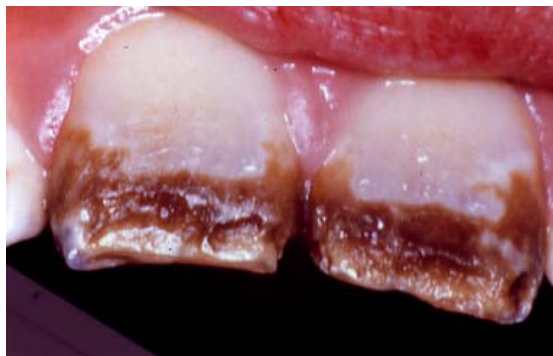


Fig. 2. Hypomineralized teeth.

The secretory surfaces of the ameloblast are called “Tomes processes”. During matrix deposition, they retract toward the apical epithelial surface, leaving behind a self assembly nanosphere of the matrix which rapidly arranges into ribbons (Fincham et al., 1999; Moradian-Oldak et al., 2006; Du et al., 2005).

Nanosized crystallites of carbonated apatite form in the channels created by these ribbons of matrix so that long polycrystalline rods of carbonated apatite are formed; the matrix proteins are degraded by some metalloproteinase (i.e. MPP20) (Li et al., 1999; Tan et al., 1998). The enamel matrix in fact disappears during enamel maturation. The degraded matrix is replaced by rapid infilling with more carbonated apatite crystallites. In the final stages the bulk of enamel is formed by a pack of crystals called “enamel prisms” surrounded by an amorphous lattice. “Aprismatic enamel” is found at the surface and at the dentin-enamel junction (Fig.1).

The matrix of enamel is particularly interesting. It is mainly constituted by a group of hydrophobic proteins called “amelogenins”. The most important seems to be a 180 amino acid long water soluble protein which is degraded from carboxyl-terminals during enamel maturation leaving its residual degradation peptides in the enamel matrix. Amelogenin aminoacid sequences are highly conserved among most species. The human amelogenin gene is expressed primarily (90%) from a single gene on the X chromosome, with minor expression on the Y chromosome.

Amelogenin interacts with carbonated apatite, *in vitro*, to limit crystallite growth, just as it might act to channel mineral crystallite accumulation into rods *in vivo*. Other hydrophilic proteins such as “enamelin” have been discovered in the enamel matrix but their function is still unknown.

The University of Helsinki offers a tutorial on teeth morphogenesis and a data-base of genes and signals molecules involved, at the web-site <http://bite-it.helsinki.fi/>

Over 300 genes have been associated with the patterning and morphogenesis of the teeth. Any alteration to these may lead to dental defects (Paine et al., 2001; Thesleff, 2006).

Defects of enamel mineralization are relatively common and vary from slight to very severe features. They are related to some break in the enamel formation process related or not to

genetic alteration involving the aminoacid sequence of amelogenins or to an alteration of the protease responsible for enamel matrix degradation (Paine et al., 2000; Gibson et al., 2001). Other histological alterations are related to a disrupting of some signal sequences at the very beginning of the dental papillae formation or any disturbance in matrix deposition.. For instance an excessive fluoride uptake causes detrimental effects on ameloblast activity and diabetes early induced in animals provokes deformities of the mineralized structures of the calvaria and maxilla and teeth prone to wear (Atar et al., 2007).

2.2 Dentin

In contrast to enamel, dentin is soft, flexible and tough, and able to absorb energy and resist fracture.

It is less mineralized than enamel and it is a sort of sponge crossed by channels of 1 micron wide radially departing from the pulp. The channels called "dentinal tubules" are occupied by a part of the cytoplasm of the odontoblasts whose cytoplasm body underlies the dentin-pulp interface. The tubules are also occupied by the dentinal fluids. The dentin is formed by mineralization of the dentinal matrix mainly composed of collagen type I and some specific proteins previously mentioned. The deposition of dentin occurs from the pulp front over the life of the teeth. Sometimes the immature dentin appears like globules which are fusing during the maturation of the tissue (Fig.1).

3. The remineralization strategies for enamel regeneration

Enamel is a definitive tissue. It has no chance to grow, heal or regenerate after eruption even if it may be subjected to absorption and desorption of molecules and ions at the surfaces. Even though enamel is highly mineralized it loses substance under acid conditions. Therefore to preserve its integrity and aesthetic it is important to remineralize enamel already at the early stages of acid etching.

For this purpose, various approaches have been attempted. They include application of inorganic and amorphous materials or nanostructured crystalline forms. Inorganic materials in combination with proteins or polymers are also reported. Physical transformations of enamel substances as occurs after laser treatment have also been proposed. Irradiations of tooth enamel ArF excimer Laser alter the structure and chemical composition and increase the Ca/P ratio and decrease the amount of carbonate and proteins (Feuerstein et al., 2005).

The results obtained in terms of "remineralization" are dependent on both the models and the technologies used to characterize the treated enamel.

The depth of demineralization of the enamel influences the degree of remineralization achievable (Lynch et al., 2007).

Supersaturated solutions containing stoichiometric hydroxyapatite are observed to be very effective to remineralize, *in vitro*, superficial lesions but less efficient than less crystalline calcium phosphate to treat deep demineralization (Lynch et al., 2007).

Fluoride compounds are traditionally claimed as remineralizing agents for damaged enamel both *in vitro* (Gaengler et al., 2009) and *in vivo*. A high concentration of fluoride seems to be more effective in *in vitro* models. *In vivo* clinical experimentations of different modalities of application (ionophoresis using 2% sodium fluoride solution, 1.23% acidulated phosphate fluoride gel application, and 5% sodium fluoride varnish application) seem to be equally

effective in reducing the dimension of demineralised areas and increase microhardness (Lee et al., 2009).

Glass ionomers applied on etched enamel have been observed to be transformed *in vitro* into enamel-like material when studied with SEM and EDAX analysis (Van Duinen et al., 2004) as well as other compounds containing fluoride such as TiF and aminated Fluoride (Am.F). Carbon dioxide Laser irradiation is observed to enhance the formation of fluoride precipitates from TiF and Am-F onto demineralized enamel (Wiegand et al., 2009).

Particular attention has recently been focused on the role of some milk proteins which are postulated to stabilise calcium phosphate. Remineralization of enamel subsurface lesions was observed *in vitro* using transverse microradiography and electron microprobe after application of a solution of casein phosphopeptide stabilised amorphous calcium phosphate and amorphous calcium fluoride phosphate solutions (Ranjitkar et al., 2009; Willershausen et al., 2009; Yengopal et al., 2009, Walker et al., 2009; Elsayad et al. 2009). The remineralization, consistent with hydroxyapatite and fluorapatite, was pH dependent with a maximum at pH 5.5. Fluoridated materials obtained better results than non fluoridated (Cochrane et al., 2008). Proteins contained in milk and its derivatives are also suggested to be effective in reducing the demineralising effect of acid. In particular proteose-peptone fractions 3 and 5 characterized by gel electrophoresis were found to be sufficient to reduce the extent of demineralisation of enamel by acid buffer solutions in *in vitro* models (Gremby et al., 2001).

Phosphate and calcium solution alone is also observed to be effective to reduce subsurface demineralization of enamel obtained with immersion of teeth in demineralising solution. The subsurface demineralization in enamel was reduced by 95% by increasing the calcium concentration of the demineralizing solution from 7 to 21 mmol/l. A similar reduction (87%) was observed by increasing the phosphate concentration. However, the amount of phosphate needed was approximately 20 times more than that of calcium (Tanaka et al., 2000).

Different modalities of calcium intake such as chewing gum with added calcium have recently been observed to promote white remineralization of enamel (Cai et al., 2009).

The application of 20 nm carbonate hydroxyapatite nanocrystals was recently described as a remineralizing technique for enamel (Huang et al., 2009; Nakashima et al., 2009) and dentin (Rimondini et al., 2007).

Hydroxyapatite nanocrystals have been synthesized with a nearly stoichiometric in bulk Ca/P molar ratio of about 1.6-1.7 and containing $4 \pm 1\text{wt}\%$ of carbonate ions replacing prevalently phosphate groups. CHA nanocrystals have been synthesized both at about 100 nm and 20 nm in size and used to remineralize *in vitro* the surface of enamel previously etched with 37% of ortho-phosphoric acid. After treatment for 10 minutes by aqueous slurry of both 20 nm and 100 nm sized synthetic CHA nanocrystals, the surface of the demineralized enamel appears covered by the CHA phase arranged thick and homogeneous apatitic layer (Roveri et al, 2009) which rebuilt the lost mineral tissue even if prismatic enamel structures cannot be built (Fig.3). The surface Ca/P molar ratio determined by XPS analysis for demineralized enamel slabs before and after *in vitro* remineralization by application of fluoride or CHA showed an increase of Ca/P molar ratio after fluoride application and the maintenance of the apatite stoichiometric one (Ca/P = 1.7) when CHA nanocrystals were used. These results suggest that the use of CHA nanocrystals leads to

remineralization by means of the addition of a layer of apatite similar to those of natural tissues whereas fluoride act more by changing the chemical composition of the enamel.

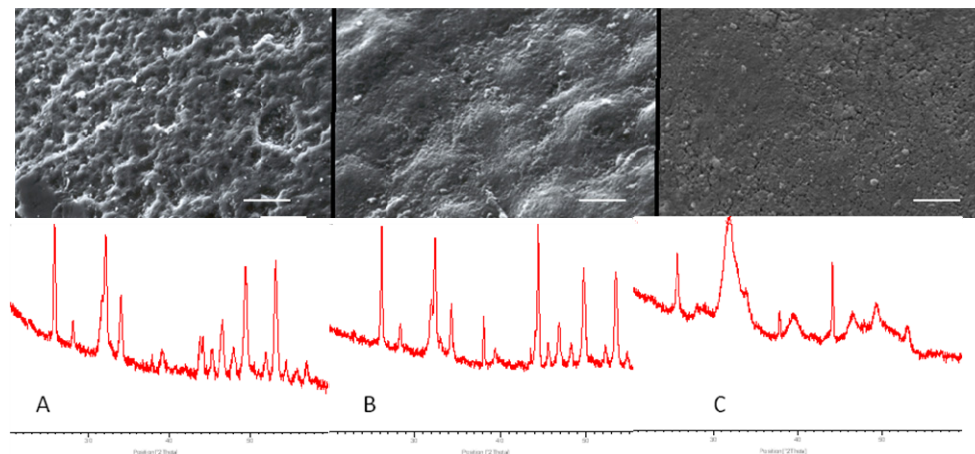


Fig. 3. A. Scanning electron microscopic graph and XRD spectrum of enamel surface demineralised with 37% orthophosphoric acid and brushed *in vitro* 2 times (1 min) a day for 15 days without any past application. Pits obtained by chemical attack and disruption by mechanical wear may be observed. Original magnification 5000X Bar=10 μ m.

B. Scanning electron microscopic graph and XRD spectrum of enamel surface demineralised with 37% orthophosphoric acid and brushed *in vitro* 2 times (1 min) a day for 15 days with fluoridated toothpastes. Pits are covered by a layer. The underneath surface is still perceptible. Original magnification 5000X Bar=10 μ m.

C. Scanning electron microscopic graph and XRD spectrum of enamel surface demineralised with 37% orthophosphoric acid and brushed *in vitro* 2 times (1 min) a day for 15 days with a paste containing a mix of 100nm and 20 nm CHA. The surface is completely covered by a globular layer. The XRD spectrum are compatible with those of CHA. Original magnification 5000X Bar=10 μ m.

In both cases the prism form of crystallization is not obtainable. To reach this goal the use of the described biomimetic carbonate-hydroxyapatite nanocrystals together with a suitable scaffold is suggested as being the promising strategy (Kirkam et al., 2007).

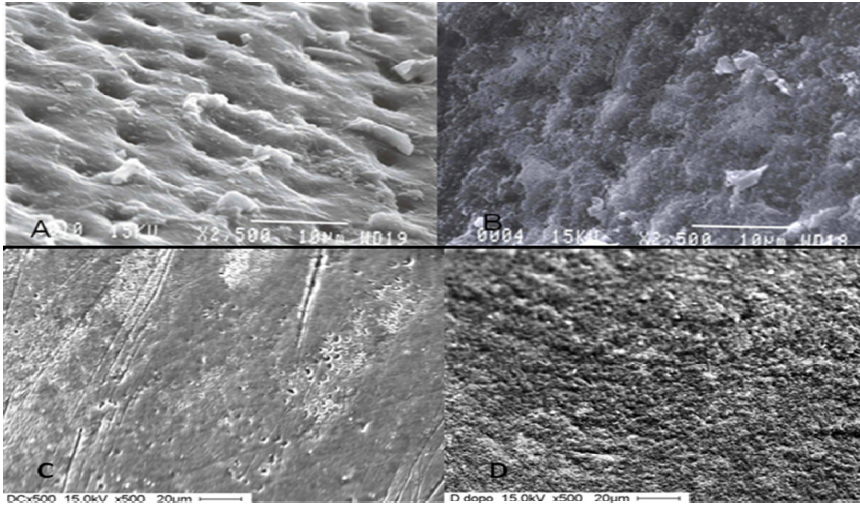


Fig. 4. Scanning electron microscope of *in vitro* demineralized dentin (A) and remineralized dentin with CHA (B); Scanning electron microscope of replica model obtained *in vivo* of demineralized dentin (C) and remineralized dentin with CHA (D).

An interesting application of nanocrystals of CHA could also be to obtain remineralization of dentin in order to reduce dentin hypersensitivity or improve mineralization of the dentinal tissues, for instance in the case of abutment preparation. The application of CHA nanocrystals closes the patent tubules of the exposed dentin *in vitro* (Fig. 4, A-B) and also *in vivo* as observable with a replica model technique (Fig. 4, C-D).

4. The application of stem cells in dental tissue regeneration

As already described, the traditional approach in the treatment of oral diseases often involves replacing teeth with artificial components. This approach is relatively successful. Biomaterials used may be not fully compliant with native tissues and often require multi-steps surgery and delayed healing (Hacking & Khademhosseini, 2009).

Tooth regeneration offers new and innovative approaches to difficulties encountered in oral and dental surgery. The aim of regenerative medicine is to simulate natural processes *in vitro* in order to re-create a tissue or an organ. This approach can involve cells, biomaterials and molecular factors; in this context, stem cells offer a great potential for tissue repair and regeneration. Stem cells are unspecialized cells capable of renewing themselves and under certain physiologic or experimental conditions, they can be addressed to more specialized committed lineages.

There are two main kinds of stem cells: adult stem cells (ASC) and embryonic stem cells (ESC). The first derive from adult tissue whereas the second derive from blastocysts. Both of them are largely used in the research field of tissue regeneration for their capability of self-renewal, their differentiation potential and their low immunogenicity.

4.1 Endodontic regeneration

Pulp and dentin tissue engineering may be an interesting alternative to traditional methods to treat compromised teeth endodontically. Sharpe and Young (Sharpe & Young, 2005) introduced the concept of using stem cells for dental tissue engineering and demonstrated that it is possible to engineer murine teeth by using adult stem cells of non-dental or dental origin.

Dental pulp contains highly proliferative cells that can be activated upon injury and undergo proliferation and differentiation toward osteoblastic phenotypes to provide for dentin repair. The first isolation of such kind of cells was reported in 2000; Gronthos and al. isolated a clonogenic population of cells from adult human dental pulp and assessed their differentiation potential (Gronthos et al., 2000). These cells, called dental pulp stem cells (DPSCs), had the capacity to form dense calcified nodules *in vitro*; moreover, STRO-1 + cells extracted from dental pulp of adult rat can differentiate toward adipogenic, neurogenic, myogenic and chondrogenic lineages.

In the same work, it was demonstrated that DPSCs can generate a dentin/pulp-like structure *in vivo*. DPSCs were transplanted in conjunction with HA/TPC powder, a scaffold "odonto-conductive", into immunocompromised mice and after 6 weeks a collagenous matrix was deposited. Besides, transplanted DPSCs expressed dentin matrix components and the gene DSPP, which encode for dentin sialoprotein and dentin phosphoprotein.

An osteo-dentin like matrix was observed to be formed only two weeks after subcutaneous implantation in rabbits, when poly (lactic-co-glycolic acid) polymeric porous scaffolds grafted with dental pulp stem cells were engineered (El-Backly et al., 2008). In this study, they observed that cells formed mineralised-like structures even without the addition of any differentiation chemicals. These cells may undergo differentiation into hard tissue forming cells when provided with an appropriate substrate.

Other cells known as SHED, stem cells isolated from dental pulp of human exfoliated deciduous teeth, have been observed to be capable of regenerating pulp and dentin if proper biochemical stimuli are provided. SHED exhibited a high plasticity, since they are able to differentiate *in vitro* into neurons, adipocytes, osteoblasts and odontoblast (Miura et al., 2003).

In 2008 Cordeiro et al. (Cordeiro et al., 2008) seeded SHED onto dentine slices and implanted them subcutaneously in immunodeficient mice. After 14-28 days, they observed a new dental pulp-like tissue, whose cellularity and architecture are very similar to that of physiologic pulp. SHED seeded on tooth slices/scaffolds were capable of differentiating into odontoblast-like cells and showed characteristics of dentin-secreting odontoblast. Moreover, in the same work it was demonstrated that SHED co-implanted with human endothelial cells HDMEC improve the new-formed tissue organization, microvascular network and oxygen and nutrient influx.

4.2 Periodontal regeneration

The periodontum is a complex organ consisting of epithelial tissue and connective tissue, both soft and mineralized. The periodontum comprises the alveolar bone, gingiva, cementum and periodontal ligament. Several diseases affecting periodontal integrity can lead to tooth loss.

The loss of numerous teeth can entail difficulties in eating and talking, moreover a significant loss of surrounding bone can imply limitations to future options of surgical

intervention. In particular periodontal ligament regeneration is a major concern in periodontology and an ambitious aim in implantology.

Periodontal ligament itself contains progenitor cells; recently human stem cells have been isolated from periodontal ligament. They express stemness markers such as STRO-1, CD146 and they are able to form alizarin red-positive nodules and cementoblastic/osteoblastic markers (alkaline phosphatase, osteocalcin and bone sialoprotein) *in vitro*. These cells have been called periodontal ligament stem cells (PDLSC). *In vitro* expanded PDLSCs were transplanted subcutaneously into the dorsal surfaces of immunocompromised mice using hydroxyapatite tricalcium phosphate (HA/TCP) as a carrier. These cells showed the capacity to differentiate into cementoblasts and to form cementum/PDL-like structures. (Seo et al., 2004).

Moreover, PDLSCs showed the capacity to form collagen fibres connecting to the cementum-like tissue; these fibres are similar to Sharpey's fibres and they suggest the potential to regenerate PDL attachment.

A recent study of a preclinical model made in miniature pigs (Liu et al., 2008) showed that autologous PDLSCs are capable of forming bone, cementum and periodontal ligament if they are transplanted onto HA/TCP carrier into surgical, created periodontal defects.

Not only PDL derived cells have periodontal regeneration capability. Precursor cells (PCs) from human dental follicles of wisdom teeth have been isolated and characterized for their periodontal regeneration potential. These cells formed *in vitro* a membranous structure that can be compared to PDL, consisting of a connective-like matrix and a mesothelium-like cellular structure with nuclei of granular calcification. *In vivo* differentiation potential of PCs was assessed by their transplantation in conjunction with hydroxyapatite powder into immunocompromised mice, but no sign of cementum or bone formation was found in histological sections of transplants (Morszeck et al., 2005).

More recently, in 2007 Yokoi et al. demonstrated that immortalized mouse dental follicle cells are able to re-generate *in vivo* a PDL-like tissue (Yokoi et al., 2007).

Also non-dental derived stem cells have been tested in order to obtain periodontal regeneration. In a work of Tobita M. (Tobita et al., 2008), ASCs (Adipose-derived Stem Cells) isolated from rat and mixed with platelet-rich plasma (PRP) were implanted into the periodontal tissue defect generated in the test rat. A partial alveolar bone regeneration and a periodontal ligament-like structure was observed 8 weeks after implantation.

Even bone marrow could represent an alternative source of MSCs for the treatment of periodontal disease (Kawaguchi et al., 2004). Its potential in periodontal regeneration was assessed *in vivo*, when bone marrow derived MSCs isolated from beagle dogs were mixed with atelocollagen and transplanted into experimental periodontal defects.

Transplanted stem cells have been able to differentiate into cementoblasts, osteoblasts, osteocytes, fibroblasts and four weeks after transplantation the defects were almost regenerated with periodontal tissue. (Hasegawa et al., 2006).

4.3 Tooth regeneration

Humans are genetically programmed to replace their teeth once during childhood. Therefore, when adult teeth are lost or damaged, they cannot be regenerated or re-grown. However, with the advancement of stem cell biology and tissue engineering, regenerating the whole tooth has become a realistic and attractive option to replace a lost or damaged tooth. The loss of teeth because of caries, periodontal disease, or trauma is a relatively

common problem among older people. Several therapies such as artificial dentition, tooth transplantation, and dental implants are often necessary to recover lost masticatory function. However, at present, complete restoration therapy to compensate for complete tooth loss has not been achieved (Masaki et al., 2008).

Teeth and their surrounding structures (tooth/periodontal complexes) are typical of complicated organs and consist of both hard tissue (dentin, enamel, cementum, alveolar bone) and soft tissue (dental pulp, periodontal ligament and gingiva). Because of its complexity, tooth regeneration presents some limits which regard the traditional principles of tissue engineering, related to whole tooth regeneration with correct morphology. Tooth development is regulated by the interaction between the dental epithelium and the dental mesenchyme. For this reason two populations of stem cells need to be considered in the development of the tooth: epithelial (EpSC) and mesenchymal stem cells (MSC), EpSCs differentiate into ameloblasts whereas MSCs give rise to odontoblasts, cementoblasts, osteoblasts and fibroblasts of the periodontal ligament.

Numerous attempts have been made in order to regenerate teeth *in vivo* with an association of odontogenic, mesenchymal and epithelial cells with encouraging results.

Some experiments were done by Sharpe's group. They discovered that recombinations between an *in vitro* created mesenchyme (with non-dental stem cell from different sources) and embryonic oral epithelium stimulate an odontogenic response in the stem cells (Ohazama et al., 2004). When this engineered tissue was implanted into adult renal capsules it resulted in the development of tooth structures and associated bone.

Other studies demonstrated that cells isolated from both porcine (Young et al., 2005) and rat (Duailibi et al., 2004) tooth buds, seeded onto polyglycolide/poly-L-lactide (PGA/PLLA) scaffolds, lead to the formation of an ectopic bioengineered tooth with pulp, dentin and enamel tissues, even though in an anomalous special arrangement. In fact, the main limitation of the new formed tooth is the abnormal shape and the relative diminution of the dental tissues generated.

In a recent study (Nakao et al., 2007) a new approach was proposed for the formation of a bioengineered tooth in the mouse mandible. Mesenchymal and epithelial cells, before the transplantation, were sequentially seeded into adjacent regions within a collagen gel drop. The implantation of both early primordia and a tooth that had partially developed in a subrenal capsule was tested. With this method, a correct tooth structure comprising enamel, dentin, root, dental pulp and bone could be observed, showing penetration of blood vessels and nerve fibers.

Encouraging results have also been obtained by Duailibi et al. (Duailibi et al., 2008) using rat tooth bud cells implanted into the jaw of an adult rat for 12 weeks. This study demonstrated that stem cells could be a useful future tool in the replacement of missing or lost teeth.

Lesot et al. showed that also bone-marrow-derived cells can be reprogrammed to give rise to ameloblast-like cells, offering novel possibilities for tooth-tissue engineering and the study of the simultaneous differentiation of one bone marrow cell subpopulation into cells of two different embryonic lineages (Unda et al., 2006).

However the odontogenic potential of bone marrow and dental derived stem cells do not seem to be the same. A work of Yu et al. (Yu et al., 2007) showed that DPSC STRO-1 + co-cultured with apical bud cells (ABCs) possess more active odontogenic differentiation ability than STRO-1 + BMSCs/ABCs. Recombined DPSCs/ABCs were able to form a tooth shaped tissue with balanced amelogenesis and dentinogenesis, whereas BMSCs/ABCs

formed an atypical dentin-pulp complex and they were not able to form enamel. These data indicate that mesenchymal stem cells derived from different embryonic origins; in fact DPSCs derive from neural crest whereas BMSCs from mesoderm and they could not be equivalent in their differentiation pathway.

5. Conclusion

Remineralization of enamel represents a useful tool to counteract the loss of mineral tissue due to bacteria metabolism and foods and drinks ingestion. The technologies now available are based on the substitution of hydroxyapatite with fluor-hydroxyapatite in order to reduce solubility. The use of nanotechnology as well as the crystallization of hydroxypapptite starting from amorphous compound are effective strategies to gain mineralization even if they fail to reconstruct the histological and crystallographic integrity of enamel tissue.

The therapeutic potential of adult stem cells for regenerative purposes is well-accepted, but further studies are necessary in order to furnish experimental data useful in clinic. Recently it was hypothesized that bone-marrow-derived mesenchymal stem cells could be a source of carcinoma-associated fibroblasts (CAF), which has an important role in the growth of epithelial solid tumors (Mishra et al., 2009). In the regenerative medicine, using stem cells may comport some risks. In particular a thorough understanding is necessary of all the molecular events that control tissues development, repair and regeneration. The pathology and consequence involved should be considered and investigated in order to avoid any problems.

6. References

- Atar, M.; Davis, G.R.; Verry, P.; Wong, F.S. (2007). Enamel mineral concentration in diabetic rodents. *Eur Arch Paediatr Dent*, 8(4):195-200
- Cai, F.; Shen, P.; Walker, G.D.; Reynolds, C.; Yuan, Y.; Reynolds, E.C. (2009). Remineralization of enamel subsurface lesions by chewing gum with added calcium. *J Dent*, 37(10):763-8.
- Chabala, J.M.; Edward, S.; Levi-Setti, R.; Lodding, A.; Lundgren, T.; Norén, J.G.; Odelius, H. (1988). Elemental imaging of dental hard tissues by secondary ion mass spectrometry. *Swed Dent*, 12(5):201-12
- Cochrane, N.J.; Saranathan, S.; Cai, F.; Cross, K.J.; Reynolds, E.C. (2008). Enamel subsurfacelesion remineralisation with casein phosphopeptide stabilised solutions of calcium, phosphate and fluoride. *Caries Res*, 42(2):88-97
- Cordeiro, MM.; Dong, Z.; Kaneko, T.; Zhang, Z.; Miyazawa, M.; Shi, S.; Smith, A.J.; Nör, J.E. (2008). Dental pulp tissue engineering with stem cells from exfoliated deciduous teeth. *J Endod*; 34(8): 962-9
- Dolphin, A.E.; Goodman, A.H.; Amarasiriwardena, D.D. (2005). Variation in elemental intensities among teeth and between pre- and postnatal regions of enamel. *Am J Phys Anthropol*, 128(4):878-88
- Du, C.; Falini, G.; Fermani, S.; Abbott, C.; Moradian-Oldak, J. (2005). Supramolecular assembly of amelogenin nanospheres into birefringent microribbons. *Science*, 4:307(5714):1450-4. Erratum in: *Science*. 2005 Sep 30;309(5744):2166.

- Duailibi, MT.; Duailibi, SE.; Young, CS.; Bartlett, JD.; Vacanti, JP.; Yelick, PC. (2004). Bioengineered teeth from cultured rat tooth bud cells. *J Dent Res*, 83: 523-528
- Duailibi, SE.; Duailibi, MT.; Zhang, W.; Asrican, R.; Vacanti, JP.; Yelick, PC. (2008) Bioengineered dental tissues grown in the rat jaw. *J Dent Res*, 87: 745-50
- El-Backly, RM.; Massoud, AG.; El-Badry, AM.; Sherif, RA.; Marei, MK. (2008). Regeneration of dentine/pulp-like tissue using a dental pulp stem cell/poly(lactic-co-glycolic) acid scaffold construct in New Zealand white rabbits *Aust Endod J*, 34(2): 52-67
- Elsayad, I.; Sakr, A.; Badr, Y. (2009). Combining casein phosphopeptide-amorphous calcium phosphate with fluoride: synergistic remineralization potential of artificially demineralized enamel or not? *J Biomed Opt*, 14(4):044039
- Fincham, A.G., Moradian-Oldak, J.M., Simmer, J.P., 1999. The structural biology of the developing dental enamel matrix. *J. Struct. Biol.* 126:270- 299.
- Fuerstein, O.; Mayer, I.; Deutsch, D. (2005). Physico-chemical changes of human enamel irradiated with ArF excimer laser. *Lasers Surg Med*, 37(3):245-51
- Gaengler, P.; Kremniczky, T.; Arnold, W.H. (2009). *In vitro* effect of fluoride oral hygiene tablets on artificial caries lesion formation and remineralization in human enamel. *BMC Oral Health*, 2;9(1):25. [Epub ahead of print]
- Gibson, C.W., Yuan, Z.A., Hall, B., Longenecker, G., Chen, E., Thyagarajan, T., Sreenath, T., Wright, J.T., Decker, S., Piddington, R., Harrison, G., Kulkarni, A.B., 2001. Amelogenin-deficient mice display an amelogenesis imperfects phenotype. *J. Biol. Chem.* 276,31871- 31875.
- Grenby, T.H.; Andrews, A.T.; Mistry, M.; Williams, R.J. (2001). Dental caries-protective agents in milk and milk products: investigations *in vitro*. *J Dent.* 29(2):83-92.
- Gronthos, S.; Mankani, M.; Brahimi, J.; Robey, P.G.; Shi, S. (2000) Postnatal human dental pulp stem cells (DPSCs) *in vitro* and *in vivo*. *Proc Natl Acad Sci USA*, 97: 13625-30
- Hacking, SA. & Khademhosseini, A. (2009). Applications of microscale technologies for regenerative dentistry. *J Dent Res*, 88 :409-21 Review
- Hasegawa, N.; Kawaguchi, H.; Hirachi, A.; Takeda, K.; Mizuno, N.; Nishimura, M.; Koike, C.; Tsuji, K.; Iba, H.; Kato, Y.; Kurihara, H. (2006). Behavior of transplanted bone marrow-derived mesenchymal stem cells in periodontal defects. *J Periodontol*, 77(6): 1003-7
- Honda, M.J.; Fong, H.; Iwatsuki, S.; Sumita, Y.; Sarikaya, M. (2008). Tooth-forming potential in embryonic and postnatal tooth bud cells. *Med Mol Morphol*, 41:183-1
- Huang, S.B.; Gao, S.S.; Yu, H.Y. (2009). Effect of nano-hydroxyapatite concentration on remineralization of initial enamel lesion *in vitro*. *Biomed Mater*, 4(3):34104. Epub 2009 Jun 5
- Jälevik, B.; Odellius, H.; Dietz, W.; Norén, J. (2001). Secondary ion mass spectrometry and X-ray microanalysis of hypomineralized enamel in human permanent first molars. *Arch Oral Biol*, 46(3):239-47
- Järvinen, E.; Tummers, M.; Thesleff, I. (2009). The role of the dental lamina in mammalian tooth replacement. *J Exp Zool B Mol Dev Evol.* 15;312B(4):281-91
- Karlinsey, R.L.; Mackey, A.C.; Stookey, G.K. (2009). *In vitro* remineralization efficacy of NaF systems containing unique forms of calcium. *Am J Dent*, 22(3):185-8
- Kawaguchi, H.; Hirachi, A.; Hasegawa, N.; Iwata, T.; Hamaguchi, H.; Shiba, H.; Takata, T.; Kato, Y.; Kurihara, H. (2004). Enhancement of periodontal tissue regeneration by transplantation of bone marrow mesenchymal stem cells. *J Periodontol*, 75(9): 1281-7

- Kirkham, J.; Firth, A.; Vernals, D.; Boden, N.; Robinson, C.; Shore, R. C.; Brookes, S. J.; Aggeli, A. (2007). Self-assembling Peptide Scaffolds Promote Enamel Remineralization. *J Dent Res*, 86: 426-430.
- Lee, Y.E.; Baek, H.J.; Choi, Y.H.; Jeong, S.H.; Park, Y.D.; Song, K.B. (2009). Comparison of remineralization effect of three topical fluoride regimens on enamel initial carious lesions. *J Dent*, Oct 8. [Epub ahead of print]
- Li, W.; Macule, D.; Gao, C.; DenBesten, P.K. (1999). Activation of recombinant bovine matrix metalloproteinase-20 and its hydrolysis of two amelogenin oligopeptides. *Eur J Oral Sci*, 107(5):352-9
- Liu, Y.; Zheng, Y.; Ding, G.; Fang, D.; Zhang, C.; Bartold, P.M.; Gronthos, S.; Shi, S.; Wang, S. (2008). Periodontal ligament stem cell-mediated treatment for periodontitis in miniature swine. *Stem Cells*, 26(4): 1065-73
- Luo, Z.X. (2007). Transformation and diversification in early mammal evolution. *Nature*, 13;450(7172):1011-9
- Lynch, R.J.; Mony, U.; ten Cate, J.M. (2007). Effect of lesion characteristics and mineralizing solution type on enamel remineralization *in vitro*. *Caries Res*, 41(4):257-62
- Mishra, P.J.; Glod, J.W.; Banerjee, D. (2009) Mesenchymal Stem Cells: Flip Side of the Coin. *Cancer Res*, 69:(4)
- Miura, M.; Gronthos, S.; Zhao, M.; Lu, B.; Fisher, L.W.; Robey PG.; Shi, S. (2003). SHED: stem cells from human exfoliated deciduous teeth. *Proc Natl Acad Sci USA*, 100: 5807-12
- Moradian-Oldak, J.; Du, C.; Falini, G. (2006). On the formation of amelogenin microribbons. *Eur J Oral Sci*, 114 Suppl 1:289-96; discussion 327-9, 382
- Morsczeck, C.; Götz, W.; Schierholz, J.; Zeilhofer, F.; Kühn, U.; Möhl, C.; Sippel, C.; Hoffmann, KH. (2005). Isolation of precursor cells (PCs) from human dental follicle of wisdom teeth. *Matrix Biol*, 24(2): 155-65
- Nakao, K.; Morita, R.; Saji, Y.; Ishida, K.; Tomita, Y.; Ogawa, M.; Saitoh, M.; Tomooka, Y.; Tsuji, T. (2007). The development of a bioengineered organ germ method. *Nat Methods*, 4(3): 227-30
- Nakashima, S.; Yoshie, M.; Sano, H.; Bahar, A. (2009). Effect of a test dentifrice containing nano-sized calcium carbonate on remineralization of enamel lesions *in vitro*. *J Oral Sci*, 51(1):69-77
- Ohazama, A.; Modino, S.A.; Miletich, I.; Sharpe, P.T. (2004). Stem-cell-based tissue engineering of murine teeth. *J Dent Res*, 83: 518-522
- Paine, M.L., White, S.N., Luo, W., Fong, H., Sarikaya, M., Snead, M.L., 2001. Regulated gene expression dictates enamel structure and tooth function. *Matrix Biol*, 20, 273-292.
- Paine, M.L., Zhu, D.-H., Luo, W., Bringas, P., Goldberg, M., White, S.N., Lei, K.Y.J.-P., Sarikaya, M., Fong, H.K., Snead, M.L. (2000). Enamel biomineralization defects result from alterations to amelogenin self-assembly. *J. Struct. Biol*, 132, 191- 200.
- Petersen, E.P. (2003). The World Oral Health Report: Continuous improvement of oral health in the 21st century - the approach of the WHO Global Oral Health. http://www.who.int/oral_health/media/en/orh_report03_en.pdf.
- Ranjitkar, S.; Narayana, T.; Kaidonis, J.A.; Hughes, T.E.; Richards, L.C.; Townsend, G.C. (2009). The effect of casein phosphopeptide-amorphous calcium phosphate on erosive dentine wear. *Aust Dent J*, 54(2):101-7

- Rimondini, L.; Palazzo, B.; Iafisco, M.; Canegallo, L.; Demarosi, F.; Merlo, M.; Roveri, R. (2007). The remineralizing effect of carbonate-hydroxyapatite nanocrystals on dentine. *Materials Science Forum*, 539-543: 602-605.
- Roveri, N.; Battistella, E.; Bianchi, CL.; Fortran, I.; Foresti, E.; Iafisco, M.; Lelli, M.; Naldoni, A.; Palazzo, B.; Rimondini, L. (2009). Surface enamel remineralization: biomimetic apatite nanocrystals and fluoride ions different effects. *Journal of Nanomaterials*; Article ID 746383, doi:10.1155/2009/746383
- Seo, BM.; Miura, M.; Gronthos, S.; Bartold, PM.; Batouli, S.; Brahim, J.; Young, M.; Robey, PG.; Wang, CY.; Shi, S.(2004) Investigation of multipotent postnatal stem cells from human periodontal ligament. *Lancet*, 364: 149-55
- Sharpe, PT. & Young, CS. (2005). Test-tube teeth. *Sci Am*, 293: 34-41
- Tan, J.; Leung, W.; Moradian-Oldak, J.; Zeichner-David, M.; Fincham, A.G. (1998). Quantitative analysis of amelogenin solubility. *J Dent Res*, 77(6):1388-96.
- Tanaka, M. & Kadoma, Y. (2000) Comparative reduction of enamel demineralization by calcium and phosphate *in vitro*. *Caries Res*, 34(3):241-5
- Thesleff, I. (2006). The genetic basis of tooth development and dental defects. *Am J Med Genet A*, 140(23):2530-5.
- Thesleff, I.; Järvinen, E.; Suomalainen, M. (2007). Affecting tooth morphology and renewal by fine-tuning the signals mediating cell and tissue interactions. *Novartis FoundSymp*, 284:142-53; discussion 153-63. Review.
- Tobita, M.; Uysal, AC.; Ogawa, R.; Hyakusoku, H.; Mizuno, H. (2008). Periodontal tissue regeneration with adipose-derived stem cells. *Tissue Eng Part A*, 14(6): 945-53
- Tummers, M.; Thesleff, I. (2009). The importance of signal pathway modulation in all aspects of tooth development. *J Exp Zool B Mol Dev Evol*, 312B(4):309-19
- Uhen, M.D. (2007). Evolution of marine mammals: back to the sea after 300 million years. *Anat Rec (Hoboken)*, 290(6):514-22.
- Unda, F.; Bopp-Kuchler, S.; Jimenez, L.; Wang, XJ.; Haïkel, Y.; Wang SL.; Lesot, H. (2006). Bone Marrow Cells Can Give Rise to Ameloblast-like Cells. *J Dent Res*, 85; 416
- Van Duinen, R.N.; Davidson, C.L.; De Gee, A.J.; Feilzer, A.J. (2004). In situ transformation of glass-ionomer into an enamel-like material. *Am J Dent*, 17(4):223-7.
- Walker, G.D.; Cai, F.; Shen, P.; Bailey, D.L.; Yuan, Y.; Cochrane, N.J.; Reynolds, C.; Reynolds E.C. (2009). Consumption of milk with added casein phosphopeptide-amorphous calcium phosphate remineralizes enamel subsurface lesions in situ. *Aust Dent J*, 54(3):245-9
- Wiegand, A.; Magalhães, A.C.; Navarro, R.S.; Schmidlin, P.R.; Rios, D.; Buzalaf, M.A.; Attin, T. (2009). Effect of Titanium Tetrafluoride and Amine Fluoride Treatment Combined with Carbon Dioxide Laser Irradiation on Enamel and Dentin Erosion. *Photomed Laser Surg*, Oct 1. [Epub ahead of print]
- Willershausen, B.; Schulz-Dobrick, B.; Gleissner, C. (2009). *In vitro* evaluation of enamel remineralisation by a casein phosphopeptide-amorphous calcium phosphate paste. *Oral Health Prev Dent*, 7(1):13-21. PubMed PMID: 19408810.
- Wilt, F.H. (2005). Developmental biology meets materials science: Morphogenesis of biomineralized structures. *Dev Biol*. 280(1):15-25. Review
- Yengopal, V.; Mickenautsch, S. (2009). Caries preventive effect of casein phosphopeptide-amorphous calcium phosphate (CPP-ACP): a meta-analysis. *Acta Odontol Scand*, 21:1-12. [Epub ahead of print]

- Yokoi, T.; Saito, M.; Kiyono, T.; Iseki, S.; Kosaka, K.; Nishida, E.; Tsubakimoto, T.; Harada, H.; Eto, K.; Noguchi, T.; Teranaka, T. (2007). Establishment of immortalized dental follicle cells for generating periodontal ligament *in vivo*. *Cell Tissue Res*, 327(2): 301-11
- Young, CS.; Kim, SW.; Qin, C.; Baba, O.; Butler, WT.; Taylor, RR.; Bartlett, JD.; Vacanti, JP.; Yelick, PC. (2005). Developmental analysis and computer modelling of bioengineered teeth. *Arch Oral Biol*, 50: 259-265
- Yu, J.; Wang, Y.; Deng, Z.; Tang, L.; Li, Y.; Shi, J.; Jin, Y. (2007). Odontogenic capability: bone marrow stromal stem cells versus dental pulp stem cells. *Biol Cell*, 99(8): 465-74

Biomimetic Porous Titanium Scaffolds for Orthopedic and Dental Applications

Alireza Nouri, Peter D. Hodgson and Cui'e Wen
*Institute for Technology Research and Innovation, Deakin University,
Waurrn Ponds, Victoria 3217
Australia*

1. Introduction

The development of artificial organs and implants for replacement of injured and diseased hard tissues such as bones, teeth and joints is highly desired in orthopedic surgery. Orthopedic prostheses have shown an enormous success in restoring the function and offering high quality of life to millions of individuals each year. Therefore, it is pertinent for an engineer to set out new approaches to restore the normal function of impaired hard tissues.

Over the last few decades, a large number of metals and applied materials have been developed with significant improvement in various properties in a wide range of medical applications. However, the traditional metallic bone implants are dense and often suffer from the problems of adverse reaction, biomechanical mismatch and lack of adequate space for new bone tissue to grow into the implant. Scientific advancements have been made to fabricate porous scaffolds that mimic the architecture and mechanical properties of natural bone. The porous structure provides necessary framework for the bone cells to grow into the pores and integrate with host tissue, known as osteointegration. The appropriate mechanical properties, in particular, the low elastic modulus mimicking that of bone may minimize or eliminate the stress-shielding problem. Another important approach is to develop biocompatible and corrosion resistant metallic materials to diminish or avoid adverse body reaction. Although numerous types of materials can be involved in this fast developing field, some of them are more widely used in medical applications. Amongst them, titanium and some of its alloys provide many advantages such as excellent biocompatibility, high strength-to-weight ratio, lower elastic modulus, and superior corrosion resistance, required for dental and orthopedic implants. Alloying elements, i.e. Zr, Nb, Ta, Sn, Mo and Si, would lead to superior improvement in properties of titanium for biomedical applications.

New processes have recently been developed to synthesize biomimetic porous titanium scaffolds for bone replacement through powder metallurgy. In particular, the space holder sintering method is capable of adjusting the pore shape, the porosity, and the pore size distribution, notably within the range of 200 to 500 μm as required for osteoconductive applications. The present chapter provides a review on the characteristics of porous metal scaffolds used as bone replacement as well as fabrication processes of porous titanium (Ti)

scaffolds through a space holder sintering method. Finally, surface modification of the resultant porous Ti scaffolds through a biomimetic chemical technique is reviewed, in order to ensure that the surfaces of the scaffolds fulfill the requirements for biomedical applications.

Outline:

The chapter is constructed as follows:

1. Introduction
 - 1.1 The structure and mechanical properties of bone
 - 1.2 Orthopedic metal alloys
 - 1.3 Titanium and its alloys as orthopedic biomaterials
2. Biomimetic Porous Scaffolds for Bone Tissue Engineering
 - 2.1 Characteristics of porous metal scaffolds
 - 2.1.1 Type of porous structure and porosity
 - 2.1.2 Density and porosity
 - 2.1.3 Shape and size of pores
 - 2.1.4 Mechanical properties of porous metal scaffolds
 - 2.2 Fabrication of porous titanium scaffolds through powder metallurgy
 - 2.2.1 Space holder method
3. Chemical Surface Modification of Porous Titanium Scaffolds
 - 3.1 Alkali treatment
4. Summary

1.1 The structure and mechanical properties of bone

Bone is an open cell composite material composed of a complex vascular system and a significant fraction of protein-related materials. At the architectural level, bone is made up of two types of different tissues tightly packed together. The outer shell is of dense compact or cortical bone, while the inner core is comprised of porous cellular, cancellous or trabecular bone, as shown in Figure 1. Cortical bone is highly dense and contains cylindrically organized osteons, also known as Haversian system, ranges between 10 to 500 μm . It is notable that the Haversian canal is composed of blood vessels in parallel to the long axis of the bone. These blood vessels are interconnected with vessels on the surface of the bone through perforating canals. Contrary to cortical bone, cancellous bone is highly porous, consisting of an interconnected network of trabeculae which is about 50-300 μm in diameter. These two types of bone tissues differ in porosity or density. The porosity of cortical bone is 5-10%, while in cancellous bones the porosity ranges between 75% and 90% (Burr & Martin, 1989; Choi et al., 1990; Rho et al., 1998; Parente et al., 2006).

The (wet) apparent density of cortical bone is 1.99 g/cm^3 (Currey, 1998), while this value for cancellous bone varies substantially and is typically in the range 0.05-1.0 g/cm^3 (Keaveny, 1998). The porosity of cancellous bone is the total volume that is not occupied by bone tissue and is usually filled with marrow. Although for the porosities less than 50% the distinction between the two bone tissues is fairly difficult, the change from compact to cancellous bone is usually clear and takes place over a small distance.

The fraction of cancellous bone varies in different living forms. For instance, birds flying in the sky have larger fraction of cancellous bone compared to those of animals crawling on the ground (Nakajima, 2007). The difference between the cortical bone and cancellous bone is

also manifested by histological evaluation of the tissue's microstructure. The microstructure of cortical bone is made up of regular, cylindrically shaped lamellae, whilst cancellous bone is identified by irregular, sinuous convolutions of lamellae. In addition, cancellous bone tissue is metabolically active and can be remodeled more frequently than that of cortical bone (Rho et al., 1998).

The porosity of bone can be characterized by the small pores of canaliculi and smaller lacunae and larger pores of osteons, and Volkmann's canals, as shown in Figure 1. In normal cortical bone, the size of the smaller canaliculi and vasculature channels are in the range of 1-5 μm (Ascenzi & Bonucci, 1976). In addition, bone is a reservoir for calcium in the body, containing 99% of the body's calcium. Bone mineral is mostly in the form of hydroxyapatite ($\text{Ca}_{10}(\text{PO}_4)_6(\text{OH})_2$). Biological hydroxyapatite contains carbonate ions as replacement groups in phosphate and hydroxyl sites of the hydroxyapatite structure.

The successful implantation of bone scaffolds not only needs to meet biological requirements but also demands to have adequate mechanical strength. The mechanical characteristics of bone can be defined by its interaction with other bones, joints, or muscles in the body. However, the total geometry of the bone and the distribution of the tissue favor the mechanical strength of the structure. Principally, bone is an anisotropic material and its mechanical properties vary with anatomical location and the loading direction. There is also a great variability of modulus between the longitudinal and transverse directions (Rho et al., 1998; Silva et al., 2007).

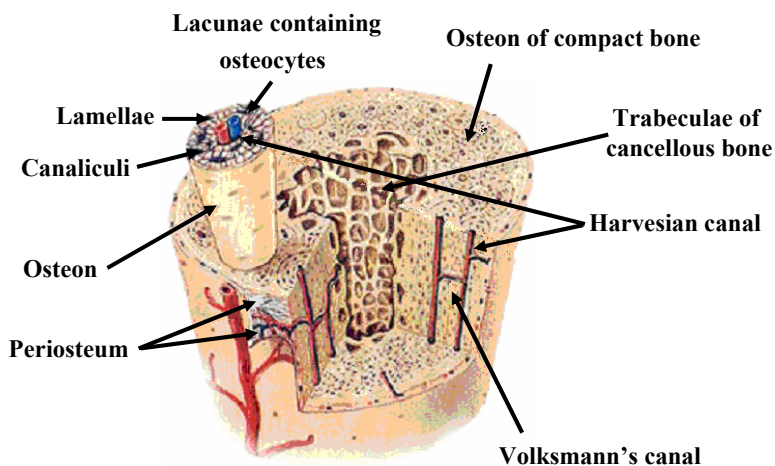


Fig. 1. The structure of bone (<http://training.seer.cancer.gov/anatomy/skeletal/tissue.html>).

It is reported that the strength of cortical bone in the longitudinal direction is about 79-151 MPa in tension and 131-224 MPa in compression (Thomson et al., 1995). However, the experiments carried out in the transverse direction show strength of 51-56 MPa in tension and 106-133 MPa in compression. The elastic moduli of compact bone range from 17 to 20 GPa in the longitudinal direction and 6 to 13 GPa in the transverse direction (Thomson et al., 1995; Veisoh & Edmondson, 2003). On the other hand, cancellous bone does not show a consistent mechanical strength and varies both longitudinally and from one bone to another.

As a result, cancellous bone exhibits much broader mechanical properties compared to those of cortical bone. The trabeculae of cancellous bone follow the lines of stress and can be realigned by changes in the direction of stress. The compression strength is reported in the range of 2-5 MPa, and the elastic modulus ranges from 0.76 to 4 GPa (Veisoh & Edmondson, 2003). In a study by Wang *et al.* (Wang *et al.*, 2007) on a dry cancellous bovine bone, the elastic modulus in the longitudinal and transverse directions were 20 ± 2 GPa and 14.7 ± 1.9 GPa, respectively.

1.2 Orthopedic metal alloys

The main goal of design and fabrication of an orthopedic biomaterial is to restore the function and mobility of the native tissue that is considered to be replaced. In order to select an ideal biomaterial for orthopedic and dental applications specific property requirements must be fulfilled. The ideal materials for hard tissue replacement should be biocompatible and bioadhesive, possess adequate mechanical properties to tolerate the applied physiological load, be corrosion/wear resistant and finally show good bioactivity to ensure sufficient bonding at the material/bone interface. The materials used in orthopedic surgery can be divided into five major classes of metals, polymers, ceramics, composites, and natural materials (Hoffman, 2004). However, this chapter focuses mainly on orthopedic metal alloys.

Compared to other biomaterials like ceramics and polymers, the metallic biomaterials offer a wider range of mechanical properties such as high strength, ductility, fracture toughness, hardness, formability, as well as corrosion resistance, and biocompatibility. These are the required properties for most load-bearing applications in fracture fixation and bone replacement (total joint arthroplasty) (Breme & Biehl, 1998a; Hallab *et al.*, 2004).

Metallic biomaterials can also be used as functional constructions such as valves and heart pacemakers (Breme & Biehl, 1998a). In view of their mechanical properties, ceramics and carbon can be highly loaded under compression stresses while polymers show a poor strength under both tensile and compression loads. However, ceramic materials are brittle and exhibit low toughness under compression loads. Taking these limitations into account, metals are preferred in most cases for structural biomedical constructions. The structural metallic biomaterials fall into two classes of low-loaded implants (e.g. plates, screws, staples) or high-loaded implants (e.g. hip and knee prostheses) (Breme & Helsen, 1998b).

However, the main concern regarding the application of bulk (dense) metallic biomaterials is their higher stiffness than that of bone. The magnitude of elastic modulus for bulk metallic implant materials surpasses that of cortical bone by far and results in a failed stress transmission from biomaterial to bone, the so-called stress-shielding effect. The stress-shielding may lead to bone resorption or even fretting, due to micro motions occurring at the bone/implant interface (Kawalec *et al.*, 1995). The idea of preparing a porous material is to bridge this biomechanical mismatch. A decrease in elastic modulus (or lowering the stiffness) would result in a higher elastic elongation of the cells in the vicinity of the implant, whereby stimulating bone formation by producing calcium (Natali & Meroi, 1989).

Metals used for implant materials must have a high corrosion resistance and should be stable in physiological environments. Although there are a few metallic elements (e.g. Cr, Co, Ni and V) possessing a relatively high corrosion resistance, they may cause adverse biological reactions (Steinemann, 1980; Okazaki *et al.*, 1998). The metallic ions of these metals may also combine with patient's proteins and trigger allergic immune response

(Kramer, 2000). In general, compared to cobalt-chromium alloys (Co-Cr) (Varma et al., 2002), and stainless steels (Winters & Nutt, 2003), titanium and some of its alloys (Ashraf Imam & Fraker, 1996) are the more suitable metallic materials used for orthopedic applications.

It is notable that the materials used for fabricating orthopedic metallic implants are mostly metal alloys rather than pure metals. In this chapter, the application of stainless steels and cobalt-chromium alloys are described briefly, whilst the characteristics of Ti and its alloys and their application in orthopedics are reviewed in more details.

Stainless steel: Stainless steels were the first reliable metals used as prosthesis in orthopedics. The basic elements in steels are iron and carbon and may usually contain chromium, nickel, and molybdenum as additional elements. The most common stainless steel in orthopedics is designated 316L. This is an austenitic steel with a low amount of carbon (0.03 wt.%). Compared to other metallic implants, stainless steels exhibit lower strength and much higher corrosion resistance, but possess greater ductility and lower production cost (Hallab et al., 2004). Their high stiffness makes them inferior to Ti in bone replacement applications (Williams, 2001).

Cobalt-chromium alloys: The two Co-Cr alloys widely used as implant materials are: (1) cobalt-chromium-molybdenum (Co-Cr-Mo), and (2) cobalt-nickel-chromium-molybdenum (Co-Ni-Cr-Mo). The possible toxicity of released Ni ions from Co-Ni-Cr alloys and also their poor frictional properties are a matter of concern in using these alloys as articulating components. Thus, Co-Cr-Mo is distinguished as the dominant class for total joint arthroplasty. However, wear debris from Co-Cr alloys have been considered as a cause of implant loosening and soft tissue adverse reaction (Browne & Gregson, 1995).

1.3 Titanium and its alloys as orthopedic biomaterials

In selecting a material for orthopedic applications, a few general criteria should be considered. The first criterion is a series of properties required for biomedical applications, such as good biocompatibility, no adverse tissue reaction with host tissue, as well as high corrosion and wear resistance. Meanwhile, an orthopedic implant should also meet the requirements of certain mechanical properties, whether the function is related to fracture fixation or total joint arthroplasty (bone replacement). In particular, an ideal orthopedic implant must exhibit an elastic modulus mimicking that of the bone selected. Secondly, the candidate material should meet the requirement of a certain processing profile, meaning that they are capable of being processed to the required shape by feasible manufacturing techniques with the minimum overall cost (Abel et al., 1994; Gasser, 2001). This requires a profound knowledge of all aspects of the implant's properties.

Titanium (Ti) is a lightweight, high strength metal located in the fourth horizontal row of the periodic table, grouped with transition metals. Ti exists in two allotropic structures with different crystal lattices. At room temperature, it is characterized by the hexagonal closely-packed crystal structure (hcp) known as α phase. Upon heating to temperatures over 883°C, it transforms into the body-centered cubic crystal structure (bcc) referred to as β phase (Molchanova, 1965; Lütjering & Williams, 2003). However, the temperature of the allotropic transformation of Ti depends on the degree of purity of the metal. The properties of Ti and its alloys are relatively sensitive to even small amounts of interstitial elements (H, O, N and C) (Brooks, 1982).

The microstructure of Ti alloys is rather complex and depends upon the alloying elements and thermomechanical process (cold working and annealing). Depending on the type and amount of alloying elements, commercial Ti alloys are typically classified into three different categories: α , β , and $\alpha+\beta$ alloys. Some alloying elements lead to an increase in the transition temperature of Ti, referred to α stabilizing elements, whilst others lower the transition temperature known as β stabilizing elements. Most of the body-centered cubic elements (bcc) would be expected as β stabilizing elements. Amongst them, Mo, V, Nb, Ta, Mn, Fe, Cr, Co, Ni and Cu are the most common β -stabilizers. On the other hand, most of the interstitial elements (e.g. O, N, and C, except H) as well as some substitutional elements such as Al, Ga, Ge and Sn fall into the category of α -stabilizer. In addition, the final microstructure of Ti alloys can be affected by the cooling process from β phase, as this affects the $\beta\leftrightarrow\alpha$ transition temperature, as well as the obtained α grain size and shape.

Ti alloys were first used in orthopedics in the mid-1940s and have continued to gain attention because of their unique properties, including high specific strength, light weight, excellent corrosion resistance and biocompatibility. Due to the aforementioned properties, this class of materials exhibits tremendous clinical advantages in terms of reduced recovery time and rehabilitation, and improved comfort for patients (Nyberg et al., 2005a). However, for bone replacement components, the strength of pure Ti is not sufficient and Ti alloys are preferred due to their superior mechanical properties. In general, alloying elements would lead to an improvement in the properties of Ti for orthopedic applications.

Ti-6Al-4V ELI and NiTi shape memory alloys (SMA) are the most commonly used Ti alloys in orthopedic applications because of their good combination of mechanical properties and corrosion resistance (Baumgart et al., 1980; Andreasen & Fahl, 1987; Li et al., 2005). However, the possible release of toxic ions from aluminum (Al), vanadium (V) and nickel (Ni) during in vivo corrosion of the implant remains the matter of concern. Al for exceeding content of 7% at low temperature would lead to possible embrittlement and it may also cause severe neurological, e.g. Alzheimer's disease (Mjoberg B, 1997) and metabolic bone diseases, e.g. osteomalacia (Boyce et al., 1992; Zaffea et al., 2004). Similarly, V can alter the kinetics of the enzyme activity associated with the cells and results in potential cytotoxic effects and adverse tissue reactions (Zwicker et al., 1980; Woodman et al., 1984; Semlitsch et al., 1985; Pimenova & Starr, 2006). Moreover, the oxide layer of Al_2O_3 and VO_2 are less thermodynamically stable than that of TiO_2 , as their harmful debris may take place in living organism (Lewis & Shaw, 1995). Evident cytotoxic and allergic responses of Ni have also been reported (Castleman & Motzkin, 1981; McKay et al., 1996). Thus, it is necessary to develop new Ti alloys that contain non-toxic elements.

Over the last two decades, the researchers working on Ti alloys have discovered new alloys for orthopedic applications. For instance, Ti-Al-Nb and Ti-Al-Nb-Ta (Semlitsch et al., 1992; Sasaki et al., 1996), Ti-Nb-Ta-Zr (Niinomi et al., 2004), Ti-Zr-Nb (Yu et al., 2001), Ti-Zr-Nb-Ta-Pd (Okazaki et al., 1996), Ti-Sn-Nb (Nouri et al., 2008a), and Ti-Ni-Ta (Lekston & Goryczka, 2007), have been developed or used as implant biomaterials. Some of the Ti alloys developed for biomedical applications are given in Table 1.

In general, most of the Ti alloys offer appropriate mechanical properties for orthopedic applications. The torsional and axial stiffness (modulus) of Ti alloys are closer to those of bone and theoretically provide less stress shielding than those of stainless steel and Co-Cr alloys. Figure 2 presents elastic moduli of some important materials used in bone tissue engineering (Niinomi et al., 2004).

Perhaps the most unfavorable properties of Ti alloys with respect to mechanical behavior are their susceptibility to crack propagation, their relative softness and relatively poor wear and frictional properties compared to Co-Cr-Mo alloys. In terms of biocompatibility, the clinical success of Ti and its alloys is based on the presence of a passive oxide layer on their surface. The naturally occurring oxide of titanium is TiO_2 which has a thickness of 5-29 nm and can be restored quickly (milliseconds) after damage (Breme & Biehl, 1998a; Bram et al., 2006a). However, there is some disagreement about the exact oxide chemistry in pure Ti versus alloyed Ti (Brunski, 2004). A comparison between the properties of Ti with their metallic biomaterial counterparts are tabulated in Table 2.

Composition	Type
Pure Ti	α
Ti-6Al-4V ELI (ASTM F136084, F620-87)	$\alpha+\beta$
Ti-6Al-4V (ASTM F1108-88)	$\alpha+\beta$
Ti-6Al-7Nb	$\alpha+\beta$
Ti-5Al-2.5Fe	$\alpha+\beta$
Ti-5Al-3Mo-4Zr	$\alpha+\beta$
Ti-15Sn-4Nb-2Ta-0.2Pd	$\alpha+\beta$
Ti-15Zr-4Nb-2Ta-0.2Pd	$\alpha+\beta$
Ti-13Nb-13Zr	near β (low modulus)
Ti-12Mo-6Zr-2Fe	β (low modulus)
Ti-15Mo	β (low modulus)
Ti-16Nb-10Hf	β (low modulus)
Ti-15Mo-5Zr-3Al	β (low modulus)
Ti-15Mo-2.8Nb-0.2Si-0.26O	β (low modulus)
Ti-35Nb-7Zr-5Ta	β (low modulus)
Ti-29Nb-13Ta-4.6Zr	β (low modulus)
Ti-40Ta, Ti-50Ta	β (high corrosion resistance)

Table 1. Titanium alloys for biomedical applications (Niinomi et al., 2004).

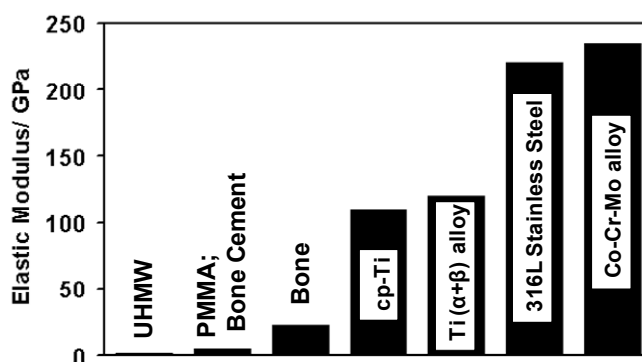


Fig. 2. Elastic modulus of some widely used orthopedic biomaterials (Niinomi et al., 2004).

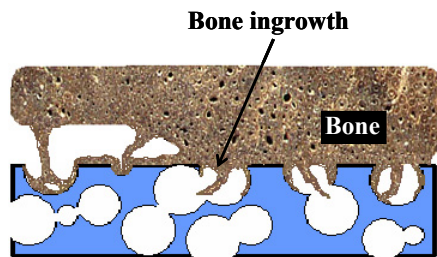
Characteristics	Stainless Steel	Cobalt-Chromium	Titanium
Stiffness	High	Medium	Low
Strength	Medium	Medium	High
Corrosion resistance	Low	Medium	High
Biocompatibility	Low	Medium	High

Table 2. Comparison between the properties of three major metallic biomaterials.

2. Biomimetic Porous Scaffolds for Bone Tissue Engineering

Bone tissue implants require not only a material with adequate composition, but also a good structure that mimics the mechanical properties and architecture of bone. Despite the great progress in manufacturing of bulk (dense) metallic implants for orthopedic applications, there are major concerns associated with their use in the human body. Two major problems are the biomechanical mismatch of stiffness between the implant and bone, as well as micromotion of the implants due to inadequate initial fixation with host tissue (Robertson et al., 1976; Cameron et al., 1978; Ryan et al., 2006). Consequently, bone surrounding the implant is subjected to negligible mechanical stress, which may result in detrimental bone resorption (Turner et al., 1986; Breme & Helsen, 1998b; Thieme et al., 2001; Thelen et al., 2004). In this situation, the bone holding the implant in place becomes weakened, causing a loosening of the device. Any approach towards solving the raised problems in providing a good load transfer and bone anchorage is of foremost importance in designing the material and structure of orthopedic implants.

Recently, a great deal of attention has been given to a new class of materials, known as porous materials. Because bone is a porous tissue material, there is a physiological rationale for the use of porous materials in its replacement. Introducing pores into a material structure reduces the stiffness values close to that of natural bone which can subsequently provide a good load transfer and stimulate the formation of new bones (Griss & Heimke, 1976). In addition, the porosity allows new bone tissue to grow into the porous structure, providing an adequate biological fixation. Figure 3 illustrates the bone growing into the open pores of an implant, creating a highly convoluted interface.



Stable Fixation

Fig. 3. The bone ingrowth into the pores of an orthopedic porous scaffold providing a stable fixation (Nouri, 2008).

Due to the anchorage of porous materials in bone, they are also considered as a preferred alternative to bone cement fixation (Oliveira et al., 2002). A number of different porous materials have been developed in the past three decades including porous ceramic, polymeric and metallic materials. Despite the excellent corrosion resistance and biocompatibility of ceramic materials, they are inherently brittle and crack easily (Breme & Helsen, 1998b; Shannon & Rush, 2005). Similarly, porous polymeric systems cannot sustain the mechanical forces present in joint replacement surgery. This leads researchers to seek for porous metal scaffolds for their appropriate mechanical properties of load-bearing applications (Breme & Helsen, 1998b). Porous Ti scaffolds possess a unique combination of properties required for orthopedic and dental applications including strength, stiffness, durability and biocompatibility.

2.1 Characteristics of porous metal scaffolds

The structure of porous metal scaffolds is extremely important for their biological and mechanical properties, and can determine their performance in orthopedic applications (Bobynd et al., 1980; Li et al., 2004a). In order to manufacture an orthopedic implant with appropriate mechanical properties and an ability to allow biological anchorage with surrounding bone tissue, the geometry of the porous structure must be taken into account (Wen et al., 2001; Banhart, 2002; Li et al., 2005).

2.1.1 Type of porous structure and porosity

The structure of porous metal scaffolds can be classified into closed cells and open cells or the combination of both, depending on the fabrication methods. Typical configurations of closed- and open cells are shown in Figure 4. In the closed-cell porous metal scaffolds, pores are surrounded by pore walls and disconnected from each other, while in open-cell porous scaffolds, pores are connected to each other through various channels such as voids, interstices, etc. Biomedical applications are challenging, as they often have requirements in both structural and functional aspects. However, for orthopedic surgery, open cells are often required since new bone tissue grows into the porosity and ensures the fixation of the implant with the surrounding host tissue (Ishizaki et al., 1998; Banhart, 2002; Shehata Aly et al., 2005). The interconnected pore networks also support the vascular system required for continuing bone development (Murray & Semple, 1981; Li et al., 2005). In view of biocompatibility, the open pores allow the access of oxygen throughout the porous structure, facilitating the formation of an important resistant passive layer (Seah et al., 1998). Porous metal scaffolds are classified into three major groups: (1) partly or fully porous-coated solid substrates, (2) fully porous body, and (3) porous metal part joined to a solid metallic part (Pilliar, 1983; Li et al., 2005; Ryan et al., 2006). However, the porosity can also be gradually changed from the surface to the centre of the sample, known as gradient porosity (Kutty et al., 2001; Zhang et al., 2007; Wen et al., 2007a).

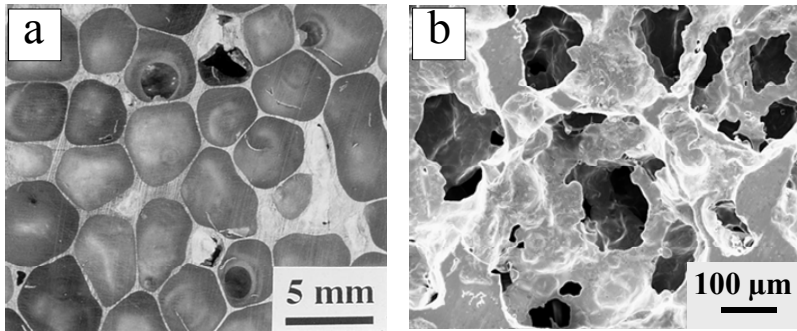


Fig. 4. Typical cell structures of (a) a closed cell aluminum foam ALPORAS (Miyoshi et al., 1999); and (b) open cell Ti-16Sn-4Nb (wt.%) scaffold (Nouri, 2008).

2.1.2 Density and porosity

The density of porous metal with an open-cellular structure is an important parameter for predicting permeability and mechanical properties. The permeability of a porous material is defined as the degree to which bone can grow into the pores and pass through it (Despois & Mortensen, 2005). By increasing the porosity, the mechanical strength is reduced and the permeability is increased (Eisenmann, 1998). However, a trade-off should be made between these two parameters to achieve a suitable implant for orthopedic applications.

In the porous metal field, the term 'relative density' is often used to describe the porous materials. It is the ratio of the density of porous metal to the density of its parent metal. The relative density of porous metals depends on the volume fraction of metal and pores. Typical porous metal scaffolds have relative densities less than 0.3 (Gibson & Ashby, 1997; Kriszt et al., 2002).

To stimulate the growth of new bone tissue into the pores, the material must have at least 60% porosity (Bram et al., 2006a). Similarly, in a study by Esen and Bor (Esen & Bor, 2007) a minimum porosity of 55% was reported for direct connectivity of macropores. These degrees of porosity would lead to an interconnected porous structure which favors the cell ingrowth to the porous space, vascularization, and transport of metabolic products. The degree of porosity is also considered to be crucial for biocompatibility. In an experiment performed by Tuchinskiy and Loutfy (Tuchinskiy & Loutfy, 2003), two materials with the same chemical composition but different porosities, were implanted in mice for a period of up to four weeks. The less porous material provoked a more vigorous foreign body reaction, and was encapsulated in a dense, highly collagenous bag with few blood vessels running through it. Consequently, the more porous material had a thinner sac with far greater vascularity.

2.1.3 Shape and size of pores

In order to increase bone growth into porous material, appropriate pore size must be provided. The pore size should be at least in the order of bone trabeculae and osteons which are tens of micrometer thick, otherwise bone ingrowth will not occur (Jasty et al., 2007). However, the optimum pore size for humans use has not been exactly defined. According to

Pilliar (Pilliar, 1987), pore size suitable for bone ingrowth is in the range of 75-250 μm ; while Elema *et al.* (Elema *et al.*, 1990) proposed that the pore size should range from 200 to 300 μm for bone tissue ingrowth in the porous samples. In general, implants with pore sizes in the range of 100 to 500 μm are suitable for bone ingrowth (Engh, 1983; Hungerford & Kenna, 1983; Bucholtz, 2002; Laptev *et al.*, 2004). Pore size from 500 μm to a millimeter would resemble a macro-structured surface rather than a three dimensionally interconnecting porous surface and theoretically would lead to loss of interface shear strength (Jasty *et al.*, 2007). It has also been suggested that the degree of interconnectivity is more important for new bone formation than the pore size itself (Kuhne *et al.*, 1994; Lu *et al.*, 1999).

The porous structure of the alloys is crucial for the growth of bone tissue and thus for improving the fixation and remodeling between the implant and the human tissue (Zhang *et al.*, 2007). However, Ayers *et al.* (Ayers *et al.*, 1999) addressed that there is no apparent correlation between pore size and bone ingrowth during the cartilaginous period of bone growth in the NiTi implant. This fact is attributed to the use of thin implants with the same thickness order as the pore size.

In addition to size, it appears that the shape of the pores will affect the extent of cell ingrowth. Goodman *et al.* (Goodman *et al.*, 1993) have reported the increase of bone ingrowth with square-shaped pores as compared with round-shaped pores. Pores with more ragged and rough surfaces also offer larger surface area for bone ingrowth (Li *et al.*, 2004a). However, depending on the various function and location of the bones in the human body, the same pore shape may not be ideal for all potential uses (Oh *et al.*, 2006).

It has been reported that the rate of bone growth into the pores can also be influenced by other factors. Bobyne *et al.* (Bobyne *et al.*, 1980) have demonstrated that ingrowth rate of bone is higher in parts placed in cancellous than in cortical bone. According to Clemow *et al.* (Clemow *et al.*, 2004), the percentage of bone growing into the surface was inversely proportional to the square root of the pore size.

2.1.4 Mechanical properties of porous metal scaffolds

One of the most important properties of porous metal scaffolds in orthopedics is their mechanical properties. Porous metals should have sufficient strength to resist stresses and physiological loadings that are imposed on them while maintaining their original size and shape. The scaffold should provide sufficient mechanical strength to support itself until the new bone tissue is completely formed into the pores.

As previously mentioned, the elastic modulus of dense metallic implants is much higher than that of natural bone. For the three most commonly used metallic orthopedic materials, the elastic modulus ranges from 55-110 GPa for Ti alloys to 205 GPa for stainless steel and 230 GPa for Co-Cr-Mo type alloys, as shown in Figure 2. However, the elastic moduli of human compact and cancellous bones are 17-20 GPa and less than 4 GPa, respectively (Gibson & Ashby, 1997; Niinomi *et al.*, 2004). Therefore, the adaptation of the elastic modulus or stiffness is one of the crucial tasks in the development of a suitable bone substitute material.

Although increased porosity and pore size facilitate bone ingrowth, it deteriorates the structural integrity of the scaffold, leading to a very low mechanical strength. The compromise in mechanical properties of the scaffold with increasing porosity sets an upper limit on the porosity and pore size (Dewidar & Lim, 2008). Thus, a trade-off must be maintained between the biomechanical properties and porosity of the material needed for

orthopedic surgery (Ryan et al., 2006; Gutierrez et al., 2008). The mechanical properties of a porous structure can be determined by various methods including compression, tensile, bending, fatigue, impact, and torsion tests. Since the compressive mechanical properties are most important for the implant applications, the present chapter summarizes only the compressive properties of porous metal materials.

Figure 5 shows a schematic compressive stress-strain curve for porous metal scaffolds with high porosity. In principle, the compressive behavior of a porous sample is characterized by three different regions. Firstly, there is a linear-elastic region which is manifested by an initial increase in stress. This initial high slope is associated with the elastic modulus (stiffness) of the porous samples. Subsequently, due to the collapse of the pores, the flow stress no longer increases with strain and there appears a wide stress plateau known as plateau or collapse region.

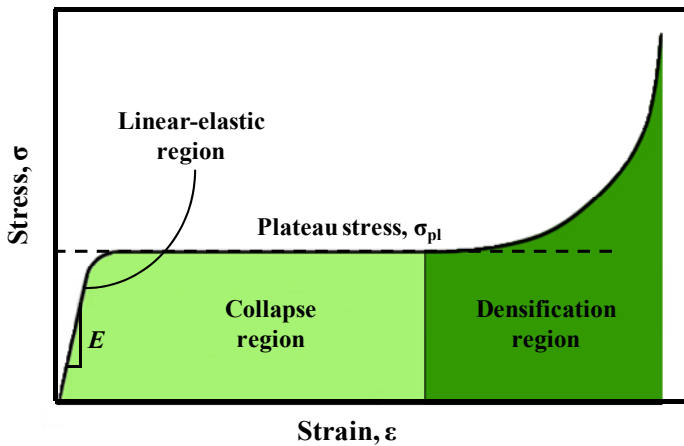


Fig. 5. A schematic illustration of compression curve of porous metal scaffolds (Nouri, 2008).

The smoothness of the plateau is highly dependent on the degree of porosity as well as the deformation behavior of the pore walls under compression. The brittle fracture of pore walls would lead to fluctuations in this region. Following the plateau region, the stress-strain curve gradually changes into a densification region where the pore walls touch each other, accompanied by a steep increase in stress (Gibson & Ashby, 1997; Banhart & Baumeister, 1998a).

2.2 Fabrication of porous titanium scaffolds through powder metallurgy

In view of the manufacturing process, Ti alloys can be classified into two groups of casting and powder metallurgy (P/M). At present, however, the fabrication of Ti-based implants through the casting method is limited to a costly, multi-step process of vacuum arc melting, hot rolling, scale removal (resulting in wasting the material), vacuum annealing, machining, and surface treatment. The casting limitations in manufacturing Ti alloys mostly arise from the high melting temperature of Ti and its affinity for oxygen (Gasser, 2001; Nyberg et al., 2005b). Moreover, as a raw material, Ti is relatively expensive compared to stainless steel

and Co-Cr alloys. The aforementioned difficulties drive the designers to search for more cost effective manufacturing methods with minimal waste production (Gasser, 2001).

The P/M process is an established method to produce Ti alloys for biomedical applications. On one hand, it reduces the cost and complexity of processing, and on the other hand, it improves the biological activity of the implant surface without compromising its structural integrity, *i.e.* its strength, fatigue resistance, and biocompatibility (Nyberg et al., 2005b). Furthermore, the P/M process is an established method for manufacturing dimensionally precise pieces finished without the need of machining work (Justino et al., 2006), which is more pronounced for Ti and its alloys due to their difficulties in machining (Kutty et al., 2001).

Powder metallurgy products are synthesized by either blending of elemental metals, or pre-alloying process. In the process of blending elemental metals, the proper proportions of elements are thoroughly mixed to obtain the alloy composition; whilst in the pre-alloying process, a homogeneous casting ingot is made into a fine alloyed powder via melting and gas atomization (Froes et al., 1980; Freese et al., 2001). Cost effectiveness of the former method offers strong potential in commercial products (Fujita et al., 1996). The metal powder from each process is cold pressed into the desired final shape and is hot sintered in vacuum. A post-sintering hot isostatic pressing (HIP) may be employed to further densify the powder-fabricated parts. Finished parts are usually annealed or heat treated, depending on the specific requirements (Freese et al., 2001). However, the high affinity of Ti and its alloys for interstitial elements like oxygen and nitrogen requires a non-oxidizing sintering environment in a high vacuum furnace as well as controlled processing media. This is due to the fact that the particle contamination hinders the particle bonding and, thus, degrades the ductility of Ti particles (Froes et al., 1980; Ryan et al., 2006; Nouri et al., 2008b).

Various processes are available for manufacturing porous metal scaffolds including casting, powder metallurgy, metallic deposition and sputter deposition (Davis & Zhen, 1983; Banhart & Baumeister, 1998b). However, to date, the choice has been between the cost and quality (Yu et al., 1998). Conventional processing of molten metal to fabricate porous metal scaffolds is suffering from limited part geometries, contamination, and limited control over the size, shape and distribution of porosities (Krishna et al., 2008). In particular, the casting method is unsuitable for manufacturing of porous Ti based scaffolds, due to the high melting temperature and the associated reactivity of Ti with oxygen and refractory materials during the melting process (Ryan et al., 2006).

The P/M method for fabricating porous metals, on the other hand, offers low cost and direct net-shaped parts with a wide range of alloys and a relatively homogeneous pore structure (Wen et al., 2001; Wen et al., 2002a; Santos et al., 2005). In addition, this method allows further control over the degree of porosity and pore size. However, depending on the method and availability of powders to be used, the P/M process could sometimes be less economic than other methods (Gasser, 2001). This is mostly pronounced when hot isostatic pressing (HIP) is involved in Ti alloy parts using pre-alloyed powder (Liu et al., 2006).

The first application of P/M technology in fabrication of porous metals for orthopedics was investigated by Hirschhorn and Reynolds, on cobalt based alloys (Hirschhorn & Reynolds, 1969). The work performed by Weber and White (Weber & White, 1972) in 1972 is also considered a pioneering study in the application of porous metals in osseointegration.

In the present chapter, due to the importance of open-cell porous implants in orthopedic surgery, the fabrication processes associated with closed-cell porous metal scaffolds are

ruled out. Based on this consideration, the P/M methods of fabricating open-cell porous materials are highlighted as follows:

1. Sintering of partially compacted or loose powder (Hirschhorn et al., 1971; Upadhyaya, 1997),
2. Space holder method (Bram et al., 2000; Wen et al., 2002a; Nouri et al., 2007a),
3. Replication (Li et al., 2002; Bansiddhi & Dunand, 2007),
4. Combustion synthesis (Li et al., 2000; Whitney et al., 2008),
5. Microwave sintering (Kutty et al., 2001).

The choice of fabrication method is usually driven by the powder characteristics, the required type of porosity and the overall cost (Eisenmann, 1998). Moreover, in order to fabricate uniform and repeatable porous structures, the sintering conditions (i.e. temperature, time and atmosphere) should be controlled precisely. More information regarding other aforementioned processes has been described in a previous study by Ryan *et al.* (Ryan et al., 2006).

2.2.1 Space holder method

A variety of methods for producing porous Ti scaffolds and other metals have been developed and commercialized. However, there are still some limitations in those methods. For instance, sintering of loose powder allows a high level of porosity to be reached, but the strength and fatigue properties of parts are lowered. Mechanical characteristics can be improved by compaction of the powder before sintering, but at the same time compaction often causes an undesirable decrease in porosity (Laptev et al., 2004). Major challenges remain in the ability to control pore morphology, pore size, porosity, product purity, and most importantly, production cost. Therefore, appropriate methods which can satisfy these requirements are desirable.

One of the most promising methods for manufacturing open porous Ti scaffolds is the P/M technique using removable space holder materials. This process can provide open porosities, which is essential for the implant bone fixation by growing the bone tissue into the pores. This method is a cost effective process, capable of adjusting the pore size distribution, pore shape, and the level of porosity by adjustment of mixing ratio of space holder and metal powder, as well as the size of space particles into a very narrow pore size distribution (Wen et al., 2001; Wen et al., 2002a; Wen et al., 2002b; Kotan & Bor, 2007).

The weight ratio of metal powder to the space holder is dependent on the predefined porosity of the final sample. The metal powders and space holder material are mixed and compacted into a green form. The compaction lends itself to better green strength to the metal powder upon removal of the space holder material during sintering process. The compaction can be uniaxial or isostatic. During the heat treatment at relatively low temperatures, the space holder is removed by decomposition, leaving the occupied spaces to become pores. Figure 5 schematically represents the space holder removal during heat treatment process. It is worth noting that fabrication of porous parts using the space holder method requires metal particles considerably smaller than the space holder particles, as seen in Figure 5 (Nouri, 2008).

After removal of the space holder the green samples are sintered at temperatures of 1100-1400 °C. The shapes and sizes of the pores are predominantly controlled by the initial shapes

and sizes of the space-holder particle. Thus, high porosity samples with spherical and angular pores in the range of 0.1-2.5 mm can be obtained (Rausch & Banhart, 2002).

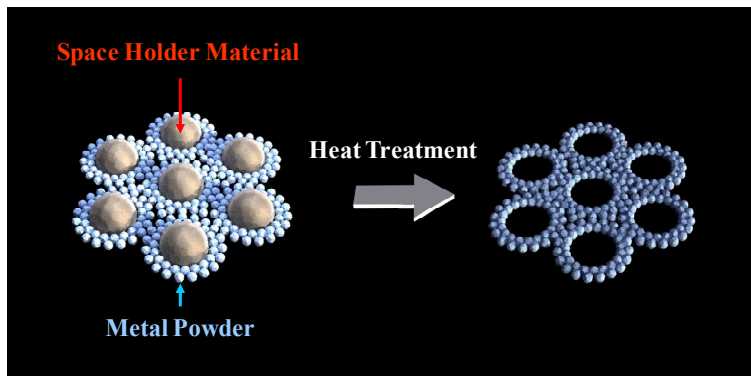


Fig. 5. Schematic illustration of the space holder method, showing a mixture consisting of metal matrix with embedded space holder material and the final metal porous structure after heat treatment (Nouri, 2008).

Several studies have already been reported about using the space holder method for manufacturing porous metallic scaffolds, in particular Ti-based materials. Esen and Bor (Esen & Bor, 2007) used magnesium (Mg) as a space holder, which was removed by slowly heating to 1200 °C and keeping for 1 h under high purity argon gas. In this experiment, Ti scaffolds with a porosity range of 45-70% and an average pore size of around 525 μm were manufactured. The yield strength and elastic moduli values of the resultant scaffolds were varying in the range 15-116 MPa and 0.42-8.80 GPa, respectively. The advantage of using Mg as space holder is its low boiling point (1107 °C) and complete immiscibility with Ti (Wheeler et al., 1983).

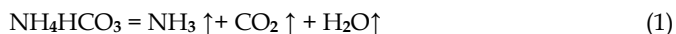
In two different experiments, Bansiddhi and Dunand distinctively used the ionic compounds of NaF (Bansiddhi & Dunand, 2007) and NaCl (Bansiddhi & Dunand, 2008) as space holder material in the mixture with shape memory NiTi powder. NiTi scaffolds consisting of 35-40% open pores with shape memory properties were fabricated by isostatic pressing at 950 and 1065 °C. The NaF and NaCl phases were then removed by water dissolution. The samples fabricated with NaCl as a space holder showed a wider range of pore size between 70 to 400 μm , compared to 240 μm for the samples with NaF. The metastable austenitic scaffold showed average stiffness of 6-12 GPa and 4-25 GPa for the porous samples made from NaF and NaCl as space holders, respectively. However, using NaCl is preferred over the NaF due to its lower cost, ease of dissolution in water and lower toxicity.

Polymer granules were used as a space holder at Fraunhofer IFAM, Bremen, Germany for synthesizing iron-based scaffolds. The polymer granules were decomposed at temperatures around 130 °C, followed by sintering in vacuum at temperatures of 1100-1250 °C. As a result, porous scaffolds with 55-80% porosity with a tensile strength range of 1.5-30.0 MPa and elastic modulus of 0.3-16.0 GPa were produced. Depending on the particle size of the granules, the resultant scaffolds exhibited average pore diameters in the range of 200-300 μm (Rausch & Banhart, 2002).

Although most of the aforementioned space holder materials have their individual merits, they also have their own limitations. The application of conventional, high-melting, organic space holders is limited by the strong reaction of Ti, stainless steel, or Ni-based alloys with the cracking products of these compounds in a temperature range of 350-600 °C. In this case, high concentrations of impurities remain in the samples. Similar problems occur if alkali salts or low-melting metals such as Mg, Sn, or Pb are used (Bram *et al.*, 2000; Buchkremer *et al.*, 2001). For instance, in the complete removal of NaCl, any residual NaCl can lead to contamination or corrosion of the base metal (Bakan, 2006). Therefore, it is important to select an appropriate space holder material which can be completely removed at low temperatures (< 200 °C) to keep the level of impurities low.

Carbamide ((NH₂)₂CO, also called urea) and ammonium hydrogen carbonate (NH₄HCO₃, also known as ammonium bicarbonate) were successfully used to produce porous samples from Ti, stainless steel (316L), and Ni-based superalloys with porosities between 60 and 80%. Depending on the shape and size distribution of the space holder, spherical and angular pores in the range of 0.1-2.5 mm were obtained. Wen *et al.* (Wen *et al.*, 2001; Wen *et al.*, 2002b; Wen *et al.*, 2006; Wen *et al.*, 2007a) and Bram *et al.* (Bram *et al.*, 2006a; Bram *et al.*, 2006b) have successfully used carbamide and ammonium hydrogen carbonate as space holder for the fabrication of porous Ti scaffolds. Successful results of using these space holders in fabricating porous materials have also been reported by other authors (Imwinkelried, 2007; Li *et al.*, 2008).

Both carbamide and ammonium hydrogen carbonate can be burnt out and then removed at temperatures below 200 °C with minimal contamination of the Ti powders. In the case of ammonium hydrogen carbonate, it can be decomposed to ammonia, carbon dioxide and water by the following reaction:



The removal process can be carried out in the air. In this respect, less exposure time of green sample during annealing is preferred (approximately 170 °C for 3 h). Low annealing temperature and longer exposure time has also been reported (80 °C for 14 h) (Bram *et al.*, 2006a). A general difficulty of this method is the removal of large quantities of organic or inorganic space holder from the sample. After heat treatment at low temperature, the porous metal scaffold is prone to collapse before the formation of strong bonding between the metal particles (Andersen & Stephani, 2002; Zhao *et al.*, 2005). Therefore, the sample after the removal of space holder must be handled with care. To achieve a sufficient stability of the compacts after removal of the space holder material, ductile metal powders with an irregular particle shape are preferred. The interlocking of adjacent powder particles enables the formation of a stable network without the need of an additional organic binder. Furthermore, the excessive size of the space holder material or the loose packing of the powder mixture may lead to a loss in interconnectivity between the powder particles, and thereby the loss of strength of the material.

Upon the removal of the space holder, the pore-space structure in the sintered material contains two types of pores: macro-pores, determined by the number and size of the space holder materials, and micro-pores, formed by particles of the metal powder or by incomplete sintering. The distribution of micro- and macro-pores in a porous Ti-16Sn-4Nb (wt.%) scaffold is depicted in Figure 6 (Nouri, 2008).

Wen *et al.* (Wen et al., 2001) synthesized an open porous Ti scaffold with a pore size distribution in the range of 200-500 μm . For the Ti scaffold with 78% porosity, the compressive strength and stiffness were 35 MPa and 5.3 GPa, respectively, showing excellent characteristics tailored for bone replacements. A wide range of strength and stiffness was reported in the Ti scaffolds with 35-80% porosity using ammonium hydrogen carbonate, suggesting that they have the adequate strength to meet the practical requirements for use as cortical and cancellous bone (Wen et al., 2002b). In another study by Niu *et al.* (Niu et al., 2009) porous Ti scaffolds with a similar pore size of 200-500 μm and porosity range of 55-75% were fabricated using carbamide. Subsequently, a plateau stress and Young's modulus were in the range of 10-35 MPa and 3.0-6.4 GPa, respectively. In an experiment conducted by Bram *et al.* (Bram et al., 2000), a plateau stress of approximately 10 and 100 MPa was reported for Ti scaffolds with porosities of 77% and 60%, respectively. Later on, the same authors produced 60% porous Ti scaffolds using different sizes of ammonium hydrogen carbonate. The result showed a stiffness of 3 GPa which is distinctively lower than the theoretical value of 18 GPa and almost independent of the size of the macropores (Bram et al., 2006a). The lower mechanical properties of the scaffold compared to the theoretical values can be attributed to the residual microporosity in the pore walls, as well as the irregular pore shape and the surface roughness of the pore walls.

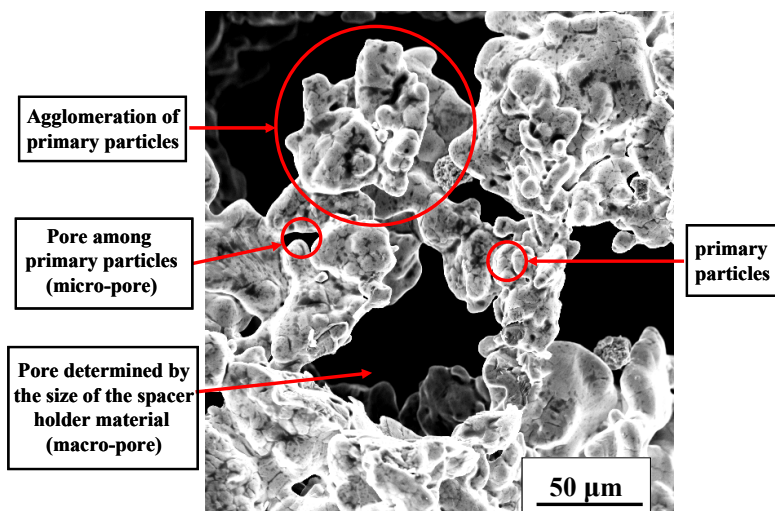


Fig. 6. SEM micrograph showing macro-pores and micro-pores in the Ti-16Sn-4Nb (wt.%) scaffold with 76% porosity (Nouri, 2008).

However, it has been reported that the mechanical properties of the porous structure can be affected by the shape of the space holder material. In an experiment performed by Jiang *et al.* (Jiang et al., 2005), open-cell Al scaffolds were synthesized using spherical- and strip-shaped carbamide particles. The scaffolds with spherical-shaped pores revealed higher compressive strength than those of the strip-shaped pores. In another experiment performed by Imwinkelried (Imwinkelried, 2007), it was found that the nonspherical space holder

particles are preferentially arranged along their elongated sides during compaction. The scaffolds obtained were anisotropic in their mechanical properties, as they were stronger perpendicular to the compaction direction, and weaker along the compaction axis. It was also found that the number of pore walls perpendicular to the compaction direction is consequently larger than those along the compaction direction, thus explaining the higher stiffness and strength.

Zhang *et al.* (Zhang *et al.*, 2007) have recently developed a method of producing gradient porosities using the space holder technique. The addition of 0%, 10%, 20% and 30% ammonium hydrogen carbonate in four layers led to an increase in porosity from 25.5% to 61.3%. For the sample with radial gradient porosities, the outside layer (about 2.5 mm thick) had a much higher porosity (60.9%) and larger pore size (433 μm) compared with the inner part which displayed a porosity of 19.5% and pore size of 84 μm .

3. Chemical Surface Modification of Porous Titanium Scaffolds

The biological performance of metallic orthopedic implants is significantly influenced by its surface properties. The surface of implant controls new bone tissue formation and long term bone-implant biological fixation. The response of bone to implants is attributable to the wide range of factors including anatomical location, the type of bone, surgical procedure, the mechanical load applied on the implant-bone system, gender and age, and, in particular, surface characteristics of the material (Williams, 1987). For this reason, extensive investigations have been attempted aiming at modifying the implant surface composition and morphology so as to optimize implant-to-bone contact and improve integration.

As previously discussed, orthopedic Ti alloys are classified as biocompatible materials; however, being bioinert materials, they do not possess the required bioactivity to bond to bone directly, resulting in a longer recovery time for bone regeneration (Anselme, 2000). Although a porous implant is capable of providing a primary stability between implant and living bone structures, when implanted into the human body, Ti alloys are generally encapsulated by soft-fibrous connective tissue. A fibrous layer intervenes between the implant and bone which reduces the stability of the implant and contribute to the loosening of the implant (Plenk, 1998; Cannas *et al.*, 2000). This phenomenon is illustrated in Figure 7 (Nouri, 2008). Apart from the biocompatibility of biomaterials, the thickness of fibrous connective tissue can also be influenced by other factors. Brunski (Brunski, 1991) has reported that the interfacial bone reaction may be affected by the anatomical location of the implant, the method of implantation, and the biomechanical performance of the implant under the load. Therefore, it is desirable to introduce a method to provoke active bone growth onto the surfaces throughout the porous structure of a Ti scaffold and therefore, maintain a stable biological fixation.

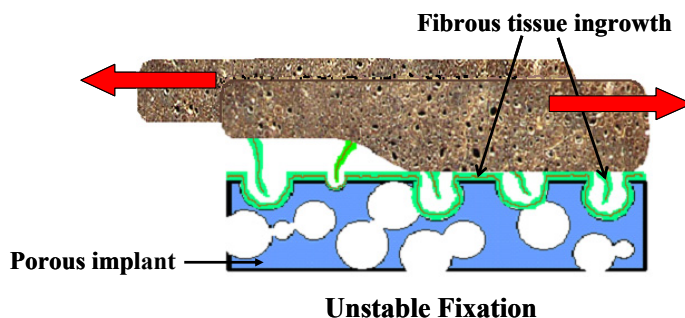


Fig. 7. The intervention of fibrous tissue with porous metallic scaffold leading to the loosening of the implant, known as unstable fixation (Nouri, 2008).

Hydroxyapatite (HA) coating on the surface of Ti implants is an effective method to enhance bioactive properties. Synthetic HA, $\text{Ca}_{10}(\text{PO}_4)_6(\text{OH})_2$, is regarded as a bioactive and biocompatible material and can directly bond to bone without the occurrence of an encapsulation with fibrous tissue. Apatite is a main component of bone crystal, and also preferentially adsorbs proteins that serve as growth factors (Hench, 1991). Despite the excellent bioactivity of hydroxyapatite, its application has been limited in clinics due to its intrinsic brittleness and high modulus of elasticity.

The bioactivity of Ti implants can be improved using various surface modification technologies. These methods can be categorized into three classes: mechanical, physical and chemical. In mechanical methods, a rough or smooth surface is formed by machining (Lausmaa et al., 1990), grinding (Hignett et al., 1987), or blasting (Wennerberg et al., 1996). In the physical method, the formation of films or coating on Ti and its alloys are mostly attributed to the thermal, kinetic, and electrical energy. Thermal spraying is one of the most demanding processes of coating in this method, in which the coating materials are thermally melted into liquid droplets and coated to the substrate at a high speed (Liu et al., 2004). The surface modification of Ti implants through mechanical and physical methods lies outside the scope of this chapter and will not be discussed further.

Currently, chemical methods are attracting more attention for the lower cost, easier control and stronger adhesion between bones and implant surfaces compared to mechanical and physical methods. This method is aimed to modify the surface of metal implant materials without significantly altering the surface morphology. The chemical reactions are predominantly occurring at the interface between the metal and chemical solution, providing unique properties required in the biological environments. The most common chemical treatments are acid, hydrogen peroxide (H_2O_2), alkali treatments, sol-gel and anodic oxidation (i.e. hydrothermal treatment). In addition, the chemical method helps to achieve better and thinner hydroxyapatite coating which possesses high bonding strength and sufficient bioactivity (Kim et al., 1996). Table 3 presents various processes used in the surface modification of Ti and its alloys through the chemical methods.

Method	Modified layer	Objective
Chemical treatment		
Acidic treatment	< 10 nm of surface oxide layer	Remove oxide scales and contamination
Alkaline treatment	~ 1 μm of sodium titanate gel	Improve biocompatibility, bioactivity or bone conductivity
Hydrogen peroxide treatment	~ 5 nm of dense inner oxide and porous outer layer	Improving biocompatibility, bioactivity or bone conductivity
Sol-gel	~ 10 μm of thin film, such as calcium phosphate, TiO_2 and silica	Improve biocompatibility, bioactivity or bone conductivity
Anodic oxidation	~ 10 nm to 40 μm of TiO_2 layer, adsorption of electrolyte anions	Produce specific surface topographies, improved corrosion resistance; improve biocompatibility, bioactivity or bone conductivity

Table 3. Various chemical methods used for surface modification of Ti and its alloys (Liu et al., 2004).

Sol-gel approach, for instance, possesses many benefits, such as fine grain structure and homogeneous substrate coverage, low cost and technical simplification, and effectiveness for the coating of implants with complex shape and porous scaffold (Wen et al., 2007b; Li et al., 2009a; Xiong et al., 2009a). However, higher bonding strength of hydroxyapatite coating on the metal surface is produced when hydrothermal treatment is used as compared to sol-gel method (Liu et al., 2005). The hydrothermal treatment usually provides materials with a high degree of crystallinity and with a calcium/phosphate ratio close to that of stoichiometric hydroxyapatite (1.67). The hydroxyapatite particles in the coating layer exhibits a polygonal shape with size in the range nanometer to micrometer (Tang et al., 2005; Xiong et al., 2009b).

Acid treatment is usually used to remove oxide scales and contamination, in order to obtain clean and uniform surface finishes. Only several acids, hydrofluoric acid (HF), nitric acid (HNO_3), hydrochloric acid (HCl), and sulfuric acid (H_2SO_4) possess the capability to react with the oxide on Ti surface whilst providing very low chemical reactivity on the surface. However, the degree of acidic reaction on the surface of Ti and its alloys is dependent on the acid concentration, temperature, and processing time, which is usually kept in the range of 1-60 min (Lausmaa, 2001). The strongly etched parts may predominantly affect the extent of material removed from the surface, and thus change the surface topography. For instance, Ti alloys containing both α and β phases react differently in etching rates resulting in surface topography where β phase sticks out from the α phase, which is etched faster (Ask et al., 1988). In general, acidic treatments would lead to the formation of a thin oxide layer

(< 10 nm), predominantly TiO₂, on the surface of Ti alloys. Absorption of hydrogen into the Ti surface due to acid treatment can cause embrittlement of the surface layer.

Hydrogen peroxide treatment is based on the reaction of Ti surface with hydrogen peroxide, H₂O₂, producing Ti-peroxy gels. Titania gel coating can improve the bioactivity of Ti implants because titania gels can induce the formation of apatite when soaked in a simulated body fluid (SBF). This process may result in roughening of the surface on the submicron scale and a considerable growth in thickness of oxide layer. However, a shorter processing time gives rise to a thinner gel layer with higher porosity in submicron size. The oxide layer consists of mainly TiO₂, as well as hydroxyl groups (Pan et al., 1998; Liu et al., 2004).

The detailed process of the aforementioned chemical treatments has been described in the literature (Tengvall et al., 1989; Wen et al., 1997; Pan et al., 1998; Sittig et al., 1999; Liu et al., 2004; Yang et al., 2004). However, the focus of the present chapter is on alkaline method for surface modification of the porous Ti scaffolds.

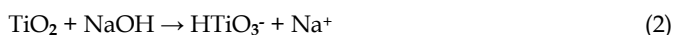
3.1 Alkali treatment

Alkali treatment provides a novel and simple technique for modification of Ti surfaces. This method was first introduced by Kim and Kokubo (Kim et al., 1996; Kokubo et al., 1996) to enhance the bioactivity of Ti and its alloys. They found, after this simple chemical treatment, that the treated surface of Ti and its alloys, such as pure Ti, Ti-6Al-4V, Ti-6Al-2Nb-Ta and Ti-15Mo-5Zr-3Al, form a thin sodium titanate layer on their surfaces. Thus, treated materials formed a dense and uniform bonelike apatite layer on their surfaces after soaking in SBF. SBF is an electrolyte solution which reproduces the inorganic part of human blood plasma. Therefore, it can be assumed that the structure of coatings precipitated from SBF will be close to that biological apatite present in human bone (Müller & Müller, 2008). Using SBF for the formation of apatite on the surface of Ti offers a promising alternative to plasma spraying and other coating methods.

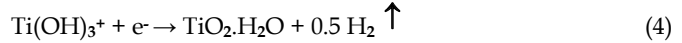
Treatment of Ti in 5-10 M NaOH at 60 °C for 24 h has been shown to produce a surface layer consisting of a sodium titanate gel (Lausmaa, 2001). The surface layers are of the order of 1 μm thick, with an irregular topography and a high degree of open porosity on the submicron scale. Subsequent heat treatments can be used for modifying the composition and structure of the surface layers.

The surface structural change of pure Ti with the alkali and heat treatments, and the mechanism of apatite formation on the treated surface in SBF have been reported in detail by Kokubo *et al.* (Kokubo et al., 2003). The mechanism of apatite formation on the surface of the porous Ti scaffold after alkali- and heat treatment process and during soaking in a SBF solution is schematically illustrated in Figure 8 (Kokubo et al., 2003; Nouri, 2008). This process is based on the induction of hydroxyl groups on the Ti surface that involves the heterogeneous nucleation and the growth of bone-like apatite layer on the surface of the porous material at physiological temperatures and pH conditions.

The structural changes during alkali treatment are described as follows. The first step is the partial dissolution of TiO₂ layer in an alkaline solution by hydroxyl groups.



The reaction is assumed to continue with hydration of Ti (Kim et al., 1996; Gil et al., 2002; Liu et al., 2004):



By proceeding the alkali treatment, more hydroxyl reacts with the hydrated TiO_2 , leading to negatively charged hydrates on the surface of the sample as follows:

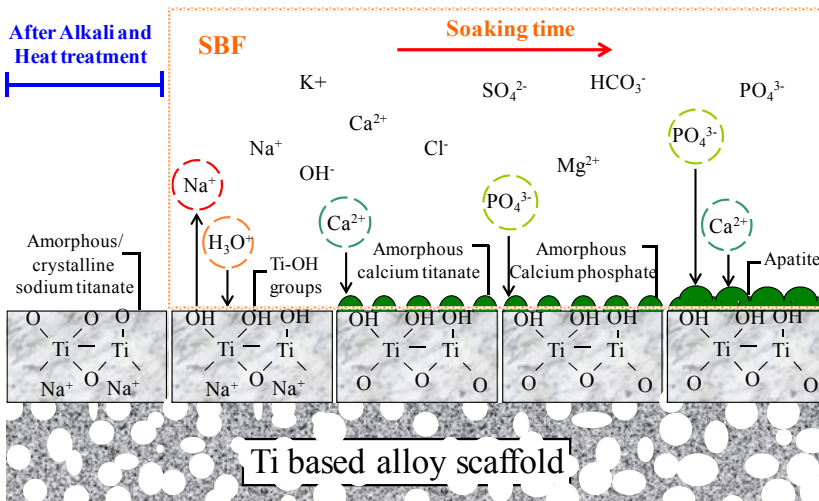
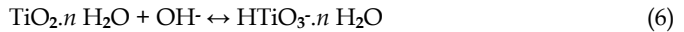


Fig. 8. A schematic illustration of the apatite formation on the surface of alkali and heat treated porous Ti based alloy scaffold soaking in SBF (Kokubo et al., 2003; Nouri, 2008).

These negatively charged species are partially dissolved into the alkaline solution to form a sodium titanate hydrogel layer. This gel layer is, however, unstable and needs to be dehydrated and densified using heat treatment to convert to a more mechanically stable layer. According to Kim *et al.* (Kim et al., 1997a), heat treatment around 600 °C results in a mechanically strong amorphous sodium titanate layer containing a small amount of crystalline sodium titanate and rutile; therefore, it induces a moderately short time for apatite nucleation. Kokubo and Takadama (Kokubo & Takadama, 2006) have shown that if a sodium titanate layer could be formed on the surface of Ti and its alloys after alkali- and heat treatment process, the following soaking in SBF can induce an apatite on the surface. As a result, the formation of apatite can provide a strong bond between the coated surface and living bone.

During the SBF soaking, sodium ions (Na^+) releases from the sample via exchange with H_3O^+ ions, resulting in the formation of a Ti-OH layer. The rate of the Na^+ ion release from the sample remarkably decreases when the surface changes from the gel to amorphous phase and then crystalline phases. The Ti-OH layer is negatively charged and can selectively combine with the positively charged Ca^{2+} through an electrostatic force and forms calcium titanate. Consequently, the positively charged surface combines with negatively charged phosphate ions (PO_4^{3-}) to form amorphous calcium phosphate. Upon the formation of the apatite nuclei, they spontaneously grow on the surface by consuming the calcium and phosphate ions from the surrounding SBF solution (Kim et al., 1996; Kim et al., 1997a; Gil et al., 2002; Liu et al., 2004). The formation of HA in SBF is according to the following equilibrium:



Apart from the hydroxide groups, the presence of titanium oxide also aids the formation of apatite on the Ti surface. Amongst the three forms of TiO_2 , known as anatase, rutile and brookite, anatase is the lower temperature phase and possesses higher activities than rutile of higher temperature phase. The reason is that anatase can provide a proper atomic arrangement in its crystal structure that suits the formation of apatite. However, the activities can be affected by other factors such as the crystallinity, impurities, lattice defect, and reaction conditions (Yoshida & Watanabe, 2005; Narayanan et al., 2008).

Kim *et al.* (Kim et al., 1997b; Kim et al., 1999) compared the bonding strength of bonelike apatite layer to Ti metal substrates pre-treated by alkali- and heat treatment at different temperatures from 500 to 800 °C. The results revealed that the heat treatment at 500 and 600 °C has the highest bonding strength. The rate of apatite formation on Ti substrate, however, decreases with increasing the temperature, especially at 800 °C. This is attributed to the lower release rate of Na^+ ion from the crystallized sodium titanate at 800 °C. Under tensile stress, the substrates heat treated at 600 °C showed higher bonding strength of the apatite to the substrates than those of heat treated at 800 °C. This is because the former introduced a smooth and graded interface structure between the apatite and the substrates while the latter had the graded interface structure disturbed by a thick Ti oxide.

The alloy composition also appeared to have an important effect on the apatite formation after alkali- and heat-treatment and soaking in SBF. Lee *et al.* (Lee et al., 2002; Lee et al., 2003) have reported better bioactivity for Ti-In-Nb-Ta alloy compared to that of Ti-6Al-4V ELI alloy in vitro. After surface modification by alkali heat treatment, porous network layers of sodium titanate ($\text{Na}_2\text{Ti}_5\text{O}_{11}$ or $\text{Na}_2\text{Ti}_6\text{O}_{13}$) were formed on both alloys surfaces. However, the finer and thinner porous layers of the former exhibited more physical stability and stronger bone-bonding strength than the coarse and thick layer of the latter.

The deposition coatings from aqueous solutions can be accelerated by several methods. Wang (Wang et al., 2003) and Yang (Yang et al., 2004) and their co-workers have demonstrated the electrodeposition of calcium phosphate by applying a current in a Ti cathode and a platinum. This method provides a perfect control over the thickness of the coating layer within a short time. Others have multiplied the concentration of calcium and phosphate ions in SBF to form a thin layer on the Ti surface. Such a procedure led to a considerable enhancement of coating rate in a very short time (2-6 h) (Habibovic et al., 2002; Tas & Bhaduri, 2004). The surface characteristics of implant material directly or indirectly

influence the way bone cells act and bone apatite nucleates. For instance, the cell response to the surface roughness of Ti and some of Ti alloys has been extensively investigated both *in vitro* and *in vivo* (Carinci et al., 2003; Li et al., 2004b; Chen et al., 2008) and there is a commonly held belief that the surface roughness of the metal substrate plays an important role in this respect. For instance, the optimum surface roughness range of 0.15–0.35 μm exhibited the improved adhesion and proliferation of human SaOS₂ osteoblast-like cells on the surface of the solid Ti₆Ta₄Sn alloy (Li et al., 2009b). In another study by Wang *et al.* (Wang et al., 2008; Wang et al., 2009) the better apatite induce ability was obtained for the Ti surface with a nanofiber-like structure than nanoporous or nanoplate surface structures. In addition to alkali- and heat treatments on bulk Ti and its alloys, a few experiments have been conducted on the effect of alkali- and heat treatment on the porous structures. Nishiguchi *et al.* (Nishiguchi et al., 2001) studied the effects of the alkali- and heat treatments on the bone-bonding ability of porous Ti scaffolds with a solid core and a 0.7 mm thick porous outer layer. Good clinical results were obtained by alkali- and heat treatment of such porous Ti, showing extremely high bonding shear strength in the canine femora push-out model after implantation for 4 weeks. In another study, the apatite formation was investigated on the porous Ti, with maximal pore size of approximately 250 μm and 40% porosity (Liang et al., 2003). The samples were soaked in 0.5, 1.0, 5.0, and 10.0 M NaOH aqueous solutions at 60 °C for 24 h, respectively. The results indicated no apatite nucleation on the small pores of samples soaked in 0.5 and 1.0 M NaOH solutions, whilst the apatite coating was formed on all other samples. Recently, Xiong *et al.* (Xiong et al., 2008) have conducted the alkali- and heat treatment on a porous Ti-18Nb-4Sn (at.%) scaffold using an aqueous solution of 10 M NaOH at 50 °C. A thick layer of spherical precipitate with small cracks was formed after soaking in SBF for 7 days. Nouri *et al.* (Nouri et al., 2007b) have also investigated the apatite forming ability of porous Ti alloy scaffold by soaking the porous samples in a concentrated simulated body fluid (10×SBF) from 1 to 6 h. The results indicated the deposition of bone-like apatite globules throughout the alkali- and heat treated porous Ti alloy scaffold after soaking in the 10×SBF for 1 h. Proceeding the soaking time to 6 h, a uniform layer of bone-like apatite granules deposited on the entire surface throughout the scaffold showing considerable apatite forming ability after the thermochemical treatment and soaking in a 10×SBF solution. Figure 9 depicts the morphology evolution of the apatite coating on the surface of the porous Ti alloy scaffold after the alkali- and heat treatment and soaking in a 10×SBF for 6 h.

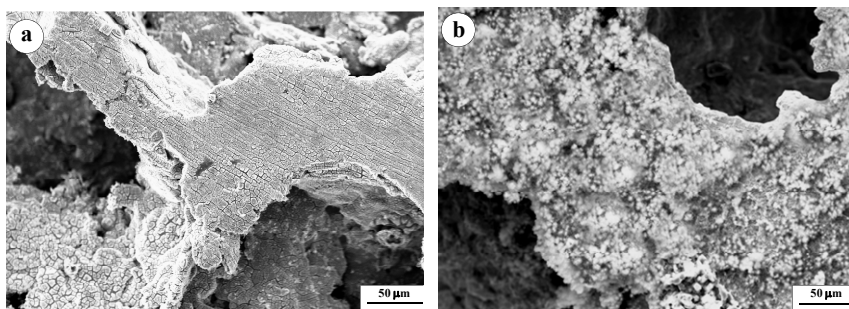


Fig. 9. SEM micrographs of the porous Ti-16Sn-4Nb (wt.%) scaffold after (a) alkali- and heat treatment and (b) soaking in the concentrated 10×SBF for 6 h (Nouri et al., 2007b).

4. Summary

This chapter presented a summary of the fabrication and characteristics of the biomimetic porous Ti scaffold for orthopedic and dental applications. In order to design and characterize an implant for orthopedic applications, a brief discussion was presented regarding the structure and mechanical properties of the natural bone. The chapter continued with the growing consensus regarding the use of Ti and its alloys for orthopedic and dental applications. Some of the issues related to porous Ti scaffolds including their physical properties, microstructure and biomedical characteristics were demonstrated and compared to their nonporous counterparts. Within the scope of the orthopedic applications, Ti alloys with biocompatible alloying elements, i.e. Zr, Nb, Ta, Sn, Mo and Si, are considered as promising candidate for bone tissue engineering.

A brief overview was also given to several potential powder metallurgical approaches for developing new advanced porous Ti alloys. In particular, the space holder method was introduced as a feasible method for fabricating biomimetic porous Ti scaffold as bone tissue replacement. This technique allows the control of pore size, pore shape and porosity in porous titanium scaffolds and the adjustment of the chemical compositions of the titanium alloys, providing excellent scaffolds for bone ingrowth. Finally, the choice of an appropriate surface technique for enhancing the bone-bonding ability of porous Ti scaffolds was discussed using the alkali- and heat treatment.

It is hoped that some basic concepts have been relayed to the reader that will provide a basis for the understanding of these biomimetic porous scaffolds in orthopedics.

5. References

- Abel, C.A. ; Edwards, K.L. & Ashby, M.F. (1994). Materials, processing and environment engineering design: the issues. *Materials and Design*, Vol. 15, 179-193
- Andersen, O. & Stephani, G. (2002). Solid-state and deposition methods, In: *Handbook of Cellular Metals, Production, Processing, Applications*, Degischer, H.P. and B. Kriszt, (Ed.), 56-70, Wiley-VCH Verlag, Weinheim
- Andreasen, G.F. & Fahl, J.L. (1987). Alloys, shape memory, In: *Encyclopedia of Medical Devices and Instrumentation*, Webster, J.G., (Ed.), 2, 15-20, Wiley, New York
- Anselme, K. (2000). Osteoblast adhesion on biomaterials. *Biomaterials*, Vol. 21, 667-681
- Ascenzi, A. & Bonucci, E. (1976). Relationship between ultrastructure and "pin test" in osteons. *Clinical Orthopaedic and Related Research*, Vol. 121, 275-294
- Ashraf Imam, M. & Fraker, A.C. (1996). Titanium alloys as implant materials, In: *Medical applications of titanium and its alloys: The material and biological issues*, Brown, S.A. and Lemons, J.E., (Ed.), 3-16, ASTM, West Conshohocken, PA
- Ask, M. ; Lausmaa, J. & Kasemo, B. (1988). Preparation and surface spectroscopic characterization of oxide films on Ti6Al4V. *Applied Surface Science*, Vol. 35, 283-301
- Ayers, R.A. ; Simske, S.J. ; Bateman, T.A. ; Petkus, A. ; Sachdeva, R.L.C. & Gyunter, V.E. (1999). Effect of nitinol implant porosity on cranial bone ingrowth and apposition after 6 weeks. *Journal of Biomedical Materials Research*, Vol. 45, 42-47
- Bakan, H.L. (2006). A novel water leaching and sintering process for manufacturing highly porous stainless steel. *Scripta Materialia*, Vol. 55, 203-206

- Banhart, J. (2002). Functional applications, In: *Handbook of cellular metals: Production, Processing, Applications*, Degischer, H.P. and Kriszt, B., (Ed.), 313-320, Wiley-VCH Verlag, Weinheim
- Banhart, J. & Baumeister, J. (1998a). Deformation characteristics of metal foams. *Journal of Materials Science*, Vol. 33, 1431-1440
- Banhart, J. & Baumeister, J. (1998b). Production methods for metallic foams. *MRS Symposium*, pp. 121-132, San Francisco
- Bansiddhi, A. & Dunand, D.C. (2007). Shape-memory NiTi foams produced by solid-state replication with NaF. *Intermetallics*, Vol. 15, 1612-1622
- Bansiddhi, A. & Dunand, D.C. (2008). Shape-memory NiTi foams produced by replication of NaCl space-holders. *Acta Biomaterialia*, Vol. 4, 1996-2007
- Baumgart, F.; Bensmann, G. & Haasters, J. (1980). Memory alloys-new material for implantation in orthopedic surgery. Part 1, In: *Current Concepts of Internal Fixation of Fractures*, Uthof, H.K., (Ed.), 122-127, Springer-Verlag, Berlin
- Boby, J.D.; Pilliar, R.M.; Cameron, H.U. & Weatherly, G.C. (1980). The optimum pore size for the fixation of porous-surfaced metal implants by the ingrowth of bone. *Clinical Orthopaedics and Related Research*, Vol. 150, 263-270
- Boyce, B.F.; Byars, J.; McWilliams, S.; Mocan, M.Z.; Elder, H.Y.; Boyle, I.T., et al. (1992). Histological and electron microprobe studies of mineralisation in aluminium-related osteomalacia. *Journal of Clinical Pathology*, Vol. 45, 502-550
- Bram, M.; Laptev, A.; Stoeber, D. & Buchkremer, H.P. (2006b). Method for producing highly porous metallic moulded bodies close to the desired final contours. US patent 7147819, Forschungszentrum Julich GmbH, Julich (DE).
- Bram, M.; Schiefer, H.; Bogdanski, D.; Köller, M.; Buchkremer, H.P. & Stöver, D. (2006a). Implant surgery: How bone bonds to PM titanium. *Metal Powder Report*, Vol. 61, 26-31
- Bram, M.; Stiller, C.; Buchkremer, H.P.; Stöver, D. & Baur, H. (2000). High-Porosity Titanium, Stainless Steel, and Superalloy Parts. *Advanced Engineering Materials*, Vol. 2, 196-199
- Breme, H.J. & Helsen, J.A. (1998b). Selection of Materials, In: *Metals as Biomaterials*, Breme, H.J. and Helsen, J.A., (Ed.), 1-35, John Wiley & Sons, Chichester
- Breme, J. & Biehl, V. (1998a). Metallic Biomaterials, In: *Handbook of Biomaterial Properties*, Black, J. and Hastings, G., (Ed.), 135-144, Chapman and Hall, London
- Brooks, C.R. (1982). *Heat treatment, structure and properties of nonferrous alloys*, American Society for Metals, Metals Park, Ohio
- Browne, M. & Gregson, P.J. (1995). Metal ion release from wear particles produced by Ti-6Al4V and Co-Cr alloy surfaces articulating against bone. *Materials Letters*, Vol. 24, 1-6
- Brunski, J.B. (1991). Influence of biomechanical factors at the bone-biomaterial interface, In: *The Bone-Biomaterial Interface*, Davies, J.E., (Ed.), 391-405, University of Toronto Press, Toronto
- Brunski, J.B. (2004). Metals, In: *Biomaterials Science: An Introduction to Materials in Medicine*, Ratner, B.D., Hoffman, A.S., Schoen, F. and Lemons, J.E., (Ed.), 137-153, Elsevier Academic Press, Amsterdam; Boston

- Buchkremer, H.P. ; Bram, M. & Newmann, P. (2001). Processing and characterization of new porous materials, In: *Recent developments in computer modeling of powder metallurgy processes*, Zavaliangos, A. and Laptev, A., (Ed.), 243-255, IOS press, Kiev, Ukraine
- Bucholtz, R.W. (2002). Nonallograft osteoconductive bone graft substitutes. *Clinical Orthopaedic and Related Research*, Vol. 395, 44-52
- Burr, D.B. & Martin, R.B. (1989). Errors in bone remodeling: toward a unified theory of metabolic bone disease. *American Journal of Anatomy*, Vol. 186, 186-216
- Cameron, H.U. ; Macnab, I. & Pilliar, R.M. (1978). A porous metal system for joint replacement surgery. *The International Journal of Artificial Organs*, Vol. 1, 104-109
- Cannas, M. ; Bosetti, M. ; Santin, M. & Mazzarelli, S. (2000). Tissue response to implants: Molecular interactions and histological correlation, In: *Biomaterials and Bioengineering Handbook*, Wise, R.L., (Ed.), 95-115, Marcel Dekker
- Carinci, F. ; Pezzetti, F. ; Volinia, S. ; Francioso, F. ; Arcelli, D. & Marchesini, J. (2003). Analysis of osteoblast-like MG63 cells' response to a rough implant surface by means of DNA microarray. *The Journal of Oral Implantology*, Vol. 29, (5), 215-220
- Castleman, L.S. & Motzkin, S.M. (1981). The biocompatibility of nitinol, In: *Biocompatibility of Clinical Implant Materials*, Williams, D.F., (Ed.), 129-154, CRC Press, Boca Raton, USA
- Chen, X.B. ; Nouri, A. ; Li, Y.C. ; Hodgson, P.D. & Wen, C.E. (2008). Effect of surface roughness of Ti, Zr, and TiZr on apatite precipitation from simulated body fluid. *Biotechnology and Bioengineering*, Vol. 101, 378-387
- Choi, K. ; Kuhn, J.L. ; Ciarelli, M.J. & Goldstein, S.A. (1990). The elastic moduli of human subchondral, trabecular, and cortical bone tissue and the size-dependency of cortical bone modulus. *Journal of Biomechanics*, Vol. 23, 1103-1113
- Clemow, A.J.T. ; Weinstein, A.M. ; Klawitter, J.J. ; Koeneman, J. & Anderson, J. (2004). Interface mechanics of porous titanium implants. *Journal of Biomedical Materials Research*, Vol. 15, 73 - 82
- Currey, J. (1998). Cortical bone, In: *Handbook of Biomaterial Properties*, Black, J. and Hastings, G., (Ed.), 3-14, Chapman and Hall, London
- Davis, G.J. & Zhen, S. (1983). Metallic foams - their production, properties and applications (Review). *Journal of Materials Science*, Vol. 18, 1899-1911
- Despois, J.F. & Mortensen, A. (2005). Permeability of open-pore microcellular materials. *Acta Materialia*, Vol. 53, 1381-1388
- Dewidar, M.M. & Lim, J.K. (2008). Properties of solid core and porous surface Ti-6Al-4V implants manufactured by powder metallurgy. *Journal of Alloys and Compounds*, Vol. 454, 442-446
- Eisenmann, M. (1998). Porous powder metallurgy technology, In: *ASM Handbook: Powder Metal Technologies and Applications*, (Ed.), 7, 1031-1042, ASM International, Materials Park, OH, USA
- Elema, H. ; de Groot, J.H. ; Nijenhuis, A.J. ; Pennings, A.J. ; Veth, R.P.H. ; Klompmaker, J., et al. (1990). Biological evaluation of porous biodegradable polymer implants in menisci. *Colloid and Polymer Science*, Vol. 268, 1082-1088
- Engh, C.A. (1983). Hip arthroplasty with a Moore prosthesis with porous coating. *Clinical Orthopaedic and Related Research*, Vol. 176, 52-66
- Esen, Z. & Bor, S. (2007). Processing of titanium foams using magnesium spacer particles. *Scripta Materialia*, Vol. 56, 341-344

- Freese, H.L. ; Volas, M.G. & Wood, J.R. (2001). Metallurgy and technological properties of titanium and its alloys, In: *Titanium in Medicine*, Brunette, D.M., Tengvall, P., Textor, M. and Thomsen, P., (Ed.), 23-51, Springer
- Froes, F.H. ; Eylon, D. ; Eichelman, G.E. & Burte, H.M. (1980). Developments in Titanium Powder Metallurgy. *Journal of Metals*, Vol. 32, 47-54
- Fujita, T. ; Ogawa, A. ; Ouchi, C. & Tajima, H. (1996). Microstructure and properties of titanium alloy produced in the newly developed blended elemental powder metallurgy process. *Materials Science and Engineering A*, Vol. 213, 148-153
- Gasser, B. (2001). Design and engineering criteria for titanium devices, In: *Titanium in Medicine*, Brunette, D.M., Tengvall, P., Textor, M. and Thomsen, P., (Ed.), 673-701, Springer
- Gibson, L.J. & Ashby, M.F. (1997). *Cellular Solids: Structure and Properties*, Cambridge University Press, UK
- Gil, F.J. ; Padrós, A. ; Manero, J.M. ; Aparicio, C. ; Nilsson, M. & Planell, J.A. (2002). Growth of bioactive surfaces on titanium and its alloys for orthopaedic and dental implants. *Materials Science and Engineering C*, Vol. 22, 53-60
- Goodman, S. ; Toksvig-Larsen, S. & Aspenberg, P. (1993). Ingrowth of bone into pores in titanium chambers implanted in rabbits: Effect of pore cross-sectional shape in the presence of dynamic shear. *Journal of Biomedical Materials Research*, Vol. 27, 247-253
- Griss, P. & Heimke, G. (1976). Record of discussion on stability of joint prostheses, In: *Biocompatibility of implant materials*, Williams, D., (Ed.), 52-68, Sector publishing, London
- Gutierrez, M. ; Lopes, M.A. ; Sooraj Hussain, N. ; Lemos, A.F. ; Ferreira, J.M.F. ; Afonso, A., et al. (2008). Bone ingrowth in macroporous bonelike for orthopaedic applications. *Acta Biomaterialia*, Vol. 4, 370-377
- Habibovic, P. ; Barrère, F. ; van Blitterswijk, C.A. ; de Groot, K. & Layrolle, P. (2002). Biomimetic hydroxyapatite coating on metal implants. *Journal of the American Ceramic Society*, Vol. 85, 517-22
- Hallab, N.J. ; Jacobs, J.J. & Katz, J.L. (2004). Application of Materials in Medicine, Biology, and Artificial Organs: Orthopedic Applications, In: *Biomaterials Science: An Introduction to Materials in Medicine*, Ratner, B.D., Hoffman, A.S., Schoen, F. and Lemons, J.E., (Ed.), 526-555, Elsevier Academic Press
- Hench, L.L. (1991). Surface reaction kinetics and adsorption of biological moieties: A mechanistic approach to tissue attachment, In: *The Bone-Biomaterial Interface*, Davies, J.E., (Ed.), 33-48, University of Toronto, Toronto
- Hignett, B. ; Andrew, T.C. ; Downing, W. ; Duwell, E.J. ; Belanger, J. & Tulinski, E.H. (1987). Surface cleaning, finishing and coating, In: *Metals Handbook, vol. 5*, Wood, W.G., (Ed.), 107-127, American Society for Metals, Metals Park, OH
- Hirschhorn, J.S. ; Mcbeath, A.A. & Dustoor, M.R. (1971). Porous Titanium Surgical Implant Materials. *Journal of Biomedical Materials Research Symposium*, Vol. 1, 49-67
- Hirschhorn, J.S. & Reynolds, J.T. (1969). Powder metallurgy fabrication of cobalt alloy surgical implant materials, In: *Research in dental and medical materials*, Korostoff, E., (Ed.), 137-150, Plenum Press, NY
- Hoffman, A.S. (2004). Classes of Materials used in medicine: Introduction, In: *Biomaterials Science: An Introduction to Materials in Medicine*, Ratner, B.D., Hoffman, A.S., Schoen, F. and Lemons, J.E., (Ed.), 67, Elsevier Academic Press

- <http://training.seer.cancer.gov/anatomy/skeletal/tissue.html>. Epidemiology and End Results (SEER) Program. from *SEER Training Modulus*, National Cancer Institute.
- Hungerford, D.S. & Kenna, R.V. (1983). Preliminary experience with a total knee prosthesis with porous coating used without cement. *Clinical Orthopaedic and Related Research*, Vol. 176, 95-107
- Imwinkelried, T. (2007). Mechanical properties of open-pore titanium foam. *Journal of Biomedical Materials Research*, Vol. 81A, 964-970,
- Ishizaki, K. ; Komarneni, S. & Nanko, M. (1998). *Porous Materials: Process technology and applications*, Kluwer Academic Publishers
- Jasty, M. ; Kienapfel, H. & Griss, P. (2007). Fixation by Ingrowth, In: *The adult hip*, Callaghan, J.J., Rosenberg, A.G. and Rubash, H.E., (Ed.), 1, 195-206, Lippincott Williams and Wilkins, Philadelphia
- Jiang, B. ; Zhao, N.Q. ; Shi, C.S. & Li, J.J. (2005). Processing of open cell aluminum foams with tailored porous morphology. *Scripta Materialia*, Vol. 53, 781-785
- Justino, J.G. ; Alves, M.K. ; Klein, A.N. & Al-Qureshi, H.A. (2006). A comparative analysis of elasto-plastic constitutive models for porous sintered materials. *Journal of Materials Processing Technology*, Vol. 179, 44-49
- Kawalec, J.S. ; Brown, S.A. ; Payer, J.H. & Merritt, K. (1995). Mixed-metal fretting corrosion of Ti6Al4V and wrought cobalt alloy. *Journal of Biomedical Materials Research*, Vol. 29, 867-873
- Keaveny, T.M. (1998). Cancellous bone, In: *Handbook of Biomaterial Properties*, Black, J. and Hastings, G., (Ed.), 15-23, Chapman and Hall, London
- Kim, H.M. ; Miyaji, F. ; Kokubo, T. & Nakamura, T. (1996). Preparation of bioactive Ti and its alloy via simple chemical surface treatment. *Journal of Biomedical Materials Research*, Vol. 32, 409-417
- Kim, H.M. ; Miyaji, F. ; Kokubo, T. & Nakamura, T. (1997a). Effect of heat treatment on apatite-forming ability of Ti metal induced by alkali treatment. *Journal of Materials Science: Materials in Medicine*, Vol. 8, 341-347
- Kim, H.M. ; Miyaji, F. ; Kokubo, T. & Nakamura, T. (1997b). Bonding strength. of bonelike apatite layer to Ti metal substrate. *Journal of Biomedical Materials Research: Applied Biomaterials*, Vol. 38, 121-127
- Kim, H.M. ; Miyaji, F. ; Kokubo, T. ; Nishiguchi, S. & Nakamura, T. (1999). Graded surface structure of bioactive titanium prepared by chemical treatment. *Journal of Biomedical Materials Research Part A*, Vol. 45, 100 - 107
- Kokubo, T. ; Kim, H.M. & Kawashita, M. (2003). Novel bioactive materials with different mechanical properties. *Biomaterials*, Vol. 24, 2161-2175
- Kokubo, T. ; Miyaji, F. & Kim, H.M. (1996). Spontaneous formation of bonelike apatite layer on chemically treated titanium metals. *Journal of American Ceramic Society*, Vol. 4, 1127-1129
- Kokubo, T. & Takadama, H. (2006). How useful is SBF in predicting in vivo bone bioactivity. *Biomaterials*, Vol. 27, 2907-2915
- Kotan, G. & Bor, A.S. (2007). Production and characterization of high porosity Ti-6Al-4V foam by space holder technique in powder metallurgy. *Turkish Journal of Engineering and Environmental Sciences*, Vol. 31, 149-156

- Kramer, K.H. (2000). Implants for surgery-A survey on metallic materials, In: *Materials for Medical Engineering, Proceedings of Euromat 99*, Stallforth, H. and Revell, P., (Ed.), 2, 9-29, Wiley-VCH, Weinheim
- Krishna, B.V. ; Xue, W. ; Bose, S. & Bandyopadhyay, A. (2008). Engineered Porous Metals for Implants. *JOM*, Vol. 60, 45-48
- Kriszt, B. ; Martin, U. & Mosler, U. (2002). Characterization of cellular and foamed metals, In: *Handbook of cellular metals*, Degischer, H.P. and Kriszt, B., (Ed.), 127-145, Wiley-VCH Verlag, Weinheim
- Kuhne, J.H. ; Bartl, R. ; Frisch, B. ; Hammer, C. ; Jansson, V. & Zimmer, M. (1994). Bone formation in coralline hydroxyapatite. Effects of pore size studied in rabbits. *Acta Orthopaedica Scandinavica*, Vol. 65, 246-252
- Kutty, M.G. ; Bhaduri, S. ; Jokisaari, J.R. & Bhaduri, S.B. (2001). Development of gradient porosities in Ti dental implant. *Ceramic Engineering and Science Proceedings*, Vol. 22, 587-592
- Laptev, A. ; Bram, M. ; Buchkremer, H.P. & Stöver, D. (2004). Study of production route for titanium parts combining very high porosity and complex shape. *Powder Metallurgy*, Vol. 47, 85-92
- Lausmaa, J. (2001). Mechanical, thermal, chemical and electrochemical surface treatment of titanium, In: *Titanium in Medicine*, Brunette, D.M., Tengvall, P., Textor, M. and Thomsen, P., (Ed.), 231-266, Springer-Verlag, Berlin
- Lausmaa, J. ; Kasemo, B. & Mattsson, H. (1990). Surface spectroscopic characterization of titanium implant materials. *Applied Surface Science*, Vol. 44, 133-146
- Lee, B.H. ; Kim, Y.D. & Lee, K.H. (2003). XPS study of bioactive graded layer. in Ti-In-Nb-Ta alloy prepared by alkali and heat treatments. *Biomaterials*, Vol. 24, 2257-2266
- Lee, B.H. ; Kim, Y.D. ; Shin, J.H. & Lee, K.H. (2002). Surface modification by alkali and heat treatments in titanium alloys. *Journal of Biomedical Materials Research*, Vol. 61, 466-473
- Lekston, Z. & Goryczka, T. (2007). Phase Transformation in Ti-Ni-Ta Shape Memory Alloy. *Solid State Phenomena*, Vol. 130, 147-150
- Lewis, G. & Shaw, K.M. (1995). Orthopaedic alloy electrochemical behavior: the case of Ti-6Al-7Nb. *Biomedical Engineering Conference, Proceedings of the 1995 Fourteenth Southern*, pp. 235-238, Shreveport, LA, USA
- Li, B.Y. ; Rong, L.J. ; Li, Y.Y. & Gjunter, V.E. (2000). A recent development in producing porous NiTi shape memory alloys. *Intermetallics*, Vol. 8, 881-4
- Li, D.S. ; Zhanga, Y.P. ; Eggeler, G. & Zhang, X.P. (2008). High porosity and high-strength porous NiTi shape memory alloys with controllable pore characteristics. *Journal of Alloys and Compounds*, Vol. 470, L1-L5
- Li, H. ; Oppenheimer, S.M. ; Stupp, S.I. ; Dunand, D.C. & Brinson, L.C. (2004a). Effects of pore morphology and bone ingrowth on mechanical properties of microporous titanium as an orthopaedic implant material. *Materials Transactions*, Vol. 45, 1124-1131
- Li, J.P. ; Li, S.H. ; de Groot, K. & Layrolle, P. (2002). Preparation and characterization of porous titanium. *Key Engineering Materials*, Vol. 218, 51-4
- Li, J.P. ; Li, S.H. ; van Blitterswijk, C.A. & de Groot, K. (2005). A novel porous Ti6Al4V: Characterization and cell attachment. *Journal of Biomedical Materials Research*, Vol. 73A, 223-233

- Li, L.H. ; Kong, Y.M. ; Kim, H.W. ; Kim, Y.W. ; Kim, H.E. & Heo, S.J. (2004b). Improved biological performance of Ti implants due to surface modification by micro-arc oxidation. *Biomaterials*, Vol. 25, 2867-2875
- Li, Y.C. ; Xiong, J.Y. ; Wong, C.S. ; Hodgson, P.D. & Wen, C.E. (2009a). Bioactivating the surfaces of titanium by sol-gel process. *Materials Science Forum*, Vol. 614, 67-71
- Li, Y.C. ; Xiong, J.Y. ; Wong, C.S. ; Hodgson, P.D. & Wen, C.E. (2009b). Ti6Ta4Sn alloy and subsequent scaffolding for bone tissue engineering. *Tissue Engineering: Part A*, Vol. 15, 1-9
- Liang, F. ; Zhou, L. & Wang, K. (2003). Apatite formation on porous titanium by alkali and heat-treatment. *Surface and Coatings Technology*, Vol. 165, 133-139
- Liu, F. ; Song, Y. ; Wang, F. ; Shimizu, T. ; Igarashi, K. & Zhao, L. (2005). Formation characterization of hydroxyapatite on titanium by microarc oxidation and hydrothermal treatment. *Journal of Bioscience and Bioengineering*, Vol. 100, 100-104
- Liu, X. ; Chu, P.K. & Ding, C. (2004). Surface modification of titanium, titanium alloys, and related materials for biomedical applications. *Materials Science and Engineering R*, Vol. 47, 49-121
- Liu, Y. ; Chen, L.F. ; Tang, H.P. ; Liu, C.T. ; Liu, B. & Huang, B.Y. (2006). Design of powder metallurgy titanium alloys and composites. *Materials Science and Engineering A*, Vol. 418, 25-35
- Lu, J.X. ; Flautre, B. ; Anselme, K. ; Hardouin, P. ; Gallur, A. ; Descamps, M., et al. (1999). Role of interconnections in porous bioceramics on bone recolonization in vitro and in vivo. *Journal of Materials Science: Materials in Medicine*, Vol. 10, 111-120
- Lütjering, G. & Williams, J.C. (2003). *Titanium*, Springer-Verlag, Berlin
- McKay, G.C. ; Macnair, R. ; MacDonald, C. & Grant, M.H. (1996). Interactions of orthopaedic metals with an immortalized rat osteoblast cell line. *Biomaterials*, Vol. 17, 1339-1344
- Miyoshi, T. ; Itoh, M. ; Mukai, T. ; Kanahashi, H. ; Kohzu, H. ; Tanabe, S., et al. (1999). Enhancement of energy absorption in a closed-cell aluminum by the modification of cellular structures. *Scripta Materialia*, Vol. 41, 1055-1060
- Mjoberg B, H.E., Mallmin H, Lindh U. (1997). Aluminum, Alzheimer's disease and bone fragility. *Acta Orthopaedica Scandinavica*, Vol. 68, 511-514
- Molchanova, E.K. (1965). *Phase Diagrams of Titanium Alloys (Translation of Atlas Diagram Sostoyaniya Titanovykh Splavov)*, Israel Program for Scientific Translations, Jerusalem
- Müller, F.A. & Müller, L. (2008). Biomimetic apatite formation, In: *Metallic Biomaterial Interfaces*, Breme, J., Kirkpatrick, C.J. and Thull, R., (Ed.), 71-81, Wiley-VCH, Weinheim
- Murray, G.A. & Semple, J.C. (1981). Transfer to tensile load from a prosthesis to bone using porous titanium. *Journal of Bone and Joint Surgery*, Vol. 63B, 138-141
- Nakajima, H. (2007). Fabrication, properties and application of porous metals with directional pores. *Progress in Materials Science*, Vol. 52, 1091-1173
- Narayanan, R. ; Seshadri, S.K. ; Kwon, T.Y. & Kim, K.H. (2008). Review: Calcium phosphate-based coatings on titanium and its alloys. *Journal of Biomedical Materials Research Part B: Applied Biomaterials*, Vol. 85B, 279-299
- Natali, A.N. & Meroi, E.A. (1989). A review of biomedical properties of bone as a material. *Journal of Biomedical Engineering*, Vol. 11, 212-219

- Niinomi, M. ; Hattori, T. & Niwa, S. (2004). Material characteristics and biocompatibility of low rigidity titanium alloys for biomedical applications, In: *Biomaterials in Orthopedics*, Yaszemski, M.J., Trantolo, D.J., Lewandrowski, K.U. et al, (Ed.), 41-62, Marcel Dekker.Inc, New York
- Nishiguchi, S. ; Kato, H. ; Neo, M. ; Oka, M. ; Kim, H.M. ; Kokubo, T., et al. (2001). Alkali and heat-treated porous titanium for orthopedic implants. *Journal of Biomedical Materials Research*, Vol. 54, 198-208
- Niu, W. ; C.G., B. ; Qiu, G.B. & Wang, Q. (2009). Processing and properties of porous titanium using space holder technique. *Materials Science and Engineering A*, Vol. 506, 148-151
- Nouri, A. (2008). Novel metal structures through powder metallurgy for biomedical applications. *Institute for Technology Research and Innovation, Deakin University*, PhD Thesis
- Nouri, A. ; Chen, X.B. ; Hodgson, P.D. & Wen, C.E. (2007a). Preparation and characterisation of new titanium based alloys for orthopaedic and dental applications. *Advanced Materials Research*, Vol. 15-17, 71-76
- Nouri, A. ; Chen, X.B. ; Hodgson, P.D. & Wen, C.E. (2007b). Preparation of bioactive porous Ti-Sn-Nb alloy for biomedical applications. *Proceeding of 5th International Conference on Porous Metals and Metallic Foams (MetFoam 2007)*, pp. 307-310, Montreal, Canada
- Nouri, A. ; Chen, X.B. ; Li, Y.C. ; Yamada, Y. ; Hodgson, P.D. & Wen, C.E. (2008a). Synthesis of Ti-Sn-Nb alloy by powder metallurgy. *Materials Science and Engineering A*, Vol. 485, 562-570
- Nouri, A. ; Li, Y.C. ; Yamada, Y. ; Hodgson, P.D. & Wen, C.E. (2008b). Effects of process control agent (PCA) on the microstructural and mechanical properties of Ti-Sn-Nb alloy prepared by mechanical alloying. *World Congress on Powder Metallurgy and Particulate Materials (PM 2008)*. Washington D.C., USA: 222-233.
- Nyberg, E. ; Miller, M. ; Simmons, K. & Scott Weil, K. (2005a). Microstructure and mechanical properties of titanium components fabricated by a new powder injection molding technique. *Materials Science and Engineering C*, Vol. 25, 336-342
- Nyberg, E. ; Miller, M. ; Simmons, K. & Scott Weil, K. (2005b). Manufacturers 'need better quality titanium PM powders'. *Metal Powder Report*, Vol. 60, 8-13
- Oh, S. ; Oh, N. ; Appleford, M. & Ong, J.L. (2006). Bioceramics for Tissue Engineering Applications - A Review. *American Journal of Biochemistry and Biotechnology*, Vol. 2, 49-56
- Okazaki, Y. ; Ito, Y. ; Kyo, K. & Tateishi, T. (1996). Corrosion resistance and corrosion fatigue strength of new titanium alloys for medical implants without V and Al. *Materials Science and Engineering A*, Vol. 213, 138-147
- Okazaki, Y. ; Rao, S. ; Tateishi, T. & Ito, Y. (1998). Cytocompatibility of various metal and development of new titanium alloys for medical implants. *Materials Science and Engineering A*, Vol. 243, 250-256
- Oliveira, M.V. ; Pereira, L.C. & Cairo, C.A.A. (2002). Porous Structure Characterization in Titanium Coating for Surgical Implants. *Materials Research*, Vol. 5, 269-273
- Pan, J. ; Liao, H. ; Leygraf, C. ; Thierry, D. & Li, J. (1998). Variation of oxide films on titanium induced by osteoblast-like cell culture and the influence of an H₂O₂ pretreatment. *Journal of Biomedical Materials Research*, Vol. 40, 244-256

- Parente, M.A. ; Geil, M. & B., M. (2006). In the future: prosthetic advances and challenges, In: *Prosthetics and patient management : a comprehensive clinical approach*, Carroll, K. and Edelstein, J., (Ed.), 215-232, SLACK Incorporated, Thorofare, NJ
- Pilliar, R.M. (1983). Powder metal-made orthopedic implants with porous surface for fixation by tissue ingrowth. *Clinical Orthopaedic and Related Research*, Vol. 176, 42-51
- Pilliar, R.M. (1987). Porous-surfaced metallic implants for orthopaedic applications. *Journal of Biomedical Materials Research*, Vol. 21, 1-33
- Pimenova, N.V. & Starr, T.L. (2006). Electrochemical and corrosion behavior of Ti-xAl-yFe alloys prepared by direct metal deposition method. *Electrochimica Acta*, Vol. 51, 2042-2049
- Plenk, H. (1998). Prosthesis-bone interface. *Journal of Biomedical Materials Research*, Vol. 43, 350-355
- Rausch, G. & Banhart, J. (2002). Making Cellular Metals from Metals other than Aluminium, In: *Handbook of Cellular Metals, Production, Processing, Applications*, Degischer, H.P. and B. Kriszt, (Ed.), 21-28, Wiley-VCH Verlag, Weinheim
- Rho, J.Y. ; Spearing, L.K. & Zioupos, P. (1998). Mechanical properties and the hierarchical structure of bone. *Medical Engineering and Physics*, Vol. 20, 92-102
- Robertson, D.M. ; Pierre, L. & Chahal, R. (1976). Preliminary observations of bone ingrowth into porous materials. *Journal of Biomedical Materials Research*, Vol. 10, 335-344
- Ryan, G. ; Pandit, A. & Apatsidis, D.P. (2006). Fabrication methods of porous metals for use in orthopaedic applications. *Biomaterials*, Vol. 27, 2651-2670
- Santos, D.R. ; Henriques, V.A.R. ; Cairo, C.A.A. & Pereira, M.S. (2005). Production of a low young modulus titanium alloy by powder metallurgy. *Materials Research*, Vol. 8, 439-442
- Sasaki, Y. ; Doi, K. & Matsushita, T. (1996). New titanium alloys for artificial hip joints. *Kinzoku*, Vol. 66, 812-817
- Seah, K.H.W. ; Thampuran, R. & Teoh, S.H. (1998). The influence of pore morphology on corrosion. *Corrosion Science*, Vol. 40, 547-556
- Semlitsch, M. ; Staub, F. & Weber, H. (1985). Titanium-aluminium-niobium alloy, development for biocompatible, high strength surgical implants. *Biomedical Technology*, Vol. 30, 334-339
- Semlitsch, M.F. ; Weber, H. ; Streicher, R.M. & Schon, R. (1992). Joint replacement components made of hot-forged and surface treated Ti6Al6Nb alloy. *Biomaterials*, Vol. 13, 781-788
- Shannon, M. & Rush, D.P.M. (2005). Bone Graft Substitutes: Osteobiologics. *Clinics in Podiatric Medicine and Surgery*, Vol. 22, 619-630
- Shehata Aly, M. ; Bleck, W. & Scholz, P.F. (2005). How metal foams behave if the temperature rises. *Metal Powder Report*, Vol. 60, 38-45
- Silva, G.A. ; Coutinho, O.P. ; Ducheyne, P. & Reis, R.L. (2007). Materials in particulate form for tissue engineering.2. Applications in bone. *Journal of Tissue Engineering and Regenerative Medicine*, Vol. 1, 97-109
- Sittig, C. ; Textor, M. ; Spencer, N.D. ; Wieland, M. & Vallotton, P.H. (1999). Surface characterization of implant materials CP Ti, Ti-6Al-7Nb and Ti-6Al-4V with different pretreatments. *Journal of Materials Science: Materials in Medicine*, Vol. 10, 35-46

- Steinemann, S.G. (1980). Corrosion of surgical implant—In vivo and in vitro test, In: *Evaluation of Biomaterials*, Winter, G.D., Leray, J.L. and de Groot, K., (Ed.), 1-34, John Wiley & Sons, New York
- Tang, X.L.; Xiao, X.F. & Liu, R.F. (2005). Structural characterization of silicon-substituted hydroxyapatite synthesized by a hydrothermal method. *Materials Letters*, Vol. 59, 3841-3846
- Tas, A.C. & Bhaduri, S.B. (2004). Rapid coating of Ti6Al4V at room temperature with a calcium phosphate solution similar to 10× simulated body fluid. *Journal of Materials Research*, Vol. 19, 2742-2749
- Tengvall, P.; Elwing, H.; Sjoqvist, L.; Lundstrom, I. & Bjursten, L.M. (1989). Interaction between hydrogen peroxide and titanium: a possible role in the biocompatibility of titanium. *Biomaterials*, Vol. 10, 118-120
- Thelen, S.; Barthelat, F. & Brinson, L.C. (2004). Mechanics Considerations for Microporous Titanium as an orthopedic implant material. *Journal of Biomedical Materials Research*, Vol. 69A, 601-610
- Thieme, M.; Wieters, K.P.; Bergner, F.; Scharnweber, D.; Worch, H.; Ndop, J., et al. (2001). Titanium powder sintering for preparation of a porous functionally graded material destined for orthopaedic implants. *Journal of Materials Science: Materials in Medicine*, Vol. 12, 225±231
- Thomson, R.C.; Wake, M.C.; Yaszemski, M.J. & Mikos, A.G. (1995). Biodegradable polymer scaffolds to regenerate organs. *Advances in Polymer Science*, Vol. 122, 245-274
- Tuchinskiy, L. & Loutfy, R. (2003). Titanium foams for medical applications. *Materials & Processes for Medical Devices*, pp. 377-381, Anaheim, California, ASM International
- Turner, T.M.; Sumner, D.R.; Urban, R.M.; Rivero, D.P. & Galante, J.O. (1986). A comparative study of porous coatings in a weight-bearing total hip-arthroplasty model. *Journal of Bone and Joint Surgery*, Vol. 68, 1396-1409
- Upadhyaya, G.S. (1997). *Powder Metallurgy Technology*, Cambridge International Science Publishing, Cambridge
- Varma, A.; Li, B. & Mukasyan, A. (2002). Novel synthesis of orthopaedic implant materials. *Advanced Engineering Materials*, Vol. 4, 482-487
- Veiseh, M. & Edmondson, D. (2003). Bone as an Open Cell Porous Material: ME 599K: Special Topics in Cellular Solids.
- Wang, X.; Yan, W.; Hayakawa, S.; Tsuru, K. & Osaka, A. (2003). Apatite deposition on thermally and anodically oxidized titanium surfaces in a simulated body fluid. *Biomaterials*, Vol. 24, 4631-4637
- Wang, X.J.; Li, Y.C.; Hodgson, P.D. & Wen, C.E. (2007). Nano- and macro-scale characterisation of the mechanical properties of bovine bone. *Materials Forum*, Vol. 31, 156-159
- Wang, X.J.; Li, Y.C.; Lin, J.G.; Yamada, Y.; Hodgson, P.D. & Wen, C.E. (2008). In vitro bioactivity evaluation of titanium and niobium metals with different surface morphologies. *Acta Biomaterialia*, Vol. 4, 1530-1535
- Wang, X.J.; Xiong, J.Y.; Li, Y.C.; Hodgson, P.D. & Wen, C.E. (2009). Apatite formation on nano-structured titanium and niobium surface. *Materials Science Forum*, Vol. 614, 85-92
- Weber, J.N. & White, E.W. (1972). Carbon-metal graded composites for permanent osseous attachment of non-porous metals. *Materials Research Bulletin*, Vol. 7, 1005-1016

- Wen, C.E. ; Mabuchi, M. ; Yamada, Y. ; Shimojima, K. ; Chino, Y. & Asahina, T. (2001). Processing of biocompatible porous Ti and Mg. *Scripta Materialia*, Vol. 45, 1147-1153
- Wen, C.E. ; Xu, W. ; Hu, W.Y. & Hodgson, P.D. (2007b). Hydroxyapatite/titania sol-gel coatings on titanium-zirconium alloy for biomedical applications. *Acta Biomaterialia*, Vol. 3, 403-410
- Wen, C.E. ; Yamada, Y. & Hodgson, P.D. (2006). Fabrication of novel TiZr alloy foams for biomedical applications. *Materials Science and Engineering C*, Vol. 26, 1439-1444
- Wen, C.E. ; Yamada, Y. ; Nouri, A. & Hodgson, P.D. (2007a). Porous titanium with porosity gradients for biomedical applications. *Materials Science Forum*, Vol. 539-543, 720-725
- Wen, C.E. ; Yamada, Y. ; Shimojima, K. ; Chino, Y. ; Asahina, T. & Mabuchi, M. (2002b). Processing and mechanical properties of autogenous titanium implant materials. *Journal of Material Science: Materials in Medicine*, Vol. 13, 397-401
- Wen, C.E. ; Yamada, Y. ; Shimojima, K. ; Chino, Y. ; Hosokawa, H. & Mabuchi, M. (2002a). Novel titanium foam for bone tissue engineering. *Journal of Materials Research*, Vol. 17, 2633-2639
- Wen, H.B. ; Wolke, J.G.C. ; de Wijn, J.R. ; Liu, Q. ; Cui, F.Z. & de Groot, K. (1997). Fast precipitation of calcium phosphate layers on titanium induced by simple chemical treatments. *Biomaterials*, Vol. 18, 1471-1478
- Wennerberg, A. ; Albrektsson, T. ; Johansson, C. & Andersson, B. (1996). Experimental study of turned and grit-blasted screw-shaped implants with special emphasis on effects of blasting material and surface topography. *Biomaterials*, Vol. 17, 15-22
- Wheeler, K.R. ; Karagianes, M.T. & Sump, K.R. (1983). Porous Titanium Alloy for Prosthesis Attachment. *Titanium alloys in surgical implants*, pp. 241, Philadelphia, ASTM
- Whitney, M. ; Corbin, S.F. & Gorbet, R.B. (2008). Investigation of the mechanisms of reactive sintering and combustion synthesis of NiTi using differential scanning calorimetry and microstructural analysis. *Acta Materialia*, Vol. 56, 559-570
- Williams, D.F. (1987). Tissue-biomaterial interactions. *Journal of Materials Science*, Vol. 22, 3421-3445
- Williams, D.F. (2001). Titanium for medical applications, In: *Titanium in Medicine*, Brunette, D.M., Tengvall, P., Textor, M. and Thomsen, P., (Ed.), 11-24, Springer
- Winters, G.L. & Nutt, M.J. (2003). *Stainless Steels for Medical and Surgical Applications*, ASTM International
- Woodman, J.L. ; Jacobs, J.J. ; Galante, J.O. & Urban, R.M. (1984). Metal ion release from titanium-based prosthetic segmental replacements of long bones in baboons: a long-term study. *Journal of Orthopaedic Research*, Vol. 1, 421-30
- Xiong, J.Y. ; Li, Y.C. ; Hodgson, P.D. & Wen, C.E. (2009a). Bioactive hydroxyapatite coating on titanium-niobium alloy through a sol-gel process. *Materials Science Forum*, Vol. 618-619, 325-328
- Xiong, J.Y. ; Li, Y.C. ; Hodgson, P.D. & Wen, C.E. (2009b). Nano-hydroxyapatite coating on a titanium-niobium alloy by a hydrothermal process. *Acta Biomaterialia*, Vol.?, In press
- Xiong, J.Y. ; Li, Y.C. ; Wang, X.J. ; Hodgson, P.D. & Wen, C.E. (2008). Mechanical properties and bioactive surface modification via alkali-heat treatment of a porous Ti-18Nb-4Sn alloy for biomedical applications. *Acta Biomaterialia*, Vol. 4, 1963-1968
- Yang, B. ; Uchida, M. ; Kim, H.M. ; Zhang, X. & Kokubo, T. (2004). Preparation of bioactive titanium metal via anodic oxidation treatment. *Biomaterials*, Vol. 25, 1003-1010

- Yoshida, N. & Watanabe, T. (2005). Sol-gel processed photocatalytic titania films, In: *Handbook of sol-gel science and technology; processing, characterization and applications*, Sakka, S., (Ed.), 3, Kluwer Academic Publishers, Boston
- Yu, C.J. ; Eifert, H.H. ; Banhart, J. & Baumeister, J. (1998). Metal foaming by a powder metallurgy method: Production, properties and applications. *Materials Research Innovations*, Vol. 2, 181-188
- Yu, S.Y. ; Scully, J.R. & Vitus, C.M. (2001). Influence of niobium and zirconium alloying additions on the anodic dissolution behavior of activated titanium in HCl solutions. *Journal of the Electrochemical Society*, Vol. B148, 68-78
- Zaffea, D. ; Bertoldi, C. & Consolo, U. (2004). Accumulation of aluminium in lamellar bone after implantation of titanium plates, Ti-6Al-4V screws, hydroxyapatite granules. *Biomaterials*, Vol. 25, 3837-3844
- Zhang, Y.P. ; Li, D.S. & Zhang, X.P. (2007). Gradient porosity and large pore size NiTi shape memory alloys. *Scripta Materialia*, Vol. 57, 1020-1023
- Zhao, Y.Y. ; Fung, T. ; Zhang, L.P. & Zhang, F.L. (2005). Lost carbonate sintering process for manufacturing metal foams. *Scripta Materialia*, Vol. 52, 295-298
- Zwicker, R. ; Buehler, K. ; Beck, H. & H.J., S. (1980). Mechanical properties and tissue reaction of a titanium alloy for implant material, In: *Titanium'80*, Kimura, H. and Izumi, O., (Ed.), 2, 505-514, Warrendale, PA

Improved Properties of Optical Surfaces by Following the Example of the “Moth Eye”

Theobald Lohmueller^{1,2,3}, Robert Brunner⁴ and Joachim P. Spatz^{1,2}

¹Max Planck Institute for Metals Research, Stuttgart, Germany

²Heidelberg University, Germany

³Current address: University of California, Berkeley, USA

⁴Carl Zeiss AG, Jena, Germany

1. Antireflective Surfaces - The “Moth Eye” Principle

The versatile visual systems of animals are intriguing examples for the ingenuity of nature's design. Complex optical concepts evolved as a result of adaptation of individual species to their environment. Identifying innovative applications for modern optics from the broad biological repertoire requires two steps: First, to understand how a system works and second, appropriate process technology to reproduce nature's design on non-living matter. A concrete example of this concept is the antireflective surface found on the eyes of certain butterfly species. The compound eyes of these insects are equipped with a periodic array of sub-wavelength structured protuberances. This structure, referred to as “Moth eye” structure after the moths were it was observed for the first time, thereby reduces reflection, while transmission of the chitin-lens is increased. The evolutionary benefit for the moth is improved vision in a dim environment while chances to be seen by a predator are lowered. But reflection of light at optical interfaces is also a problem for many technological applications (Kikuta *et al.* 2003). The reflection loss at a single air-glass interface is about 4 % due to the abrupt change of the refractive index. In state-of-the-art lithography systems and microscope devices, with dozens of lenses incorporated, losses of untreated surfaces would add up resulting in a substantial decrease of the overall performance. In the case of semiconductors, reflectance can reach up to 40% due to high refractive indices of the materials (Singh 2003), with impact on the efficiency of solar cells and optoelectronic devices (Partain 1995). Disturbing light reflection from computer monitors, television screens and LCD displays are further examples from daily experience.

Antireflection coatings are most frequently single or multilayer interference structures with alternating high and low refractive indices (Walheim *et al.* 1999) (Sandrock *et al.* 2004) (Xi *et al.* 2007). Reflection is reduced for normal incidence due to destructive interference of reflected light from the layer-substrate and the air-layer interface. However, there are factors limiting the applicability of layer systems like radiation damage and adhesion problems due to different thermal expansion coefficients of substrate and coating material. This is a particular problem for high-power laser applications. State-of-the-art optical lithography for example employs exposure wavelengths in the deep-ultraviolet (DUV) range in order to

address manufacturing demands for high-resolution processing (Chiu *et al.* 1997; Holmes *et al.* 1997). Coatings in this spectral range are difficult to implement, extremely expensive, and only a limited number of materials meet the optical requirements (Ullmann *et al.* 2000; Dobrowolski *et al.* 2002; Kikuta *et al.* 2003; Kaiser 2007).

“Moth eye” surfaces may offer an intriguing solution for these problems: They were first discovered by Bernhard (Bernhard 1967), who proposed that the function of these ‘nipple arrays’ might be the suppression of light reflection from the eye of the insect in order to avoid fatal consequences for the moth. The origin of these antireflective properties emerge from a gradation of the refractive index between air and the cornea surface (Clapham *et al.* 1973; Wilson *et al.* 1982). SEM micrographs of the surface structure of a genuine moth are shown in Figure 1.

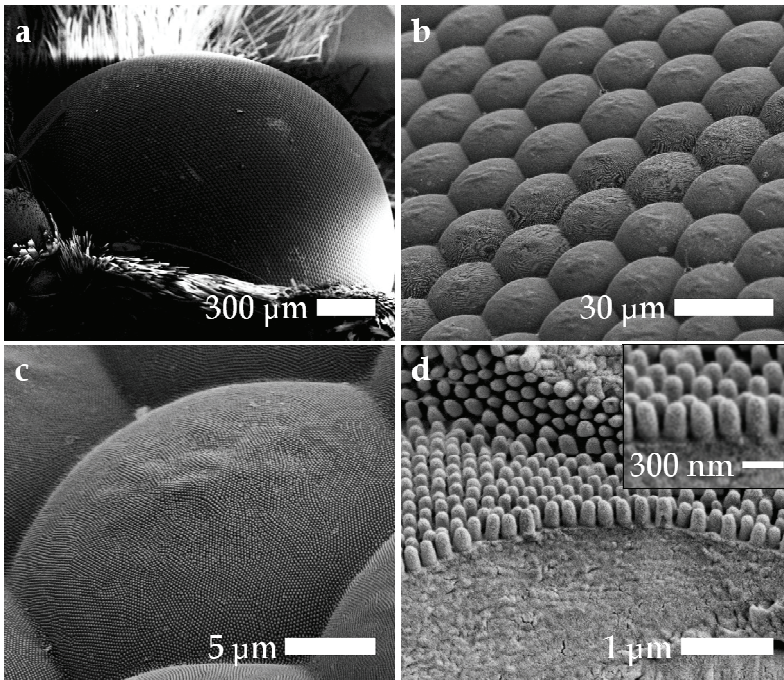


Fig. 1. SEM micrographs of the surface of a genuine moth eye. The compound eye of insects consists of an arrangement of identical units, the ommatidia. Each ommatidia itself represents an independent optical system with its own cornea and lens to focus light on the subjacent photoreceptor cells. a,b Compound eye of a moth build up by a microlens array of several thousand single lenslets. c, d, The surface of a single ommatidia is equipped with a fine nanoscopic array of protuberances. A detailed overview of structural properties for different butterfly species can be found in literature (Stavenga *et al.* 2006).

Since the distance between the pillars is sufficiently small, the structure cannot be resolved by incident light. Transition between the air-material interface thus appears as a continuous boundary with the effect of decreased reflection and improved transmittance of all light with a wavelength larger than the spacing period. The “Moth-eye” approach has thereby an

advantage compared to state-of-the-art antireflective coatings: Common single- and multi-layer configurations are only applicable within a small wavelength range and near to normal incidence of light. “Moth-eye”-structured surfaces, in contrast, show reduced and angle-independent reflectance over a broad spectral bandwidth (Clapham *et al.* 1973).

In this chapter we want to discuss the physical origin of these exceptional properties and how they can be transferred to optical functional materials. We used metallic nanoparticles as a lithographic mask to generate a quasi-hexagonal pattern of hollow, pillar-like protuberances into glass and fused silica substrates. We report on a combination of self-assembly based nanotechnology and reactive ion etching as a cost-effective and straightforward way for the fabrication of moth-eye inspired interfaces fully integrated in the optical material itself. The structures were found to exhibit broadband antireflective properties ranging from deep-ultraviolet to infrared light at oblique angles of incidence (Lohmueller *et al.* 2008b).

2. Theoretical Considerations

According to their complexity antireflection coatings can be classified by two basic models. Reduced reflectance can either be achieved by a homogeneous single-layer or digital type coating or by a more complex inhomogeneous multilayer configuration or gradual profile pattern respectively, that provides a gradual refractive index transition at the air/material interface (Dobrowolski *et al.* 2002). In the simplest case, a single homogeneous layer with a refractive index n will suppress reflectance between a substrate n_s and air n_a for normal incidence of light and an optical thickness of $\lambda/4$, if the constraint $n = (n_s n_a)^{0.5}$ is fulfilled. The demand for $\lambda/4$ thickness is based on both effects, the optical path difference and also the phase change at the low-to-high refractive index interface. It is important to point out that such configurations are always limited to a single wavelength.

An improvement is achieved by the introduction of multilayer systems which show an increased but still limited spectral bandwidth and also allow only a narrow variation of the incidence angle. Further optimizations are possible by using gradient optical coatings which show broadband antireflective characteristics for omnidirectional incidence of light (Poitras *et al.* 2004). The first theoretical description of this characteristic was published by J. S. Rayleigh in 1880, who mathematically demonstrated the broadband antireflection properties of graded-refractive index layers (Rayleigh 1880). For a discontinuous boundary the reflection coefficient at the interface of two media can be expressed as (Wilson *et al.* 1982)

$$R = [(n_1 - n_2)/(n_1 + n_2)]^2 \quad (1)$$

where n_1 and n_2 are the refractive indices. For a series of refractive indices, the total reflectance is a result of the interference of all reflections at each incremental step along the gradient. Each reflection has a different phase, as they come from a different depth of the substrate. The overall reflectance will therefore be suppressed, if the height of the antireflective structure equals to $\lambda/2$ and all phases are present.

In case of the “Moth eye” surface, the quasi periodical structure of the protuberances is characterized by a lateral period which is much smaller than the optical wavelength. The structure thus acts as a diffraction grating where only the zeroth order is allowed to propagate and all other orders are evanescent. The “moth eye” cornea is optically equivalent

to a laterally nonstructured film with a gradual change of the refractive index in depth. Figure 2 shows schematically the continuous increase of the physical thickness along the antireflective structure from air to bulk.

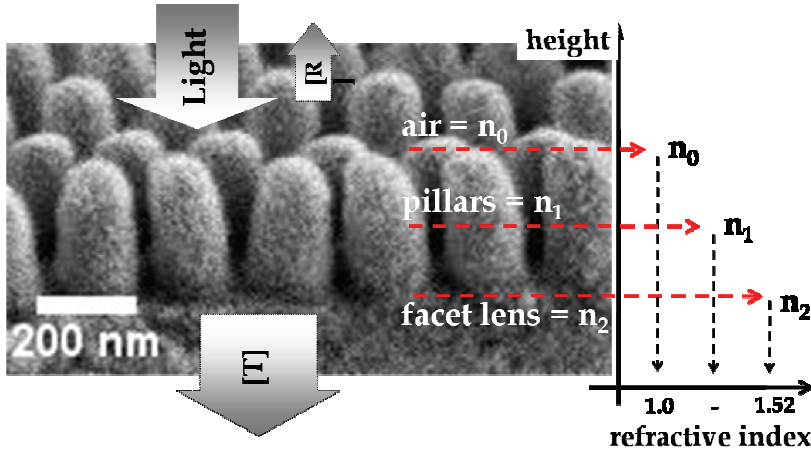


Fig. 2. Effective refractive index profile of a genuine moth eye. The fine array of protuberances on the lens of an insect eye has a structural period, smaller than the wavelength of the incoming light. This special profile is leading to a gradient increase of the material density and thus the refractive index at the air-cornea interfaces responsible for the antireflective properties.

This model of gradual index change is also the underlying principle for various effective medium approaches with the intention to introduce numerical methods which allow the determination of the dielectric constant of subwavelength structured composite materials (Lalanne *et al.* 2003). These approaches, however, represent only a rough approximation of the reality with a poor account for the individual profile geometry, especially if the structural period is infinitely smaller than the wavelength. A more exact form is given by the effective medium theory (EMT). Considering a 1D periodic structure with a gradual index profile, the effective refractive index n_{eff} of the whole interface can be expanded in a power series according to (Lalanne *et al.* 1996):

$$n_{eff} = n^{(0)} + n^{(2)}(\Lambda / \lambda)^2 + n^{(4)}(\Lambda / \lambda)^4 + \dots \quad (2)$$

Here, $n^{(0)}$ represents the effective index in the long-wavelength limit $n^{(2)}$ and $n^{(4)}$ are dimensionless coefficients depending on the structural geometry. Λ / λ denotes the period-to-wavelength ratio between the grating period of the 1D profile and the respective wavelength. While closed-form expressions like equation (2) are feasible up to the fourth order, an exact expression of n_{eff} for 2D periodic structures, like the moth eye, has not been achieved.

Alternatively, rigorous coupled wave analysis (RCWA), represents a method for the numerical calculation and simulation of light waves, as they are propagating in periodic media. The RCWA thereby represents an approximation of the Maxwell Equations

(Moharam *et al.* 1981). For RCWA, the geometry of a periodic pattern is divided into a define number of incremental optical layers. This stack region represents a transition between two semi-infinite regions such as air and the substrate. The light propagation is now calculated by the interaction of the incoming electromagnetic field with the layer stack where especially mutual interdependency has to be taken into account. The surface profile of a nanopatterned optical interface can thus be modeled by dividing the structure in a sufficiently small number of stack layers where each layer has a higher filling factor (and a higher optical thickness, respectively) than the previous one. The RCWA approach can be extended to accurately calculate the optimum surface-relief profile with respect to the refractive index of the material. Southwell *et al.* showed that the side-walls of a pyramid-like gradient profile would have an optimum shape (and thus optimum antireflective properties), for a fifth-order (quintic) functional dependence of the refractive index on the optical thickness (Southwell 1983; Southwell 1991):

$$n = n_s - (n_s - 1)(10u^3 - 15u^4 + 6u^5) \quad (3)$$

where u denotes the normalized optical thickness of the material ranging from zero at the dense substrate to unity at the air/substrate interface. The optimum slope of the pyramid sidewalls is thereby depending on the refractive index of the medium. Calculating the quintic surface profile reveals that curved, rather than flat-sided pyramids result in an index-matching layer with optimum antireflective properties at dielectric interfaces (Southwell 1991).

3. Subwavelength Structured Optical Interfaces

3.1 Fabrication of Artificial “Moth Eye” Structures

Different techniques such as e-beam writing (Kanamori *et al.* 1999; Kanamori *et al.* 2000; Toyota *et al.* 2001), mask lithography (Motamedi *et al.* 1993), and Interference Lithography (Gombert *et al.* 1998) have been applied to realize master structures for sub-wavelength structured gratings. To avoid scattering from the optical interface, the structural dimensions have to be smaller than the wavelength of the incoming light ('lower wavelength limit') (Wilson *et al.* 1982; Southwell 1991; Dobrowolski *et al.* 2002). For UV and DUV applications, very small feature sizes below 200 nm are required. At the same time, the overall reflectance is a function of the AR-layer thickness d and the wavelength λ (Rayleigh 1880). For a graded-index transition, substantial anti-reflection is obtained, if the ratio d/λ is about 0.4 or higher (Wilson *et al.* 1982; Lalanne *et al.* 2003). Thus, for optimum anti-reflection conditions in the DUV region the height of the structure should be at least 100 nm. In this size range, conventional fabrication technologies suffer from being time-consuming, expensive and rather complicated. Moreover, processing of non-planar substrates like lenses, especially with a small radius of curvature is challenging. An alternative is offered by self-assembly based methods. Porous alumina membranes (Kanamori *et al.* 2001) or block copolymer layers were used in combination with subsequent dry-etching (Park *et al.* 1997; Cao *et al.* 2003) (Asakawa *et al.* 2002). In the latter example, the etch selectivity between acrylic and aromatic polymer components results in a surface topography of the underlying material. Structure depths between 8 and 30 nm have been reported in silicon, too thin to obtain a substantial anti-reflective effect. Alternative approaches like porous sol-gel (Thomas 1992),

and optical polymer thin film coatings (Walheim *et al.* 1999; Ibn-Elhaj *et al.* 2001) are not useful for UV applications.

Colloidal monolayers of SiO₂ and polystyrene spheres have also been used in a combination with reactive ion etching (RIE) to lower the substrate reflectance (Nositschka *et al.* 2003) (Cheung *et al.* 2006) but the fabrication of small nanostructures below 200 nm covering large surface areas is challenging. An alternative route is offered by rough metal films or colloidal gold particles as masking material (Lewis *et al.* 1998) (Lewis *et al.* 1999; Seeger *et al.* 1999; Haupt *et al.* 2002). The etch mask in these examples is placed on top of silicon wafers by either sputter coating of metal islands or random deposition of colloidal gold particles out of solution. Stochastic relief structures with a spatial resolution smaller than 100 nm have been realized but both methods do not allow control of structural parameters such as feature size and spacing.

We applied Block Copolymer Micelle Nanolithography (BCML) in order to create extended and highly ordered arrays of gold nanoparticles on optical functional materials like fused silica and glass by means of pure self assembly (Spatz *et al.* 2000; Glass *et al.* 2003). Polystyrene-block-poly(2)-vinylpyridine, (PS-b-P2VP) diblock copolymers were dissolved in toluene forming uniform spherical micelles. Tetrachloroaurate, HAuCl₄ was added to the solution with a stoichiometric loading parameter defined as $L = n[\text{Me}]/n[\text{P2VP}]$ (Me = metal salt), in order to neutralize the vinylpyridine block, which mainly represents the micellar core. After stirring for 24 h, all metal salt is dissolved. Glass cover slips ($n = 1,52$) and fused silica wafers ($n = 1,46$) are immersed into solution. During the retraction, a self-assembled monolayer of metal salt loaded micelles is formed on top of the substrate driven by the evaporation of the solvent. Dipping the substrate has a certain advantage over other methods in that it enables a fast and homogeneous coating of plane as well as curved substrates like e.g. lenses with high reproducibility. BCML has no special requirements for the substrate composition besides it has to be resistant to the solvent. The polymer matrix is entirely removed by hydrogen plasma treatment of the sample leaving a template of hexagonally ordered gold particles on the surface. Various materials such as glass, silica, GaAs, mica as well as sapphire or diamond can be completely structured with nanosized particles over a large area $\gg \text{cm}^2$ within minutes. Advantageous of this technique is that the interparticle distance and the average colloidal diameter can be adjusted independently of one another enabling particle spacing between 15 and 250 nm and a precise control of the particle size (Lohmueller *et al.* 2008a). These particles act as a shadow mask for subsequent reactive ion etching (RIE) leading to a surface texture with anti-reflective properties (Figure 3).

We realized antireflective nanostructures on glass and on both, plane and biconvex fused silica surfaces. The structural period was set to 100 nm with a structure depth between 60 nm and 120 nm.

The gold nanoparticles are functioning as a protective resist during the etching process due to their high stability against the plasma treatment compared to the underlying material. Since the RIE process represents an unselective physical ion bombardment of the sample, the gold particles are continuously reduced in size until they are used up completely. From that moment on, the whole surface is uniformly etched and the structure is destroyed. Artificial moth eye structures were prepared on glass and fused silica as shown in Figure 4.

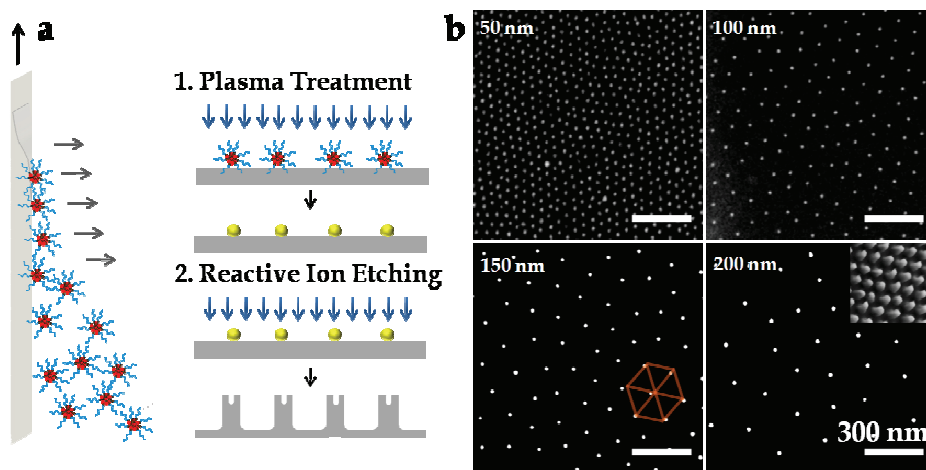


Fig. 3. Schematic of the fabrication process. a, The substrate is immersed into a toluene solution of metal salt loaded micelles. During retraction, a micellar monolayer self-assembles on top of the substrate driven by capillary forces due to the evaporation of the solvent. The polymer matrix is removed entirely by hydrogen plasma treatment and results in the deposition of an extended array of elemental gold particles on top of the substrate. Gold nanoparticles act as an efficient mask for etching hollow cone-like pillars into the underlying silica support by Reactive Ion Etching (RIE). b, The distance between the nanoparticles can be controlled over several hundreds of nanometers. The hexatic arrangement of the particles on the surface is similar to the orientation of the protuberances found on the eye of moths.

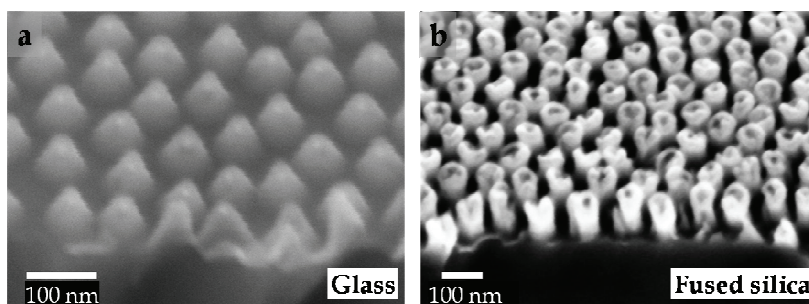


Fig. 4. “Moth-eye” structured glass cover slips and fused silica samples. a, High magnification micrograph showing the triangular shape of the glass cones. b, Side-view image of the pillar array measured with a tilt angle of 45°

The nanostructure profiles were different depending on the substrate material. On the glass-cover slips, the process resulted in a homogeneously patterned array of nano-cones with a diameter of 80 ± 5 nm at the base and a structural depth of app. 60 nm, representing the effective thickness of the antireflective layer. The sidewalls of the cones had an inclination angle of app. $\theta = 60^\circ$. The triangular shape found on top of the normal glass is a consequence

of a mixed isotropic-anisotropic etching at a moderate plasma power with an etch rate of app. 10 nm/min. According to theory, the optimum quintic profile for glass corresponds to the form of a nearly flat sided pyramid (Southwell 1991). Therefore, the process values were elaborated in order to generate an array of glass cones, which continuously converge towards the bottom. The sharp cone tips are indicating the optimum etching time. The samples were processed until the colloidal metal spheres were completely removed. For longer sample processing or higher RF power, the tips of the structure are blunted and the height is reduced. In both cases the optical performance declines considerably. For fused silica, a rather anisotropic etch profile was observed with an etch rate of 30 nm/min, three times higher than in the case of normal glass. Instead of sloping side walls, the structure had a vertical, pillar-like shape with a diameter of 60 ± 8 nm and a lateral spacing of 114 ± 3 nm (center to center) respectively. The different result can be explained by the lower resistance of the fused silica against the plasma treatment compared to normal glass. The height of the structure was measured to be 120 nm, which corresponds to the effective thickness of the antireflective layer (Figure 5).

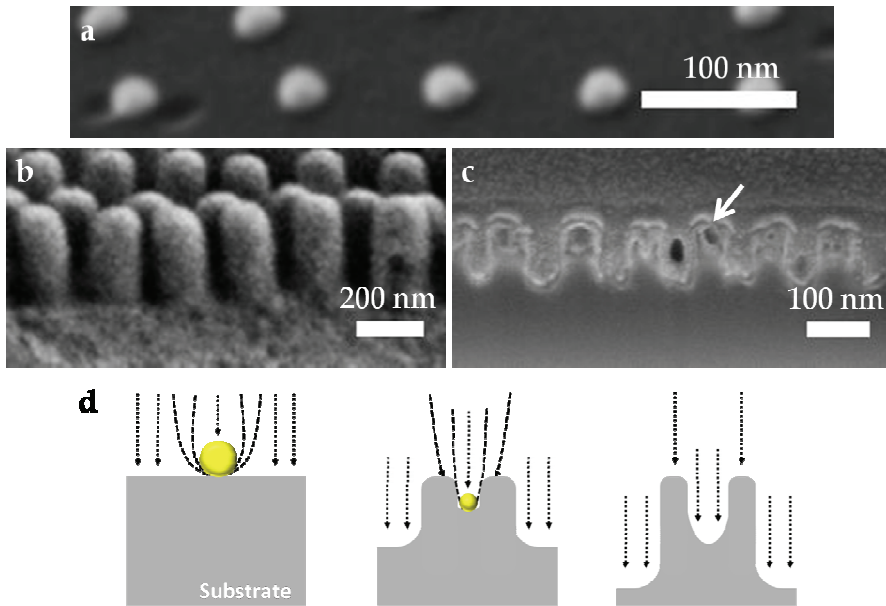


Fig. 5. a, 60° side-view SE-micrograph of the gold nanoparticles used as an etch mask. Comparison between a cross section of the cornea of a b, moth eye and the c, artificial moth eye profile in fused silica. Focused Ion Beam (FIB) cross section through the antireflective structure. The pillars have a diameter of 60 ± 4 nm and a lateral spacing of 110 ± 7 nm (center to center), respectively. The height of the structure was measured to be 120 ± 5 nm which corresponds to the effective thickness of the antireflective layer. A cone-type hole is etched into each pillar tip to approximately half of the pillar height. e, Schematic displaying the fabrication of hollow cone-like pillars during the reactive ion etching process in the presence of gold nanoparticles.

Remarkably, the tips of the pillars are hollow and pores are formed at the spots where the gold particle had been placed originally. A hole is etched into each pillar tip to app. half of the pillar height. This is caused by a electrostatic sheath ("Debye Sheath") (Langmuir 1923; Hull *et al.* 1929), formed above the sample during the plasma process (Figure 5 d). In the sheath region a strong electric field is generated perpendicular to the surface. The presence of electrical conductive gold clusters on top of the insulating material, however, causes a sheath distortion in the vicinity of the conductor/insulator interface (Kim *et al.* 2004). The reactive ions of the plasma are thereby focused to the contact area of the metallic nanoparticles with the underlying fused silica substrate. This causes a depletion of the plasma-generated reactive ion concentration around the metal islands. As a consequence, the particles act as an etching mask for processing hollow, cone-like pillars oriented perpendicular to the substrate. During the etching process, the particles sink into the material and the particle diameter continuously decreases until they are completely used up. The outer diameter of the pillars is larger than the nanoparticles due to depletion of ion concentration, while the inner diameter of the hollow structure reflects the original particle size. As mentioned earlier, a gradual increase of material from air to bulk is responsible for the substrate's anti-reflection properties (Moharam *et al.* 1981) (Kikuta *et al.* 2003). Consequently, the partly hollow, cone-type pillars are expected to improve the anti-reflective quality of the structure.

3.2 Optical Characterization

Different sub-wavelength profiles were obtained depending on the substrate material showing significant anti-reflective properties over a broad wavelength range from the deep UV up to the IR region. The optical properties of the fabricated samples were investigated by wavelength dependent transmission measurements. The incidence direction of the probe beam was oriented perpendicular to the surface. An unstructured substrate was measured in each case as a reference. For quantification, the reference measurement was also used to subtract the reflex from the backside of the single-sided structured samples. Figure 6 shows the measured transmission in dependence on the wavelength for glass and fused silica.

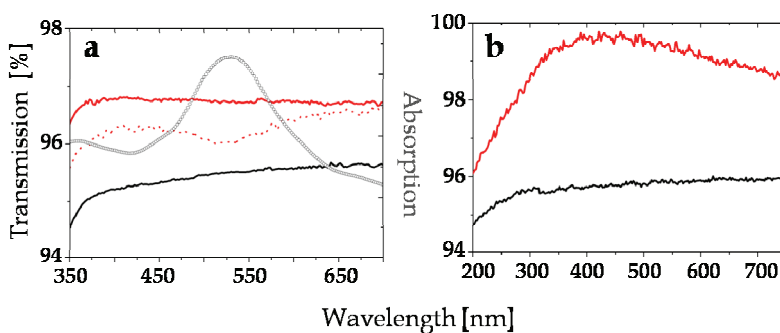


Fig. 6. Transmittance of an untreated and antireflective structured substrate of a, glass and b, fused silica. Residuals of the gold particles are visible in the spectra by a minimum of the transmission curve (red dotted line) that correlates with the maximum of the absorbance spectra (grey line) of the plasmon resonance of the gold particles. The reflex contribution of the sample backsides was subtracted for all spectra.

The distinct antireflective properties are clearly observable over the whole observed spectral region. Increased transmission of nearly 2% at a wavelength of 350 nm was detected compared to a reference glass cover slip. Residual gold may be left over on top of the substrate after RIE. However, if there are any remains of the particles, they are visible in the transmission spectrum. This is shown in Figure 6 a by the curve minimum that appears around 530 nm overlapping with the maximum of the absorbance spectra that was taken from the same sample. After five minutes no vestiges of the gold were detectable. By an alternate measurement of plasmon absorbance and overall transmission it is thus possible to determine the point of time when the particles are completely used off during the RIE process. Beside their role as plasma resist, the gold particles are thereby acting as an indicator for the course of the experiment. The transmission efficiency for the pillar-like structures was higher compared to the cone-shaped profile found on the glass cover slips. The reason is the smaller height of the glass indentations of only 60 nm, where the fused silica samples reached a structural depth of up to 120 nm. The effective thickness of the structure is mainly responsible for the efficiency of the antireflective properties and should therefore be in the order of half the wavelength or more. In the case of the VIS spectral region, ideal structure depth would therefore be between 200 nm and 400 nm. The desired parameters for an artificial moth eye design imply a structural spacing as small as possible and a structural depth as great as possible to achieve the least reflection and highest transmission over a broad bandwidth. The obtained pillar height, however, should show an optimum performance for the aspired wavelength range below 300 nm. The topology of the fused silica sample was similar to the corneal surface of a real moth.

As already mentioned, the moth eye lens shows a superior optical performance compared to many non-natural materials, since the overall reflection is reduced, while at the same time the transmission of light in the visible range is increased for omni-directional incidence of light. This is in contrast to non-reflecting coatings based on compound films or unspecific surface roughness, where diffuse scattering reduces the reflection but transmission is damped at the same time. The optical properties of plane fused silica samples were investigated by angle dependent reflection measurements at a particular as shown in Figure 7.

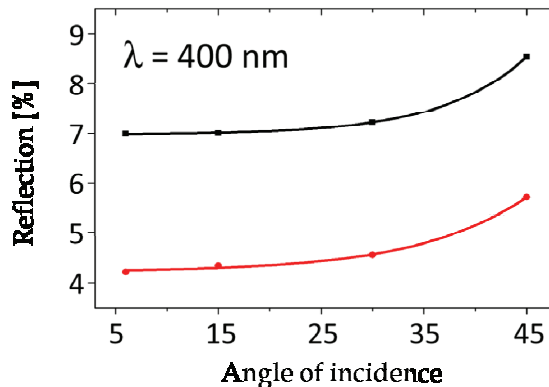


Fig. 7. Reflectance of an antireflective structured (red line) and a reference (black line) sample as a function of incident angle. The reflex contribution of the sample backsides was not subtracted in this case.

An increase of the total transmission was observed over a spectral range from 300 to 800 nm. At $\lambda = 400$ nm the transmittance reached a maximum value of 99.3 % (Figure 6 b), while the reflectivity of the same sample was damped to 0.7 %. Since the improved transmission is in accordance with a reduced reflectance, it is apparent that light scattering defects or absorption losses, which might have been introduced by the fabrication process, play, if at all existing, a minor role. The reflection and transmission under a certain angle is dependent on the polarization of the incoming light due to Fresnel’s law as demonstrated in Figure 8.

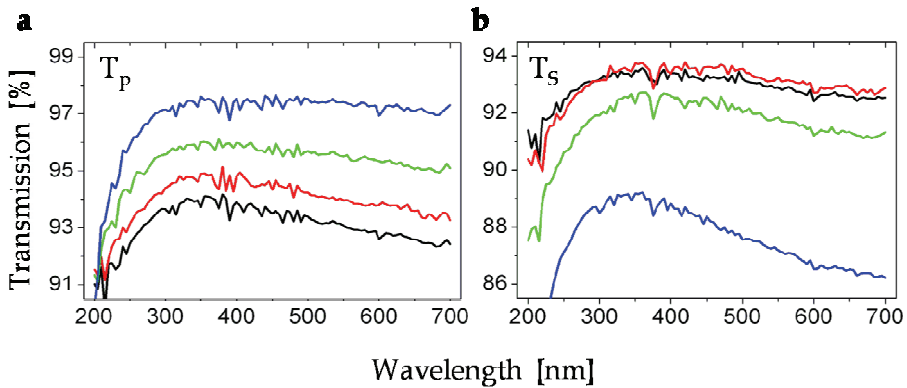


Fig. 8. Angle dependent transmission with polarized light. a,b,Spectral transmission of p- and s-polarized light for different angles of incidence(black: 0; red: 15; green: 30; blue: 45)

As expected, the difference between the transmittance for p - and s - polarized light is increasing towards larger polarization angles with a maximum dispartment at the Brewster angle (55.4° for fused silica, $n = 1.46$) (Hecht 2002).

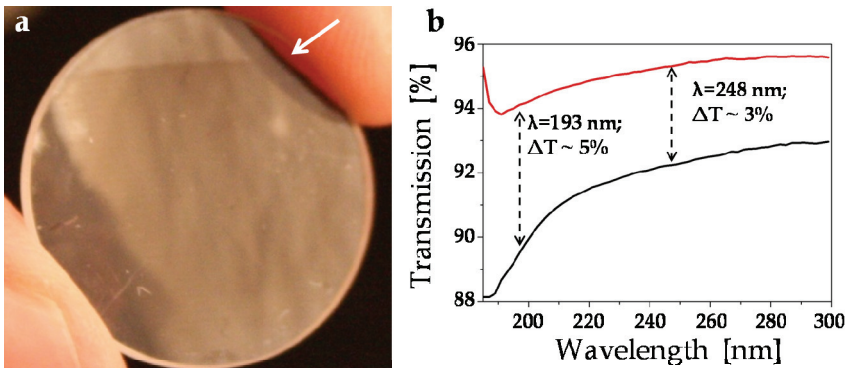


Fig. 9. Optical properties of an antireflective structured lens. a, Photograph of the processed lens demonstrating the anti-reflective effect. The borderline between the structured (bottom) and unstructured (top) area is indicated by the white arrow. b, Transmission spectra of the same lens before (black line) and after (red line) processing. An increase of transmission was observed for the DUV range from 185 to 300 nm. The improved transmission values for the excimer laser wavelengths 193 nm (ArF) and 248 nm (KrF) are shown exemplarily.

To demonstrate the excellent applicability of the method to non-planar optical components, the convex side of a fused silica lens was processed and characterized by sub-300 nm transmission measurements. The planconvex lens had a diameter of 22.4 mm and a focal distance of 100 mm, which corresponds to a radius of curvature of 46 mm. The reduced reflectivity in the visible light region of the structured part of the lens surface is shown in Figure 9. More intense light reflectivity is seen above the line indicated by the white arrow which is the border line between the nanostructured and the unstructured part of the lens surface, whereas, the antireflective structured part of the lens appears less bright. Transmission in the DUV range was measured between 185 and 300 nm (Figure 9b). The performance was improved over the entire DUV spectral region, by 5 % for 193 nm and 3 % for 248 nm at the excimer laser wavelengths of ArF and KrF, respectively. The high increase of transmission of about 5 % therefore relate to a virtual elimination of reflection at the modified optical interface.

3.3 Wettability of Nanostructured Interfaces

Beside the improved optical performance, a substantial change of the surface wettability was observed for the antireflective structured fused silica samples. This observation is advantageous, since an additional self-cleaning property of the optical interface would even enhance its practical applicability. Contact angle measurements were performed to investigate the hydrophobic effect of the antireflective structured fused silica interface. A difference of the contact angle of about 100° was observed between a plain and structured fused silica sample, which is a clear change of the surface wettability from hydrophilic to hydrophobic as shown in Figure 10.

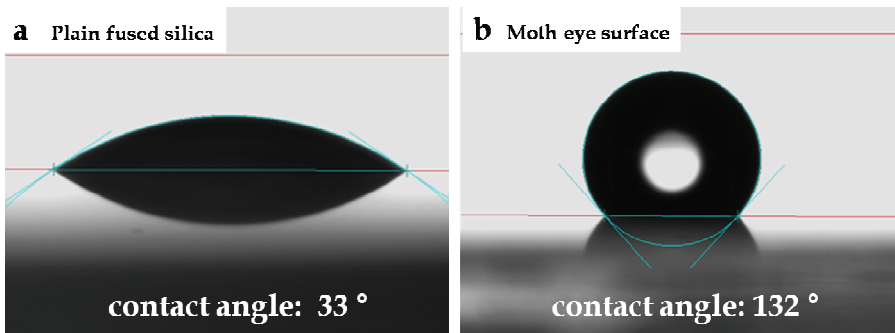


Fig. 10. Wetting of “Moth-eye” nanostructured fused silica samples. The contact angle for water of a, plane and b, nanostructured fused silica samples is increased from 33° to 132° .

A famous example for topology induced superhydrophobicity is the lotus effect (Neinhuis *et al.* 1997). The leaves of lotus plants, although they usually grow in a swamp like, muddy habitat, stay clean, since a certain microscopic structure and surface chemistry prevent the leaves from being moistened. Instead of a liquid film, water droplets are formed which pick up dirt as they roll off the leaf. In contrast to the lotus leaf, no additional change of the surface chemistry was introduced to amplify the water repellent properties. The hydrophobicity in this case is solely a result of the special surface topology. This observation can be explained according to the Cassie’s approach of surface wettability on rough

substrates (Cassie 1948). As shown in Fig 5 c the antireflective structure is build up by half-hollow protuberances with steep sidewalls. Grooves between the pillars, as well as the hollow pillar heads are leading to a strong lowering of the water-solid contact area. Furthermore, air bubbles are trapped within the structure forming a material-air-water composite interface. Wetting of the pillar structure is hindered, due to the steep sidewalls and the surface tension of water resulting in a liquid meniscus between the nanoscopic features and a high Laplace pressure. The effect of the sidewall angle α and the Laplace pressure Δp can be expressed according to (Patankar 2003; Xiu *et al.* 2007):

$$\Delta p = p - p_0 = -\frac{\gamma \cos(\theta - \alpha)}{R_0 + h \tan \alpha} \quad (4)$$

In this equation, γ denotes the surface tension of water, θ is the contact angle of water on the structure, R_0 is half of the width between two individual pillar sidewalls, p is the pressure on the liquid side of the meniscus and p_0 is the atmospheric pressure. The geometry of the structure is considered in this equation by the inclination angle α perpendicular to the surface. For steep sidewalls $\alpha = 0^\circ$, the Laplace equation is reduced to:

$$\Delta p = -\frac{\gamma \cos \theta}{R_0} \quad (5)$$

In this state, the Laplace pressure Δp has its highest value for a small R_0 which results in an increase of the water contact angle on top of the substrate.

4. Conclusion

We have demonstrated a new approach for the low-cost fabrication of antireflective structured materials is demonstrated by utilizing the advantage of self-assembly based nanolithography and reactive ion etching. Quasi hexagonal arrays of gold nanoparticles are used as an etch mask for plasma processing of glass cover slips and fused silica wafers. Cone-shaped and pillar-like protuberances with a structural period of 100 nm and a height of 60 nm and 120 nm, respectively, have been fabricated. Anti-reflective properties of these structures were demonstrated by transmission and reflection measurements for wavelengths ranging from deep UV to IR for oblique angles of incidence. Applicability of the fabrication method has been demonstrated on planconvex fused silica lenses with the result of a substantially increased transmittance of light in the DUV spectral region between 185 and 300 nm. Beside the remarkable optical properties, these structures offer additional advantages compared to thin-film coatings in terms of mechanical stability and durability. “Moth eye” structured devices can be used over a broad thermal range since they are essentially free of adhesion problems and tensile stress between the substrate and the antireflective layer. In addition, “Moth eye” structured fused silica samples were found to show a strong hydrophobicity caused by air that is trapped in the grooves between the hollow pillar features and the water-material interface. Overall, the method represents a fast, inexpensive, and very reproducible way for the fabrication of highly light-transmissive, anti-

reflective optical materials to be used for display panels, projection optics and heat-generating microscopic and excimer laser applications.

5. References

- Asakawa, K. and T. Hiraoka (2002). "Nanopatterning with microdomains of Block Copolymers using reactive-Ion etching selectivity." Japanese Journal of Applied Physics **41**: 6112-6118.
- Bernhard, C. G. (1967). "Structural and functional adaptation in a visual system." Endeavour **26**: 79-84.
- Cao, L., J. A. Massey, et al. (2003). "Reactive ion etching of cylindrical polyferrocenylsilane block copolymer micelles: Fabrication of ceramic nanolines on semiconducting substrates." Advanced Functional Materials **13**: 271-276.
- Cassie, A. B. D. (1948). "Contact angles." Discussions of the Faraday Society **33**: 11-16.
- Cheung, C. L., R. J. Nikoli, et al. (2006). "Fabrication of nanopillars by nanosphere lithography." Nanotechnology **17**: 1339-1343.
- Chiu, G. L. T. and J. M. Shaw (1997). "Optical Lithography: Introduction." IBM Journal of Research and Development **41**(1/2).
- Clapham, P. B. and M. C. Hutley (1973). "Reduction of lens reflection by the moth eye principle." Nature **244**(3): 281-282.
- Dobrowolski, J. A., D. Poitras, et al. (2002). "Toward perfect antireflection coatings: numerical investigation." Applied Optics **41**(16): 3075-3083.
- Glass, R., M. Moeller, et al. (2003). "Block copolymer micelle nanolithography." Nanotechnology **14**: 1153-1160.
- Gombert, A., K. Rose, et al. (1998). "Antireflective submicrometer surface-relief gratings for solar applications." Solar Energy Materials & Solar Cells **54**: 333-342.
- Haupt, M., S. Miller, et al. (2002). "Semiconductor nanostructures defined with self-organizing polymers." Journal of Applied Physics **91**: 6057-6059.
- Hecht, E. (2002). Optics. Addison Wesley.
- Holmes, S. J., P. H. Mitchell, et al. (1997). "Manufacturing with DUV lithography." IBM Journal of Research and Development **41**.
- Hull, A. W. and I. Langmuir (1929). "Control of an arc discharge by means of an grid." PNAS **15**(3): 218-225.
- Ibn-Elhaj, M. and M. Schadt (2001). "Optical polymer thin films with isotropic and anisotropic nano-corrugated surface topologies." Nature **410**(6830): 796-799.
- Kaiser, N. (2007). "Old rules useful to the designer of optical coatings." Vakuum in Forschung und Praxis **19**(4): 17-23.
- Kanamori, Y., K. Hane, et al. (2001). "100 nm eriod silicon antireflection structures fabricated using a porous alumina membrane mask." Applied Physics Letters **78**(142-143).
- Kanamori, Y., H. Kikuta, et al. (2000). "Broadband antireflection gratings for glass substrates fabricated by fast atom beam etching." Japanese Journal of Applied Physics **39**: L735-L737.
- Kanamori, Y., M. Sasaki, et al. (1999). "Antireflection gratings fabricated upon silicon substrates." Optics Letters **24**: 1422-1424.
- Kikuta, H., H. Toyota, et al. (2003). "Optical elements with subwavelength structured surfaces." Optical Review **10**(2): 63-73.

- Kim, D. and D. J. Economou (2004). "Simulation of a two-dimensional sheath over a flat insulator-conductor interface on a radio-frequency biased electrode in a high-density plasma." Journal of Applied Physics **95**: 3311-3318.
- Lalanne, P. and M. Hutley (2003). Encyclopedia of Optical Engineering - Artificial Media Optical Properties – Subwavelength Scale, Marcel Dekker, Inc.
- Lalanne, P. and D. Lemerrier-Lalanne (1996). "On the effective medium theory of subwavelength periodic structures." Journal of Modern Optics **43**(10): 2063-2086.
- Langmuir, I. (1923). "Positive ion currents from the positive column of mercury arcs." Science **58**(1502): 290-291.
- Lewis, P. A. and H. Ahmed (1999). "Patterning of silicon nanopillars formed with a colloidal gold etch mask." Journal of Vacuum Science and Technology B **17**: 3239-3243.
- Lewis, P. A., H. Ahmed, et al. (1998). "Silicon nanopillars formed with gold colloidal particle masking." Journal of Vacuum Science and Technology B **16**(6): 2938-2941.
- Lohmueller, T., E. Bock, et al. (2008a). "Synthesis of quasi hexagonal ordered arrays of metallic nanoparticles with tuneable particle size." Advanced Materials **20**(12): 2297-2302
- Lohmueller, T., M. Helgert, et al. (2008b). "Biomimetic Interfaces for high-performance optics in the Deep-UV light range." Nano Letters **8**(5): 1429-1433
- Moharam, M. G. and T. K. Gaylord (1981). "Rigorous coupled-wave analysis of grating diffraction." Journal of the Optical Society of America A: Optics, Image Science, and Vision **71**: 811-818.
- Motamedi, M. E., W. H. Southwell, et al. (1993). "Antireflection surfaces in silicon using binary optics technology." Applied Optics **31**(22): 4371-4376.
- Neinhuis, C. and W. Barthlott (1997). "Characterization and distribution of water repellent, self-cleaning plant surfaces." Annals of Botany **6**: 667-677.
- Nositschka, W. A., C. Beneking, et al. (2003). "Texturisation of multicrystalline silicon wafers for solar cells by reactive ion etching through colloidal masks." Solar Energy Materials & Solar Cells **76**: 155-166.
- Park, M., C. Harrison, et al. (1997). "Block Copolymer Lithography: Periodic arrays of $\sim 10^{11}$ holes in 1 square centimeter." Science **276**: 1401-1404.
- Partain, L. D. (1995). Solar cells and their applications, Wiley Series in Microwave and Optical Engineering.
- Patankar, N. A. (2003). "On the modeling of hydrophobic contact angles on rough surfaces." Langmuir **19**: 1249-1253.
- Poitras, D. and J. A. Dobrowolski (2004). "Toward perfect antireflection coatings. 2. Theory." Applied Optics **43**(6): 1286-1295.
- Rayleigh, J. S. (1880). "On reflection of vibrations at the confines of two media between which the transition is gradual." Proceedings of the London Mathematical Society **11**: 51-56.
- Sandrock, M., M. Wiggins, et al. (2004). "A widely tunable refractive index in a nanolayered photonic material." Applied Physics Letters **84**(18): 3621-3623.
- Seeger, K. and R. E. Palmer (1999). "Fabrication of silicon cones and pillars using rough metal films as plasma etching masks." Applied Physics Letters **74**: 1627-1629.
- Singh, J. (2003). Electronic and optoelectronic properties of semiconductor structures, Cambridge University Press.

- Southwell, W. H. (1983). "Gradient-index antireflection coatings." Optics Letters **8**(11): 584-586.
- Southwell, W. H. (1991). "Pyramid-array surface-relief structures producing antireflection index matching on optical surfaces." Journal of the Optical Society of America A: Optics, Image Science, and Vision **8**(3): 549-553.
- Spatz, J. P., S. Moessmer, et al. (2000). "Ordered deposition of inorganic clusters from micellar block copolymer films." Langmuir **16**: 407-415.
- Stavenga, D. G., S. Foletti, et al. (2006). "Light on the moth-eye corneal nipple array of butterflies." Proceedings of the Royal Society B: Biological Sciences **273**(1587): 661-667.
- Thomas, I. M. (1992). "Method for preparing porous silica antireflection coatings varying in refractive index from 1,22 to 1,44." Applied Optics **34**: 6145-6149.
- Toyota, H., K. Takahara, et al. (2001). "Fabrication of microcone array for antireflection structured surface using metal dotted pattern." Japanese Journal of Applied Physics **40**: 747-749.
- Ullmann, J., M. Mertin, et al. (2000). "Coated Optics for DUV-Excimer Laser Applications." Proc. SPIE **3902**: 514-527.
- Walheim, S., E. Schaeffer, et al. (1999). "Nanophase-separated polymer films as high-performance antireflection coatings." Science **283**: 520-522.
- Wilson, S. J. and M. C. Hutley (1982). "The optical properties of 'moth eye' antireflection surfaces." Optica Acta **7**: 993-1009.
- Xi, J. Q., M. F. Schubert, et al. (2007). "Optical thin-film materials with low refractive index for broadband elimination of Fresnel reflection." nature photonics **1**: 176-179.
- Xiu, Y., L. Zhu, et al. (2007). "Hierarchical silicon etched structures for controlled hydrophobicity/superhydrophobicity." Nano Letters **7**(11): 3388-3393.

Wood wasp inspired planetary and Earth drill

Thibault Gouache and Yang Gao
*Surrey Space Centre
United-Kingdom*

Yves Gourinat
*Institut Supérieur de l'Aéronautique et de l'Espace
France*

Pierre Coste
*ESTEC
European Space Agency*

1. Introduction

The exploration of the solar system is known to be very challenging to scientists, engineers and, technicians alike. One of the most difficult engineering challenges in extra-terrestrial exploration is gaining access to sub-surface samples and data. The fact that there have only been three successful drilling missions on extraterrestrial bodies (Russian Luna missions to the Moon, American Apollo missions to the Moon and Russian Venera missions to Venus) illustrates the high difficulty of sub-surface exploration on other planetary bodies than the Earth. However the potential scientific return of a sub-surface exploration mission is immense. For example, if we wish to detect the presence of organic molecules on Mars, we must dig through the first layers of the soil. Indeed, any organic molecule in these first layers is subject to high concentrations of oxidizing elements and is exposed to high ultraviolet fluxes which rapidly decompose it.

In this chapter, we will explain why the low gravity encountered on Mars or on the Moon and, the low mass of the probes, landers and rovers that carry drilling devices limit classical drilling techniques. Novel boring solutions optimised in mass and power consumption are thus needed for space applications. Biologists have identified the wood wasp, an insect that is capable of "drilling" into wood to lay its eggs. A low mass and low power system, like an insect, capable of drilling into wood is of the highest interest for planetary drilling and terrestrial drilling alike. The general working principle of the wood wasp drill ("dual reciprocating drilling") will be exposed and the potential benefits of imitating the wood wasp for planetary drilling will be highlighted.

Since the nature of wood is highly fibrous but the nature of extraterrestrial and terrestrial soils are not, it is necessary to adapt the wood wasp ovipositor to our target soils. A test bench to evaluate the influence of the different geometries and operational parameters was produced and is presented here. The dual reciprocating drilling experimental results obtained

on this test bench are also highlighted. They should lead to a new and enhanced model and comprehension of dual-reciprocating-drilling.

2. The challenges of drilling in extra-terrestrial bodies

2.1 Why drill in planetary bodies?

Drilling and subsurface exploration is called upon regularly in space missions. It is needed for producing samples for scientific payloads or sample return missions. But sampling is not the only reason for creating a borehole. The existence of the borehole allows a robot or a human to place captors in it for in-situ experimentation: for instance a neutron probe for water detection, an amino-acid bio-marker detection Skelley et al. (2005) or a thermal sensor for temperature gradient and flux evaluation Komle, Hiltner, Kargl, Ju, Gao & Grygorczuk (2008); Komle, Kaufmann, Kargl, Gao & Rui (2008). A borehole also gives access to the stratigraphy of the terrain. This access is of utmost importance since it allows numerous studies. The study of the planets past and thus the solar systems past, the evaluation of potential usable resources for manned exploration and, the assessment of soil mechanical properties for future man constructions are a few examples. The process of drilling itself and the telemetry recorded during this operation contains a large amount of scientific information. For instance, the operational parameters of the NASA (National Aeronautics and Space Administration) RAT (Rock Abrasion Tool) operating on Mars were used to evaluate the grindability or specific grind energy of the different tested Martian rocks. By comparing these values to tests done on Earth, it has been established that Martian rocks resemble (in terms of grindability) a range of Earth rocks going from gypsum to low strength basalts Myrick et al. (2004).

The four goals of future Mars scientific exploration outlined by the MEPAG (Mars Exploration Program Analysis Group) illustrate the importance of subsurface access. Indeed, each of the four identified goals require boring capabilities (Goal I: Determine if life ever arose on Mars; Goal II: Understanding the processes and history of climate on Mars; Goal III: Determine the evolution of the surface and interior of Mars; Goal IV: Prepare for human exploration) (MEPAG). The NASA Solar System Exploration Roadmap published in 2006 also put emphasis on the necessity of developing surface and subsurface mobility for solar system exploration missions Directorate (2006). There are numerous missions that are currently under development and that will require sub-surface exploration capabilities: MoonLite Gao, Phipps, Taylor, Clemmet, Parker, Crawford, Ball, Wilson, Curiel, Davies et al. (2007); Gao, Phipps, Taylor, Crawford, Ball, Wilson, Parker, Sweeting, da Silva Curiel, Davies et al. (2007); Gowen et al. (2008), ExoMars Van Winnendael et al. (2005), MSL (Mars Science Laboratory) Steltzner et al. (2006) and MSR (Mars Sample Return) O'Neil & Cazaux (2000).

2.2 Classical drilling methods and their performance in low-gravity

Drilling can be seen as a two-step process. First, it is necessary to break the drilled substrate. Then, the created cuttings must be evacuated. These two steps can either be conducted simultaneously or independently. There are four different general ways of creating drilling debris: with heat that vaporizes or sublimates the bored substrate or that generates cracks in it, by chemicals or by mechanical action Zacny et al. (2002). Since planetary drilling is exclusively used for scientific exploration, samples and the local environment must not be drastically altered by the drilling process. Thus only mechanical action is suitable.

Rotary drilling is the most commonly used technique in the oil and gas industry Azar & Samuel (2007). To successfully create a vertical or directional hole thanks to rotary drilling

three components are necessary: a force acting on the drill bit or WOB (Weight On Bit), the rotation of the drill bit and the evacuation of the drillings. The rotation of the drill bit is created by a motor (incorporated in the drill stem or above the drill stem on ground level). Usually the drillings are evacuated by drilling fluids injected at the bottom of the hole. Because of contamination issues and mass issues this is not acceptable. Generally planetary rotary drilling relies on dry auger evacuation of drillings. The danger of dry auger evacuation is jamming the drill stem. This happened to Apollo 15 astronauts who had great difficulties drilling more than one meter into the Lunar regolith Heiken et al. (1991). The astronauts had to use tools to remove the jammed drill from the ground and exceeded their nominal extra-vehicular activity time by doing so.

Despite the difficulties due to drillings evacuation, the biggest limit of classical drilling techniques in low-gravity is the WOB requirement. Indeed, for a rotary drill to cut into a rock formation, it is necessary to have a sufficient WOB. On Earth generating the correct WOB is quite easy. In deep oil drilling, the oil rig pulls on the drill stem to lower the WOB, rather than having to push on it. The mass of the drilling systems and Earth's gravity are more than sufficient to generate the proper WOB. On Mars or on the Moon where the gravity is respectively one third and one sixth of Earth's gravity, the same mass will create a third or a sixth of the WOB it would create on Earth. Furthermore, space systems are highly mass constrained. Engineers and mission architects spend most of their energy to reduce the mass of their systems. Thus the systems carrying rotary drills in space have low mass. Their low mass combined to the low-gravity environment allows little WOB and thus limits classical rotary drilling.

Many research efforts have been made to propose alternatives to classical rotary drilling. For instance the sonic and ultra-sonic drilling technique (USDC) uses high frequency oscillations and resonance to impose important accelerations to the drill head thanks to a free mass. These high level accelerations induce high stresses on the drilled formation and fracture it without requiring important WOB. Two teams, one from JPL and the other one from UK based company Magna Parva Peter Thomas (2009), have developed this concept. Another concept developed is the "mole". A mole is capable of burying itself into planetary soil. A mole can reach much larger depths than its own length without needing complex drill string assembly. To progress, a mole can use many drilling principles like classical rotary drilling. A very simple and efficient manner of making a mole progress is percussive action. In this case percussive action will not fracture rock but will allow soil penetration by compression and displacement. This was used on the PLUTO (PLANetary Underground TOol) Mole Sampling Device on ESA Mars Express lander Beagle 2 Richter et al. (2002). This mole can be deployed vertically or horizontally Richter et al. (2001). A DC electric motor displaces a mass and compresses a spring inside the mole. The energy accumulated in the spring is then released and the mass hits the mole casing. This shock allows the mole to progress. The design also allowed for reverse hammering to facilitate mole retrieval Richter et al. (2004).

Some researchers have turned themselves towards Nature to draw inspiration. In Europe, with the help of the ESA (European Space Agency) Advanced Concept Team, a number of bio-inspired solutions for sub-surface exploration have been explored. The two most promising solutions that have been identified are a locust inspired design and a wood wasp inspired design. The locust can dig into soil to lay its eggs. To do so it uses the two valves of its ovipositor that are capable of spreading apart and closing to enlarge the borehole and pull the locust abdomen further into the drilled soil. A simple physical model and a numerical model of this drilling mechanism were developed and showed promising results, though more work

is necessary before a fully functional 3D engineering model exists Menon et al. (n.d.). The wood-wasp inspired drill is the subject of this work.

3. The wood wasp ovipositor

3.1 Ovipositor morphology

Large numbers of insects have ovipositors allowing them to lay their eggs. Some insects commonly named “wood wasps” have ovipositors capable of drilling into wood to lay their eggs. Ovipositors also have numerous other functions like envenomation, defensive stinging or host location. For a more detailed description of ovipositors (evolutionary considerations, morphology, structures, oviposition strategies, etc.) refer to Quicke et al. (1999). Figure 1 is a middle region schematic of a typical ovipositor. The ovipositor has an upper or dorsal valve and two lower or ventral valves Rahman et al. (1998). Vincent and King Vincent & King (1995) described the morphology of two ovipositors: the short and rigid one of *Sirex noctilio* (10mm long and 0.26mm diameter) and the long and thin one of *Megarhyssa nortoni nortoni* (50mm long and 0.2mm diameter). They chose these two species because their ovipositors represent the large diversity of observed ovipositor morphologies of wood drilling wasps. They observed the ovipositors thanks to a Leica S440 scanning electron microscope. These observations revealed that the two ovipositors have different structures. Each ovipositor tip is covered with teeth. For both of these species the four first teeth at the tip of the ovipositor point proximally. In the case of *M. n. nortoni* the rest of the teeth also point proximally but decrease in size. For *S. noctilio* the following teeth progressively point distally. Differences in morphologies naturally induce differences in drilling mechanism.

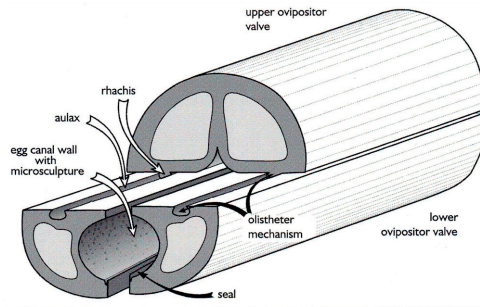


Fig. 1. Schematic of the middle region of a typical ovipositor Rahman et al. (1998).

3.2 Drilling Mechanism

Vincent and King described the “drilling” mechanism of both of these species. The insect moves its two lower valves back and forth: when one valve is protruding the other is retracted and then the protruding valve is retracted and the retracted valve is deployed (see Figure 2). For both insects, the first teeth pointing proximally will engage in the cell wall of the wood cells and then break these cell walls in tension with the part of the ovipositor pulling upwards. The advantage of using such mechanism is that the available force is not limited by buckling considerations but only by the limit of insect muscular power. Before the upward stroke of the ovipositor can break the cell walls in tension, the downward stroke must allow the pushing part of the ovipositor to traverse the wood cell wall. To do so the required force is partially

generated by the overhead push of the insect on its ovipositor. This overhead push is limited by the critical buckling force of the ovipositor. To generate extra push the insect uses the tensile forces generated by its proximally facing teeth that are engaged in the wood cell walls. This also allows the receding valve to be in tension and to stabilize the ovipositor and reduces buckling risks. For *M. n. nortoni*, Vincent and King estimated the tension force to be ten times higher than the critical buckling load of the ovipositor. Thus the load that the insect can impose on the tip of the downward going valve of its ovipositor is principally generated by the resistance of the wood to the tensile forces of the upward moving valve (see Figure 2).

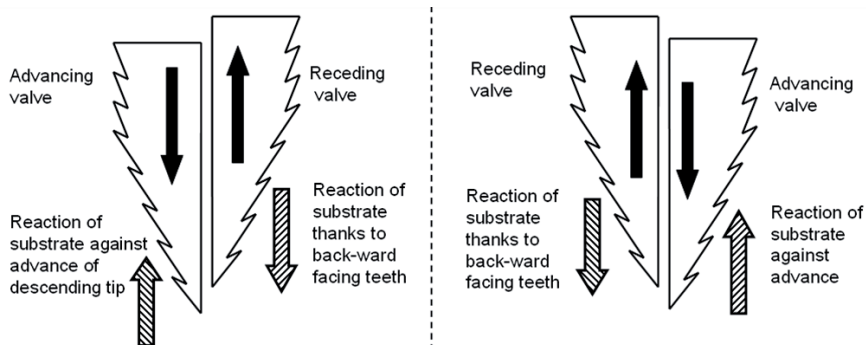


Fig. 2. Schematic of reciprocation movement and dual-reciprocating drill principle used by wood wasps.

3.3 Lessons learnt

When observing in detail the anatomy of the wood wasps' ovipositor and the possible mechanisms that could explain its capacity to drill into wood, two main "lessons" for drilling engineering can be learnt: "reaction generation" and "tension stabilisation". Reaction generation is the use of backward facing teeth to generate a reaction of the substrate in direction of drilling. The microstructures or the friction coefficient of the valve must be sufficient for the valve to mobilise the shearing resistance of the substrate and not slip on the surface of the substrate. Tension stabilisation is using the reaction of the substrate generated by the "reaction generation" to create tension forces in the receding valve. The valve in tension is no longer subject to Euler buckling issues. Thanks to the ovipositor's *olistheter* (sliding joint made of a T-shaped groove (*aulax*) on the lower valve and of a corresponding T-section ridge (*rachis*) on the upper valve) the progressing valve which is in compression is linked to the valve in tension. If the critical buckling load of the compressed valve were to be exceeded, it would become unstable and tend to buckle. But because it is linked to the other valve which is stabilized by the tension, the compressed valve can not deviate from its position. The valve in tension acts as a guide or support structure to the compressed valve. Thus the critical buckling load of the compressed valve can be exceeded without buckling issues. Many other observations of ovipositor morphology could lead to bio-mimetic applications (the ovipositors *olistheter* or the ovipositor steering mechanisms for instance).

4. DRD technologies

4.1 Planetary Drill

The wood-wasp drilling mechanism proposed in Vincent & King (1995) fostered high hopes in the planetary drilling and sampling community. Apart from the general potential of biomimetic systems to be low-mass and efficient, the perspective of being able to generate the drilling forces between two valves with “no net external force required” (the receding valve generating the force required for the advancing valve) was of premium interest Gao et al. (2005). Indeed, as explained previously, space systems are constrained in mass and must operate in low gravity environments, thus the total over head force available for a drilling system is low. Classical rotary drilling techniques need high over-head forces and thus have limited performance in space applications Gao et al. (2005).

To assess the feasibility of the wood-wasp inspired drill a first experimental setup was built to measure the necessary cutting forces. The drill bits were manufactured in ABS plastic and the drilled substrate was polystyrene. The rack angle of the drill bit was varied as well as the cutting speed. Authors concluded thanks to these test that there is an optimal cutting speed to maximise drilling output power. The effects of the rack angle were also shown. Higher rake angles were shown to produce higher cutting forces. It was also shown that after increasing with cutting speed, the cutting force passes through a maximum and then decreases whatever the rack angle Gao et al. (2005). Further on a simple DRD mechanism with metal drill bits was built. A pin and crank mechanism that was positioned over the drill bits was used (see Figure 3).



Fig. 3. Picture of the planetary DRD first prototype (right) and of its drill bits (left) Gao, Ellery, Jaddou, Vincent & Eckersley (2007).

Three different drilled substrates were tested (condensed chalk, non fired clay and lime mortar) and drilled at 9 different power levels. This first prototype drilled faster in softer substrates (lower compressive strength) than in harder ones with the same input power. The fact that drilling speed generally grew with penetration depth was identified. This was explained by potential cracks that could have formed in the drilled substrate Gao, Ellery, Sweeting & Vincent (2007). Another potential explanation proposed here is that the deeper the drilled hole the more the backward facing teeth can engage in the drilled surface, thus allowing a higher WOB for penetrating valve. In Gao, Ellery, Sweeting & Vincent (2007) authors also proposed an empirical model allowing to predict the penetration speed v_d of their DRD mechanism based on input power P and substrate compressive strength ϵ as model inputs.

$$v_d \propto k \cdot P \cdot \frac{1}{\sqrt{\epsilon}} \quad (1)$$

But above all the experimental work presented was the first implementation of DRD and proved the feasibility of DRD in soil and low strength rocks. Thanks to these first two studies, a light (< 10kg) micro penetrator concept housing a DRD was proposed Gao, Ellery, Jaddou, Vincent & Eckersley (2007).

4.2 Brain Probe

The wood wasp drilling mechanism described in Vincent & King (1995) has also fired new technological developments in neurosurgical probes (see Fig. 4). The possibility of being able to insert a fine probe under very low normal force into a brain could allow lowering the damage done to a brain during minimal invasive surgery Parittotokkaporn et al. (2009). The flexibility and the possibility of being able to steer a flexible neurosurgical probe like an ovipositor is steered would enable surgeons to avoid key zones of the brain when operating. For the moment this is limited by the rigid probes used Frasson, Parittotokkaporn, Schneider, Davies, Vincent, Huq, Degenaar & Baena (2008). However it is important to note that the main function of the ovipositor is to remove wood whereas the neurosurgical probe should displace tissue.



Fig. 4. Picture of the brain probe prototype (left) and pen as size reference (right) Frasson, Parittotokkaporn, Davies & Rodriguez y Baena (2008).

Inspired by the texture of the ovipositor of *Sirex Noctilio*, surfaces having different tribological properties depending on the direction in which they are moved were manufactured. To emulate the surface of an ovipositor, fin and tooth like microstructures with high-aspect ratios were manufactured thanks to advanced microelectronic mechanical systems (MEMS) fabrication technique. A large range of micro-structure size were manufactured (ranging from $10\mu\text{m}$ to $500\mu\text{m}$). For more details on manufacturing and related issues refer to Schneider et al. (2008; 2009).

A first series of tests were conducted thanks to the manufactured micro-structures. The goal was to determine whether or not the reciprocating motion of the microstructures was sufficient to induce the displacement of a specimen. The specimens tested ranged from in-organic materials to organic and also biological ones. The microstructures were reciprocated on the surface of each tested specimen. A specific air bearing was designed to lower the friction the specimen was subject to. It was showed that most soft organic tissues and most inorganic materials did not allow the micro structures to have sufficient grip on the specimen for it to move significantly. A good correlation between the microtexture size and the slip on the specimen was found. Five different microstructure/specimen interaction mechanisms were proposed. The damage created by the microstructures during the reciprocation motion was also investigated. This first work proved the feasibility of soft tissue traversal thanks to anisotropic

frictional properties and reciprocating motions with minimal tissue damage Parittotokkaporn et al. (2009).

The microstructures were then mounted onto a neurosurgical probe. The dynamic properties of the probes in a bi-directional axial displacement test done in brain tissues were explored. The forces necessary for their surgical probe to progress and the forces generated during the retraction of the probe were recorded. Since these two forces are of the same order of magnitude they have concluded that a brain probe using dual-reciprocating-drilling is feasible. Such a surgical tool would thus take benefit of the anisotropic tribological properties of its surface to progress thanks to reciprocating motion. It was even showed that the presence of the microstructures on the probe reduces the necessary amount of force to insert the probe in the brain tissues (when compared to a smooth probe)Frasson, Parittotokkaporn, Davies & Rodriguez y Baena (2008). The future work planned on this development include: the understanding of the tissue/probe interaction and the exploration of the effects of the normal force, of tissue properties and of reciprocating speed on soft tissue traversal.

4.3 Dual-Reciprocating-Drilling

As shown above, the wood-wasp drilling mechanism has inspired different technological developments. Here and in further publications the wood-wasp inspired drilling mechanism will be referred to as dual-reciprocating drilling. Indeed the drilling mechanism is based on the reciprocation motion of two tools or valves. Any drilling mechanism which disrupts or progresses into the drilled substrate thanks to the reciprocation of two tools in opposition one to another will be referred to as dual-reciprocating drilling (DRD). In DRD, the two reciprocated tools will be referred to as valves like in the wood-wasp morphology or drill bits.

4.4 Study Rationales

In Gao, Ellery, Sweeting & Vincent (2007), Gao et. al. highlighted some interesting research to be done on their DRD: optimize the geometry of drill bit, experiment on a wide variety of substrates, work on sample extraction method and build a prototype. In Frasson, Parittotokkaporn, Davies & Rodriguez y Baena (2008), Frasson et. al. have also insisted on the numerous studies needed before a fully functional brain probe can be proposed to neurosurgeons. Even the observations of the morphology of ovipositors still have much room for progress: "Almost nothing is known about the mechanics of substrate penetration and the interactions between the ovipositor valves and the substrate. No measurements of the rate or extents of ovipositor valve movements are available [...]." Quicke et al. (1999). Before an operational and space-qualified DRD can be proposed to solar system exploration missions it is key that more knowledge be collected. Two main questions need answering

4.4.1 What fundamental mechanism does DRD use to penetrate planetary soils?

Vincent and King proposed a basic drilling mechanism for the wood wasp's ovipositor. Though there is still room for more in depth understanding, it is very satisfying. However it is very unlikely that the mechanism they have described is applicable to a planetary DRD advancing in lunar regolith. Indeed wood is made of fibres but regolith is not. It is thought that the teeth of the wood wasp ovipositor have been optimised (through natural selection) to the size of wood cell walls. Further more, it is unclear whether or not a planetary DRD would use the same basic mechanism of progression in a granular material and in a soft rock formation. However understanding the fundamental drilling mechanism is key. This would allow engineers to optimize their designs.

For the moment three possible basic drilling mechanisms have been identified: displacement, compression and local shear/evacuation (see Fig. 5). In order to penetrate the substrate a mole, like the Beagle 2 Pluto mole, will displace the substrate around it. The substrate directly in front of the tip will be pushed down; the substrate further away will be pushed to the side and up. Upheaval of the substrate at the surface will be observed around the DRD. It is also likely that the displacement of the substrate will be accompanied by compression of the substrate. In some cases (high initial void ratio or low relative density of the substrate) compression will dominate. The compression of the substrate in the local vicinity of the drill will be sufficient to create enough room for the drill to progress. In such cases the substrate directly around the drill will be compressed and the substrate further away from the drill will not be affected (no displacement nor compression). A dip in the ground level around the DRD will be observed. The final mechanism is local shear and evacuation. It is possible to locally shear and displace the substrate and evacuate it. This method is the most similar to classical rotary drilling. Since this mechanism allows very localised action, it intuitively has the best low-energy potential. Whether these are applicable to a planetary DRD in planetary regolith is the first major contribution envisaged for this work. It is possible that none of the three mechanisms proposed allow a correct interpretation of our future observations and that a new mechanisms will have to be proposed.

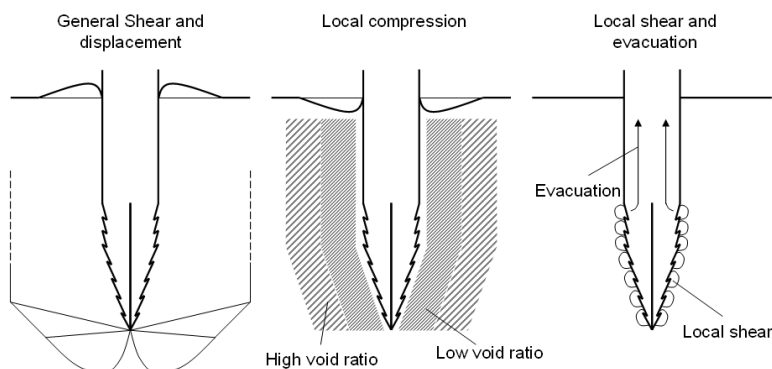


Fig. 5. Illustration of the three proposed basic drilling processes.

A very closely linked issue is the identification of the progression mechanism. Indeed it is unclear whether the force generated by the backward facing teeth of the receding valve is sufficient to make the entire drill progress. This is unclear even in the biological system. Little detail is given on the progression of the entire ovipositor and the role of the third valve.

4.4.2 Which parameters influence DRD performance?

For the moment only substrate compressive strength and input power have been explored and linked to drilling speed (see Equation 1). However a large number of parameters could play a role in DRD performance and force and power requirements. Before optimised planetary DRD designs can be proposed it is necessary that the key parameters driving DRD be identified. Parameters potentially playing a role in DRD have been identified and split into 3 categories: geometry of the drill head, operational parameters and substrate properties.

4.4.2.1 Geometry of drill head

The wood wasp ovipositor morphology being highly complex, it is impossible to mimic it fully. A simplified geometry has been adopted. Each DRD valve will be a half cone on top of a half cylinder. Such a general form is defined by three parameters: cone apex angle α , cylinder radius R , and cylinder length L . Each part of the DRD valve (cone and cylinder) will have specific tooth geometry. To define each tooth we need to know: two angles (respectively α_1 , γ_1 and α_2 , γ_2) and the number of teeth on each part (respectively N_1 and N_2). The geometry of the DRD valves is thus fully defined by nine geometrical parameters (see Figure 6).

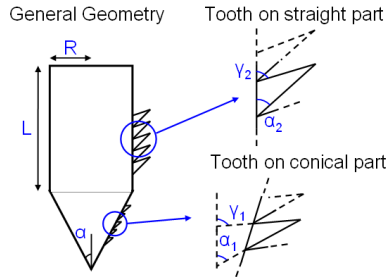


Fig. 6. Schematic of drill head geometry.

4.4.2.2 Operational parameters

How the valves are displaced must also be defined. The reciprocation motion is defined by its amplitude (δ) and its frequency (f). These two parameters are linked to others like input voltage, input current, input power and drilling speed. The depth d of the DRD valves and the over-head force or mass available to push on the drill are also very important operational parameters.

4.4.2.3 Substrate parameters

DRD technology is very novel and its full potential is not yet understood. It is thus important that it be tested in a wide variety of substrates: high void ratio sands, low void ratio regolith simulants and low unconfined strength rocks like the ones used in Gao, Ellery, Sweeting & Vincent (2007). Defining a set of parameters to describe the mechanical properties of rocks and granular materials alike is not feasible. For granular materials, angle of internal friction, cohesion, particle size distribution, angularity, density and void ratio can be considered. For soft cohesive formations unconfined compressive strength, elastic modulus and shear modulus can be considered.

5. Experimental Setup

5.1 A new DRD test bench

5.1.1 Design constraints

To answer the two main questions exposed in subsection 4.4, a new DRD test bench was designed. This new test bench presents added functionality compared to the first planetary DRD prototype. Indeed it allows the exploration of a wider range of parameters: variation of drill valve geometry, reciprocation movement amplitude and frequency. Apart from reciprocation

movement frequency, this was not feasible in the first planetary DRD prototype. But above all, this new DRD test bench was designed to allow the control of the over-head weight or force acting on the DRD valves. Indeed the added-value foreseen in a planetary DRD is its ability to drill with little or no over-head force requirements. A strict control of the over-head force on the DRD valves was not implemented on the first planetary DRD prototype. The new DRD test bench has a counter-mass and pulley system to control the vertical force acting upon the DRD. However, because of the numerous new functions, the mass of the test bench is significantly higher than the mass of previous setup.

5.1.2 Test bench description

A schematic, CAD-view and a picture of the new DRD test bench are presented Figure 7. The main elements of the test bench are the DRD mechanism (made of a motor, a movement transformation mechanism and the DRD valves) fixed on an aluminium plate, two rails guiding the aluminium plate (vertical translation), a counter mass system with two pulleys, and the data acquisition and control chains.

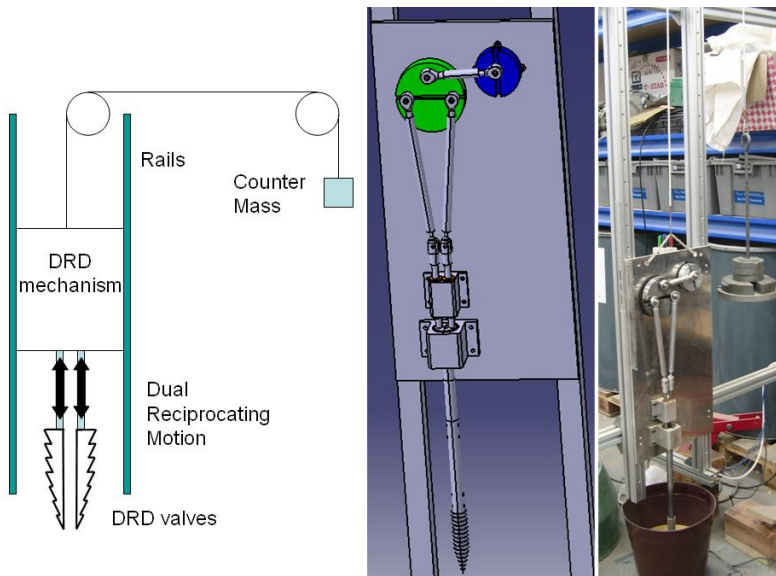


Fig. 7. Schematic and picture of DRD test bench.

The DRD mechanism is made of a continuous current motor, a movement transformation mechanism and the DRD valves. To transform the rotation of the motor into a dual reciprocating motion, a three rod, double pin and crank mechanism was manufactured. In order to allow modification of the amplitude without deeply transforming the reciprocation cycle and its symmetry, it is possible to modify the lengths as well as the fixation points of the rods. Figure 8 illustrates some possible valve movements that the DRD test bench can produce (grey lines) and some valve movements it would have produced if the length of the rods had not been modifiable (black lines).

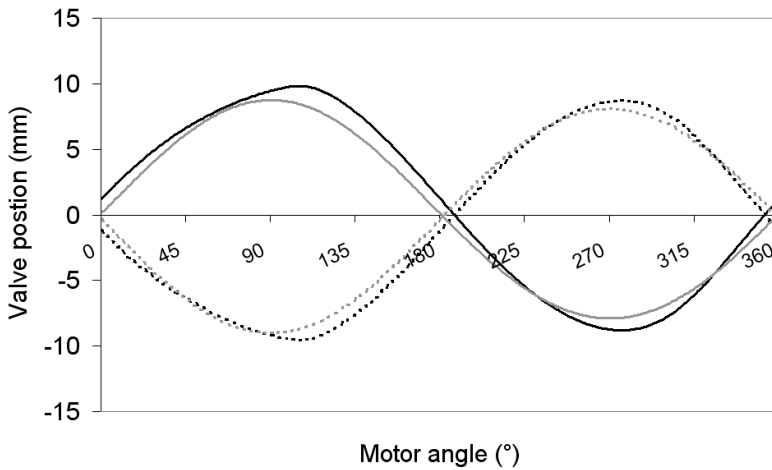


Fig. 8. Possible valve movements of the DRD test bench versus motor angle. Grey lines represent valve movements obtained thanks to the modifiable rod length; black lines represent movement obtained if rod had a set length. Dotted lines are left valve, full lines are right valve.

The counter-mass is setup with two pulleys. Interpretation of the role of the counter-mass must be done with caution. Indeed the counter-mass does not allow to mimic low gravity. If the global equilibrium of the plate supporting the DRD mechanism is considered, it can be seen that the vertical force on the valves does depend on the value of the counter-mass, but the maximum difference between the two valves does not. It is the strength of the rails that determine this value. If the DRD were housed in a rover or robot on the surface of the Moon or Mars, the maximum allowable force difference between the valves would be determined in part by gravity (and also by the carrier's geometrical setup). Another element that the counter-mass does not allow to control is the role of gravity on the drilled substrate. Experimental studies have been lead in partial gravity conditions to show the influence of gravity on bearing capacity of soils and have showed that gravity must be taken into account Bui et al. (2009). The electric motor frequency is controlled by varying input voltage. The input current and input voltage are monitored by TTI Multimeters and recorded automatically by a data acquisition desk top computer (at 0.5 Hz). The depth of the drill is recorded thanks to an image capture system. Its data acquisition frequency is also set to 0.5 Hz. For further details refer to Gouache et al. (2009b).

5.2 Substrates

As described by Neil Armstrong (Tranquillity Base, Apollo 11, July 20, 1969), the surface of the Moon appears to be "very, very fine-grained, as you get close to it, it's almost like a powder; down there, it's very fine [...] I can see the footprints of my boots and the treads in the fine sandy particles." . The samples brought back to Earth by the Luna and Apollo missions have widely been studied Heiken et al. (1991). The Moon is covered by regolith, a granular material. The surface of Mars is also covered by regolith though its origin (most probably weathering and communitation through impacts and wind more than chemical, biological and

water action) is believed to be different than Lunar regolith's origin (micrometeorites and meteorite impacts) Seiferlin et al. (2008). Since no large quantities of Lunar or Martian regolith are available on Earth, it is mandatory to rely on simulants. For mechanical testing (drilling, trafficability, etc.) the mechanical properties of the simulant are more important than its chemical composition. Sands have already been used to simulate regolith. For instance the Beagle 2 mole was tested in sand Richter et al. (2001). Two sands have been identified and characterised as suitable Mars simulants at the Surrey Space Centre: SSC-1 and SSC-2. SSC-1 is a coarse-silty quartz sand and SSC-2 is a fine garnet sand. The mechanical properties of these two simulants and their particle distributions are given in Scott & Saaj (2009).

It has been noticed that the void ratio or relative density of a sand can influence (or even dominate) the behaviour of a structure interacting with it: trafficability of rovers Brunskill & Vaios (2009); Scott & Saaj (2009) or penetration forces El Shafie et al. (2009) for instance. Thus, two substrate preparation methods were designed: one to obtain a low relative density substrate and the other one to obtain a high relative density substrate. Efforts have been focused on proposing a robust method able to reproduce the same relative density for a given substrate. The low relative density substrate is obtained by pouring the substrate into its container. The height of pouring and flow rate can have an incidence on the obtained density. It was observed that for heights above 40cm, there is little influence on final density. Thus all pouring were done from at least 50 cm high. The high relative density substrate is obtained by pouring the substrate into its container that is positioned on a vibrating table. Here the height of pouring has no influence on final density. Each of these methods was tested five times on both SSC-1 and SSC-2 (a total of 20 runs). The results of these tests are shown in table 1. The levels of relative density obtained are sufficiently spaced out (over 80% and under 10%) and low levels of deviation are observed (less than 5%). On the poured technique two runs (one with SSC-1 and one with SSC-2) gave anomalous results and were disregarded.

Relative density		SSC-1	SSC-2
High	Mean (%)	83	87
	Deviation (%)	4.6	1.8
Low	Mean (%)	7.4	0.0
	Deviation (%)	4.4	1.1

Table 1. Mean relative density and relative density deviation of SSC-1 and SSC-2 with high and low relative density preparation methods.

5.3 Design of experiment

The wide range of parameters potentially influencing DRD performance and the novelty of the technique have pushed authors to use design of experiment techniques. Indeed they allow to assess the influence of a large number of parameters by screening experiments while minimising the number of experiments to be done. A very complete presentation of such techniques is given in Montgomery (2009).

5.3.1 Inputs and outputs

Here we have chosen to keep the same drill head geometry. The studied inputs with their low and high levels are:

- over-head mass (*OHM*): 2 kg and 5 kg

- frequency of reciprocation motion (F): 0.5 Hz and 2.5 Hz
- amplitude of reciprocation motion (A): 5 mm and 12 mm
- substrate type (S): SSC – 1 and SSC – 2
- relative density (RD): low and high

The studied outputs are:

- final depth of penetration (FD)
- total power during drilling (P)
- difference between power used during drilling and before drilling (ΔP)
- total current during drilling (I)
- difference between the current required during drilling and before drilling (ΔI)
- initial drilling velocity (IV)

5.3.2 Choice of experimental design

A two-level factorial design was chosen to evaluate the influence of the inputs on the outputs. The two levels adopted for each parameter were presented above. To be able to determine the influence of each input and their one-to-one interactions independently, it is necessary to choose a resolution V design. The adopted design is a 16 experiment, 5 parameter, 2^{5-1} partial factorial resolution V design of experiment. The 16 experiments done are presented in table 2. For further details please refer to Gouache et al. (2009a).

Experiment	OHM	F	A	S	VR
1	-	-	-	-	+
2	+	-	-	-	-
3	-	+	-	-	-
4	+	+	-	-	+
5	-	-	+	-	-
6	+	-	+	-	+
7	-	+	+	-	+
8	+	+	+	-	-
9	-	-	-	+	-
10	+	-	-	+	+
11	-	+	-	+	+
12	+	+	-	+	-
13	-	-	+	+	+
14	+	-	+	+	-
15	-	+	+	+	-
16	+	+	+	+	+

Table 2. Description of the 16 experiments planned done with the DRD test bench.

6. Parameters driving DRD

6.1 Typical drilling results

6.1.1 Drilling profiles

Of the 16 experiments done, 7 drilled to the maximum depth allowed by the test bench and 9 reached their FD. An example of each of these depth profiles are shown in 9(a). The drilling experiments that did not reach the maximum allowable depth levelled off in an exponential manner, the speed of penetration progressively decreasing to zero. The other experiments maintained a more or less constant speed through the drilling experiment. Before the drilling starts ($t < 0$), the tip of the drill is placed at ground level. At $t = 0$ the drill is released and it plunges into the substrate. The initial jump in depth can be seen in Figure 9(a). A typical power and current record are shown in figure 9(b). Before drilling starts ($t < 0$) the power and current oscillate around a constant value. At $t=0$ the drill is set free and penetrates the surface. Power and current go up. Finally the power and current oscillate around a new constant value.

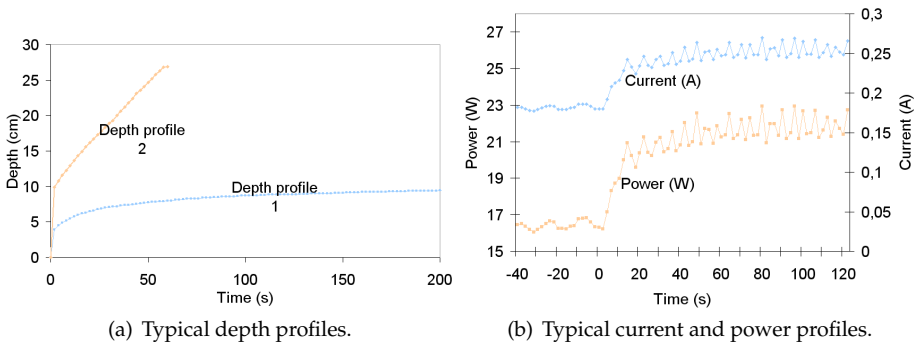


Fig. 9. Typical depth, current and power profiles observed during experiments on DRD test bench.

6.1.2 Surface deformation

Fig. 10(a) is a picture of the drill head advancing into SSC-1. Fig. 10(b) is a picture of DRD advancing in SSC-2. When observing the surface of the drilled SSC-1 in Fig. 10(a), clear upheaval can be seen. For the SSC-2 case a clear dip can be seen in Fig. 10(b). For the test represented in Fig. 10(a), SSC-1 had been vibrated and for the test in Fig. 10(b), SSC-2 had been poured. These observations indicate that in high void ratio sand, the basic drilling mechanism is "local compression" and in low void ratio sand it is "general shear and displacement". (The low void ratio case could be also explained by the "local shear" basic mechanism but without evacuation, since the drill head is barely submerged by the drilled medium).

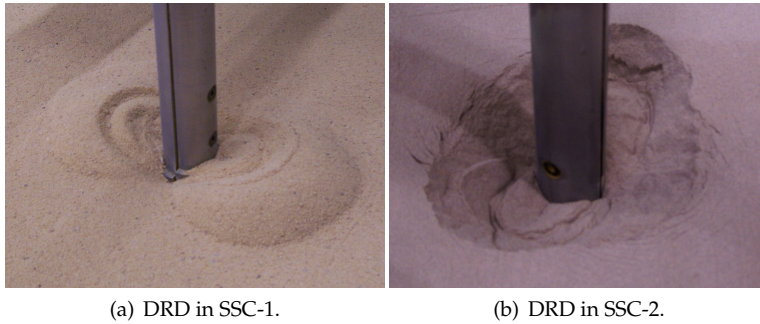


Fig. 10. Pictures of the deformation of substrate surface after drilling of DRD.

6.2 Analysis of main effects

Figure 11 represents the analysis of the 16 experiments done. It represents in % the modification of an output (ie: power, etc.) following the modification of an input (ie: frequency, etc.) from low level to high level. In figure 11, only the principle effects are shown. As can be seen in figure 11, FD is mainly driven by relative density. The higher relative density the lower FD is. For the 7 experiments that reached the maximum allowable depth, an arbitrary value of 100 cm was given as FD. This value was changed from 50 cm to 500 cm without any major differences in our conclusions. F and A also have influence on FD, almost as much as OWM. Thus by choosing a correct set of F and A, important depths should be reached. Power is evidently driven by frequency. OHM and A have a high influence on ΔP and little influence on P. Indeed OHM and A only have influence on the drilling phase and do not modify the power needed to overcome friction in the test bench. A higher F induces higher current (or torque) requirements but lower ΔI . Indeed, as frequency goes up, the power required to compensate the friction in the DRD prototype goes up. However a higher drilling frequency can lower the forces needed for the drilling process. Indeed in granular materials the critical state friction can be lower than the peak friction. Higher amplitude and higher OHM require higher drilling forces. IV is mainly determined by OHM. This is quite logical, since the higher the OHM, the more force the DRD valves have on them.

6.3 Analysis of interactions

Following the analysis of the main effects, a linear model was built. The high levels of dispersion showed that the interactions between main parameters must be taken into account to explain the experimental results obtained. The main interactions identified are presented. For FD, interactions between frequency and OHM and frequency and amplitude play an important role. For ΔP interaction amongst frequency, amplitude and OHM play are of interest. OHM and RD interaction as well as F and RD interaction influence ΔI . IV is highly affected by the interaction between relative density and amplitude.

7. Conclusion

The need for planetary sub-surface exploration techniques (to discover life on Mars for instance) and the limitations of classical drilling techniques in low gravity environments have fostered many technological developments. Amongst these a bio-mimetic solution inspired by

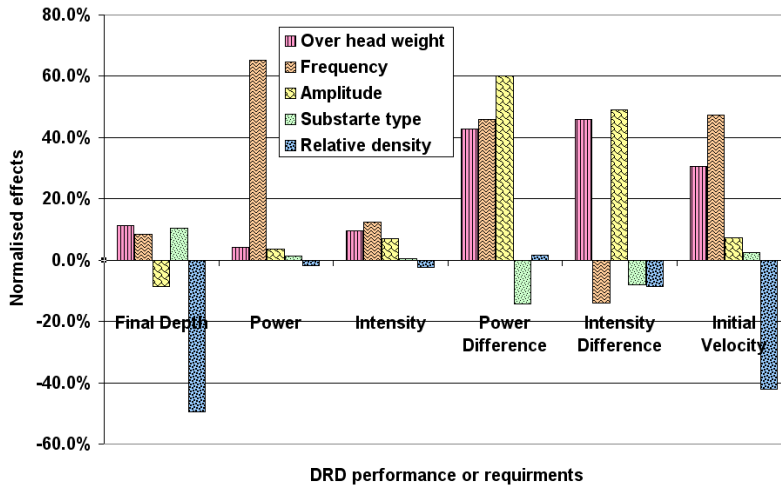


Fig. 11. Analysis of the 16 experiments: in % the modification of an output following the change in an input from low level to high level.

the wood wasp's ovipositor was proposed: dual-reciprocating drilling. Even though the principle was demonstrated thanks to a first prototype, further work was needed to determine the mechanisms used by DRD to progress in granular mediums like regolith and to identify the main parameters driving DRD performance. To do so a DRD test bench was designed and was presented in this paper. A series of 16 experiments were planned and analysed using design of experiment techniques. This allowed authors to identify the parameters affecting DRD performance and requirements. The main finding of this analysis is the importance of the interaction between parameters. However, because of the high dispersion inherent to any drilling experiment, it is necessary to repeat the 16 experiments to gain higher confidence in the conclusions of this work. Future work includes repeating experiments to take into account dispersion of results; exploring the influence of the other parameters that were held constant during this series of experiments; focusing on the driving parameters and interactions thanks to dedicated experiments; proposing numerical and analytical models of system and; enhancing DRD test bench (reduce mass for instance). Such research efforts would then lead to a series of laws and models allowing engineers to propose an optimised space-qualified DRD.

Acknowledgments

The authors would like to thank the European Space Agency for fostering their cooperation and research thanks to its Networking and Partnership Initiative. They also thank the French Ministry of Research for funding PhD students.

8. References

- Azar, J. & Samuel, G. (2007). *Drilling engineering*, Pennwell Corp.
- Brunskill, C. & Vaios, L. (2009). The effect of soil density on microrover trafficability under low ground pressure conditions, *11th European Regional Conference of the International Society for Terrain-Vehicle Systems*.

- Bui, H., Kobayashi, T., Fukagawa, R. & Wells, J. (2009). Numerical and experimental studies of gravity effect on the mechanism of lunar excavations, *Journal of Terramechanics* .
- Directorate, N. S. M. (2006). Solar system exploration.
- El Shafie, A., Ulrich, R. & Roe, L. (2009). Penetration Forces for Subsurface Regolith Probes, *40th Lunar and Planetary Science Conference, March 23-27, 2009, The Woodlands, Texas, USA*.
- Frasson, L., Parittotokkaporn, T., Davies, B. & Rodriguez y Baena, F. (2008). Early developments of a novel smart actuator inspired by nature, *Mechatronics and Machine Vision in Practice, 2008. M2VIP 2008. 15th International Conference on*, pp. 163–168.
- Frasson, L., Parittotokkaporn, T., Schneider, A., Davies, B., Vincent, J., Huq, S., Degenaar, P. & Baena, F. R. (2008). Biologically inspired microtexturing: Investigation into the surface topography of next-generation neurosurgical probes, *Engineering in Medicine and Biology Society, 2008. EMBS 2008. 30th Annual International Conference of the IEEE*, pp. 5611–5614.
- Gao, Y., Ellery, A., Jaddou, M., Vincent, J. & Eckersley, S. (2005). A novel penetration system for in situ astrobiological studies, *International Journal of Advanced Robotic Systems* **2**(4): 281–286.
- Gao, Y., Ellery, A., Jaddou, M., Vincent, J. & Eckersley, S. (2007). Planetary micro-penetrator concept study with biomimetic drill and sampler design, *IEEE Transactions on Aerospace and Electronic Systems* **43**(3): 875–885.
- Gao, Y., Ellery, A., Sweeting, M. & Vincent, J. (2007). Bioinspired Drill for Planetary Sampling: Literature Survey, Conceptual Design, and Feasibility Study, *Journal of Spacecraft and Rockets* **44**(3): 703–709.
- Gao, Y., Phipps, A., Taylor, M., Clemmet, J., Parker, D., Crawford, I., Ball, A., Wilson, L., Curiel, A., Davies, P. et al. (2007). UK lunar science missions: MoonLITE & moonraker, *Proc. DGLR Int. Symposium To Moon and Beyond, Bremen, Germany*.
- Gao, Y., Phipps, A., Taylor, M., Crawford, I., Ball, A., Wilson, L., Parker, D., Sweeting, M., da Silva Curiel, A., Davies, P. et al. (2007). Lunar science with affordable small spacecraft technologies: MoonLITE and Moonraker, *Planetary and Space Science* .
- Gouache, T., Gao, Y., Coste, P. & Gourinat, Y. (2009a). Experimental Parametric Evaluation of Dual-Reciprocating-Drilling Mechanism Performance, *Proceedings of the 11th European Conference on Spacecraft Structures, Materials and Mechanical Testing, Toulouse, France*.
- Gouache, T., Gao, Y., Coste, P. & Gourinat, Y. (2009b). Experimental Study of Dual-Reciprocating-Drilling Mechanism using Design of Experiment Approach, *Proceedings of the 13th European Space Mechanisms and Tribology Symposium, Vienna, Austria*.
- Gowen, R., Smith, A., Crawford, I., Ball, A., Barber, S., Church, P., Gao, Y., Griffiths, A., Hagermann, A., Pike, W. et al. (2008). An update on the MoonLite lunar mission, *Geophysical Research Abstracts*, Vol. 10, pp. 1607–7962.
- Heiken, G., Vaniman, D. & French, B. (1991). *Lunar sourcebook: A user's guide to the Moon*, Cambridge University Press.
- Komle, N., Hißjter, E., Kargl, G., Ju, H., Gao, Y. & Grygorczuk, J. (2008). Development of Thermal Sensors and Drilling Systems for Application on Lunar Lander Missions, *Earth, Moon, and Planets* **103**(3): 119–141.
- Komle, N., Kaufmann, E., Kargl, G., Gao, Y. & Rui, X. (2008). Development of thermal sensors and drilling systems for lunar and planetary regoliths, *Advances in Space Research* **42**(2): 363–368.

- Menon, C., Vincent, J., Lan, N., Bilhaut, L., Ellery, A., Gao, Y., Zangani, D., Carosio, S., Manning, C., Jaddou, M. et al. (n.d.). Bio-inspired micro-drills for future planetary exploration, *Proceedings of CANEUS, August 27 - September 1, 2006, Toulouse, FRANCE* 20: 21.
- (MEPAG), M. E. P. A. G. (2006). Mars Scientific Goals, Objectives, Investigations, and Priorities: 2006.
URL: <http://mepag.jpl.nasa.gov/reports/index.html>
- Montgomery, D. (2009). *Design and analysis of experiments.*, John Wiley & Sons New York.
- Myrick, T., Chau, J., Carlson, L. et al. (2004). The RAT as a rock physical properties tool, *Proceedings of AIAA Space 2004 Conference and Exhibit/AIAA*, Vol. 6096, pp. 1–11.
- O'Neil, W. & Cazaux, C. (2000). The Mars sample return project, *Acta Astronautica* 47(2-9): 453–465.
- Parittotokkaporn, T., Frasson, L., Schneider, A., Huq, S., Davies, B. L., Degenaar, P., Biesenack, J. & Rodriguez y Baena, F. M. (2009). Soft tissue traversal with zero net force: Feasibility study of a biologically inspired design based on reciprocal motion, *Robotics and Biomimetics, 2008. ROBIO 2008. IEEE International Conference on*, pp. 80–85.
- Peter Thomas, M. P. L. (2009). Ultrasonic Drill Tool (UDT) & Rock Abrasion Tool (RAT), *Mechanisms Final Presentation Days and Tribology Forum 2009*.
- Quicke, D., Leralec, A. & Vilhelmsen, L. (1999). Ovipositor structure and function in the parasitic hymenoptera with an exploration of new hypotheses, *Atti dell'Accademia Nazionale Italiana di Entomologia* 47: 197–239.
- Rahman, M., Fitton, M. & Quicke, D. (1998). Ovipositor internal microsculpture in the Braconidae (Insecta, Hymenoptera), *Zoologica Scripta* 27(4): 319–332.
- Richter, L., Coste, P., Gromov, V. & Grzesik, A. (2004). The mole with sampling mechanism (MSM)–Technology development and payload of beagle 2 mars lander, *Proceedings, 8th ESA Workshop on Advanced Space Technologies for Robotics and Automation (ASTRA 2004), Noordwijk, The Netherlands, November*, pp. 2–4.
- Richter, L., Coste, P., Gromov, V., Kochan, H., Nadalini, R., Ng, T., Pinna, S., Richter, H. & Yung, K. (2002). Development and testing of subsurface sampling devices for the Beagle 2 lander, *Planetary and Space Science* 50(9): 903–913.
- Richter, L., Coste, P., Gromov, V., Kochan, H., Pinna, S. & Richter, H. (2001). Development of the “planetary underground tool” subsurface soil sampler for the Mars express “Beagle 2” lander, *Advances in Space Research* 28(8): 1225–1230.
- Schneider, A., Frasson, L., Parittotokkaporn, T., Rodriguez y Baena, F., Davies, B. & Huq, S. (2008). Microfabrication of Components for a Novel Biomimetic Neurological Endoscope, in S. Dimov & W. Menz (eds), *In: International Conference on Multi-Material Micro Manufacture, 4th, Cardiff, UK, September 9-11, 2008, Proceedings*, Whittles Publishing Ltd.
- Schneider, A., Frasson, L., Parittotokkaporn, T., Rodriguez y Baena, F., Davies, B. & Huq, S. (2009). Biomimetic microtexturing for neurosurgical probe surfaces to influence tribological characteristics during tissue penetration, *Microelectronic Engineering*.
- Scott, G. & Saaj, C. (2009). Measuring and Simulating the Effect of Variations in Soil Properties on Microrover Trafficability, *AIAA Space 2009 Conference and Exposition. Pasadena, CA, USA*.
- Seiferlin, K., Ehrenfreund, P., Garry, J., Gunderson, K., Hütter, E., Kargl, G., Maturilli, A. & Merrison, J. (2008). Simulating Martian regolith in the laboratory, *Planetary and Space Science*.

- Skelley, A., Scherer, J., Aubrey, A., Grover, W., Ivester, R., Ehrenfreund, P., Grunthaner, F., Bada, J. & Mathies, R. (2005). Development and evaluation of a microdevice for amino acid biomarker detection and analysis on Mars, *Proceedings of the National Academy of Sciences* **102**(4): 1041–1046.
- Steltzner, A., Kipp, D., Chen, A., Burkhart, D., Guernsey, C., Mendeck, G., Mitcheltree, R., Powell, R., Rivellini, T., San Martin, M. et al. (2006). Mars Science Laboratory entry, descent, and landing system, *2006 IEEE Aerospace Conference*, p. 15.
- Van Winnendael, M., Gardini, B., Roumeas, R. & Vago, J. (2005). The ExoMars Mission of ESA's Aurora Programme, ASCE.
- Vincent, J. & King, M. (1995). The mechanism of drilling by wood wasp ovipositors, *Biomimetics (USA)* .
- Zacny, K., Quayle, M., McFadden, M., Neugebauer, A., Huang, K. & Cooper, G. (2002). A novel method for cuttings removal from holes during percussive drilling on Mars, *RASC-AL (Revolutionary Aerospace Systems Concepts-Academic Linkage): 2002 Advanced Concept Design Presentation*, p. 107-121 .

Biomimetic Architectures for Tissue Engineering

Jianming Li, Sean Connell and Riyi Shi
Purdue University
USA

1. Introduction

Within the human body, there is a vast array of uniquely arranged biologic structures. The elegance of these geometries is only matched by their equally varied functional sophistication. The harmony at which all components operate is truly awe-inspiring and from an engineering perspective, daunting to replicate. Yet in depth analysis of body tissues reveals a unique story. Many complex hierarchal structures can be deconstructed into simple recurring forms. Two ubiquitous geometries native to soft tissue are fibrillar networks and thin walled tubules. For instance, much of the extracellular matrix (ECM) that lends mechanical support to cells and tissues are fibrillar in nature. Vessels involved in either fluid transport or filtration are also high aspect ratio tubes of varying diameters. Furthermore, fibrillar and tubular themes are even found in hard tissues such as bone and cartilage.

In this chapter, we describe how researchers are synthetically recreating three-dimensional matrix analogs for regenerative medicine. We first highlight the complexities and nuances of real tissue and discuss the challenges in designing, fabricating and implementing biomimetic scaffolds for implantation. Applications of state of the art research pertaining to soft tissues and stem cell work will also be examined. We finally address current technological shortcomings and provide strategies for recreating function-specific tissue/organ systems with appropriate biophysical parameters

1.1 Structure-Function Relationships

The unique architectures found in biology have been evolutionarily shaped to perform particular tasks and this marriage between form and function is well manifested in the human body. For example, the layout of the nervous system is closely tied to cellular specialization. Neurons that perform signal integration are endowed with complex, multi-dendritic processes, while transmission neurons have axons that span several meters in length in some mammals. A similar undercurrent is observed in the circulatory system, where the biconcave geometry of red blood cells is optimized to facilitate oxygen exchange, mobility in a fluid medium and clotting (Wang, Pan et al. 2009; Wang, Gao et al. 2009). Injury or pathology can affect cell morphology, inducing problematic physiologic abnormalities. In the discussion of blood, conditions such as sickle cell anemia can alter flow dynamics and cause unwanted blood clots.

The forces at work that determine cell shape are also evident in the extracellular matrix (Figure 1). Mechanically mediated adaptation occurs frequently in the musculoskeletal system. For instance, bone undergoes a structural remodeling process in the presence or absence of loading (Wolffe's law). Recent studies into bone's nanostructure also reveal heterogeneous patterns that may impart load dispersal properties (Ortiz 2009). The axial hierarchal organization of supporting ligaments and tendons also reflect their functional role. Much like cables, these aligned elastic tissues are well suited to bearing tensile loads (Frank 2004). We emphasize that biologic structure-function relationships exist at all length scales- even down to the nanometer level of DNA and proteins.

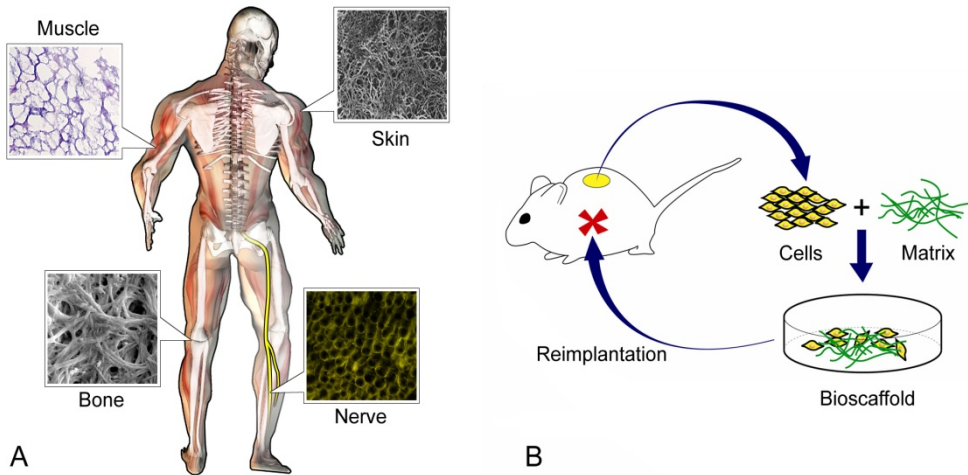


Fig. 1. (A) Many body tissues depict fibrillar and tubular thematic elements. Muscle and skin cross sections reprinted with permission (Singelyn, DeQuach et al. 2009) and (Chen, Ho et al. 2004), respectively. Bone micrograph courtesy of O. Akkus. (B) Tissue engineering aims to restore function by repair, replacement or regeneration of damaged tissue. Cellular therapies involve harvesting healthy cells (adult or stem cells), culturing in a matrix and subsequent reimplantation into the damaged site. Alternatively, acellular (cell free) biomatrices may also be used to promote endogenous healing and remodelling.

1.2 The Role of Architecture in Tissue Engineering

Like most machines, components of the body eventually fail. Disease states, mechanical insult or normal wear may initiate the process of tissue degradation. The goal of tissue engineering is the restoration of lost function. Recently, cellular therapies have drawn significant interest, with stem cell research at the forefront of biomedical innovation. The pluripotent nature of stem cells makes them attractive candidates for regenerating all organ types. In contrast, acellular treatments designed to promote endogenous wound healing are also tenable strategies. However, regardless of the therapeutic regime it has become evident that matrix architecture plays an active role in tissue remodeling. The matrix contributes to how a cell transduces input from the external physical environment into biochemical signals that dictate cell response. A wealth of evidence has shown that cells grown in 3-D culture

systems demonstrate altered morphologies and gene expression compared to traditional 2-D platforms. Affecting the cell's physical environment may be used to ultimately control cell behavior and fate (Sands and Mooney 2007; Ingber 2008). Thus, the structure-function relationships that govern normal physiology are equally instrumental during the repair process. This dogma underpins tissue engineered replacements: restorative devices should emulate the natural order of the body.

Interestingly, while there are countless architectural schemes *in vivo*, two elements found in high frequency are fibrils and tubules. Most body tissues are hierarchal fibrillar or tubular arrangements. It is the variation in size, organization and composition of these simple building blocks that dictates the wide range of observed mechanical and biophysical properties (Figure 2). Replicating these diverse structures from the macroscopic to the nanoscale level is a significant scientific undertaking. However, advancements in micro and nanofabrication have paved the path for constructing biologic analogs beginning at the molecular level. In the following sections, we discuss unique manufacturing methods capable of producing ECM-like architectures. Specifically, we emphasize emergent manufacturing techniques such as electrospinning, phase separation and nanoscale self-assembly. These methods provide invaluable tools for developing the next generation of biointegrative implants.

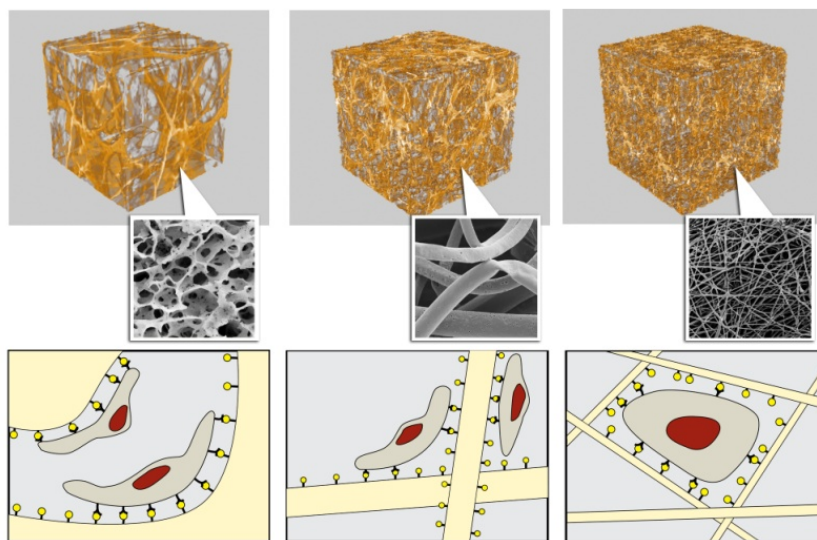


Fig. 2. The role of length scales on cellular behavior. As geometric features become smaller, changes in cell morphology and fate can be observed. Micrometer based lengths induce more 2-D (planar) geometries, while cells are more spatially interactive on 3-D nanoscaled meshes. Adapted from (Stevens and George 2005).

1.3 Emulating Nature: Fabrication of Micro and Nanoscale Architectures

1.3.1 Electrospinning

Electrospinning is a fabrication technique that utilizes electrostatic forces to draw continuous fibers from a viscoelastic medium. The process of electrospinning is quite archaic, dating back to 1902. However, in the mid 1990's electrospinning was resurrected in the laboratory as many researchers recognized its utility in the growing nanoengineering discipline (Doshi and Reneker 1995). Since then, a multitude of materials ranging from synthetic and natural polymers, ceramics, semiconductors, biomacromolecules and even cell suspensions have been electrostatically spun (Pham, Sharma et al. 2006; Jayasinghe, Irvine et al. 2007). Resultant fibers can be as large as 10 μ m or as small as 5nm. The material versatility, ease of manufacture, combined with fibers within biologically relevant length scales makes electrospinning a highly attractive method for scaffold production.

The fundamental principle guiding electrospinning is uniaxial stretching of a fluid. Figure 3 describes a typical laboratory configuration for electrospinning. A high voltage (5-30kV) is applied to a dissolved polymer solution. The repulsive force in the fluid accumulates until at a critical point, the electrostatic repulsion overcomes surface tension and a bead erupts from the spinneret (tip). The exiting jet soon enters a dynamic instability phase, which is marked by a chaotic swirling motion. Continued elongation of the jet coincides with solvent evaporation and the fluid stream eventually lands on the grounded collector plate. At this point, the charges dissipate and the fiber solidifies/cures.

The dynamics of the spray jet is a well studied phenomenon and computational models have been made to describe the thinning event. Variables such as viscosity, conductivity, voltage, tip to collector distance and humidity can have an effect on fiber morphology. Details for these can be found elsewhere (Rutledge and Fridrikh 2007). Since electrospinning generates shear stresses within the thinning jet, large scale alignment at the molecular level can be achieved (Stephens, Fahnestock et al. 2005).

One of the primary challenges facing electrospinning is the control of architecture. Since the spinning process is predominately chaotic, the final mat of fiber is unwoven and randomly oriented. However, multiple strategies have been devised to fabricate hierarchal or oriented fibrils. These include focusing of the falling jet with external electric fields or modifications to the collecting plate. For example, one technique used for obtaining aligned fibers is the placement of a rotating disc/drum as the collector (Figure 3). Electrospun fibers are deposited on the edge of the disc, with alignment being parallel to the edge width. Electrospinning may also be used to coat various shapes such as tubes for cardiovascular applications. Alternatively, Xia and co-workers developed a unique split plate collector system to create aligned fibers over a span of several centimeters (Li, Wang et al. 2004). If alternating split plates are used, the ground can be cycled between each electrode pair, creating layer by layer stacked mats of orthogonal alignment (Xie, Macewan et al. 2009).

Others have also used field assisted approaches to create braided fibers (Theron, Zussman et al. 2001). These particular structures have promise in use for axially loaded tissue such as ligaments and tendons. Coaxial spinning with two concentric spinnerets has also shown potential for creating composite fibers (Jiang, Hu et al. 2005; McCann, Marquez et al. 2006). In this process a hybrid fiber with a different core material can be produced. The core can be retained or selectively dissolved to fashion microtubular entities.

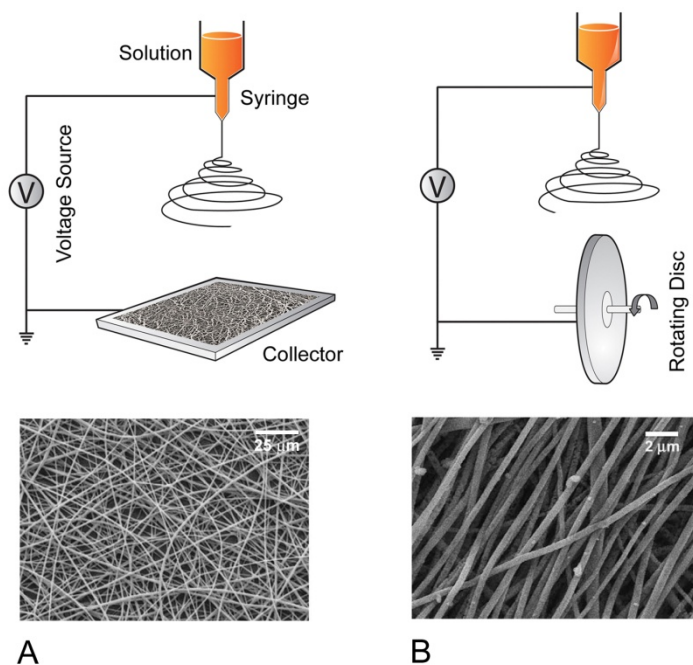


Fig. 3. (A) Schematic depiction of the electrospinning process. A charged solution is drawn from the tip and the residual random fibers collect on a grounded plate. (B) A spinning disc technique commonly employed to create aligned electrospun fibers. Fibers aggregate on the disc edge. Corresponding random and aligned fibers produced from shown setup. Reproduced with permission from (Prabhakaran, Venugopal et al. 2009) and (Lee, Bashur et al. 2009).

1.3.2 Phase Separation and Selective Dissolution

Phase separation is a unique process that has the capacity to form both fibrillar and tubular constructs. There are multiple variations to phase separation, but a common modality is solid-liquid phase extraction. One novel strategy involves creating a thermal gradient to separate two constituent phases. For example, Ma and Zhang used this method to manufacture nanofibrous foams and networks (Ma and Zhang 1999). In this process, the parent polymer was first dissolved in a solvent. The solution was then placed in a refrigerator to gel. Solvent exchange was carried out with distilled water and the subsequent compound frozen and freeze dried. Resultant fibrillar architectures showed fibril diameters between 50-500nm. Local porosity was high, reaching 98% in some cases. Fiber matrix properties were controlled primarily by the gelation temperature. The same group also manipulated this technique to form microtubular arrays. In this case, a dissolved polymer solution was laterally insulated and placed on a cold source. The uniaxial thermal gradient induced a directional precipitation of the dissolved polymer (Figure 4). The solid-liquid separated solution was subsequently freeze dried. Stokols and Tuszynski also used a uniaxial thermal gradient with agarose to form linear channels (Stokols and Tuszynski 2004). These channels were continuous for up to 1cm and had pore sizes (channel diameter)

on the order of 30-100 μm . These structures swelled in the presence of water due to hydrophilicity and resembled endogenous myotubes and endoneurial tubes.

Recently, Li et al. devised an inexpensive method to form single and aggregate high aspect ratio tubules with sacrificial sugar (Li, Rickett et al. 2009). Initially, sugar filaments formed from melt spinning were coated with a degradable polymer (PLLA). After polymer curing, the sugar core was dissolved with water, leaving a thin continuous tubular membrane. The final tubules also showed nanoscopic pores which are desirable for nutrient and waste diffusion. Multiple tube aggregates were made by fusion. The use of "cotton candy" as a core template was also employed by Bellan et al. for simulated microvasculature (Bellan, Singh et al. 2009). In this case, PDMS polymer was poured around long sugar filaments. The sugar was dissolved with water, leaving a solid PDMS block with embedded microtubes. The winding tubes were capable of supporting fluid media at physiologic flow rates.

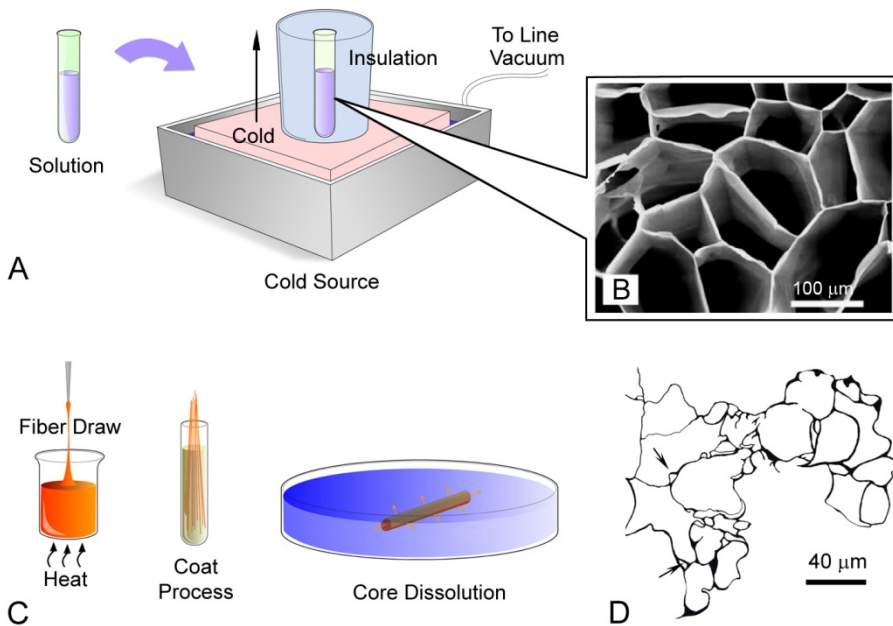


Fig. 4. (A) Diagram of thermal phase separation technique. A solution of dissolved polymer is placed on a cold source. The induced thermal gradient causes precipitation of the solute in a uniaxial fashion. Reprinted and adapted from (Stokols and Tuszynski 2004). (B) Corresponding microstructure of microchannels from phase separation (Stokols and Tuszynski 2004). (C) Depiction of selective dissolution for fabricating microchannels. Sucrose templates are coated with a polymer. The core is preferentially dissolved with another solvent. (D) Cross sectional images of microtubular geometries created by sacrificial templating. Reprinted with permission from (Li, Rickett et al. 2009).

One of the primary advantages of using phase separation approaches is the simplicity of the process. Phase separation generally requires minimal equipment, resources and the gamut of structures can range from nanoscale fibrils to micrometer tubes capable of sustaining

fluid flow. In addition to the basic underlying structure, additional pores or discontinuities may be imparted via particulate leaching. Thus, scaffolds with several orders of architectural complexity may be realized.

1.3.3 Self Assembly

Self assembly is a process that describes the spontaneous formation of material patterns or structures without external influence. The forces that govern the aggregation phenomenon are local molecular interactions such as electrostatic forces, hydrophobic interactions and hydrogen bonding (Tu and Tirrell 2004). Self assembly is a key concept in “bottoms up” nanofabrication, where structures are constructed from individual molecular units. Self assembly is a fundamental theme in nature and is responsible for simple or complex hierarchal shapes including lipid bilayers (micelles), DNA, proteins and viral capsids. Consequently, understanding the basic tenants of self assembly has given researchers insight into forming biocompatible supramolecular structures. The key in self-assembled structures is design of base units that have two distinguishing components: a segment for directing the aggregation process and a biologically active moiety that encodes cell-specific instruction (Tu and Tirrell 2004).

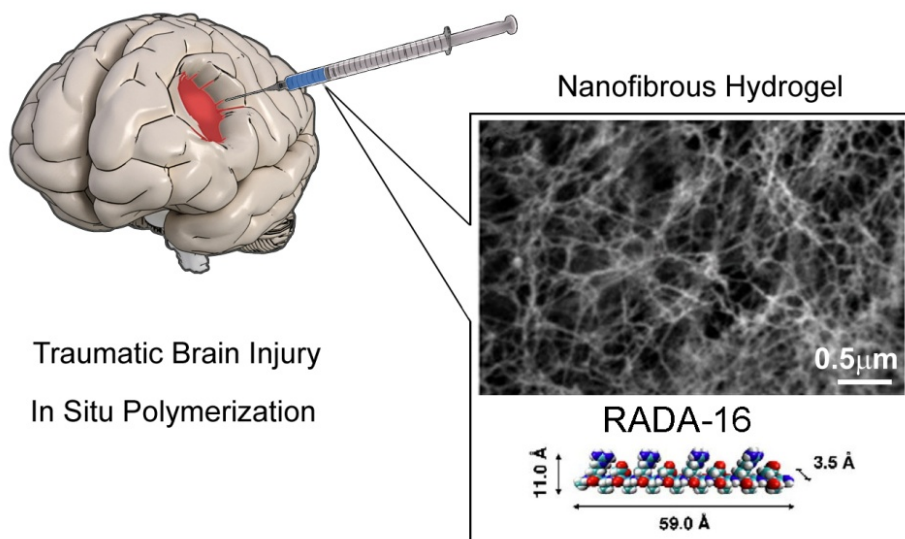


Fig. 5. *In situ* hydrogel polymerization for instances where significant soft tissue damage occurs. Inset shows the nanofibrillar arrangement of RADA-16 peptide amphiphiles. Reprinted with permission (Nagai, Unsworth et al. 2006).

Peptide amphiphiles (PA) are common building blocks for use in self assembly. This approach was first used to fabricate membranes composed of nanofibrillar meshes based on repeating amino acid ((Ala-Glu-Ala-Glu-Ala-Lys-Ala-Lys)₂) sequences (Zhang, Holmes et al. 1993). Recently, the same group developed an arginine, alanine, aspartate, and alanine (RADA-16) sequence that assembled into three-dimensional hydrogels composed of

nanofibrils (Figure 5). The primary base sequences were additionally functionalized with an osteogenic growth peptide and two other cell adhesion motifs via direct solid phase extension of the C-termini (Horii, Wang et al. 2007).

Similarly, Silva et al. incorporated a pentapeptide amino acid sequence (isolucineylsine-valine-alanine-valine, IKVAV) onto a hydrocarbon tail (Silva, Czeisler et al. 2004). The IKVAV epitope is found in laminin protein and enhances neural cell adhesion and growth (Chen 2003). A special glutamine residue was added to give the amphiphile a net negative charge at physiologic pH. Exposure to positive charges, such as from the cell medium or body fluid would trigger the polymerization event, causing the amphiphile to form a network of nanofibers. Other attributes of individual nanorods include high aspect ratios (micrometer length vs 5-8 nanometer diameter) and high IKVAV epitope density for cell interaction. Other designer hydrogels based on peptide amphiphile self assembly have also been created. Unique characteristics of hydrogels include high water content (99%), compatibility with *in situ* application and resemblance to natural ECM.

1.4 Application of Biomimetic Architectures

1.4.1 Vasculature

Blood vessels are a major constituent of the human cardiovascular system and function as a vehicle for metabolic and gaseous transport. In arteries, three layers exist. The outmost wall consists of fibroblasts embedded within a randomly aligned collagen type I matrix for structural support. Smooth muscle cells (SMC) surrounded by elastin fibers and collagen types I and III compose the elastic medial zone. Finally, the innermost layer is an endothelial (EC) monolayer rich in collagen type IV and elastin that provides a smooth surface for blood flow.

Atherosclerosis is a common cardiovascular disease characterized by the pathological reduction in arterial elasticity and narrowing of the arteries. Decreased diameter of the interior lumen subsequently leads to loss of circulation. Once blood flow is compromised, the preferred treatment option is vascular bypass surgery. Autologous replacement of damaged arteries frequently involves the internal mammary artery or the saphenous vein. However, such treatments yield donor site morbidity and are often unable to bridge large diameter vessels (Conte 1998). Alternative options using traditional synthetic grafts, including expanded polytetrafluoroethylene (e-PTFE) and woven polyethylene terephthalate (PET) fibers are suitable for medium (6-10mm) and large (>10 mm) vascular substitutes, but are not successful as small diameter prosthetics (Ma, Kotaki et al. 2005). Development of a small-diameter vascular graft capable of withstanding the immense environmental pressures of the circulatory system presents a significant challenge. Conquering this remaining obstacle is often seen as the Holy Grail of tissue engineering (Conte 1998).

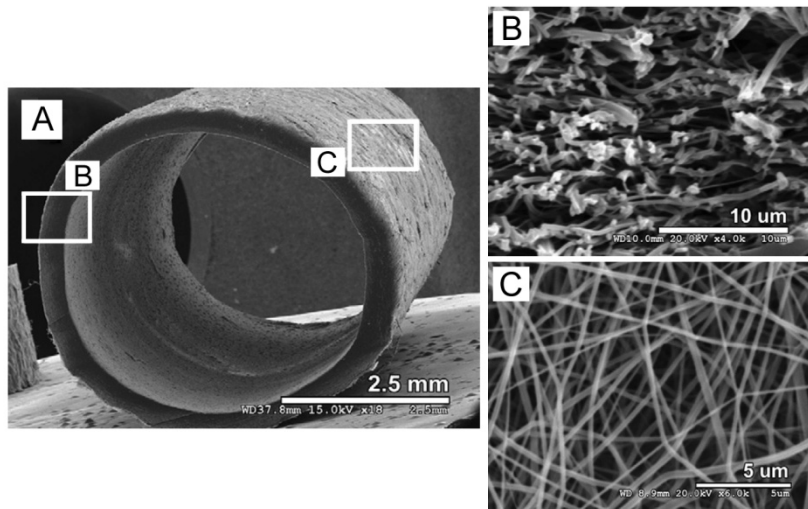


Fig. 6. Tissue engineered vascular grafts. (A) Gross overview of an electrospun composite scaffold composed of collagen type I and poly(ϵ -caprolactone) (PCL). (B) SEM image of the circumferential morphology (x4.0K) and (C) Exterior surface (x6.0K) (Lee, Liu et al. 2008).

New advancements in nanofiber-based scaffold production (i.e. electrospinning, phase separation and self-assembly) allow for the creation of grafts that imitate the molecular and structural properties of the vasculature ECM. For instance, Ramakrishna et al. developed a synthetic biodegradable aligned poly(L-lactide-co- ϵ -caprolactone) [PLLA-CL] nanofibrous scaffold (Mo, Xu et al. 2004; Xu, Inai et al. 2004; Xu, Inai et al. 2004). Aligned fibers produced a scaffold topography that mimicked the circumferential orientation of cells and fibrils found in the medial layer of arteries. When cultured with SMC and ECs, the scaffold promoted cell attachment and migration along the axis of the aligned nanofibers and demonstrated increased levels of cell proliferation when compared to an inert control. Integration of cells within the nanofibers formed a three-dimensional cellular network while maintaining phenotypic shape (Mo, Xu et al. 2004; Xu, Inai et al. 2004; Xu, Inai et al. 2004). Alternatively, Boland et al. produced a natural, three-layered vascular construct composed of collagen and elastin. Outer layers of the construct were seeded with SMC and FB with the interior lumen seeded with ECs. This cell seeded scaffold allows for natural tissue development in the injured site by promoting cell motility, proliferation and matrix deposition/remodeling (Matthews, Wnek et al. 2002). Figure 6 demonstrates a composite vascular system composed of poly(ϵ -caprolactone) (PCL) and collagen. The composite scaffolds exhibited adequate tensile strength (4 ± 0.4 MPa), and elasticity (2.7 ± 1.2 MPa) for appropriate physiological performance. Composite scaffolds aided the formation of a confluent outer layer and interior lumen when seeded with smooth muscle cells and endothelial cells, respectively (Lee, Liu et al. 2008).

Similar tri-laminate vascular constructs were developed using cell self-assembly as reported by L'Heureux et al. (L'Heureux, Paquet et al. 1998; L'Heureux, McAllister et al. 2007). Intact layers of human vascular cells were cultured past confluency to form a uniform cell sheet with a naturally produced randomly aligned ECM. The sheet was then rolled over a support

mandrel to create a tubular arrangement. An outermost layer was constructed in the same fashion by placing a sheet of fibroblasts on top of the previous SMC layer. Further maturation of the tube allowed for prolific ECM production before the interior lumen was seeded with ECs (L'Heureux, Paquet et al. 1998; L'Heureux, McAllister et al. 2007).

1.4.2 Ligament and Tendon Tissue Engineering

Ligaments are comprised of dense, parallel collagen (types I and III) bundles that serve as load bearing tissues. Fibroblasts preferentially aligned along the longitudinal axis of the crosslinked bundles regulate mechanical attributes through matrix remodeling. The high tensile strength of this configuration and elastic properties of the collagen fibrils allow for controlled movement and joint stability.

Mechanical trauma disrupting the integrity of the ligament produces significant joint dysfunction resulting in abnormal kinematics and potentially long term degenerative joint diseases (Lin, Lee et al. 1999). Conventional reconstructive surgical procedures using autografts have had limited success (Arnoczky, Tarvin et al. 1982). Major shortfalls include donor site morbidity, stress shielding and tendonitis (Lee, Shin et al. 2005).

Ligament tissue engineering is a viable alternative to surgical approaches. However, several challenges remain in the realization of scaffolds capable of withstanding the large cyclic loads. Nanofiber manipulation techniques provide promising solutions by replicating the natural orientation and spatial distribution of molecules and cells within an engineered construct.

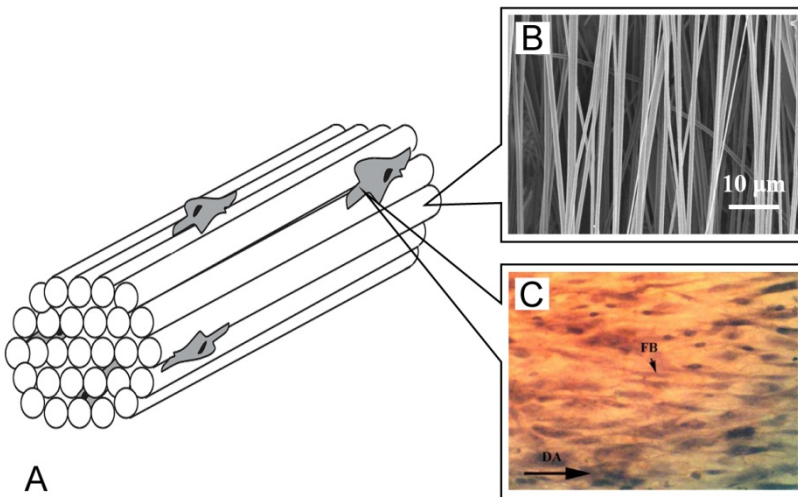


Fig. 7. Ligament Engineering (A) Ligament schema showing parallel fibers with adhered fibroblasts (Doroski, Brink et al. 2007). (B) SEM micrograph of aligned PU fibers (500 to 800 nm) (C) cultured with fibroblasts (FB) indicating the direction of alignment (DA) along aligned fibers (Lee, Shin et al. 2005).

For example, using a modified electrospinning process, Lee et al. collected polyurethane (PU) nanofibers on a rotating collecting target to produce a uniformly aligned matrix as

shown in Figure 7. Fibers were then seeded with human ligament fibroblasts (HLFs) to investigate the affects of fiber alignment on cell behavior. Results demonstrated cellular alignment with fiber orientation and increased matrix deposition under longitudinal load compared to HLFs seeded on randomly oriented fibers (Lee, Shin et al. 2005).

An alternative method for controlled collagen assembly was proposed by Akkus and collaborators. The novel electrochemical technique passed electric current through a dialyzed collagen solution placed between two parallel electrodes to promote molecular migration. This process allowed for the generation of highly oriented and densely packed elongated collagen bundles ranging between 50-400 μ m in diameter and 3-7cm in length. Polarized imaging was used to assess collagen orientation and fibrillar assembly as shown in Figure 8. Electrochemically oriented collagen bundles showed color patterning similar to natural tendon fibers, indicating a comparable degree of fiber orientation. Furthermore, the synthetically aligned fibers exhibited a 30-fold increase in mechanical strength compared to randomly oriented collagen fibers. Mechanically robust and highly oriented bundles formed using this method highlight a promising tissue engineering approach for tendon and ligament repair (Cheng, Gurkan et al. 2008).

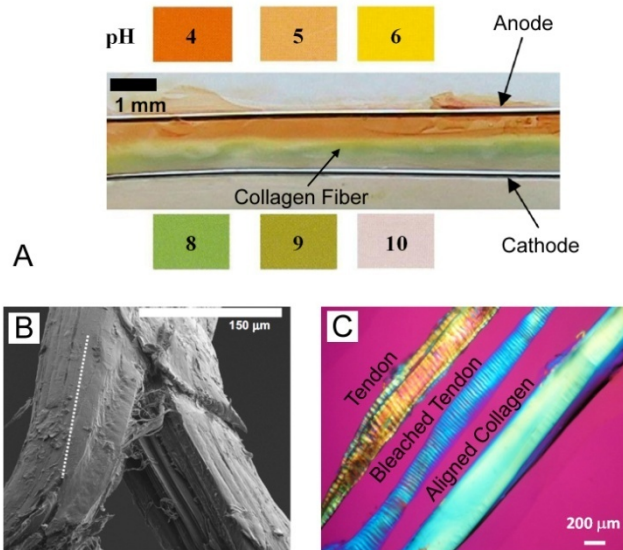


Fig. 8. Synthetic alignment of collagen fibers using an electrochemical technique. (A) Electrochemical cell with collagen solution between two parallel electrodes and color coded pH gradient required for rotational alignment. (B) SEM image of an intentionally split collagen bundle, indicating uniform orientation and alignment along the longitudinal axis (C) Polarized image of bleached native tendon and electrochemically aligned collagen construct. Both tissues depict the blue retardation coloring, indicating comparable fiber orientation (Cheng, Gurkan et al. 2008).

1.4.3 Skin

Skin is the largest organ in the body and consists of two main layers: dermis and epidermis. The keratinized stratified epidermis is the primary cell layer while the dermal zone provides structural support and nutrient renewal. Skin engineering has a history spanning 100 years yet autografts remain the gold standard for treating full thickness skin injuries. A design goal for therapeutic skin substitutes resides in emulating the skin's stratified composition. Since the dermal layer is a dense network of collagen and elastin, porous fibrillar constructs make excellent candidates as a substrate for skin reconstruction. Indeed, this approach has been used since the 1970's as the basis for artificial skin (Yannas and Burke 1980). The first skin constructs used a scaffold composed of a collagen base with added glycosaminoglycans to promote wound healing (Schulz, Tompkins et al. 2000). An additional silicone membrane ("pseudo-epidermis") was overlaid on the collagen layer to function as a heat and moisture barrier. Variations in this bilayered theme are presently employed in skin graft products (Falanga and Sabolinski 1999).

However, a significant drawback in artificial skin is the lack of vasculature, pigmentation and anti-bacterial properties. To circumvent these deficiencies, scientists are using either stem cells or genetically modified cells in combination with biomatrices. The goal is to develop artificial skin fragments that are vascularised and have the ability to ward off infection, sweat and protect against UV radiation. In one report, researchers transfected keratinocytes to secrete an antimicrobial protein (Smiley, Gardner et al. 2007). Bacterial growth was suppressed on these skin cultures, which suggests genetic manipulation to be a viable method for reducing post-operative infection. Alternatively, Katti et al. employed electrospinning to produce nanofibrous poly(lactide-coglycolide) membranes incorporating a broad spectrum antibiotic (Katti, Robinson et al. 2004).

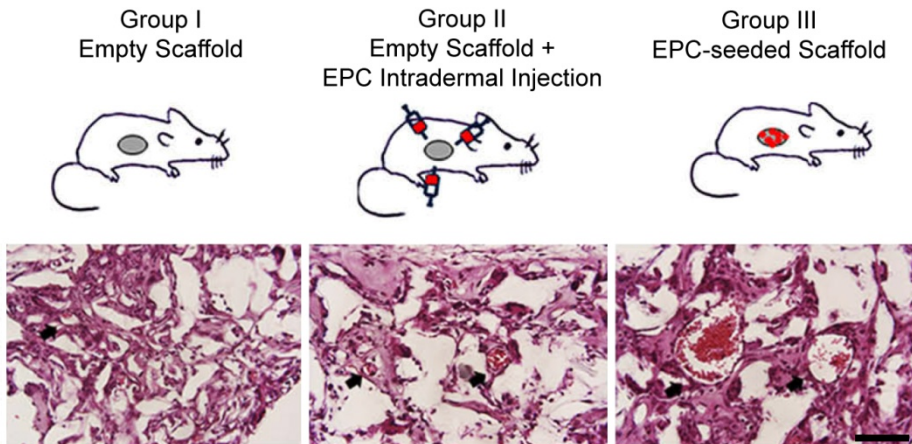


Fig. 9. Schematic showing the presence of endothelial progenitor cells in a mouse model of skin trauma (Kim, Han et al. 2009). Empty (cell free) scaffolds showed some endogenous remodeling and blood vessel formation. Injection of EPCs improved the degree of vascularization while pre-seeded scaffolds provided the best results. Reprinted with permission.

To recreate other salient features of skin, research groups have suggested using bulb stem cells residing in hair follicles to reproduce epidermis (Larouche, Tong et al. 2008). Similarly, Kim et al harvested endothelial progenitor cells (EPCs) for use in a mouse skin excision injury model (Figure 9). Experimental data showed EPC seeded scaffolds promoted angiogenesis and microvasculature at the wound site (Kim, Han et al. 2009). Newer developments in skin technology have added combinations of fibroblasts, keratinocytes or epithelial cells into biodegradable scaffolds (Priya, Jungvid et al. 2008; Schulz, Tompkins et al. 2000). After a designated culture time, the cells populate and remodel the matrix, creating a rudimentary living skin. Other studies on substrate architecture shed light on optimum fibril diameters and packing density for enhancing collagen expression (Kumbar, Nukavarapu et al. 2008) microbial infiltration (Powell and Boyce 2008).

The collective cellular and scaffolding data suggests a promising future for patients with severe skin damage. The combination of appropriately modified physical substrates coupled with cell seeding may lead to skin products that provide necessary protection while simultaneously reducing the appearance of scar (Metcalf and Ferguson 2007).

1.4.4 Nervous system

Neurons are highly ordered cells specializing in a variety of integrative and signal transmission functions. When damaged, neurons have the intrinsic ability to regenerate, although the degree of regeneration is heavily dependent upon the local microenvironment. In the central nervous system (CNS) damaged neurons undergo a form of abortive regeneration. Multiple avenues are being pursued to coax adult neurons to recapitulate developmental processes (Rossignol, Schwab et al. 2007; Ruff, McKerracher et al. 2008). In contrast, peripheral nervous system (PNS) axons readily sprout and extend after injury. However, the quality of regeneration is lacking due to insufficient guidance cues (Lundborg 2000). It has been postulated that in addition to biochemical signals, physical guidance may further aid and direct the regeneration process.

For treating brain and spinal cord injuries hydrogels have been proposed. Hydrogels form a loose network of fibers representative of the endogenous CNS matrix. For example, Silva et al. (Silva, Czeisler et al. 2004), used a pentapeptide IKVAV sequence mounted onto a hydrophobic tail to create self assembling peptide amphiphiles. These amphiphiles directed differentiation of neural progenitor cells while inhibiting astrocyte differentiation *in vitro*. Additional investigation using a spinal cord compression model showed IKVAV nanofibers reduced glial scar formation, cell death and encouraged migration of oligodendrocytes into the implant region (Tysseling-Mattiace, Sahni et al. 2008).

In another study, peptide amphiphiles consisting of RADA16 were used to successfully restore vision in an optic nerve guinea pig animal model (Ellis-Behnke, Liang et al. 2006). In this case, the peptide hydrogel created a permissive environment that promoted neural tissue bridging of severed tracts. Other studies with hydrogels have shown promising outcomes. Stokols et al. reported a unique agarose guidance scaffold consisting of long linear channels (Stokols and Tuszynski 2004). These constructs had pore diameters (channels) of $119 \pm 26 \mu\text{m}$ and were capable of sustained growth factor release. Follow-up assessment of the scaffolds in a spinal cord injury paradigm showed organized axonal regeneration through the agarose channels (Stokols and Tuszynski 2006).

In contrast to the brain, nerves within the PNS have a unique global structural arrangement. Peripheral nerve axons are longitudinally oriented, with individual axons ensheathed in

collagen based tubes (endoneurial tube). Following axotomy, these continuous tubes facilitate the regeneration process by providing a physical template that directs axon extension. Imitating this structural feature is therefore vital for encouraging outgrowth and reducing fiber misdirection (Sumner 1990).

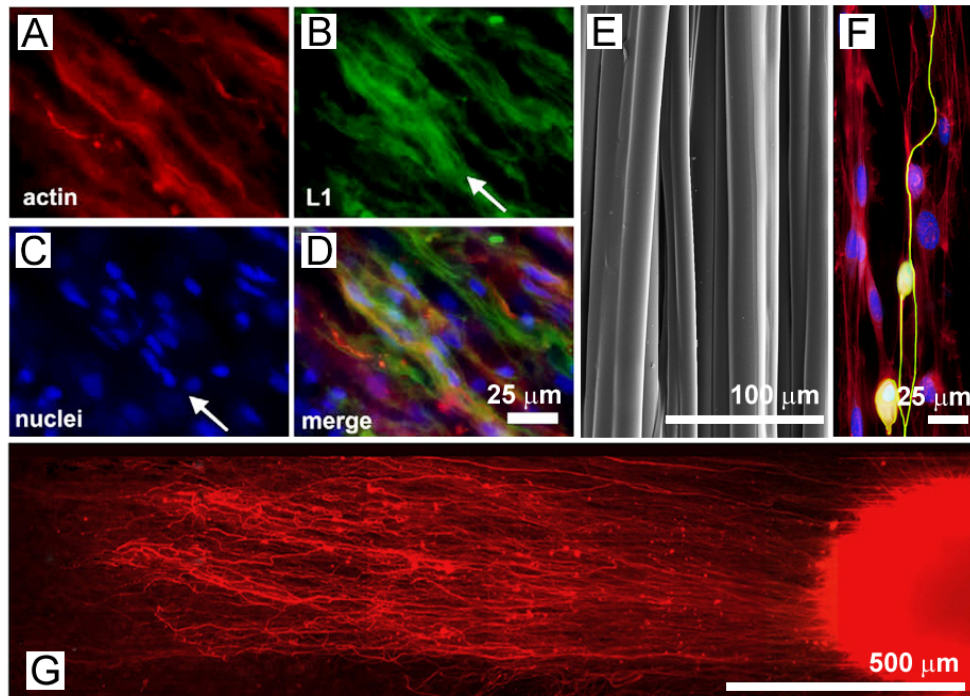


Fig. 10. (A)-(D) Fluorescent longitudinal sections of rat sciatic nerve and the structural arrangement. Reprinted from (Ribeiro-Resende, Koenig et al. 2009). (E) Microtubular polymeric arrays which mimic the oriented nature of peripheral nerves. (F) Dorsal root ganglia neurons and Schwann cells co-cultures align on tubules depicted in (E). Reprinted with permission from (Li, Rickett et al. 2009). (G) Dorsal root ganglia neurons extend along electrospun nanofibers (Kim, Haftel et al. 2008).

Conduits containing aligned electrospun fibers have been used to mimic the function of endoneurial tubes (Figure 10). For instance, Kim et al. created a 17mm gap defect in rat sciatic nerve and used an artificial conduit to bridge the damage site (Kim, Haftel et al. 2008). Acrylonitrile-co-methylacrylate (PAN-MA) polymer was spun into aligned or unaligned configurations. Both types of conduits were implanted and after 16 weeks, animals were sacrificed for analysis. Histological and functional data showed superior axonal regeneration in animals receiving the aligned fiber conduits. This study showed that for the PNS, aligned fiber morphology can be used to facilitate the regeneration process. Moreover, Li et al. used microtubular arrays to emphasize oriented Schwann cell and neurite alignment *in vitro* (Li, Rickett et al. 2009). The microtubes supported cell growth on the exterior surface and within the lumen. Other investigations have demonstrated

improved regeneration on polymer filaments in long gap injuries with rats (Cai, Peng et al. 2005).

1.5 Future Directions and Conclusion

Bioengineering has evolved from the simple notion of biocompatibility to an age which values intelligent materials for providing cell-specific instructional cues. One of these signaling mechanisms is physical and is intimately tied to cell mechanotransduction. Indeed, the local spatial arrangement of the extracellular environment plays a pivotal role in governing morphogenesis, migration and differentiation. Thus, understanding how nano and microscale architectures influence cell response and the subsequent macroscopic properties is fundamental in developing restorative constructs.

Recent manufacturing innovations have yielded tissue analogs approximating the natural ECM at multiple length scales. However, significant challenges remain. In terms of the three-dimensional aspect, most artificial scaffolds are relatively homogeneous and do not represent the stratified or graded physiochemical properties found *in vivo*. Therefore, a design challenge for future 3-D structures lies in implementation of zonal transitions. Such scaffolds would encourage heterotypic cell interactions essential to the constructive remodeling process. Additionally, we now recognize that the ECM is more than a framework for cell residence. Natural ECM contains multiple support proteins and biochemical factors that maintain local dynamic homeostasis, reinforce mechanical properties and direct wound healing (Badylak 2007). Incorporating such compounds synergistically within the material architecture is critical for optimum success.

Finally, stem cells and biomolecular delivery are inevitably going to play a larger role in regenerative medicine. Current investigations with stem cells have already demonstrated promise in various experimental injury models. New insights into controlling stem cell fate are necessary in realizing safe and effective therapies. Nonetheless, the confluence of cellular methods with biomimetic architectures bodes well for functional restoration of damaged or diseased tissues.

Acknowledgments

We would like to thank Michel Schweinsberg for his contributions in artwork.

2. References

- Arnoczky, S. P., Tarvin, G. B. & Marshall, J. L. (1982). Anterior Cruciate Ligament Replacement Using Patellar Tendon - an Evaluation of Graft Revascularization in the Dog. *Journal of Bone and Joint Surgery-American Volume* **64**(2): 217-224.
- Badylak, S. F. (2007). The extracellular matrix as a biologic scaffold material. *Biomaterials* **28**(25): 3587-93.
- Bellan, L. M., Singh, S. P., Henderson, P. W., Porri, T. J., Craighead, H. G. & Spector, J. A. (2009). Fabrication of an artificial 3-dimensional vascular network using sacrificial sugar structures. *Soft Matter* **5**: 1354-1357.
- Cai, J., Peng, X., Nelson, K. D., Eberhart, R. & Smith, G. M. (2005). Permeable guidance channels containing microfilament scaffolds enhance axon growth and maturation. *J Biomed Mater Res A* **75**(2): 374-86.

- Chen, R. N., Ho, H. O., Tsai, Y. T. & Sheu, M. T. (2004). Process development of an acellular dermal matrix (ADM) for biomedical applications. *Biomaterials* **25**(13): 2679-86.
- Chen, Z., Strickland, S. (2003). Laminin gamma1 is critical for Schwann cell differentiation, axon myelination, and regeneration in the peripheral nerve. *J Cell Biol* **163**(4): 889-899.
- Cheng, X. G., Gurkan, U. A., Dehen, C. J., Tate, M. P., Hillhouse, H. W., Simpson, G. J. & Akkus, O. (2008). An electrochemical fabrication process for the assembly of anisotropically oriented collagen bundles. *Biomaterials* **29**(22): 3278-3288.
- Conte, M. S. (1998). The ideal small arterial substitute: a search for the Holy Grail? *Faseb Journal* **12**(1): 43-45.
- Doroski, D. M., Brink, K. S. & Temenoff, J. S. (2007). Techniques for biological characterization of tissue-engineered tendon and ligament. *Biomaterials* **28**(2): 187-202.
- Doshi, J. & Reneker, D. H. (1995). Electrospinning process and applications of electrospun fibers. *J. Electrostat.* **35**: 151.
- Ellis-Behnke, R. G., Liang, Y. X., You, S. W., Tay, D. K., Zhang, S., So, K. F. & Schneider, G. E. (2006). Nano neuro knitting: peptide nanofiber scaffold for brain repair and axon regeneration with functional return of vision. *Proc Natl Acad Sci U S A* **103**(13): 5054-9.
- Falanga, V. & Sabolinski, M. (1999). A bilayered living skin construct (APLIGRAF) accelerates complete closure of hard-to-heal venous ulcers. *Wound Repair Regen* **7**(4): 201-7.
- Frank, C. B. (2004). Ligament structure, physiology and function. *J Musculoskelet Neuronal Interact* **4**(2): 199-201.
- Horii, A., Wang, X., Gelain, F. & Zhang, S. (2007). Biological designer self-assembling Peptide nanofiber scaffolds significantly enhance osteoblast proliferation, differentiation and 3-D migration. *PLoS One* **2**(2): e190.
- Ingber, D. E. (2008). Tensegrity-based mechanosensing from macro to micro. *Prog Biophys Mol Biol* **97**(2-3): 163-79.
- Jayasinghe, S. N., Irvine, S. & McEwan, J. R. (2007). Cell electrospinning highly concentrated cellular suspensions containing primary living organisms into cell-bearing threads and scaffolds. *Nanomed* **2**(4): 555-67.
- Jiang, H., Hu, Y., Li, Y., Zhao, P., Zhu, K. & Chen, W. (2005). A facile technique to prepare biodegradable coaxial electrospun nanofibers for controlled release of bioactive agents. *J Control Release* **108**(2-3): 237-43.
- Katti, D. S., Robinson, K. W., Ko, F. K. & Laurencin, C. T. (2004). Bioresorbable nanofiber-based systems for wound healing and drug delivery: optimization of fabrication parameters. *J Biomed Mater Res B Appl Biomater* **70**(2): 286-96.
- Kim, K. L., Han, D. K., Park, K., Song, S. H., Kim, J. Y., Kim, J. M., Ki, H. Y., Yie, S. W., Roh, C. R., Jeon, E. S., Kim, D. K. & Suh, W. (2009). Enhanced dermal wound neovascularization by targeted delivery of endothelial progenitor cells using an RGD-g-PLLA scaffold. *Biomaterials* **30**(22): 3742-8.
- Kim, Y. T., Haftel, V. K., Kumar, S. & Bellamkonda, R. V. (2008). The role of aligned polymer fiber-based constructs in the bridging of long peripheral nerve gaps. *Biomaterials* **29**(21): 3117-27.

- Kumbar, S. G., Nukavarapu, S. P., James, R., Nair, L. S. & Laurencin, C. T. (2008). Electrospun poly(lactic acid-co-glycolic acid) scaffolds for skin tissue engineering. *Biomaterials* **29**(30): 4100-7.
- L'Heureux, N., McAllister, T. N. & de la Fuente, L. M. (2007). Tissue-engineered blood vessel for adult arterial revascularization. *New England Journal of Medicine* **357**(14): 1451-1453.
- L'Heureux, N., Paquet, S., Labbe, R., Germain, L. & Auger, F. A. (1998). A completely biological tissue-engineered human blood vessel. *Faseb Journal* **12**(1): 47-56.
- Larouche, D., Tong, X., Fradette, J., Coulombe, P. A. & Germain, L. (2008). Vibrissa hair bulge houses two populations of skin epithelial stem cells distinct by their keratin profile. *FASEB J* **22**(5): 1404-15.
- Lee, C. H., Shin, H. J., Cho, I. H., Kang, Y. M., Kim, I. A., Park, K. D. & Shin, J. W. (2005). Nanofiber alignment and direction of mechanical strain affect the ECM production of human ACL fibroblast. *Biomaterials* **26**(11): 1261-1270.
- Lee, J. Y., Bashur, C. A., Goldstein, A. S. & Schmidt, C. E. (2009). Polypyrrole-coated electrospun PLGA nanofibers for neural tissue applications. *Biomaterials* **30**(26): 4325-35.
- Lee, S. J., Liu, J., Oh, S. H., Soker, S., Atala, A. & Yoo, J. J. (2008). Development of a composite vascular scaffolding system that withstands physiological vascular conditions. *Biomaterials* **29**(19): 2891-2898.
- Li, D., Wang, Y. & Xia, Y. (2004). Electrospinning Nanofibers as Uniaxially Aligned Arrays and Layer-by-Layer Stacked Films. *Adv. Mater.* **16**: 361-366.
- Li, J., Rickett, T. A. & Shi, R. (2009). Biomimetic nerve scaffolds with aligned intraluminal microchannels: a "sweet" approach to tissue engineering. *Langmuir* **25**(3): 1813-7.
- Lin, V. S., Lee, M. C., O'Neal, S., McKean, J. & Sung, K. L. P. (1999). Ligament tissue engineering using synthetic biodegradable fiber scaffolds. *Tissue Engineering* **5**(5): 443-451.
- Lundborg, G. (2000). A 25-year perspective of peripheral nerve surgery: evolving neuroscientific concepts and clinical significance. *J Hand Surg Am* **25**(3): 391-414.
- Ma, P. X. & Zhang, R. (1999). Synthetic nano-scale fibrous extracellular matrix. *J Biomed Mater Res* **46**(1): 60-72.
- Ma, Z. W., Kotaki, M., Yong, T., He, W. & Ramakrishna, S. (2005). Surface engineering of electrospun polyethylene terephthalate (PET) nanofibers towards development of a new material for blood vessel engineering. *Biomaterials* **26**(15): 2527-2536.
- Matthews, J. A., Wnek, G. E., Simpson, D. G. & Bowlin, G. L. (2002). Electrospinning of collagen nanofibers. *Biomacromolecules* **3**(2): 232-238.
- McCann, J. T., Marquez, M. & Xia, Y. (2006). Melt coaxial electrospinning: a versatile method for the encapsulation of solid materials and fabrication of phase change nanofibers. *Nano Lett* **6**(12): 2868-72.
- Metcalfe, A. D. & Ferguson, M. W. (2007). Tissue engineering of replacement skin: the crossroads of biomaterials, wound healing, embryonic development, stem cells and regeneration. *J R Soc Interface* **4**(14): 413-37.
- Mo, X. M., Xu, C. Y., Kotaki, M. & Ramakrishna, S. (2004). Electrospun P(LLA-CL) nanofiber: a biomimetic extracellular matrix for smooth muscle cell and endothelial cell proliferation. *Biomaterials* **25**(10): 1883-1890.

- Nagai, Y., Unsworth, L. D., Koutsopoulos, S. & Zhang, S. (2006). Slow release of molecules in self-assembling peptide nanofiber scaffold. *J Control Release* **115**(1): 18-25.
- Ortiz, G. (2009). Nanocontacts: The importance of being entangled. *Nat Mater* **8**(7): 541-2.
- Pham, Q. P., Sharma, U. & Mikos, A. G. (2006). Electrospinning of polymeric nanofibers for tissue engineering applications: a review. *Tissue Eng* **12**(5): 1197-211.
- Powell, H. M. & Boyce, S. T. (2008). Fiber density of electrospun gelatin scaffolds regulates morphogenesis of dermal-epidermal skin substitutes. *J Biomed Mater Res A* **84**(4): 1078-86.
- Prabhakaran, M. P., Venugopal, J. R. & Ramakrishna, S. (2009). Mesenchymal stem cell differentiation to neuronal cells on electrospun nanofibrous substrates for nerve tissue engineering. *Biomaterials* **30**(28): 4996-5003.
- Priya, S. G., Jungvid, H. & Kumar, A. (2008). Skin tissue engineering for tissue repair and regeneration. *Tissue Eng Part B Rev* **14**(1): 105-18.
- Ribeiro-Resende, V. T., Koenig, B., Nichterwitz, S., Oberhoffner, S. & Schlosshauer, B. (2009). Strategies for inducing the formation of bands of Bungner in peripheral nerve regeneration. *Biomaterials* **30**(29): 5251-9.
- Rossignol, S., Schwab, M., Schwartz, M. & Fehlings, M. G. (2007). Spinal cord injury: time to move? *J Neurosci* **27**(44): 11782-92.
- Ruff, R. L., McKerracher, L. & Selzer, M. E. (2008). Repair and neurorehabilitation strategies for spinal cord injury. *Ann N Y Acad Sci* **1142**: 1-20.
- Rutledge, G. C. & Fridrikh, S. V. (2007). Formation of fibers by electrospinning. *Adv Drug Deliv Rev* **59**(14): 1384-91.
- Sands, R. W. & Mooney, D. J. (2007). Polymers to direct cell fate by controlling the microenvironment. *Curr Opin Biotechnol* **18**(5): 448-53.
- Schulz, J. T., 3rd, Tompkins, R. G. & Burke, J. F. (2000). Artificial skin. *Annu Rev Med* **51**: 231-44.
- Silva, G. A., Czeisler, C., Niece, K. L., Beniash, E., Harrington, D. A., Kessler, J. A. & Stupp, S. I. (2004). Selective differentiation of neural progenitor cells by high-epitope density nanofibers. *Science* **303**(5662): 1352-5.
- Singelyn, J. M., DeQuach, J. A., Seif-Naraghi, S. B., Littlefield, R. B., Schup-Magoffin, P. J. & Christman, K. L. (2009). Naturally derived myocardial matrix as an injectable scaffold for cardiac tissue engineering. *Biomaterials* **30**(29): 5409-16.
- Smiley, A. K., Gardner, J., Klingenberg, J. M., Neely, A. N. & Supp, D. M. (2007). Expression of human beta defensin 4 in genetically modified keratinocytes enhances antimicrobial activity. *J Burn Care Res* **28**(1): 127-32.
- Stephens, J. S., Fahnestock, S. R., Farmer, R. S., Kiick, K. L., Chase, D. B. & Rabolt, J. F. (2005). Effects of electrospinning and solution casting protocols on the secondary structure of a genetically engineered dragline spider silk analogue investigated via Fourier transform Raman spectroscopy. *Biomacromolecules* **6**(3): 1405-13.
- Stevens, M. M. & George, J. H. (2005). Exploring and engineering the cell surface interface. *Science* **310**(5751): 1135-8.
- Stokols, S. & Tuszynski, M. H. (2004). The fabrication and characterization of linearly oriented nerve guidance scaffolds for spinal cord injury. *Biomaterials* **25**(27): 5839-46.

- Stokols, S. & Tuszynski, M. H. (2006). Freeze-dried agarose scaffolds with uniaxial channels stimulate and guide linear axonal growth following spinal cord injury. *Biomaterials* **27**(3): 443-51.
- Sumner, A. J. (1990). Aberrant reinnervation. *Muscle Nerve* **13**(9): 801-3.
- Theron, A., Zussman, E. & Yarin, A. L. (2001). Electrostatic field-assisted alignment of electrospun nanofibers. *Nanotechnology* **12**(384): 2001.
- Tu, R. S. & Tirrell, M. (2004). Bottom-up design of biomimetic assemblies. *Adv Drug Deliv Rev* **56**(11): 1537-63.
- Tysseling-Mattiace, V. M., Sahni, V., Niece, K. L., Birch, D., Czeisler, C., Fehlings, M. G., Stupp, S. I. & Kessler, J. A. (2008). Self-assembling nanofibers inhibit glial scar formation and promote axon elongation after spinal cord injury. *J Neurosci* **28**(14): 3814-23.
- Wang, T., Pan, T. W., Xing, Z. W. & Glowinski, R. (2009). Numerical simulation of rheology of red blood cell rouleaux in microchannels. *Phys Rev E Stat Nonlin Soft Matter Phys* **79**(4 Pt 1): 041916.
- Wang, X., Gao, W., Peng, W., Xie, J. & Li, Y. (2009). Biorheological properties of reconstructed erythrocytes and its function of carrying-releasing oxygen. *Artif Cells Blood Substit Immobil Biotechnol* **37**(1): 41-4.
- Xie, J., Macewan, M. R., Li, X., Sakiyama-Elbert, S. E. & Xia, Y. (2009). Neurite Outgrowth on Nanofiber Scaffolds with Different Orders, Structures, and Surface Properties. *ACS Nano*.
- Xu, C. Y., Inai, R., Kotaki, M. & Ramakrishna, S. (2004). Aligned biodegradable nanofibrous structure: a potential scaffold for blood vessel engineering. *Biomaterials* **25**(5): 877-886.
- Xu, C. Y., Inai, R., Kotaki, M. & Ramakrishna, S. (2004). Electrospun nanofiber fabrication as synthetic extracellular matrix and its potential for vascular tissue engineering. *Tissue Engineering* **10**(7-8): 1160-1168.
- Yannas, I. V. & Burke, J. F. (1980). Design of an artificial skin. I. Basic design principles. *J Biomed Mater Res* **14**(1): 65-81.
- Zhang, S., Holmes, T., Lockshin, C. & Rich, A. (1993). Spontaneous assembly of a self-complementary oligopeptide to form a stable macroscopic membrane. *Proc Natl Acad Sci U S A* **90**(8): 3334-8.

Lipid-based Biomimetics in Drug and Vaccine Delivery

Ana Maria Carmona-Ribeiro

*Biocolloids Lab, Instituto de Química, Universidade de São Paulo
Brazil*

1. Introduction

Lipids provide adequate matrixes for supporting important biomolecules (proteins, DNA, oligonucleotides and polysaccharides) on model surfaces (latex, silica, silicon wafers, self-assembled monolayers, metals, polymers, insoluble drugs, biological cells and viruses). For example, biomolecular recognition between receptor and ligand can be isolated and reconstituted by means of receptor immobilization into supported lipidic bilayers on silica. This is an overview on novel lipid-based assemblies for drug and vaccine delivery. Especial emphasis will be on assemblies produced from the cationic, synthetic and unexpensive lipid dioctadecyldimethylammonium bromide (DODAB). DODAB vesicles interacted with negatively charged prokaryotic or eukaryotic cells with high affinity changing the cell surface charge from negative to positive and reducing cell viability. DODAB effects on cell viability (bacteria, fungus and cultured mammalian cells) revealed its high antimicrobial activity and differential cytotoxicity *in vitro*. DODAB bilayer fragments were combined with drugs, biomolecules or particles producing novel lipid-based biomimetics to deliver difficult drugs or design vaccines. Hydrophobic drug granules or aggregated recombinant antigens became well dispersed in water solution via lipid adsorption on drug particles as nanocapsules or protein adsorption onto supported DODAB bilayers. In other instances, hydrophobic drug molecules were attached as monomers to borders of lipid bilayer fragments yielding drug formulations effective *in vivo* at low drug-to-lipid-molar ratio. Cationic biomimetic particles from silica or latex covered with one cationic lipid bilayer proved effective for adsorption, presentation and targeting of biomolecules *in vivo*. Thereby antigens were effectively presented to the immune system by particles at defined and controllable sizes. The problem of delivering drugs, antigens or biomolecules to their targets *in vivo* is central and multidisciplinary and biomimetic assemblies are a major asset to improved and less toxic drug and vaccine delivery.

2. The self-assembly of natural and synthetic lipids

Liposomes were first produced in 1965 by Alec Bangham in Cambridge UK and looked like myelin figures forming coherent and closed concentric spheroidal bilayers. From these early days up to the present, the development and diversification of the liposome "membrane"

model was astonishing (Bangham, 1983). Much of our present knowledge of membrane properties has been obtained with models prepared with phospholipids. From the late 1970's and early eighties, a variety of bilayer structures, formed by dialkyldimethylammonium halides (Kunitake et al., 1977) and other synthetic amphiphiles (Hargreaves & Deamer, 1978; Mortara et al., 1978; Czarniecki & Breslow, 1979; Suedholter et al., 1980) were introduced to mimic membrane properties and furnished unique opportunities to investigate structure-function relationships. Since the major requirement to form a supramolecular assembly of the bilayer type was an approximately cylindrical amphiphilic molecule with a geometric parameter between 0.5 and 1.0 (Israelachvili et al., 1977), not only natural phospholipids were prone to form bilayers. Structural and functional aspects of biological membranes were also copied in a variety of biomimetic systems. Bilayers were the preferential supramolecular assembly for several synthetic amphiphiles as dialkyldimethylammonium bromide or chloride (Kunitake et al., 1977), sodium dihexadecylphosphate (Mortara et al., 1978, Carmona-Ribeiro et al., 1991) and many other molecules (Furhhop & Fristch, 1986; Segota & Tezak, 2006). **Figure 1** shows closed unilamellar vesicles and bilayer fragments of synthetic lipids.

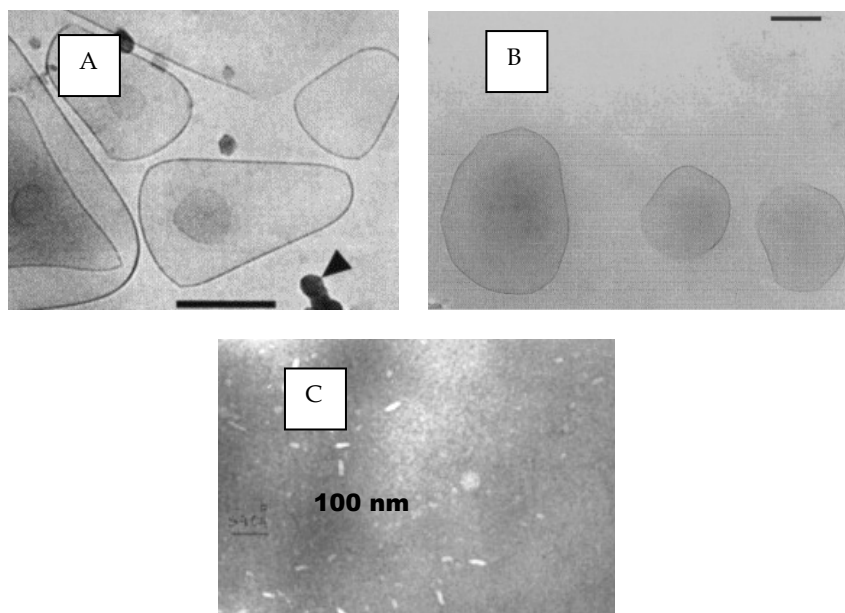


Fig. 1. Cryo-TEM images of DODAB vesicles obtained by vortexing (A) or extrusion (B) adapted with permission from Feitosa et al., 2006 and Lopes et al., 2008. Copyright 2006 and 2008 Elsevier. Ultrasonic vesicle disruption produced the bilayer fragments of DHP (C) adapted with permission from Carmona-Ribeiro et al., 1991. Copyright 1991 American Chemical Society. In (A, B) bars correspond to 100 nm whereas in (C) 1 μm = 100 nm.

In the eighties, new possibilities for the synthesis of bilayer-forming compounds were just appearing. Novel amphiphiles were similar to natural phospholipid systems regarding bilayer structure and physical state, range of sizes, preparation methods available, water

and solutes permeabilities and impermeability towards salts (Carmona-Ribeiro & Chaimovich, 1983; Carmona-Ribeiro et al. 1984). **Table 1** shows calculations of the geometric parameter for DODAB and DHP synthetic lipids.

Synthetic lipid	C/M	pH	v/nm^3	l/nm	a/nm^2	v/al
DODAB	0	6.5	0.969	2.3	0.66	0.64
	0.0001				0.54	0.79
	0.001				0.52	0.81
	0.01				0.52	0.81
DHP	0	7.8	0.862	2.1	0.425	0.99
	0.0001	7.3			0.427	0.985
	0.001	6.9			0.426	0.988
	0.01	6.2			0.421	1

Table 1. Calculation of the geometric parameter v/al for DODAC and DHP assuming that the area per monomer a is equal to the limiting area per monomer at 25 mN/m in DODAC and DHP monolayers. C is the NaCl concentration. Adapted with permission from Claesson et al., 1989. Copyright 1989 American Chemical Society.

Vesicles exhibited basically 4 different operational types of stability: physical (mechanical), chemical, colloidal, and biological stability (Lasic, 1994). In the physical sense, vesicles were thermodynamically unstable because the symmetric membrane is curved and the excess energy of each vesicle due to its curvature is $8\pi K$, where K is the elastic bending module of the membrane. Vesicles could be formed spontaneously only in the case of bilayers with very low values of K (Talmon et al., 1983). A vesicle, however, was a much more stable physical entity than a micelle since the residence lifetime of one single molecule in the vesicle and in the micelle were ca. 10^4 and 10^{-4} s, respectively (Israelachvili et al., 1977). The much higher residence lifetime of one single molecule in the vesicle explained why micelles or microemulsions droplets quickly disintegrated upon dilution whereas vesicles and liposomes made from phospholipids or double-chained synthetic amphiphiles (with very low values of critical micelle concentration) remained stable against dilution. Mechanical properties of bilayers as measured by the micropipette manipulation technique indicated that mechanical properties such as stretching modulus can be correlated with liposome physical stability (Bloom et al., 1991). For example, a general observation was that cholesterol made more cohesive bilayers. Mechanical stabilization may also be achieved by polymerization (Hueb et al., 1980) or by using lipids with fluorocarbon chains (Kunitake, 1992). The chemical stability of liposomes was low because acid/base catalyzed hydrolysis might pinch off one or both hydrocarbon chains from the backbone of the lipid (Traueble & Eibl, 1974) or oxidation might form cyclic peroxides at adjacent double bonds of the hydrocarbon chains resulting ultimately in the breakage of chains via lipoperoxidation (Chatterjee & Agarwal, 1988). Hydrolysis rate of soybean lecithin in liposomes was pH and temperature dependent being at highest at extreme pH values where acid-base catalysis was enhanced and/or at the highest temperatures tested (Gritt & Crommelin, 1992). Oxidation could be prevented by using saturated lipids and oxidation rates could be greatly reduced by adding antioxidants such as vitamin E or butylated hydroxytoluene (Lasic, 1994).

Synthetic amphiphiles such as DODAB and DHP that form bilayers certainly are chemically more stable than natural lipids (Fuhrhop & Fritsch, 1986). However, in contrast to natural lipids, which formed colloiddally stable bilayer membranes at 150 mM monovalent salt, pH 7.4, their colloid stability was low and their biological stability, ie their stability in the biological millieu, was poorly investigated (Carmona-Ribeiro & Chaimovich, 1983; Carmona-Ribeiro et al. 1984). Furthermore, cytotoxicity for some synthetic amphiphiles as DODAB had been reported to be high, an apparent drawback that found useful applications in the design of liposomal antimicrobials where the liposomal carrier was not at all innocuous: vesicles and/or bilayer fragments playing an antimicrobial role by themselves (Tapias et al., 1994; Campanhã et al., 1999). Fig. 2 illustrated the efficacy of DODAB bilayer fragments against *Escherichia coli*.

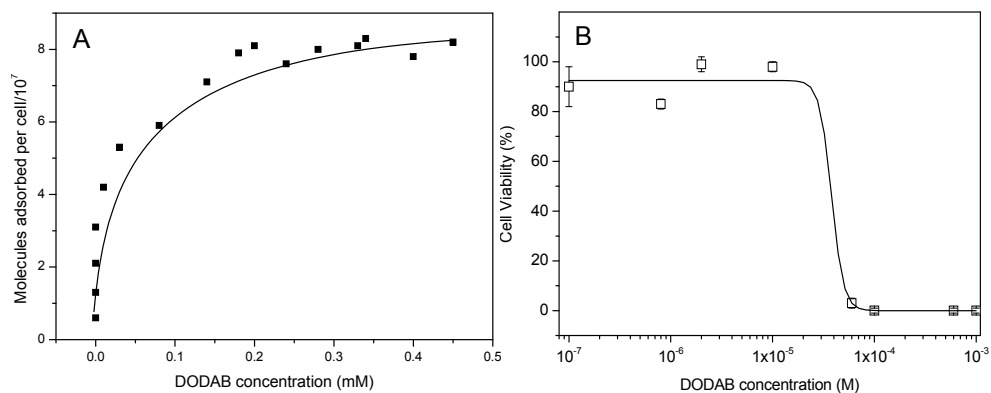


Fig. 2. Adsorption of DODAB BF onto *Escherichia coli* (A) profoundly affects *E. coli* viability (B). Adapted with permission from Campanhã et al., 1999, Tapias et al., 1994, Martins et al., 1997. Copyright 1994 and 1997 American Chemical Society.

In spite of its dose dependent-toxicity (Carmona-Ribeiro et al., 2006; Lincopan et al., 2006), DODAB capability to induce retarded hypersensibility, a marker for cellular immune responses, allowed DODAB to find important uses as an efficient immunoadjuvant mainly for veterinary uses but also in humans in a few instances (Gall, 1966; Dailey & Hunter, 1974; Hilgers & Snippe, 1992; Tsuruta et al., 1997; Klinguer-Harmour et al., 2002; Korsholm et al., 2007). Furthermore, we have been developing novel DODAB-based immunoadjuvants at reduced doses and toxicity.

3. Surface functionalization by lipids

Over the last two decades, lipid self-assembly at solid surfaces started to be better understood. In the eighties liposome adsorption was incidentally reported on clays, asbestos, Biobeads, gel filtration columns and membrane filters (Jackson et al., 1986). Lipid deposition from a lipidic vesicle onto a solid surface would be determined initially by the classical combination of a repulsive force arising from the interaction of the electrical double layers associated with the vesicle and the surface and the attractive dispersion force between the vesicle and the solid. Vesicles are not, however, permanent rigid structures, and

depending on their size and chemical composition and that of the aqueous medium they can distort, aggregate, disrupt and fuse with each other. Deposition of vesicles onto a solid surface could give rise to any particular one or a combination of these processes. Unilamellar phosphatidylcholine vesicles were reported to break open and adhere to a mica surface to form a bilayer coating, in spite of the evidence for this being indirect as obtained from the measured separation between two surfaces when pushed together (Horn, 1984). Further compression of the closely apposed bilayers resulted in fusion into a single bilayer. Phospholipid monolayers with lipid haptens inserted were supported by hydrophobic glass and useful for specific adherence of macrophages and cell surface recognition studies, but did not serve as hosts for transmembrane proteins (Lin et al., 1982). Dipalmitoylphosphatidylcholine (DPPC) and phosphatidylinositol (PI) from vesicles adsorbed onto negatively charged ballottini (hydrophobic) glass beads as a monolayer with their head groups uppermost (Jackson et al., 1986). The easiest method for preparing high quality phospholipid bilayers on a flat hydrophilic surface was the direct fusion of small unilamellar vesicles, a method originated to make unilamellar membranes on glass coverslips for spectroscopic studies (Brian & McConnell, 1984). Phospholipid fusion at the hydrophilic surface such as freshly cleaved mica could be induced at elevated temperatures for those lipids of higher transition temperature with traces of divalent cations such as Ca^{2+} . The other method for preparing supported membranes of biological interest was the controlled transfer of monolayers to the surface using the Langmuir trough. Using this method the content in each leaflet was easily controlled, and the transfer pressure could be at a desirable value (Tamm & McConnell, 1985). The main advantages of the vesicle fusion method seemed to be simplicity and the most natural lateral pressure in the bilayer in comparison to the lateral pressures obtained with the Langmuir trough. However, the content in each leaflet could not be controlled using fusion. A central problem in biology has been the structure of membranes and membrane proteins. Despite many years of intense effort, direct imaging of unsupported membranes such as the plasma membrane of an intact cell, did not appear very promising due to low resolution (20 nm). When such membranes, either artificially made or purified, were placed on a solid support, such as mica or glass cover slips, much higher resolution was demonstrated using the atomic force microscope AFM (Butt et al., 1990; Yang et al., 1993). This advance came with the AFM itself invented in 1986 (Binnig et al., 1986) and substantially improved in 1990, though AFM imaging of cells has not yielded sufficiently high resolution to identify membrane proteins (Shao & Yang, 1995). In contrast, supported membranes on mica, obtained either via vesicle fusion or deposition from monolayers prepared in the Langmuir trough, were stable under the AFM for repeated scans and in various buffers; even the defects were found useful as a nice internal control that permitted determination of bilayer thickness (Shao & Yang, 1995). The optical detection AFM could easily operate in aqueous buffers transparent to the visible light and this capability was very important for biological applications that required full hydration for retention of the native structures. When a membrane of appropriate composition was made on a mica surface, peripheral membrane proteins could be easily added to the buffer to allow binding to the membrane. The most straightforward example was the case of the cholera toxin bound to supported bilayers that contained the cholera toxin receptor, the monosialoganglioside GM1. Shao and Yang found that the stability of the toxin on fluid phase bilayers, such as egg-PC could be as good as the one on gel phase bilayers, such as DPPC (Shao and Yang, 1995). The success of AFM imaging this toxin at

intermediate ionic strength (up to 150 mM) opened the real possibility of imaging reconstituted membrane proteins under true physiological conditions. A second example was reconstitution of gramicidin A, a short trans-membrane peptide, incorporated in such supported bilayers resolved as a channel like depression of 1–2 nm (Mou et al., 1996). For integral membrane proteins, methods to incorporate the proteins into the supported planar membrane required vesicle fusion: either directly fusing vesicles that contained integral membrane proteins onto a supported substrate such a piece of quartz or glass coverslip or fusing them onto a substrate which was previously coated with a monolayer of lipids (Yang et al., 1993). The mechanism of such events was not understood. Palmitoyl-oleoylphosphatidylcholine (POPC) vesicles without major protruding molecular moieties spread on a glass surface and formed a supported planar bilayer whereas *Escherichia coli* lipid vesicles adsorbed as entire vesicles to the surface forming a supported vesicle layer on glass (Nollert et al., 1995). *Escherichia coli* lipids, a lipid mixture rich in lipopolysaccharides with bulky and strongly hydrated polarheads, did not form a supported bilayer on glass, vesicles simply adhered and formed a supported vesicle layer, lipopolysaccharides accounting for the steric repulsion that prevented fusion inbetween vesicles attached to the surface (Nollert et al., 1995). For DPPC and DSPC bilayers on hydrophilic silicon/water interface, single and double bilayers have been prepared and characterized via neutron reflectivity to determine the structure, hydration and roughness of the layers; the distance between the two bilayers identified the second bilayer highly hydrated and floating at 2 to 3 nm above the first one (Charitat et al., 1999). Adhesion of a vesicle layer of dioctadecyldimethylammonium bromide (DODAB), a synthetic lipid with a poorly hydrated polar headgroup, onto the rough and highly hydrated surface of cells was electrostatically driven with cationic vesicles at low ionic strength attracted to the negatively charged cell surface and surrounding the cell as a vesicle layer (Tapias et al., 1994). Absence of [¹⁴C]-sucrose leakage from vesicles in experiments where this marker was used to label the inner water compartment of the vesicles (Martins et al., 1997). The differential cytotoxicity of DODAB lipid was illustrated in Table 2 (adapted from Carmona-Ribeiro, 2003; Carmona-Ribeiro, 2006; Mamizuka & Carmona-Ribeiro, 2007).

Cell type	Viable cells/mL	[DODAB] for 50% survival /mM	Reference
Normal Balb-c 3T3 (clone A31) mouse fibroblasts	10 ⁴	1.000	Carmona-Ribeiro et al., 1997
SV40-transformed mouse fibroblasts SVT2	10 ⁴	1.000	Carmona-Ribeiro et al., 1997
<i>C. albicans</i>	2X10 ⁶	0.010	Campanhã et al., 2001
<i>E. coli</i>	2X10 ⁷	0.028	Martins et al., 1997; Campanhã et al., 1999
<i>S. typhimurium</i>	2X10 ⁷	0.010	Campanhã et al., 1999
<i>P. aeruginosa</i>	3X10 ⁷	0.005	Campanhã et al., 1999
<i>S. aureus</i>	3X10 ⁷	0.006	Campanhã et al., 1999

Table 2. Differential cytotoxicity of DODAB cationic lipid.

In conjunction with amphotericin B, DODAB bilayer fragments provided a novel drug formulation with excellent activity against systemic candidiasis in mice (Vieira & Carmona-Ribeiro, 2001; Lincopan et al. 2003) but low nephrotoxicity (Lincopan et al., 2005) (Figure 3).

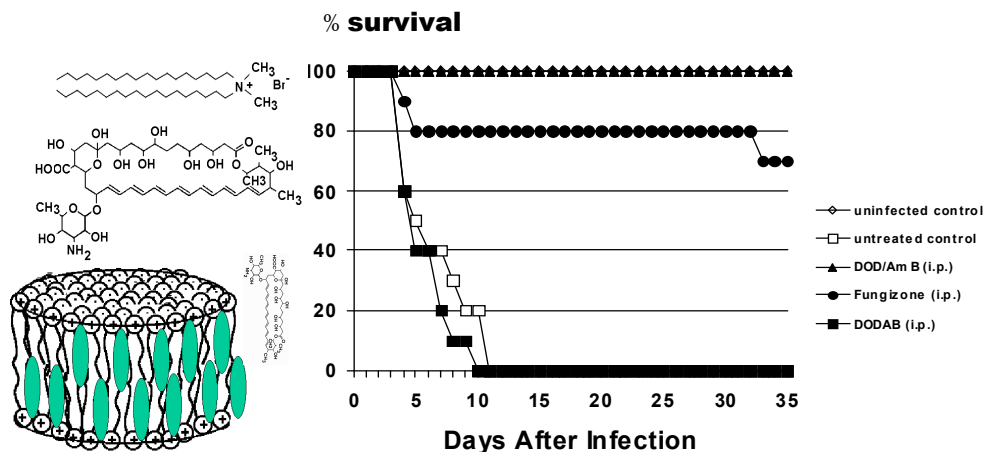


Fig. 3. Therapeutic activity of DODAB BF carrying monomeric amphotericin B in mice with candidiasis at low drug to lipid molar ratios. Adapted with permission from Vieira & Carmona-Ribeiro, 2001. Copyright 2001 Elsevier; and from Lincopan et al., 2003. Copyright 2003 Oxford University Press.

4. Particle functionalization by lipids

A particle can be understood as a lipid particle (eg, a bilayer fragment), a polymeric particle, a mineral particle, a drug particle, a bacterium cell, a virus or a whole biological cell with several organelles. Even a supramolecular assembly of the coacervate type forming a microgel can be understood as a particle. Therefore, a broad variety of particulates can be functionalized by lipids depending on their interaction forces, intervening media and nature of the interacting pair. Bayerl and coworkers first demonstrated the formation of supported phospholipid bilayers on spherical silica beads (Bayerl & Bloom, 1990), Esumi and coworkers deposited a DODAB layer (Esumi et al., 1992) and reported phospholipid adsorption on silica (Esumi & Yamada, 1993) and Carmona-Ribeiro and coworkers first demonstrated deposition of a synthetic lipid bilayer onto oppositely charged latex via electrostatic attraction (Carmona-Ribeiro & Midmore, 1992) or deposition of a neutral phospholipid monolayer on amidine latex via hydrophobic interaction between hydrocarbon chains of the phospholipid and the hydrophobic latex surface (Carmona-Ribeiro & Herrington, 1993). Electrostatic attraction drove physical adsorption of charged bilayers onto oppositely charged polymeric particles (Carmona-Ribeiro & Midmore, 1992). Adsorption isotherms were of the Langmuir type and for the three different lipids studied the limiting areas at the polymer/water interface were consistent with bilayer deposition. Electrokinetic properties of the covered particles were very similar to those of vesicles; the mean-z-average diameter of particles in the latex/vesicle mixtures increased of 10 nm, consistently with the increase in diameter expected from deposition of one bilayer on the

particles (Carmona-Ribeiro & Midmore, 1992). The interaction between lipids and particles has been reviewed over the last two decades in a few review articles and book chapters (Carmona-Ribeiro, 1992; Carmona-Ribeiro and Lessa, 1999; Carmona-Ribeiro, 2001 a,b; Carmona-Ribeiro, 2003; Carmona-Ribeiro et al., 2006; Carmona-Ribeiro, 2006; Carmona-Ribeiro, 2007; Petri & Carmona-Ribeiro, 2007; Mamizuka & Carmona-Ribeiro, 2007) and lately other excellent reviews appeared in the literature (Bulte & De Cuyper, 2003; Troutier & Ladavière, 2007; Al-Jammal & Kostarelos). Figure 4 illustrated possible assemblies resulting from the interaction between bilayer-forming lipids and particles as depicted from experimental evidences (Carmona-Ribeiro & Midmore, 1992; Carmona-Ribeiro & Herrington, 1993; Tsuruta et al., 1995; Rapuano & Carmona-Ribeiro, 1997; Carmona-Ribeiro & Lessa, 1999; Moura & Carmona-Ribeiro, 2003; Moura & Carmona-Ribeiro, 2005; Moura & Carmona-Ribeiro, 2007).

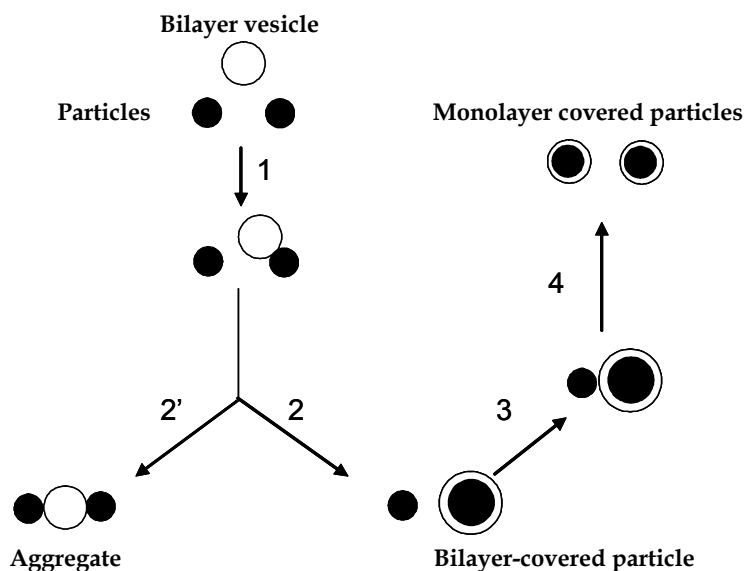


Fig. 4. The interaction between one bilayer vesicle and two particles. Adapted with permission from Carmona-Ribeiro & Lessa, 1999. Copyright 1999 Elsevier.

For neutral phospholipids such as PC and DPPC, lipid adsorption was evaluated from adsorption isotherms and determination of mean-z-average diameter of particles in the latex/vesicle mixtures for three different latex dispersions: polystyrene with amidine, sulfate or carboxylate as functional groups (Carmona-Ribeiro & Herrington, 1993). Small unilamellar phospholipid vesicles and polystyrene microspheres indeed interacted in aqueous solution to form homodisperse and stable phospholipid covered latexes. The amidine latex adsorbed neutral PC or DPPC vesicles revealing deposition of an odd number of monolayers: 1, 3, 5, etc (Carmona-Ribeiro & Herrington, 1993). In a first step of the phospholipid vesicle / latex interaction, the vesicle would break open and the bilayer would adhere to the latex; in a second step the hydrophobic attraction between the phospholipid hydrocarbon chains in the bilayer and the hydrophobic polystyrene surface would disrupt the bilayer structure inducing coverage of the hydrophobic surface with one phospholipid

monolayer with polar heads uppermost. Thereafter, upon increasing phospholipid concentration in the mixtures, the van der Waals attraction between the phospholipid layer on latex and free vesicles in the dispersion would drive deposition of a phospholipid bilayer onto the monolayer covered latex (Carmona-Ribeiro & Herrington, 1993). The lipid covered-latexes are useful as hosts for receptors (Sicchierolli & Carmona-Ribeiro, 1995; Sicchierolli & Carmona-Ribeiro, 1996; Moura & Carmona-Ribeiro, 2006), reduced protein adsorption on the polymer (Sicchierolli & Carmona-Ribeiro, 1996) and chromatography (Hautala et al., 2003; Haratake et al., 2007; Gulcev & Lucy, 2008). Figure 5 showed cholera toxin immobilization onto cationic (A) or neutral biomimetic particles (B) schematically shown from Petri and Carmona-Ribeiro, 2007; Lincopan & Carmona-Ribeiro, 2009; Moura & Carmona-Ribeiro, 2005 and Moura & Carmona-Ribeiro, 2006.

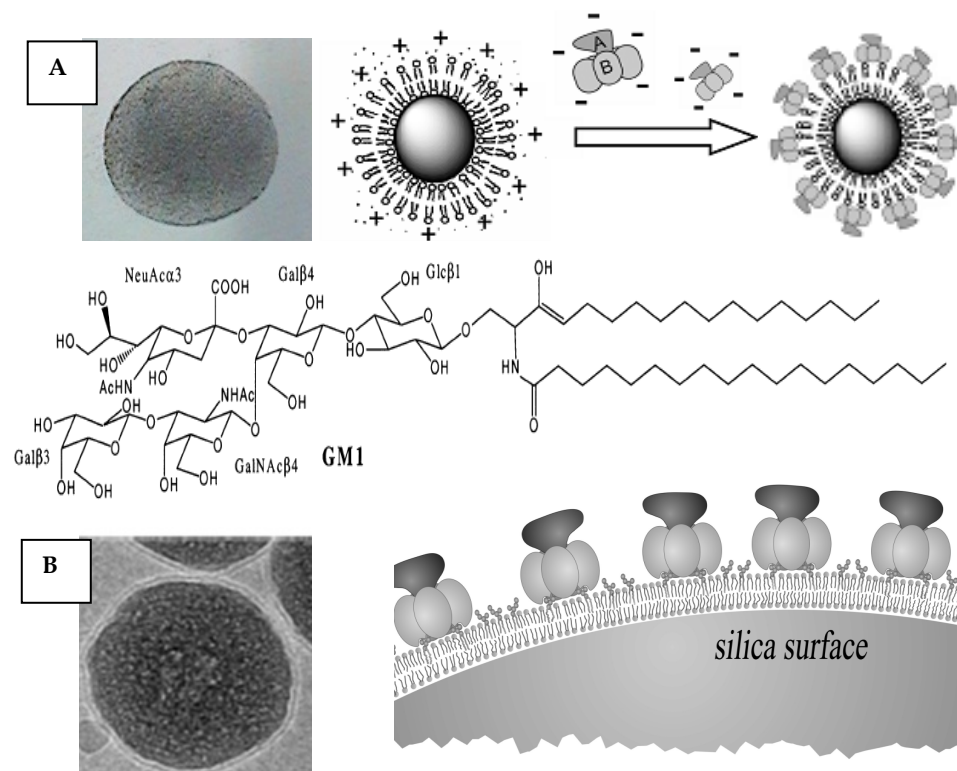


Fig. 5. Protein reconstitution onto biomimetic particles. Cholera toxin (CT) assembly onto polystyrene sulfate latex covered by a DODAB cationic bilayer (A) or CT specific binding to its GM1 receptor in phosphatidylcholine bilayers supported on silica particles (B). TEM (A) or cryo-TEM (B) revealed the cationic bilayer surrounding a polystyrene sulfate latex particle (A) or a PC bilayer surrounding a silica particle (B), respectively. Micrograph (B) was adapted with permission from Mornet et al., 2005. Copyright 2005 American Chemical Society.

Although DODAC or DHP electrostatically adsorbed to oppositely charged polystyrene microspheres, forming homodisperse bilayer-covered lattices, this took place only over a certain range of low lipid concentration. Beyond bilayer deposition, there was vesicle adhesion to the bilayer-covered latex (Tsuruta et al., 1995). For DODAC vesicles the extent of vesicle adhesion to the covered latex was much higher than for DODAB vesicles; no rupture of adhered vesicles being detected for DODAC but with rupture taking place for DODAB vesicles. Rupture for DODAB vesicles was associated with the absence of hydration repulsion in between adhered adjacent vesicles on the covered latex whereas absence of rupture for DODAC was related to occurrence of the short-ranged hydration repulsion (Tsuruta et al., 1995a). Using radiolabeled D-glucose inside the cationic vesicles at very low ionic strength, cationic liposome adsorption was accompanied of vesicle disruption evidencing formation of a bilayer on the solid particle surface (Tsuruta et al., 1995a). A series of monodisperse sulfate polystyrene latex dispersions (76–412 nm mean diameter) were covered with DODAB bilayers (Tsuruta et al., 1995b). The zeta-potential of these bilayer-covered particles in water remained constant (and positive) over the entire range of sizes tested. The kinetics of NaCl-induced flocculation for the bilayer-covered microspheres were obtained and the results used to construct curves of the logarithm of the stability ratio against the log of electrolyte concentration. At a given salt concentration, colloid stability increased, reached a maximum, and then decreased as a function of size. Slopes of the stability curves were calculated theoretically and compared with those obtained experimentally. The DLVO approximation by Reerink and Overbeek for an ideal colloid predicted an increase of slope with particle size which was not observed experimentally but DLVO models which include aggregation at the secondary minimum turned out to be qualitatively consistent with the experimental dependence of colloidal stability on particle size (Tsuruta et al., 1995b). DODA bromide (DODAB), chloride (DODAC), and acetate (DODAAc) bilayer-covered microspheres were more stable than vesicles of similar sizes under identical medium composition, vesicle colloidal instability due to asymmetry of charge distribution that occurs when salt is added to the vesicle outside, i. e. counterions bind at the outer vesicle surface but cannot bind at the inner vesicle surface because salt does not penetrate into the vesicle interior (Tsuruta & Carmona-Ribeiro, 1996). With acetate as the counterion at pH 5.1–5.3, specific acetate binding at the inner vesicle surface due to permeation of the neutral acetic acid through the vesicle membrane, thereby resulting in a high colloid stability. This stability was the highest ever observed for DODA vesicles. As counterion size and hydration increased (from bromide to acetate) so did colloid stability of vesicles and covered microspheres (Tsuruta & Carmona-Ribeiro, 1996). The effect of increasing particle size was to decrease colloid stability due to reversible aggregation at a secondary minimum (Tsuruta & Carmona-Ribeiro, 1996). Contact angle measurements on polystyrene or poly(styrene/methacrylate) surfaces with aqueous DODAB, DODAC or DODAAc dispersions over a range of lipid concentrations (10^{-6} – 10^{-4} M) were reported (Lessa & Carmona-Ribeiro, 1996). For the polystyrene surface without charge, angles decreased as a function of lipid concentration for the three lipids, an indication that lipid molecules would be lying on the hydrophobic homopolymer whereas for the charged copolymers angles first increased and then attained a plateau value as a function of lipid concentration. Counterion effect on nature of the deposited lipid layer was to increase hydrophilicity according to: acetate > chloride > acetate whereas the effect of increasing the copolymer surface charge was to promote a higher degree of vertical orientation of the

hydrocarbon chains facilitating bilayer deposition (Lessa & Carmona-Ribeiro, 1996). The most hydrophobic surface under air was the one obtained from the interaction between DODAB and the most charged copolymer. A DLVO model without free parameters did not account for the experimental colloid stability of a presumably ideal colloid such as latex covered with one DODAB bilayer (Carmona-Ribeiro & Lessa, 1999). The experimental stability measured from NaCl-induced flocculation was much smaller than the theoretical stability ratios suggesting either aggregation at a secondary minimum or an additional attractive force acting between the bilayer-covered particles not considered in the framework of the DLVO theory. Zeta-potential increased whereas experimentally measured colloid stability displayed a maximum as a function of particle size. Thus, over the range of larger particle sizes, upon increasing zeta-potential, there was a decrease in colloid stability. Possibly, calculations using adequate models that take into account this aggregation will shed new light on this issue. Whereas polystyrene microspheres have an hydrophobic surface, silica particles are good models for hydrophilic surfaces. Silica interacts with erythrocytes, lysosomes, macrophage plasma membranes and liposomes (Nash et al., 1966) but the mechanism of the interaction between silica and phospholipid membranes is still controversial. The main possibilities are: 1) silica particles binding DPPC through hydrogen bonds between Si-OH and O=P- groups; 2) tetraalkylammonium groups at the extracellular region of the erythrocyte membrane forming ion pairs with dissociated silanol on the silica particle and generating hemolytic effects observed for silica. Adsorption isotherms of 4 different bilayers on hydrophilic silica over a range of experimental conditions helped to clarify this issue (Rapuano & Carmona-Ribeiro, 1997). The separate use of synthetic charged membranes with phosphate or tetraalkylammonium groups as polarheads such as are DODAB and DHP bilayer vesicles, to obtain adsorption isotherms on silica established the relative importance of phosphate or tetraalkylammonium on the mechanism of phospholipid deposition onto hydrophilic silica particles. Formation of ion pairs between the quaternary ammonium in the choline moiety of the phospholipid and the deprotonated silanol drove vesicle adhesion to the particle but vesicle rupture and bilayer deposition was determined by the cooperative occurrence of several hydrogen bridges between silanol and the phosphate moiety on the phospholipid (Rapuano & Carmona-Ribeiro, 1997). A low affinity between neutral phospholipids and the silica surface and a high affinity for the cationic amphiphile over a range of pH values was obtained (Rapuano & Carmona-Ribeiro, 2000). Tris-hydroxymethylaminomethane (Tris) used as buffer increased affinity between PC and silica at $\text{pH} \leq 7.4$ due to Tris adsorption on silica with an increase in the surface density of hydroxyls on the surface available to hydrogen bridging with phosphate phospholipid groups. Bilayer deposition, however, was unambiguously confirmed by the three techniques only for the interaction DPPC vesicles/silica over 1 h at 65 °C and for the interaction DODAB vesicles/silica over the all range of experimental conditions tested (Rapuano & Carmona-Ribeiro, 2000). A simple spectrophotometric method for identifying entire bilayer deposition onto solid particles was developed from incorporation of the optical probe merocyanine 540 onto the outer bilayer vesicle surface. Upon bilayer deposition on the particle, sandwiching the marker between bilayer and solid particle reduced light absorption, this reduction being quantitatively related to bilayer deposition. For the interaction between cationic DODAB/DPPC and anionic PI/DPPC vesicles with zinc citrate dispersions the majority of the adsorption was in the form of intact liposomes (Catuogno & Jones, 2000). Also, for several types of liposomes interacting with hydrophilic

solid surfaces containing ionizable groups such as citrate or silanol, the pH affected the extent of adsorption, adsorption increasing with decreasing pH for anionic liposomes and increasing with increasing pH for cationic liposomes. The fusion and spreading of phospholipid bilayers on negatively charged glass surfaces is dependent on pH and ionic strength with membrane fusion of negatively charged membranes being favoured by low pH and high ionic strength as driven by the van der Waals attraction and membrane fusion of positively charged membranes onto the surface taking place under all conditions tested (Cremer & Boxer, 1999). Figure 6 illustrated optimized bilayer deposition for PC on silica.

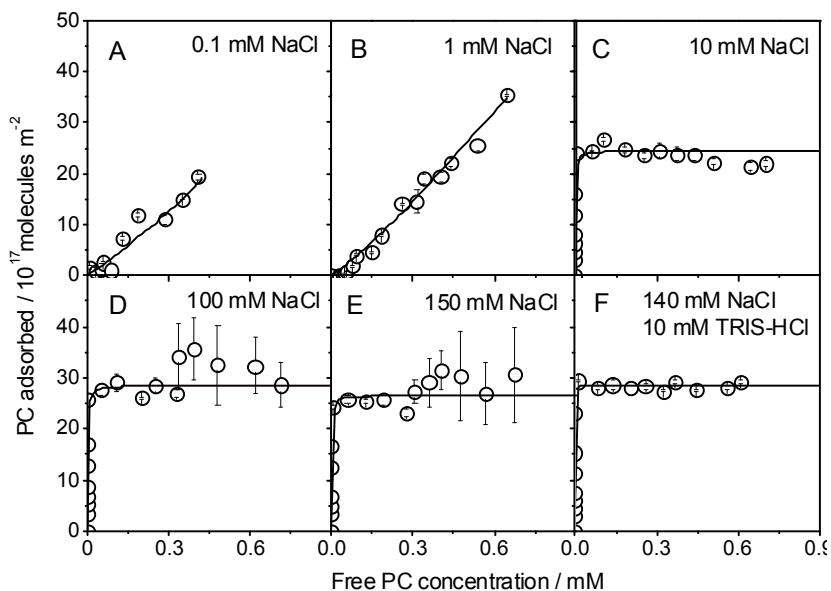


Fig. 6. Optimal bilayer coverage on silica from PC adsorption over a range of ionic strength. At maximal adsorption in C, D, E and F there is deposition of one PC bilayer onto particles. Reprinted with permission from Moura & Carmona-Ribeiro, 2005. Copyright 2005 American Chemical Society.

Jones and coworkers prepared cationic and anionic liposomes from DPPC and in mixtures with cholesterol and DODAB and with phosphatidylinositol (PI) respectively covering a range of composition from 0 to 19 mole % DODAB and PI producing supported vesicles on solid particles of silica and titanium dioxide (Bennet et al., 2000). Using encapsulation of radiolabeled D-glucose in the vesicles, they have shown that lipid adsorption on particles did not release the marker, an indication of adsorption of an intact vesicle layer onto the particles. Indeed, in the rigid gel state, bilayers are more difficult to disrupt as was the case for DODAB/DPPC vesicles adsorbing on silica (Moura & Carmona-Ribeiro, 2007), with tightly packed bilayers (Sobral et al., 2008). There were important differences between the interactions that involve liposomes in the liquid-crystalline or in the gel state. Furthermore, differences in molecular geometry as predicted from the self-assembly model may lead to differences in packing of these molecules also at the solid surface. A cylindrical molecule

prefers to deposit as a flat aggregate on a flat surface instead of depositing on highly curved particles. Molecular shapes departing from the cylindrical geometry such as the one of micelle-forming amphiphiles, adsorb onto hydrophobic surfaces as hemicylinders of liquid-crystalline aggregates (Manne & Gaub, 1995). The bilayer bending for deposition on curved surfaces requires energy that can be offered by electrostatic attraction between oppositely charged groups on the bilayer or on the surface and/or highly cooperative hydrogen bonding between phospholipid polarheads and certain groups on the surface, e.g. silanols. From the comparison between langmuirian adsorption isotherms for PC, DPPC or DODAB deposition on silica particles (50 nm mean diameter), affinity constants for the surface increased in the following order $PC < DPPC < DODAB$ (Rapuano and Carmona-Ribeiro, 1997; Rapuano and Carmona-Ribeiro, 2000). The molecular shape for PC in the bilayer is more cylindrical for PC than for DPPC, the geometric parameter for PC is larger than the geometric parameter for DPPC and it becomes difficult for the PC bilayer to bend and deposit on a curved silica particle but bending is easier for a DPPC bilayer. The contrary should be expected for PC and DPPC deposition on a silicon wafer as indeed observed (Salay & Carmona-Ribeiro, 1999). Covering silica with a DODAB cationic bilayer in the rigid gel state was possible from the interaction between silica and bilayer fragments over a range of ratios between total surface areas for bilayer and silica particles (A_b/A_s) and over a range of ionic strengths (Moura & Carmona-Ribeiro, 2003). Thereby the difficulty of breaking open a vesicle that was in the rigid gel state was conveniently circumvented. Figure 7 illustrated colloid stability of silica/DODAB or silica/PC systems.

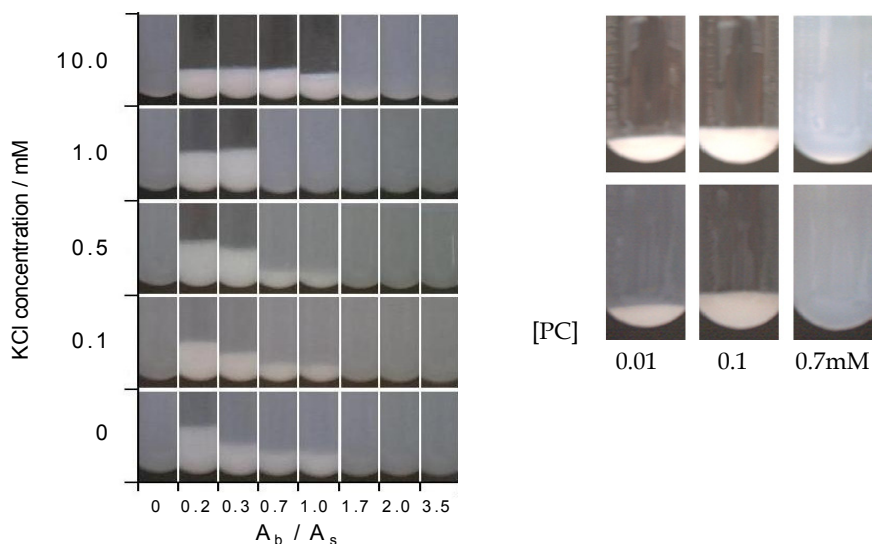


Fig. 7. Pictures of silica/DODAB (on the left) and silica/PC mixtures (on the right) at pH 6.3 on top or 7.4 on the bottom. Adapted with permission from Moura & Carmona-Ribeiro, 2003 and Moura & Carmona-Ribeiro, 2005. Copyright 2003 and 2005 American Chemical Society.

The use of membrane-coatings on colloidal particles offered an extensive repertoire of chemical functionality (Bayerl, 2004; Baksh et al., 2004). Glass microspheres coated with phospholipid layers evaluated the binding specificity of enzymes on cell surface (Obringer et al. 1995) or quantified lipid-antibodies binding (Kiser et al., 1998). Recent work continues to investigate lipid-supporting particles based on minerals (Lincopan et al. 2009; Nordlund et al. 2009; Ahmed & Wunder, 2009; Xu et al., 2009; Oleson & Sahai, 2008; Pyiasena et al., 2008; Senarath-Yapa et al. 2007; Moura & Carmona-Ribeiro, 2007; Parida et al., 2006), polymers (Lincopan & Carmona-Ribeiro, 2009; Jha & Bose, 2009; Thevenot et al., 2008; Lincopan et al., 2007; Bershteyn et al. 2008; Zuzzi et al., 2008; Troutier et al., 2005; Pereira et al., 2004), metals eg magnetoliposomes for biomedical applications or contrast agents in magnetic resonance imaging (Bulte & De Cuyper, 2003) or biological cells as templating cores to be dissolved to obtain capsules (Ge et al., 2003) or viruses for enhancing adenovirus tumor targeting *in vivo* (Singh et al., 2008). Polymer hollow capsules were produced by Möhwald and coworkers (Ge et al., 2003) from the polyelectrolyte layer-by-layer technique on biological cells. Permeability control of ions and small neutral molecules was achieved by analogy with the barrier function of biological membranes from the lipid coating on these capsules. Essentially, biomimetic particles composed of a particle core coated with lipids associated the advantages of particles and lipids. The solid core conferred mechanical stability to the lipid layers and, for biodegradable cores, particles could eventually be used *in vivo* as a carrier for bioactive compounds. The main advantages of the lipid envelop were biocompatibility, a biomimetic behavior of cell membranes and the ability to interact with a wide variety of molecules, either within the membrane or on the surface, depending on the physico-chemical properties of the carried species. The functionalization of colloidal particles with novel organoalkoxysilane-based lipids (Si-lipids) (Katagiri et al., 1999) pointed out the mechanic stability of a robust siloxane network at the particle-water interface (Katagiri & Caruso, 2004).

5. Lipid-based biomimetics for drug and vaccine delivery

Liposomes and particles are both very versatile structures that are finding a large variety of biomedical and pharmaceutical applications. In general, particulate systems are naturally targeted to antigen presenting cells (APC) so that particles deliver antigens to APC more efficiently than soluble antigen (Kovacovics-Bankowski et al., 1993; Vidard et al., 1996). For example, positively charged particles with diameters of 500 nm and below were shown to be optimal for dendritic cells uptake (Foged et al., 2005). Furthermore, it was recently shown that particles with positive charge showed higher internalization into human breast cancer cells than the nanoparticles with negative charge, while the degree of internalization of the positively- and negatively-charged nanoparticles into human umbilical vein endothelial cells was almost the same (Osaka et al., 2009). On the other hand, cationic lipids electrostatically combine with a vast variety of negatively charged biomolecules or biological structures besides being excellent antimicrobial agents by themselves (Carmona-Ribeiro et al., 2006). Silica (Rapuano and Carmona-Ribeiro, 1997, 2000; Moura and Carmona-Ribeiro, 2005, 2006, 2007), latex (Carmona-Ribeiro and Midmore, 1992; Carmona-Ribeiro, 2001) or hydrophobic drug particles (Pacheco and Carmona-Ribeiro, 2003; Vieira et al., 2006; Lincopan and Carmona-Ribeiro, 2006) have been coated with cationic lipids. Optimal cationic bilayer deposition on particles was achieved by coalescence of bilayer fragments at

adequate experimental conditions for the intervening medium such as pH, ionic strength and concentrations of the interacting components (Moura & Carmona-Ribeiro, 2003; Moura & Carmona-Ribeiro, 2005; Pereira et al., 2004; Pereira et al., 2006). Recently, the optimal bilayer coverage of polystyrene sulfate (PSS) nanoparticles with a cationic dioctadecyldimethylammonium bromide (DODAB) bilayer found an important application adsorbing and successfully presenting antigens to the immune system (Lincopan et al., 2007; Lincopan et al., 2009a). From the literature, the potential of hybrid particle-lipid systems in diagnostics and therapeutics is starting to be realized (Carmona-Ribeiro, 2003; Katagiri et al., 2004; Pichot, 2004; Troutier et al. 2005; Urban and Lestage, 2006; Al-Jamal and Kostarelos, 2007; Petri and Carmona-Ribeiro, 2007; Singh et al., 2008; Soo et al., 2009). Bilayer-coated or solid lipid nanoparticles have also been employed to formulate other drugs. Recently, lipid nanoparticles of the anticancer drug chlorambucil were prepared by ultrasonication, using stearic acid as the core lipid and DODAB as surface modifier; it was observed that the presence of DODAB on the lipid nanoparticles resulted in greater accumulation of the drug in tumors (Sharma et al., 2009). For the encapsulation of cisplatin, bilayer-coating circumvented the limited solubility of cisplatin in water and produced cisplatin nanocapsules, bean-shaped nanoprecipitates of cisplatin coated by a lipid bilayer (Burger et al., 2002). The nanocapsules represented a novel lipid formulation of cisplatin characterized by a very high cisplatin-to-lipid ratio and cytotoxicity against tumor cells *in vitro* as compared to the free drug. The formation of the nanocapsules critically depended on the presence of negatively charged phospholipids and positively charged aqua-species of cisplatin (Burger et al., 2002; Chupin et al., 2004). The effect of PEG on the stability of the cisplatin nanocapsules was studied by incorporating PEG conjugated to phosphatidylethanolamine (DSPE-PEG2000) (Velinova et al., 2004). Cisplatin release from the nanocapsules depended on the temperature, the surrounding medium, and the lipid composition of the bilayer coat. Sterically stabilized cisplatin nanocapsules containing 6 mol% DSPE-PEG served as the starting formulation for *in vivo* studies addressing the anti-tumor efficacy of cisplatin nanocapsules in tumor-bearing mice; there was a requirement of anionic phospholipid for successful nanoencapsulation of the cationic aqua-cisplatin (Velinova et al., 2004). DODAB or DHP bilayer fragments have been used to formulate hydrophobic drugs (Vieira & Carmona-Ribeiro, 2001; Pacheco & Carmona-Ribeiro, 2003; Lincopan et al., 2003; Carmona-Ribeiro, 2003; Vieira et al. 2006; Lincopan & Carmona-Ribeiro, 2006). Amphotericin B or miconazole were solubilized by bilayer fragments at low drug to lipid molar ratios (Vieira & Carmona-Ribeiro, 2001; Pacheco & Carmona-Ribeiro, 2003; Lincopan & Carmona-Ribeiro, 2003) whereas at high drug to lipid molar ratios, drug particles were covered with synthetic bilayers from DODAB or DHP bilayer fragments (Pacheco & Carmona-Ribeiro, 2003; Lincopan & Carmona-Ribeiro, 2006). The combined action of lipid-covered miconazole and amphotericin B particles against *Candida* and *C. neoformans* was shown to depend on drug-to-lipid-molar proportion and interaction time (Lincopan and Carmona-Ribeiro, 2006). BF loading capacity for monomeric amphotericin B was 0.1 mM amphotericin B at 2 mM DODAB. Above this low drug-to-lipid molar proportion, all solubilization sites at the rim of the bilayer fragments were saturated and amphotericin B aggregated in the dispersion. At high drug-to-lipid molar proportions, addition of chaotropic K_2HPO_4 (0.2-2 mM) converted miconazole or amphotericin B aggregates into negatively charged particles with affinity for cationic lipid, which then surrounded each drug particle with a cationic layer. DODAB by itself killed *C. neoformans*

and *Candida* at 2 and 2 to >250 mg/L minimal fungicidal concentration (MFC). In combination, over the first hour, fungicidal activity was due to DODAB with lipid capsules retarding drug action. At 48 h and 10^4 cfu/mL, MFC (mg/L) against *Candida albicans* was reduced from 4 to 1 amphotericin B (at 2 DODAB), and from 8 to 1 miconazole (at 1 DODAB). DODAB may be a suitable candidate for use in combination with miconazole for antifungal therapy due to reconfirmed synergistic action of both antimicrobial drugs: the cationic DODAB lipid and the microbicidal drug (Vieira et al., 2006; Lincopan and Carmona-Ribeiro, 2006). Poly(ethylene glycol) (PEG) decorated lipid bilayers are widely used in drug delivery (Lasic, 1994). In these hybrid polymer/lipid systems, there is a transition from a dispersed lamellar phase (liposomes) to a micellar phase mediated by the formation of small discoidal micelles. The onset of disk formation took place at low PEG-lipid concentrations (<5 mol %) and the size of the disks decreased as more PEG-lipid was added to the lipid mixture (Johnsson & Edwards, 2003). Stable dispersions dominated by flat bilayer disks could be prepared from a carefully optimized mixture of 1,2-distearoyl-sn-glycero-3-phosphocholine (DSPC), cholesterol, and 1,2-distearoyl-sn-glycero-3-phosphoethanolamine-N-[methoxy(polyethyleneglycol)-5000][PEG-DSPE(5000)]. By varying the content of PEG - DSPE (5000), the disks diameter varied from about 15 to 60 nm. Disks compared favourably to uni- and multilamellar liposomes for hydrophilic drug partitioning employing immobilized disks in glass capillaries (Johansson et al., 2005). The major repulsive interactions preventing fusion of bilayer fragments and discs in dispersion are electrostatic, steric and/or electrosteric (Carmona-Ribeiro, 2006). In particular, probe sonication of the synthetic and cationic lipid dioctadecyldimethylammonium bromide (DODAB) can yield disrupted vesicles: the bilayer fragments, BF, or disks (Carmona-Ribeiro, 2006). Bilayer disks are an attractive and sometimes superior alternative to liposomes (Nath et al., 2007; Johansson et al., 2007). Table 3 illustrated the efficacy of miconazole (MCZ) in DODAB or DHP bilayer fragments.

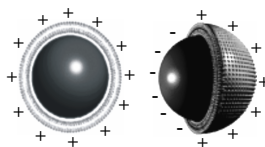
Drug or drug/lipid dispersion	MFC	
	μM	mg/mL
Zoltec® (FCZ)	6.5	2
DODAB	4000	250
MCZ	8	4
MCZ and DODAB	2	1
MCZ and DHP	4	2

Table 3. Minimal fungicidal concentration (MFC) for miconazole (MCZ) in ethanol 4.3%, MCZ/DODAB or DHP and Zoltec® (trade name for fluconazol) against *Candida albicans* ATCC 90028. Adapted with permission from Vieira et al 2006. Copyright 2006 Elsevier.

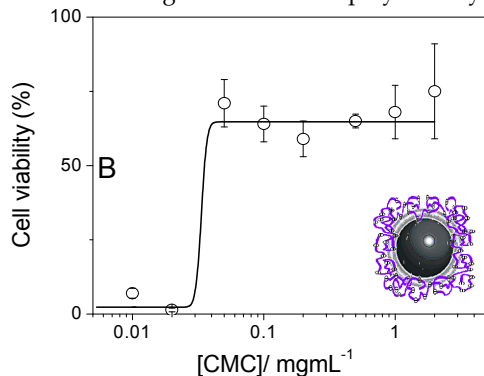
DODAB bilayer fragments (BF) were used for solubilization of hydrophobic drugs at low or high drug-to-lipid molar ratios (Vieira and Carmona-Ribeiro, 2001; Vieira and Carmona-Ribeiro, 2008), as antimicrobial agent (Campanhã et al., 2000), or in the production of lipid-covered drug particles at high drug-to lipid molar ratios (Lincopan and Carmona-Ribeiro, 2006; Vieira and Carmona-Ribeiro, 2008) or bilayer-coated silica (Rapuano and Carmona-Ribeiro, 2000; Moura and Carmona-Ribeiro, 2003) or latex (Carmona-Ribeiro and Midmore, 1992; Carmona-Ribeiro and Lessa, 1999). These cationic, bilayer-covered latex or silica particles where the bilayer is solely composed of DODAB were recently employed to

present antigens to the immune system with better results than alum as adjuvants (Lincopan et al., 2007; Lincopan et al., 2009a,b,c). At low ionic strength, charged bilayer fragments (BF) were colloiddally stable due to electrostatic repulsion. At low drug-to-lipid molar ratios, BF provided excellent solubilization sites for hydrophobic antifungal drugs so that drug granules of amphotericin B or miconazole could be completely solubilized at the rim of BF: monomolecular drug could be found well dispersed in water solution due to its self-assembly to the BF structure (Vieira and Carmona-Ribeiro, 2001; Pacheco and Carmona-Ribeiro, 2003; Lincopan et al., 2003). At high drug-to-lipid molar ratios, minute amounts of bilayer fragments coalesced around each drug granule forming a lipidic capsule (Pacheco and Carmona-Ribeiro, 2003; Vieira et al., 2006; Lincopan and Carmona-Ribeiro, 2006). Therefore, these discoidal, charged bilayer fragments dispersed the hydrophobic drug particles in water both at low and at high drug-to-lipid molar ratios. Figure 8 showed effective formulations for amphotericin B at high drug to lipid molar ratio. Encapsulation of the drug particle by the cationic bilayer was followed by deposition of two more layers of polyelectrolytes (Pacheco & Carmona-Ribeiro, 2003; Lincopan & Carmona-Ribeiro, 2006; Vieira & Carmona-Ribeiro, 2008).

STEP 1: Coverage of drug particle with cationic bilayer



STEP 2: Coverage with anionic polymer layer



STEP 3: Coverage with cationic layer

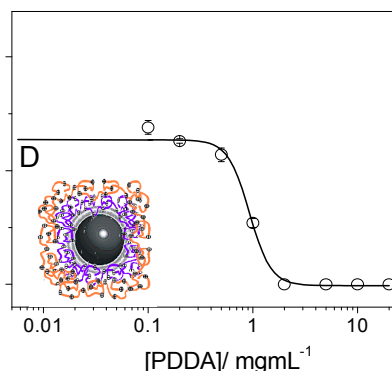


Fig. 8. Encapsulation of amphotericin B at high drug to lipid molar ratio. The insoluble drug particle is covered with a cationic bilayer, then covered by a layer of carboxymethylcellulose (CMC) and an outer layer of polydiallyldimethylammonium polymer (PDDA) becoming again positively charged and active against *Candida albicans* (Vieira & Carmona-Ribeiro, 2008).

Electrostatically driven bilayer coverage from bilayer fragments onto oppositely charged latex produced a highly homodisperse particulate for biomolecules adsorption (Carmona-Ribeiro and Midmore, 1992; Carmona-Ribeiro, 2001; Carmona-Ribeiro, 2003; Pereira et al., 2004; Lincopan et al., 2006; Lincopan et al., 2007; Rosa et al., 2008). Polystyrene sulfate (PSS) particles which are anionic can be covered with single cationic DODAB bilayers forming

biomimetic particles prone to be used for DNA, proteins or antigen immobilization (Lincopan et al., 2006; Lincopan et al., 2007; Lincopan et al., 2009). Firstly, the DODAB/PSS assembly was characterized at 1 mM NaCl and 5×10^9 PSS particles/mL over a range of DODAB concentrations (0.001 -1 mM) by means of dynamic light scattering for particle sizing and zeta-potential analysis. 0.01 mM DODAB was enough to produce perfectly homodisperse and cationic bilayer-covered particles. Secondly, under these experimental conditions, biomolecules or antigens adsorbed onto biomimetic particles with high affinity. Biomimetic particles were obtained in two-steps first covering the originally bare latex with a lipid layer and then, with a monomolecular biomolecule (protein or DNA) layer (Rosa et al., 2008; Lincopan & Carmona-Ribeiro, 2009). PSS/DODAB/biomolecule assemblies were also characterized by means of dynamic light scattering and zeta-potential analysis yielding highly monodisperse particles at and above maximal adsorption. Cationic bilayer-covered particles were a highly organized and general support for biomolecules immobilization. The narrow size distribution and low polydispersity correlated well with superior cellular immune response towards the antigen (Lincopan et al., 2007) also observed for silica/DODAB particulates (Lincopan et al. 2009). Latex or polymeric particles can be useful as models for hydrophobic drug particles whereas silica or silicon wafers can mimic hydrophilic supports. Biomimetic particles as silica covered by one PC bilayer were obtained from quantification of PC adsorption onto silica (Moura and Carmona-Ribeiro, 2005). The effect of ionic strength and pH on phosphatidylcholine (PC) adsorption from vesicles on silica nanoparticles was investigated over a range of [NaCl] (0.1-150 mM) at pH 6.3 and 7.4 by determining adsorption isotherms, colloid stability, particle size and zeta-potentials. At and above 10 mM ionic strength, pH 6.3, high-affinity adsorption with limiting adsorption at one-bilayer deposition on each silica particle was obtained. At 10 mM ionic strength, adsorption isotherms indicated lower affinity between PC and silica at pH 7.4 than at pH 6.3, reconfirming the important role of hydrogen bonding between silanoyl on silica and phosphate on PC in promoting bilayer deposition at pH of water. Under conditions where high affinity and bilayer deposition took place, silica sedimentation was absent, suggesting particle stabilization induced by bilayer coverage. At 150 mM NaCl, the large colloid stability similarly achieved at pH 6.3 or 7.4 suggested the major role of van der Waals attraction between the PC bilayer vesicle and the silica particle in determining bilayer deposition. Van der Waals attraction increased with ionic strength, causing PC vesicle disruption with bilayer deposition and silica stabilization. Major applications of supported bilayers on silica particles were isolation and reconstitution of receptor-ligand specific interaction (Moura and Carmona-Ribeiro, 2006) and antigens (proteins or DNA) presentation for vaccines (Rosa et al., 2008; Lincopan et al., 2009). Cholera toxin (CT) and its receptor, the monosialoganglioside GM1, a cell membrane glycolipid, self-assembled on PC bilayer-covered silica at 1 CT/5 GM1 molar ratio in perfect agreement with literature. Fig. 9 illustrated particles uptake by dendritic cells and the novel cationic immunoadjuvants.

6. Conclusion

Lipid association to polymeric, mineral, metal or drug particles has been optimized in order to achieve optimal bilayer deposition onto particles. Vesicle disruption, difficult for bilayers in the rigid gel state, was circumvented by employing previously disrupted charged vesicles: the bilayer fragments or disks. At appropriate intervening media, bilayer fragments

coalesced around particles. Uses for biomimetic particles in drug and vaccine delivery were encapsulation of hydrophobic drugs, reconstitution of cell receptors, antigen presentation and antimicrobial therapy.

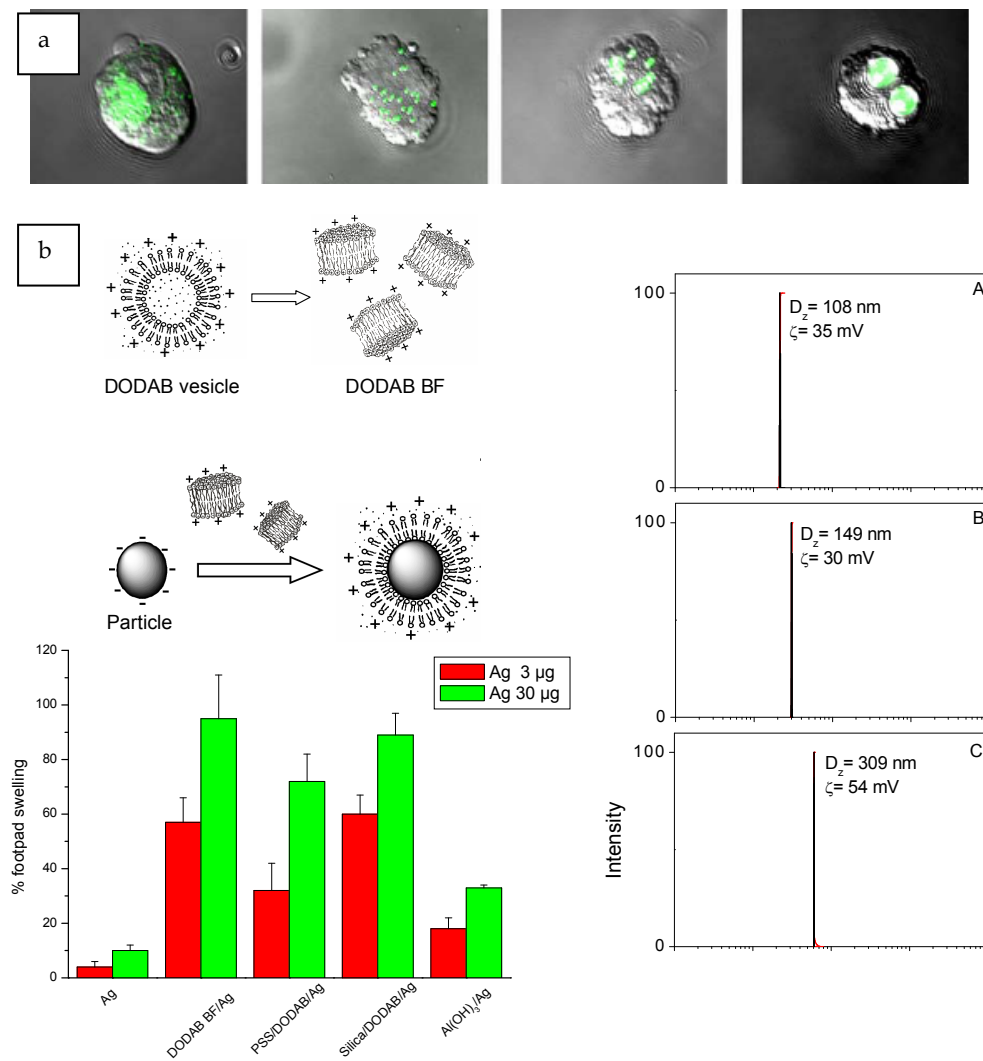


Fig. 9. (a) Uptake of carboxylated polystyrene particles (labeled in green) by dendritic cells from confocal overlaid with transmission pictures. From left to right microspheres were 0.1, 0.5, 1.0 and 4.5 μm mean diameter. Adapted with permission from Foged et al, 2005, copyright 2005 Elsevier. (b) Cationic biomimetic particles (PSS/DODAB) with very narrow size distributions can be obtained over a range of sizes being effective as immuno adjuvants that elicit footpad swelling in mice and cellular immune response. Size distributions were reproduced with permission from Rosa et al., 2008. Copyright 2008 American Chemical Society.

Acknowledgments

Financial support from FAPESP and CNPq is gratefully acknowledged.

7. References

- Ahmed, S. & Wunder, S. L. (2009). Effect of High Surface Curvature on the Main Phase Transition of Supported Phospholipid Bilayers on SiO₂ Nanoparticles. *Langmuir*, 25, 6, (Mar 2009) 3682-91, ISSN 1053-0509.
- Al-Jamal, W. T. & Kostarelos, K. (2007). Liposome-nanoparticle hybrids for multimodal diagnostic and therapeutic applications. *Nanomedicine*, 2, 1, (Feb 2007) 85-98, ISSN 1743-5889.
- Baksh, M. M.; Jaros, M. & Groves, J. T. (2004). Detection of molecular interactions at membrane surfaces through colloid phase transitions. *Nature*, 427, 6970, (Jan 2004) 139-41, ISSN 0028-0836.
- Bangham, A. D. (1983). *Liposome Letters*, Bangham, A. D., (Ed.), 1-405, Academic Press, ISBN 10: 0120777800, London.
- Bayerl, T. M. (2004). A glass bead game. *Nature*, 427, 6970, (Jan 2004) 105-6, ISSN 0028-0836.
- Bayerl, T. M. & Bloom, M. (1990). Physical properties of single phospholipid bilayers adsorbed to micro glass beads. A new vesicular model system studied by ²H-nuclear magnetic resonance. *Biophys. J.*, 58, 2, 357-62, ISSN (electronic) 1542-0086.
- Bennett, T. C. ; Creeth, J. E. & Jones, M. N. (2000). Solid supported vesicles for bactericide delivery. *J. Liposome Res.*, 10, 4, 303-20, ISSN: 0898-2104.
- Bershteyn, A.; Chaparro, J.; Yau, R.; Kim, M. ; Reinherz, E. ; Ferreira-Moita, L. & Irvine, D. J. (2008). Polymer-supported lipid shells, onions, and flowers. *Soft Matter*, 4, 9, (Apr 2008) 1787-91, ISSN 1744-683X.
- Binnig, G. ; Quate, C. F. & Gerber, C. H. (1986). Atomic Force Microscope. *Phys Rev Lett.*, 56, 9, (Mar 1986) 930-33, ISSN 0031-9007.
- Bloom, M.; Mouritsen, O. & Evans, E. (1991). Physical properties of the fluid lipid-bilayer component of cell membranes: a perspective. *Q. Rev. Biophys.*, 24, 3, (Aug 1991) 293-397, ISSN 0033-5835.
- Brian, A. A. & McConnell, H. M. (1984). Allogeneic stimulation of cytotoxic T cells by supported planar membranes. *Proc Natl Acad Sci U S A*, 81, 19, (Oct 1984) 6159-63, ISSN 0027-8424.
- Bulte, J. W. & De Cuyper, M. (2003). Magnetoliposomes as contrast agents. *Method. Enzymol.*, 373, 175-98, ISSN 0076-6879.
- Burger, K. N. ; Staffhorst, R. W. ; de Vijlder, H. C. ; Velinova, M. J. ; Bomans, P. H. ; Frederik, P. M. & de Kruijff, B. (2002). Nanocapsules: lipid-coated aggregates of cisplatin with high cytotoxicity. *Nat. Med.*, 8, 1, (Jan 2002) 81-4, ISSN 1078-8956.
- Butt, H. J.; Downing, K. H. & Hansma, P. K. (1990). Imaging the membrane protein bacteriorhodopsin with the atomic force microscope. *Biophys. J.*, 58, 6, (Dec 1990) 1473-80, ISSN (electronic) 1542-0086.
- Campanhã, M. T. N.; Mamizuka, E. M. & Carmona-Ribeiro, A. M. (1999). Interactions between cationic liposomes and bacteria: the physical-chemistry of the bactericidal action. *J. Lipid Res.*, 40, 8, (1999 Aug) 1495-500, ISSN 0022-2275.

- Campanhã, M. T. N. ; Mamizuka, E. M. & Carmona-Ribeiro, A. M. (2001). Interactions between cationic vesicles and *Candida albicans*. *J. Phys. Chem. B*, 105, 34, (Aug 2001), 8230-36, ISSN 1089-5647.
- Carmona-Ribeiro, A. M. & Chaimovich, H. (1983). Preparation and characterization of large dioctadecyldimethylammonium chloride liposomes and comparison with small sonicated vesicles. *Biochim. Biophys. Acta*, 733, 1, (Aug 1983) 172-9, ISSN 0006-3002.
- Carmona-Ribeiro, A. M. ; Yoshida, L. S. ; Sesso, A. & Chaimovich, H. (1984). Permeabilities and stabilities of large dihexadecylphosphate and dioctadecyldimethylammonium chloride vesicles. *J. Colloid Interface Sci.*, 100, 2, (Aug 1984) 433-43, ISSN 0021-9797.
- Carmona-Ribeiro, A. M. ; Castuma, C. E. ; Sesso, A. & Schreier, S. (1991). Bilayer structure and stability in dihexadecyl phosphate dispersions. *J. Phys. Chem.*, 95, 13, (June 1991) 5361-66, ISSN 0022-3654.
- Carmona-Ribeiro, A. M. & Midmore, B. R. (1992). Synthetic bilayer adsorption onto polystyrene microspheres. *Langmuir*, 8, 3, (Mar 1992) 801-6, ISSN 1053-0509.
- Carmona-Ribeiro, A. M. (1992). Synthetic amphiphile vesicles. *Chem. Soc. Rev.*, 21, 3, (1992) 209-14, ISSN 0306-0012.
- Carmona-Ribeiro, A. M. & Herrington, T. M. (1993). Phospholipid adsorption onto polystyrene microspheres. *J. Colloid Interface Sci.*, 156, 1, (Mar 1993) 19-23, ISSN 0021-9797.
- Carmona-Ribeiro, A. M. ; Ortis, F. ; Schumacher, R. I. & Armelin, M. C. S. (1997). Interactions between cationic vesicles and cultured mammalian cells. *Langmuir*, 13, 8, (Apr 1997) 2215-18, ISSN 1053-0509.
- Carmona-Ribeiro, A. M. & Lessa, M. M. (1999). Interactions between bilayer vesicles and latex. *Colloids Surf. A*, 153, (1-3), (Aug 1999) 355-61, ISSN 0927-7757.
- Carmona-Ribeiro, A. M. (2001). Bilayer vesicles and liposomes as interface agents. *Chem. Soc. Rev.*, 30, 4, (Jun 2001), 241-47, ISSN 0306-0012.
- Carmona-Ribeiro, A. M. (2001). Interactions between bilayer vesicles, biomolecules, and interfaces. In: *Handbook of Surfaces and Interfaces of Materials*, Nalwa, H. S., (Ed.), Vol. 5, 129-165, Academic Press, ISBN: 1588830690. San Diego.
- Carmona-Ribeiro, A. M. (2003). Bilayer-forming synthetic lipids: drugs or carriers? *Current Medicinal Chemistry*, 10, 22, (Nov 2003) 2425-46, ISSN 0929-8673.
- Carmona-Ribeiro, A. M.; Vieira, D. B. & Lincopan, N. (2006). Cationic surfactants and lipids as anti-infective agents. *Anti-Infective Agents in Medicinal Chemistry*, 5, 1, (Jan 2006) 33-51, ISSN 1871-5214.
- Carmona-Ribeiro, A. M. (2006). Lipid bilayer fragments and disks in drug delivery. *Current Medicinal Chemistry*, 13, 12, (May 2006) 1359-70, ISSN 0929-8673.
- Carmona-Ribeiro, A. M. (2007). Biomimetic Particles in Drug and Vaccine Delivery. *J. Liposome Res.*, 17, 3-4, (Dec 2007) 165-72, ISSN 0898-2104.
- Catuogno, C. & Jones, M. N. (2000). The interaction of cationic and anionic vesicles with zinc citrate dispersions. *Colloids Surf. A*, 163, (2000) 165-76, ISSN 0927-7757.
- Charitat, T. ; Bellet-Amalric, E. ; Fragneto, G. & Graner, F. (1999). Adsorbed and free lipid bilayers at the solid-liquid interface. *Eur. Phys. J. B*, 8, 4, (1999) 583-93, ISSN 1434-6028.
- Chatterjee, S. N. & Agarwal, S. (1988). Liposomes as membrane model for study of lipid peroxidation. *Free Radicals Biology & Medicine*, 4, 1, (1988) 51-72, ISSN:0891-5849.

- Chupin, V. ; de Kroon, A. I. P. M. & de Kruijff, B. (2004). Molecular architecture of nanocapsules, bilayer-enclosed solid particles of cisplatin. *J. Am. Chem. Soc.*, 126, 42, (Oct 2004) 13816-21, ISSN 0002-7863.
- Claesson, P. M. ; Carmona-Ribeiro, A. M. & Kurihara, K. (1989). Dihexadecyl phosphate monolayers: intralayer and interlayer interactions. *J. Phys. Chem.*, 93, 2, (Jan 1989) 917-22, ISSN 0022-3654.
- Cremer, P. S. & Boxer, S. G. (1999). Formation and Spreading of Lipid Bilayers on Planar Glass Supports. *J. Phys. Chem.*, 103, 13, (Mar 1999) 2554-59, ISSN 0022-3654.
- Czarniecki, M. F. & Breslow, R. (1979). Photochemical probes for model membrane structures. *J. Am. Chem. Soc.*, 101, 13, (Jun 1979) 3675-6, ISSN 0002-7863.
- Dailey, M. O. & Hunter, R. L. (1974). The role of lipid in the induction of hapten-specific delayed hypersensitivity and contact sensitivity. *J. Immunol.*, 112, 4, (Apr 1974) ISSN 1526-34.
- Esumi, K. ; Sugimuro, T. ; Yamada, T. & Meguro, K. (1993). Adsorption of dioctadecyldimethylammonium chloride on silica. *Colloids & Surfaces*, 62, 5, (Feb 1992) 249-54, ISSN 0927-7757.
- Esumi, K. & Yamada, T. (1993). Characterization of a phospholipid adsorbed layer on silica from small unilamellar vesicles. *Langmuir*, 9, 2, (Feb. 1993) 622-4, ISSN 1053-0509.
- Feitosa, E., Karlsson, G. & Edwards, K. (2006). Unilamellar vesicles obtained by simply mixing dioctadecyldimethylammonium chloride and bromide with water. *Chem. Phys. Lipids*, 140, 1-2, (Apr 2006) 66-74, ISSN 0009-3084.
- Foged, C., Brodin, B., Frokjaer, S. & Sundblad, A. (2005). Particle size and surface charge affect particle uptake by human dendritic cells in an *in vitro* model. *Int. J. Pharm.*, 298, 2, (Jul 2005) 315-22, ISSN 0378-5173.
- Fuhrhop, J-H. & Fritsch, D. (1986). Bolaamphiphiles form ultrathin, porous and unsymmetric monolayer lipid membranes. *Acc. Chem. Res.*, 19, 5, (May 1986) 130-7, ISSN 0001-4842.
- Gall, D., (1966). The adjuvant activity of aliphatic nitrogenous bases. *Immunology* 11, 4, (Oct 1966) 369-86, ISSN: 0019 2805.
- Ge, L. ; Möhwald, H. & Li, J. (2003). Polymer-stabilized phospholipid vesicles formed on polyelectrolyte multilayer capsules. *Biochem. Biophys. Res. Commun.*, 303, 2, (Apr 2003) 653-9, ISSN: 0006-291X.
- Gritt, M. & Crommelin, D. J. A. (1992). The effect of aging on the physical stability of liposome dispersions. *Chem. Phys. Lipids*, 62, 2, (Sept 1992) 113-22, ISSN 0009-3084.
- Gulcev, M. D. & Lucy, C. A. (2008). Factors Affecting the Behavior and Effectiveness of Phospholipid Bilayer Coatings for Capillary Electrophoretic Separations of Basic Proteins. *Anal. Chem.*, 80, 5, (Mar 2008) 1806-12, ISSN 0003-2700.
- Haratake, M., Hidaka, S.; Ono, M. & Nakayama, M. (2007). Preparation of an ion-exchangeable polymer bead wrapped with bilayer membrane structures for high performance liquid chromatography. *Anal. Chim. Acta*, 589, 1, (Apr 2007) 76-83, ISSN 0003-2670.
- Hargreaves, W. R. & Deamer, D. W. (1978). Liposomes from ionic, single-chain amphiphiles. *Biochemistry*, 17, 18, (Sep 1978) 3759-68, ISSN 0006-2960.

- Hautala, J. T. ; Linden, M. V. ; Wiedmer, S. K. ; Ryhanen, S. J. ; Saily, M. J. ; Kinnunen, P. K. J. & Riekkola, M.-L. (2003). Simple coating of capillaries with anionic liposomes in capillary electrophoresis. *Journal of Chromatography A*, 1004, 1-2, (Jul 2003) 81-90, ISSN 0021-9673.
- Hilgers, L. A. & Snippe, H. (1992). DDA as an immunological adjuvant. *Res. Immunol.*, 143, 5, (Jun 1992) 494-503, ISSN 0923-2494.
- Horn, R. G. (1984). Direct measurement of the force between two lipid bilayers and observation of their fusion. *Biochim. Biophys. Acta*, 778, 1, (Nov 1984) 224-8, ISSN 0005-2736.
- Hueb, H. H. ; Hupfer, B. ; Koch, H. & Ringsdorf, H. (1980). Polymerizable phospholipid analogues--new stable biomembrane and cell models. *Angew. Chem. Int. Ed. Engl.*, 1980, 19, (Dec 1980) 938-40, ISSN 1433-7851.
- Israelachvili, J. N. ; Mitchell, D. J. & Ninham, B. W. (1977). Theory of self-assembly of lipid bilayers and vesicles. *Biochim. Biophys. Acta*, 470, 2, (Oct 1977) 185-201, ISSN 0005-2736.
- Jackson, S. ; Reboiras, M. D. ; Lyle, I. G. & Jones, M. N. (1986). Adsorption of phospholipid vesicles on solid surfaces. *Faraday Discuss. Chem. Soc.*, 81, 291-301, ISSN 0301-7249.
- Jha, A. K. & Bose, A. (2009). Surfactant Microstructure and Particle Aggregation Control Using Amphiphile Adsorption on Surface-Functionalized Polystyrene Spheres. *Langmuir*, 25, 1, (Jan 2009) 123-6, ISSN 1053-0509.
- Johansson, E. ; Lundquist, A. ; Zuo, S. & Edwards, K. (2007). Nanosized bilayer disks: attractive model membranes for drug partition studies. *Biochim. Biophys. Acta* 1768, 6, (Jun 2007) 1518-25, ISSN 0006-3002.
- Johansson, E. ; Engvall, C. ; Arfvidsson, M. ; Lundahl, P. & Edwards, K. (2005). Development and initial evaluation of PEG-stabilized bilayer disks as novel model membranes. *Biophys. Chem.*, 113, 2, (Feb 2005) 183-92, ISSN 0301-4622.
- Johansson, M. & Edwards, K. (2003). Liposomes, disks, and spherical micelles: aggregate structure in mixtures of gel phase phosphatidylcholines and poly(ethylene glycol)-phospholipids. *Biophys J.*, 85, 6, (Dec 2003) 3839-47, ISSN(electronic) 1542-0086.
- Katagiri, K. & Caruso, F. (2004). Functionalization of Colloids with Robust Inorganic-Based Lipid Coatings. *Macromolecules*, 37, 26, (Dec 2004) 9947-53, ISSN 0024-9297.
- Katagiri, K. ; Ariga, J. & Kikuchi, J. (1999). Preparation of Organic-Inorganic Hybrid Vesicle "Cerasome" Derived from Artificial Lipid with Alkoxysilyl Head. *Chem. Lett.*, 28, 7, (Aug 1999) 661-2, ISSN 0366-7022.
- Kiser, P. F. ; Wilson, G. & Needham, D. (1998). A synthetic mimic of the secretory granule for drug delivery. *Nature*, 394, 6692, (Jul 1998) 459-62, ISSN 0028-0836.
- Klinguer-Hamour, C. ; Libon, C. ; Plotnicky-Gilquin, H. ; Bussat, M. C. ; Revy, L. ; Nguyen, T. ; Bonnefoy, J. Y. ; Corvaia, N. & Beck, A. (2002). *Vaccine*, 20, 21-22, (Jun 2002) 2743-51, ISSN 0264-410X.
- Korsholm, K. S. ; Agger, E. M. ; Foged, C. ; Christensen, D. ; Dietrich, J. ; Andersen, C. S. ; Geisler, C. ; Andersen, P. (2007). The adjuvant mechanism of cationic dimethyldioctadecylammonium liposomes. *Immunology*, 121, 2, (Jun 2007) 216-26, ISSN 0019 2805.

- Kovacsovics-Bankowski, M. ; Clark, K. ; Benacerraf, B. & Rock, K. L. (1993). Efficient major histocompatibility complex class I presentation of exogenous antigen upon phagocytosis by macrophages. *Proc. Natl. Acad. Sci. U.S.A.*, 90, 11, (Jun 1993) 4942-6, ISSN(electronic) 1091-6490.
- Kunitake, T. (1992). Synthetic Bilayer Membranes: Molecular Design, Self-Organization, and Application. *Angew. Chem. Int. Ed. Engl.*, 31, 6, (Jun 1992) 709-26, ISSN 1433-7851.
- Kunitake, T. ; Okahata, Y. ; Tamaki, K. ; Kumamaru, F. & Takayanagi, M. (1977). Formation of the bilayer membrane from a series of quaternary ammonium salts. *Chem. Lett.* 6, 4, 387-90, ISSN 0366-7022.
- Lasic, D. D. (1994). Sterically stabilized vesicles. *Angew. Chem. Int. Ed. Engl.*, 33, 17, (Dec 1994) 1685-3, ISSN 1433-7851.
- Lessa, M. M. & Carmona-Ribeiro, A. M. (1996). Bilayer Wetting on Polymer Surfaces. *J. Colloid Interface Sci.*, 182, 1, (Sep 1996) 166-71, ISSN 0021-9797.
- Lin, L-C. ; Weis, R. M. & McConnell, H. M. (1982). Induction of helical liposomes by Ca²⁺-mediated intermembrane binding. *Nature*, 296, 5853, (Mar 1982) 164-5, ISSN 0028-0836.
- Lincopan, N. ; Mamizuka, E. M. & Carmona-Ribeiro, A. M. (2003). In vivo activity of a novel amphotericin B formulation with synthetic cationic bilayer fragments. *J Antimicrob Chemother.*; 52, 3, (Sep 2003) 412-8, ISSN 0305-7453.
- Lincopan, N. ; Mamizuka, E. M. & Carmona-Ribeiro, A. M. (2005). Low nephrotoxicity of an effective amphotericin B formulation with cationic bilayer fragments. *J Antimicrob Chemother.*, 55, 5, (Mar 2005) 727-34, ISSN 0305-7453.
- Lincopan, N. & Carmona-Ribeiro, A. M. (2006). Lipid-covered drug particles: combined action of dioctadecyldimethylammonium bromide and amphotericin B or miconazole. *J Antimicrob Chemother.*, 58, 1, (Jul 2006) 66-75, ISSN 0305-7453.
- Lincopan, N., Borelli, P., Fock, R., Mamizuka, E. M. & Carmona-Ribeiro, A. M. (2006). Toxicity of an effective amphotericin B formulation at high cationic lipid to drug molar ratio. *Exp Toxicol Pathol.*, 58, 2-3, (Nov 2006) 175-83, ISSN 0940-2993.
- Lincopan, N. ; Rosa, H. & Carmona-Ribeiro, A. M. (2006). Biomimetic Particles. *Macromol. Symposia*, 245-246, 1, (Feb 2007), 485-90, ISSN (electronic) 1521-3900.
- Lincopan, N. ; Espíndola, N. M. ; Vaz, A. J. & Carmona-Ribeiro, A. M. (2007). Cationic supported lipid bilayers for antigen presentation. *Int. J. Pharm.*, 340, 1-2, (Aug 2007) 216-22, ISSN 0378-5173.
- Lincopan, N. ; Santana, M. R. A. ; Faquim-Mauro, E. ; da Costa, M. H. B. & Carmona-Ribeiro, A. M. (2009). Silica-based cationic bilayers as immunoadjuvants. *BMC Biotechnol.*, 9, article 5, (Jan 2009) E-ISSN 1472-6750.
- Lincopan, N. & Carmona-Ribeiro, A. M. (2009). Protein assembly onto cationic supported bilayers. *J. Nanosci. Nanotechnol.*, 9, 6, (Jun 2009) 3578-86, ISSN 1533-4880.
- Lincopan, N. ; Espíndola, N. M. ; Vaz, A. J. ; da Costa, M. H. B. ; Faquim-Mauro, E. & Carmona-Ribeiro, A. M. (2009). Novel immunoadjuvants based on cationic lipid : preparation, characterization and activity *in vivo*. *Vaccine*, 27, 42, (Sep 2009) 5760-71, ISSN 0264-410X.
- Lopes, A. ; Edwards, K. & Feitosa, E. (2008). Extruded vesicles of dioctadecyldimethylammonium bromide and chloride investigated by light scattering and cryogenic transmission electron microscopy. *J. Colloid Interface Sci.*, 322, 2, (Jun 2008) 582-8, ISSN 0021-9797.

- Mamizuka, E. M. & Carmona-Ribeiro, A. M. (2007). Cationic Liposomes as Antimicrobial Agents, In: *Communicating Current Research and Educational Topics and Trends in Applied Microbiology*. Antonio Méndez Vilas, (Ed.), Vol. 2, 636-47. Formatex, ISBN: 978-84-611-94, Badajoz.
- Manne, S. & Gaub, H. (1995) Molecular Organization of Surfactants at Solid-Liquid Interfaces. *Science*, 270, 5241, (Dec 1995) 1480-2, ISSN 0036-8075.
- Martins, L. M. S. ; Mamizuka, E. M. & Carmona-Ribeiro, A. M. (1997). Cationic Vesicles as Bactericides. *Langmuir*, 13, 21, (Oct 1997) 5583-87, ISSN 1053-0509.
- Messerschmidt, S. K. E., Musyanovych, A., Altvater, M., Scheurich, P., Pfizenmaier, K., Landfester, K., Kontermann, R. E. (2009). Targeted lipid-coated nanoparticles: Delivery of tumor necrosis factor-functionalized particles to tumor cells. *J. Control. Release*, 137, 1, (Jul 2009) 69-77, ISSN 0168-3659.
- Mornet, S. ; Lambert, O. ; Duguet, E. & Brisson, A. (2005). The Formation of Supported Lipid Bilayers on Silica Nanoparticles Revealed by Cryoelectron Microscopy. *Nano Letters*, 5, 2, (Feb 2005) 281-285.
- Mortara, R. A. ; Quina, F. H. & Chaimovich, H. (1978). Formation of closed vesicles from a simple phosphate diester. Preparation and some properties of vesicles of dihexadecyl phosphate. *Biochem. Biophys. Res. Commun.*, 81, 4, (Apr 1978) 1080-6, ISSN 0006-291X.
- Mou, J. ; Czajkowsky, D. M. ; Shao, Z. (1996). Gramicidin A aggregation in supported gel state phosphatidylcholine bilayers. *Biochemistry*, 35, 10, (Mar 1996) 3222-6, ISSN 0006-2960.
- Moura S. P. & Carmona-Ribeiro A. M. (2003). Cationic Bilayer Fragments on Silica at Low Ionic Strength: Competitive Adsorption and Colloid Stability. *Langmuir*, 19, 17, (Jul 2003) 6664-67, ISSN 1053-0509.
- Moura, S. P. & Carmona-Ribeiro, A. M. (2005). Biomimetic Particles: Optimization of Phospholipid Bilayer Coverage on Silica and Colloid Stabilization. *Langmuir*, 21, 22, (Jul 2005) 10160-4. ISSN 1053-0509.
- Moura S. P., & Carmona-Ribeiro A. M. (2007). Adsorption behavior of DODAB/DPPC vesicles on silica. *J Colloid Interface Sci.*, 313, 2, (Sep 2007) 519-26, ISSN 0021-9797.
- Moura, S. P. & Carmona-Ribeiro, A. M. (2006). Biomimetic particles for isolation and reconstitution of receptor function. *Cell Biochem Biophys*. 44, 3, (Mar 2006) 446-52, ISSN1085-9195.
- Nash, T. ; Allison, A. C. & Harington, J. S. (1966). Physico-chemical properties of silica in relation to its toxicity. *Nature*, 210, 5033, (Apr 1966) 259-61, ISSN 0028-0836.
- Nath, A.; Atkins, W. M. & Sligar, S. G. (2007) Applications of Phospholipid Bilayer Nanodiscs in the Study of Membranes and Membrane Proteins. *Biochemistry.*, 46, 8, (Feb 2007) 2059-69, ISSN 0006-2960.
- Nollert, P. ; Kiefer, H. & Jaehrig, F. (1995). Lipid vesicle adsorption versus formation of planar bilayers on solid surfaces. *Biophys. J.*, 69, 4, (Oct 1995) 1447-55, ISSN (electronic) 1542-0086.
- Nordlund, G. ; Lonneborg, R. & Brzezinski, P. (2009). Formation of Supported Lipid Bilayers on Silica Particles Studied Using Flow Cytometry. *Langmuir*, 25, 8, (Apr 2009) 4601-6, ISSN 1053-0509.

- Obringer, A. N. ; Rote, N. S. & Walter, A. (1995). Antiphospholipid antibody binding to bilayer-coated glass microspheres. *J. Immunol. Methods.*, 185, 1, (Sep 1995) 81-93, ISSN 0022-1759.
- Oleson, T. A. & Sahai, N. (2008). Oxide-Dependent Adsorption of a Model Membrane Phospholipid, Dipalmitoylphosphatidylcholine: Bulk Adsorption Isotherms. *Langmuir*, 24, 9, (May 2008) 4865-73, ISSN 1053-0509.
- Osaka, T., Nakanishi, T., Shanmugam, S., Takahama, S. & Zhang, H. (2009). Effect of surface charge of magnetite nanoparticles on their internalization into breast cancer and umbilical vein endothelial cells. *Colloids & Surf. B: Biointerfaces*, 71, 2, (Jul 2009) 325-30, ISSN 0927-7765.
- Pacheco, L. F. & Carmona-Ribeiro, A. M. (2003). Effects of synthetic lipids on solubilization and colloid stability of hydrophobic drugs. *J. Colloid Interface Sci.*, 258, 1, (Feb 2003) 146-54, ISSN 0021-9797.
- Pacheco, L. F.; Vieira, D. B.; Correia, F. M. & Carmona-Ribeiro, A. M. (2004). Interactions between cationic bilayers and *Candida albicans* cells, In: *Surface and Colloid Science*, Galembeck, F., (Ed.), 175-77., Springer, ISBN 978-3-540-21247-8, Heidelberg.
- Parida, S. K.; Dash, S. ; Patel, S. & Mishra, B. K. (2006). Adsorption of organic molecules on silica surface. *Adv. Colloid and Interface Sci.*, 121, 1-3, (2006)77-110. ISSN:0001-8686.
- Pereira, E. M. A. ; Vieira, D. B. & Carmona-Ribeiro, A.M. (2004). Cationic bilayers on polymeric particles: effect of low NaCl concentration on surface coverage. *J. Phys. Chem. B*, 108 (31), (Jun 2004) 11490-5, ISSN 1089-5647.
- Pereira, E. M. A. ; Petri, D. F. S. & Carmona-Ribeiro, A. M. (2006). Adsorption of Cationic Lipid Bilayer onto Flat Silicon Wafers: Effect of Ion Nature and Concentration. *J. Phys. Chem. B.*, 110, 20, (May 2006) 10070-74, ISSN 1089-5647.
- Petri, D. F. S. & Carmona-Ribeiro, A. M. (2007). Biomimetic particles, In: *Polymeric Nanostructures and Their Applications*. Nalwa, H. S. (Ed.), Vol. 1, 485-530, American Scientific Publishers, ISBN 1-58883-068-3, Valencia CA.
- Pichot, C. (2004) Surface-functionalized latexes for biotechnological applications. *Curr. Op. Coll. Interface Sci.* 9, 3-4, (Nov 2004) 213-21, 1359-0294.
- Piyasena, M. E. ; Zeineldin, R. ; Fenton, K. ; Buranda, T. & Lopez, G. P. (2008). Biosensors based on release of compounds upon disruption of lipid bilayers supported on porous microspheres. *Biointerphases*, 3, 2, (Jun 2008) ISSN 1559-4106.
- Rapuano, R. & Carmona-Ribeiro, A. M. (1997). Physical adsorption of bilayer membranes on silica. *J. Colloid Interface Sci.*, 193, 1, (Sep 1997) 104-11, ISSN 0021-9797.
- Rapuano, R. & Carmona-Ribeiro, A. M. (2000). Supported bilayers on silica. *J. Colloid Interface Sci.*, 226, 2, (Jun 2000) 299-307, ISSN 0021-9797.
- Rosa, H. ; Petri, D. F. S. & Carmona-Ribeiro, A. M. (2008). Interactions between bacteriophage DNA and cationic biomimetic particles. *J. Phys. Chem. B.*, 112, 51, (Dec 2008) 16422-30, ISSN 1089-5647.
- Salay, L. C. & Carmona-Ribeiro, A. M. (1999). Wetting of SiO₂ surfaces by phospholipid dispersions. *J. Adhes. Sci. Technol.*, 13, 10, (1999) 1165-79, ISSN 0169-4243.
- Segota, S. & Tezak, D. (2006). Spontaneous formation of vesicles. *Adv. Colloid Interface Sci*, 121, 1-3, (Sep 2006) 51-75. ISSN 0001-8686.

- Senarath-Yapa, M. D. ; Phimphivong, S. ; Coym, J. W. ; Wirth, M. J. ; Aspinwall, C. A. & Saavedra, S. S. (2007). Preparation and Characterization of Poly(lipid)-Coated, Fluorophore-Doped Silica Nanoparticles for Biolabeling and Cellular Imaging. *Langmuir*, 23, 25, (Dec 2007) 12624-33, ISSN 1053-0509.
- Shao, Z. & Yang, J. (1995). Progress in high resolution atomic force microscopy in biology. *Q. Rev. Biophys.*, 28, 2, (May 1995) 195-251, ISSN 0033-5835.
- Sharma, P. ; Ganta, S. ; Denny, W. A. & Garg, S. (2009). Formulation and pharmacokinetics of lipid nanoparticles of a chemically sensitive nitrogen mustard derivative: Chlorambucil. *Int. J. Pharm.*, 367, 1-2, (Feb 2009) 187-94, ISSN 0378-5173.
- Sicchierolli, S. M. & Carmona-Ribeiro, A. M. (1996). Biomolecular recognition at phospholipid-covered polystyrene microspheres. *J. Phys. Chem.*, 100, 41, (Oct 1996) 16771-5, ISSN 0022-3654.
- Sicchierolli, S. M. & Carmona-Ribeiro, A. M. (1995). Incorporation of the cholera toxin receptor in phospholipid-covered polystyrene microspheres. *Colloids and Surfaces B: Biointerfaces*, 5, 1-2, (Sep 1995) 57-64, ISSN 0927-7765.
- Singh, R. ; Tian, B. & Kostarelos, K. (2008). Artificial envelopment of nonenveloped viruses: enhancing adenovirus tumor targeting in vivo. *FASEB J.*, 22, 9, (Sep 2008) 3389-402, ISSN 0892-6638.
- Sobral, C. N. C. ; Soto, M. A. & Carmona-Ribeiro, A. M. (2008). Characterization of DODAB/DPPC vesicles. *Chem Phys Lipids.*, 152, 1, (2008 Mar) 38-45, ISSN 0009-3084.
- Soo, P. L. ; Dunne, M. ; Liu, J. & Allen, C. (2009). Nano-sized advanced delivery systems as parenteral formulation strategies for hydrophobic anti-cancer drugs. In: *Biotechnology: Pharmaceutical Aspects*, Villiers, M. M. De ; Aramwit, P. ; Kwon, G. S. (Eds.), 349-383, Vol. 10 (Nanotechnology in Drug Delivery), Springer, ISBN 978-0-387-77667-5, Heidelberg.
- Suedholter, E. J. R.; Engberts, J. B. F. N.; Hoekstra, D. J. (1980). Vesicle formation by two novel synthetic amphiphiles carrying micropolarity reporter head groups. *J. Am. Chem. Soc.*, 102, 7, (Mar 1980) 2467-69, ISSN0002-7863.
- Talmon, Y.; Evans, D. F.; Ninham, B. W. (1983). Spontaneous Vesicles Formed from Hydroxide Surfactants: Evidence from Electron Microscopy. *Science.*, 221, 4615, (Sep 1983) 1047-48, ISSN 0036-8075.
- Tamm, L. K. & McConnell, H. M. (1985). Supported phospholipid bilayers. *Biophys J.*, 47, 1, (Jan 1985) 105-13, ISSN(electronic) 1542-0086.
- Tápias, G. N. ; Sicchierolli, S. M. ; Mamizuka, E. M. & Carmona-Ribeiro, A. M. (1994). Interactions between Cationic Vesicles and *Escherichia coli*. *Langmuir*, 10, 10, (Oct 1994) 3461-65, ISSN 1053-0509.
- Thevenot J, Troutier AL, Putaux JL, Delair T, Ladavière C. (2008). Effect of the Polymer Nature on the Structural Organization of Lipid/Polymer Particle Assemblies. *J Phys Chem B.*, 112, 44, (Nov 2008) 13812-22, ISSN 1089-5647.
- Trauble, H. & Eibl, H. (1974). Electrostatic effects on lipid phase transitions: membrane structure and ionic environment. *Proc Natl Acad Sci U S A.*, 71, 1, (Jan 1974) 214-9, ISSN 0027-8424.
- Troutier, A.-L. ; Delair, T. ; Pichot, C. & Ladavière, C. (2005). Physicochemical and Interfacial Investigation of Lipid/Polymer Particle Assemblies. *Langmuir* 21, 4, (Feb 2005) 1305-13, ISSN 1053-0509.

- Troutier, A.-L. & Ladavière, C. (2007). An overview of lipid membrane supported by colloidal particles. *Adv. Colloid Interface Sci.*, 133, 1, (May 2007) 1-21, ISSN:0001-8686.
- Tsuruta, L. R. ; Lessa, M. M. & Carmona-Ribeiro, A. M. (1995). Interactions between dioctadecyldimethylammonium chloride or bromide bilayers in water. *Langmuir*, 11, 8, (Aug 1995) 2938-43, ISSN 0743-7463.
- Tsuruta, L. R. ; Lessa, M. M. & Carmona-Ribeiro, A. M. (1995). Effect of particle size on colloid stability of bilayer-covered polystyrene microspheres. *J. Colloid Interface Sci.*, 175, 2, (Nov 1995) 470-5, ISSN: 0021-9797.
- Tsuruta, L. R. & Carmona-Ribeiro, A. M. (1996). Counterion Effects on Colloid Stability of Cationic Vesicles and Bilayer-Covered Polystyrene Microspheres. *J. Phys. Chem.*, 25, 100, 17, (Apr 1996) 7130-4, ISSN 0022-3654.
- Tsuruta, L. R. ; Quintilio, W. ; Costa, M. H. B. & Carmona-Ribeiro, A. M. (1997). Interactions between cationic liposomes and an antigenic protein: the physical chemistry of the immunoadjuvant action. *J Lipid Res.*, 38, 10, (Oct 1997) 2003-11, ISSN 0022-2275.
- Urban, M. W. & Lestage, D. (2006). Colloidal particle morphology and film formation; the role of bio-active components on stimuli-responsive behavior. *Polymer Rev.*, 46, 4, (Dec 2006) 445-66, ISSN 1558-3724.
- Velinova, M. J. ; Staffhorst, R. W. ; Mulder, W. J. ; Dries, A. S. ; Jansen, B. A. ; de Kruijff, B. & de Kroon, A. I. (2004). Preparation and stability of lipid-coated nanocapsules of cisplatin: anionic phospholipid specificity. *Biochim. Biophys. Acta.*, 1663, 1-2, (May 2004) 135-42, ISSN 0006-3002.
- Vidard, L. ; Kovacovics-Bankowski, M. ; Kraeft, S. K. ; Chen, L. B. ; Benacerraf, B. & Rock, K. L. (1996). Analysis of MHC class II presentation of particulate antigens of B lymphocytes. *J. Immunol.*, 156, 8, (Apr 1996) 2809-18, ISSN 1526-34.
- Vieira, D. B. & Carmona-Ribeiro, A. M. (2001). Synthetic Bilayer Fragments for Solubilization of Amphotericin B. *J. Colloid Interface Sci.*, 244, 2, (Dec 2001) 427-31, ISSN 0021-9797.
- Vieira, D. B. ; Pacheco, L. F. & Carmona-Ribeiro, A.M. (2006). Assembly of a model hydrophobic drug into cationic bilayer fragments. *J. Colloid Interface Sci.*, 293, 1, (Jan 2006) 240-7, ISSN 0021-9797
- Vieira, D. B. & Carmona-Ribeiro, A. M. (2006). Cationic lipids and surfactants as antifungal agents: mode of action. *J Antimicrob Chemother.*, 58, 4, (Aug 2006) 760-7, ISSN 0305-7453.
- Vieira, D. B. & Carmona-Ribeiro, A.M. (2008) Cationic nanoparticles for delivery of amphotericin B: preparation, characterization and activity *in vitro*. *Journal of Nanobiotechnology*, 6, article 6, (May 2008) E-ISSN:1477-3155.
- Xu, J. ; Stevens, M. J. ; Oleson, T. A. ; Last, J. A. & Sahai, N. (2009). Role of Oxide Surface Chemistry and Phospholipid Phase on Adsorption and Self-Assembly: Isotherms and Atomic Force Microscopy. *J. Phys. Chem. C*, 113, 6, (Feb 2009) 2187-96, ISSN 1932-7447.
- Yang, J. ; Tamm, L. K. ; Tillack, T. W. & Shao, Z. (1993). New approach for atomic force microscopy of membrane proteins. The imaging of cholera toxin. *J. Mol. Biol.*, 229, 2, (Jan 1993) 286-90, ISSN 0022-2836
- Zuzzi, S. ; Cametti, C. & Onori, G. (2008). Polyion-Induced Aggregation of Lipidic-Coated Solid Polystyrene Spheres: The Many Facets of Complex Formation in Low-Density Colloidal Suspensions. *Langmuir*, 24, 12, (Jun 2008) 6044-49, ISSN 0743-7463.